

De-Shuang Huang
Vitoantonio Bevilacqua
Abir Hussain (Eds.)

LNCS 12463

Intelligent Computing Theories and Application

16th International Conference, ICIC 2020
Bari, Italy, October 2–5, 2020
Proceedings, Part I

1
Part I

 Springer

Founding Editors

Gerhard Goos

Karlsruhe Institute of Technology, Karlsruhe, Germany

Juris Hartmanis

Cornell University, Ithaca, NY, USA

Editorial Board Members

Elisa Bertino

Purdue University, West Lafayette, IN, USA

Wen Gao

Peking University, Beijing, China

Bernhard Steffen 

TU Dortmund University, Dortmund, Germany

Gerhard Woeginger 

RWTH Aachen, Aachen, Germany

Moti Yung

Columbia University, New York, NY, USA

More information about this series at <http://www.springer.com/series/7409>

De-Shuang Huang · Vitoantonio Bevilacqua ·
Abir Hussain (Eds.)

Intelligent Computing Theories and Application

16th International Conference, ICIC 2020
Bari, Italy, October 2–5, 2020
Proceedings, Part I

Editors

De-Shuang Huang
Institute of Machine Learning
and Systems Biology
Tongji University
Shanghai, China

Vitoantonio Bevilacqua
Electrical and Electronics Department
Polytechnic University of Bari
Bari, Italy

Abir Hussain
School of Computer Science
and Mathematics
Liverpool John Moores University
Liverpool, UK

ISSN 0302-9743 ISSN 1611-3349 (electronic)
Lecture Notes in Computer Science
ISBN 978-3-030-60798-2 ISBN 978-3-030-60799-9 (eBook)
<https://doi.org/10.1007/978-3-030-60799-9>

LNCS Sublibrary: SL3 – Information Systems and Applications, incl. Internet/Web, and HCI

© Springer Nature Switzerland AG 2020

This work is subject to copyright. All rights are reserved by the Publisher, whether the whole or part of the material is concerned, specifically the rights of translation, reprinting, reuse of illustrations, recitation, broadcasting, reproduction on microfilms or in any other physical way, and transmission or information storage and retrieval, electronic adaptation, computer software, or by similar or dissimilar methodology now known or hereafter developed.

The use of general descriptive names, registered names, trademarks, service marks, etc. in this publication does not imply, even in the absence of a specific statement, that such names are exempt from the relevant protective laws and regulations and therefore free for general use.

The publisher, the authors and the editors are safe to assume that the advice and information in this book are believed to be true and accurate at the date of publication. Neither the publisher nor the authors or the editors give a warranty, expressed or implied, with respect to the material contained herein or for any errors or omissions that may have been made. The publisher remains neutral with regard to jurisdictional claims in published maps and institutional affiliations.

This Springer imprint is published by the registered company Springer Nature Switzerland AG
The registered company address is: Gewerbestrasse 11, 6330 Cham, Switzerland

Preface

The International Conference on Intelligent Computing (ICIC) was started to provide an annual forum dedicated to the emerging and challenging topics in artificial intelligence, machine learning, pattern recognition, bioinformatics, and computational biology. It aims to bring together researchers and practitioners from both academia and industry to share ideas, problems, and solutions related to the multifaceted aspects of intelligent computing.

ICIC 2020, held in Bari, Italy, during October 2–5, 2020, constituted the 16th edition of this conference series. It built upon the success of ICIC 2019 (Nanchang, China), ICIC 2018 (Wuhan, China), ICIC 2017 (Liverpool, UK), ICIC 2016 (Lanzhou, China), ICIC 2015 (Fuzhou, China), ICIC 2014 (Taiyuan, China), ICIC 2013 (Nanning, China), ICIC 2012 (Huangshan, China), ICIC 2011 (Zhengzhou, China), ICIC 2010 (Changsha, China), ICIC 2009 (Ulsan, South Korea), ICIC 2008 (Shanghai, China), ICIC 2007 (Qingdao, China), ICIC 2006 (Kunming, China), and ICIC 2005 (Hefei, China).

This year, the conference concentrated mainly on the theories and methodologies as well as the emerging applications of intelligent computing. Its aim was to unify the picture of contemporary intelligent computing techniques as an integral concept that highlights the trends in advanced computational intelligence and bridges theoretical research with applications. Therefore, the theme for this conference was “Advanced Intelligent Computing Technology and Applications.” Papers that focused on this theme were solicited, addressing theories, methodologies, and applications in science and technology.

ICIC 2020 received 457 submissions from 21 countries and regions. All papers went through a rigorous peer-review procedure and each paper received at least three review reports. Based on the review reports, the Program Committee finally selected 162 high-quality papers for presentation at ICIC 2020, included in three volumes of proceedings published by Springer: two volumes of *Lecture Notes in Computer Science* (LNCS), and one volume of *Lecture Notes in Artificial Intelligence* (LNAI).

This volume of LNCS includes 54 papers.

The organizers of ICIC 2020, including Tongji University, China, and Polytechnic University of Bari, Italy, made an enormous effort to ensure the success of the conference. We hereby would like to thank the members of the Program Committee and the referees for their collective effort in reviewing and soliciting the papers. We would like to thank Alfred Hofmann, executive editor from Springer, for his frank and helpful advice and guidance throughout as well as his continuous support in publishing the proceedings. In particular, we would like to thank all the authors for contributing their papers. Without the high-quality submissions from the authors, the success of the

conference would not have been possible. Finally, we are especially grateful to the International Neural Network Society and the National Science Foundation of China for their sponsorship.

August 2020

De-Shuang Huang
Vitoantonio Bevilacqua
Abir Hussain

Organization

General Co-chairs

De-Shuang Huang, China
Vitoantonio Bevilacqua, Italy

Program Committee Co-chairs

Eugenio Di Sciascio, Italy
Kanghyun Jo, South Korea

Organizing Committee Co-chairs

Ling Wang, China
Phalguni Gupta, India
Vincenzo Piuri, Italy
Antonio Frisoli, Italy
Eugenio Guglielmelli, Italy
Silvestro Micera, Italy
Loreto Gesualdo, Italy

Organizing Committee Members

Andrea Guerriero, Italy
Nicholas Caporusso, USA
Francesco Fontanella, Italy
Vincenzo Randazzo, Italy
Giacomo Donato Cascarano, Italy
Irio De Feudis, Italy
Cristian Camardella, Italy
Nicola Altini, Italy

Award Committee Co-chairs

Kyungsook Han, South Korea
Jair Cervantes Canales, Mexico
Leonarda Carnimeo, Italy

Tutorial Co-chairs

M. Michael Gromiha, India
Giovanni Dimauro, Italy

Publication Co-chairs

Valeriya Gribova, Russia
Antonino Staiano, Italy

Special Session Co-chairs

Abir Hussain, UK
Antonio Brunetti, Italy

Special Issue Co-chairs

Mario Cesarelli, Italy
Eros Pasero, Italy

International Liaison Co-chairs

Prashan Premaratne, Australia
Marco Gori, Italy

Workshop Co-chairs

Laurent Heutte, France
Domenico Buongiorno, Italy

Publicity Co-chairs

Giansalvo Cirrincione, France
Chun-Hou Zheng, China
Salvatore Vitabile, Italy

Exhibition Contact Co-Chairs

Michal Choras, Poland
Stefano Cagnoni, Italy

Program Committee Members

| | | |
|------------------------|-------------------------|-----------------------|
| Daqi Zhu | Guoquan Liu | Laurent Heutte |
| Xinhong Hei | Wei Chen | Leonarda Carnimeo |
| Yuan-Nong Ye | Valeriya Gribova | Bo Li |
| Abir Hussain | Michael Gromiha | Junqing Li |
| Khalid Aamir | Maria Siluvay | Juan Liu |
| Kang-Hyun Jo | Guoliang Li | Yunxia Liu |
| Andrea Guerriero | Huiyu Zhou | Zhendong Liu |
| Angelo Ciaramella | Tianyong Hao | Jungang Lou |
| Antonino Staiano | Mohd Helmy Abd Wahab | Fei Luo |
| Antonio Brunetti | Honghuang Lin | Jiawei Luo |
| Wenzheng Bao | Jian Huang | Haiying Ma |
| Binhua Tang | Hao Lin | Marzio Pennisi |
| Bin Qian | Hongmin Cai | Nicholas Caporusso |
| Bingqiang Liu | Xinguo Lu | Nicola Altini |
| Bo Liu | Ho-Jin Choi | Giansalvo Cirrincione |
| Bin Liu | Hongjie Wu | Gaoxiang Ouyang |
| Chin-Chih Chang | Irio De Feudis | Pu-Feng Du |
| Wen-Sheng Chen | Dong Wang | Shaoliang Peng |
| Michal Choras | Insoo Koo | Phalguni Gupta |
| Xiyuan Chen | Daowen Qiu | Ping Guo |
| Chunmei Liu | Jiansheng Wu | Prashan Premaratne |
| Cristian Camardella | Jianbo Fan | Qinghua Jiang |
| Zhihua Cui | Jair Cervantes | Qingfeng Chen |
| Defu Zhang | Junfeng Xia | Roman Neruda |
| Dah-Jing Jwo | Junhui Gao | Rui Wang |
| Dong-Joong Kang | Juan Carlos | Stefano Squartini |
| Domenico Buongiorno | Juan Carlos | Salvatore Vitabile |
| Domenico Chiaradia | Figueroa-García | Wei-Chiang Hong |
| Ben Niu | Gangyi Jiang | Jin-Xing Liu |
| Shaoyi Du | Jiangning Song | Shen Yin |
| Eros Pasero | Jing-Yan Wang | Shiliang Sun |
| Fengfeng Zhou | Yuhua Qian | Saiful Islam |
| Haodi Feng | Joaquín Torres-Sospedra | Shulin Wang |
| Fei Guo | Ju Liu | Xiaodi Li |
| Francesco Fontanella | Jinwen Ma | Zhihuan Song |
| Chuleerat Jaruskulchai | Ji Xiang Du | Shunren Xia |
| Fabio Stroppa | Junzhong Gu | Sungshin Kim |
| Gai-Ge Wang | Ka-Chun Wong | Stefano Cagnoni |
| Giacomo Donato | Kyungsook Han | Stefano Mazzoleni |
| Casarano | K. R. Seeja | Surya Prakash |
| Giovanni Dimauro | Yoshinori Kuno | Tar Veli Mumcu |
| L. J. Gong | Weiwei Kong | Xu-Qing Tang |

Vasily Aristarkhov
 Vincenzo Randazzo
 Vito Monaco
 Vitoantonio Bevilacqua

Waqas Bangyal
 Bing Wang
 Wenbin Liu
 Weidong Chen

Weijia Jia
 Wei Jiang
 Shanwen Zhang
 Takashi Kuremoto

Reviewers

Wan Hussain Wan Ishak
 Nureize Arbaiy
 Shingo Mabu
 Lianming Zhang
 Xiao Yu
 Shaohua Li
 Yuntao Wei
 Jinglong Wu
 Wei-Chiang Hong
 Sungshin Kim
 Tianhua Guan
 Shutao Mei
 Yuelin Sun
 Hai-Cheng Yi
 Zhan-Heng Chen
 Suwen Zhao
 Medha Pandey
 Mike Dyll-Smith
 Xin Hong
 Ziyi Chen
 Xiwei Tang
 Khanh Le
 Shulin Wang
 Di Zhang
 Sijia Zhang
 Na Cheng
 Menglu Li
 Zhenhao Guo
 Limin Jiang
 Kun Zhan
 Cheng-Hsiung Chiang
 Yuqi Wang
 Anna Esposito
 Salvatore Vitabile
 Bahattin Karakaya
 Tejaswini Mallavarapu
 Sheng Yang
 Heutte Laurent

Seeja
 Pu-Feng Du
 Wei Chen
 Jonggeun Kim
 Eun Kyeong Kim
 Hansoo Lee
 Yiqiao Cai
 Wuritu Yang
 Weitao Sun
 Shou-Tao Xu
 Min-You Chen
 Yajuan Zhang
 Guihua Tao
 Jinzhong Zhang
 Wenjie Yi
 Miguel Gomez
 Lingyun Huang
 Chao Chen
 Jiangping He
 Jin Ma
 Xiao Yang
 Sotanto Sotanto
 Liang Xu
 Chaomin Iuo
 Rohitash Chandra
 Hui Ma
 Lei Deng
 Di Liu
 María I. Giménez
 Ansgar Poetsch
 Dimitry Y. Sorokin
 Jill F. Banfield
 Can Alkan
 Ji-Xiang Du
 Xiao-Feng Wang
 Zhong-Qiu Zhao
 Bo Li
 Zhong rui Zhang

Yanyun Qu
 Shunlin Wang
 Jin-Xing Liu
 Shravan Sukumar
 Long Gao
 Yifei Wu
 Qi Yan
 Tianhua Jiang
 Fangping Wan
 Lixiang Hong
 Sai Zhang
 Tingzhong Tian
 Qi Zhao
 Leyi Wei
 Lianrong Pu
 Chong Shen
 Junwei Wang
 Zhe Yan
 Rui Song
 Xin Shao
 Xinhua Tang
 Claudia Guldemann
 Saad Abdullah Khan
 Bangyal
 Giansalvo Cirrincione
 Bing Wang
 Xiao Xiancui
 X. Zheng
 Vincenzo Randazzo
 Huijuan Zhu
 DongYuan Li
 Jingbo Xia
 Boya Ji
 Manilo Monaco
 Xiao-Hua Yu
 Pierre Leblond
 Zu-Guo Yu
 Jun Yuan

| | | |
|---------------------|------------------------|------------------------|
| Shenggen Zheng | Yuxiang Tian | Tuozhong Yao |
| Xiong Chunhe | Zhenjia Wang | Xuzhao Chai |
| Punam Kumari | Shuqin Zhang | Zhenhu Liang |
| Li Shang | Angelo Riccio | Yu Lu |
| Sandy Sgorlon | Francesco Camastra | Hua Tang |
| Bo Wei Zhao | Xiong Yuanpeng | Liang Cheng |
| X. J. Chen | Jing Xu | Jiang Hui |
| Fang Yu | Zou Zeyu | Puneet Rawat |
| Takashi Kurmeoto | Y. H. Tsai | Kulandaisamy Akila |
| Huakuang Li | Chien-Yuan Lai | Niu Xiaohui |
| Pallavi Pandey | Guo-Feng Fan | Zhang Guoliang |
| Yan Zhou | Shaoming Pan | Egidio Falotico |
| Mascot Wang | De-Xuan Zou | Peng Chen |
| Chenhui Qiu | Zheng Chen | Cheng Wang |
| Haizhou Wu | Renzhi Cao | He Chen |
| Lulu Zuo | Ronggen Yang | Giacomo Donato |
| Jiangning Song | Azis Azis | Cascarano |
| Rafal Kozik | Shelli Shelli | Vitoantonio Bevilacqua |
| Wenyan Gu | Zhongming Zhao | Shaohua Wan |
| Shiyin Tan | Yongna Yuan | Jaya Sudha J. S. |
| Yaping Fang | Kamal Al Nasr | Sameena Naaz |
| Xiuxiu Ren | Chuanxing Liu | Cheng Chen |
| Antonino Staiano | Panpan Song | Jie Li |
| Aniello Castiglione | Joao Sousa | Ruxin Zhao |
| Qiong Wu | Min Li | Jiazhou Chen |
| Atif Mehmood | Wenying He | Abeer Alsadhan |
| Wang Guangzhong | Kaikai Xu | Guoliang Xu |
| Zheng Tian | Ming Chen | Fangli Yang |
| Junyi Chen | Laura Dominguez Jalili | Congxu Zhu |
| Meineng Wang | Vivek Kanhangad | Deng Li |
| Xiaorui Su | Zhang Ziqi | Piyush Joshi |
| Jianping Yu | Davide Nardone | Syed Sadaf Ali |
| Jair Cervantes | Liangxu Liu | Qin Wei |
| Lizhi Liu | Huijian Han | Kuan Li |
| Junwei Luo | Qingjun Zhu | Teng Wan |
| Yuanyuan Wang | Hongluan Zhao | Hao Liu |
| Jiayin Zhou | Chyuan-Huei Thomas | Yexian Zhang |
| Mingyi Wang | Yang | Xu Qiao |
| Xiaolei Zhu | R. S. Lin | Ce Li |
| Jiafan Zhu | N. Nezu | Lingchong Zhong |
| Yongle Li | Chin-Chih Chang | Wenyan Wang |
| Hao Lin | Hung-Chi Su | Xiaoyu Ji |
| Xiaoyin Xu | Antonio Brunetti | Weifeng Guo |
| Shiwei Sun | Xie conghua | Yuchen Jiang |
| Hongxuan Hua | Caitong Yue | Yuanyuan Huang |
| Shiping Zhang | Li Yan | Zaixing Sun |

| | | |
|---------------------|--------------------------|---------------------------|
| Honglin Zhang | Balachandran Manavalan | José Sergio Ruiz Castilla |
| Yu Jie He | Bingqiang Liu | Juan de Jesus Amador |
| Benjamin Soibam | Lianrong Pu | Nanxun Wang |
| Sungroh Yoon | Di Wang | Rencai Zhou |
| Mohamed Chaabane | Fangping Wan | Moli Huang |
| Rong Hu | Guosheng Han | Yong Zhang |
| Youjie Yao | Renmeng Liu | Daniele Loiacono |
| NaiKang Yu | Yinan Guo | Grzegorz Dudek |
| Carlo Bianca | Lujie Fang | Joaquín Torres-Sospedra |
| Giulia Russo | Ying Zhang | Xingjian Chen |
| Dian Liu | Yinghao Cao | Saifur Rahaman |
| Cheng Liang | Xhize Wu | Olutomilayo Petinrin |
| Iyyakutti Iyappan | Le Zou | Xiaoming Liu |
| Ganapathi | G. Brian Golding | Xin Xu |
| Mingon Kang | Viktoriya Coneva | Zi-Qi Zhu |
| Zhang Chuanchao | Alexandre Rossi Paschoal | Punam Kumari |
| Hao Dai | Ambuj Srivastava | Pallavy Pandey |
| Geethan | Prabakaran R. | Najme Zehra |
| Brendan Halloran | Xingquan Zuo | Zhenqing Ye |
| Yue Li | Jiabin Huang | Hao Zhang |
| Qianqian Shi | Jingwen Yang | Zijing Wang |
| Zhiqiang Tian | Liu Qianying | Lida Zhu |
| Yang Yang | Markus J. Ankenbrand | Lvzhou Li |
| Jalilah Arijah Mohd | Jianghong Meng | Junfeng Xia |
| Kamarudin | Tongchi Zhou | Jianguo Liu |
| Jun Wang | Zhi-Ping Liu | Jia-Xiang Wang |
| Ke Yan | Xinyan Liang | Gongxin Peng |
| Hang Wei | Xiaopeng Jin | Junbo Liang |
| David A. Hendrix | Jun Zhang | Linjing Liu |
| Ka-Chun Wong | Yumeng Liu | Xian Geng |
| Yuyan Han | Junliang Shang | Sheng Ding |
| Hisato Fukuda | L. M. Xiao | Jun Li |
| Yaning Yang | Shang-han Li | Laksono Kurnianggoro |
| Lixiang Xu | Jianhua Zhang | Minxia Cheng |
| Yuanke Zhou | Han-Jing Jiang | Meiyi Li |
| Shihui Ying | Daniele Nardi | Qizhi Zhu |
| Wenqiang Fan | Kunikazu | Peng Chao Li |
| Zhao Li | Shenglin Mu | Ming Xiao |
| Zhe Zhang | Jing Liang | Guangdi Liu |
| Xiaoying Guo | Jialing Li | Jing Meng |
| Yiqi Jiang | Yu-Wen-Tian Sun | Kang Xu |
| Zhuoqun Xia | Zhe Sun | Cong Feng |
| Jing Sun | Wentao Fan | Arturo Yee |
| Na Geng | Wei Lan | Yi Xiong |
| Chen Li | Jiancheng Zhong | Fei Luo |
| Xin Ding | Josue Espejel Cabrera | Xionghui Zhou |

| | | |
|---------------------|------------------------|----------------------|
| Kazunori Onoguchi | Chunfeng Shi | Donghyeon Lee |
| Hotaka Takizawa | Shuo Jiang | Mohamed Hasan |
| Suhang Gu | Xiaoke Hao | ChangHwan Kim |
| Zhang Yu | Lei Wang | Vivek Thangavelu |
| Bin Qin | Minghua Zhao | Alvaro Costa-Garcia |
| Yang Gu | Cheng Shi | David Parent |
| Zhibin Jiang | Jiulong Zhang | Oskar Ljungqvist |
| Chuanyan Wu | Shui-Hua Wang | Long Cheng |
| Wahyono Wahyono | Xuefeng Cui | Huajuan Huang |
| Van-Dung Hoang | Sandesh Gupta | Vasily Aristarkhov |
| My-Ha Le | Nadia Siddiqui | Zhonghao Liu |
| Kaushik Deb | Syeda Shira Moin | Lichuan Pan |
| Danilo Caceres | Sajjad Ahmed | Yongquan Zhou |
| Alexander Filonenko | Ruidong Li | Zhongying Zhao |
| Van-Thanh Hoang | Mauro Castelli | Kunikazu Kobayashi |
| Ning Guo | Leonardo Bocchi | Masato Nagayoshi |
| Deng Chao | Leonardo Vanneschi | Atsushi Yamashita |
| Soniya Balram | Ivanoe De Falco | Wei Peng |
| Jian Liu | Antonio Della Cioppa | Haodi Feng |
| Angelo Ciaramella | Kamlesh Tiwari | Jin Zhao |
| Yijie Ding | Puneet Gupta | Shunheng Zhou |
| Ramakrishnan | Zuliang Wang | Xinguo Lu |
| Nagarajan Raju | Luca Tiseni | Xiangwen Wang |
| Kumar Yugandhar | Francesco Porcini | Zhe Liu |
| Anoosha Paruchuri | Ruizhi Fan | Pi-Jing Wei |
| Dhanusa | Grigorios Skaltsas | Bin Liu |
| Jino Blessy | Mario Selvaggio | Haozhen Situ |
| Agata Gie | Xiang Yu | Meng Zhou |
| Lei Che | Abdurrahman Eray Baran | Muhammad Ikram Ullah |
| Yujia Xi | Alessandra Rossi | Hui Tang |
| Ma Haiying | Jacky Liang | Sakthivel Ramasamy |
| Huanqiang Zeng | Robin Strudel | Akio Nakamura |
| Hong-Bo Zhang | Stefan Stevsic | Antony Lam |
| Yewang Chen | Ariyan M. Kabir | Weilin Deng |
| Farheen Sidiqqi | Lin Shao | Haiyan Qiao |
| Sama Ukyo | Parker Owan | Xu Zhou |
| Parul Agarwal | Rafael Papallas | Shuyuan Wang |
| Akash Tayal | Alina Kloss | Rabia Shakir |
| Ru Yang | Muhammad Suhail | Shixiong Zhang |
| Junning Gao | Saleem | Xuanfan Fei |
| Jianqing Zhu | Neel Doshi | Fatih Ad |
| Joel Ayala | Masaki Murooka | Aysel Ersoy Yilmaz |
| Haizhou Liu | Huitan Mao | Haotian Xu |
| Nobutaka Shimada | Christos K. Verginis | Zekang Bian |
| Yuan Xu | Joon Hyub Lee | Shuguang Ge |
| Ping Yang | Gennaro Notomista | Dhiya Al-Jumeily |

| | | |
|----------------------|-----------------------|---------------------|
| Thar Baker | Yudong Zhang | Alex Akinbi |
| Haoqian Huang | Zafaryab Haider | Fuyi Li |
| Siguo Wang | Mahreen Saleem | Fan Xu |
| Huan Liu | Quang Do | Guangsheng Wu |
| Jianqing Chen | Vladimir Shakhov | Yuchong Gong |
| Chunhui Wang | Daniele Leonardis | Weitai Yang |
| Xiaoshu Zhu | Simona Crea | Mohammed Aledhari |
| Wen Zhang | Byungkyu Park | Yanan Wang |
| Yongchun Zuo | Pau Rodr´ute | Bo Chen |
| Dariusz Pazderski | Alper GÜN | Binbin Pan |
| Elif Hocaoglu | Mehmet Fatih Demirel | Chunhou Zheng |
| Hyunsoo Kim | Elena Battini | Abir Hussain |
| Park Singu | Radzi Ambar | Chen Yan |
| Saeed Ahmed | Mohamad Farhan | Dhanjay Singh |
| Youngdoo Lee | Mohamad Mohsin | Bowen Song |
| Nathan D. Kent | Nur Azzah Abu Bakar | Guojing |
| Areesha Anjum | Noraziah ChePa | Weiping Liu |
| Sanjay Sharma | Sasalak Tongkaw | Yeguo Liao |
| Shaojin Geng | Kumar Jana | Laura Jalili |
| Andrea Mannini | Hafizul Fahri Hanafi | Quan Zou |
| Van-Dung Hoang | Liu Jinxing | Xing Chen |
| He Yongqiang | Alex Moopenn | Xiujuan Lei |
| Kyungsook Han | Liang Liang | Marek Pawlicki |
| Long Chen | Ling-Yun Dai | Haiying Ma |
| Jialin Lyu | Raffaele Montella | Hao Zhu |
| Zhenyang Li | Maratea Antonio | Wang Zhanjun |
| Tian Rui | Xiongtao Zhang | Mohamed Alloghani |
| Khan Alcan | Sobia Pervaiz Iqbal | Yu Hu |
| Alperen Acemoglu | Fang Yang | Haya Alaskar |
| Duygun Erol Barkana | Si Liu | Baohua Wang |
| Juan Manuel Jacinto | Natsa Kleanthous | Hanfu Wang |
| Villegas | Zhen Shen | Hongle Xie |
| Zhenishbek Zhakypov | Jing Jiang | Guangming Wang |
| Domenico Chiaradia | Shamrie Sainin | Yongmei Liu |
| Huiyu Zhou | Suraya Alias | Fuchun Liu |
| Yichuan Wang | Mohd Hanafi Ahmad | Farid Garcia-Lamont |
| Sang-Goo Jeong | Hijazi | Yang Li |
| Nicolò Navarin | Mohd Razali Tomari | Hengyue Shi |
| Eray A. Baran | Chunyan Fan | Gao Kun |
| Jiakai Ding | Jie Zhao | Wen Zheng Ma |
| Dehua Zhang | Yuchen Zhang Casimiro | Jin Sun |
| Giuseppe Pirlo | Dong-Jun Yu | Xing Ruiwen |
| Alberto Morea | Jianwei Yang | Zhong Lianxin |
| Giuseppe Mastronardi | Wenrui Zhao | Zhang Hongyuan |
| Insoo Koo | Di Wu | Han Xupeng |
| Dah-Jing Jwo | Chao Wang | Mon Hian Chew |

| | | |
|---------------------|---------------------|-------------------------|
| Jianxun Mi | Qinhu Zhang | Fabio Bellavia |
| Michele Scarpiniti | Jiang Liu | Giosue' Lo Bosco |
| Hugo Morais | Yuzhen Han | Giuseppe Salvi |
| Alamgir Hossain | Pengcheng Xiao | Giovanni Acampora |
| Felipe Saraiva | Harry Haoxiang Wang | Zhen Chen |
| Xuyang Xuyang | Fengqiang Li | Enrico De Santis |
| Yasushi Mae | Chenggang Lai | Xing Lining |
| Haoran Mo | Dong Li | Wu Guohua |
| Pengfei Cui | Shuai Liu | Dong Nanjiang |
| Yoshinori Kobayashi | Cuiling Huang | Jhony Heriberto Giraldo |
| Qing Yu Cui | Lian-Yong Qi | Zuluaga |
| Kongtao Chen | Qi Zhu | Waqas Haider Bangyal |
| Feng Feng | Wenqiang Gu | Cong Feng |
| Wenli Yan | Haitao Du | Autilia Vitiello |
| Zhibo Wang | Bingbo Cui | TingTing Dan |
| Ying Qiao | Qinghua Li | Haiyan Wang |
| Qiyue Lu | Xin Juan | Angelo Casolaro |
| Geethan Mendiz | Emanuele Principi | Dandan Lu |
| Dong Li | Xiaohan Sun | Bin Zhang |
| Liu Di | Inas Kadhim | Raul Montoliu |
| Feilin Zhang | Jing Feng | Sergio Trilles |
| Haibin Li | Xin Juan | Xu Yang |
| Heqi Wang | Hongguo Zhao | Fan Jiao |
| Wei Wang | Masoomah Mirrashid | Li Kaiwen |
| Tony Hao | Jialiang Li | Wenhua Li |
| Yingxia Pan | Yaping Hu | Ming Mengjun |
| Chenglong Wei | Xiangzhen Kong | Ma Wubin |
| My Ha Le | Mi-Xiao Hou | Cuco Cristanno |
| Yu Chen | Zhen Cui | Chao Wu |
| Eren Aydemir | Juan Wang | Ghada Abdelmoumin |
| Naida Fetic | Na Yu | Han-Zhou Wu |
| Bing Sun | Meiyu Duan | Antonio Junior Spoleto |
| Zhenzhong Chu | Pavel Osinenko | Zhenghao Shi |
| Meijing Li | Chengdong Li | Ya Wang |
| Wentao Chen | Stefano Rovetta | Tao Li |
| Mingpeng Zheng | Mingjun Zhong | Shuyi Zhang |
| Zhihao Tang | Baoping Yuan | Xiaoqing Li |
| Li keng Liang | Akhilesh Mohan | Yajun Zou |
| Alberto Mazzoni | Srivastatva | Chuanlei Zhang |
| Domenico Buongiorno | Vivek Baghel | Berardino Prencipe |
| Zhang Lifeng | Umarani Jayaraman | Feng Liu |
| Chi Yuhong | Somnath Dey | Yongsheng Dong |
| Meng-Meng Yin | Guanghai Li | Yatong Zhou |
| Yannan Bin | Lihong Peng | Carlo Croce |
| Wasiq Khan | Wei Zhang | Rong Fei |
| Yong Wu | Hailin Chen | Zhen Wang |

| | | |
|-------------------|-------------------------|-----------------------|
| Huai-Ping Jin | Yong-Wan Kwon | Guohong Qi |
| Mingzhe She | Heng Chen | Xiaoyan Hu |
| Sen Zhang | S. T. Veena | Li Guo |
| Yifan Zheng | J. Anita Christaline | Xia-an Bi |
| Christophe Guyeux | R. Ramesh | Xiuquan Du |
| Jun Sang | Shadrokh Samavi | Ping Zhu |
| Huang Wenzhun | Amin Khatami | Young-Seob Jeong |
| Jun Wu | Min Chen | Han-Gyu Kim |
| Jing Luo | He Huang | Dongkun Lee |
| Wei Lu | Qing Lei | Jonghwan Hyeon |
| Heungkyu Lee | Shuang Ye | Chae-Gyun Lim |
| Yinlong Qian | Francesco Fontanella | Nicola Altini |
| Hong wang | Kang Jijia | Claudio Gallicchio |
| Daniele Malitesta | Rahul Kumar | Dingna Duan |
| Fenqiang Zhao | Alessandra Scotto Freca | Shiqiang Ma |
| Xinghuo Ye | Nicole Cilia | Mingliang Dou |
| Hongyi Zhang | Alessandro Aliberti | Jansen Woo |
| Xuexin Yu | Gabriele Ciravegna | Shanshan |
| Guanshuo Xu | Jacopo Ferretti | ShanShan Hu |
| Mehdi Yedroudj | Jing Yang | Hai-tao Li |
| Xujun Duan | Zheheng Jiang | Francescomaria Marino |
| Xing-Ming Zhao | Dan Yang | Jiayi Ji |
| Jiayan Han | Dongxue Peng | Jun Peng |
| Yan Xiao | Wenting Cui | Jie Hu |
| Weizhong Lu | Francescomaria Marino | Jipeng Wu |
| Weiguo Shen | Wenhao Chi | Shirley Meng |
| Hongzhen Shi | Ruobing Liang | Prashan Premaratne |
| Zeng Shangyou | Feixiang Zhou | Lucia Ballerini |
| Zhou Yue | Jijia Kang | Haifeng Hu |
| TaeMoon Seo | Xinshao Wang | JianXin Zhang |
| Sergio Cannata | Huawei Huang | Xiaoxiao Sun |
| Weiqi Luo | Zhi Zhou | Shaomin Mu |
| Feng Yanyan | Yanrui Ding | Yongyu Xu |
| Pan Bing | Peng Li | Jingyu Hou |
| Jiwen Dong | Yunfeng Zhao | Zhixian Liu |

Contents – Part I

Evolutionary Computing and Learning

| | |
|--|----|
| Entry Deterrence Game Under Ambiguity | 3 |
| <i>Lan Sun</i> | |
| Identification of Cell Types from Single-Cell Transcriptomes Using a Novel Clustering Framework | 17 |
| <i>Xinguo Lu, Yan Gao, Jinxin Li, Keren He, Guanyuan Chen, and Qiang Qu</i> | |
| Two-Stage Learning Brain Storm Optimizer | 28 |
| <i>Yan Xu, Jingwei Wang, Lianbo Ma, Junfeng Zhao, and Xiaolong Shen</i> | |
| A Modified Bacterial Foraging Optimizer with Adaptive Chemotactic Step in Dynamic Search Region. | 41 |
| <i>Yibo Yong, Lianbo Ma, Junfeng Zhao, and Xiaolong Shen</i> | |
| Novel Mutation Operators of a Variable-Length Representation for EC-Based Feature Selection in High-Dimensional Data. | 53 |
| <i>Nicole Dalia Cilia, Claudio De Stefano, and Francesco Fontanella</i> | |

Swarm Intelligence and Optimization

| | |
|---|----|
| Phasor Symbiotic Organisms Search Algorithm for Global Optimization | 67 |
| <i>Fahui Miao, Li Yao, Xiaojie Zhao, and Yawen Zheng</i> | |

Compressed Sensing and Sparse Coding

| | |
|--|----|
| Essential Proteins Identification Based on Integrated Network. | 81 |
| <i>Chang-Gang Wen, Jin-Xing Liu, Lei Qin, Juan Wang, and Yun Fang</i> | |

Neural Networks

| | |
|---|-----|
| Time Sequence Features Extraction Algorithm of Lying Speech Based on Sparse CNN and LSTM | 95 |
| <i>Yan Zhou and Li Shang</i> | |
| An Improved Conditional Generative Adversarial Network for Microarray Data. | 105 |
| <i>Sheng Fang, Fei Han, Wan-Yun Liang, and Jing Jiang</i> | |

A Cognitive Model of Morphological Neural Network. 115
Naiqin Feng, Lijuan Qin, and Bin Sun

SharedNet: A Novel Efficient Convolutional Architecture Based on Group Sharing Convolution 128
Jian-Xun Mi and Jie Feng

Paying Deep Attention to Both Neighbors and Multiple Tasks 140
Gaoyuan Liang, Haoran Mo, Ying Qiao, Chuxin Wang, and Jing-Yan Wang

Image Classification Based on Deep Belief Network and YELM. 150
ChengYong Zhang, Zhengwei Li, Ru Nie, Lei Wang, and Huan Zhao

Double Channel Neural Non Invasive Blood Pressure Prediction. 160
Annunziata Paviglianiti, Vincenzo Randazzo, Giansalvo Cirrincione, and Eros Pasero

Unsupervised Multi-omic Data Fusion: The Neural Graph Learning Network 172
Pietro Barbiero, Marta Lovino, Mattia Siviero, Gabriele Ciravegna, Vincenzo Randazzo, Elisa Ficarra, and Giansalvo Cirrincione

Random Occlusion Recovery with Noise Channel for Person Re-identification 183
Kun Zhang, Di Wu, Changan Yuan, Xiao Qin, Hongjie Wu, Xingming Zhao, Lijun Zhang, Yuchuan Du, and Hanli Wang

Detection of Abnormal Behavior Based on the Scene of Anti-photographing 192
Wei Zhang and Fan Lin

Signal Processing

Emergency Siren Recognition in Urban Scenarios: Synthetic Dataset and Deep Learning Models 207
Michela Cantarini, Luca Serafini, Leonardo Gabrielli, Emanuele Principi, and Stefano Squartini

Pattern Recognition

Cucumber Disease Recognition Based on Depthwise Separable Convolution. 223
Xianfeng Wang, Zhen Wang, and Shanwen Zhang

| | |
|---|-----|
| Noise Robust Illumination Invariant Face Recognition via Contourlet Transform in Logarithm Domain. | 231 |
| <i>Guangyi Chen and Wenfang Xie</i> | |
| License Plate Detection and Recognition Technology for Complex Real Scenarios | 241 |
| <i>Zhipeng Li, Fei Wang, Hamdan Taleb, Changan Yuan, Xiao Qin, Hongjie Wu, Xingming Zhao, and Lijun Zhang</i> | |
| Biometrics Recognition | |
| Shallow Neural Network for Biometrics from the ECG-WATCH | 259 |
| <i>Vincenzo Randazzo, Giansalvo Cirrincione, and Eros Pasero</i> | |
| Image Processing | |
| Component Tree Computation of 2D Images | 273 |
| <i>Rui Tao and Yuqing Song</i> | |
| An Efficient Method for Computation of Entropy and Joint Entropy of Images. | 282 |
| <i>Debapriya Sengupta, Phalguni Gupta, and Arindam Biswas</i> | |
| A Hybrid Convolutional Neural Network for Complex Leaves Identification | 291 |
| <i>Daniel Ayala Niño, Jair Cervantes Canales, Farid García Lamont, Joel Ayala de la Vega, and Guillermo Calderón Zavala</i> | |
| Low Contrast Chinese Rubbing Image Segmentation Based on Gradient Filtering | 302 |
| <i>Zhi-Kai Huang, Huan Wang, Xian-Chang Xi, Yi-Ning Ning, and Ling-Ying Hou</i> | |
| Industrial Smoke Image Segmentation Based on a New Algorithm of Cross-Entropy Model. | 311 |
| <i>Qian-Jing Huang, Le Zou, Zhi-Ze Wu, Huan-Yi Li, Xiao-Feng Wang, and Yan-Ping Chen</i> | |
| Efficient Segmentation Using Gamma Correction with Complement Image of Chinese Rubbing Image | 323 |
| <i>Han Huang and Yong-Li Ma</i> | |
| State Spatial Selectivity and Its Impacts on Urban Sprawl: Insights from Remote Sensing Images of Zhuhai. | 329 |
| <i>Lingyue Li, Zhixin Qi, and Shi Xian</i> | |

A Tversky Loss-Based Convolutional Neural Network for Liver Vessels Segmentation 342
Nicola Altini, Berardino Prencipe, Antonio Brunetti, Gioacchino Brunetti, Vito Triggiani, Leonarda Carnimeo, Francescomaria Marino, Andrea Guerriero, Laura Villani, Arnaldo Scardapane, and Giacomo Donato Cascarano

A Classification Algorithm for Real Collar Images 355
Xiao Qin, Chengcheng Huang, Junhua Wu, and Changan Yuan

Accurate and Efficient Traffic Sign Detection with a Guided Region Enlarging Algorithm 367
Qing Tang, Ge Cao, and Kanghyun Jo

Plant Leaf Recognition Network Based on Feature Learning and Metric Learning 378
Hongwei Yang, Di Wu, Changan Yuan, Xiao Qin, Hongjie Wu, Xingming Zhao, and Zhongqiu Zhao

Position Attention-Guided Learning for Infrared-Visible Person Re-identification 387
Yong Wu, Sizhe Wan, Di Wu, Chao Wang, Changan Yuan, Xiao Qin, Hongjie Wu, and Xingming Zhao

A Novel Approach Based on Region Growing Algorithm for Liver and Spleen Segmentation from CT Scans 398
Berardino Prencipe, Nicola Altini, Giacomo Donato Cascarano, Andrea Guerriero, and Antonio Brunetti

Information Security

A Novel Approach of Steganalysis to Deal with Steganographic Algorithm Mismatch 413
Pengfei Shi, Donghui Hu, Yuchen Li, Shuli Zheng, and Zhongqiu Zhao

Research on User Information Security in the Context of New Media 423
Haiyu Wang

Research on Software Community Division Method Based on Inter-node Dependency 430
Jun Dong, Chengqian Hao, Jiadong Ren, and Haitao Lu

Blockchain-Based Group Key Management Scheme in IoT 445
Haiying Ma and Guorong Sun

Research on Ideological and Political Education of College Students Based on Network Information Security 458
Xiao-yu Liu, Yu-hang Zhu, Yan Ma, Pan Zhou, and Guang-yue Tian

Artificial Intelligence in Biological and Medical Information Procession

| | |
|---|-----|
| A Novel Plastic Neural Model with Dendritic Computation for Classification Problems | 471 |
| <i>Junkai Ji, Minhui Dong, Cheng Tang, Jiajun Zhao, and Shuangbao Song</i> | |

| | |
|---|-----|
| Improving Approximate Logic Neuron Model by Means of a Novel Learning Algorithm | 484 |
| <i>Jiajun Zhao, Minhui Dong, Cheng Tang, Junkai Ji, and Ying He</i> | |

Recent Advances in Deep Learning Methods and Techniques for Medical Image Analysis

| | |
|--|-----|
| Detection of COVID-19 by GoogLeNet-COD | 499 |
| <i>Xiang Yu, Shui-Hua Wang, Xin Zhang, and Yu-Dong Zhang</i> | |

| | |
|---|-----|
| A Big Data Driven Model for Screening Electricity Customers | 510 |
| <i>Liu Xingping, Xie Zhihan, Zhang Chenmin, Zhou Chenhui, and Zhuang Chen</i> | |

| | |
|---|-----|
| The Evaluation Model Research of Power Supply Service Under the Background of “Running Once at Most”. | 517 |
| <i>Liu Xingping, Wang Xiaoyu, and Zhang Chenmin</i> | |

| | |
|---|-----|
| Customer Characteristics Analysis Module for Operation Platform | 526 |
| <i>Zhang Wei, Wang Qingjuan, and Lou Fei</i> | |

| | |
|---|-----|
| Reconstruction and Re-ranking: A Simple and Effective Approach for Question Answering | 531 |
| <i>Shen Ran, Wang Yifan, Lv Shining, Chen Jinwei, and Xiong Jianfeng</i> | |

| | |
|---|-----|
| Research on Offline State Management Technology of Metered Assets Based on Internet of Things | 539 |
| <i>Linhu, Jiang Yong, and Zhang Jimin</i> | |

| | |
|--|-----|
| Assessment and Application Research on the Carrying Capacity of Township Power Supply Station Based on Big Data Analysis | 548 |
| <i>Pan Weiwei, Shen Guang, Wu Yuebo, and Huang Xiang</i> | |

| | |
|--|-----|
| Research on the Optimization of Mobile Work Terminal Positioning Function Based on LBS | 556 |
| <i>Pan Weiwei, Shen Guang, Wu Yuebo, and Huang Xiang</i> | |

| | |
|--|-----|
| Study on Line Loss Prediction of Low-Voltage Platform Area Based on Internet of Things | 565 |
| <i>Sun Gang, Gu Hongjie, and He Yun</i> | |

Research on Unstructured Electronic Archives Query Based on Visual Retrieval Technology. 576
Hui Yang

Gingivitis Detection by Fractional Fourier Entropy and Standard Genetic Algorithm. 585
Yan Yan and Elijah Nguyen

Logical Analysis and Enlightenment of Credit Management System Design in Electricity Market 597
Ye Hongdou and Chen Xiaoxiao

Author Index 609

Contents – Part II

Gene Expression Array Analysis

| | |
|---|---|
| A Novel Clustering-Framework of Gene Expression Data Based on the Combination Between Deep Learning and Self-organizing Map | 3 |
| <i>Yan Cui, Huacheng Gao, Rui Zhang, Yuanyuan Lu, Yuan Xue, and Chun-Hou Zheng</i> | |

| | |
|---|----|
| Tumor Gene Selection and Prediction via Supervised Correlation Analysis Based F-Score Method. | 14 |
| <i>Jia-Jun Cheng and Bo Li</i> | |

| | |
|---|----|
| A Machine Learning Based Method to Identify Differentially Expressed Genes. | 21 |
| <i>Bolin Chen, Li Gao, and Xuequn Shang</i> | |

| | |
|---|----|
| Multi-omics Classification on Kidney Samples Exploiting Uncertainty-Aware Models. | 32 |
| <i>Marta Lovino, Gianpaolo Bontempo, Giansalvo Cirrincione, and Elisa Ficarra</i> | |

Gene Regulation Modeling and Analysis

| | |
|--|----|
| Inference Method for Reconstructing Regulatory Networks Using Statistical Path-Consistency Algorithm and Mutual Information. | 45 |
| <i>Yan Yan, Xinan Zhang, and Tianhai Tian</i> | |

| | |
|---|----|
| Exploring lncRNA-MRNA Regulatory Modules Based on lncRNA Similarity in Breast Cancer. | 57 |
| <i>Lei Tian, Shu-Lin Wang, and Xing Zhong</i> | |

| | |
|---|----|
| Three-Layer Dynamic Transfer Learning Language Model for E. Coli Promoter Classification | 67 |
| <i>Ying He, Zhen Shen, Qinhu Zhang, Siguo Wang, Changan Yuan, Xiao Qin, Hongjie Wu, and Xingming Zhao</i> | |

| | |
|--|----|
| A New Method Combining DNA Shape Features to Improve the Prediction Accuracy of Transcription Factor Binding Sites | 79 |
| <i>Siguo Wang, Zhen Shen, Ying He, Qinhu Zhang, Changan Yuan, Xiao Qin, Hongjie Wu, and Xingming Zhao</i> | |

| | |
|---|----|
| Predicting <i>in-Vitro</i> Transcription Factor Binding Sites with Deep Embedding Convolution Network | 90 |
| <i>Yindong Zhang, Qinhu Zhang, Changan Yuan, Xiao Qin, Hongjie Wu, and Xingming Zhao</i> | |

Protein-Protein Interaction Prediction

| | |
|---|-----|
| Prediction of Membrane Protein Interaction Based on Deep Residual Learning | 103 |
| <i>Tengsheng Jiang, Hongjie Wu, Yuhui Chen, Haiou Li, Jin Qiu, Weizhong Lu, and Qiming Fu</i> | |

| | |
|---|-----|
| GCNSP: A Novel Prediction Method of Self-Interacting Proteins Based on Graph Convolutional Networks | 109 |
| <i>Lei Wang, Zhu-Hong You, Xin Yan, Kai Zheng, and Zheng-Wei Li</i> | |

| | |
|--|-----|
| Predicting Protein-Protein Interactions from Protein Sequence Using Locality Preserving Projections and Rotation Forest. | 121 |
| <i>Xinke Zhan, Zhuhong You, Changqing Yu, Jie Pan, and Ruiyang Li</i> | |

| | |
|---|-----|
| Predicting Protein-Protein Interactions from Protein Sequence Information Using Dual-Tree Complex Wavelet Transform | 132 |
| <i>Jie Pan, Zhu-Hong You, Chang-Qing Yu, Li-Ping Li, and Xin-ke Zhan</i> | |

Biomarker Discovery and Detection

| | |
|---|-----|
| Biomarkers Selection of Abnormal Functional Connections in Schizophrenia with $\ell_{2,1-2}$ -Norm Based Sparse Regularization Feature Selection Method | 145 |
| <i>Na Gao, Chen Qiao, Shun Qi, Kai Ren, Jian Chen, and Hanfeng Fang</i> | |

Systems Biology

| | |
|---|-----|
| Identification and Analysis of Genes Involved in Stages of Colon Cancer . . . | 161 |
| <i>Bolin Chen, Teng Wang, and Xuequn Shang</i> | |

Modeling, Simulation, and Optimization of Biological Systems

| | |
|---|-----|
| Take It or Leave It: A Computational Model for Flexibility in Decision-Making in Downregulating Negative Emotions | 175 |
| <i>Nimat Ullah, Sander L. Koole, and Jan Treur</i> | |

| | |
|---|-----|
| A Network-Driven Approach for LncRNA-Disease Association Mapping. . . . | 188 |
| <i>Lin Yuan, Tao Sun, Jing Zhao, Song Liu, Ai-Min Li, Qin Lu, Yu-Shui Geng, and Xin-Gang Wang</i> | |

Intelligent Computing in Computational Biology

| | |
|--|-----|
| A Graph Convolutional Matrix Completion Method for miRNA-Disease Association Prediction | 201 |
| <i>Wei Wang, Jiawei Luo, Cong Shen, and Nguye Hoang Tu</i> | |
| An Efficient Computational Method to Predict Drug-Target Interactions Utilizing Structural Perturbation Method | 216 |
| <i>Xinguo Lu, Fang Liu, Li Ding, Xinyu Wang, Jinxin Li, and Yue Yuan</i> | |
| Predicting Human Disease-Associated piRNAs Based on Multi-source Information and Random Forest | 227 |
| <i>Kai Zheng, Zhu-Hong You, Lei Wang, Hao-Yuan Li, and Bo-Ya Ji</i> | |
| Inferring Disease-Associated Piwi-Interacting RNAs via Graph Attention Networks | 239 |
| <i>Kai Zheng, Zhu-Hong You, Lei Wang, Leon Wong, and Zhan-Heng Chen</i> | |
| A Novel Improved Algorithm for Protein Classification Through a Graph Similarity Approach | 251 |
| <i>Hsin-Hung Chou, Ching-Tien Hsu, Hao-Ching Wang, and Sun-Yuan Hsieh</i> | |
| LncRNA-Disease Association Prediction Based on Graph Neural Networks and Inductive Matrix Completion | 262 |
| <i>Lin Yuan, Jing Zhao, Tao Sun, Xue-Song Jiang, Zhen-Yu Yang, Xin-Gang Wang, and Yu-Shui Geng</i> | |
| Prediction of lncRNA-miRNA Interactions via an Embedding Learning Graph Factorize Over Heterogeneous Information Network | 270 |
| <i>Ji-Ren Zhou, Zhu-Hong You, Li Cheng, Xi Zhou, and Hao-Yuan Li</i> | |
| Inferring Drug-miRNA Associations by Integrating Drug SMILES and MiRNA Sequence Information | 279 |
| <i>Zhen-Hao Guo, Zhu-Hong You, Li-Ping Li, Zhan-Heng Chen, Hai-Cheng Yi, and Yan-Bin Wang</i> | |
| Identification of Rice Drought-Resistant Gene Based on Gene Expression Profiles and Network Analysis Algorithm. | 290 |
| <i>Yujia Gao, Yiqiong Chen, Zhiyu Ma, Tao Zeng, Iftikhar Ahmad, Youhua Zhang, and Zhenyu Yue</i> | |
| Identification of Human LncRNA-Disease Association by Fast Kernel Learning-Based Kronecker Regularized Least Squares | 302 |
| <i>Wen Li, Shu-Lin Wang, Junlin Xu, and Jialiang Yang</i> | |

| | |
|---|------------|
| A Gaussian Kernel Similarity-Based Linear Optimization Model for Predicting miRNA-lncRNA Interactions | 316 |
| <i>Leon Wong, Zhu-Hong You, Yu-An Huang, Xi Zhou, and Mei-Yuan Cao</i> | |
| Identification of Autistic Risk Genes Using Developmental Brain Gene Expression Data | 326 |
| <i>Zhi-An Huang, Yu-An Huang, Zhu-Hong You, Shanwen Zhang, Chang-Qing Yu, and Wenzhun Huang</i> | |
| A Unified Deep Biological Sequence Representation Learning with Pretrained Encoder-Decoder Model | 339 |
| <i>Hai-Cheng Yi, Zhu-Hong You, Xiao-Rui Su, De-Shuang Huang, and Zhen-Hao Guo</i> | |
| Predicting Drug-Target Interactions by Node2vec Node Embedding in Molecular Associations Network | 348 |
| <i>Zhan-Heng Chen, Zhu-Hong You, Zhen-Hao Guo, Hai-Cheng Yi, Gong-Xu Luo, and Yan-Bin Wang</i> | |
| Intelligent Computing in Drug Design | |
| Prediction of Drug-Target Interactions with CNNs and Random Forest | 361 |
| <i>Xiaoli Lin, Minqi Xu, and Haiping Yu</i> | |
| DTIFS: A Novel Computational Approach for Predicting Drug-Target Interactions from Drug Structure and Protein Sequence | 371 |
| <i>Xin Yan, Zhu-Hong You, Lei Wang, Li-Ping Li, Kai Zheng, and Mei-Neng Wang</i> | |
| HGAlinker: Drug-Disease Association Prediction Based on Attention Mechanism of Heterogeneous Graph | 384 |
| <i>Xiaozhu Jing, Wei Jiang, Zhongqing Zhang, Yadong Wang, and Junyi Li</i> | |
| Computational Genomics | |
| A Probabilistic Matrix Decomposition Method for Identifying miRNA-Disease Associations | 399 |
| <i>Keren He, Ronghui Wu, Zhenghao Zhu, Jinxin Li, and Xinguo Lu</i> | |
| Artificial Intelligence in Biological and Medical Information Procession | |
| CT Scan Synthesis for Promoting Computer-Aided Diagnosis Capacity of COVID-19 | 413 |
| <i>Heng Li, Yan Hu, Sanqian Li, Wenjun Lin, Peng Liu, Risa Higashita, and Jiang Liu</i> | |

Traffic Data Prediction Based on Complex-Valued S-System Model 423
Bin Yang and Wei Zhang

Classification of Protein Modification Sites with Machine Learning. 432
Jin Sun, Wenzheng Bao, Yi Cao, and Yuehui Chen

RFQ-ANN: Artificial Neural Network Model for Predicting Protein-Protein Interaction Based on Sparse Matrix 446
Wenzheng Ma, Wenzheng Bao, Yi Cao, and Yuehui Chen

Recent Advances in Swarm Intelligence: Computing and Applications

A Novel Hybrid Algorithm Based on Bacterial Foraging Optimization and Grey Wolf Optimizer. 457
Xiaobing Gan and Baoyu Xiao

An Analysis of K-Means, Particle Swarm Optimization and Genetic Algorithm with Data Clustering Technique. 469
Maja Gulan and Kaishan Huang

A Novel Computational Approach for Predicting Drug-Target Interactions via Network Representation Learning 481
Xiao-Rui Su, Zhu-Hong You, Ji-Ren Zhou, Hai-Cheng Yi, and Xiao Li

Predicting LncRNA-miRNA Interactions via Network Embedding with Integrated Structure and Attribute Information 493
Bo-Wei Zhao, Ping Zhang, Zhu-Hong You, Ji-Ren Zhou, and Xiao Li

Machine Learning Techniques in Bioinformatics

A Novel Computational Method for Predicting LncRNA-Disease Associations from Heterogeneous Information Network with SDNE Embedding Model. 505
Ping Zhang, Bo-Wei Zhao, Leon Wong, Zhu-Hong You, Zhen-Hao Guo, and Hai-Cheng Yi

Expression and Gene Regulation Network of *ELF3* in Breast Invasive Carcinoma Based on Data Mining. 514
Chenxia Ren, Pengyong Han, Chandrasekhar Gopalakrishnan, Caixia Xu, Rajasekaran Ramalingam, and Zhengwei Li

Embracing Disease Progression with a Learning System for Real World Evidence Discovery. 524
Zefang Tang, Lun Hu, Xu Min, Yuan Zhang, Jing Mei, Kenney Ng, Shaochun Li, Pengwei Hu, and Zhuhong You

High-Performance Modelling Methods on High-Throughput Biomedical Data

| | |
|--|-----|
| Robust Graph Regularized Extreme Learning Machine Auto Encoder and Its Application to Single-Cell Samples Classification | 537 |
| <i>Liang-Rui Ren, Jin-Xing Liu, Ying-Lian Gao, Xiang-Zhen Kong, and Chun-Hou Zheng</i> | |

Intelligent Computing and Swarm Optimization

| | |
|--|-----|
| A Short Survey of Multi-objective Immune Algorithm Based on Clonal Selection | 549 |
| <i>Lingjie Li, Qiuzhen Lin, and Zhong Ming</i> | |

| | |
|--|-----|
| Adaptive Artificial Immune System for Biological Network Alignment | 560 |
| <i>Shiqiang Wang, Lijia Ma, and Xiao Zhang</i> | |

| | |
|---|-----|
| A Novel Decomposition-Based Multimodal Multi-objective Evolutionary Algorithm | 571 |
| <i>Wu Lin, Yuan Li, and Naili Luo</i> | |

| | |
|--|-----|
| GTCN: Dynamic Network Embedding Based on Graph Temporal Convolution Neural Network | 583 |
| <i>Zhichao Huang, Jingkuan Zhang, Lijia Ma, and Fubing Mao</i> | |

| | |
|--|-----|
| Resource Scheduling Algorithm Based on Evolutionary Computation in Dynamic Cloud Environment | 594 |
| <i>Qiyuan Yu, Shen Zhong, Naili Luo, and Peizhi Huang</i> | |

| | |
|---|-----|
| An Ensemble Classification Technique for Intrusion Detection Based on Dual Evolution. | 607 |
| <i>Qiuzhen Lin, Chao Hu, Shuo Chen, and Peizhi Huang</i> | |

Construction of Large-Scale Heterogeneous Molecular Association Network and Its Application in Molecular Link Prediction

| | |
|--|-----|
| A Novel Stochastic Block Model for Network-Based Prediction of Protein-Protein Interactions. | 621 |
| <i>Xiaojuan Wang, Pengwei Hu, and Lun Hu</i> | |

| | |
|-------------------------------|------------|
| Author Index | 633 |
|-------------------------------|------------|

Contents – Part III

Intelligent Computing in Robotics

| | |
|--|----|
| Automatic Pose Estimation of Micro Unmanned Aerial Vehicle for Autonomous Landing | 3 |
| <i>Manish Shrestha, Sanjeeb Prasad Panday, Basanta Joshi, Aman Shakya, and Rom Kant Pandey</i> | |
| A New Robotic Manipulator Calibration Method of Identification Kinematic and Compliance Errors | 16 |
| <i>Phu-Nguyen Le and Hee-Jung Kang</i> | |
| Person-Following Shopping Support Robot Using Kinect Depth Camera Based on 3D Skeleton Tracking | 28 |
| <i>Md Matiqul Islam, Antony Lam, Hisato Fukuda, Yoshinori Kobayashi, and Yoshinori Kuno</i> | |

Intelligent Computing in Computer Vision

| | |
|--|-----|
| Real-Time Object Detection Based on Convolutional Block Attention Module | 41 |
| <i>Ming-Yang Ban, Wei-Dong Tian, and Zhong-Qiu Zhao</i> | |
| Image Super-Resolution Network Based on Prior Information Fusion | 51 |
| <i>Cheng Ding, Wei-Dong Tian, and Zhong-Qiu Zhao</i> | |
| TFPGAN: Tiny Face Detection with Prior Information and GAN | 62 |
| <i>Dian Liu, Zhong-Qiu Zhao, and Wei-Dong Tian</i> | |
| Regenerating Image Caption with High-Level Semantics | 74 |
| <i>Wei-Dong Tian, Nan-Xun Wang, Yue-Lin Sun, and Zhong-Qiu Zhao</i> | |
| Aggregated Deep Saliency Prediction by Self-attention Network | 87 |
| <i>Ge Cao, Qing Tang, and Kang-hyun Jo</i> | |
| Identification of Diseases and Pests in Tomato Plants Through Artificial Vision | 98 |
| <i>Ernesto García Amaro, Jair Cervantes Canales, Josué Espejel Cabrera, José Sergio Ruiz Castilla, and Farid García Lamont</i> | |
| Depth Guided Attention for Person Re-identification | 110 |
| <i>Md Kamal Uddin, Antony Lam, Hisato Fukuda, Yoshinori Kobayashi, and Yoshinori Kuno</i> | |

| | |
|--|-----|
| Improved Vision Based Pose Estimation for Industrial Robots via Sparse Regression | 121 |
| <i>Diyar Khalis Bilal, Mustafa Unel, and Lutfi Taner Tunc</i> | |
| LiDAR-Camera-Based Deep Dense Fusion for Robust 3D Object Detection . . . | 133 |
| <i>Lihua Wen and Kang-Hyun Jo</i> | |
| PON: Proposal Optimization Network for Temporal Action Proposal Generation | 145 |
| <i>Xiaoxiao Peng, Jixiang Du, and Hongbo Zhang</i> | |
| Intelligent Computing in Communication Networks | |
| A Second-Order Adaptive Agent Network Model for Social Dynamics in a Classroom Setting | 161 |
| <i>Kasper Nicholas, Eric Zonneveld, and Jan Treur</i> | |
| Intelligent Control and Automation | |
| A Fast Terminal Sliding Mode Control Strategy for Trajectory Tracking Control of Robotic Manipulators | 177 |
| <i>Anh Tuan Vo, Hee-Jun Kang, and Thanh Nguyen Truong</i> | |
| An Active Disturbance Rejection Control Method for Robot Manipulators . . . | 190 |
| <i>Thanh Nguyen Truong, Hee-Jun Kang, and Anh Tuan Vo</i> | |
| A Fault Tolerant Control for Robotic Manipulators Using Adaptive Non-singular Fast Terminal Sliding Mode Control Based on Neural Third Order Sliding Mode Observer | 202 |
| <i>Van-Cuong Nguyen and Hee-Jun Kang</i> | |
| Fuzzy PID Controller for Adaptive Current Sharing of Energy Storage System in DC Microgrid | 213 |
| <i>Duy-Long Nguyen and Hong-Hee Lee</i> | |
| Deep Learning Based Fingerprints Reduction Approach for Visible Light-Based Indoor Positioning System | 224 |
| <i>Huy Q. Tran and Cheolkeun Ha</i> | |
| Intelligent Data Analysis and Prediction | |
| Anomaly Detection for Time Series Based on the Neural Networks Optimized by the Improved PSO Algorithm | 237 |
| <i>Wenxiang Guo, Xiyu Liu, and Laisheng Xiang</i> | |

| | |
|---|------------|
| An Integration Framework for Liver Cancer Subtype Classification and Survival Prediction Based on Multi-omics Data | 247 |
| <i>Zhonglie Wang, Rui Yan, Jie Liu, Yudong Liu, Fei Ren, Chunhou Zheng, and Fa Zhang</i> | |
| Short-Term Rainfall Forecasting with E-LSTM Recurrent Neural Networks Using Small Datasets. | 258 |
| <i>Cristian Rodriguez Rivero, Julián Pucheta, Daniel Patiño, Paula Otaño, Leonardo Franco, and Gustavo Juarez</i> | |
| A Highly Efficient Biomolecular Network Representation Model for Predicting Drug-Disease Associations | 271 |
| <i>Han-Jing Jiang, Zhu-Hong You, Lun Hu, Zhen-Hao Guo, Bo-Ya Ji, and Leon Wong</i> | |
| DAAT: A New Method to Train Convolutional Neural Network on Atrial Fibrillation Detection. | 280 |
| <i>Jian Zhang, Juan Liu, Pei-Fang Li, and Jing Feng</i> | |
| Prediction of lncRNA-Disease Associations from Heterogeneous Information Network Based on DeepWalk Embedding Model. | 291 |
| <i>Xiao-Yu Song, Tong Liu, Ze-Yang Qiu, Zhu-Hong You, Yue Sun, Li-Ting Jin, Xiao-Bei Feng, and Lin Zhu</i> | |
| Phishing Attacks and Websites Classification Using Machine Learning and Multiple Datasets (A Comparative Analysis). | 301 |
| <i>Sohail Ahmed Khan, Wasiq Khan, and Abir Hussain</i> | |
| A Survey of Vision-Based Road Parameter Estimating Methods | 314 |
| <i>Yan Wu, Feilin Liu, Linting Guan, and Xinneng Yang</i> | |
| Intelligent Fault Diagnosis | |
| The TE Fault Monitoring Based on IPCR of Adjustable Threshold | 329 |
| <i>Aihua Zhang, Chengcong Lv, and Zhiqiang Zhang</i> | |
| Fuzzy Theory and Algorithms | |
| Notes on Supervisory Control of Fuzzy Discrete Event Systems | 341 |
| <i>Chongqing Lin and Daowen Qiu</i> | |
| Kernel Methods and Supporting Vector Machines | |
| A Multi-class Classification Algorithm Based on Geometric Support Vector Machine | 355 |
| <i>Yuping Qin, Xueying Cheng, and Qiangkui Leng</i> | |

Machine Learning

| | |
|--|-----|
| A Network Embedding-Based Method for Predicting miRNA-Disease Associations by Integrating Multiple Information | 367 |
| <i>Hao-Yuan Li, Zhu-Hong You, Zheng-Wei Li, Ji-Ren Zhou, and Peng-Wei Hu</i> | |
| BP Neural Network-Based Deep Non-negative Matrix Factorization for Image Clustering | 378 |
| <i>Qianwen Zeng, Wen-Sheng Chen, and Binbin Pan</i> | |
| Parameters Selection of Twin Support Vector Regression Based on Cloud Particle Swarm Optimization | 388 |
| <i>Xiuxi Wei, Huajuan Huang, and Weidong Tang</i> | |
| A MapReduce-Based Parallel Random Forest Approach for Predicting Large-Scale Protein-Protein Interactions | 400 |
| <i>Bo-Ya Ji, Zhu-Hong You, Long Yang, Ji-Ren Zhou, and Peng-Wei Hu</i> | |
| Feature Extraction and Random Forest to Identify Sheep Behavior from Accelerometer Data | 408 |
| <i>Natasa Kleanthous, Abir Hussain, Wasiq Khan, Jenny Sneddon, and Alex Mason</i> | |
| Multi-core Twin Support Vector Machines Based on Binary PSO Optimization. | 420 |
| <i>Huajuan Huang and Xiuxi Wei</i> | |
| Multi-stage Hierarchical Clustering Method Based on Hypergraph. | 432 |
| <i>Yue Xi and Yonggang Lu</i> | |
| Knowledge Discovery and Data Mining | |
| Discovery of Cancer Subtypes Based on Stacked Autoencoder | 447 |
| <i>Bo Zhang, Rui-Fen Cao, Jing Wang, and Chun-Hou Zheng</i> | |
| A Meta Graph-Based Top-k Similarity Measure for Heterogeneous Information Networks | 455 |
| <i>Xiangtao Chen, Yonghong Jiang, Yubo Wu, Xiaohui Wei, and Xinguo Lu</i> | |
| Joint Deep Recurrent Network Embedding and Edge Flow Estimation | 467 |
| <i>Gaoyuan Liang, Haoran Mo, Zhibo Wang, Chao-Qun Dong, and Jing-Yan Wang</i> | |
| An Effective Multi-label Classification Algorithm Based on Hypercube | 476 |
| <i>Yuping Qin, Xueying Cheng, Xiangna Li, and Qiangkui Leng</i> | |

Using Self Organizing Maps and K Means Clustering Based on RFM Model for Customer Segmentation in the Online Retail Business 484
Rajan Vohra, Jankisharan Pahareeya, Abir Hussain, Fawaz Ghali, and Alison Lui

An Adaptive Seed Node Mining Algorithm Based on Graph Clustering to Maximize the Influence of Social Networks 498
Tie Hua Zhou, Bo Jiang, Yu Lu, and Ling Wang

Wavelet-Based Emotion Recognition Using Single Channel EEG Device. 510
Tie Hua Zhou, Wen Long Liang, Hang Yu Liu, Wei Jian Pu, and Ling Wang

Dense Subgraphs Summarization: An Efficient Way to Summarize Large Scale Graphs by Super Nodes. 520
Ling Wang, Yu Lu, Bo Jiang, Kai Tai Gao, and Tie Hua Zhou

Uncertainty of Multi-granulation Hesitant Fuzzy Rough Sets Based on Three-Way Decisions 531
Hong Wang and Huanhuan Cheng

WGMFDDA: A Novel Weighted-Based Graph Regularized Matrix Factorization for Predicting Drug-Disease Associations 542
Mei-Neng Wang, Zhu-Hong You, Li-Ping Li, Zhan-Heng Chen, and Xue-Jun Xie

Natural Language Processing and Computational Linguistics

Word Embedding by Unlinking Head and Tail Entities in Crime Classification Model 555
Qinhua Huang and Weimin Ouyang

Recent Advances in Swarm Intelligence: Computing and Applications

A Novel Hybrid Bacterial Foraging Optimization Algorithm Based on Reinforcement Learning 567
Ben Niu, Churong Zhang, Kaishan Huang, and Baoyu Xiao

Improved Water Cycle Algorithm and K-Means Based Method for Data Clustering 579
Huan Liu, Lijing Tan, Luoxin Jin, and Ben Niu

Information Security

The Research of Music AI in the Context of Information Security. 593
Hui Sun

**Intra-frame Adaptive Transform Size for Video Steganography
in H.265/HEVC Bitstreams 601**
Hongguo Zhao, Menghua Pang, and Yunxia Liu

Towards a Universal Steganalyser Using Convolutional Neural Networks 611
*Inas Jawad Kadhim, Prashan Premaratne, Peter James Vial,
Osamah M. Al-Qershi, and Qasim Al-Shebani*

A HEVC Steganography Method Based on QDCT Coefficient 624
Si Liu, Yunxia Liu, Cong Feng, Hongguo Zhao, and Yu Huang

Author Index 633

Evolutionary Computing and Learning



Entry Deterrence Game Under Ambiguity

Lan Sun^(✉)

School of Economics and Management, Yunnan Normal University,
Kunming 650500, People's Republic of China
l. sun@ynnu.edu.cn

Abstract. In this paper, we introduce ambiguity into an entry deterrence game between a better-informed established firm and a less informed potential entrant, in which the potential entrant has multiple priors on the true state of aggregate demand. In this model, the established firm is also uncertain about the state but is informed of the distribution of the state. We characterize the conditions under which limit pricing emerges in equilibria, and thus ambiguity decreases the probability of entry. Welfare analysis shows that limit pricing is more harmful in a market with higher expected demand than in a market with lower expected demand.

Keywords: Entry deterrence game · Asymmetric information · Ambiguity

1 Introduction

Games with incomplete information typically involve the situation in which the players are uncertain about some important parameters of the game, such as the payoff functions, the strategies available to various players, or the information other players have about the game. The normal form of such games is well studied. Extensive-form games with incomplete information in which one informed player, who possesses private information, sends a signal to a second party, who thereupon takes an action have been also widely considered as signalling games (Spence 1973, Cho and Kreps, 1987, etc.). However, in most of the literature, it is assumed that the probability distributions entertained by the different players are mutually “consistent”, in the sense that they can be regarded as conditional probability distributions derived from a certain “basic probability distribution” or “common prior” over the parameters unknown to the various players.

In this paper, we introduce a different concept of the asymmetric information structure in an entry deterrence game between one more informed player and one less informed player. The established firm is more informed since it has already made investment commitment. Either it has knowledge of the true state of the market (the aggregate demand, costs, for example), or at least, it has confidence in the probability distribution of the state. While the potential entrant has little information and hence little confidence regarding to the true state of the market, it may have a set of probability measures over the state space. These two different situations with respect to uncertainty are distinguished by Knight (2012). The situation in which the uncertainty can be governed by a unique probability measure is called “measurable uncertainty” or

“risk”. In contrast, we use “Knightian uncertainty” or “ambiguity” to refer to situations in which individuals cannot or do not assign subjective probabilities to uncertain events. The Ellsberg Paradox (Ellsberg 1961) has shown that this distinction is behaviourally meaningful since people treat ambiguous bets differently from risky bets. Importantly, the lack of confidence reflected by choices in the Ellsberg Paradox cannot be rationalized by any probabilistic belief; see Ellsberg (1961). In the literature, theoretical models of individual preferences for decisions under ambiguity include Maxmin Expected Utility (MEU) (Gilboa and Schmeidler, 1989), smooth ambiguity preference (Klibanoff et al., 2005), and variational representation of preferences (Maccheroni, et al., 2006).

In a seminal study of limiting pricing and entry deterrence models with incomplete information, Milgrom and Roberts (1982) formulated a two-period two-firm model in which the firms know the realizations of their own unit costs but those of their opponent. However, the joint distribution of the costs is common knowledge. In their setting, both firms face “measurable uncertainty” regarding their opponent’s costs. They studied the impact of the information asymmetries on the entry probability compared with the complete information case. We introduce “Knightian uncertainty” in a simplified version of the Milgrom-Roberts model and discuss two cases of information asymmetry between the established firm and the potential entrant.

We formulate a two-period game in which the payoffs of the two players depend on an aggregate demand function with two possible alternatives. In this model, both of the firms face uncertainty, but firm 1 is under risk, while firm 2 is under ambiguity. Since we employ a linear demand function, choosing quantity as firm 1’s strategy in the first period is equivalent to choosing price. In this model, firm 1 chooses a price to charge in the first period, and it will learn the realization of the uncertain demand in the first period. Firm 2 updates its set of priors after observing the price charged by firm 1 in the first period and decides whether to enter the market. If firm 2 enters, it also makes an investment commitment and learns the real prior immediately; then the two firms engage in Cournot competition. Otherwise, firm 1 remains its monopoly. From the information structure, we can see that firm 1 has an informational advantage in both pre- and post-entry markets.

A welfare analysis reveals that the changes in expected consumer surplus due to limit pricing are increasing in the expected aggregate demand under certain standard conditions. However, limit pricing decreases the expected industry surplus and total welfare. Further, it is more harmful in a market with higher expected demand than in a market with lower expected demand.

The remainder of this chapter is organized as follows. Section 2 describes a model in which both firms are uncertain about the demand function, but there is asymmetric information with respect to uncertainty. The established firm is under risk, but the entrant is under ambiguity. This section characterizes one message-monotone equilibrium and discusses the impact of ambiguity. Section 3 discusses the impact of information asymmetry on welfare. Finally, Sect. 4 presents the conclusion.

2 Entry Deterrence Game with Asymmetric Information on Uncertainty

2.1 Description of the Asymmetric Information Structure

Consider a market for a homogeneous good in which there are an established firm, denoted firm 1, and a potential entrant, firm 2. The inverse demand function for the industry output is $P = a - bQ$. The parameter a is assumed to be one of the two possible values a^H and a^L , with $0 < a^L < a^H$. Thus $a = a^H$ reflects a higher aggregate demand state than $a = a^L$. A two-period model of entry deterrence and entry under incomplete information proceeds as follows: At stage 0, nature selects the value of a according to a distribution $\mathbb{P}(a = a^H) = 1 - \mathbb{P}(a = a^L) = x \in [0, 1]$ and fixes a through the next two periods. Firm 1 is informed the probability distribution of a , that is, firm 1 knows the value of $x = x_0$. But firm 2 only has knowledge that $x \in [\underline{x}, \bar{x}] \subseteq [0, 1]$. We assume that $x_0 \in [\underline{x}, \bar{x}]$ for consistency. The asymmetric information situation is common knowledge but not the information itself.

At stage 1, firm 1 has to choose a price to charge for the production. Observing the price charged by firm 1, firm 2 decides to enter the market or not.

At stage 2, if firm 2 decides to enter the market and makes commitment on the investment with a fixed cost K , it also can learn the value of a and the two firms proceed Cournot competition in this stage. Otherwise, if firm 2 doesn't enter, firm 1 will enjoy the monopoly profit.

We assume that the firms are risk neutral and ambiguity averse. The unit cost c_i , $i = 1, 2$ is constant, and the description of the game are common knowledge.

2.2 Strategies and Payoffs

In order to simplify the payoff functions, we take the method by Milgrom and Roberts (1982) to normalize the profit to firm 1 in the second period to be zero if entry occurs. Otherwise firm 1 gets a reward which equals to the difference between the monopoly profit and the Cournot profit if entry doesn't occur. We assume that firm 2 can learn the distribution of a immediately as soon as it decides to enter the market and makes investment commitment with a fixed cost K . Firm 1 learnt the true state of a by observing its demand in the first period. Under this framework, firm 1 has information advantage both in the pre-entry market and in the post-entry market.

We analyze the post-entry Cournot duopoly market first, which is a typical one shot game with incomplete information on one side. In this sub-game, firm 1's pure strategy is to choose an output level conditional on a , $Q_1(\cdot) : \{a^H, a^L\} \rightarrow \mathbb{R}_+$, to maximize its profit:

$$\max_{Q_1} [a - b(Q_1 + Q_2) - c_1]Q_1.$$

Given the quantity of production of firm 2, Q_2 , the reaction curve of firm 1 is:

$$Q_1(Q_2; a) = \frac{a - bQ_2 - c_1}{2b}.$$

Firm 2's pure strategy is to choose an output level Q_2 conditional on x , $Q_2(\cdot) : [0, 1] \rightarrow \mathbb{R}_+$, to maximize its expected profit:

$$\begin{aligned} & \max_{Q_2} E_a[a - b(Q_1(a) + Q_2) - c_2]Q_2 \\ &= \max_{Q_2} [a^e(x) - b(Q_1^e(x) + Q_2) - c_2]Q_2, \end{aligned}$$

where $a^e(x) = xa^H + (1-x)a^L$ and $Q_1^e(x) = xQ_1(a^H) + (1-x)Q_1(a^L)$. Then the reaction curve of firm 2 is:

$$Q_2(Q_1; x) = \frac{a^e(x) - bQ_1^e(x) - c_2}{2b}.$$

We can get the Equilibrium Cournot quantities from Eq. (4.5) and (4.6):

$$\begin{aligned} Q_2(x) &= \frac{a^e(x) + c_1 - 2c_2}{3b}, \\ Q_1(a) &= \frac{3a - a^e(x) - 4c_1 + 2c_2}{6b}, \quad \text{for } a \in \{a^H, a^L\}. \end{aligned}$$

According to the aggregate demand function, we can obtain the ex post equilibrium price which firm 1 can anticipate ex ante:

$$P(a) = \frac{3a - a^e(x) + 2c_1 + 2c_2}{6}, \quad \text{for } a \in \{a^H, a^L\}.$$

Now we can compute the Cournot profit of firm 1 conditional on a :

$$\begin{aligned} \Pi_{1C}(a, x) &= [P(a) - c_1]Q_1(a) \\ &= \frac{(3a - a^e(x) - 4c_1 + 2c_2)^2}{36b}, \end{aligned}$$

and the expected Cournot profit of firm 2:

$$\begin{aligned} \Pi_{2C}^e(x) &= E_a[P(a) - c_2]Q_2(x) \\ &= \frac{(a^e(x) + c_1 - 2c_2)^2}{9b}. \end{aligned}$$

As long as we pin down the Cournot competition game in the second period, we can analyze the strategies and payoffs of the two firms in the two periods. As we illustrated in the game description, firm 1's strategy in the first period influences its

total payoff, and it also serves as a signal transferred to firm 2 to influence firm 2's decision in the second period. We restrict attention to pure strategy equilibria. Denote the pure strategy of firm 1 as:

$$s : [0, 1] \rightarrow \mathbb{R}_+,$$

then $s(x)$ is the price chosen by firm 1 in the first period conditional on the probability distribution of a . Denote the pure strategy of firm 2 as:

$$t : \mathbb{R}_+ \rightarrow \{0, 1\}.$$

If firm 2 decides to stay out of the market observing s , then $t(s) = 0$. Otherwise, if firm 2 decides to enter the market, then $t(s) = 1$. Given these strategies, we can write down the total expected payoffs of the two firms. Let $\Pi_1^e(s; x, t)$ and $\Pi_2^e(t; x, s)$ be the total expected profits of firm 1 and firm 2 respectively. Then

$$\begin{aligned} \Pi_1^e(s; x, t) &= \Pi_1^{0e}(s; x) + \delta_1 R^e(x)(1 - t) \\ &= \Pi_1^{0e}(s; x) + \delta_1 E_x[\Pi_M(a) - \Pi_{1C}(a, x)](1 - t), \end{aligned}$$

and

$$\Pi_2^e(t; x, s) = \delta_2 t(s) [\Pi_{2C}^e(x) - K],$$

where δ_i is the discount factor of firm i , $i = 1, 2$, $\Pi_1^{0e}(s; x)$ is firm 1's expected profit in the first period if it chooses price s , and $R^e(x)$ is firm 1's expected reward profit if it succeeds in deterring firm 2 which is equal to the expected monopoly profit $E_a[\Pi_M(a)]$ minus the expected Cournot profit $E_a[\Pi_{1C}(a, x)]$. If firm 1 decides to reveal itself in the first period, then knowing the probability distribution of a , firm 1 chooses a monopoly price to maximize its expected profit:

$$\max_s E \left[\frac{(s - c_1)(a - s)}{b} \right].$$

Solving this optimization problem,

$$s_M^e(x) = \frac{a^e(x) + c_1}{2},$$

then we can get the expected monopoly profit.

$$E_a[\Pi_M(a)] = \Pi_{1M}^e(x) = \frac{[a^e(x) - c_1]^2}{4b}.$$

To make things interesting, we assume that firm 1's expected monopoly profit is greater than its expected Cournot profit, that is, $\Pi_{1M}^e(x) > \Pi_{1C}^e(x)$.

2.3 Equilibrium Analysis

Again, we adopt the Maxmin Expected Utility to represent the ambiguity aversion of firm 2 with multiple priors. Assume that firm 1 plays some strategy $\bar{s} : [0, 1] \rightarrow \mathbb{R}_+$, then any P (price) in the range of \bar{s} , firm 2 updates its set of priors by $x \in \bar{s}^{-1}(P)$. Firm 2's best response is "enter" if and only if the minimum expected value of the post-entry profit, $\inf_{x \in \bar{s}^{-1}(P)} (\Pi_{2C}^e(x) - K)$, is positive. Formally, we give the definition of Nash equilibrium as follows:

Definition 1.

A strategy profile (s^*, t^*) is a Nash equilibrium of the entry deterrence game if it satisfies the following conditions:

(i) for any $x \in [0, 1]$ and any $s : [0, 1] \rightarrow \mathbb{R}_+$

$$\begin{aligned} \Pi_1^{0e}(s^*; x) + \delta_1 R^e(x)(1 - t^*(s^*)) &\geq \\ \Pi_1^{0e}(s; x) + \delta_1 R^e(x)(1 - t^*(s)). & \end{aligned}$$

(ii) for any $\{0, 1\}$, for all $P \in \mathbb{R}_+$, such that $\exists x \in [0, 1]$, $s^*(x) = P$,

$$\inf_{x \in \{x: s^*(x)=P\}} t^*(P)(\Pi_{2C}^e(x) - K) \geq \inf_{x \in \{x: s^*(x)=P\}} t(P)(\Pi_{2C}^e(x) - K).$$

For simplicity, we analyze the equilibrium under the following assumptions:

Assumption 1.

- (i). $\Pi_C^2(a^L) - K < 0$ and $\Pi_C^2(a^H) - K > 0$.
- (ii). $a^L - 2c_2 + c_1 > 0$.

Assumption 2. Firm 2's optimal choice is staying out of the market under it's original information.

Assumption 1(i) just simply means that firm 2 won't enter the market if it is informed that $a = a^L$ and it will enter the market if $a = a^H$. Assumption 1(2) implies that if firm 2 enters the market, then it produces positive quantity in the Cournot market even at the low state of demand.

Assumption 3. $[\underline{x}, \bar{x}] = [0, 1]$, $c_2 \geq c_1$ and $\delta_1 = 1$.

In the equilibrium analysis, we focus on message-monotone equilibrium.

Definition 2

In a message-monotone equilibrium in the entry deterrence game, the strategy of firm 1, $s(x)$, is weakly increasing in x .

The continuity of the duopoly Cournot payoff function together with assumption 1 imply that there exists a belief $\hat{x} \in (0, 1)$ such that firm 2 is indifferent between “enter” and “not enter”. With a simple calculation, we can get the indifferent point which is:

$$\hat{x} = \frac{\sqrt{9bK} - (a^L + c_1 - 2c_2)}{a^H - a^L}.$$

Since we assume that $\Pi_M^e(x) > \Pi_{1C}^e(a, x)$ for all $x \in [0, 1]$, which implies that firm 1 has incentive to deter the entrant by sacrificing the profit in the first period due to charging a lower price. And it's getting more and more costly to deter the entrant as x increases. Under assumption $\delta_1 = 1$, the indifference point of firm 1, \tilde{x} , satisfies the following condition:

$$\frac{(a^e(\hat{x}) - c_1)^2}{4} = \frac{(a^e(\tilde{x}) - 2c_1 + c_2)^2}{9}.$$

Given these two critical points \hat{x} and \tilde{x} together with assumptions A1–A3, we can get the following property of a Nash equilibrium:

Proposition 1

In this entry deterrence model, under A1–A3, a Nash equilibrium (s^*, t^*) is a message-monotone equilibrium.

The proof is given in Appendix A.

An increasing x indicates a higher expected aggregate demand. With message-monotone strategies, firm 1 sends a more attractive message to firm 2 by choosing a non-decreasing price when the expected aggregate demand increases. On the other hand, observing a higher price, firm 2 can induce a higher expected demand. Therefore, firm 2's strategy is also non-decreasing with respect to the price it observed. The following theorem characterizes such a message-monotone equilibrium.

Theorem 1

Under the assumptions A1–A3, there exists a message-monotone equilibrium (s^*, t^*) in the entry deterrence game in two different cases:

(i) if $\tilde{x} \leq \hat{x}$, then there exists a separating equilibrium (s^*, t^*) :

$$\begin{aligned} s^*(x) &= s_M^e(x) \quad \forall x \in [0, 1], \\ t^*(s) &= \begin{cases} 0, & \text{if } s \leq s_M^e(\hat{x}) \\ 1, & \text{otherwise} \end{cases} \end{aligned}$$

(ii) if $\tilde{x} \geq \hat{x}$, then there exists a semi-separating equilibrium (s^*, t^*) :

$$s^*(x) = \begin{cases} s_M^e(x) & \text{if } x \in [0, \hat{x}] \cup (\min\{\tilde{x}, 1\}, 1] \\ s_M^e(\hat{x}) & \text{if } x \in [\hat{x}, \min\{\tilde{x}, 1\}], \end{cases}$$

$$t^*(s) = \begin{cases} 0, & \text{if } s \leq s_M^e(\hat{x}) \\ 1, & \text{otherwise} \end{cases}$$

Proof (see the appendix B)

Remark: In the first case, for any level of expected demand, it's so costly to deter the entrant that the reward is not enough to compensate the lost if firm 1 conducts limit pricing in the first period, therefore, limit pricing doesn't emerge in this situation. In the second case, in contrast, when the expected demand is low enough such that the entrant is not interested in entering the market, firm 1 doesn't need to conduct limit pricing. Or the expected demand is high enough that the signal sent by firm 1 is high enough such that the entrant will enter the market observing the signal, then it's not necessary for firm 1 to conduct limit pricing. But when the expected demand is between the two thresholds, limit pricing emerges.

3 Welfare Analysis

3.1 The Impact of Ambiguity on Expected Welfare

In this sector, we discuss the impact of ambiguity comparing with the situation where firm 2 is also informed the probability distribution of a . If there doesn't exist information asymmetries between firm 1 and firm 2, then firm 1 can't deter firm 2 by conducting limit pricing because firm 2 doesn't need to induce any information from the behavior of firm 1 in the first period. Firm 2 will choose to enter the market when $x > \hat{x}$ and stay out the market otherwise. Therefore, limit pricing doesn't emerge and firm 1 just charges the expected monopoly price in the first period for any $x \in [0, 1]$. In order to discuss the impact of ambiguity on expected welfare, we just need to analyze the impact of limit pricing on the expected welfare.

To focus on the impact of limit pricing, we assume that $\hat{x} < \tilde{x} \leq 1$. Consumer's surplus: In the previous section, we have shown that the price decreases from the expected monopoly price $P_M(x) = s_M^e(x)$ to the limit price $P_M(\hat{x}) = s_M^e(\hat{x})$ when $x \in [\hat{x}, \tilde{x}]$ in the first period, and

$$P_M(\hat{x}) - P_M(x) = \frac{a^e(\hat{x}) - a^e(x)}{2} < 0.$$

Due to limit pricing, the entrant is deterred in the second period, the monopoly price is greater than the Cournot price:

$$\begin{aligned} P_M(a) - P_C(a) &= \frac{a + c_1}{2} - \frac{3a - a^e(x) + 2c_1 + 2c_2}{6} \\ &= \frac{a^e(x) + c_1 - 2c_2}{6} > 0. \end{aligned}$$

Therefore, the consumer's surplus increases in the first period and decreases in the second period. The change of total consumer's surplus is ambiguous. However, we still can analyze the changes of consumer's surplus with respect to the state of the market. We can clearly see that the price decreases in the first period faster than it increases in the second period as x increases, i.e.

$$\left| \frac{\partial(P_M(\hat{x}) - P_M(x))}{\partial x} \right| > \frac{\partial(P_M(a) - P_C(a))}{\partial x}.$$

Therefore, we expect that the consumer's surplus increases in x . Formally, The net consumer's surplus from without limit pricing to limit pricing is:

$$\begin{aligned} \Delta S^C &= - \int_{P_M(x)}^{P_M(a)} \frac{a-p}{b} dp - \int_{P_C(a)}^{P_M(a)} \frac{a-p}{b} dp \\ \frac{\partial \Delta E(S^C)}{\partial x} &= \frac{a^H - a^L}{2} \left[E \left[\frac{a - P_M(x)}{b} \right] - \frac{1}{3} E \left[\frac{a - P_C(a)}{b} \right] \right] \\ &= \frac{a^H - a^L}{2} \left(E_x[Q_M] - \frac{1}{3} E_x[Q_C] \right) \\ &= \frac{a^H - a^L}{2} \left(Q_M^e(x) - \frac{1}{3} Q_C^e(x) \right) \end{aligned}$$

We can see that the expected consumer's surplus is increasing in x as long as the expected aggregate monopoly production $E_x[Q_M]$ at x is greater than one third of the expected aggregate Cournot production $E_x[Q_C]$.

Firm's surplus: Firm's surplus is equal to firm's profit. The net firm's surplus from without limit pricing to limit pricing is:

$$\begin{aligned} E[\Delta S^F] &= \Pi_{1M}^e(\hat{x}) + \Pi_{1M}^e(a) - (\Pi_{1M}^e(x) + \Pi_{1C}(a) + \Pi_{2C}^e(x)) \\ &= \{(P_M(\hat{x}) - c_1)Q_M(\hat{x}) + (P_M(a) - c_1)Q_M(a)\} \\ &\quad - \{(P_M(x) - c_1)Q_M(x) + (P_C(a) - c_1)Q_{1C} + (P_C(a) - c_2)Q_{2C}\} \\ &= \frac{(P_M(\hat{x}) - c_1)^2}{4b} + \frac{(P_M(a) - c_1)^2}{4b} \\ &\quad - \left\{ \frac{(P_M(x) - c_1)^2}{4b} + \frac{(P_C(a) - c_1)^2}{b} + \frac{(P_C(a) - c_2)(a^e(x) + c_1 - 2c_2)}{3b} \right\} \\ &= \frac{(a^e(\hat{x}) - c_1)^2}{4b} - \left(\frac{(a^e(x) - 2c_1 + c_2)^2}{9b} + \frac{(a^e(x) - 2c_2 + c_1)^2}{9b} \right). \end{aligned}$$

The net industry' surplus equals to the difference between the expected monopoly profit at \hat{x} and the total expected Cournot profits at x . Since $x > \hat{x}$, the net industry's surplus is negative if c_2 is not very large. We conclude that deterring an moderate cost entrant by limit pricing harms the industry. Moreover,

$$\begin{aligned}\frac{\partial E[\Delta S^F]}{\partial x} &= -\frac{2(a^H - a^L)(a^e(x) - c_1 - c_2)}{9b} \\ &= -\frac{2(a^H - a^L)Q_C^e(x)}{3} < 0,\end{aligned}$$

where $Q_C^e(x)$ is the expected total Cournot production at x if firm 2 enters the market in the second period. This result shows that the limit pricing harms the industry more in a market with higher expected demand than a lower one.

Total welfare: The total welfare is the sum of the consumer's surplus and the firm's surplus. Therefore,

$$\Delta TW = \Delta S^C + \Delta S^F,$$

and

$$\begin{aligned}\frac{\partial E[\Delta TW]}{\partial x} &= -\frac{(a^H - a^L)}{6} (3Q_M^e(x) - 5Q_C^e(x)) \\ &\begin{cases} > 0 & \text{if } 3Q_M^e(x) - 5Q_C^e(x) < 0 \\ < 0 & \text{if } 3Q_M^e(x) - 5Q_C^e(x) > 0. \end{cases}\end{aligned}$$

Limit pricing decreases the total social welfare more in a higher expected demand market than in a lower one when the expected Cournot output is less than 60% of the expected monopoly output.

In a general framework, if firm 2 has a set of priors $x \in [\underline{x}, \bar{x}]$, the impact of ambiguity on expected welfare occurs only when an increase of ambiguity changes the strategy of firm 1 from non-limit pricing to limit pricing, or vice versa. As we can see from the equilibrium analysis, limit pricing doesn't occur as long as the realization of x is in the region $[\underline{x}, \hat{x}] \cup [\underline{x}, \bar{x}]$. Therefore, the ambiguity doesn't influence the strategy of firm 1 or the welfare when $x \in [\underline{x}, \hat{x}] \cup [\bar{x}, \bar{x}]$. Ambiguity decreases the total expected welfare when $x \in [\hat{x}, \bar{x}]$ comparing with symmetric information situation. However, the change of the degree of ambiguity influences the welfare only when firm 2's set of priors changes such that \underline{x} moves from one side of \hat{x} to the other. We present an example in the next section to illustrate the results.

3.2 An Example

In this section, we provide a numerical example to compute the equilibrium strategies in the entry deterrence game with asymmetric information on uncertainty. Suppose that $a^H = 10$, $a^L = 5$, $b = 1$, $\delta_1 = \delta_2 = 1$, $c_1 = c_2 = 1$, $K = 3.5$. The probability distribution of a is $\mathbb{P}(a = a^H) = 1 - \mathbb{P}(a = a^L) = x \in [0, 1]$. The set of priors of firm 2 on the distribution of a is $[0, 1]$. One can compute that the indifferent point of firm 2 is

$\hat{x} = 0.322$, and the indifferent point of firm 1 is $\tilde{x} = 0.884$. The expected monopoly price charged by firm 1 at $x = \hat{x}$ is: $s_M^e(\hat{x}) = \frac{a^e(\hat{x}) + c_1}{2} = 3.805$. At equilibrium, the message-monotone strategy of firm 1 is:

$$s^*(x) = \begin{cases} 3.805 & \text{if } x \in [0.322, 0.884) \\ \frac{5x+6}{2} & \text{if } x \in [0, 0.322) \cup [0.884, 1], \end{cases}$$

and the strategy of firm 2 is

$$t^*(s) = \begin{cases} 0 & \text{if } s \leq 3.805 \\ 1 & \text{if } s > 3.805. \end{cases}$$

In this example firm 1 can take the advantage of the information asymmetries by using pooling strategy to deter the entrant if the probability of the higher aggregate demand is not too low or too high. In this example, we can see (Fig. 1) that both the expected consumer's surplus and the expected industry's surplus decrease due to the limit pricing, and limit pricing also decreases the expected total welfare. The expected net consumer's surplus is increasing in x but the expected total welfare is decreasing in x , which means that the established firm has to sacrifice more profits in the first period in order to deter the entrant in a market with higher expected demand. This result suggests that an antitrust policy is more important in a market with higher expected demand.

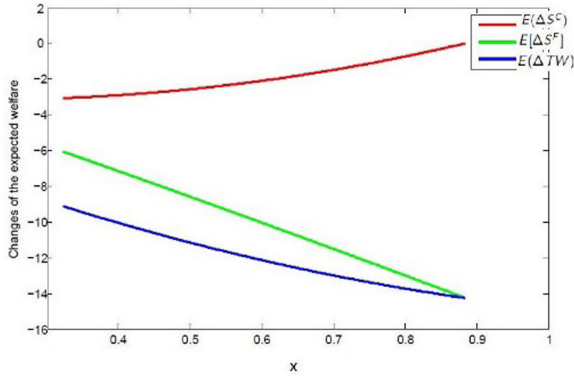


Fig. 1. The changes of welfare due to limit pricing

4 Conclusions

In this chapter we re-examine the entry deterrence game in which two firms have asymmetric information (Milgrom and Roberts 1982) but under different information structures. We formulate a model with asymmetric information. The entrant faces ambiguity about the true state, in the sense that it has multiple priors on the true state. While the established firm is informed of the distribution of the true state. The

informational advantage encourages the established firm to send an unattractive signal to the entrant by engaging in limit pricing in the first period and deters the entrant under certain circumstances. Compared with symmetric information, ambiguity decreases the probability of entry under certain conditions, but it is also possible for it to have no influence on the probability of entry. A numerical example reveals that both the expected consumer surplus and the expected industry surplus are decreased due to limit pricing, and thus total welfare is decreased. Deterring a moderate-cost entrant harms social welfare to a greater extent in a market with higher expected demand than in one with lower expected demand. However, in our analysis, we assume, for simplicity, that firm 1 is also informed of firm 2's set of priors. An extension of the analysis in which firm 2 also has private information on its set of priors is not trivial and the results would be different.

Acknowledgement. This work is Granted by Doctoral Research Program of Yunnan Normal University (No. XJBS2018122014).

Appendix

A. Proof of Proposition 1

Proof. In this proposition, we intent to prove that at equilibrium, for $\forall x_1, x_2 \in [0, 1]$, if $x_1 < x_2$, then $s_1^* = s^*(x_1) \leq s^*(x_2) = s_2^*$. For the case that $\hat{x} < \tilde{x}$, there are four possibilities that can occur at equilibrium:

- (i). $t^*(s_1^*) = t^*(s_2^*) = 0$;
- (ii). $t^*(s_1^*) = 0$, and $t^*(s_2^*) = 1$;
- (iii). $t^*(s_1^*) = 1$, and $t^*(s_2^*) = 1$.
- (iv). $t^*(s_1^*) = 1$, and $t^*(s_2^*) = 0$;

In each case, we can show that a violation of the monotonicity leads to a deviation from the equilibrium. Let $A_1 = \{x : s^*(x) = s_1^*\}$ and $A_2 = \{x : s^*(x) = s_2^*\}$ be the strategies of firm 1 at the particular equilibrium. By contradiction, assume that $s_1^* > s_2^*$.

For case (i), let $x_1^* = \inf\{x : s^*(x) = s_1^*\}$ and $x_2^* = \inf\{x : s^*(x) = s_2^*\}$. Due to the strictly increasing of $\Pi_{2C}^e(x)$ in x , firm 2 takes x_1^* and x_2^* as the worst case by MaxMin utility. If firm 2 doesn't enter the market at x_1^* and x_2^* , then the optimal response of firm 1 will be

$$s_1^* = \frac{a^e(x_1^*) + c_1}{2b}, \quad \text{and} \quad s_2^* = \frac{a^e(x_2^*) + c_1}{2b}.$$

If $s_1^* > s_2^*$, then $x_2^* < x_1^* \leq x_1 < x_2$. Then the type x_2 of firm 1 would deviate to s_1^* . By deviation, $x_2 \in A_1$, and still we have $x_1^* = \inf A_1$, which doesn't influence the decision of firm 2. The x_2 type of firm 1 can get higher profit in the first period and the same monopoly profit in the second period.

For case (ii), we have similar argument. If $s_1^* > s_2^*$, and firm 2 enters the market observing s_2^* , then type x_2 of firm 1 would deviate to get higher profit in the first period and deter the entry by choosing s_1^* .

For case (iii), since both s_1^* and s_2^* can't deter the entry, type x_2 of firm 1 would deviate to get higher profit in the first period by choosing s_1^* .

For case (iv), Firstly, we show $x_1^* = x_1$. If $x_1^* < x_1$, then $s_1^* < \frac{a^e(x_1) + c_1}{2b}$. Since s_1^* induces entry, x_1 type of firm 1's profit is $\Pi_{1M}^e(x_1^*)$. However, the worst case by choosing s_1 is inducing entry and the profit is $\Pi_{1M}^e(x_1)$, and $\Pi_{1M}^e(x_1^*) < \Pi_{1M}^e(x_1)$. The x_1 type of firm 1 would deviate to $s_1 = \frac{a^e(x_1) + c_1}{2b}$. So $x_1^* = x_1$. Now let's show that if $s_1^* > s_2^*$, one type of firm 1 would deviate. At equilibrium, $x_2^* < x_1 < x_2$ and the profits of firm 1 given by:

$$\begin{aligned}\Pi_1^e(s_1^*; x_1) &= \Pi_M^e(x_1) \\ \Pi_1^e(s_2^*; x_2) &= \Pi_M^e(x_2^*) + R^e(x_2)\end{aligned}$$

If $\Pi_1^e(s_1^*; x_1) > \Pi_1^e(s_2^*; x_2)$, then x_2 type of firm 1 would deviate. Choosing a higher price s_1^* induces entry but it can get higher profit.

If $\Pi_1^e(s_1^*; x_1) < \Pi_1^e(s_2^*; x_2)$, The condition for existence of a pooling equilibrium implies that

$$\Pi_M^e(x_2^*) + R^e(x_2) - \Pi_1^e(x_2) < \Pi_M^e(x_2^*) + R^e(x_1) - \Pi_1^e(x_1).$$

Since s_2^* is the optimal choice for x_2 type of firm 1,

$$\Pi_M^e(x_2^*) + R^e(x_2) - \Pi_1^e(x_2) \geq 0.$$

We obtain

$$\Pi_M^e(x_2^*) + R^e(x_1) - \Pi_1^e(x_1) > 0,$$

which implies that x_1 type of firm 1 would deviate to get higher payoff by choosing a lower price s_2^* .

B. Proof of Theorem 1

Proof. To prove this theorem, we just follow the definition of Nash Equilibrium (Def. 2.1). Given the strategy of firm 1, observing $s < \frac{a^e(\hat{x}) - c_1}{2}$, firm 2 induces that $x < \hat{x}$. Firm 2 chooses to stay out of the market with maximin preference. So t^* is an optimal response to s^* . On the other hand, Given the strategy of firm 2, t^* , firm 1's optimal strategy is to maximize its total expected profit. Let $\delta_1 = 1$, then the total expected profits of firm 1 is:

$$\Pi_1^e(s; x) = \begin{cases} \Pi_1^{0e}(s; x) + R^e(x) & \text{if } s \leq \frac{a^e(\hat{x}) + c_1}{2b} \\ \Pi_1^{0e}(s; x) & \text{if } s > \frac{a^e(\hat{x}) + c_1}{2b}, \end{cases}$$

We can show that the difference of the profits of firm 1 between deterring and not deterring the entrant is decreasing in x if $\delta_1 = 1$:

$$\frac{d(\Pi_1^e(\hat{x}, x) - \Pi_{1M}^e(x))}{dx} = -\frac{2(a^H - a^L)(a^e(x) - 2c_1 + c_2)}{9b} < 0.$$

And we have shown that firm 1 is indifferent at $x = \tilde{x}$. So firm 1 prefers deterring to accommodating the entrant when $x < \tilde{x}$. When $\tilde{x} < \hat{x}$, for any $x \in [0, 1]$, firm 1 will choose the monopoly price in the first period because it is too costly to deter the entrant. But when $\tilde{x} > \hat{x}$, firm 1 has incentive to deter the entrant by pooling strategies for $x \in [\hat{x}, \tilde{x}]$ and what it can do the best is to choose the monopoly price at $x = \hat{x}$. Given the strategy of firm 2, for any $x \in [0, 1]$, firm 1 doesn't want to deviate.

References

- Cho, I.K., Kreps, D.M.: Signaling games and stable equilibria. *Q. J. Econ.* **102**, 179–221 (1987)
- Ellsberg, D.: Risk, ambiguity, and the Savage axioms. *The Q. J. Econ.* **75**, 643–669 (1961)
- Gilboa, I., Schmeidler, D.: Maxmin expected utility with non-unique prior. *J. Math. Econ.* **18**(2), 141–153 (1989)
- Klibanoff, P., Marinacci, M., Mukerji, S.: A smooth model of decision making under ambiguity. *Econometrica* **73**(6), 1849–1892 (2005)
- Knight, F.H.: *Risk, Uncertainty and Profit*. Courier Corporation, Chelmsford (2012)
- Maccheroni, F., Marinacci, M., Rustichini, A.: Ambiguity aversion, robustness, and the variational representation of preferences. *Econometrica* **74**(6), 1447–1498 (2006)
- Milgrom, P., Roberts, J.: Limit pricing and entry under incomplete information: an equilibrium analysis. *Econometrica J. Econometric Soc.* **50**, 443–459 (1982)
- Spence, M.: Job market signaling. *Q. J. Econ.* **87**, 355–374 (1973)



Identification of Cell Types from Single-Cell Transcriptomes Using a Novel Clustering Framework

Xinguo Lu^(✉), Yan Gao, Jinxin Li, Keren He, Guanyuan Chen,
and Qiang Qu

College of Computer Science and Electronic Engineering, Hunan University,
Changsha, China
hnluxinguo@126.com

Abstract. Quantifying or labeling biological sample types based on single-cell gene expression patterns is the key to deepening understanding of complex diseases or tissues. Usually the clustering method is the main computing tool for this purpose. In particular, due to the noise and high dimensional limitations of scRNA-seq data, it poses great challenges to clustering. To overcome this challenges, researchers have developed many protocols for detecting cell clusters from scRNA-seq data. However, there are still deficiencies. In this paper, we propose a novel unsupervised clustering framework SDPUF, which integrates several effective single-cell data preprocessing procedures including filtering, normalization and dimension transformation, to eliminate the noise impact caused by sequencing technology limitations and biological factors. Moreover, the clustering results are two-dimensionalized. Finally, we identify cell clusters on the scRNA-seq data, and use the adjusted RAND index (ARI) to measure the accuracy of clustering and compare it with other classic clustering methods. The results are encouraging, it shows that SDPUF has a competitive advantage compared with existing methods.

Keywords: Single cell · Clustering · Normalization

1 Introduction

The emergence of high-throughput single-cell sequencing technology has changed the study of transcriptomics, allowing whole-genome expression analysis at single-cell resolution to reveal the heterogeneity of cell composition, which brings new insights into complex biological phenomena opportunity. Single cell sequencing technology is based on single-cellomics research, and large-scale single-cell data is measured, which can more fully reflect the more comprehensive gene expression of multicellular organisms. This makes it the primary choice for studying exciting biological processes such as gene expression variability between cells or tissues and early embryonic development, discovering novel medical insights and key clinical issues for effective clinical applications [1, 2, 3].

Generally, clustering is a common analysis method for single-cell data, which is used to help find the heterogeneity of cells or tissues, and also facilitates downstream

related analysis [4, 5]. A large number of calculation methods for clustering cell types based on cell transcriptome maps have been proposed. For example, the classical SC3 method [6], firstly, the distance matrix of cells was found through three similar calculation formulas, and then PCA and Laplace were used to realize the feature transformation. Then, the k-means method is reused to cluster several different types of projections to build consensus matrix. Finally, the consensus matrix is used for hierarchical clustering. Seurat [7] is a friendly interaction mode, which uses PCA for feature selection on highly variable genes to obtain statistically significant principal components, and uses t-SNE [8] to project it to Two-dimensional space. Finally, a density clustering algorithm is used to identify cell clusters. SNN-Cliq [9] is a graph-based clustering method that uses clique detection to cluster cells with scRNA-seq data. Since factions are usually rare in sparse graphs, SNN-Cliq will detect dense but not fully connected quasi-clique in SNN graphs. RcaReduce [10] is a method based on hierarchical clustering, which also uses PCA to reduce the dimension of gene expression matrix, and then continues to use K-means to obtain the mean and covariance matrix of different clusters, and iterate to meet the conditional principal components.

Single-cell RNA-Seq data cluster analysis often faces complex data calculation problems. Since single-cell RNA-Seq data usually has tens of thousands of dimensions, this leads to huge computational complexity and huge overhead of clustering problems. For this widely used dimensionality reduction method, there are PCA and t-SNE nonlinear dimensionality reduction method, such as the above mentioned method SC3 [6], Seurat [7], RcaReduce [10] also incorporates such dimensionality reduction methods. At the same time, due to the influence of biological experiments and sequencing technologies, the clustering method has poor clustering effect on scRNA-seq data. It is usually to filter some non-expressed genes or cells to eliminate the effect of noise. The filtering step will greatly remove the meaningless data and reduce the data scale to a certain extent. However, most of the existing problems have complicated calculations and sensitive parameter settings. Therefore, in order to overcome the above difficulties, we propose a novel unsupervised clustering framework, which can use scRNA-seq data to detect and visualize cell level heterogeneity and reveal a variety of interesting biological knowledge.

2 Materials and Method

2.1 Dataset Description

Yan [11]: This data is downloaded from the GEO website under the login number GSE36552. This data is from Yan et al., Which obtained the transcriptome information of 124 individual cells from pre-implantation embryos and human embryonic stem cells [1–4]. This data set includes each mouse embryo cell Developmental transcriptome information: oocyte cell samples ($n = 3$), zygote cell samples ($n = 3$), 2-cell cell samples ($n = 6$), 4-cell cell samples ($n = 12$), 8-cell samples ($n = 2$), Morula cell samples ($n = 26$) and late blastocyst at hatching stage cell samples ($n = 30$).

Biase [12]: The second data is downloaded from the GEO website through the login number GSE57249. This data is transcriptome information of 56 mouse samples obtained by Biase et al. through smart-seq protocol. This data set included transcriptome information for each developmental stage of mouse embryonic cells: zygote ($n = 9$), 2-cell-stage ($n = 20$), 4-cell-stage ($n = 20$), and blast stage ($n = 7$).

Goolam [13]: The last Goolam data is also from mouse embryonic stem cells and can be downloaded from <https://www.ebi.ac.uk/arrayexpress/experiments/E-MTAB-3321/>. This data was obtained by Scialdone et al. Through Smart-seq protocol, which are 2-cell-stage ($n = 16$), 4-cell-stage ($n = 64$), and 8-cell-stage ($n = 32$), 16-cell-stage ($n = 6$), blast-stage ($n = 6$).

2.2 Method Overview

The overview of the proposed framework is presented in Fig. 1, where whole pipeline is divided into three overlapping steps.

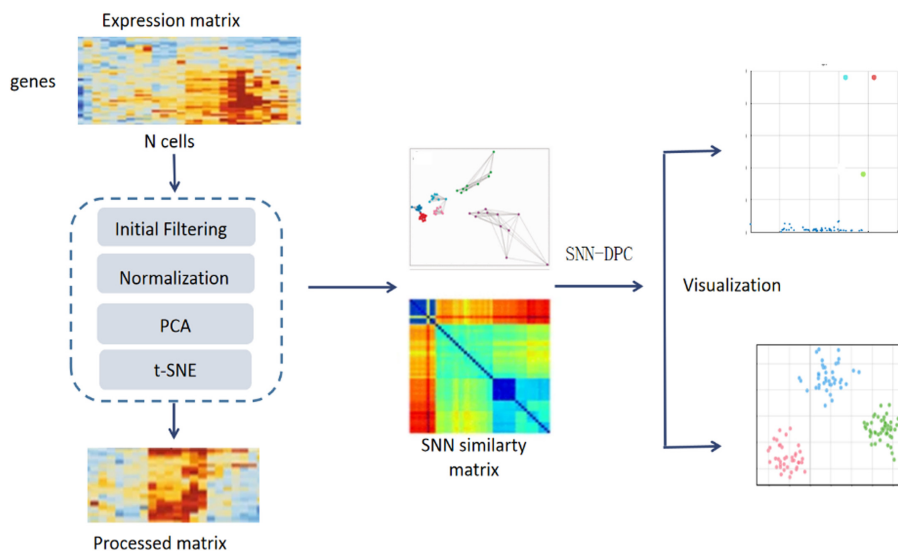


Fig. 1. Schematic of the framework.

As we all know, in recent years, single-cell data, researchers have gradually discovered that an important step of cluster analysis based on single-cell data is the pre-processing of the data, including filtering, normalization, feature transformation [6, 7]. We will get a meaningful data to prepare for subsequent analysis.

For most clustering methods, similarity measurement is a very important step. For example, hierarchical clustering and density clustering. However, studies have shown that commonly used similarity measures (such as Euclidean distance or cosine measure) will become less reliable as the dimensionality increases. The reason is that data becomes sparse in high-dimensional space, so the similarity between objects measured

by these indicators is usually low. Many clustering methods based on these measures are not effective enough for single-cell high-dimensional data with few objects. Here we use the clustering method is density peak clustering [14], this method is efficient and simple, using decision graphs, you can easily find the cluster center, but it does not perform well for high-dimensional data clustering. Therefore, consider using a density clustering based on the concept of shared nearest neighbors to realize single-cell data analysis. More specifically, there are literatures that show that in high dimensions [15], SNN metrics are more robust than related main metrics and lead to more stable performance. The similarity between two data points is captured by the connectivity of two nodes in the vicinity. Moreover, SNN technology has been successfully applied to some clustering problems [16]. Therefore, we define a new similarity based on the ranking of the shared neighborhood of two data points.

2.3 Data Preprocessing

In our proposed method, the pre-processing consists of four important steps.

Step1: Initial filtering.

There is a lot of noise in single-cell data sequencing techniques and biological properties, especially for clustering methods. Because the method is to classify similar cells into one group by calculating the similarity of expression levels between cells, the accuracy of clustering will be severely reduced by the large number of genes that are not meaningful for clustering. In order to effectively discover the heterogeneity of single-cell expression data, we filtered out rare and ubiquitous genes, and identified the most variable genes in the entire single-cell data set.

Step2: Normalization of scRNA-seq Data.

The transcriptome data has a technical deviation due to the sampling effect. In many normalization methods for batch gene expression, the above problems are solved by scaling the count data [7]. However, these methods are not suitable for scRNA-seq data, so in recent years, researchers have developed some normalization methods for scRNA-seq [8, 17]. In this paper, we use the Linnorm Rpackage [18] with default parameter Settings to normalize the data.

Step3: Reduce technical noise using PCA.

Prior to this, the data obtained in the preprocessing step was normalized, and then a few principal component information onto which the data was projected was selected to eliminate some of the technical noise of single-cell data in the data [19]. Although cell-type-specific expression patterns show strong genetic correlations, technical noise does not show any important correlation structures.

Step4: Reduce the dimension using t-SNE

In this step, we use the non-linear dimensionality reduction method t-SNE, which is commonly used in single-cell data, to reduce high-dimensional data to low-dimensional subspaces to achieve the purpose of reducing data size. The main parameter affecting the t-SNE method is perplexity, which is a smooth measure of the number of effective neighbors. Here, we set the default value of the confusion to 10 and use t-SNE to reduce the scRNA expression data obtained in the previous step to two dimensions.

2.4 SNN-Based Density Peaks Clustering

DPC is a new clustering algorithm based on density and distance. It is widely cited in various fields. This algorithm is based on the assumption that the cluster center density is surrounded by lower local density neighbors, and the distance between the cluster center point and the high density point is large. By calculating two important indicators describing each data point, its local density ρ_i the distance between each data point and the high density point δ_i , the heuristic method of the decision graph is used to identify the cluster center [20]. After the cluster center is selected, each remaining point will be assigned to the cluster where its nearest high density neighbor is located. The points are assigned to the designated cluster centers round by round, which makes the method fast and scalable for a variety of data sets. The local density δ_i of data object ρ_i and the cutoff distance are given by Eq. 1:

$$\rho_i = \sum_{i \neq j} \chi(d_{ij} - d_{cutoff}), \quad \chi = \begin{cases} 1, & x < 0 \\ 0, & x \geq 0 \end{cases} \quad (1)$$

Where, d_{ij} represents the distance between data points i and j , d_{cutoff} represents the cut-off distance, the meaning of χ . Formula is to find the number of data points whose distance from the first data point is less than the cutoff distance, and use it as The i -th data point is really dense. At this time, the distance between the data point i and the data point with higher local density can be defined by Eq. 2:

$$\delta_i = \begin{cases} \min(d_{ij}), & \text{if } \exists j. \text{s.t. } \rho_i > \rho_j \\ \max(\delta_i), & i \neq j \end{cases} \quad (2)$$

However, the density peak clustering algorithm directly calculates the distance and density between points, ignoring the influence of neighbors around the data points, and may cluster some complex data sets, and the results are not ideal. For example, single-cell data, cells do not exist independently, they interact with each other to a certain extent. Therefore, in order to make clustering more robust and objective, we used a density peak clustering algorithm based on shared nearest neighbors to cluster single-cell RNA sequence data [21]. This method introduces SNN similarity to consider the effect of nearest neighbor and shared neighbor information on local density. The available representation of SNN similarity is Eq. 3:

$$\text{Sim}(i, j) = |SNN(i, j)| \times \frac{1}{\frac{1}{|SNN(i, j)|} \sum_{P \in SNN(i, j)} (d_{ip} + d_{jp})} \quad (3)$$

Where, $SNN(i, j) = \Gamma(i) \cap \Gamma(j)$, which represents the common neighbor set of the shared neighbors of data points i and j , $\Gamma(i)$ and $\Gamma(j)$ represent the K number of points i and j , respectively set of nearest neighbors. d means that the local density ρ_i , which is the set of k points with the highest similarity to point i . The right part is the reciprocal of the average distance between data point i and data j to all their shared neighbors,

which represents the density around the two points within a certain range. The left part of the equation represents the number of shared neighbors of data point i and data point j . By simultaneously checking the shared neighbors and the density of two points, SNN similarity can improve the applicability of the clustering effect. For the SNN-DPC method, the calculation of ρ_i can be expressed by the Eq. 4:

$$\rho_i = \sum_{j \in L(i)} Sim(i, j) \quad (4)$$

Where, $L(i) = \{x_1, x_2, \dots, x_k\}$ represents the set of k points, which with the highest similarity to data point i . Then the calculation of δ_j can be expressed by the Eq. 5:

$$\delta_i = \begin{cases} \min \left[d_{ij} \left(\sum_{\mathcal{P} \in \Gamma(i)} d_{ip} + \sum_{\mathcal{P} \in \Gamma(j)} d_{iq} \right) \right], & \text{if } \exists j. s. t. \rho_i > \rho_j \\ \max(\delta_i), & j \in (X - i) \end{cases} \quad (5)$$

By drawing the calculated statistics (ρ_i, δ_i) on the decision chart, you can intuitively find the selection of potential cell types, where highdensity potential abnormal points are regarded as the center of the cluster. When the potential cluster center is identified, the remaining points are assigned to the nearest cluster center according to the nearest neighbor with higher density. After identifying the clusters, we can see in the decision map that the discovered cell types are visualized as different colors, show as Fig. 2.

2.5 Evaluation of Clustering Performance

Clustering algorithms often use an adjusted Rand index (ARI) to quantify how well our clustering results match another given set of labels. ARI ranges from 0 to 1. Given a set of n samples in the data and two clusterings of these samples, the overlap between the two groupings can be summarized in a contingency table, where each entry n_{ij} represents the number of samples in common between i -th group of the first clustering and the j -th group of the second clustering, and. The adjusted Rand index is defined as:

$$ARI = \frac{\sum_{ij} \binom{n_{ij}}{2} - \left[\sum_i \binom{a_i}{2} \sum_j \binom{b_j}{2} \right] / \binom{n}{2}}{\frac{1}{2} \left[\sum_i \binom{a_i}{2} + \sum_j \binom{b_j}{2} \right] - \left[\sum_i \binom{a_i}{2} \sum_j \binom{b_j}{2} \right] / \binom{n}{2}} \quad (6)$$

Where a_i and b_j are the sums of rows and columns of the contingency table respectively.

3 Results

3.1 Visualization of Clustering Results

Usually for scRNA-seq data, we try to describe the transcriptome data of each cell in the low-dimensional space without distortion, and have an intuitive interpretation of the data. Therefore, our method uses t-SNE to two-dimensionalize the clustering results.

Human Embryo Devel Cells. When detecting the center of the cluster, outliers with a higher density are regarded as potential cluster centers, which are visually displayed on the decision map. In particular, the selection of the k value of the data points will directly affect the clustering results of SDPUCF. Experience shows that the value of k performs well between 5–30. Through experiments, for Yan data, we set the value of k to 16. As shown in Fig. 2(b).

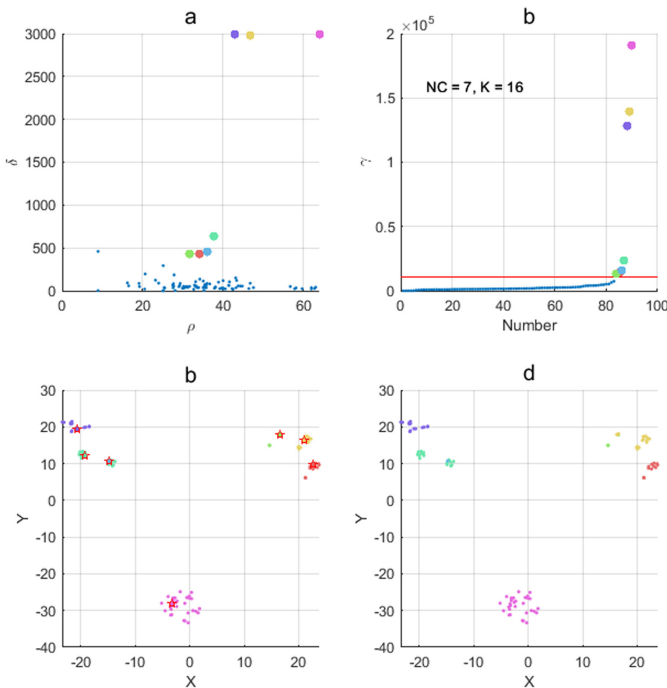


Fig. 2. Visual clustering results of Yan dataset

The 7 different colored abnormal points in Fig. 2(a) represent the cluster centers of 7 clusters, and the remaining points are data points to be allocated. Our method successfully detected yan data as oocyte, zygote, 2-cell, 4-cell, 8-cell, and late blastocyst at hatching stage. Seven types of cells were identified.

Mouse Embryo Devel Cells. Through experiments, for bias data, k value in the range of 5–15, can achieve the optimal clustering performance, we set the value of k to 7, as shown in Fig. 3(b). In Fig. 3(a), four outliers with different colors are identified, representing four cluster centers. In Fig. 3(c), we successfully completed the method of bias data detection, that is, zygote, 2 cells, 4 cells, blast identified four types of cell.

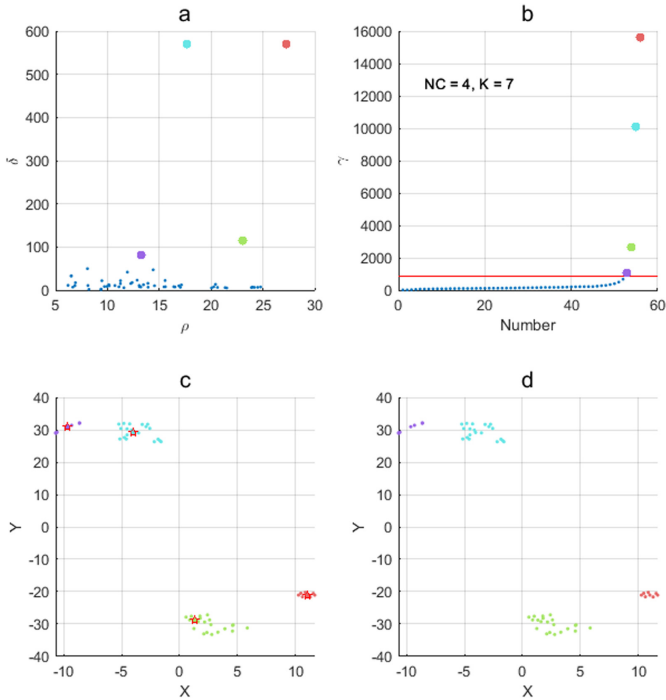


Fig. 3. Visual clustering results of Bias dataset

For the Goolam data (figure omitted), we set the value of k to 17, and finally marked five outliers with different colors to identify five types of cell clusters, namely the zygote, 2-cell, 4-cell, blast cell.

3.2 Compare with State-of-the-Art Approach

Analysis of Time Complexity. Most of the data we use in this article are small data sets, so the comparison with the running time of other methods is omitted. Here we analyze the time complexity analysis of several comparative methods to briefly discuss the computational performance of each algorithm.

PcaReduce [10] is an agglomerative hierarchical clustering approach with PCA which provides clustering results in a hierarchical. As a simple pipeline, SINCERA [22] uses hierarchical clustering and concentrated Pearsona’s age correlation, and the average

link method to identify cell types. SC3 [6] also applies the hierarchical clustering method to the consensus matrix obtained by combining the clustering results of k-means in the ensemble. The above several methods are based on agglomerative hierarchical clustering to reveal the relationship between cells/genes, but agglomerated hierarchical clustering has a higher time complexity, which is $O(N^3)$. Seurat [7] is based on Louvain algorithm to discover cell types. Louvain is a community detection algorithm that uses a greedy method to assign nodes to communities and update the network to obtain more coarse-grained representations. The time complexity of Louvain is $O(N\log N)$. The time complexity of the SUDPC algorithm is $(O(k + m)N^2)$, m is the number of cluster centers, k is the number of neighbors, and both k and m are relatively small in the experiment. Therefore, they will not affect the running time to a large extent. In summary, Seurat has the lowest time complexity among all comparison methods, while SUDPC has a slightly higher time complexity. Although the calculation performance of our algorithm is affected by other parameters to a certain extent. However, our clustering results are better than Seurat [7], as shown in Fig. 4, which makes up for the lack of computational performance of the method.

Analysis of Clustering Results. Here, we compare our proposed method with the most advanced four single-cell clustering methods. Including SC3 [6], Seurat [7], pcaReduce [10], SINCERA [21]. And use the ARI index to measure the performance of each clustering method show in Fig. 4.

It shows that for Biase data, our proposed method has a higher ARI score than SINCERA, which is 0.95. For Yan data, SDPUCF's ARI score is 0.85, while other clustering methods score far below 0.8. Even in the clustering in the class experiments, the clustering results generally fail the Goolam data. SDPUCF can also successfully identify 5 cell clusters, and the ARI score is 0.64. This reflects the superiority of SUDPC clustering performance.

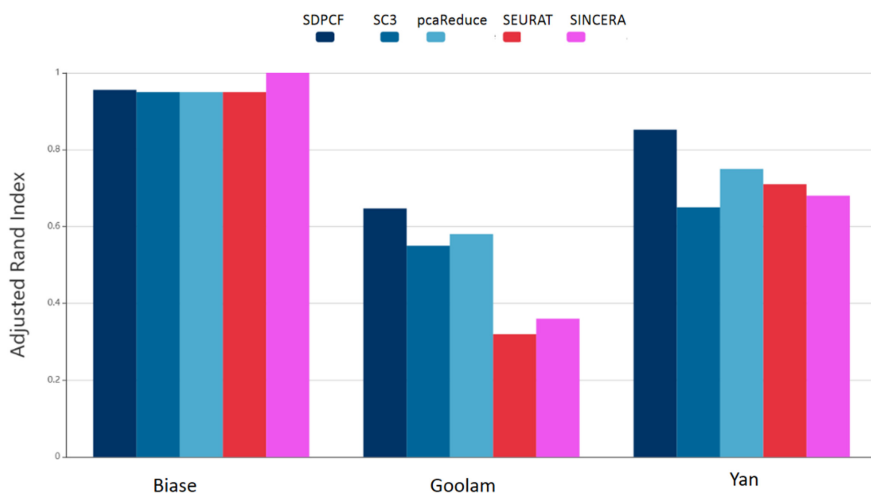


Fig. 4. The bar graph shows the display of ARI scores of five clustering methods on three single-cell sets.

4 Conclusion

In this paper, we propose a new unsupervised clustering framework to discover the heterogeneity of single-cell data. Our method integrates important procedures including filtering, normalization, feature selection, clustering, and visualization. It realizes effective pre-processing of high-dimensional, high-noise single-cell data, reduces the impact of sequencing technology and biological factors, and reduces the calculation complexity of the method. The nonlinear dimensionality reduction method is used to project the result into a low-dimensional space, which intuitively displays the identified cell clusters. Through experiments on the single-cell data set, using ARI to compare the experimental results with the most advanced single-cell clustering methods published, we have shown good clustering performance of our method to identify cell types.

Acknowledgements. This work was supported by Natural Science Foundation of China (Grant No. 61972141) and Natural Science Foundation of Hunan Province, China (Grant No. 2018JJ2053).

References

1. Wagner, A., Regev, A., Yosef, N.: Revealing the vectors of cellular identity with single-cell genomics. *Nat. Biotechnol.* **34**, 1145–1160 (2016)
2. Kolodziejczyk, A.A., Kim, J.K., Svensson, V., Marioni, J.C., Teichmann, S.A.: The technology and biology of single-cell RNA sequencing. *Mol. Cell* **58**, 610–620 (2015)
3. Jaitin, D.A., Kenigsberg, E., Keren-Shaul, H., Elefant, N., Paul, F., Zaretsky, I., et al.: Massively parallel single-cell RNA-seq for marker-free decomposition of tissues into cell types. *Science* **343**, 776–779 (2014)
4. Kharchenko, P.V., Silberstein, L., Scadden, D.T.: Bayesian approach to single-cell differential expression analysis. *Nat. Methods* **11**(7), 740 (2014)
5. Ji, Z., Ji, H.: Tscan: pseudo-time reconstruction and evaluation in single-cell rna-seq analysis. *Nucleic Acids Res.* **44**(13), e117 (2016)
6. Kiselev, V.Y., Kirschner, K., Schaub, M.T., Andrews, T., Yiu, A., Chandra, T., et al.: SC3: consensus clustering of single-cell RNA-seq data. *Nat. Methods* **14**, 483–486 (2017)
7. Macosko, E.Z., et al.: Highly parallel genome-wide expression profiling of individual cells using nanoliter droplets. *Cell* **161**(5), 1202–1214 (2015)
8. Maaten, L.V.D., Hinton, G.: Visualizing data using TSNE. *J Mach Learn Res.* **9**(Nov), 2579–2605 (2008)
9. Chen, X., Zhengchang, S.: Identification of cell types from single-cell transcriptomes using a novel clustering method. *Bioinformatics* **12**, 12 (2015)
10. Yau, C., et al.: Pcareduce: hierarchical clustering of single cell transcriptional profiles. *BMC Bioinf.* **17**(1), 140 (2016)
11. Yan, L., et al.: Single-cell RNA-seq profiling of human preimplantation embryos and embryonic stem cells. *Nat. Struct. Mol. Biol.* **20**(9), 1131–1139 (2013)
12. Biase, F.H., Cao, X., Zhong, S.: Cell fate inclination within 2-cell and 4-cell mouse embryos revealed by single-cell RNA sequencing. *Genome Res.* **24**(11), 1787–1796 (2014)
13. Goolam, M., et al.: Heterogeneity in Oct4 and Sox2 targets biases cell fate in 4-cell mouse embryos. *Cell* **165**(1), 61–74 (2016)

14. Rodriguez, A., Laio, A.: Clustering by fast search and find of density peaks. *Science* **344** (6191), 1492–1496 (2014). <https://doi.org/10.1126/science.1242072>
15. Houle, M.E., Kriegel, H.-P., Kröger, P., Schubert, E., Zimek, A.: Can shared-neighbor distances defeat the curse of dimensionality? In: Gertz, M., Ludäscher, B. (eds.) *SSDBM 2010. LNCS*, vol. 6187, pp. 482–500. Springer, Heidelberg (2010). https://doi.org/10.1007/978-3-642-13818-8_34
16. Ertöz, L., et al.: Finding clusters of different sizes, shapes, and densities in noisy, high dimensional data. In: *Proceedings of 2nd SIAM International Conference on Data Mining* (2003)
17. Jiang, L., Chen, H., Pinello, L., Yuan, G.C.: GiniClust: detecting rare cell types from single-cell gene expression data with Gini index. *Genome Biol.* **17**, 144 (2016)
18. Yip, S.H., Wang, P., Kocher, J.-P.A., Sham, P.C., Wang, J.: Linnorm: improved statistical analysis for single cell RNA-seq expression data. *Nucleic Acids Res.* **45**(22), e179 (2017)
19. Kristofer, D., Jasper, J., Duygu, K., et al.: A single-cell transcriptome atlas of the aging drosophila brain. *Cell* **174**(4), 982–998 (2018)
20. Xu, J., Wang, G., Deng, W.: DenPEHC: density peak based efficient hierarchical clustering. *Inf. Sci.* **373**, 200–218 (2016)
21. Liu, R., Wang, H., Yu, X.: Shared-nearest-neighbor-based clustering by fast search and find of density peaks. *Inf. Sci. Int. J.* **450**, 200–226 (2018)
22. Guo, M., Wang, H., Potter, S.S., Whitsett, J.A., Xu, Y.: SINCERA: a pipeline for single-cell RNA-Seq profiling analysis. *PLoS Comput. Biol.* **11**, e1004575 (2015)



Two-Stage Learning Brain Storm Optimizer

Yan Xu¹, Jingwei Wang^{1(✉)}, Lianbo Ma^{1(✉)}, Junfeng Zhao²,
and Xiaolong Shen²

¹ College of Software, Northeastern University, Shenyang, China
jingwei.wang2018@outlook.com, malb@swc.neu.edu.cn
² 2012 Laboratories, Huawei Technologies Co., Ltd., Shenzhen, China

Abstract. Brain storm optimizer (BSO), a new swarm intelligence paradigm inspired from the human brainstorming process, have received a surge of attentions. However, the original BSO easily suffers from the premature convergence due to its ineffective solution generation operation. In this paper, a two-stage learning strategy is proposed to accelerate the efficiency of the solution generation operation in BSO, thereby enhancing the convergence speed as well as the diversity of population. At the first stage, a learning automaton strategy is conducted to select an appropriate learning exemplar to guide the updating of each solution (i.e., idea). This strategy learns from the feedback information from the environment to enhance the exploration and exploitation. At the second stage, a comprehensive learning strategy is used to generate a set of directional learning exemplars, using utilize useful search experiences during the search. The experimental results on a set of CEC2017 benchmarks validate the effectiveness of the proposed strategy. Then, the resultant algorithm called ACLBSO is applied to resolving the quantitative association rule mining problem. Simulation results show that ACLBSO is a satisfactory optimizer to deal with the complex association rule mining problems.

Keywords: Brain storm optimization · Comprehensive learning · Swarm intelligence · ACLBSO · Association rule mining

1 Introduction

Brain storm optimization (BSO) is a young yet promising Swarm intelligence paradigm [1], which is based on the simulation of the brainstorming process of human beings solving complex tasks [2]. In BSO, a population of ideas, i.e., solutions in the optimization, are evolved via the convergent operation and divergent operation in a cooperative manner. At the convergent stage, the population is divided into a number of clusters. The best individual in each cluster is regarded as a cluster center. At the divergent stage, a number of ideas termed as Sold ideas are generated by using cluster information including one inter-cluster idea and two intra-cluster ideas, and then a Gaussian-based random search is imposed on each Sold to generate a new idea Snew. In a sense, the convergent operation provides cluster information, which is used to guide the exploration and exploitation search in the divergent operation. Note that, the clustering information can reveal the problem's landscapes in an extent, since the clusters can be viewed as a set of local-optima regions and the information of good

ideas can be propagated from one cluster to another cluster [3]. However, such clustering information has not been exploited thoroughly, making the algorithm suffer from premature convergence. The reasons are as follows:

First, the construction of Sold (as shown in Eq. (2) in Sect. 2-A) is rather simple, just depending on a linear summation of ideas from one or two clusters, which neglects the effect of bad dimensions in the cluster information. Each parent idea used to generate Sold has some good dimensions as well as some bad dimensions, and unfortunately these bad dimensions may have a greater impact on Sold than the good ones. This may cause the evolution stagnation or degeneration of individuals, which makes BSO easily trapped into local optima. Second, the search equation of generating a new idea Snew (as shown in Eq. (3) in Sect. 2-A) in BSO is a blind disturbance operator, only offering random noise on each dimension of Sold, thus it lacks of an directional guidance, being poor at exploitation.

Many studies [4–6] have demonstrated that learning automata (LA) and comprehensive learning (CL) are effective improvement strategies for SI algorithms to enhance the search ability of exploration and exploitation, and have been adopted in some algorithms, such as PSO [7–9], GA [10], DE [11], ABC [12].

In this paper, a two-stage learning strategy based on comprehensive learning and learning automata is proposed to accelerate the efficiency of the solution generation operation in BSO. In this way, the convergence speed and diversity of population can be enhanced. At first, comprehensive learning is used to generate a set of directional learning exemplars, by using utilize useful search experiences during the search. Then, learning automation is performed to determine appropriate exemplar to guide the updating of each solution. In this process, the feedback information from the environment is learnt to enhance the exploration and exploitation. The main contributions of the work include:

- A two-stage learning strategy is proposed to accelerate the efficiency of the solution generation operation in BSO. In this way, the exploration and exploitation search can be enhanced in a learning manner. The effectiveness and efficiency of the proposed strategy are validated experimentally on a set of benchmarks.
- The resultant algorithm is applied to ARM problem. Simulation results on a set of real-world ARM test instances show the effectiveness of the proposed approach.

The rest of this paper is organized as follows. Section 2 reviews the related work. Section 3 describes the proposed strategy and the resultant algorithm in detail. Section 4 gives the benchmark test. Section 5 presents the application of the proposed algorithm on ARM problems. Section 6 outlines the conclusion.

2 Related Work

2.1 Brain Storm Optimization Algorithm

BSO was proposed by Shi [2] in 2011, inspired from the brainstorming process in human beings solving complex task. In BSO, each idea represents a solution of

problem, a population of ideas are first initialized randomly. Afterwards, the main procedures are as follows:

- 1) Idea clustering. All ideas are clustered into a number of clusters using K-means. The best idea in each cluster is selected as the cluster center.
- 2) Cluster center disruption. A cluster center $C_j^k = [C_{j1}^k, C_{j2}^k, \dots, C_{jD}^k]$ is randomly selected, and it is updated by a new idea $Q = [q_1, q_2, \dots, q_D]$ with a probability of P_{r1} , as

$$C_{jd}^k = \begin{cases} q_d, & \text{if } \text{rand} < P_{r1} \\ C_{jd}^k, & \text{elsewise} \end{cases}, d \in \{1, 2, \dots, D\} \quad (1)$$

- 3) Idea updating: Each parent idea $S_{old}^k = [S_1^k, S_2^k, \dots, S_D^k]$ is constructed based on one or two clusters with a predetermined possibility.
 - a) S_{old} is generated based on one cluster. The preset possibility pch is computed by

$$pch = \frac{f(c_j^k)}{\sum_{m=1}^M F(c_m^k)} \quad (2)$$

where $F(\cdot)$ is the fitness function, c_j^k and c_m^k are the selected centers of the clusters j and m , respectively.

Then, for an idea $\Psi^k = [\Psi_1^k, \Psi_2^k, \dots, \Psi_D^k]$, which is selected randomly from cluster j , solution $S_{old}^k = [S_{old1}^k, S_{old2}^k, \dots, S_{oldD}^k]$ is constructed by

$$S_{old}^k = \begin{cases} C_{jd}^k, & \text{if } \text{rand} < P_{r2} \\ \Psi_d^k, & \text{elsewise} \end{cases}, d \in \{1, 2, \dots, D\} \quad (3)$$

where C_{jd}^k is the d th dimension of the cluster center C_j^k , and Ψ_d^k is the d th dimension of Ψ^k , and P_{r2} is a preset probability, which is proportional to the size of cluster j .

- b) S_{old} is generated based on two clusters. Two clusters j and h are selected randomly from M clusters by the possibility pc defined in Eq. (1). Then, $S_{old}^k = [S_1^k, S_2^k, \dots, S_D^k]$ is generated using a linear summation approach, which is

$$S_{old}^k = \begin{cases} r_d C_{jd}^k + (1 - r_d) C_{hd}^k, & \text{if } \text{rand} < P_{r3} \\ r_d \Psi_d^k + (1 - r_d) \phi_d^k, & \text{elsewise} \end{cases}, d \in \{1, 2, \dots, D\} \quad (4)$$

Where $C_j^k = [C_{j1}^k, C_{j2}^k, \dots, C_{jD}^k]$ and $C_h^k = [C_{h1}^k, C_{h2}^k, \dots, C_{hD}^k]$ are two centers of the clusters j and h , respectively, C_{jd}^k and C_{hd}^k are the d th dimensions of C_j^k and C_h^k , respectively, $\Psi^k = [\Psi_1^k, \Psi_2^k, \dots, \Psi_D^k]$ and $\phi^k = [\phi_1^k, \phi_2^k, \dots, \phi_D^k]$ are two different

parent ideas selected randomly from the clusters i and h , respectively, Ψ_{jd}^k and ϕ_{hd}^k are the d th dimensions of Ψ_j^k and ϕ_h^k , respectively, and r_d is a random value uniformly distributed in $[0, 1]$.

- 4) Idea updating: Random disturbances are added on S_{old} to form a new idea S_{new} (i.e., S_i^{k+1}), as following:

$$S_{newd}^{k+1} = S_{oldd}^{k+1} + \xi \eta_d(\mu, \sigma) \quad (5)$$

where S_{newd}^{k+1} is the d th dimension of a new idea S_{new} , S_{oldd}^k is the d th dimension of S_{old} , η_d is a Gaussian random function with a mean μ and variance σ , $\xi(k)$ is a step size for η_d .

Then, the newly generated ideas are compared with the old ideas and the better ones survive into the next generation.

2.2 Learning Automata (LA)

Learning automaton (LA) is an adaptive decision-making machine, also as an effective reinforcement learning method, aiming to select the current action based on past experiences from the random environment. Figure 1 shows how the automaton interacts with its corresponding environment and receives reward and penalty signals. Detailed formulations of LA are provided in [13].

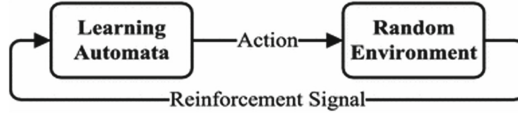


Fig. 1. The interaction between learning automata and environment

2.3 Comprehensive Learning Strategy

Algorithm 1 shows the main procedure of comprehensive learning (CL) [9]. In comprehensive learning (CL), individuals are allowed to have chance to learn from the search experience from the best individual in the population and the information of the best dimension of other individuals. In this way, individuals are able to learn from the useful experiences from best individual, itself and other ordinary individuals. In this process, a learning probability P_c is used to determine the probability of learning from the individual i self, which is:

$$P_{c_i} = 0.05 + 0.45 \frac{\exp\left(\frac{10(i-1)}{\text{pop}-1}\right) - 1}{\exp(10) - 1} \quad (6)$$

where pop is the size of population, and i is the index of current individual. A smaller P_c value indicates a smaller probability of learning from the dimension of the individual itself.

3 The Proposed Algorithm

3.1 Dynamic Learning Probability Pc for Each Idea

In the original comprehensive learning process, as shown in Eq. (6), the probabilities are fixed according to the idea's index during the search. This may be inefficient to deal with the dynamics of the population. Intuitively, P_{ci} needs to be adaptive to the quality of the idea, rather than the index of idea. Therefore, it is essential that P_{ci} needs to be set to be large for an idea with better fitness.

Algorithm1 Comprehensive learning

Input: P(Refer set), popu(current population), k (current index of idea)

D (the dimension of the idea)

Output: LE (learning example of current idea)

1. $d=1$;
 2. While $d \leq D$
 3. If $\text{rand()} < P_{ci}$;
 4. Randomly choose two ideas p_1, p_2 in P;
 5. If $\text{fitness}(p_1) > \text{fitness}(p_2)$
 $LE^d = p_1^d$
 6. Else
 $LE^d = p_2^d$
 7. end if
 8. Else
 9. $LE^d = \text{popu}_k^d$
 10. End if
 11. $d=d+1$
 12. End while
 - 13 if $LE == \text{popu}_k$
 14. $D_{rand} = \text{rand()} * D$
 15. $P_{rand} = \text{rand()} * \text{Size}(\text{popu})$
 16. $LE^{D_{rand}} = \text{popu}_{P_{rand}}^{D_{rand}}$
 17. end-if
 18. **Return** LE
-

Algorithm 2 Fitness-based grouping

Input: m(the number of cluster), popu(current population)

1. Rank ideas according to fitness in descending order
 2. for each idea i in popu do
 3. $g = (i-1) \% m + 1$
 4. Add idea i to group g
 5. calculate the value of the P_c
 6. end for
-

3.2 LA to Construct the Learning Example

In original BSO algorithm, the idea updating operator of Eq. (5) is a random search operator, only generating a random disturbance on each dimension of X_{old} . The Gaussian random function is used to perform a random local search around X_{old} . However, the optimal search directions of dimensions of X_{old} are usually different from each other. Due to the lack of necessary direction guidance, Eq. (5) is inefficient at exploitation. To solve the above issue, we use the comprehensive learning to generate ideas' direction vector LE. Accordingly, the updating equation is designed as follow:

$$X_{old}^d = X_{old}^d + rand_i^d \left(LE_{fi(d)}^d - X_{old}^d \right) \quad (7)$$

where $fi = [fi(1), fi(2), \dots, fi(D)]$ defines which ideas' learning example the idea i should follow. $LE_{fi(d)}^d$ is the corresponding dimension of any ideas in the population. Therefore, the selection of refer set P (Algorithm 1) is particularly important. The selection of different refer sets directly affects the process of algorithm exploitation and exploration.

Figure 2 shows two situations. If the cluster center idea Cbest and the global best idea Gbest are on opposite sides of the idea's current position X (as shown in Fig. 2a), the Cbest and Gbest may make idea X oscillate. However, if we just focus on the Gbest's information, the idea X will be dragged in a local optimum region, as in Fig. 2a. When Cbest and Gbest are on the same side of the X's current position (Fig. 2b), the idea X may be led to a local optimum region. the idea X may be able to move in the opposite direction towards the global optimum region by learning from a neighbor idea X_N, as in Fig. 2b. In these situations, each idea (or individual) may need a different learning exemplar to correct the direction of current evolution, which is more flexible to search for multiple local optima. Therefore, we propose a learning-based strategy for BSO. In this strategy, a learning automaton (LA) is mounted on each individual, and a set of LAs optimizes the process of generation of ideas learning examples. Especially the LA makes interactions with the environment and receives their reinforcement signal from individuals.

3.3 Main Framework

By integrating the above strategies, Algorithm 3 presents the main framework of ACLBSO. In ACLBSO. The population is clustered by using an objective-fitness-based grouping. Meanwhile, Changing the learning probability P_{ci} dynamically depends on idea's own fitness can help better ideas keep their own features and properties and help the worse ideas have more chance to learn other idea with better fitness (Line 4) and then distinguish ordinary ideas from cluster central ideas. (Line 5). At the first stage, a learning automaton (LA) is mounted on each idea (Line 7), we use learning automata to choose the way to exploration or exploration. At the second stage, we use the comprehensive learning method to construct learning exemplar (Lines 9–10), in order to keep the better search ability and diversity of population. For exploitation, we use the information of cluster centers to construct learning example, to improve convergence

speed. For exploration, to avoid being prone to local optimum. we use original ideas' dimension information to construct learning example to improve the diversity.

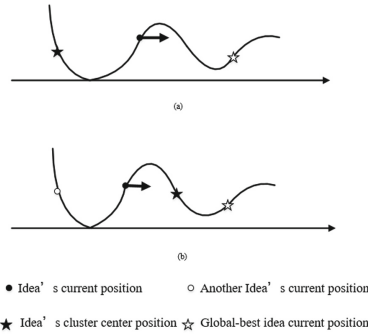


Fig. 2. The Example in a multimodal function

Algorithm 3 Main procedures of ACLBSO

- 1: Randomly initialize population P^0
 - 2: **While** $k < \text{Max_FEs}$ **do**
 - 3: Evaluate all individuals in P^k
 - 4: The clustering process and calculate Pc_i using Algorithm 2
 - 5: $\text{nor_popu} = P^0(\text{centers} = 0)$;
 - 6: for each idea i_idea in P^0 do
 - 7: Select an action of LA_i
 - 8: Switch(action)
 - 9: Case 1: $\text{indi_direction} = \text{Algorithm 1 is activated}(\text{centers}, P^0, i)$
 - 10: Case 2: $\text{indi_direction} = \text{Algorithm 1 is activated}(\text{nor_popu}, P^0, i)$
 - 11: If $\text{rand}() < P_{\text{one-cluster}}$ then
 - 12: Select a cluster
 - 13: choose cluster center or normal individual to generate new individual named $nIdea$
 - 14: else
 - 15: Select *two* cluster
 - 16: choose cluster center or normal individual to generate new individual named $nIdea$
 - 17: end if
 - 18: $nIdea = nidea + \text{rand}() * (\text{indi_direction} - nidea) + \xi * N(0, 1)$
 - 19: if $\text{fitness}(nidea) < \text{fitness}(i_idea)$
 - 20: $i_idea = nidea$;
 - 21: update LA ;
 - 22: end
 - 23: End for
 - 24: Update population
 - 25: **End While**
-

4 Benchmark Test

4.1 Parameter Settings and Test Functions

To validate the performance of ACLBSO, we test it on a set of 15 benchmark functions from CEC2017 test suits including unimodal function F1, multimodal functions F4, F5, F6, F7, F8, F9, F10, hybrid functions F12, F14, F16, F18, and composition functions F24, F27, F30. Parameters of the involved test functions follow the settings suggested in [18]. All algorithms use the same population size n and the same number of cluster m , where n is set to 100 and m is set to 5. All the algorithms run 30 times on each benchmark function with dimensions 30. The maximum number of function evaluations is set to 300,000. The ACLBSO is compared against several state-of-the-art BSOs, including BSO [2], PPBSO [14], MBSO [15], SBSO [16] and BSOLS [17]. Their parameters follow the default settings in their original references [2, 14–17].

4.2 Parameter Settings and Test Functions

Table 1 reports the mean and SD results obtained by BSO, PPBSO, MBSO, SBSO, BSOLS and ACLBSO on the test instances with 30 dimensions. From the table, it can be clearly observed that ACLBSO obtains the best overall performance, especially on the multimodal functions such as F4, F5, F6, F7, F8, F9, F10. ACLBSO obtains first ranks on all the 30-D test instances. The superior performance of ACLBSO may be due to the two-stage learning strategy, which reasonably uses the useful dimensional information of other ideas to help the algorithm avoid falling into the local optimal. For unimodal function F1, ACLBSO performs several orders of magnitude better than compared algorithms. This is mainly because that the information of the cluster center ideas is helpful to speed up the mining ability. On the hybrid and composite functions F12, F14, F16, F18, whose variables are randomly divided into several subcomponents, ACLBSO always ranked first or second. These observations show that the proposed two-stage learning strategy indeed improves the performance of ACLBSO on complex single objective optimization.

Table 1. Results of ACLBSO, origin BSO and other BSO variants algorithm with 30D

| Function | ACLBSO | BSO | PPBSO | MBSO | SBSO | BSOLS | |
|----------|--------|-----------------|----------|-----------|-----------|----------|-----------|
| F1 | Mean | 9.02E+03 | 5.88E+07 | 1.41E+07 | 2.44E+07 | 2.77E+10 | 4.32E+08 |
| | Std | 3.29E+03 | 5.88E+07 | 1.41E +07 | 2.34E+06 | 3.47E+09 | 2.29E +08 |
| | Rank | 1 | 4 | 2 | 3 | 6 | 5 |
| F4 | Mean | 4.89E+02 | 6.03E+02 | 4.98E+02 | 4.92E+02 | 1.51E+03 | 5.54E +02 |
| | Std | 1.78E+00 | 5.31E+00 | 2.31E+01 | 7.81E+00 | 2.88E+02 | 5.44E+01 |
| | Rank | 1 | 5 | 3 | 2 | 6 | 4 |
| F5 | Mean | 5.69E+02 | 5.88E+07 | 1.41E+07 | 2.44E+07 | 2.77E+10 | 4.32E +08 |
| | Std | 3.29E+03 | 5.88E+07 | 1.41E+07 | 2.34E +06 | 3.47E+09 | 2.29E+08 |
| | Rank | 1 | 4 | 2 | 3 | 6 | 5 |

(continued)

Table 1. (continued)

| Function | ACLBSO | | BSO | PPBSO | MBSO | SBSO | BSOLS |
|----------|--------|-----------------|-----------------|------------------|-----------|-----------|-----------|
| F6 | Mean | 6.01E+02 | 6.55E+02 | 6.50E+02 | 6.34E +02 | 6.48E+02 | 6.50E+02 |
| | Std | 1.13E-01 | 9.94E-01 | 5.52E+00 | 3.23E+00 | 4.91E-01 | 2.53E+00 |
| | Rank | 1 | 6 | 5 | 2 | 3 | 4 |
| F7 | Mean | 7.72E+02 | 1.32E+03 | 1.23E+03 | 1.01E+03 | 1.23E +03 | 1.20E+03 |
| | Std | 6.72E+00 | 2.52E+01 | 2.05E +01 | 9.57E+00 | 4.13E+01 | 1.33E+02 |
| | Rank | 1 | 6 | 4 | 2 | 5 | 3 |
| F8 | Mean | 8.80E+02 | 9.78E+02 | 1.02E+03 | 9.40E +02 | 9.61E+02 | 9.95E+02 |
| | Std | 1.49E+01 | 9.45E+00 | 3.23E +01 | 8.31E-01 | 5.47E+00 | 1.44E+01 |
| | Rank | 1 | 4 | 6 | 2 | 3 | 5 |
| F9 | Mean | 9.01E+02 | 3.93E+03 | 4.31E+03 | 6.70E +03 | 4.11E+03 | 4.86E+03 |
| | Std | 7.82E-01 | 5.19E+02 | 1.48E +02 | 5.25E+02 | 3.37E+02 | 7.90E+02 |
| | Rank | 1 | 2 | 4 | 6 | 3 | 5 |
| F10 | Mean | 2.99E+03 | 6.03E+03 | 5.62E+03 | 4.86E+03 | 4.26E+03 | 6.26E+03 |
| | Std | 1.00E+02 | 5.40E+02 | 6.29E+02 | 2.22E+02 | 6.04E +01 | 7.61E +01 |
| | Rank | 1 | 5 | 4 | 3 | 2 | 6 |
| F12 | Mean | 5.08E+07 | 4.65E+07 | 6.99E+07 | 1.48E+08 | 1.75E+09 | 7.06E+07 |
| | Std | 1.45E+07 | 1.79E+07 | 2.87E+07 | 6.25E +07 | 1.49E+09 | 2.72E+07 |
| | Rank | 2 | 1 | 3 | 5 | 6 | 4 |
| F14 | Mean | 3.52E+04 | 3.79E+04 | 1.87E +03 | 2.12E+05 | 8.57E +04 | 5.24E+04 |
| | Std | 1.05E +03 | 2.10E+04 | 6.24E+01 | 2.59E+04 | 3.21E+04 | 4.82E+04 |
| | Rank | 2 | 3 | 1 | 6 | 5 | 4 |
| F16 | Mean | 2.40E+03 | 2.63E +03 | 3.19E+03 | 3.70E+03 | 2.84E+03 | 3.30E+03 |
| | Std | 6.71E+00 | 1.21E+02 | 1.31E +02 | 1.49E+02 | 2.79E+02 | 5.24E+01 |
| | Rank | 1 | 2 | 4 | 6 | 3 | 5 |
| F18 | Mean | 3.64E+05 | 1.60E+06 | 4.57E+05 | 3.53E+06 | 1.17E+06 | 7.20E +05 |
| | Std | 8.18E+04 | 5.55E+05 | 2.38E+04 | 1.73E+06 | 8.00E+05 | 3.68E+05 |
| | Rank | 1 | 5 | 2 | 6 | 4 | 3 |
| F23 | Mean | 2.99E+03 | 4.41E+03 | 3.45E+03 | 3.03E+03 | 4.40E+03 | 4.76E +03 |
| | Std | 5.68E+01 | 1.13E+01 | 2.05E+01 | 8.20E+01 | 4.59E +02 | 3.94E +02 |
| | Rank | 1 | 5 | 3 | 2 | 4 | 6 |
| F27 | Mean | 3.59E+03 | 5.04E+03 | 3.20E +03 | 3.21E +03 | 5.16E+03 | 5.26E+03 |
| | Std | 5.17E+01 | 5.43E+02 | 1.54E-05 | 7.83E+00 | 2.60E+00 | 2.94E +02 |
| | Rank | 3 | 4 | 1 | 2 | 5 | 6 |
| F30 | Mean | 1.52E+06 | 1.42E+06 | 1.02E+04 | 6.90E+06 | 3.69E+06 | 9.77E+05 |
| | Std | 7.05E+05 | 2.81E+05 | 3.13E+03 | 1.27E+06 | 1.63E+06 | 5.96E+05 |
| | Rank | 4 | 3 | 1 | 6 | 5 | 2 |

5 Real-Word Application: Association Rule Mining

5.1 Association Rule Mining

Association rules (AR) are used to represent and identify dependencies between items in a dataset [22]. They are expressions of the type $X \rightarrow Y$, where X and Y are sets of items, and $X \cap Y = \emptyset$. There are many previous studies of mining association rules that

mainly focus on datasets with binary or discrete values [19–21]. However, there are usually quantitative data in real-world applications, and accordingly the quantitative association rules (QAR) have become a challenging task to be tackled [24].

5.2 Association Rule Mining

There are four objective functions which should be optimized in model of QAR [23], namely support(fsup) [22], confidence(fconf) [22], CF(fcf) [25], and Combined Measure(fm).

Combined Measure (fm)

In this paper, the overall optimal solution for QAR is represented by a linear combination of the four objective functions:

$$f_m = \sum_{i=1}^3 \frac{w_i f_i}{f_{i\max}}; w_1 + w_2 + w_3 = 1, w_i > 0 \quad (8)$$

where f_i is the objective function for the i th requirement normalized to its maximum value $f_{i\max}$. The normalization is necessary because these four objectives represent non-homogeneous quantities and are very different in values.

The real-world dataset used here is the called Stock Prince dataset, which is available in the repository KEEL-dataset [26]. This dataset consists of 10 real attributes and 950 examples. In this experiment, the comprehensive learning PSO algorithm, i.e., CLPSO, and two basic SI algorithms, i.e., BSO and PSO, are adopted for ARM optimization to compare with the proposed ACLBSO algorithm.

5.3 Result

All involved algorithms are first tested on the three objective functions (fsup, fconf, and fcf), respectively. Then, the test of the combined objective function fm is implemented. The weighted coefficients used in this instance are set as $w_1 = 0.4$, $w_2 = 0.3$, and $w_3 = 0.3$, which can be regulated according to the demand of different users. The results consisting of the best, worst, mean and standard deviation of the optimal solutions over 20 sample runs are listed in Table 2. The average measure values (i.e., fsup, fconf, fcf and fm) of the top 10 association rules generated by each algorithm are shown in Table 3. It is apparent that ACLBSO presents an obvious improvement over its counterparts CLPSO, BSO and PSO for support (fsup) and confidence (fconf) and combined measure (fm). It can be seen that the comprehensive learning strategy can improve the accuracy of confidence. Both ACLBSO and CLPSO that use comprehensive learning can obtain the most optimal result (0) on CF, which prevents misleading rules that are not detected by confidence.

Table 2. The measure values obtained by each algorithm on the dataset

| Obj | f_m | | | | f_{sup} | | | | f_{conf} | | | | F_{cf} | | | |
|--------|--------------|--------------|--------------|--------------|--------------|--------------|--------------|--------------|------------|----------|----------|-------|----------|-------|-------|-------|
| | Max | Min | Mean | Std | Max | Min | Mean | Std | Max | Min | Mean | Std | Max | Min | Mean | Std |
| PSO | 1.947 | 1.646 | 1.765 | 0.159 | 0.335 | 0.001 | 0.136 | 0.176 | 1.11 | 0.981 | 0.993 | 0.010 | 1 | 0.967 | 0.989 | 0.018 |
| CLPSO | 1.988 | 1.730 | 1.848 | 0.130 | 0.689 | 0.601 | 0.507 | 0.159 | 1 | 1 | 1 | 0 | 0 | 0 | 0 | 0 |
| BSO | 1.855 | 1.038 | 1.511 | 0.423 | 0.597 | 0.015 | 0.332 | 0.294 | 1 | 0.535 | 0.845 | 0.268 | 0.488 | 0 | 0.162 | 0.282 |
| ACLBSO | 1.986 | 1.858 | 1.920 | 0.063 | 0.728 | 0.388 | 0.662 | 0.063 | 1 | 1 | 1 | 0 | 0 | 0 | 0 | 0 |

Table 3. The average measure values of the top 10 association rules generated by each algorithm on the dataset

| Obj | f_m | | | | f_{sup} | | | | f_{conf} | | | | F_{cf} | | | |
|--------|--------------|--------------|--------------|--------------|--------------|--------------|--------------|--------------|------------|--------------|--------------|--------------|----------|-------|-------|-------|
| | Max | Min | Mean | Std | Max | Min | Mean | Std | Max | Min | Mean | Std | Max | Min | Mean | Std |
| PSO | 1.535 | 0.465 | 1.198 | 0.709 | 0.315 | 0.010 | 0.122 | 0.167 | 0.925 | 0.195 | 0.590 | 0.368 | 0.089 | -0.50 | 0.305 | 0.723 |
| CLPSO | 1.428 | 1.262 | 1.341 | 0.083 | 0.270 | 0.297 | 0.246 | 0.037 | 0.9 | 0.805 | 0.838 | 0.053 | 0 | -0.05 | -0.01 | 0.034 |
| BSO | 1.618 | 0.485 | 1.116 | 0.577 | 0.360 | 0.033 | 0.193 | 0.163 | 1 | 0.170 | 0.658 | 0.434 | 0 | -0.37 | -0.15 | 0.194 |
| ACLBSO | 1.882 | 1.381 | 1.474 | 0.081 | 0.379 | 0.177 | 0.340 | 0.041 | 0.903 | 0.826 | 0.871 | 0.039 | 0.033 | 0 | 0.011 | 0.019 |

6 Conclusion

This paper proposes a two-stage learning strategy for BSO to enhance its effectiveness and efficiency and then develops an enhanced BSO variant called ACLBSO. This two-stage learning strategy is based on the principle of reinforcement learning, aiming to learn from the feedback information from the environment to enhance the exploration and exploitation. At the first stage, the learning automaton is utilized to choose the way to exploration or exploitation for guide the updating of each solution. At the second stage, a comprehensive learning strategy is used to generate a set of directional learning exemplars.

Experiments have been conducted on a set of the CEC2017 benchmark functions where ACLBSO is compared with several art-of-the-state BSO algorithms. Experimental results demonstrate that the ACLBSO is a powerful optimizer, doing better than other BSO algorithms in terms of the accuracy and convergence on multimodal and unimodal test problems, and it also obtains satisfactory results on more complex hybrid and composition functions.

Experiments have been conducted on a real-world application of association rule mining, and comparison results have shown that ACLBSO indeed obtains significant improvements over BSO and its variants. the proposed approach using ACLBSO exhibits a significant potential to deal with the QAR problems, in terms of solution accuracy and computation efficiency. In the future, BSO algorithms should be added to try association rules and other application problems.

Acknowledgment. This work was supported in part by National Natural Science Foundation of China under Grant No. 61773103 and Huawei HIRP project under No. HO2019085002.

References

1. Kennedy, J., Eberhart, R.C., Shi, Y.H.: *Swarm Intelligence*. Morgan Kaufmann, San Mateo (2001)
2. Shi, Y.: Brain storm optimization algorithm. In: *Proceedings of 2nd International Conference Swarm Intelligence*, Chongqing, China, 12–15 June 2011, pp. 303–309 (2011)
3. Ma, L., Cheng, S., Shi, Y.: Enhancing learning efficiency of brain storm optimization via orthogonal learning design. *IEEE Trans. Syst. Man Cybern. Syst.* (2020). <https://doi.org/10.1109/tsmc.2020.2963943>
4. Ni, J.C., Li, L., Qiao, F., Wu, Q.D.: A novel memetic algorithm based on the comprehensive learning PSO. In: *2012 IEEE Congress on Evolutionary Computation (CEC) IEEE* (2012)
5. Goudos, S.K., Moysiadou, V., Samaras, T., Siakavara, K., Sahalos, J.N.: Application of a comprehensive learning particle swarm optimizer to unequally spaced linear array synthesis with sidelobe level suppression and null control. *IEEE Ant. Wirel. Propag. Lett.* **9**(1), 125–129 (2010)
6. Liang, J.J., Qin, A.K., Suganthan, P.N., Baskar, S.: Comprehensive learning particle swarm optimizer for global optimization of multimodal functions. *IEEE Trans. Evol. Comput.* **10**(3), 1–295 (2006)
7. Azad, A.R., Jhariya, D., Mohan, A.: Synthesis of cross-coupled resonator filters using comprehensive learning particle swarm optimization (CLPSO) algorithm. In: *2016 Asia-Pacific Microwave Conference (APMC)*. IEEE (2016)
8. Mohammad, M.H., Meybodi, R., Ebadzadeh, M.M.: A robust heuristic algorithm for cooperative particle swarm optimizer: a learning automata approach. *Electrical Engineering IEEE* (2012)
9. Liang, J.J., Qin, A.K., Suganthan, P.N., Baskar, S.: Particle swarm optimization algorithms with novel learning strategies. In: *Proceedings of International Conference Systems Man Cybernetics* (2004)
10. Xin, S., Liu, Q., Zhang, L.: A BP neural network model based on genetic algorithm for comprehensive evaluation. In: *Conference on Circuits, Communications and System* (2011)
11. Sengupta, A., et al.: An adaptive memetic algorithm using a synergy of differential evolution and learning automata. *IEEE Evolutionary Computation* (2012)
12. Lynn, N., Suganthan, P.N.: Modified artificial bee colony algorithm with comprehensive learning re-initialization strategy. In: *2015 IEEE International Conference on Systems, Man, and Cybernetics (SMC)*. IEEE (2015)
13. Najim, K., Poznyak, A.S.: *Learning Automata: Theory and Applications*. Pergamon Press, Oxford (1994)
14. Haibin, D., Li, S., Shi, Y.: Predator–Prey brain storm optimization for DC Brushless Motor. *IEEE Trans. Magn.* **49**(10), 5336–5340 (2013)
15. Zhan, Z.H., Zhang, J., Shi, Y.H., Liu, H.L.: A modified brain storm optimization. In: *Proceedings of IEEE Congress on Evolutionary Computer*, Brisbane, Australia, pp. 1C8 (2012)
16. Li, J., Duan, H.: Simplified brain storm optimization approach to control parameter optimization in F/A-18 automatic carrier landing system. *Aerosp. Sci. Technol.* **42**, 187–195 (2015)
17. Cao, Z., Rong, X., Du, Z.: An improved brain storm optimization with dynamic clustering strategy. In: *Proceedings of 3th International Conference on Mechatronics and Mechanical Engineering* (2016)

18. Awad, N.H., Ali, M.Z., Suganthan, P.N., Liang, J.J., Qu, B.Y.: Problem Definitions and Evaluation Criteria for the CEC 2017 Special Session and Competition on Single Objective Real-Parameter Numerical Optimization. Technical Report (2016)
19. Ma, L., Zhang, T., Wang, R., Yang, G., Zhang, Y.: PBAR: parallelized brain storm optimization for association rule mining. In: 2019 IEEE Congress on Evolutionary Computation (CEC), Wellington, New Zealand, pp. 1148–1156 (2019)
20. Zhang, T., Ma, L., Yang, G.: MOPNAR-II: an improved multi-objective evolutionary algorithm for mining positive and negative association rules. In: IEEE 31st International Conference on Tools with Artificial Intelligence (ICTAI), Portland, Oregon (2019)
21. Zhang, T., Shi, M., Wang, J., Yang, G.: P-EAARM: a generic framework based on spark for EAs-based association rule mining. In: 2019 IEEE 4th International Conference on Cloud Computing and Big Data Analysis (ICCCBDA), Chengdu, China, pp. 99–104 (2019)
22. Zhang, C., Zhang, S. (eds.): Association Rule Mining. LNCS (LNAI), vol. 2307. Springer, Heidelberg (2002). <https://doi.org/10.1007/3-540-46027-6>
23. Brin, S., Motwani, R., Ullman, J., Tsur, S.: Dynamic itemset counting and implication rules for market basket data. *ACM SIGMOD Record* **26**(2), 255–264 (1997)
24. Silverstein, C., Brin, S., Motwani, R.: Beyond market baskets: generalizing association rules to dependence rules. *Data Min. Knowl. Disc.* **2**(1), 39–68 (1998)
25. Shortliffe, E., Buchanan, B.: A model of inexact reasoning in medicine. *Math. Biosci.* **23**(3–4), 351–379 (1975)
26. Alcalá-Fdez, J., Fernández, A., Luego, J., Derrac, J., García, S., Sánchez, L., et al.: Keel data-mining software tool: data set repository, integration of algorithms and experimental analysis framework. *J Multiple Valued Logic Soft Comput.* **17**(23), 255–287 (2011)



A Modified Bacterial Foraging Optimizer with Adaptive Chemotactic Step in Dynamic Search Region

Yibo Yong¹, Lianbo Ma^{1(✉)}, Junfeng Zhao², and Xiaolong Shen²

¹ College of Software, Northeastern University, Shenyang, China
malb@swc.neu.edu.cn

² 2012 Laboratories, Huawei Technologies Co., Ltd., Shenzhen, China

Abstract. Bacterial foraging optimization (BFO), inspired from the foraging process of bacterium called *E.coli*, has been applied successfully to a variety of real world optimization problems. However, BFO easily encounters the issue of poor convergence when dealing with complex landscapes of optimization problems due to its inherent fixed chemotactic strategy. Aiming at the above issue, an adaptive bacterial foraging optimizer is presented in this paper, which is able to obtain a good balance between exploration and exploitation during the search. In this approach, the chemotactic step-length is adjusted dynamically, that is a larger chemotactic step is for global search and a smaller chemotactic step is conducive to local search. Moreover, the outstanding swarming pattern is incorporated to perform information sharing in population during the evolution, aiming to maintain diversity and convergence. Simulation results on a set of benchmark functions validate the effectiveness of the proposed algorithm.

Keywords: Bacteria foraging optimization · Adaptive chemotactic step · Swarm intelligence

1 Introduction

As an important computation paradigm in artificial intelligence, swarm intelligence algorithms, which are usually based on bio-inspired computation paradigms, have received a surge of attentions recently. The promising examples include Genetic Algorithm (GA) [1], Artificial Bee Colony (ABC) [2, 3], Particle Swarm Optimization (PSO) [4], Brain Storm Optimization (BSO) [5], Ant Colony Optimization [6], etc. Such biologically inspired algorithms are frequently used to optimize many-objective problems [7]. Among them, bacterial foraging optimization (BFO) algorithm [8] was firstly proposed by Passino in 2002 [9], based on the principle of foraging behaviors of *E.coli* bacteria. The bacterial swarm is essentially a complex adaptive system, where the foraging behaviors show the features of self-organization and self-adaptation. These interesting patterns inspire to develop an optimization paradigm based on bacterial foraging behaviors. Up to now, many improved BFO algorithms have been proposed such as citations [10–14]. BFO algorithm has been applied to many real-world problems, such as harmonic signal estimation [15], PID controller design [16], optimal

power flow [17] and optimal power system stabilizers design [18], load forecasting [19], stock market prediction [20], optimum economic dispatch [21].

BFO algorithm solves single-objective the problem, which is different from multi-objective algorithm [22]. When dealing with complex optimization problems, however, BFO suffers from low convergence speed and being trapped into local optima easily. According, this paradigm can't obtain convincing results in a certain range of optimization problems, due to a chemotactic step-length is always set as a constant no matter which phase the optimization is. For this weakness, a modified adaptive bacterial foraging optimization (MABFO) algorithm is devised by incorporating a modified adaptive chemotactic strategy including adaptive step-length and adaptive tumbling in this paper.

The remainder of this paper is organized as follows: Sect. 2 provides a brief introduction to BFO. Section 3 introduces the proposed MABFO. The simulation results of evaluating MABFO on nine benchmark functions and discussions are shown in Sect. 4. The conclusion is drawn in Sect. 5.

2 Bacterial Foraging Optimization

In principle, bacteria tend to gather towards the nutrient-rich areas in the living environment. In such dynamical environment, the most adapted bacteria survive into the next generation and have a change to reproduce via natural selection, passing on their genetic traits to their offspring. At the same time, those that can't survive are eliminated. Some bacteria may migrate to other places, leading to extinction and migration operations in real bacterial population. In the search process, bacteria in population share information via cell-to-cell communication. This foraging activity can inspire the researchers to use it as optimization process.

The classical BFO algorithm comprises four processes, namely, chemotaxis, swarming, reproduction and elimination-dispersal. The following is brief description of these four processes.

2.1 Chemotaxis

This process simulates swimming behavior and tumbling behavior behavior of *E.coli* bacteria via flagella. The movement ways of bacteria include two types: swimming and tumbling. Biologically, bacteria can move in the above two ways alternatively, that is, swimming in the same direction or possibly tumbling for a period of time. Suppose $\theta^i(j, k, l)$ represents the position of *i*th bacterial after the *j*th chemotaxis operation, *k*th reproduction operation and *l*th extinction and migration operation. $C(i)$ represents the swimming step-length of the *i*th individual in random selected direction, $\angle\phi(j)$ represents a vector of random direction. The mathematical expression of bacterial chemotaxis phase is defined as follows:

$$\theta^i(j+1, k, l) = \theta^i(j, k, l) + C(i)\angle\phi(j) \quad (1)$$

2.2 Swarming

In this process, a cell-to-cell communication is simulated by releasing different signals. As all bacteria are on the move, they release signals to attract other bacteria swimming toward it. At the same time, each bacterium releases a rejection signal to warn other bacteria maintaining a safe distance in face of harmful substances. Bacterial foraging optimization algorithm simulates the social behavior of information sharing and cooperation among bacteria. In the search process, bacteria should not only remember their own information, but also consider the information of their companions to transmit to each other. The numerical sequence expression of the influence value of swarming can be formulated as follows:

$$\begin{aligned}
J_{cc}(\theta, P(j, k, l)) &= \sum_{i=1}^s J_{cc}^i(\theta, \theta^i(j, k, l)) \\
&= \sum_{i=1}^s [h_{repellent} \exp(-w_{repellent} \sum_{m=1}^p (\theta_m - \theta_m^i)^2)] \\
&\quad + \sum_{i=1}^s [-d_{attract} \exp(-w_{attract} \sum_{m=1}^p (\theta_m - \theta_m^i)^2)]
\end{aligned} \tag{2}$$

where s is the total number of bacteria. p is the number of optimized parameters for each bacterium, that is, the position of individuals in the population. $d_{attract}$, $w_{attract}$, $h_{repellent}$, $w_{repellent}$ are different coefficients.

2.3 Reproduction

The evolution and development of bacteria follow principle of ‘The survival of the fittest in natural selection’. After the chemotaxis process, some selections are obviously failed, and the individuals with weak foraging ability are eliminated. The individuals with strong foraging ability maintain stability of population quantity and improve quality of population through reproduction.

Health status of each bacterium is represented by sum of adaptive values of each chemotactic step-length in its life cycle:

$$J_{health}^i = \sum_{j=1}^{N_c} J(i, j, k, l) \tag{3}$$

In order to avoid the disappearance of good feasible solutions in the search process, this strategy eliminates the inferior ones and retain the excellent ones. All bacteria are ordered according to the fitness function. Half of these bacteria with poor fitness will be eliminated, and the remaining bacteria will replicate, so as to keep the number of bacterial population unchanged.

2.4 Elimination-Dispersal

E.coli bacterium may trap into local optimum. In order to improve the global search ability, the bacteria will die or migrate after N_{re} reproduction operation. With the probability of P_{ed} , bacteria are dispersed to any location within the optimized region. This elimination-dispersal operation can reduce the possibility of bacteria falling into local optimal solution. The number of elimination-dispersal operation is denoted as N_{ed} .

3 Modified Adaptive Bacterial Foraging Optimization

During the search process of BFO, the search region size of population at different phases is shown in Fig. 1 and Fig. 2. Figure 1 shows distribution of population at the initial phase, and Fig. 2 demonstrates distribution of population at the later period. As the algorithm runs, the search region becomes smaller. If a chemotactic step-length is too small, the convergence speed will be slow. On the contrary, it may occur oscillation phenomenon, as shown in Fig. 3, causing the bacteria to trap into local optimum easily. Therefore, it is difficult to balance exploration and exploitation with a fixed chemotactic step-length, which affects both the accuracy and speed of algorithm search. To summarize, a proper chemotactic step-length is critical to the performance of BFO.

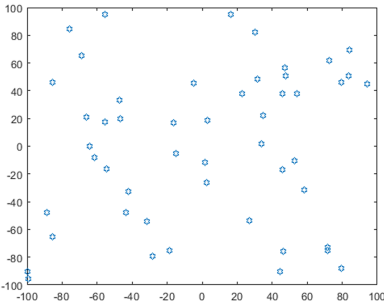


Fig. 1. Population distribution-1

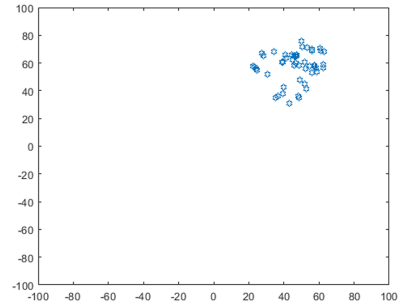


Fig. 2. Population distribution-2

The size of chemotactic step-length is dynamically adjusted in the reproduction process, which ensures the bacteria moving towards the global optimum quickly at the beginning of whole search process, and converging to the global optimum accurately in the end. In this way, it could balance exploration and exploitation of BFO.

Based on the above-mentioned analysis about changing chemotactic step-length, we proposed an adaptive step-length based on dynamic search region in which at each

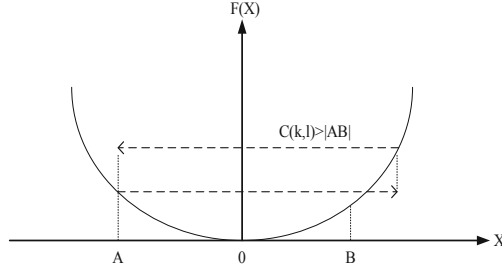


Fig. 3. Oscillation phenomenon of solution

reproduction and elimination-dispersal process of algorithm. The novel adaptive chemotactic step-length formula is shown as follows:

$$\begin{cases} C^i(k, l) = \lambda * R_f^{T_i / T_{\max}} \\ R_f = \frac{R(k, l)}{R(1, 1)} \\ R(k, l) = \frac{1}{n} * \sum_{i=1}^n |x_i - x_{best}| \end{cases} \quad (4)$$

where λ is a constant controlling the step-length that the beginning of whole search process. x_i is position of the i th bacterium x_{best} is the best position in current population. T_i is total number of motion steps of i th bacterium in current reproduction phase. T_{\max} is the ideally maximal number of motion steps in a reproduction phase. If T_i is larger, the area i th bacterium searches is more likely to get the optimal value. Thus, a large value C^i is needed to increase ability of exploitation. On the contrary, the value of C^i for i th bacterium is less than other bacteria. This strategy is inspired by non-uniform mutation [23]. This means that step-length of each bacterium in population may be different at the same time, which greatly increases the local search ability of population.

Moreover, MABFO also introduced a mechanism that new position of each bacterium is calculated according to Eq. (5), which makes all bacteria moving towards the global optimum as far as possible at the beginning of the iteration and maintaining sufficient diversity. In this way, it can obtain expected convergence and diversity in the whole search process.

$$\begin{cases} \theta^i(j+1, k, l) = \theta^i(j, k, l) + C(i) \angle \phi(i, j) \\ \angle \phi(i, j) = (1 - R_f) * \angle \phi_{rand} + R_f * D_i \\ D_i = x_{best} - x_i \end{cases} \quad (5)$$

where $\angle \phi(i, j)$ is direction of movement (swimming or tumbling) of i th bacterium in the j th chemotaxis. $\angle \phi_{rand}$ is a random direction.

The pseudocode of MABFO is given in Table 1. pop represents the number of bacteria. N_s represents the maximum number of swimming, N_c represents the maximum number of chemotaxis, N_{re} represents the maximum number of reproduction, N_{ed} represents the maximum number of elimination and dispersal, P_{ed} represents the

maximum number of elimination-dispersal. The main process include: first, the initialization procedure generates pop initial solutions. It performs chemotactic process after initialization. Then it executes reproduction process. Finally, it carries out elimination-dispersal process. The computational complexity of MABFO isn't significantly different compared with classic BFO, because the size of chemotactic step-length is only dynamically adjusted in the reproduction process.

Table 1. Pseudocode of MABFO.

Randomly initialize positions of bacteria in the domain

FOR (Elimination-dispersal $l=1: N_{ed}$)

FOR (Reproduction loop $k=1: N_{re}$)

FOR (Chemotaxis loop $j=1: N_c$)

FOR (each bacterium $i=1: pop$)

Calculate: Calculate $J^i(j, k, l)$ and set as J_{last} ;

Tumble: Generate a random angle represented by $\angle\phi_{rand}$. Move to a random direction $\angle\phi(i, j)$ by a unit walk, the new position is calculated by equation (3-2).

Run: For bacterium i , calculate the step fitness as J_i . If $J_i(j, k) < J_{last}$, continue to swim until N_s steps. Otherwise, start another chemotactic step.

END FOR (each bacterium)

END FOR (Chemotaxis loop)

 Calculate adaptive chemotactic step-length $C(k, l)$ by equation (3-1).

END FOR (Reproduction loop)

 Perform elimination-dispersal with a probability P_{ed} for each bacterium.

END FOR (Elimination-dispersal loop)

4 Simulation Studies and Discussions

4.1 The Benchmark Function

To evaluate the performance of MABFO, nine benchmark functions selected from citation [24] as follows (Table 2):

Table 2. Test function formula.

| Functions | Formula |
|---|---|
| Shifted and Rotated Zakharov Function | $F_1(x) = f_3(M(x - o_3)) + 300$ |
| Shifted and Rotated Expanded Scaffer's Function | $F_2(x) = f_{20}(M(\frac{0.5(x-o_6)}{100})) + 600$ |
| Shifted and Rotated Lunacek Bi_Rastrigin Function | $F_3(x) = f_7(M(\frac{600(x-o_7)}{100})) + 700$ |
| Hybrid Function 1 (N = 3) | $F_4(x) = f_3(M_1z_1) + f_4(M_2z_2) + f_5(M_3z_3) + 1100$ |
| Hybrid Function 5 (N = 4) | $F_5(x) = f_1(M_1z_1) + f_{18}(M_2z_2) + f_5(M_3z_3) + f_4(M_3z_3) + 1500$ |
| Hybrid Function 6 (N = 5) | $F_6(x) = f_{16}(M_1z_1) + f_{13}(M_2z_2) + f_{19}(M_3z_3) + f_{10}(M_2z_2) + f_5(M_3z_3) + 1700$ |
| Composition Function 3 (N = 4) | $F_7(x) = \sum_{i=1}^N \{\omega_i * [\lambda_i g_i(x) + bias_i]\} + 2300$ |
| Composition Function 6 (N = 5) | $F_8(x) = \sum_{i=1}^N \{\omega_i * [\lambda_i g_i(x) + bias_i]\} + 2600$ |
| Composition Function 10 (N = 3) | $F_9(x) = \sum_{i=1}^N \{\omega_i * [\lambda_i g_i(x) + bias_i]\} + 2900$ |

The test suite includes nine benchmark functions in this paper, encompassing uni-modal, simple multi-modal, hybrid and composition problems. Function F1 is uni-modal function. Functions F2–F3, which are more complex optimization problems, are simple multi-modal functions. Functions F4–F6 are hybrid functions, and functions F7–F9 are composition functions. Both hybrid function and composition functions consist of a variety of basic functions, where the number of local minimum increases exponentially with the problem dimension. So they are considered to be the most difficult class of optimization problems. More detailed function definition is given in citation [24].

4.2 Parameter Settings

The performance of the proposed MABFO is evaluated on the benchmark functions in comparison with PPBSO [25], ABFO [13] and BFO [8]. Here, the total number of iterations for each algorithm is set as 2000. Additionally, as for other specific parameters of each algorithm, as shown in Table 3:

It can be known from the description in Sect. 3, λ is important for the performance for the proposed algorithm. We should choose an appropriate value of λ to further improve the performance of the algorithm. Table 4 shows the stimulation results of nine functions with different values of λ . There are the largest number of functions that can get the most accurate value when coefficient (λ) is set as 1.0.

Table 3. Parameter settings.

| Algorithm | Parameter |
|-----------|--|
| MABFO | $\lambda = 1.0, C_{\min} = 0.01, N_s = 4, N_c = 250, N_{re} = 4, N_{ed} = 2, P_{ed} = 0.25$ |
| PPBSO | $m = 30, N_{c_{\max}} = 200, K = 3, p_{5a} = 0.2, p_{6b} = 0.8, p_{6b3} = 0.4, p_{6c} = 0.5,$ $w_{predator} = 0.05, p_{prey} = 0.1$ |
| ABFO | $C_{\min} = 0.01, C_{\max} = 0.1, a = 4, n = 4, N_s = 4, N_c = 250,$ $N_{re} = 4, N_{ed} = 2, P_{ed} = 0.25$ |
| BFO | $N_s = 4, N_c = 250, N_{re} = 4, N_{ed} = 2, P_{ed} = 0.25$ |

Table 4. Results with different values of coefficient λ on test functions

| Functions | | $\lambda = 0.5$ | $\lambda = 0.6$ | $\lambda = 0.7$ | $\lambda = 0.8$ | $\lambda = 0.9$ | $\lambda = 1.0$ |
|-----------|-----|-------------------|-----------------|-------------------|-------------------|-------------------|-------------------|
| F1 | 10D | 3.02e + 02 | 3.02e + 02 | 3.03e + 02 | 3.05e + 02 | 3.04e + 02 | 3.06e + 02 |
| | 30D | 3.62e + 04 | 3.36e + 04 | 2.93e + 04 | 2.38e + 04 | 2.23e + 04 | 1.79e + 04 |
| F2 | 10D | 6.14e + 02 | 6.13e + 02 | 6.11e + 02 | 6.10e + 02 | 6.08e + 02 | 6.07e + 02 |
| | 30D | 6.49e + 02 | 6.48e + 02 | 6.49e + 02 | 6.46e + 02 | 6.48e + 02 | 6.45e + 02 |
| F3 | 10D | 7.34e + 02 | 7.29e + 02 | 7.28e + 02 | 7.30e + 02 | 7.28e + 02 | 7.30e + 02 |
| | 30D | 1.16e + 03 | 1.11e + 03 | 1.06e + 03 | 1.06e + 03 | 1.04e + 03 | 1.03e + 03 |
| F4 | 10D | 1.11e + 03 | 1.12e + 03 | 1.11e + 03 | 1.11e + 03 | 1.11e + 03 | 1.11e + 03 |
| | 30D | 1.39e + 03 | 1.36e + 03 | 1.34e + 03 | 1.37e + 03 | 1.34e + 03 | 1.35e + 03 |
| F5 | 10D | 1.53e + 03 | 1.53e + 03 | 1.53e + 03 | 1.54e + 03 | 1.53e + 03 | 1.54e + 03 |
| | 30D | 1.94e + 04 | 2.02e + 04 | 2.59e + 04 | 1.83e + 04 | 2.56e + 04 | 2.86e + 04 |
| F6 | 10D | 1.75e + 03 | 1.74e + 03 | 1.74e + 03 | 1.74e + 03 | 1.74e + 03 | 1.75e + 03 |
| | 30D | 2.19e + 03 | 2.16e + 03 | 2.17e + 03 | 2.10e + 03 | 2.13e + 03 | 2.10e + 03 |
| F7 | 10D | 2.79e + 03 | 2.77e + 03 | 2.78e + 03 | 2.68e + 03 | 2.69e + 03 | 2.74e + 03 |
| | 30D | 4.57e + 03 | 4.41e + 03 | 4.42e + 03 | 4.39e + 03 | 4.25e + 03 | 4.32e + 03 |
| F8 | 10D | 2.97e + 03 | 2.86e + 03 | 2.89e + 03 | 2.86e + 03 | 2.95e + 03 | 2.85e + 03 |
| | 30D | 2.88e + 03 | 3.17e + 03 | 2.90e + 03 | 2.90e + 03 | 2.91e + 03 | 2.92e + 03 |
| F9 | 10D | 3.18e + 03 | 3.17e + 03 | 3.17e + 03 | 3.17e + 03 | 3.17e + 03 | 3.16e + 03 |
| | 30D | 3.88e + 03 | 3.83e + 03 | 3.91e + 03 | 3.72e + 03 | 3.72e + 03 | 3.75e + 03 |

4.3 Simulation Results

The merits and characteristics of MABFO are discussed in comparison with PPBSO, ABFO and BFO as follows. Table 5 demonstrates simulation results obtained by MABFO, PPBSO, ABFO and BFO applied on the nine benchmark functions respectively. The simulation results for these benchmark functions are shown in Fig. 1, 2, 3 and 4 which describe the convergence process of MABFO, PPBSO, ABFO and BFO respectively.

Precision of Optimization: The proposed MABFO algorithm is evaluated on the 10-dimension and 30-dimension benchmark functions in comparison with PPBSO, ABFO and BFO respectively. Each algorithm runs 20 times to give a mean value of the best solutions and a standard deviation.

Table 5. The performance comparison of MABFO, PPBSO, ABFO and BFO.

| Functions | | | MABFO | PPBSO | ABFO | BFO |
|-----------|-----|------|---------------------|---------------------|---------------------|--------------|
| F1 | 10D | Mean | 3.0584e + 02 | 3.0000e + 02 | 1.3749e + 03 | 8.1190e + 03 |
| | | SD | 2.6261e + 00 | 4.5829e - 14 | 4.0948e + 02 | 3.7756e + 03 |
| | 30D | Mean | 1.7774e + 04 | 8.8504e + 03 | 1.2257e + 05 | 1.4437e + 05 |
| | | SD | 5.9123e + 03 | 9.3753e + 03 | 1.5786e + 04 | 1.9211e + 04 |
| F2 | 10D | Mean | 6.0759e + 02 | 6.2205e + 02 | 6.2526e + 02 | 6.4604e + 02 |
| | | SD | 4.0422e + 00 | 9.5718e + 00 | 6.2246e + 00 | 5.9501e + 00 |
| | 30D | Mean | 6.4593e + 02 | 6.5011e + 02 | 6.7454e + 02 | 6.6973e + 02 |
| | | SD | 7.7749e + 00 | 7.7364e + 00 | 5.4036e + 00 | 4.4806e + 00 |
| F3 | 10D | Mean | 7.2814e + 02 | 7.8390e + 02 | 7.6519e + 02 | 1.0776e + 03 |
| | | SD | 5.1883e + 00 | 2.9834e + 01 | 1.1577e + 01 | 9.2470e + 01 |
| | 30D | Mean | 1.0340e + 03 | 1.3067e + 03 | 1.7438e + 03 | 3.1204e + 03 |
| | | SD | 4.8066e + 01 | 1.1808e + 02 | 1.2740e + 02 | 2.7588e + 02 |
| F4 | 10D | Mean | 1.1105e + 03 | 1.1245e + 03 | 1.1108e + 03 | 1.1512e + 03 |
| | | SD | 5.1915e + 00 | 1.4632e + 01 | 3.9058e + 00 | 2.9547e + 01 |
| | 30D | Mean | 1.3347e + 03 | 1.3363e + 03 | 1.5922e + 03 | 1.8618e + 04 |
| | | SD | 4.7908e + 01 | 8.1675e + 01 | 6.6374e + 01 | 7.6777e + 03 |
| F5 | 10D | Mean | 1.5373e + 03 | 1.8244e + 03 | 1.6795e + 03 | 1.8381e + 03 |
| | | SD | 1.8705e + 01 | 4.2506e + 02 | 7.3928e + 01 | 1.4335e + 02 |
| | 30D | Mean | 2.8687e + 04 | 1.2391e + 04 | 6.3020e + 04 | 1.0596e + 08 |
| | | SD | 1.8467e + 04 | 8.9803e + 03 | 2.1868e + 04 | 1.1227e + 08 |
| F6 | 10D | Mean | 1.7471e + 03 | 1.7490e + 03 | 1.7506e + 03 | 1.8156e + 03 |
| | | SD | 1.3037e + 01 | 1.2734e + 01 | 1.7534e + 01 | 8.1156e + 01 |
| | 30D | Mean | 2.0732e + 03 | 2.5271e + 03 | 2.2469e + 03 | 2.9394e + 03 |
| | | SD | 1.6597e + 02 | 3.3938e + 02 | 1.4962e + 02 | 3.1378e + 02 |
| F7 | 10D | Mean | 2.7222e + 03 | 2.7292e + 03 | 2.7269e + 03 | 2.9380e + 03 |
| | | SD | 1.0978e + 02 | 5.0220e + 01 | 3.8044e + 01 | 6.8809e + 01 |
| | 30D | Mean | 4.2918e + 03 | 3.5391e + 03 | 3.9840e + 03 | 4.5136e + 03 |
| | | SD | 3.2712e + 02 | 2.0798e + 02 | 2.3874e + 02 | 2.3819e + 02 |
| F8 | 10D | Mean | 2.8836e + 03 | 2.9564e + 03 | 2.8490e + 03 | 3.2559e + 03 |
| | | SD | 1.7279e + 02 | 3.4298e + 02 | 5.6717e + 01 | 4.9001e + 02 |
| | 30D | Mean | 2.9342e + 03 | 3.3389e + 03 | 3.3761e + 03 | 1.2707e + 04 |
| | | SD | 1.1595e + 01 | 1.6167e + 03 | 2.7501e + 02 | 1.3268e + 03 |
| F9 | 10D | Mean | 3.1692e + 03 | 3.2022e + 03 | 3.1800e + 03 | 3.3064e + 03 |
| | | SD | 1.8905e + 01 | 8.2237e + 01 | 2.2377e + 01 | 9.0455e + 01 |
| | 30D | Mean | 3.7376e + 03 | 4.0253e + 03 | 4.0250e + 03 | 4.9156e + 03 |
| | | SD | 2.0469e + 02 | 3.0944e + 02 | 1.9343e + 02 | 2.9212e + 02 |

From Table 5, it can be seen clearly that the average convergence value of the proposed MABFO algorithm ranks first for 13 times in total among the nine functions, and has small deviation at the same time. This demonstrates that the search accuracy of MABFO algorithm is better than the other three algorithms. This is because that the

modified adaptive chemotactic step strategy of MABFO can help escape from local optimum and improve its capability of searching global optimum.

Speed of Convergence: From the results presented in Fig. 4, 5, 6 and 7, comparing MABFO and classic BFO, the adaptive chemotactic step-length mechanism of MABFO can balance exploration and exploitation on the whole phase. Because MABFO can use big chemotactic step-length for fast searching feasible solution region in exploration phase, and for local search with small chemotactic step-length in exploitation phase quickly. On the contrary, the constant chemotactic step-length of classic BFO unable to maintain high-speed search ability in different environments.

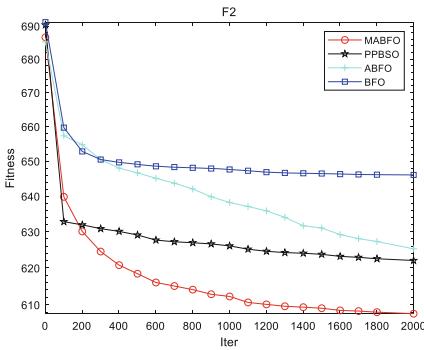


Fig. 4. Convergence curve of F2 10-D

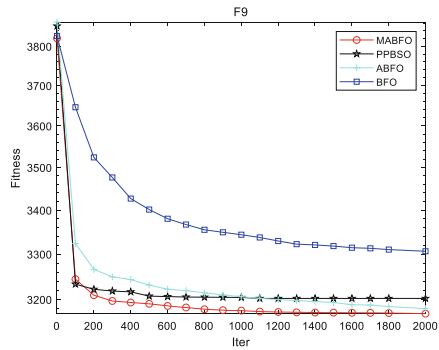


Fig. 5. Convergence curve of F9 10-D

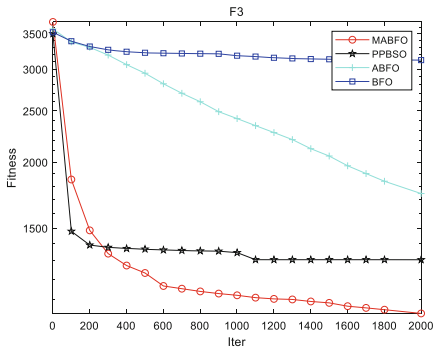


Fig. 6. Convergence curve of F3 30-D

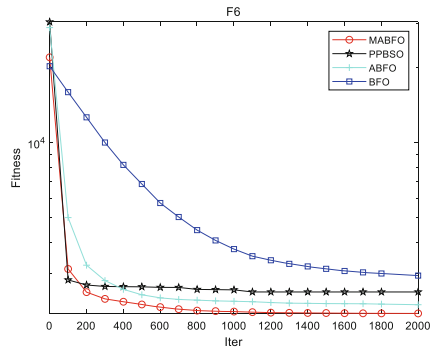


Fig. 7. Convergence curve of F6 30-D

From Fig. 4, 5, 6 and 7, we can find that the convergence speed of MABFO is better than PPBSO, ABFO and BFO. The convergence speed of MABFO and PPBSO at the same level roughly in the initial search phase. Because MABFO not only adds mechanism of adaptive chemotactic step-length, but also introduces the adaptive tumbling mode that makes full use of the information of the global best individual.

A larger chemotactic step-length and more suitable movement direction can obtain a relatively better convergence speed in the initial search phase. Moreover, MABFO also has faster convergence speed than other three algorithms in the middle and late stage of whole search process, because it has a desired chemotactic step-length and direction in the whole dynamic search region.

5 Conclusions

In this paper, a modified adaptive chemotaxis strategy in dynamic search region is proposed to improve the BFO algorithm. Nine benchmark functions were then used to test effectiveness of the proposed improvement. Compared with PPBSO, ABFO and BFO, the proposed MABFO algorithm has fast search performance according to its adaptive character in whole search phase. In a large number of scientific research and engineering application practice, people found that biologically inspired algorithm has some problems, mainly premature convergence, and easy to fall into the local optimal. Evaluation results obtained on benchmark functions have proved the effectiveness of the proposed MABFO algorithm in solving problems of premature convergence and easy to fall into the local optimal. But the performance on the 30-dimension is worse than that on the 10-dimension. This encourages us to study further to solve higher dimensions optimization problems.

Acknowledgment. This work was supported in part by National Natural Science Foundation of China under Grant No. 61773103 and Huawei HIRP project under No. HO2019085002.

References

1. Whitley, D.: A genetic algorithm tutorial. *Stat. Comput.* **4**(2), 65–85 (1994)
2. Karaboga, D., Akay, B.: A comparative study of artificial bee colony algorithm. *Appl. Math. Comput.* **214**(1), 108–132 (2009)
3. Ma, L., Hu, K., Zhu, Y., Chen, H.: Cooperative artificial bee colony algorithm for multi-objective RFID network planning. *J. Network Comput. Appl.* **42**, 143–162 (2014)
4. Shi, Y.: Particle swarm optimization: developments, applications and resources. In: *Proceedings of the 2001 Congress on Evolutionary Computation (IEEE Cat. No. 01TH8546)*, vol. 1, pp. 81–86. IEEE (2001)
5. Ma, L., Cheng, S., Shi, Y.: Enhancing learning efficiency of brain storm optimization via orthogonal learning design. *IEEE Trans. Syst. Man Cybern. Syst.* (2020). <https://doi.org/10.1109/tsmc.2020.2963943>
6. Dorigo, M., Birattari, M., Stutzle, T., et al.: Ant colony optimization: artificial ants as a computational intelligence technique. *IEEE Comput. Intell. Mag.* **1**(4), 28–39 (2006)
7. Ma, L., Wang, R., Chen, M., Wang, X., Cheng, S., Shi, Y.: A novel many-objective evolutionary algorithm based on transfer learning with kriging model. *Inf. Sci.* **509**, 437–456 (2020)
8. Das, S., Biswas, A., Dasgupta, S., et al.: Bacterial foraging optimization algorithm: theoretical foundations, analysis, and applications. In: Abraham, A., Hassanien, A.E., Siarry, P., Engelbrecht, A. (eds.) *Foundations of Computational Intelligence Volume 3*, vol. 203, pp. 23–55. Springer, Heidelberg (2009). https://doi.org/10.1007/978-3-642-01085-9_2

9. Passino, K.M.: Biomimicry of bacterial foraging for distributed optimization and control. *IEEE Control Syst. Mag.* **22**(3), 52–67 (2002)
10. Tang, W.J., Wu, Q.H., Saunders, J.R.: Bacterial foraging algorithm for dynamic environments. In: 2006 IEEE International Conference on Evolutionary Computation, pp. 1324–1330. IEEE (2006)
11. Chu, Y., Mi, H., Liao, H., et al.: A fast bacterial swarming algorithm for high-dimensional function optimization. In: 2008 IEEE Congress on Evolutionary Computation (IEEE World Congress on Computational Intelligence), pp. 3135–3140. IEEE (2008)
12. Dasgupta, S., Das, S., Abraham, A., et al.: Adaptive computational chemotaxis in bacterial foraging optimization: an analysis. *IEEE Trans. Evol. Comput.* **13**(4), 919–941 (2009)
13. Niu, B., Wang, H., Tan, L., et al.: Improved BFO with adaptive chemotaxis step for global optimization. In: 2011 Seventh International Conference on Computational Intelligence and Security, pp. 76–80. IEEE (2011)
14. Chen, H., Zhu, Y., Hu, K.: Adaptive bacterial foraging optimization. *Abstract and Applied Analysis*, Hindawi (2011)
15. Mishra, S.: A hybrid least square-fuzzy bacterial foraging strategy for harmonic estimation. *IEEE Trans. Evol. Comput.* **9**(1), 61–73 (2005)
16. Kim, D.H., Cho, J.H.: Adaptive tuning of PID controller for multivariable system using bacterial foraging based optimization. In: Szczepaniak, Piotr S., Kacprzyk, J., Niewiadomski, A. (eds.) *AWIC 2005. LNCS (LNAI)*, vol. 3528, pp. 231–235. Springer, Heidelberg (2005). https://doi.org/10.1007/11495772_36
17. Tang, W.J., Li, M.S., He, S., et al.: Optimal power flow with dynamic loads using bacterial foraging algorithm. In: 2006 International Conference on Power System Technology, pp. 1–5. IEEE (2006)
18. Das, T.K., Venayagamoorthy, G.K., Aliyu, U.O.: Bio-inspired algorithms for the design of multiple optimal power system stabilizers: SPPSO and BFA. In: *Industry Applications Conference*, pp. 1445–1457. IEEE (2006)
19. Ulagammai, M., Venkatesh, P., Kannan, P.S., et al.: Application of bacterial foraging technique trained artificial and wavelet neural networks in load forecasting. *Neuro Comput.* **70**(16–18), 2659–2667 (2007)
20. Majhi, R., Panda, G., Majhi, B., et al.: Efficient prediction of stock market indices using adaptive bacterial foraging optimization (ABFO) and BFO based techniques. *Expert Syst. Appl.* **36**(6), 10097–10104 (2009)
21. Farhat, I.A., Elhawary, M.E.: Dynamic adaptive bacterial foraging algorithm for optimum economic dispatch with valve-point effects and wind power. *IET Gener. Trans. Distrib.* **4**(9), 989–999 (2010)
22. Ma, L., Wang, X., Huang, M., Lin, Z., Tian, L., Chen, H.: Two-level master-slave RFID networks planning via hybrid multi-objective artificial bee colony optimizer. *IEEE Trans. Syst. Man Cybern. Syst.* **49**(5), 861–880 (2019)
23. Deep, K., Thakur, M.: A new mutation operator for real coded genetic algorithms. *Appl. Math. Comput.* **193**(1), 211–230 (2007)
24. Awad, N.H., Ali, M.Z., Suganthan, P.N., Liang, J.J., Qu, B.Y.: Problem definitions and evaluation criteria for the CEC 2017 special session and competition on single objective real-parameter numerical optimization. Technical report (2016)
25. Duan, H., Li, S., Shi, Y.: Predator-prey brain storm optimization for DC brushless motor. *IEEE Trans. Magn.* **49**(10), 5336–5340 (2013)



Novel Mutation Operators of a Variable-Length Representation for EC-Based Feature Selection in High-Dimensional Data

Nicole Dalia Cilia, Claudio De Stefano, and Francesco Fontanella^(✉)

Università di Cassino e del Lazio meridionale, Cassino, FR, Italy
{nicoledalia.cilia, destefano, fontanella}@unicas.it

Abstract. Because of their ability to explore large and complex search spaces, evolutionary algorithms have been widely used to solve feature selection problems. Many of them, e.g. genetic algorithms, provide a natural way to represent feature subsets, however, when the number of features is high, these representations may make the evolutionary process inefficient. In a previous paper, we presented a novel variable-length representation scheme for encoding subsets of features efficiently as well as a crossover operator to cope with the variable length representation. In this paper, we present two novel mutation operators that can generate offspring that may have a length different from that of the parent. We aim to simplify the approach presented previously, by using a single operator. We have tested the proposed approach on six datasets and the results compared with those achieved by a standard GA and two state-of-art algorithms. The results of comparisons demonstrated the effectiveness of the proposed approach when thousand of features are involved.

Keywords: Feature selection · Evolutionary algorithms · Variable length representation

1 Introduction

In machine learning, in many cases, available data are represented by a large number of features, with some, or even most of them, be redundant or irrelevant. In the first case, in the set of available features, one or more groups are made of features that are correlated each other and then, for each group, most of them can be discarded without affecting the quantity of information about the target class contained in that group. Regarding the irrelevant features, they can be safely removed because they contain few, or even none, information about the target class. Moreover, this kind of features may be harmful since they may cause a deterioration of the classification performance [1–3]. This problem can be tackled by adopting feature selection techniques, that use a search procedure to find the best feature subset, according to the criteria implemented by means of an evaluation function. These criteria typically take into account the subset size (to minimize) and the discriminative power (to maximize). Evaluation functions can be divided into two broad classes *wrapper* and *filter* [4]. Functions belonging to the first class evaluate the goodness of a given subset in terms of classification performance, whereas those belonging to the second class use statistical measures, e.g. correlation or entropy, that

make them independent of any classification algorithm. Moreover, wrapper functions typically need greater computational resources than those required by filter ones. Regarding the search strategies, the optimal subset can be found by exhaustively evaluating all the possible solutions. However, in most cases this strategy is impracticable because the number of solutions to evaluate grows exponentially with the total number of features. As a consequence, many heuristic approaches have proposed [4]. However, most of these methods suffer from stagnation in local optima, because of their greedy nature, or high computational costs.

In this framework, Evolutionary computation (EC) techniques have been widely used because of their global search ability. Among the EC based approaches, Genetic Algorithms (GAs) have been widely used since they provide a straightforward representation for feature subsets: the value 1 or 0 of the chromosome i -th element indicates whether the i -th feature is included or not [5–7]. However, the chromosome length is equal to the number of available features. As consequence, when this number grows, the GA evolution becomes inefficient. To cope with this problem, have been proposed several enhancements. In [8], for example, the authors proposed a binary vector to represent a predefined small number of selected features. This representation reduced the dimensionality of the GA search space, which resulted in better performance than the traditional representation on high-dimensional datasets. Jeong et al. [9], instead, proposed a new representation to further reduce the dimensionality, where the length of the chromosome was equal to the number of desired features. The values in chromosomes indicated the indices of the included features. When the index of a feature(s) appeared multiple times, a partial SFFS operator was applied to choose alternative features to avoid duplication. The main limitation of the just mentioned approaches is that the number of features needs to be predefined, which might not be the optimal size. To address this limitation, two approaches have been proposed. Yahya et al. [10] proposed a variable length representation, whereby each chromosome contains the selected features and different chromosomes may have different lengths. New genetic operators were accordingly developed to cope with the variable length representation. However, the performance of the proposed algorithm was only tested on a single problem, for cues phrase selection and neither compared with other GAs-based methods. Finally, Chen et al. [11] proposed a binary representation made of two parts; the first part encode the number of features to be selected, whereas the second one contains the features selected. However, in this case, the authors do not explain how to set the chromosome length and if it depends on the total number of features.

In a previous paper [12], we presented a novel variable-length representation scheme for encoding subsets of features. According to such scheme, a feature subset is represented by an ordered list of integers, where the value contained in the i -th element of the list represents the index of the i -th feature of the subset and the length of the list coincide with the cardinality of the subset. Regarding the genetic operators, we defined a crossover and a mutation operator. The first implements parent chromosomes recombination and can produce offspring with a length different from that of the parents, whereas the second generates new individuals by modifying the elements of the list. As for the fitness function, we adopted a filter one which uses correlation to evaluate feature subset quality, independently of the number of features making up the subset to be evaluated. Therefore, thanks to the crossover operator devised and the

fitness function adopted, that approach does not need to fix a priori the number of features of the target solution.

In this paper, we present two novel mutation operators that allows our EC-based feature selection algorithm to improve its ability in exploring the search space, especially when an high number of features is involved. The devised mutation operators are able to both modify the single elements of the list and its length, by adding a new element or removing one of those already in the list to be mutated. The rationale of the proposed operator is to use a single operator, with the aim of simplifying the above-mentioned approach. To test these operators we performed a set of experiments on some benchmark datasets. In particular, we first assessed the effectiveness of the proposed operators by comparing their search abilities with that achieved by the crossover and mutation ones of the previous approach. Then we compared the performance of our system with two state-of-the-art algorithms as well as a standard GA.

The remainder of the paper is organized as follows: in Sect. 2 the representation scheme proposed and the mutation operators are described, Sect. 3 illustrates the evolutionary algorithm implemented, including the fitness function. In Sect. 4 the experimental results are detailed. Finally, Sect. 5 is devoted to the conclusions.

2 The Representation Scheme and the Mutation Operators

As mentioned in the Introduction, GA binary vectors provide a natural representation for feature subsets, where the chromosome length is equal to the number N of available features and the i -th feature is represented by the i -th bit in the chromosome. On the other hand, the choice to represent also the information about the missing features (the 0's in the vector) makes the evolution inefficient when N is huge. Thus, it is needed a more efficient representation scheme, in which only the features actually included in the solution (subset) are represented. For this reason, we have chosen a direct representation scheme, in which a feature subset is encoded by a sorted list of integers and the length of the list represents the cardinality of the subset encoded.



Fig. 1. An example of the representation scheme adopted, with $N = 100$. The list represents the subset of features $S_1 = \{2, 6, 16, 29, 37, 47, 71\}$.

It is worth noting that, though the ordering may require repairing the chromosome after the application of the operators, it allows the implementation of more effective operators. As concerns the length of the list, it can be modified by the application of the a mutation operator that besides modifying single list elements, is also able to add a new element or delete one of those in the list.

Let N be the number of available features and S a subset of features of cardinality $N_s : S = \{f_1, f_2, \dots, f_{N_s}\}$ with $f_i < f_{i+1}$ and $1 \leq f_i \leq N$. In our approach S is represented by an ordered list of integers L , where the i -th element of the list contains the value f_i

and the cardinality of S is intrinsically represented by the length of L . An example of representation is shown in Fig. 1.

2.1 The Mutation Operators

We have defined two mutation operators, named *mut3* and *mut4*. Both operators scan the list making up the chromosome and modify its i -th element e_i according to a given probability p_m . The operator *mut3* can modify a chromosome only adding/deleting one or more elements, whereas *mut4* besides these options can also substitute the elements already in the chromosome with new ones, randomly generated. Note that both operators may require the reordering of the list or the removal of double indices. The pseudo-code of both operators is detailed in the following.

Mut3

Given a list L of size n_l , the operator *mut3* modifies L through the following steps:

```

for  $i \leftarrow 1$  to  $n_l$  do
  if  $flip(p_m)$  then
    if  $flip(0.5)$  then
      choose randomly a value  $v$  in the interval  $[1, N]$ ;
      add  $v$  to  $L$ 
    else
      remove  $e_i$  from  $L$ 
    end if
  end if
end for
Reorder  $L$ ;
Remove double indices from  $L$ ;

```

Mut4

Given a list L of size n_l , the operator *mut4* modifies L through the following steps:

```

for  $i \leftarrow 1$  to  $n_l$  do
  if  $flip(p_m)$  then
    if  $flip(0.5)$  then
      choose randomly a value  $v$  in the interval  $[1, N]$ ;
      substitute  $e_i$  with  $v$ 
    else if  $flip(0.5)$  then
      remove  $e_i$  from  $L$ 
    else
      Choose randomly a value  $v$  in the interval  $[1, N]$ ;
      add  $v$  to  $L$ ;
    end if
  end if
end for
Reorder  $L$ ;
Remove double indices from  $L$ ;

```

3 The Evolutionary Algorithm

The system presented here has been implemented by using a generational evolutionary algorithm. The algorithm starts by generating a population of P individuals, randomly generated. The procedure for the random generation of these individuals takes in input three terms: the number of available features N and the minimum and maximum chromosome length l_{min} and l_{max} , with the last two values expressed as a fraction of N . The procedure starts randomly generating a value l in the interval $[l_{min}, l_{max}]$. Then l values are randomly picked up from the set $\{1, \dots, N\}$, without replacement, and added to the list making up the chromosome of the individual. Finally, the list is sorted, in ascending order. In the experiments reported in Sect. 4, the values of l_{min} and l_{max} have been set to 0.1 and 0.5, respectively.

Afterwards, the fitness of the generated individuals is evaluated according to the formula in (2). After this preliminary evaluation phase, a new population is generated by selecting $P/2$ couples of individuals using the tournament method. Then the genetic operators detailed in the previous section are applied. First, the one point crossover operator is applied to each of the selected couples, according to a given probability factor p_c . Afterwards, one of the two mutation operators is applied with a probability p_m . The value of p_m has been set to $1/l_c$, where l_c is the chromosome length. This probability value allows, on average, the modification of only one chromosome element. Finally, these individuals are added to the new population. The process just described is repeated for N_g generations.

3.1 The Fitness Function

As fitness function, we chose a filter one, called CFS (Correlation-based Feature Selection) [13], which uses a correlation based heuristic to evaluate feature subsets.

Given two features X and Y , their correlation r_{XY} is computed as follows¹

$$r_{XY} = 2.0 \cdot \frac{H(X) + H(Y) - H(X, Y)}{H(X) + H(Y)} \quad (1)$$

Where the symbol H denotes the entropy function. The function takes into account the usefulness of the single features for predicting class labels along with the level of inter-correlation among them. The idea behind this approach is that good subsets contain features highly correlated with the class and uncorrelated with each other.

Given a feature selection problem in which the patterns are represented by means of a set Y of N features, the CFS function computes the merit of the generic subset, made $X \in Y$ of k features, as follows:

$$f_{CFS}(X) = \frac{k \cdot \overline{r_{cf}}}{\sqrt{k + k \cdot (k - 1) \cdot \overline{r_{ff}}}} \quad (2)$$

¹ Note that the same holds also for the feature-class correlation.

where $\overline{r_{cf}}$ is the average feature-class correlation, and $\overline{r_{ff}}$ is the average feature-feature correlation. Note that the numerator estimates the discriminative power of the features in X , whereas the denominator assesses the redundancy among them. The CFS function allows irrelevant and redundant features to be discarded. The former because they are poor in discriminating the different classes at the hand; the latter because they are highly correlated with one or more of the other features. It is worth noting that, differently from previously presented approaches, this fitness function is able to automatically find the number of features and does not need the setting of any parameter.

Table 1. The datasets used in the experiments.

| Name | attributes | samples | classes |
|----------|------------|---------|---------|
| Colon | 2000 | 62 | 2 |
| Lymphoma | 4026 | 96 | 2 |
| Musk | 166 | 476 | 14 |
| Ovarian | 2191 | 216 | 2 |
| Spam | 57 | 3037 | 2 |
| Ucihar | 561 | 2948 | 6 |

4 Experimental Results

The proposed approach was tested on six, publicly available, datasets: *Colon*, *Lymphoma*, *Musk*, *Ovarian*, *Spam* and *Ucihar*. The characteristics of these datasets are summarized in Table 1. They present different characteristics as regards the number of attributes, the number of classes (two or multiple classes problems) and the number of samples. For each dataset, we performed thirty runs. At the end of every run, the feature subset encoded by the individual with the best fitness was stored as the solution provided by that run. As for the parameters of the evolutionary algorithm, we performed some preliminary trials to set them. These parameters were used for all the experiments described below and are reported in Table 2.

Table 2. The values of the parameters used in the experiments. Note that p_m depends on the chromosome length l_c .

| Parameter | symbol | value |
|-----------------------|---------------|---------|
| Population size | \mathcal{P} | 100 |
| Crossover probability | p_c | 0.6 |
| Mutation probability | p_m | $1/l_c$ |
| Number of Generations | N_g | 1000 |

In order to test the effectiveness of the proposed approach, we performed three sets of experiments. In the first set, we compared the performance of the two mutation operators devised with that of the operator `mut2`, presented in [13]. The comparison

was performed in terms of the population average fitness during the run that achieved the best fitness. The results are shown in Fig. 2. From the plots, it can be seen that, for all the datasets considered, the mutation operator mut4 performs better than mut3. This suggests that mut4 has a better exploration ability than mut3. Most probably, this is due to the fact that, given a list L (chromosome) of length l_c representing the sub set $S = \{f_1, f_2, \dots, f_{l_c}\}$, mut4 can mutate L both by changing or adding/deleting one or more elements of L , whereas mut3 can perform only the last two operations. This choice,

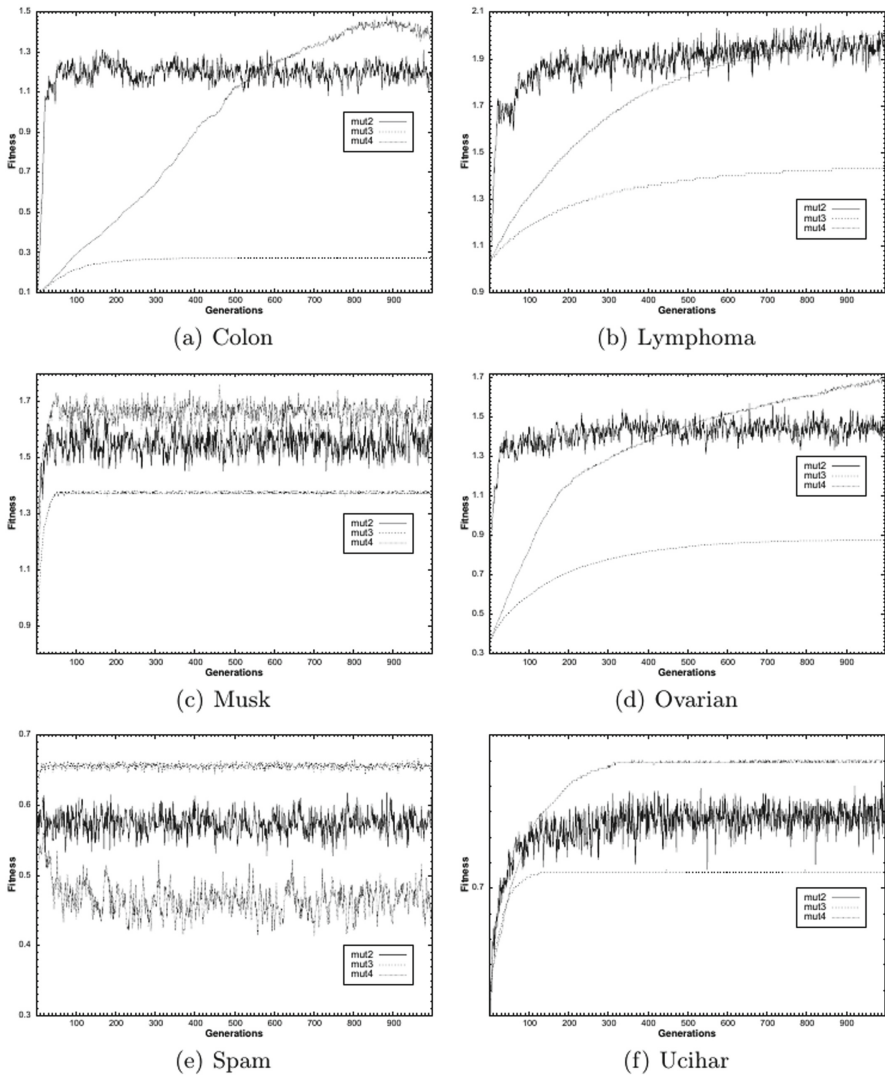


Fig. 2. Comparison results between the operators mut2, mut3 and mut4.

seems to limit the exploration ability of the operator. The plots also shows that mut4 performs better than mut2. In particular, from the plots emerges two trends. For Colon, Lymphoma and Ovarian, mut4 converges slower than mut2 toward its best fitness values, whereas for the remaining datasets both operators show similar convergence.

Table 3. Comparison results between our approach, by using the mut4 operator, and the GA.

| Dataset | Mut4 | | | | GA | | | |
|----------|-------------|------------|-------------|-----|---------|--------|-------------|------|
| | Fitness | | #iterations | | Fitness | | #iterations | |
| | avg | std | avg | std | avg | std | avg | std |
| Colon | 1.49 | 0.1 | 994 | 5 | 1.26 | 0.03 | 997 | 1.2 |
| Lymphoma | 1.94 | 0.08 | 998 | 1 | 1.88 | 0.18 | 21.5 | 2.2 |
| Musk | 1.94 | 0.001 | 136 | 100 | 1.94 | 0.004 | 220 | 150 |
| Ovarian | 1.63 | 0.1 | 998 | 2 | 1.31 | 0.01 | 990 | 1.3 |
| Spam | 0.722 | 0.00 | 67.5 | 40 | 0.722 | 0.00 | 86.7 | 62.1 |
| Ucihar | 0.751 | 0.0004 | 896 | 90 | 0.751 | 0.0001 | 613 | 200 |

Therefore, when thousands of features are involved, as is the case of Colon, Lymphoma and Ovarian, mut4 needs more time (generations) than mut2 to identify the areas of the search space containing good solutions. Nonetheless, once these areas are identified mut4 allows our algorithm to find, on average, better solutions than those found by using mut2. However, the plots also suggest that for these datasets more generations would allow the algorithm to find even better solutions. Finally, Note that in [13] the experimental results proved that our approach with mut2 together with the crossover operator, performs better a GA on the datasets with thousands of features.

After the comparison between the two mutation operators devised, we compared the performance achieved by using the operator mut4, with that of a GA. In order to have a fair comparison, it was performed by using the same fitness function and the same set of parameters. We compared the fitness values of the best individuals found, averaged over the the thirty runs performed. These results are shown in Table 3, that also reports the iterations at which the best solutions have been found. To statistically validate the obtained results, we performed the non-parametric Wilcoxon rank-sum test ($\alpha = 0.05$). For each dataset, the best result, according to the Wilcoxon test, is in bold. From the table it can be seen that our approach outperforms the GA on Colon and Ovarian, in terms of fitness of the best individuals found. Regarding Lymphoma, the difference of performance with the GA is not statistically significant. However, it is worth noting that our approach finds the best solution at the late stage of the evolutionary process (#iterations = 998) and, most probably, more generations would allow it to outperform the GA. Also for the remaining datasets (Musk, Spam and Ucihar) performance differences are not statistically significant. These last results confirm that our approach is more effective than a GA in finding good subsets when the data are represented by thousands of features.

Table 4. Comparison results between our approach, by using the mut4 operator, and the GA.

| Dataset | Our approach | | mRMR | | FCBF | |
|----------|--------------|-------------|-------|-------|--------------|--------------|
| | RR | NF | RR | NF | RR | NF |
| Colon | 93.06 | 25.8 | 75.96 | 22.00 | 89.52 | 18.00 |
| Lymphoma | 98.23 | 341 | 72.46 | 61 | 78.44 | 319 |
| Musk | 98.57 | 5.6 | 79.90 | 7.00 | 80.21 | 11.00 |
| Ovarian | 88.01 | 91 | 74.25 | 13.00 | 88.42 | 18.00 |
| Spam | 75.93 | 3.00 | 92.05 | 7.00 | 92.19 | 17.00 |
| Ucihar | 82.62 | 47.3 | 69.37 | 23.00 | 93.02 | 32.00 |

Finally, we tested the devised approach in terms of classification performance. We used decision trees (DT in the following) as classifiers, trained by using the C4.5 algorithm. To this aim, at the end of each of the thirty runs performed, the feature subset encoded by the individual with the best fitness was used to build a DT. The classification performances of the classifiers built have been obtained by using the 10-fold cross-validation approach. The results reported in the following were obtained averaging the performance of the 30 DTs built. We compared the achieved results with those obtained by the following two state-of-the-art algorithms for feature selection:

- *Fast Correlation-Based Filter*. This algorithm selects subsets made of features that are strongly relevant to the class concept and are not redundant. It evaluates non-linear correlations between the features by using the information-theoretical concept of entropy. The algorithm first ranks the features according to their correlation to the class, then the ordered list is further processed to remove redundant features. It will be denoted as *FCBF* in the following.
- *Minimum Redundancy Maximum Relevance*. This approach finds the best feature subset made up of the features that are highly correlated with the class concept and minimally correlated each other, by using the mutual information criterion for the discrete variables and the F-test for the continuous ones. It will be denoted as *mRMR* in the following.

Since the above methods are deterministic, they generate a single feature subset. In order to perform a fair comparison with the proposed approach, for each dataset, 30 DT's have been learned by using the 10-fold cross-validation technique, with different initial seeds. The results reported in the following have been obtained by averaging the performance of the 30 DT's learned. Table 4 reports the results in terms of recognition rate (RR) and number of features (NF). Also in this case, we performed the Wilcoxon test mentioned above to statistically validate the results. For each dataset, the recognition rate in bold highlights the best result, according to the Wilcoxon test. From the table, it can be seen that, on three of the six datasets considered, namely Colon, Lymphoma and Musk, the results achieved by our approach are better than those of FCBF and mRMR, in terms of RR. As for the number of features selected, they are comparable on Colon and Lymphoma, whereas on Musk our system selected about half of those selected from FCBF. As concerns Ovarian, our approach achieved results not

statistically different from those of FCBF, by selecting much more features. However, as suggested by the plot in Fig. 2, more generations would allow the algorithm to find better solutions and, most probably, to overcome the performance obtained by FCBF. Finally, the results on Spam and Ucihar, where FCBF the best performance, confirm that our approach is best suited for datasets containing thousands of features.

5 Conclusions

We presented two mutation operators specifically devised for a variable-length representation to be used in EC-based algorithms for feature selection, in which a feature subset is represented by an ordered list of integers. These operators allow the generation of offspring that may have a length different from that of the parent. We tested the proposed approach on six datasets and performed several experiments, as well as a comparison with state-of-art algorithms. The results showed that the two mutation operators perform differently. More precisely, the operator that can both change or add/delete one or more elements of the chromosome performs better than the one that can mutate the chromosome only by adding/deleting one or more elements. Regarding the comparison results, they confirmed that, for problems with a large number of features, the proposed approach outperforms both a standard GA and the two algorithms used for the comparison.

Future work will include the application of the feature selection approach devised, by using the operators presented here, to new application domains for the development of systems for cancer diagnosis [14, 15], e-health [16], or biometrics [17].

References

1. Cordella, L.P., De Stefano, C., Fontanella, F., Scotto di Freca, A.: A weighted majority vote strategy using Bayesian networks. In: Petrosino, A. (ed.) *ICIAP 2013*. LNCS, vol. 8157, pp. 219–228. Springer, Heidelberg (2013). https://doi.org/10.1007/978-3-642-41184-7_23
2. De Stefano, C., Fontanella, F., Folino, G., di Freca, A.S.: A Bayesian approach for combining ensembles of gp classifiers. In: Sansone, C., Kittler, J., Roli, F. (eds.) *MCS 2011*. LNCS, vol. 6713, pp. 26–35. Springer, Heidelberg (2011). https://doi.org/10.1007/978-3-642-21557-5_5
3. De Stefano, C., Fontanella, F., Di Freca, A.S.: A novel Naive Bayes Voting strategy for combining classifiers. In: *2012 International Conference on Frontiers in Handwriting Recognition*, pp. 467–472 (2012)
4. Xue, B., Zhang, M., Browne, W.N., Yao, X.: A survey on evolutionary computation approaches to feature selection. *IEEE Trans. Evol. Comput.* **20**(4), 606–626 (2016)
5. Cilia, N.D., De Stefano, C., Fontanella, F., Scotto di Freca, A.: A ranking-based feature selection approach for handwritten character recognition. *Pattern Recogn. Lett.* **121**, 77–86 (2018)
6. De Stefano, C., Fontanella, F., Marrocco, C.: A GA-based feature selection algorithm for remote sensing images, pp. 285–294. Springer, Berlin Heidelberg, Heidelberg (2008)

7. De Stefano, C., Fontanella, F., Marrocco, C., di Freca, A.S.: A GA-based feature selection approach with an application to handwritten character recognition. *Pattern Recogn. Lett.* **35**, 130–141 (2014)
8. Hong, J.-H., Cho, S.-B.: Efficient huge-scale feature selection with speciated genetic algorithm. *Pattern Recogn. Lett.* **27**(2), 143–150 (2006)
9. Jeong, Y.-S., Shin, K.S., Jeong, M.K.: An evolutionary algorithm with the partial sequential forward floating search mutation for large-scale feature selection problems. *J. Oper. Res. Soc.* **66**(4), 529–538 (2015)
10. Yahya, A.A., Osman, A., Ramli, A.R., Balola, A.: Feature selection for high dimensional data: an evolutionary filter approach. *J. Comput. Sci.* **7**, 800–820 (2011)
11. Chen, T.C., Hsieh, Y.C., You, P.S., Lee, Y.C.: Feature selection and classification by using grid computing based evolutionary approach for the microarray data. In: 2010 3rd International Conference on Computer Science and Information Technology, pp. 85–89 (2010)
12. Cilia, N.D., De Stefano, C., Fontanella, F., Scotto di Freca, A.: Variable-length representation for ec-based feature selection in high-dimensional data. In: Kaufmann, P., Castillo, P.A. (eds.) *EvoApplications 2019*. LNCS, vol. 11454, pp. 325–340. Springer, Cham (2019). https://doi.org/10.1007/978-3-030-16692-2_22
13. Hall, M.A.: Correlation-based Feature selection for discrete and numeric class machine learning. In: *Proceedings of the Seventeenth International Conference on Machine Learning*, San Francisco, CA, USA, pp. 359–366. Morgan Kaufmann Publishers Inc., (2000)
14. Menolascina, F., et al.: Developing optimal input design strategies in cancer systems biology with applications to microfluidic device engineering. *BMC Bioinform.* **10**, S4 (2009). <https://doi.org/10.1186/1471-2105-10-S12-S4>, (SUPPL. 12), art. no. S4
15. Bevilacqua, V., Mastronardi, G., Menolascina, F., Pannarale, P., Pedone, A.: A novel multi-objective genetic algorithm approach to artificial neural network topology optimisation: the breast cancer classification problem. In: *IEEE International Conference on Neural Networks - Conference Proceedings*, pp. 1958–1965 (2006)
16. Bevilacqua, V., et al.: A novel approach to evaluate blood parameters using computer vision techniques. In: *2016 IEEE International Symposium on Medical Measurements and Applications, MeMeA 2016 – Proceedings* (2016)
17. Bevilacqua, V., et al.: Retinal fundus biometric analysis for personal identifications. In: Huang, D.-S., Wunsch, D.C., Levine, D.S., Jo, K.-H. (eds.) *ICIC 2008*. LNCS (LNAI), vol. 5227, pp. 1229–1237. Springer, Heidelberg (2008). https://doi.org/10.1007/978-3-540-85984-0_147

Swarm Intelligence and Optimization



Phasor Symbiotic Organisms Search Algorithm for Global Optimization

Fahui Miao, Li Yao, Xiaojie Zhao^(✉), and Yawen Zheng

School of Artificial Intelligence, Beijing Normal University,
Beijing 100875, China
zhaox86@163.com

Abstract. The symbiotic organisms search algorithm is a meta-heuristic algorithm based on the establishment of symbiotic relationships between populations in recent years. In this study, a novel phasor symbiotic organisms search algorithm (PSOS) based on phasor theory is proposed. Both the phase angle and the trigonometric function in the proposed PSOS are used to set parameters that can have the same or different directions, similar or diverse values. Different combinations of these parameters can better control the local exploitation and global exploration of PSOS. This makes the PSOS algorithm have stronger global optimization ability, avoiding premature algorithm or falling into local optimization. In order to verify the effectiveness of the algorithm, this study selected 23 benchmark test functions and a classic engineering optimization problem for testing. The results show that the PSOS algorithm has higher convergence accuracy and stronger robustness.

Keywords: Phase angle · Symbiotic organisms search · Global optimization

1 Introduction

With the development of the economy and society, many complex engineering optimization and practical application problems are gradually appearing. For example, in the field of artificial intelligence, many global optimization problems are encountering with image processing [1], cloud computing [2] and Measurement matrix optimization [3], etc. Some studies show that traditional mathematical programming methods such as conjugate gradient descent and quadratic programming methods cannot effectively solve complex problems with non-differentiable, discontinuous, and multi-modal characteristics in reality [4, 12].

The meta-heuristic algorithm based on population plays an important role in engineering and practical optimization problems because of its flexibility and no gradients [5]. Meta-heuristic algorithm is a kind of global optimization algorithm inspired by various phenomena in nature [6]. Classic meta-heuristic algorithms include genetic algorithms [7], particle swarm optimization algorithms [8]. Along with the continuous development of meta heuristics, many new algorithms have been proposed in recent years, such as monarch butterfly optimization algorithm (MBO) [9], ant lion optimizer (ALO) [10], grey wolf optimizer (GOW) [11], harris hawks optimization (HHO) [12] algorithm and symbiotic organisms search algorithm (SOS) [13].

Inspired by the symbiotic relationship in nature, Chen and Prayogo proposed the symbiotic organisms search algorithm in 2014. The SOS has a simple structure and does not require extra parameters to get the optimal solution. The SOS algorithm has been improved in multiple versions and applied to many areas, such as the algorithm used in large-scale economic scheduling [14] and color image multi-threshold search optimization [1], the enhanced symbiotic organism search algorithms adopted to unrelated parallel machines manufacturing scheduling and setup time [15], and the discrete co-occurrence search methods introduced to large-scale time cost trade-offs in construction scheduling [16]. According to the no free lunch theorem (NFL) [17], no single optimization algorithm is suitable for solving all optimization problems. Therefore, modifying the original SOS algorithm is an interesting research topic. The study of the original SOS algorithm shows that the algorithm is more biased towards the guidance of global information for candidate solutions and does not make better use of local information, which makes the algorithm more precocious and is detrimental to the optimal solution. In addition, the original algorithm uses a simple normal distribution to control the update of candidate solutions, which is detrimental to the diversity of the population and reduces the algorithm's search for optimal performance. Proper use of global and local information is necessary to better balance the local exploitation and global exploration, so that the algorithm avoids falling into local optimal and precocious phenomena enable the algorithm to have a stronger performance in finding the best. For example, the global information is considered based on the average distance in paper [18], so as to avoid the original algorithm being overly biased towards local exploitation and falling into the partial optimal solution. According to phasor theory, the phase angle combined with trigonometric functions can obtain the parameters with the same or different directions, similar or different values [19]. Different combinations of these values produce more diverse values to better control local exploitation and global exploration of the algorithm. Inspired by it, this study proposes a phasor symbiotic organisms search algorithm (PSOS) based on the SOS and the phase angle control algorithm to take off the balance between local exploitation and global exploration.

The main contributions of this paper are as follows.

1. This study introduces the idea of phase angle into SOS algorithm for the first time and proposes a new PSOS algorithm.
2. The PSOS increases the use of local information and takes advantage of the diversity of the phase angle variation, so that it has the ability to balance the exploitation and exploration and enhance the algorithm's optimization performance.
3. The PSOS algorithm improves the optimization performance on benchmarking functions and three-rod truss design problems.

This paper is structured as follows, Sect. 1 is an introduction, which gives the background and the motivation for proposing the PSOS. Section 2 describes the original SOS algorithm. Section 3 describes the newly proposed PSOS in detail. Section 4 provides experiments and discussion to verify the global optimization capability of the PSOS algorithm. Section 5 is a full-text summary.

2 Symbiotic Organisms Search Algorithm

The SOS algorithm performs a search by simulating mutualism, commensalism and parasitism in nature [13]. The most surviving individual in the group is the optimal solution of the algorithm to achieve the global optimization of the algorithm. The specific model of SOS is as follows:

(1) Mutualism Phase

Mutualism relationship refers to the fact that both parties who establish a mutually beneficial relationship in nature can mutually benefit each other, thereby improving their own survivability. However, the two parties who establish a symbiotic relationship can have different benefits from each other. One of the most common examples of this symbiotic relationship in nature is the bee and the flower. The mathematical model abstracted from this relationship is as follows:

$$\begin{aligned} X_{inew} &= X_i + rand(0, 1) * (X_{best} - Mutual_Vector * BF_1) \\ X_{jnew} &= X_j + rand(0, 1) * (X_{best} - Mutual_Vector * BF_2) \\ Mutual_Vector &= \frac{X_i + X_j}{2} \end{aligned} \quad (1)$$

Among them, X_i and X_j are both sides of a mutually beneficial symbiotic relationship. $Mutual_Vector$ is the amount of benefit in a mutually beneficial symbiotic relationship. And BF_1 and BF_2 are benefit factors representing different benefit sizes, and the value is 1 or 2.

(2) Commensalism phase

Commensalism is the establishment of a symbiotic relationship among organisms in which one side benefits and the other neither benefits nor suffers. Remora fish and shark are such a commensalism relationship. One party feeds on the other's food waste, but the other party is not harmed or benefits. The mathematical model of this relationship is as follows:

$$X_{inew} = X_i + rand(-1, 1) * (X_{best} - X_j) \quad (2)$$

Among them, X_j is the individual difference from X_i and X_i is the party that benefits.

(3) Parasitism phase

Parasitic relationship is those in which one party benefits from the relationship while harming the other. The most common of such relationship in nature is mosquito and human. The mosquito abuses human blood and benefits from it, and humans are the victims. In the SOS algorithm, Lb denotes the lower boundary of the problem space and Ub denotes the upper boundary of the problem space. Lb and Ub are used to control the extent of the algorithm's search space. They are used

to control the randomly generated parasites in the problem space of the algorithm such that the value is a valid candidate solution. The artificial parasite ($X_{Parasite_Vector}$) mimicked the mosquito is obtained by randomly replacing the values of some dimensions on X_j as follows:

$$X_{Parasite_Vector} = rand(0, 1) * (Ub - Lb) + Lb \quad (3)$$

If the fitness value of $X_{Parasite_Vector}$ is higher than X_j , X_j is replaced by $X_{Parasite_Vector}$.

3 Phasor Symbiotic Organisms Search Algorithm (PSOS)

In the SOS algorithm, the random number between 0 and 1 is generated in terms of the rand function to control the magnitude of the update amount X_i . The generated random number cannot balance the exploration and exploitation capabilities of the algorithm. Additionally, in the original SOS algorithm, except the parasitic stage, the individual's benefits from the symbiotic relationship came from the global optimal value X_{best} ignoring the local optimal solution. For the symbiosis phenomenon, in addition to the biological benefits from the symbiotic relationship, the organism will also generate some benefits, such as the production of biological antibodies. In order to simulate this phenomenon, we add a part of individual self-benefit in the benefit stage of symbiotic relationship, and use the local optimal value to simulate self-benefit. Inspired by the phasor theory in mathematics, this study proposes an improved SOS algorithm based on the phase angle control algorithm for local detection and global mining balance called phasor symbiotic organisms search algorithm (PSOS). According to previous study [19], we choose sine and cosine functions to calculate parameters $p(\theta_i^{Iter})$ and $g(\theta_i^{Iter})$ of phase angle θ as follows.

$$p(\theta_i^{Iter}) = |\cos\theta_i^{Iter}|^{2*\sin\theta_i^{Iter}}, \quad g(\theta_i^{Iter}) = |\sin\theta_i^{Iter}|^{2*\cos\theta_i^{Iter}} \quad (4)$$

Where $|\sin\theta_i^{Iter}|$ and $|\cos\theta_i^{Iter}|$ represent the absolute values of sine and cosine functions that are periodic functions with values of amplitude ranging from [0,1]. These parameters are based on the combination of different values calculated by θ and are used to represent the different search strategies of the algorithm under phase angle control. The subgraph (a) in Fig. 1 shows the range of the rand function transformed randomly in the interval [0,1]. The subgraph (b) in Fig. 1 shows the distribution of parameters $p(\theta_i^{Iter})$ and $g(\theta_i^{Iter})$. If the phase angle is different, the $p(\theta_i^{Iter})$ and $g(\theta_i^{Iter})$ may have the opposite direction or the same direction. Their values may be similar or very different, producing different results in the algorithm. Therefore, the balance between algorithm exploration and exploitation can be well achieved, avoiding premature convergence or falling into a locally optimal solution.

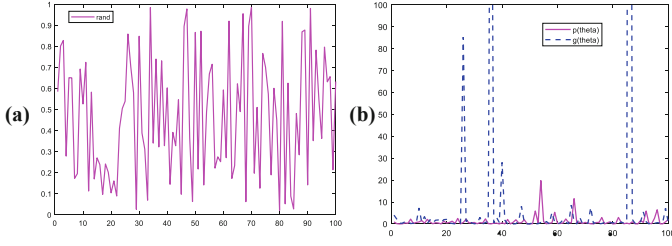


Fig. 1. Parametric data distribution curve. (a). Random function data distribution curve. (b). $p(\theta_i^{iter})$ and $g(\theta_i^{iter})$ distribution curves

In PSOS, biological populations are initially coded to be composed using an $M \times N$ Gaussian matrix, where M is the number of populations. N is the dimension of the problem space. And the range of generated biological individuals is controlled according to the upper (Ub) and lower (Lb) bounds of the problem space. In the initialization phase, a set of $M \times N$ phase angles θ is randomly generated, where θ is the value of a discrete and uniformly distributed set of randomly generated values at $[0, 2\pi]$. In this algorithm, the fitness values are used to measure the individual values. The mathematical model of the proposed PSOS algorithm in the three symbiotic stages is as follows:

(1) Mutualism Phase

$$\begin{aligned} X_{i_{new}} &= X_i + p(\theta_i^{iter}) * (X_{best} - Mutual_Vector * BF_1) + g(\theta_i^{iter}) * (X_i - Mutual_Vector * BF_1) \\ X_{j_{new}} &= X_j + p(\theta_j^{iter}) * (X_{best} - Mutual_Vector * BF_2) + g(\theta_j^{iter}) * (X_j - Mutual_Vector * BF_2) \end{aligned} \quad (5)$$

Among them, compared to the original SOS, the random function is replaced by $p(\theta_i^{iter})$ or $g(\theta_i^{iter})$, resulting in a larger range of possible solutions. The self-benefit of a biological individual is expressed by X_i or the difference between X_j and weighted $Mutual_Vector$. $Mutual_Vector$ is the amount of benefit in a mutually beneficial symbiotic relationship and It is calculated in the same way as in Eq. 1. BF_1 and BF_2 are mutually beneficial benefit factors whose values are randomly set to 1 or 2 and are used to mimic the amount of benefit that differs between two organisms.

(2) Commensalism phase

$$X_{i_{new}} = X_i + p(\theta_i^{iter}) * (X_{best} - X_j) + g(\theta_i^{iter}) * (X_i - X_j) \quad (6)$$

Similarly, in the new formula here, the random function is replaced by $p(\theta_i^{iter})$ or $g(\theta_i^{iter})$. The self-benefit of an individual organism is expressed by the difference between X_i and X_j .

(3) Parasitism phase

$$X_{parasite} = p(\theta_i^{Iter}) * (Ub - Ub) + Lb + g(\theta_i^{Iter}) * (Ub - Ub) + Lb \quad (7)$$

The artificial parasite $X_{Parasite_Vector}$ is also obtained by modifying the random dimension, where the upper and lower bounds Ub and Lb of the variable are used to calculate the random dimension, and the random function is replaced by $p(\theta_i^{Iter})$ or $g(\theta_i^{Iter})$.

After the three-phase calculation, the next phase angle is updated by the following formula:

$$\theta_i^{Iter+1} = \theta_i^{Iter} + |\cos(\theta_i^{Iter}) + \sin(\theta_i^{Iter})| * 2\pi \quad (8)$$

In order to facilitate the visualization of the PSOS, this paper draws a flowchart of the PSOS (shown in Fig. 2).

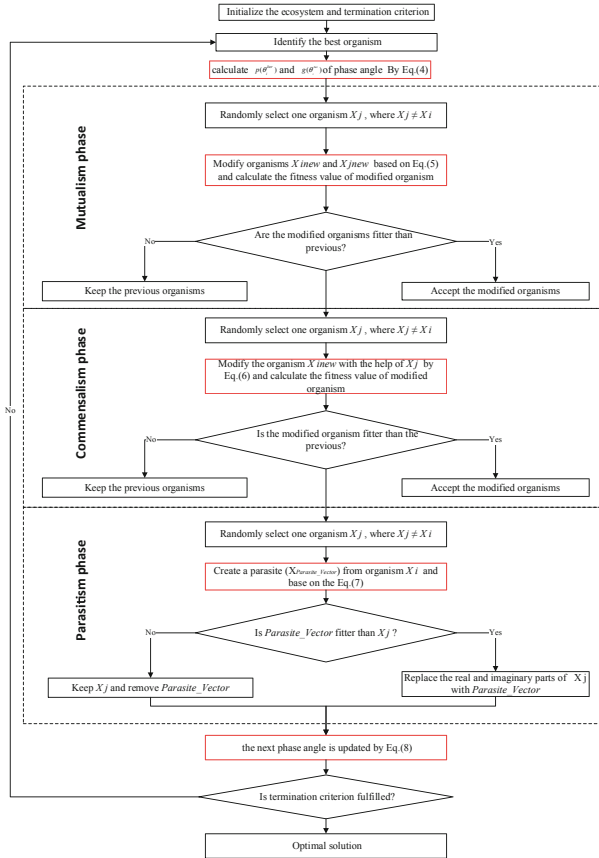


Fig. 2. The flowchart of PSOS. The red box indicates what distinguishes PSOS from SOS. (Color figure online)

4 Experimental Results and Discussion

In this study, three kinds of test functions are selected, including unimodal, multimodal, and fixed-dimensional multi-modal benchmark functions. A typical engineering example is selected to test the performance of PSOS algorithm on the three-bar truss design problem.

4.1 Experimental Setup

This study selects PSO, ALO, GWO and HHO algorithms for comparison experiments. The PSO algorithm is a classical algorithm in the field of meta-heuristics, and the ALO and GWO algorithms are the best performers in the field in recent years. HHO is the latest proposed algorithm with superior performance. So these 4 representative algorithms are chosen to compare with PSOS algorithm to measure the performance of their algorithm. The parameter settings of related comparison algorithms are shown in Table 1.

Table 1. Parameter settings of the algorithms compared with PSOS.

| Algorithm | Parameter |
|-----------|--|
| PSO [8] | $C_1 = 2, C_2 = 2, \omega = 0.1, \text{population} = 20$ |
| ALO [10] | population = 20 |
| GWO [11] | $\vec{a} = (2 \rightarrow 0), \text{population} = 20$ |
| HHO [12] | $\beta = 1.5, \text{population} = 20$ |
| SOS [13] | Population = 20 |

4.2 Results and Analysis on Benchmark Functions

- (1) The performance of PSOS algorithm on the benchmark function.

To verify the global optimization ability of the PSOS algorithm, 23 benchmark test functions were selected. Among these 23 benchmark functions, there are 7 unimodal benchmark functions, 6 multimodal benchmark functions, and 10 fixed-dimension multimodal benchmark functions. These benchmark test functions are consistent with those in previous study [12]. The results of these test functions are obtained by iterating 1000 times and running independently 10 times. Table 2 shows results of the unimodal benchmark functions with the underlined best-ranked values, indicating that the convergence accuracy is achieved by the PSOS on functions 1–4 and 7, and the theoretical optimal value in functions 1–4. In addition, the standard deviation of the five functions is the smallest.

Table 2. The fitness of the PSOS algorithms on the unimodal benchmark functions compared with the other realted algorithms. The underlined values are the best-ranked values.

| No. | | Method | | | | | |
|-----|------|---------|----------|----------|-----------------|-----------------|-----------------|
| | | PSO | ALO | GWO | HHO | SOS | PSOS |
| f1 | Mean | 6.81661 | 5.18E-05 | 1.05E-49 | 1.4E-174 | 4E-281 | <u>0</u> |
| | Std | 4.22697 | 3.34E-05 | 2.62E-49 | 0 | 0 | <u>0</u> |
| f2 | Mean | 13.8845 | 65.4021 | 1.38E-29 | 1.4E-95 | 1.1E-142 | <u>0</u> |
| | Std | 4.78017 | 50.1779 | 8.09E-30 | 4.26E-95 | 2.3E-142 | <u>0</u> |
| f3 | Mean | 385.619 | 2741.11 | 2.14E-11 | 6.9E-143 | 1.6E-102 | <u>0</u> |
| | Std | 209.202 | 1446.44 | 4.2E-11 | 2.2E-142 | 3.1E-102 | <u>0</u> |
| f4 | Mean | 9.67434 | 17.4906 | 6.36E-12 | 1.04E-89 | 4.9E-114 | <u>0</u> |
| | Std | 2.67860 | 7.85536 | 6.29E-12 | 3.14E-89 | 6.5E-114 | <u>0</u> |
| f5 | Mean | 2482.73 | 163.161 | 26.86305 | <u>0.007392</u> | 21.86642 | 11.4033 |
| | Std | 1423.96 | 239.862 | 0.603017 | <u>0.014901</u> | 0.868856 | 14.7216 |
| f6 | Mean | 7.89260 | 5.32E-05 | 0.662067 | 3.96E-05 | <u>6.2E-27</u> | 0.00153 |
| | Std | 4.95894 | 2.99E-05 | 0.326408 | 4.28E-05 | <u>1.59E-26</u> | 0.00226 |
| f7 | Mean | 5.69536 | 0.18694 | 0.001143 | 0.000129 | 0.000331 | <u>8.95E-05</u> |
| | Std | 7.19583 | 0.04036 | 0.000847 | 0.000113 | 0.000196 | <u>4.4E-05</u> |

Table 3 shows the results of multimodal benchmark functions. The PSOS algorithm achieved the smallest convergence accuracy in three of them. Except for function 12, the standard deviation of PSOS is the smallest, showing that the proposed algorithm is the most robust algorithm.

Table 3. The fitness of the PSOS algorithms on the multimodal benchmark functions compared with the other realted algorithms. The underlined values are the best-ranked values.

| No. | | Method | | | | | |
|-----|------|----------|----------|----------|-----------------|-----------------|-----------------|
| | | PSO | ALO | GWO | HHO | SOS | PSOS |
| f8 | Mean | -3136.36 | -6143.5 | -6345.99 | -12569.3 | <u>-11611.6</u> | -21526 |
| | Std | 1080.45 | 2105.95 | 752.7858 | 0.281949 | <u>533.909</u> | 90.46927 |
| f9 | Mean | 220.488 | 92.43144 | 0.337032 | <u>0</u> | <u>0</u> | <u>0</u> |
| | Std | 50.0577 | 30.1618 | 1.065789 | <u>0</u> | <u>0</u> | <u>0</u> |
| f10 | Mean | 5.81021 | 2.66713 | 1.9E-14 | <u>8.88E-16</u> | 3.38E-15 | <u>8.88E-16</u> |
| | Std | 0.85594 | 1.25889 | 3.11E-15 | <u>0</u> | 1.72E-15 | <u>0</u> |
| f11 | Mean | 0.59005 | 0.00663 | 0.003649 | <u>0</u> | <u>0</u> | <u>0</u> |
| | Std | 0.16463 | 0.00633 | 0.00595 | <u>0</u> | <u>0</u> | <u>0</u> |
| f12 | Mean | 12.1280 | 11.3234 | 0.045716 | 6.29E-06 | <u>6.27E-28</u> | 5.89E-05 |
| | Std | 8.92419 | 4.55756 | 0.017417 | 1.07E-05 | 1.93E-27 | 5.27E-05 |
| f13 | Mean | 36.8062 | 4.36172 | 0.732864 | <u>7.28E-05</u> | 0.026171 | 0.00024 |
| | Std | 31.109 | 13.2700 | 0.166067 | <u>7.65E-05</u> | 0.035954 | 0.000199 |

Table 4 shows the results of fixed-dimension multimodal benchmark function. The PSOS algorithm achieved the smallest convergence accuracy on all 10 functions, and theoretical optimal values of the model were found in 17, 18, and 21. In addition, the PSOS has the smallest standard deviation, except that the standard deviation is slightly higher than the SOS in function 18 with the same optimal value.

Table 4. The fitness of the PSOS algorithms on the fixed-dimension multimodal benchmark functions compared with the other related algorithms. The underlined values are the best-ranked values.

| No. | | Method | | | | | |
|-----|------|----------|----------|-----------|-----------|-----------------|-----------------|
| | | PSO | ALO | GWO | HHO | SOS | PSOS |
| f14 | Mean | 2.58836 | 1.990057 | 6.262057 | 1.689893 | <u>0.998004</u> | <u>0.998004</u> |
| | Std | 1.483883 | 1.04447 | 5.592337 | 1.545684 | <u>0</u> | <u>0</u> |
| f15 | Mean | 0.240851 | 0.009221 | 0.006333 | 0.000334 | 0.000307 | <u>0.000307</u> |
| | Std | 0.318335 | 0.020376 | 0.009682 | 2.43E-05 | 1.32E-19 | <u>1.08E-19</u> |
| f16 | Mean | -0.61919 | -1.03163 | -1.03163 | -1.03163 | <u>-1.03163</u> | <u>-1.03163</u> |
| | Std | 0.389019 | 4.69E-14 | 7.65E-09 | 6.69E-10 | <u>0</u> | <u>0</u> |
| f17 | Mean | -0.87204 | -0.96175 | <u>-1</u> | <u>-1</u> | <u>-1</u> | <u>-1</u> |
| | Std | 0.097589 | 0.032923 | <u>0</u> | <u>0</u> | <u>0</u> | <u>0</u> |
| f18 | Mean | 58.3756 | 3 | 3.000013 | 3.000001 | <u>3</u> | <u>3</u> |
| | Std | 77.50042 | 4.56E-13 | 1.23E-05 | 2.04E-06 | <u>2.96E-16</u> | <u>9E-16</u> |
| f19 | Mean | -3.71873 | -3.86278 | -3.85969 | -3.8597 | <u>-3.86278</u> | <u>-3.86278</u> |
| | Std | 0.111387 | 3.18E-14 | 0.003207 | 0.004626 | <u>9.36E-16</u> | <u>9.36E-16</u> |
| f20 | Mean | -2.84826 | -3.27443 | -3.2428 | -3.07909 | -3.27444 | <u>-3.29822</u> |
| | Std | 0.207444 | 0.061409 | 0.070808 | 0.089496 | 0.061396 | <u>0.05013</u> |
| f21 | Mean | -4.35089 | -5.84212 | -10.1526 | -5.04998 | -9.1336 | <u>-10.1532</u> |
| | Std | 2.390589 | 2.390184 | 0.000368 | 0.00334 | 2.149506 | <u>5.92E-16</u> |
| f22 | Mean | -6.21255 | -9.344 | -9.34342 | -5.08627 | -8.80836 | <u>-10.4029</u> |
| | Std | 2.761929 | 2.23246 | 2.232302 | 0.001831 | 2.567519 | <u>2.15E-07</u> |
| f23 | Mean | -5.79131 | -7.34603 | -10.5355 | -5.65079 | -10.5364 | <u>-10.5364</u> |
| | Std | 3.446301 | 3.48727 | 0.000593 | 1.661094 | 1.87E-15 | <u>1.67E-15</u> |

- (2) The p-value of the wilcoxon rank-sum test on the benchmark functions.

In this study, a wilcoxon rank-sum test [20] was performed on the fitness values of all algorithms with p-value as 0.05 (Table 5). The results show that the performance of PSOS is significantly better than the other related algorithms on most of benchmark function.

Table 5. p-values of Wilcoxon rank-sum test between the PSOS and other realted algorithms. The underlined values are greater than 0.05.

| No | PSO | ALO | GWO | HHO | SOS |
|-----|-------------|-----------------|-----------------|-----------------|-----------------|
| f1 | 6.38644E-05 | 6.39E-05 | 6.39E-05 | 6.39E-05 | 6.39E-05 |
| f2 | 6.38644E-05 | 6.39E-05 | 6.39E-05 | 6.39E-05 | 6.39E-05 |
| f3 | 6.38644E-05 | 6.39E-05 | 6.39E-05 | 6.39E-05 | 6.39E-05 |
| f4 | 8.74499E-05 | 8.74E-05 | 8.74E-05 | 8.74E-05 | 8.74E-05 |
| f5 | 0.000182672 | <u>0.005795</u> | <u>0.472676</u> | <u>0.850107</u> | <u>0.472676</u> |
| f6 | 0.000182672 | 0.000246 | 0.000183 | 0.00044 | 0.000183 |
| f7 | 0.000182672 | 0.000183 | 0.000583 | <u>0.73373</u> | 0.00033 |
| f8 | 0.000182672 | 0.000173 | 0.000183 | 0.000183 | 0.000183 |
| f9 | 6.38644E-05 | 6.39E-05 | 0.034424 | N/A | N/A |
| f10 | 6.38644E-05 | 6.39E-05 | 5.59E-05 | N/A | 0.001617 |
| f11 | 6.38644E-05 | 6.39E-05 | <u>0.077872</u> | N/A | N/A |
| f12 | 0.000182672 | 0.000183 | 0.000183 | 0.001008 | 0.000183 |
| f13 | 0.000182672 | 0.000246 | 0.000183 | 0.017257 | <u>0.472676</u> |
| f14 | 6.38644E-05 | 6.02E-05 | 6.39E-05 | 6.39E-05 | N/A |
| f15 | 0.000162111 | 0.000162 | 0.000162 | 0.000162 | 0.002402 |
| f16 | 6.38644E-05 | 6.39E-05 | 6.39E-05 | 6.39E-05 | N/A |
| f17 | 6.38644E-05 | 6.2E-05 | N/A | N/A | N/A |
| f18 | 0.000161177 | 0.000161 | 0.000161 | 0.000161 | <u>0.851968</u> |
| f19 | 6.38644E-05 | 6.34E-05 | 6.39E-05 | 6.39E-05 | N/A |
| f20 | 0.000182672 | <u>0.427355</u> | 0.001706 | 0.000183 | <u>0.180879</u> |
| f21 | 8.74499E-05 | 8.74E-05 | 8.74E-05 | 8.74E-05 | <u>0.122608</u> |
| f22 | 0.0001459 | 0.001452 | 0.000146 | 0.000146 | <u>0.144796</u> |
| f23 | 0.000109969 | 0.00011 | 0.00011 | 0.00011 | <u>0.167489</u> |

4.3 Performance of the PSOS Algorithm in Engineering Optimization

Three-bar truss design problem [12] is a classic engineering design problem, which is a single-objective optimization problem.

$$\text{Consider } \vec{X} = [x_1 x_2] = [A_1 A_2]$$

$$\text{Minimize } f(\vec{X}) = (2\sqrt{2}x_1 + x_2) \times L$$

$$\begin{aligned} \text{Subject to } g_1(\vec{X}) &= \frac{\sqrt{2}x_1 + x_2}{\sqrt{2}x_1^2 + 2x_1x_2} P - \sigma \leq 0, \quad g_2(\vec{X}) = \frac{x_2}{\sqrt{2}x_1^2 + 2x_1x_2} P - \sigma \leq 0, \quad g_3(\vec{X}) \\ &= \frac{1}{x_1 + \sqrt{2}x_2} P - \sigma \leq 0 \end{aligned}$$

$$\text{Variable range } 0 \leq x_1, x_2 \leq 1, \quad (L = 100\text{cm}, P = 2\text{KN}/\text{cm}^2, \sigma = 2\text{KN}/\text{cm}^2)$$

This structure consists of 3 rods, which are subject to longitudinal and lateral stresses. The areas between rods 1, rods 2, and rods 3 need to be calculated. We need to find the minimum force to withstand. The calculation results are shown in Table 7.

Table 7. The performance comparison of the optimization algorithms on three-bar truss design problem.

| Algorithm | Optimal values for variables | | Optimal weight |
|-----------|------------------------------|----------|----------------|
| | x_1 | x_2 | |
| PSOS | 0.78685 | 0.28801 | 186.3859 |
| HHO | 0.788663 | 0.408283 | 263.8958 |
| DEDS | 0.788675 | 0.408248 | 263.8958 |
| MVO | 0.788603 | 0.408453 | 263.8958 |
| GOA | 0.788898 | 0.40762 | 263.8959 |
| MFO | 0.788245 | 0.409467 | 263.896 |
| PSO-DE | 0.788675 | 0.408248 | 263.8958 |
| Ray | 0.795 | 0.395 | 264.3 |
| CS | 0.78867 | 0.40902 | 263.9716 |

The bearing capacity derived from the combination of rod areas by the PSOS is the smallest, indicating the value of the PSOS in this engineering optimization is optimal.

5 Conclusions

This study proposes a new phasor symbiotic organisms search algorithm (PSOS) based on the phase angle control algorithm to balance local exploitation and global exploration. According to the phasor theory, the directions of the phase angles may be the same or opposite, and the calculated parameters may be similar or different. Their combination can provide a wealth of strategies that is beneficial to the PSOS algorithm to enhance exploration capabilities and better balance global and local search, thereby avoiding the algorithm premature or falling into local optimization. The experimental results of 23 benchmark test functions and a practical engineering example show that the PSOS algorithm presents stronger abilities of optimization and robustness. Next, the PSOS algorithm can be extended to other practical applications such as medical images or biological signal processing.

Acknowledgement. This work is supported by the Funds for National Natural Science Foundation of China (grant number 61871040); the Key Program of National Natural Science Foundation of China (grant number 61731003) and the Engineering Research Center of Intelligent Technology and Educational Application, Ministry of Education.

References

1. Chakraborty, F., Nandi, D., Roy, P.K.: Oppositional symbiotic organisms search optimization for multilevel thresholding of color image. *Appl. Soft Comput.* **82**, 105577 (2019)
2. Ezugwu, A.E., Adewumi, A.O.: Soft sets based symbiotic organisms search algorithm for resource discovery in cloud computing environment. *Future Gener. Comput. Syst.* **76**, 33–50 (2017)
3. Zhihua, C., Chunmei, Z., Zhentao, S., Yun, N.: Observation matrix optimization algorithm based on bat algorithm. *Control Decis.* **33**(7), 1341–1344 (2018)
4. Wu, G., Pedrycz, W., Suganthan, P.N., Mallipeddi, R.: A variable reduction strategy for evolutionary algorithms handling equality constraints. *Appl. Soft Comput.* **37**, 774–786 (2015)
5. Yapici, H., Cetinkaya, N.: A new meta-heuristic optimizer: pathfinder algorithm. *Appl. Soft Comput.* **78**, 545–568 (2019)
6. Mirjalili, S., Lewis, A.: The whale optimization algorithm. *Adv. Eng. Softw.* **95**, 51–67 (2016)
7. Jesus, I.S., Barbosa, R.S.: Genetic optimization of fuzzy fractional PD+I controllers. *ISA Trans.* **57**, 220–230 (2015)
8. Pan, I., Das, S.: Fractional order fuzzy control of hybrid power system with renewable generation using chaotic PSO. *ISA Trans.* **62**, 19–29 (2016)
9. Wang, G.-G., Deb, S., Cui, Z.: Monarch butterfly optimization. *Neural Comput. Appl.* **31**(7), 1995–2014 (2015). <https://doi.org/10.1007/s00521-015-1923-y>
10. Mirjalili, S.: The ant lion optimizer. *Adv. Eng. Softw.* **83**, 80–98 (2015)
11. Mirjalili, S., Mirjalili, S.M., Lewis, A.: Grey wolf optimizer. *Adv. Eng. Softw.* **69**, 46–61 (2014)
12. Heidari, A.A., Mirjalili, S., Faris, H., Aljarah, I., Mafarja, M., Chen, H.: Harris hawks optimization: algorithm and applications. *Future Gener. Comput. Syst.* **97**, 849–872 (2019)
13. Cheng, M.Y., Prayogo, D.: Symbiotic organisms search: a new metaheuristic optimization algorithm. *Comput. Struct.* **139**, 98–112 (2014)
14. Secui, D.C.: A modified symbiotic organisms search algorithm for large scale economic dispatch problem with valve-point effects. *Energy* **113**, 366–384 (2016)
15. Ezugwu, A.E.: Enhanced symbiotic organisms search algorithm for unrelated parallel machines manufacturing scheduling with setup times. *Knowl.-Based Syst.* **172**, 15–32 (2019)
16. Liu, D., Li, H., Wang, H., Qi, C., Rose, T.: Discrete symbiotic organisms search method for solving large-scale time-cost trade-off problem in construction scheduling. *Expert Syst. Appl.* **148**, 113230 (2020)
17. Wolpert, D.H., Macready, W.G.: No free lunch theorems for optimization. *IEEE Trans. Evol. Comput.* **1**(1), 67–82 (1997)
18. Zhihua, C., Maoqing, Z., Chang, Yu., Jiangjiang, Z., Hui, W., Wensheng, Z.: NSGA-II based on average distance clustering. *J. Autom.* (2019). <https://doi.org/10.16383/j.aas.c180540>
19. Ghasemi, M., Akbari, E., Rahimnejad, A., Razavi, S.E., Ghavidel, S., Li, L.: Phasor particle swarm optimization: a simple and efficient variant of PSO. *Soft. Comput.* **23**(19), 9701–9718 (2018). <https://doi.org/10.1007/s00500-018-3536-8>
20. Wilcoxon, F.: Individual comparisons by ranking methods. In: *Breakthroughs in Statistics*, pp. 196–202. Springer, New York (1992). https://doi.org/10.1007/978-1-4612-4380-9_16

Compressed Sensing and Sparse Coding



Essential Proteins Identification Based on Integrated Network

Chang-Gang Wen¹, Jin-Xing Liu¹, Lei Qin², Juan Wang¹,
and Yun Fang¹ (✉)

¹ School of Information Science and Engineering, Qufu Normal University,
Rizhao 276826, China
chgwenqrnu@126.com

² Shandong Vocational and Technical University of International Studies,
Rizhao 276826, China

Abstract. Identifying essential proteins is important for understanding cellular life and pathogenic mechanisms. In addition to experimental methods, many computing approaches have been employed to identify essential proteins. Many of these methods usually consider the topological structure of the protein-protein interaction network (PPIN). However, the fact that the PPIN includes many false negative interactions is ignored. In this paper, an integrated PPIN that considers protein interactions and gene co-expression is presented. With more false negative interactions being considered, more meaningful essential proteins can be identified on the integrated PPIN. To verify the performance of this method, an experiment is carried out on data from *Saccharomyces cerevisiae*. The results demonstrate that ITPPIN can identify essential proteins is more effective than PPIN.

Keywords: Essential proteins · Gene co-expression · Integration · Protein-protein interaction network

1 Introduction

Protein is an important component of all cells and tissues in human body. The compositions of biology, metabolism and genetics are closely related to protein structure and function. Therefore, it is necessary to identify proteins, especially essential ones. If an essential protein in a protein complex is lost, the complex will not work properly, and this may cause the organism to be unable to survive [1]. Essential proteins are crucial to understand cellular life and practical applications, such as clinical diagnosis and drug design. Because of the importance of essential proteins, it is necessary to effectively identify them.

Originally, essential proteins were identified by biotechnology experimental methods. To address the deficiencies of biotechnology experiments, computational methods can be employed to discover essential proteins. Many machine learning algorithms have been used to detect essential proteins. The basic thought of these methods is to identify essential proteins by a trained classifier according to the features of known essential and non-essential proteins.

Since the correlation between topological centrality and protein essentiality has been confirmed [2–5], many studies tried to identify essential proteins by complex network computing. Most of the computing methods are based on topological structure characteristics of the protein-protein interaction network (PPIN). Essential proteins can be identified with low cost and improved efficiency by these methods. Therefore, the identification of essential proteins at the PPIN level has attracted the increasing attention of scholars as a hot topic in the field of proteomics.

These studies generally consider that the degree of essential proteins is likely larger than non-essential proteins, and essential proteins tend to be in densely connected clusters [6]. Degree centrality (DC) [7], betweenness centrality (BC) [8], subgraph centrality (SC) [9], eigenvector centrality (EC) [10], network centrality (NC) [11], and the local average connectivity-based methods (LAC) [12] are commonly used for essential protein identification. These methods only consider one topological feature of a PPI network. LIDC [13] is based on both local interaction density and the corresponding protein complexes. On the basis of the LIDC, BC is introduced into LBCC [14]. Together with the topological features of PPI networks, other features (such as cellular localization and gene expression) have also been used to discover essential proteins. Acencio et al. identified essential genes by using features of topological structure, which were integrated with cellular localization and biological process [15]. Yue et al. found candidate genes of breast cancer by using a common PPI network integrated with co-expression information [16].

Though these methods are effective at finding essential proteins, the fact that the protein-protein interaction network contains many false negative or false positive interactions is ignored. For example, Huang et al. noted that in the PPI network of yeast, the rates of false positive and false negative are 9.9% and 51%, respectively [17]. Thus, these rates will affect identification of essential proteins. Some methods, such as weighting methods, have been used to find false positive interactions. In addition, some literature showed that essential proteins are clearly not independent but in one cluster [18–20], and this idea was also used by Qin et al. [14]. Li et al. showed that essential proteins may be highly co-clustered and co-expressed with other proteins [6].

Based on the above points, we propose a new method in which the PPIN is integrated by the co-expression network to identify essential proteins. In our method, the original protein-protein interaction network is named PPIN, and the protein-protein network integrated with the co-expression network is named ITPPIN. First, the gene expression data are filtered according to the PPIN, and a co-expression network between genes is constructed by Pearson coefficient. Then, one edge selected from the co-expression network is searched in the PPIN. If not found, the edge is added into the PPIN, otherwise, it is considered a true positive and left as is. All the edges in the co-expression network are processed by the above process until the whole integrated network is complete. Thus, our method can find partial false negative interactions, and more essential proteins can also be identified.

In this paper, we construct two kinds of networks, named PPIN and ITPPIN, on data from *Saccharomyces cerevisiae*. To test the effect of ITPPIN, nine classical methods are employed on these two network types. The results demonstrate that almost all the nine methods are more efficient on ITPPIN than PPIN at any level.

The rest of the paper is organized as follows. Section 2 introduces the method basis and workflow. Section 3 describes the experimental process. The results are shown in Sect. 4. Section 5 provides some conclusions.

2 Related Work

To demonstrate our method, we first introduce the relevant definitions and descriptions. An undirected graph $G(V, E)$ is used to represent the PPIN. In graph $G(V, E)$, a node v ($v \in V$) represents a protein and an edge $e(u, v)$ ($e(u, v) \in E$) represents the interaction between protein u and protein v . Unlike PPIN, the co-expression network is represented by an undirected network $N(V, E)$, where a node denotes a gene and an edge $e(s, t)$ ($e(s, t) \in E$) with a weight that represents the degree of co-expression between genes s and t . Similarly, the integrated network based on the PPIN and co-expression network is also represented by an undirected graph. Moreover, the original protein-protein interaction network is named PPIN, and the protein-protein network integrated with the co-expression network is named ITPPIN.

In this section, a method by which the protein-protein interaction network can be integrated with the co-expression network is proposed in detail. The method is based on two ideas: (1) essential proteins in the same cluster are more likely to be co-expressed than essential proteins in other clusters [6], (2) co-expressed genes have a greater chance of interacting with each other [21]. The process of our method contains three phases: construction of the co-expression network, integration of the PPIN and co-expression networks, and network analysis and evaluation.

2.1 Construction of the Co-expression Network

It is generally believed that the stronger the interaction between proteins, the stronger the correlation. To evaluate the strength of the interaction between proteins, we introduced the co-expression network. Because the raw gene expression data contain noise and irrelevant data, the raw data are filtered by first referring to the protein-protein interaction data. Then, the genes that correspond to proteins in the PPIN are selected. The expression data of the selected genes are put into a matrix. A co-expression network is constructed with a Pearson coefficient between genes. The Pearson coefficient formula can be written as follows:

$$p(X, Y) = \frac{1}{(n-1)} \sum_{i=1}^n \left(\frac{X_i - \bar{X}}{S_X} \right) \left(\frac{Y_i - \bar{Y}}{S_Y} \right) \quad (1)$$

where n is the number of samples in the gene expression data; X_i (or Y_i) is the observed value of gene X (or gene Y) in the sample i ; \bar{X} (\bar{Y}) is the mean and standard variation of gene X (Y); S_X (or S_Y) is standard variance of gene X (or gene Y).

Assuming the number of selected genes is d , the size of the co-expression matrix is $d \times d$. In our method, the positive and negative correlations are equally important. Therefore, the final co-expression network contains the absolute value of all correlations.

2.2 Integration of PPI Network and Co-expression Network

As mentioned above, for most proteins, the interaction and correlation are congruent. Any PPI network contains some false positive and false negative interactions. A false negative interaction may corresponds to a strong correlation. This is the basis formation of the integrated PPI network. The integrated PPI network is constructed by the PPIN and the co-expression network that is constructed as described above.

In the co-expression network, although one pair of genes has a correlation coefficient, the corresponding proteins in the protein do not have to interact with each other. Further, if the protein pair is added into the PPI network, it is likely to be a false positive. In this paper, only the protein pairs with high correlation are considered likely to be interacting each other. First, a threshold t is given. Then, a gene pair whose correlation coefficient exceeded it is selected, and the corresponding protein pair in the PPI network is searched. If the protein pair is not found, it is considered a false negative protein-protein interaction and put into the PPI network. If the protein pair is found, the corresponding protein-protein interaction is confirmed. The above process is repeated until all the candidate gene pairs are used. Finally, the integrated PPI network, named ITPPIN, is completed.

The ITPPIN is demonstrated in Fig. 1. The first part is PPIN, in which the protein A has the highest degree and is most likely an essential protein. The degree of protein B is one, and it is less likely to be an essential protein. The basis for these findings is that a protein with a high degree is more likely to be essential than one with a low degree [6]. In ITPPIN, considering the co-expression characteristics, B has new interactions with C, D and E and is more likely to be essential. This outcome is the result of the above iterative process.

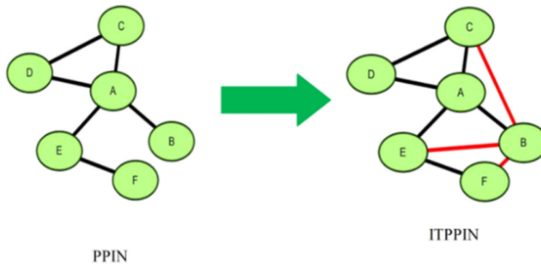


Fig. 1. An example for the construction of ITPPIN. In PPIN, the protein A has the highest degree and is most likely to be an essential protein. B has a lower degree and may not be essential. Due to co-expression in ITPPIN, B has new interactions with C, D and E, and the chance to be an essential proteins increased.

2.3 Network Analysis and Evaluation

Several algorithms, such as DC, BC, SC, EC, NC, LAC, information centrality (IC) [22], and closeness centrality (CC) [23], are classical methods to identify essential proteins. A variety of topological structure characteristics are involved in these methods. Ye et al. have integrated these methods as a plug named CytoNCA of

Cytoscape [24]. We analyze the two network types (PPIN and ITPPIN) using the plugin, LBCC, which considers the local and global topological features and was shown to be more effective than the above method by Qin et al. [14]. We also use it to validate the effectiveness of ITPPIN.

3 Experiments

3.1 Experimental Data

Because it has the most complete and reliable PPI and gene expression data [25], *S. cerevisiae* (Baker's Yeast) is used frequently in many other studies. Data from *S. cerevisiae* [6] is also used to test our method.

The PPI data of *S. cerevisiae* is obtained from the DIP database. The data include 24,743 interactions and 5093 proteins without self-interactions and repeated interactions.

The essential proteins were extracted from the following four databases: MIPS, SGD [26], DEG [27], and SGDP [28]. The extraction strategy is that an essential protein is in at least one of the above four databases. Among the 1285 extracted essential proteins, the PPI data contain 1167 proteins. In our experiment, the remaining 3296 proteins were considered non-essential.

The gene expression data of *Saccharomyces cerevisiae* are distributed by Tu et al. [29]. Among the gene expression data, containing 6777 genes and 36 samples, 4858 genes are involved in the PPI network.

3.2 Constructing Co-expression Network

First, by removing the genes not involved in the PPI network, the gene expression data is filtered. Then, a matrix that includes the Pearson coefficient of 4858 genes is created. In the matrix, rows and columns represent genes, and the data are the absolute values of the Pearson coefficient. Based on the above matrix, an undirected network is constructed. The vertices of the undirected network are genes. The edges, where the Pearson coefficient is considered as the weight, represent the co-expression relationship of gene pairs.

3.3 Constructing ITPPIN

To select appropriate gene pairs, a threshold t was first specified. Accordingly, t was defined as 3 times the mean of all the edge weights in the above gene co-expression network. A pair of genes, whose value of Pearson coefficient exceeds a threshold t , was taken out. We searched for the corresponding pair of proteins in the PPI network. If not found, the corresponding protein pair was considered false negative and added to the PPI network. This process was repeated until the integrated PPI network was completed. In total, the Pearson coefficient of 1886 gene pairs was above the threshold t , and 1814 edges were added into the PPIN. The original PPIN included 72 pairs.

3.4 Computing on ITPPIN and PPIN

We employed nine methods to test the efficiency of the ITPPIN. They were degree centrality (DC), betweenness centrality (BC), subgraph centrality (SC), eigenvector centrality (EC), network centrality (NC), the local average connectivity-based method (LAC), and LBCC. The first eight methods have been used in many studies.

4 Results

4.1 Essential Protein Identification

Similar to others, we first sorted proteins in descending order according to their scores computed by the different algorithms. Then, the top 100, 200, 300, 400, 500, and 600 proteins were selected as candidate essential proteins. Finally, based on the list of essential proteins, each candidate essential protein was verified. To compare the efficiency of the ITPPIN and the original PPIN, the original PPIN was also computed by the above nine algorithms. The results are shown in Fig. 2.

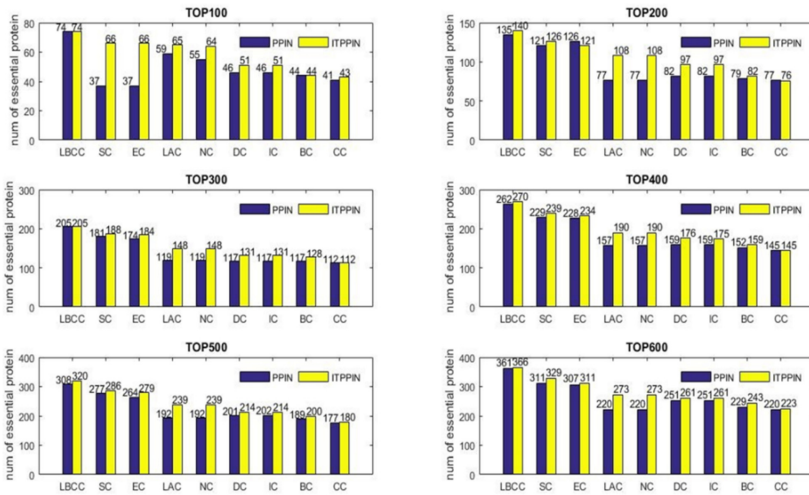


Fig. 2. The numbers of essential proteins selected by different methods on two kinds of network.

As shown in Fig. 2, almost all nine methods obtained a better result on the ITPPIN than the original PPIN. The effects of SC and EC increase by more than two-thirds at the top 100 level. For SC, LAC, NC, DC and IC, the results are improved at all six levels. At the top 100 level, LBCC and BC have the same efficiency on two network types. CC also has similar characteristics at the top 300 and 400 levels; however, LBCC is at level top 100 and top 300. LBCC always has the highest efficiency on the two networks among the nine algorithms at all levels. The best average improvement

efficiency is completed by LAC. The increased numbers, by the algorithm LAC, are 6, 41, 29, 33, 41 and 53 at the six levels, respectively.

We compare the calculated results of each method on the two network types at the top 100 level. The numbers of essential proteins identified by different methods on the two network types are shown in Table 1.

Table 1. The numbers of essential proteins

| Method | S1 | S2 | $S1 \cap S2$ | S1-S2 | S2-S1 |
|--------|----|----|--------------|-------|-------|
| LBCC | 74 | 74 | 63 | 11 | 11 |
| SC | 66 | 37 | 10 | 56 | 27 |
| EC | 66 | 37 | 10 | 56 | 27 |
| LAC | 65 | 59 | 21 | 44 | 38 |
| NC | 64 | 55 | 21 | 43 | 32 |
| DC | 51 | 46 | 39 | 12 | 7 |
| IC | 51 | 46 | 36 | 15 | 10 |
| CC | 43 | 41 | 39 | 4 | 2 |
| BC | 44 | 44 | 42 | 2 | 2 |

In Table 1, S1, S2 are the numbers of essential proteins found on ITPPIN and PPIN, respectively. $S1 \cap S2$ is the number of essential proteins found in both kinds of networks. S1-S2 denotes the number of essential proteins found on ITPPIN and not on PPIN, and S2-S1 denotes the opposite. Although LBCC and BC obtain the same number of essential proteins on ITPPIN and PPIN with all nine methods, the essential proteins found by the same method on different networks are not the same.

We count the average degree of different essential proteins at the top100 level and show the results in Table 2. AD (S1) and AD (S2) are the average degree of essential proteins found on ITPPIN and PPIN, respectively. AD ($S1 \cap S2$) is the average degree of essential proteins found in both network types. AD (S1-S2) denotes the average degree of essential proteins found on ITPPIN and not on PPIN, and AD (S2-S1) denotes the opposite. Apart from NC and CC, each of the other seven methods can find essential proteins with lower degree on ITPPIN than on PPIN. Why did this happen? Although most essential proteins are often rich in neighbors, those with few neighbors is there and were found by our method. For example, by SC, the average degree of essential proteins on ITPPIN is lower than that on PPIN. And AD (S2-S1) is also much higher than AD (S1-S2).

4.2 Result Evaluation

Referring to the literature [11, 13, 14], we evaluated the effectiveness of the measures, including works by six statistical measures, including specificity (SP), sensitivity (SN), negative predictive value (NPV), positive predictive value (PPV), accuracy (ACC), and F-measure (F). These statistical measures are often used to evaluate the effectiveness of

Table 2. Average degree of essential proteins

| Method | AD (S1) | AD (S2) | AD (S1 \cap 2) | AD (S1-S2) | AD (S2-S1) |
|--------|---------|---------|------------------|------------|------------|
| LBCC | 22.04 | 23.81 | 23.81 | 20.27 | 23.82 |
| SC | 74.59 | 106.78 | 128.60 | 20.57 | 84.96 |
| EC | 74.59 | 106.78 | 128.60 | 20.57 | 84.96 |
| LAC | 27.16 | 32.69 | 39.71 | 14.61 | 25.66 |
| NC | 82.93 | 78.94 | 103.67 | 62.19 | 54.21 |
| DC | 68.04 | 85.70 | 105.26 | 30.83 | 66.14 |
| IC | 63.83 | 102.52 | 96.83 | 30.83 | 108.20 |
| CC | 76.42 | 62.69 | 97.85 | 55.00 | 27.54 |
| BC | 73.57 | 77.82 | 99.14 | 48.00 | 56.50 |

methods for detecting essential proteins and interactions between protein pairs or gene pairs. The classical definition of the statistical measures is as follows.

We used the above six statistical methods to compare the efficiency of PPIN and ITPPIN in identifying essential proteins. Taking the BC method as an example, the calculation was carried out on the two network types. We ranked the proteins in descending order according to the score computed by BC. Then, the top 100 proteins detected by BC were identified as essential, and the remaining proteins were identified as non-essential proteins. This processing procedure is applicable to all the other eight methods. The statistical results are listed in Table 3.

From Table 3, it is found that most of the methods can obtain a better result on ITPPIN than on PPIN. Because of obtaining the same results on the two network types, SC and EC have the same trend on each statistical measure at top100 level. Because the same results were obtained by BC and LBCC for both network types, ITPPIN and PPIN are not different than BC and LBCC.

5 Conclusion

In this paper, we constructed a type of integrated network, named ITPPIN, by integrating the PPIN with the gene co-expression network. We built the ITPPIN with the data of *Saccharomyces cerevisiae* and employed nine classical algorithms, including SC, EC, NC, DC, IC, BC, CC, LAC and LBCC, on the PPIN and ITPPIN networks. As the results show, almost all the algorithms can obtain a better result on ITPPIN than PPIN at all levels. We analyzed the essential proteins found by the BC method on both networks types at top level 100. Most of the essential proteins that were simultaneously found in both networks interact with each other. The essential proteins that were found in ITPPIN but not in PPIN have more interactions with other essential proteins and fewer with those found in PPIN but not in ITPPIN.

The results reflect that more essential proteins can be found by the integrated PPI network ITPPIN, and they are more meaningful. In further study, we will consider the co-expression of one protein with all the other proteins around it at the same time.

Table 3. Statistical results

| Method | SN | | SP | | PPV | | IPV | | F | | ACC | |
|--------|--------------|-------|--------------|-------|--------------|-------|--------------|-------|--------------|-------|--------------|-------|
| | ITPPIN | PPIN | ITPPIN | PPIN | ITPPIN | PPIN | ITPPIN | PPIN | ITPPIN | PPIN | ITPPIN | PPIN |
| SC | 0.057 | 0.032 | 0.991 | 0.984 | 0.660 | 0.370 | 0.779 | 0.774 | 0.104 | 0.058 | 0.777 | 0.766 |
| DC | 0.044 | 0.039 | 0.988 | 0.986 | 0.510 | 0.460 | 0.776 | 0.775 | 0.081 | 0.073 | 0.771 | 0.769 |
| EC | 0.057 | 0.032 | 0.991 | 0.984 | 0.660 | 0.370 | 0.779 | 0.774 | 0.104 | 0.058 | 0.777 | 0.766 |
| IC | 0.044 | 0.039 | 0.988 | 0.986 | 0.510 | 0.460 | 0.776 | 0.775 | 0.081 | 0.073 | 0.771 | 0.769 |
| LAC | 0.056 | 0.051 | 0.991 | 0.990 | 0.650 | 0.590 | 0.779 | 0.778 | 0.103 | 0.093 | 0.777 | 0.774 |
| BC | 0.038 | 0.038 | 0.986 | 0.986 | 0.440 | 0.440 | 0.775 | 0.775 | 0.069 | 0.069 | 0.768 | 0.768 |
| CC | 0.037 | 0.035 | 0.985 | 0.985 | 0.430 | 0.410 | 0.775 | 0.774 | 0.068 | 0.065 | 0.768 | 0.767 |
| NC | 0.055 | 0.047 | 0.991 | 0.989 | 0.640 | 0.550 | 0.779 | 0.777 | 0.101 | 0.087 | 0.776 | 0.773 |
| LBCC | 0.063 | 0.063 | 0.993 | 0.993 | 0.740 | 0.740 | 0.781 | 0.781 | 0.117 | 0.117 | 0.780 | 0.780 |

Some other related data, such as domain information, localization, biological process, and similarity, will be introduced into our study.

Acknowledgment. This work was supported in part by the NSFC under grant Nos. 61872220, and 61873001.

References

1. Winzeler, E.A., et al.: Functional characterization of the *S. cerevisiae* genome by gene deletion and parallel analysis. *Science* **285**, 901–906 (1999)
2. Batada, N.N., Hurst, L.D., Tyers, M.: Evolutionary and physiological importance of hub proteins. *PLoS Comput. Biol.* **2**, e88 (2006)
3. Estrada, E.: Virtual identification of essential proteins within the protein interaction network of yeast. *Proteomics* **6**, 35–40 (2006)
4. Hahn, M.W., Kern, A.D.: Comparative genomics of centrality and essentiality in three eukaryotic protein-interaction networks. *Mol. Biol. Evol.* **22**, 803–806 (2005)
5. Vallabhajosyula, R.R., Chakravarti, D., Lutfeali, S., Ray, A., Raval, A.: Identifying hubs in protein interaction networks. *PLoS ONE* **4**, e5344 (2009)
6. Min, L., Zhang, H., Wang, J., Yi, P.: A new essential protein discovery method based on the integration of protein-protein interaction and gene expression data. *BMC Syst. Biol.* **6**, 15 (2012)
7. Jeong, H., Mason, S.P., Barabási, A.L., Oltvai, Z.N.: Lethality and centrality in protein networks. *Nature* **411**, 41–42 (2001)
8. Joy, M.P., Brock, A., Ingber, D.E., Huang, S.: High-betweenness proteins in the yeast protein interaction network. *J. Biomed. Biotechnol.* **2005**, 96–103 (2005)
9. Estrada, E., Rodríguez-Velázquez, J.A.: Subgraph centrality in complex networks. *Phys. Rev. E Stat. Nonlin. Soft Matter Phys.* **71**, 122–133 (2005)
10. Bonacich, P.: Power and centrality: a family of measures. *Am. J. Sociol.* **92**, 1170–1182 (1987)
11. Wang, J., Li, M., Wang, H., Pan, Y.: Identification of essential proteins based on edge clustering coefficient. *IEEE/ACM Trans. Comput. Biol. Bioinf.* **9**, 1070–1080 (2012)
12. Li, M., Wang, J., Chen, X., Wang, H., Pan, Y.: A local average connectivity-based method for identifying essential proteins from the network level. *Comput. Biol. Chem.* **35**, 143–150 (2011)
13. Luo, J., Qi, Y.: Identification of essential proteins based on a new combination of local interaction density and protein complexes. *Plos One* **10** (2015)
14. Qin, C., Sun, Y., Dong, Y.: A new method for identifying essential proteins based on network topology properties and protein complexes. *Plos One* **11** (2016)
15. Acencio, M.L., Lemke, N.: Towards the prediction of essential genes by integration of network topology, cellular localization and biological process information. *BMC Bioinf.* **10**, 290 (2009)
16. Yue, Z., Li, H.-T., Yang, Y., Hussain, S., Zheng, C.-H., Xia, J., Chen, Y.: Identification of breast cancer candidate genes using gene co-expression and protein-protein interaction information. *Oncotarget* (2016)
17. Huang, H., Bader, J.S.: Precision and recall estimates for two-hybrid screens. *Bioinformatics* **25**, 372–378 (2009)

18. Zotenko, E., Mestre, J., O'Leary, D.P., Przytycka, T.M.: Why do hubs in the yeast protein interaction network tend to be essential: reexamining the connection between the network topology and essentiality. *PLOS Comput. Biol.* **4**, e1000140 (2008)
19. Ren, J., Wang, J., Li, M., Wang, H., Liu, B.: Prediction of essential proteins by integration of PPI network topology and protein complexes information. In: *Bioinformatics Research and Applications - International Symposium, ISBRA 2011, Changsha, China, 27–29 May 2011. Proceedings*, pp. 12–24 (2011)
20. Wang, H., Li, M., Wang, J., Pan, Y.: A new method for identifying essential proteins based on edge clustering coefficient. In: Chen, J., Wang, J., Zelikovsky, A. (eds.) *ISBRA 2011. LNCS*, vol. 6674, pp. 87–98. Springer, Heidelberg (2011). https://doi.org/10.1007/978-3-642-21260-4_12
21. Chua, H.N., Wong, L.: Increasing the reliability of protein interactomes. *Drug Discovery Today* **13**, 652–658 (2008)
22. Stephenson, K., Zelen, M.: Rethinking centrality: methods and examples. *Soc. Netw. Soc. Netw.* **11**, 1–37 (1989)
23. Sabidussi, G.: The centrality of a graph. *Psychometrika* **31**, 581–603 (1966)
24. Tang, Y., Li, M., Wang, J., Pan, Y., Wu, F.X.: CytoNCA: a cytoscape plugin for centrality analysis and evaluation of protein interaction networks. *Bio Syst.* **127**, 67–72 (2015)
25. Zhong, J., Wang, J., Peng, W., Zhang, Z., Pan, Y.: Prediction of essential proteins based on gene expression programming. *BMC Genom.* **14**, S7–S7 (2013)
26. Cherry, J.M., et al.: SGD: saccharomyces genome database. *Nucleic Acids Res.* **26**, 73–79 (1998)
27. Zhang, R., Lin, Y.: DEG 5.0, a database of essential genes in both prokaryotes and eukaryotes. *Nucleic Acids Res.* **37**, D455–D458 (2009)
28. Improved multi-level protein–protein interaction prediction with semantic-based regularization.pdf
29. Tu, B.P., Kudlicki, A., Rowicka, M., Mcknight, S.L.: Logic of the yeast metabolic cycle: temporal compartmentalization of cellular processes. *Science* **310**, 1152–1158 (2005)

Neural Networks



Time Sequence Features Extraction Algorithm of Lying Speech Based on Sparse CNN and LSTM

Yan Zhou^(✉) and Li Shang

College of Electronic and Information Engineering,
Suzhou Vocational University, Suzhou, Jiangsu, China
zhyan@jssvc.edu.cn

Abstract. Time sequence feature extraction algorithm of lying speech based on CNN-LSTM deep network was proposed in this paper. The sparse representation of CNN was realized by introducing l_1 norm into the objective function of CNN. This sparse optimization algorithm overcame the disadvantage of CNN network that was easy to fall into the local minimum. Firstly, speech preprocessing had been performed, and then, the spectrograms of lying speech were sent into the sparse CNN model. This step was aim to extract the local lying features. Secondly, establishing a time sequence feature extraction model, the local lying features were sent into the LSTM network to extract lying features temporal perspective. Finally, the Softmax testing unit was used to output the lie detection results. Experimental results show that, compared with traditional methods, the model that extracted the fusion features of local features and time sequence features proposed in this paper had a higher detection rate and good scalability. In a word, the Sparse-CNN-LSTM feature extraction model provided a new idea for the research of lying speech detection.

Keywords: Lying speech · Convolutional neural network · Long short-time memory network · Detection rate

1 Introduction

Lies detection from Speech is a difficult problem of psychological calculation. At present, lie detection mainly focuses on the research of the selection of phonological features [1, 2]. For example, Ekman et al. made a statistical analysis of the fundamental frequency features, and found that the fundamental frequency of the lying speech segment was significantly improved compared with that of telling the truth [3]. Bond et al. indicated that when people tell lies, they will have shorter speaking time, fewer details, more repetition and higher fundamental frequency [4]. Gopalan et al. used an amplitude modulation and frequency-modulation model to detect lies, and found that the Tenger's energy-related features were likely to distinguish the lies [5]. Enos summarized prosodic features to analyze lying speech [6]. Kirchhbel studied the lie detection from the influence of different interview modes by using the acoustic and time sequence features of speech [8]. Zhao Li et al. introduced the development and basic principle of the lie detection technology, and focused on the research of

classification algorithm for speech lie detection, furthermore, the prospect of speech lie detection technology was put forward [9]. Yu Hua et al. proposed a SVM and GMM combined deception detection classifier approach [10].

Although researchers have carried out a lot of research work, the above research mainly focuses on the extraction and observation of the traditional prosodic features of speech, and fails to combine the research on the hidden features of lying speech such as psychoacoustics and auditory perception, and ignored the analysis of time sequence features of lying speech. So far, there is no research work to determine the effective speech features for lie detection, and the obtained lie detection rate is only slightly higher than the random probability judgment. In view of the problems above, it considers that the psychological state of lying is a dynamic process. There is a strong time-variability relation and correlation between frames of lying speech, so the features of different moments play different roles in the detection process. Recently, the neural network methods such as the Convolutional Neural Network (CNN) and Long Short-Term Memory (LSTM) network are widely used [11]. CNN is good at extracting the dependence between local complex features of speech signal, but it cannot extract the long-term effect relation between features. However, LSTM can not only deal with the remote dependence between speech time sequences, but also can avoid the problem of gradient disappearance [12].

In this paper, a sparse optimization based CNN-LSTM lying speech feature extraction model was proposed. Firstly, the sparse representation of CNN was realized by introducing l_1 norm into the objective function of CNN. The local correlations between the basic acoustic features of lying speech were extracted by sparse optimized CNN. Then, inputting the local features into the LSTM neural network, this was used to extract the long-term feature information between the acoustic features of lying speech. The feature extraction method based on the fusion of local feature and time sequence feature had achieved a reasonable detection effect. The experiment results showed that the deep network of the Sparse Convolutional Neural Network-Long Short-Term Memory Network (S-CNN-LSTM) could extract a lot of deep time sequence information which was carried by lying speech signals. This research is an effective exploration in the research field of lying detection from speech.

2 Time Sequence Feature Extraction Model of Lying Speech

2.1 The Training Process

CNN convolution based on sparse representation is mainly to extract the local interaction features and location information between lying speech signals. Meanwhile, the long short-term memory network is mainly to extract the psychoacoustic features of the internal interactions of lying speech sequences. Here, the local feature and the time sequence psychoacoustic feature information were fused to detect the lying psychology. The main training process is expressed as following.

Step 1: Lying speech preprocessing. After the frame segmentation, the sequences were cut down as the same size, and then be averaged and normalized to reduce the commonness among frames and highlight individual sample differences.

Step 2: The extraction of local lying speech features. The sparse CNN network was constructed by introducing the sparse regularization term of l_1 norm into the objective function. The spectrograms input to the constructed network to study the local feature representation of lying speech.

Step 3: Time sequence features extraction. The short-time features extracted by sparse CNN were sent into the LSTM network for further learning. The time-domain information of the past and the future was introduced into the sequence learning, which made the classification more accurate. The function of Softmax was used as the output layer of LSTM network. The output layer assigned probability to the prediction results obtained after LSTM learning, and the highest probability was the final lie detection result. The algorithm framework model of this paper is shown in Fig. 1.

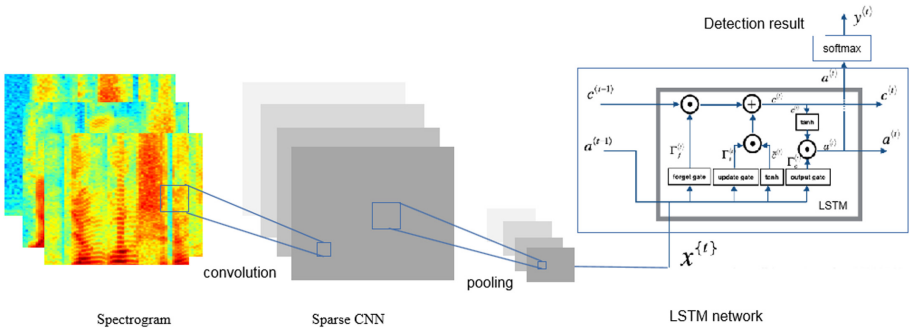


Fig. 1. The feature extraction model of lying speech

2.2 Local Features Extraction of Lying Speech

The function of CNN is too simple and sometimes prone to local minimization. Therefore, in order to solve this problem, the l_1 norm as the sparse constraint term was introduced to the least square error function in this paper. The objective function of CNN and sparse CNN are expressed as following.

Suppose a set of lying speech training sample is given like this (x^1, y^1) , $(x^2, y^2), \dots, (x^m, y^m)$, among them, $y^i (i = 1, 2, \dots, m)$ is the training sample with label, and then the objective function of the CNN can be expressed as:

$$J = \frac{1}{m} \sum_{i=1}^m \sum_{k=1}^K \frac{1}{2} \|h_{w,b}(x_k^i) - y_k^i\|^2 \quad (1)$$

Where, w is the weight of the convolutional neural network, b is the corresponding bias, k is the number of classes of expected classification, $h_{w,b}(x_k^i)$ is a vector with dimension of k which represents the actual output of the sample, and the $J(w, b)$ represent the sum of the least square error of the samples after network training. In the training process of convolutional neural network, the most important parameters are the parameters of weight w and bias b , and the method of gradient descent is usually used to minimize the error sum of these two parameters. This method firstly obtains a

residual value in the process of forward propagation, then updates the weights and deviations of the network through continuous iteration in the process of back propagation, and finally calculates the minimum loss value of the whole network.

The cost function based on l_1 norm sparse constraint can be expressed as this:

$$J_\theta = J(w, b) + \mu L(w, b) \quad (2)$$

Where, the sparse constraint function $L(w, b)$ is shown as following:

$$L(w, b) = \frac{1}{m} \sum_{i=1}^m \sum_{k=1}^K \frac{1}{2} \ln \left(1 + \frac{(h_{w,b}(x^i)_k - y_k^i)^2}{f^2} \right) \quad (3)$$

In order to make the error small enough between the actual output of the sample and the sample label, this paper introduced the sparse constraint of l_1 norm regularization function into the least square error function. Accordingly, a sparse constrained convolutional neural network was proposed. From Eq. (1), (2) and (3), the objective function based on l_1 norm regularization sparse constraint can be expressed as this:

$$J_\theta = J(w, b) + \mu \sum_{i=1}^m \sum_{k=1}^K \frac{1}{2m} \ln \left(1 + \frac{(h_{w,b}(x^i)_k - y_k^i)^2}{f^2} \right) \quad (4)$$

$$J_\theta = \frac{1}{m} \sum_{i=1}^m \sum_{k=1}^K \frac{1}{2} \|h_{w,b}(x^i)_k - y_k^i\| + \mu \sum_{i=1}^m \sum_{k=1}^K \frac{1}{2m} \ln \left(1 + \frac{(h_{w,b}(x^i)_k - y_k^i)^2}{f^2} \right) \quad (5)$$

It means

$$J_\theta = \frac{1}{2m} \sum_{i=1}^m \sum_{k=1}^K \left(\|h_{w,b}(x^i)_k - y_k^i\| + \mu \ln \left(1 + \frac{(h_{w,b}(x^i)_k - y_k^i)^2}{f^2} \right) \right) \quad (6)$$

The second term in the above equation is the sparse constraint term and μ is the regularization coefficient, which controls the sparse measurement results of the objective function. The value of μ and f affect the computational performance of the convolutional neural network. The main purpose of the sparse constrained CNN network is to improve the sparsity of the network and the efficiency of the speech features.

2.3 Time Sequence Feature Extraction of Lying Speech

In this paper, the LSTM network was adopted with single-layer structure, the number of hidden layer node was 128, the function was selected as the activation function, and the function *Softmax* was used in the output layer. In the process of training and detection, the hidden layer state of LSTM changed according to the current input and the hidden layer state of the previous moment, afterwards, the process was continuously cycled until the end. The structure of LSTM is shown in the following Fig. 2.

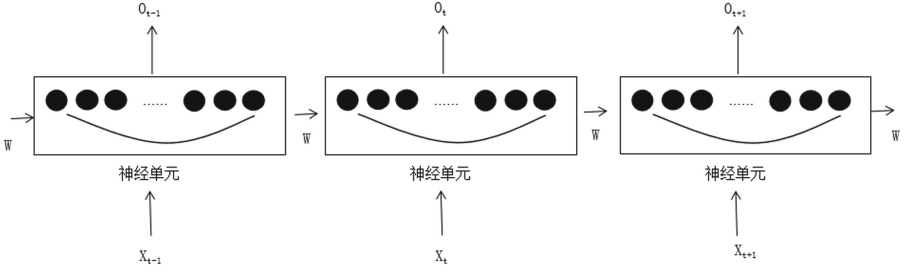


Fig. 2. The sequence diagram of LSTM

The classical Error Back Propagation (EBP) algorithm was used to train the network, and the weight was learned by continuously transferring the leading layer. The connection weight of each neural network layer was obtained by iterating the error from the output to the input layer by layer. In this way, the connection weights of each neural network layer could be obtained. Here, gradient descent algorithm was used during the training processing.

At the moment of t , the network read the input value x_t and the state value h_{t-1} of the hidden layer at the previous moment, calculated the state value of the hidden layer at this moment, and repeated this step until all the input were read. If the function represented by the cyclic neural network was denoted as f , the formula can be expressed as this:

$$h_t = f(x_t, h_{t-1}) = \sigma(W_{xh}x_t + W_{hh}h_{t-1} + b_h) \quad (7)$$

Where, $Softmax$ was the weight matrix input to the hidden layer, W_{hh} was the weight matrix from the hidden layer to the other, b_h was the bias vector of the hidden layer, and σ was the function $Softmax$. Since CNN was prone to gradient disappearance or explosion during training, LSTM network was added the memory unit c , input gate i , forgetting gate f and output gate o to solve this problem. The combination of these gates and memory units greatly improved the ability of cyclic neural networks to process long sequences of speech signal. The formulas of memory units and gate functions of LSTM-based cyclic neural network can be expressed as follows:

$$i_t = \sigma(W_{xi}x_t + W_{hi}h_{t-1} + W_{ci}c_{t-1} + b_i) \quad (8)$$

$$f_t = \sigma(W_{xf}x_t + W_{hf}h_{t-1} + W_{cf}c_{t-1} + b_f) \quad (9)$$

$$o_t = \sigma(W_{xo}x_t + W_{ho}h_{t-1} + W_{co}c_{t-1} + b_o) \quad (10)$$

$$c_t = f_t c_{t-1} + i_t \tanh(W_{xc}x_t + W_{hc}h_{t-1} + b_c) \quad (11)$$

$$h_t = o_t \tanh(c_t) \quad (12)$$

Where, i_t , f_t , c_t , and o_t respectively represented the vector values of input gate, forgetting gate, memory unit and output gate. The parameters of the weight value and

offset value of the response were the hyperbolic tangent function. The input gate controlled the intensity of new input entering the memory unit, the forgetting gate controlled the intensity of the memory unit maintaining the value of the last time, and the output gate controlled the intensity of the output memory unit. The three gates were calculated similarly, but with completely different parameters. They controlled the memory unit by their different ways. In LSTM network, the error gradient of hidden layer output was δ_{ht} , the error gradient could be obtained by calculating the following formula:

$$\delta_{ht} = \frac{\partial L}{\partial h_t} \quad (13)$$

$$\delta_{ct} = \frac{\partial L}{\partial c_t} \quad (14)$$

By further calculation, the following value could be obtained:

$$\delta_{ht} = \frac{\partial L}{\partial o_t} \frac{\partial o_t}{\partial h_t} + \frac{\partial L}{\partial h_{t+1}} \frac{\partial h_{t+1}}{\partial h_t} \quad (15)$$

$$\delta_{ct} = \frac{\partial L}{\partial c_{t+1}} \frac{\partial c_{t+1}}{\partial c_t} + \frac{\partial L}{\partial h_{t+1}} \frac{\partial h_{t+1}}{\partial h_t} \quad (16)$$

Then, the weight gradient W_f of the forgotten gate could be updated as:

$$\frac{\partial L}{\partial W_f} = \sum_{t=1}^T \frac{\partial L}{\partial c_t} \frac{\partial c_t}{\partial f_t} \frac{\partial f_t}{\partial W_f} \quad (17)$$

Therefore, by the way introduced above, all the weights of input gate, output gate and hidden layer could be calculated.

3 Experimental Design and Result Analysis

3.1 Experimental Data Preparation and Evaluation Criteria

This paper selected the polygraph database of Soochow University, including 30 testers (native speakers of Chinese) from Soochow University. The recording forms mainly include inductive talk, deliberate imitation game and natural TV program. The corpus is mandarin, the sampling frequency is 8 kHz, the quantization is 16 bits, and the storage format is WAV. In this paper, 600 segments of truth speech and 800 segments of lying speech were randomly selected. The speech frame length was set to 10 ms. The time sequence information, frequency information and speech data energy of speech were plotted into a 106 dpi \times 80 dpi spectrograms by Fourier transform, which were used as the input data of the sparse CNN network model.

In order to unify the size of the spectrum, here, the samples were divided into equal length. For the original speech signal, it was set as a time sequence $N(n_1, n_2, n_3, \dots, n_i, \dots, n_t)$ which was composed of n sample points and the original length was t . For different speech samples, the time length was different, so the sequence length was not the same. So it needs to align the sequential signals to T in time. The aligned sequence $N'(n'_1, n'_2, n'_3, \dots, n'_i, \dots, n'_t)$ could be obtained by using the following alignment method.

$$n'_i = \begin{cases} n_i, & i \leq t \\ n_{imodt}, & i > t \end{cases} \quad (18)$$

Here, the sparse CNN was directly used to convolve the original temporal signals after aligning with multi-layers. When the sampling point covered by the convolutional window was consistent with the window size of the divided frame, the output values of the CNN network could be saved as the frame features, which represented the local features of lying speech signal. The obtained frame features were spliced together along the time dimension and then input to the LSTM network to extract the time sequence features. In general, the system detection state has the following four cases (Table 1).

Table 1. Test status.

| Sample type | Test results | Test status judgment |
|-------------|--------------|----------------------|
| Truth | Truth | Correct detection |
| Truth | Lie | Error detection |
| Lie | Lie | Correct detection |
| Lie | Truth | Error detection |

In this paper, Lie Detection accuracy (LDA) was used as the evaluation standard. In the experiment, it was defined as this:

$$LDA = \frac{\sum_{i=1}^n p_i}{\sum_{i=1}^n p_i + \sum_{j=1}^n q_j} \quad (19)$$

Where, n represented the number of tested people, p_i was the probability that the i -th correctly detected person, and q_j was the probability that the j -th person who was not correctly detected.

3.2 Experimental Results and Analysis

This paper proposed the fusion of local features and time sequence features for detecting lie from speech. In order to verify the validity of the feature parameters proposed, it was compared with the traditional acoustic feature extracted based on partition window. The speech frame features and the global statistical features of statements extracted by the traditional method were compared, and the Softmax neural network was used as the classifier. Firstly, the Open source tool Open Smile was used

to extract the Basic feature set (BF) of speech frames, including energy, fundamental frequency, duration, Mel Frequency Cepstrum Coefficient, etc., in which the frame length was 10 ms, the window length was set to 25 ms, and the frame shift was set to 10 ms. In general, the 64 dimensional frame feature sequence was extracted for each sample. Secondly, based on the above speech frame feature extraction, the 64 Gaussian Function was used to extract the Global statistical feature set (GSF). The window length was set to 100 ms, and the global statistical feature sequence of the statement was obtained through the convolution function group. Thirdly, Sequential feature (SF) was extracted by the proposed S-CNN-LSTM network, and then 64 dimensional feature sequence was obtained after PCA dimension reduction. The correct detection rate based on different speech features is shown in Fig. 3.

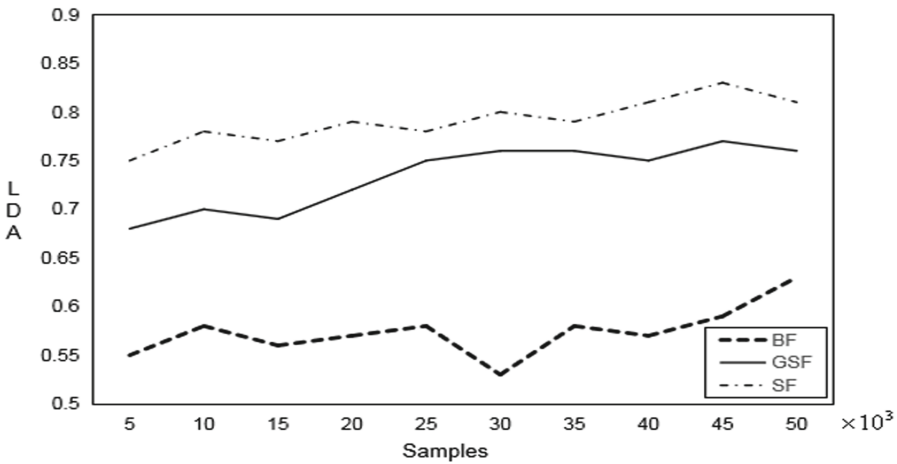


Fig. 3. Correct detection rate of lie under different characteristic parameters

It can be seen from the figure that, in the process of testing with increasing sample size, the detection rates of the three feature sets based on female and male samples were all improved. In the three schemes, the correct detection rate of time sequence features extracted based on S-CNN-LSTM model was higher than that of other features. This indicated that in the task of lie detection, the effective time sequence features in speech spectrum had an important impact on the lie detection results.

In this paper, the time sequence feature of lying speech were fully considered, and the extracted long short-length features were better than the traditional single-feature expression for the lying state. In this experiment, the average detection rate was 59.2% based on the 64 dimension of speech frame, including fundamental frequency, zero rate, MFCC, spectrum energy related features, etc. the average detection rate of 75.1% based on the 64 dimension of global statistical features, including the prosodic features, spectrum of relevant features, sound quality, etc. The average detection rate reached 79.8% based on the S-CNN-LSTM model of time sequence features.

In order to verify the effectiveness of the S-CNN-LSTM model proposed in this paper for lie detection, a comparative experiment was carried out in this paper.

The training data set was the same as the previous experiment. Here, the CNN model, LSTM model and CNN-LSTM model were compared and Softmax was used as the classifier. Due to the deep structure of the deep learning network, it required a large number of iterations to fully learn the features and fully train the network parameters. The performance of different models is shown in Fig. 4.

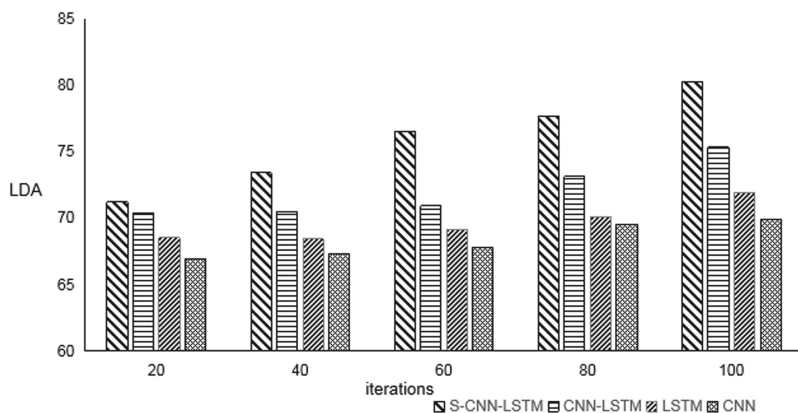


Fig. 4. The detection ability comparison of different models

The experimental iteration results are shown in Fig. 4, which represent the correct detection rates of different iteration times. When the number of iterations was small, the performance of S-CNN-LSTM network was not outstanding in the above several networks, because it was impacted by the deep structure characteristics and the setting of the network parameters. The detection accuracy of the proposed S-CNN-LSTM network increased gradually in the first 40 iterations for the learning samples of female and male. Due to the l_1 norm was introduced into the objective function of CNN to realize the sparse representation of CNN. Therefore, the disadvantage that the CNN network was easy to fall into the local minimum in the process of learning could be overcome. The computational efficiency was improved by this operation. After many experiments, when the number of iterations was 100, the S-CNN-LSTM model obtained the highest correct detection rate of 81.2%. After the experiment, it was found that when the number of iterations reached about 200, the accuracy of S-CNN-LSTM tended to be stable with 80.8%. The S-CNN-LSTM network designed in this paper could achieve higher accuracy in a fewer iterations, and it was better than the existing network in terms of time efficiency and accuracy.

4 Conclusion

Lie detection from Speech is a complex psychological calculation problem because the lying state is a complex process of gradual and reciprocating. In this paper, the psychological change information of the liar was obtained by analyzing the local feature

and time sequence feature of the acoustic features in speech signals. At present, there is no clear correlation between phonological features and lying state in the research of phonological lie detection. Therefore, this paper chose to establish a deep learning network model to explore the extraction method of feature parameters in lie detection. By comparing the performance of S-CNN-LSTM, CNN-LSTM and the CNN and LSTM network models, the lie detection performance was tested. It was found that the S-CNN-LSTM network model can learn to obtain the time sequence features of speech well, and had a high accuracy rate for lie detection, which acquired good detection result. By comparison with CNN, LSTM and CNN-LSTM network, the advantages of the proposed model in lie detection are verified, which provides a new idea and method for the practical application of lie detection.

Acknowledgement. The authors acknowledge the QingLan project of colleges and universities in Jiangsu province. Intelligent computing and knowledge learning research platform construction project of Suzhou Vocational University.

References

1. Hartwig, M., Bond, C.F.: Why do lie catchers fail? A lens model meta-analysis of human lie judgments. *Psychol. Bull.* **137**(4), 643–659 (2011)
2. Cheng, F., Heming, Z., Xueqin, C., et al.: Distinguishing deception from non-deception in Chinese speech. In: 6th International Conference on Intelligent Control and Information Proceedings. pp. 268–273. IEEE, Wuhan (2016)
3. Ekman, P., Osullivan, M., Friesen, W.V., et al.: Invited article: face, voice, and body in detecting deceit. *J. Non-verbal Behav.* **15**(2), 125–135 (1991)
4. Bond, C.F., Depaulo, B.M.: Accuracy of deception judgments. *Pers. Soc. Psychol. Rev. Official J. Soc. Pers. Soc. Psychol. Inc* **10**(3), 214 (2006)
5. Gopalan, K., Wendt, S.: Speech analysis using modulation-based features for detecting deception. In: 15th International Conference on Digital Signal Processing, pp. 619–622. IEEE, Cardiff (2007)
6. Enos, F.: Detecting Deception in Speech. Columbia University (2010)
7. Kirchhuelbel, C.: The Acoustic and Temporal Characteristics of Deceptive Speech. University of York, York (2015)
8. Li, Z., Ruiyu, L., Yue, X., et al.: Progress and outlook of lie detection technique in lie speech. *Data Acquisition Proces.* **032**(002), 246–257 (2017)
9. Hua, Yu., Chao, Ye: Deception detection based on SVM and GMM combined classifier. *Electron. Devices* **42**(1), 240–243 (2019)
10. Badshah, A.M., Ahmad, J., Rahim, N., et al.: Speech emotion recognition from spectrograms with deep convolutional neural network. In: the International Conference on Platform Technology and Service, pp. 1–5 (2017)
11. Cong, X.: Research on the multi-granularity analysis method of time sequence signal using convolutional long short time memory network. Harbin Institute of Technology (2017)
12. Palangi, H., Deng, L., Shen, Y., et al.: Deep sentence embedding using the long short-term memory network: analysis and application to information retrieval. *Trans. Audio Speech Lang. Process.* **24**(4), 694 (2016)



An Improved Conditional Generative Adversarial Network for Microarray Data

Sheng Fang¹, Fei Han^{1(✉)}, Wan-Yun Liang², and Jing Jiang¹

¹ School of Computer Science and Communication Engineering,
Jiangsu University, Zhenjiang 212013, Jiangsu, China
hanfei@ujs.edu.cn

² School of Computer Science, Jiangsu University of Science and Technology,
Zhenjiang 212000, Jiangsu, China

Abstract. Microarray data has the characteristics of high dimension and few samples, which brings much difficulty to its processing. It is necessary to expand microarray data to increase the data sample size. Although the traditional generative adversarial network (GAN) could expand the sample of microarray data set, it could not get the corresponding label value of the generated sample and may generate “dirty” samples. Although the conditional generative adversarial network could get the labels of the generated samples, it is difficult to make the algorithm converge, and there are also “dirty” samples in the generated samples. To ensure that the algorithm could converge and the generated samples have corresponding labels and eliminate the “dirty” samples in the generated samples, an improved conditional generative adversarial network based on feature matching penalty and probability model setting threshold is proposed. On one hand, to improve the convergence probability of the CGAN, a feature matching penalty strategy is proposed in this study, which consists in finding a Nash equilibrium to a two-player non-cooperative game. On the other hand, to overcome the problem of the “dirty” samples from the generated samples, a strategy of the probability model is proposed to set the threshold, which could screen high-quality samples and discard “dirty” samples. The proposed CGAN could improve the classification accuracy as well as data generation ability, which is conducive to the diagnosis of diseases and the development of functional genomics. Experimental results on several public microarray data sets verifies the effectiveness of the proposed CGAN.

Keywords: Microarray data · Conditional generative adversarial network · Generated samples · Probability model · Feature matching

1 Introduction

Microarray data sets [1] are two or multi classification related to diseases or human physiological states, which are characterized by high dimension of data and small number of samples. Moreover, most microarray data contains noise. All these characteristics bring great obstacles to the processing of microarray data.

Variational Autoencoders (VAEs) [2] are classical model of generating samples. Because VAEs focus on the approximate likelihood of the examples, they share the

limitation of the standard models and need to fiddle with additional noise terms. With the assumption that word vectors in different languages could be drawn from a same latent variable space, a novel approach was proposed in [3], which builds cross-lingual dictionaries via latent variable models and adversarial training with no parallel corpora. However, this method is difficult to be applied to microarray data, and could not generate the expected samples. The “adversarial autoencoders” (AAE) was proposed in [4], which is a probabilistic autoencoder using the generative adversarial networks (GAN) to perform variational inference by matching the aggregated posterior of the hidden code vector of the autoencoder with an arbitrary prior distribution, but this method is difficult to generate data for the specified label.

Recently the generative adversarial network (GAN) [5] has aroused much interest because of the verisimilitude of the generated images, and many methods are proposed to use generative adversarial network to generate samples [6–10]. The remote sensing sample generation method [11] adopted the generative adversarial network based on Wasserstein distance to expand the remote sensing image sample set of construction waste. DCGAN [7] used the trained discriminators for image classification tasks, showing competitive performance with other unsupervised algorithms. The method of a zero-centered gradient penalty was proposed in [13], which was used to improve the generalization of the discriminator by pushing it toward the optimal discriminator, and the penalty guaranteed the generalization and convergence of GANs. The above generative adversarial networks are suitable for the generation of samples without labels, because it could only get the generated sample data and could not get the corresponding labels of the samples.

To overcome the shortcoming of GANs, many conditional generative adversarial networks were proposed to generate the sample of the specified label. In 2014, Mehdi Mirza et al. first introduced conditional generative adversarial network (CGAN) in [14], which added constraints to the original GAN, and introduced the conditional variable y into the generation model and discrimination model to guide generating data. A structure-aware image-to-image translation network was proposed in [15], which is composed of encoders, generators, discriminators and parsing nets for the two domains, respectively, in a unified framework. The purposed network generates more visually plausible images compared to competing methods on different image-translation tasks. A camera style (CamStyle) [16] adaptation method was proposed to regularize CNN training for person re-ID. CamStyle can serve as a data augmentation approach that smooths the camera style disparities. Specifically, with CycleGAN, labeled training images can be style-transferred to each camera, and, along with the original training samples, form the augmented training set. The above methods could generate data with similar labels, but the generative samples may contain some dirty samples.

To solve the above problems, an improved conditional generative adversarial network based on feature matching penalty and probability model to set threshold is proposed. Firstly, the conditional generative adversarial network is directly applied to microarray data set, and the discriminator and generator loss could not be in the antagonistic state, which could not make the algorithm converge. Therefore, the discriminator loss function uses the feature matching [17] strategy with penalty to ensure that the discriminator and generator are in a state of confrontation, which promotes the convergence of the algorithm. Although the sample quantity has been expanded, there

are the following problems: there may be “dirty” samples in the generated samples, whose quality could not be judged. Secondly, to reduce “dirty” samples generated by the CGAN with feature matching penalty, a probabilistic model of setting thresholds is used to screen the generated samples and retain the high-quality samples.

2 Preliminaries

2.1 Conditional Generative Adversarial Network

Generation adversarial network (GAN) [5] is different from most algorithms. The algorithm has two players: generation model (G) and discrimination model (D). The purpose of the discriminant model is to distinguish the authenticity of the generated samples, and the purpose of the generation model is to make the ability of the generated samples as strong as possible. D is trained to maximize the probability of assigning the correct label to both training examples and samples from G. G is simultaneously trained to minimize $\log(1 - D(G(z)))$. In other words, D and G play the following two-player minimax game with value function $V(G, D)$:

$$\min_G \max_D V(G, D) = E_{x \sim p_{data}(x)}[\log D(x)] + E_{z \sim p_z(z)}[\log \log(1 - D(G(z)))] \quad (1)$$

where G and D are generators and discriminators, z is the input noise distribution data, and x is the input real data. When generative adversarial network is used to generate microarray data, the generated samples will be obtained. However, the tag corresponding to the generated samples could not be obtained. Therefore, the following introduction is required to conditional generative adversarial network.

Conditional generative adversarial network (CGAN) [14] could not only generate microarray data, but also specify tags to generate data sets. But the loss function of CGAN and GAN is a little difference, the loss function formula of CGAN introduced in the condition of variable y, the model can generate specific type or label samples. The objective function of a two-player minimax game would be as Eq. (2):

$$\min_G \max_D V(G, D) = E_{x \sim p_{data}(x)}[\log D(x|y)] + E_{z \sim P_z(z)}[\log(1 - D(G(z|y)))] \quad (2)$$

where G and D are the generator and discriminator respectively, z is the noise distribution data of the input, x is the real data of the input, and y is the specified label value.

2.2 Determine the Quality of the Generated Sample

Conditional generative adversarial network can generate microarray data, but there are “dirty” samples in the generated samples, so it is necessary to screen the generated samples, keep high-quality samples and discard the “dirty” samples. Therefore, the paper [17] proposes to use Inception Score to calculate the value of conditional probability to judge the quality of the images, as shown in Eq. (3):

$$IS(G) = E_x KL(p(y|x)||p(y)) \quad (3)$$

where x is the input image, y is the object in the image, and Inception Network [18] is a network with excellent local topological structure, input images into the Inception Network to determine the conditional probability of each object in the image.

3 The Proposed CGAN

In order to overcome the defects of traditional CGAN which could not converge and generate “dirty” samples, an improved conditional generative adversarial network based on feature matching penalty and probability model setting threshold is proposed. To overcome the problem that the traditional CGAN is difficult to converge, a feature matching strategy with penalty is proposed, which consists in finding a Nash equilibrium to a two-player non-cooperative game. To overcome the problem of the “dirty” samples from the generated samples, a strategy of the probability model is proposed to set the threshold, which could discard “dirty” samples and obtain high-quality samples.

3.1 The Improved Feature Matching with Penalty

When the loss function Eq. (2) above is used to generate the microarray data set, it is found that the traditional CGAN could not converge, that is, the loss of generator is small, while the loss of discriminator is large. In order to balance the loss of both, an improved method of discriminator loss function is proposed, as shown in Eq. (4):

$$\begin{aligned} \min_G \max_D V(G, D) = E_{x \sim P_{data}(x)} [\log D(x|y)] + E_{z \sim P_z(z)} [\log(1 - D(G(z|y)))] \\ + r * feature_loss \end{aligned} \quad (4)$$

where r is the penalty factor, and $feature_loss$ is feature matching, as shown in Eq. (5):

$$feature_loss = \frac{1}{N} \sum_{i=1}^N (d_i - g_i)^2 \quad (5)$$

where N is the total number of layers of the discriminant network, and d_i and g_i is the eigenvector of the real sample and generated samples respectively through the layer i discrimination network. In order to balance the loss of both, the two feature vectors d_i and g_i are calculated as the mean-square error, and the penalty factor r times of the feature vectors is taken as part of the discriminator loss, which could make the proposed CGAN become stable. At present, r is the optimum value obtained after many experiments.

3.2 The Improved Probability Model to Screen High Quality Samples

Although the feature matching strategy with penalty could improve the convergence of the CGAN, the CGAN may generate “dirty” samples. In order to filter the “dirty”

samples in the generated samples, a probabilistic model based on threshold is proposed in this study.

In GAN, the calculation of the generative picture quality is provided by Eq. (5). If the value of the conditional probability $P(y|x)$ (x represents the picture and y represents the main object in the picture) is high, the object could be highly predicted and the content of this picture is the object. Based on this idea, the samples generated by the CGAN based on the feature matching strategy with penalty are substituted into the probability model, if the classification of samples is correctly determined and the probability of discrimination is greater than or equal to the set probability threshold, the samples will be considered as high-quality samples; otherwise, the sample is considered “dirty” samples and discarded.

3.3 The Proposed Conditional Generative Adversarial Network Based on the Feature Matching Penalty and Probability Model

The flowchart of the proposed conditional generative adversarial network based on the feature matching strategy with penalty and probability model is shown in Fig. 1, and the detailed steps are described as follows.

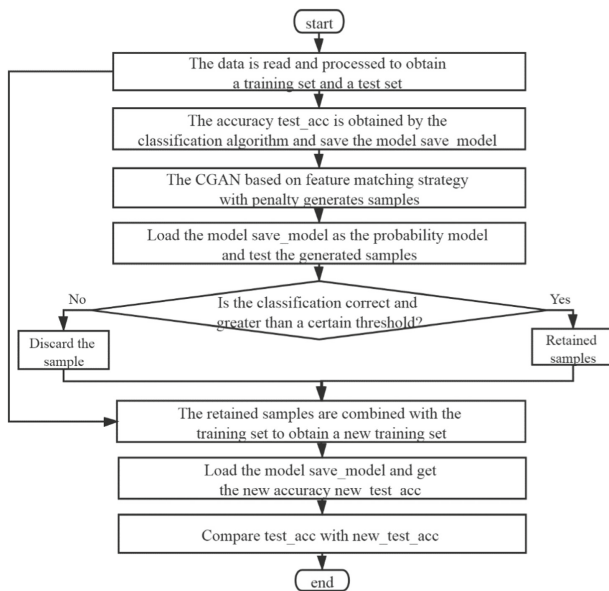


Fig. 1. The main framework of the proposed CGAN

Step1: Get the original accuracy and save the model. The original data set is preprocessed to obtain the test set and train set, as well as the label corresponding to the test set and the train set. Classification algorithm is used to train the train set, and

then the test set is tested to obtain the accuracy test_acc (TA), and the model is saved as save_model.

Step2: Get high quality samples by proposed CGAN. The CGAN based on feature matching penalty is used to train the original data set, and the sample corresponding to each label is generated, denoted as G_samples. The above model save_model could be a probability model and load the saved model save_model. The generated samples G_samples are input into the probability model to obtain the probability value of each category. The screening criteria is as follows: the probability model save_model must correctly classify the generated samples, and the conditional probability of the category is greater than a certain threshold. If the above two conditions are met, the sample is retained; otherwise the sample is discarded.

Step3: The new accuracy is obtained and compared with the original accuracy. The retained samples are mixed with the original training set to obtain the new training set. The test set is the same as the original test set. The new training set is trained by reusing classification algorithm, and the test set is tested to obtain the new accuracy new_test_acc (NTA), and the NTA is compared with the previous TA. If the NTA is higher than the original accuracy TA, it indicates that the generated samples are realistic to the real data, which could increase the sample size and facilitate classification.

4 Experimental Results and Discussion

In order to verify the feasibility and performance of the proposed algorithm, experiments are conducted on four data sets, as shown in Table 1. These data sets are selected from the paper [19], and the entire experiment is performed on Python 3.6.2, Intel(R) Core(TM) i5-5200u, 2.20 GHz, and 8 GB RAM.

Table 1. Details of the four datasets

| Dataset name | Sample size | Number of genes | Number of categories |
|--------------|-------------|-----------------|----------------------|
| Lung cancer | 32 | 56 | 3 |
| WBCD | 569 | 30 | 2 |
| Colon cancer | 62 | 2001 | 2 |
| Leukemia | 72 | 7129 | 2 |

4.1 The Effectiveness of the Feature Matching Strategy with Penalty

Through experiments, it is found that the loss of discriminator was relatively small, while the loss of generator is much larger, failing to achieve the effect of relative balance between discriminator and generator, and the model would collapse. The CGAN based on feature matching strategy with penalty keeps the discriminator

and generator in a balanced state. The discriminator loss and generator loss are shown in Fig. 2 below.

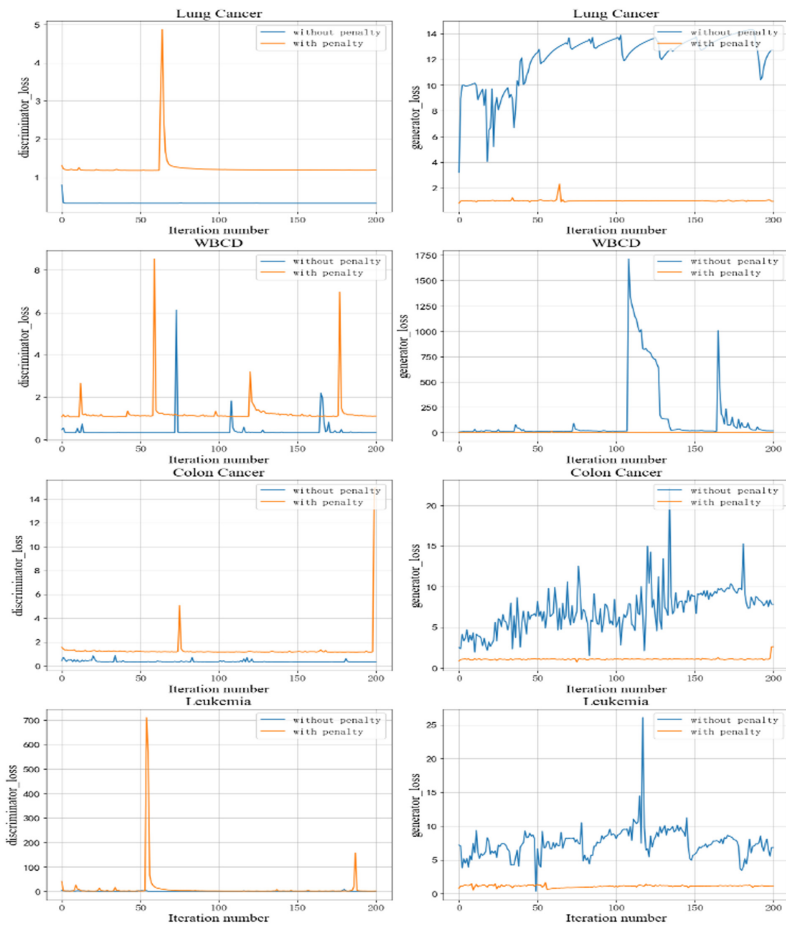


Fig. 2. The comparison between the feature matching strategy without penalty and the one with penalty on the different microarray data sets

It could be seen from the Fig. 2 that the discriminator loss without feature matching penalty strategy could not reach a relatively balanced state with the generator loss, which makes the proposed CGAN difficult to converge. Through the feature matching strategy with penalty, discriminant loss and the generator loss were similar and discriminator model and the generator model is in a state of the Nash equilibrium, which could make the algorithm converge and verify that the feature matching strategy with penalty is effective.

4.2 The Three Classification Algorithms for Generative Sample

The feature matching strategy with penalty is used to generate samples for the above four data sets, and the generated samples are screened by using probability model strategy. If the probability model classifies the samples correctly, the samples are retained; otherwise, the samples are discarded. The retained samples are mixed with the original training set to form a new training set. The test classification accuracy obtained on the original data is called TA in Table 2, and the test classification accuracy obtained on the data generated by the proposed method is called NTA in Table 2. The classification algorithm uses three different algorithms to classify the data set, namely the fully connected neural network algorithm [20], the decision tree [21] and KNN [22], to verify the feasibility of the probability model strategy. The experimental results are shown in Table 2.

Table 2. The mean classification accuracy and standard deviation obtained by the different classifiers on the original dataset and the generative dataset

| Data | Classifier | | | | | |
|--------------|-------------------------------|------------------|------------------------------|------------------|------------------------------|------------------|
| | Full connected neural network | | Decision tree | | KNN | |
| | Mean accuracy (%) \pm Std. | | Mean accuracy (%) \pm Std. | | Mean accuracy (%) \pm Std. | |
| | TA | NTA | TA | NTA | TA | NTA |
| Lung | $25.71 \pm 1e-2$ | $34.38 \pm 2e-2$ | $48.56 \pm 5e-3$ | $54.28 \pm 3e-3$ | 71.42 ± 0 | $82.85 \pm 3e-3$ |
| WBCD | $95.78 \pm 1e-5$ | $95.96 \pm 7e-5$ | $92.47 \pm 2e-5$ | $92.64 \pm 1e-5$ | 98.02 ± 0 | 98.92 ± 0 |
| Colon cancer | $73.33 \pm 4e-3$ | $74.99 \pm 6e-3$ | 58.33 ± 0 | $69.60 \pm 2e-3$ | 58.33 ± 0 | $64.99 \pm 7e-3$ |
| Leukemia | $67.99 \pm 6e-3$ | $75.99 \pm 8e-3$ | $87.30 \pm 5e-3$ | $92.72 \pm 1e-3$ | 81.33 ± 0 | $82.53 \pm 3e-5$ |

From Table 2, the CGAN based on feature matching strategy with penalty could generate similar real samples. Experimental results on several public microarray data sets show the mean accuracy has been improved for all three classifiers, which indicates that the feature matching strategy with penalty could generate realistic samples.

4.3 The Probabilistic Model of Setting the Threshold Value

On the basis of the above experiments, the probability model setting different thresholds is used for the four data sets to screen high-quality samples. If the conditional probability value about the sample calculated by the probability model is greater than the set threshold, the sample is retained; otherwise, the sample is discarded. The retained samples are expanded to obtain a new training set and the new accuracy test_acc_threshold is obtained, and compared the accuracy under different thresholds. The classification algorithm here is the full-connected neural network mentioned above. The experimental results are shown in Fig. 3.

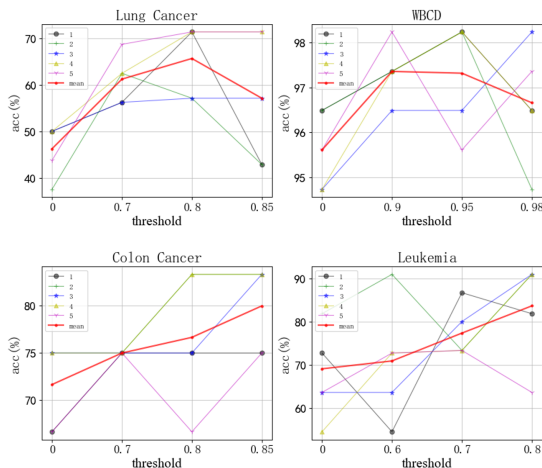


Fig. 3. The classification accuracy obtained by full connected neural network on several public microarray data sets versus the different thresholds

In Fig. 3, the accuracy of classification is different when different thresholds are set for the same data set. The accuracy after setting appropriate thresholds is higher than that without thresholds, and there is an optimal threshold to maximize the accuracy of classification. On the Lung Cancer data set, the optimal threshold is 0.8, and the accuracy of both thresholds (0.7, 0.85) decreases. On the WBCD data set, the optimal threshold is 0.9, and the accuracy of the thresholds (0.95, 0.98) decreases continuously. On the Colon Cancer data set, the optimal threshold is 0.85, and the accuracy corresponding to the threshold (0.7, 0.8) increases continuously. On the Leukemia data set, the optimal threshold is 0.8, and the accuracy corresponding to the threshold (0.6, 0.7) increases continuously.

5 Conclusions

To ensure that the traditional CGAN could converge and the generated samples had corresponding labels and eliminate the “dirty” samples in the generated samples, an improved conditional generative adversarial network based on feature matching penalty and probability model setting threshold was proposed. Among them, the feature matching strategy with penalty could make the algorithm converge, which consists in finding a Nash equilibrium to a two-player non-cooperative game. A strategy of the probability model was proposed to set the threshold, which could screen high-quality samples and discard “dirty” samples. Experimental results verified the proposed CGAN could improve the classification accuracy as well as data generation ability.

Although the experiment has verified the quality and validity of the generated samples on the four datasets, more microarray data sets need to be verified by this method. The penalty value of feature matching strategy and threshold should be adaptive.

Acknowledgments. This work was supported by the National Natural Science Foundation of China [Nos. 61976108 and 61572241], the National Key R&D Program of China [No. 2017YFC0806600].

References

1. Huang, D.S.: Study on Mining Method of Microarray Data, 1st edn. Science press, Beijing (2009)
2. Diederik, P.K., Max, W.: Auto-encoding variational bayes. CoRR, abs/1312.6114 (2013)
3. Dou, Z.Y., Zhou, Z.H. Huang, S.J.: Unsupervised bilingual lexicon induction via latent variable models. In: Proceedings of the 2018 Conference on Empirical Methods in Natural Language Processing, pp. 621–626 (2018)
4. Makhzani, A., Shlens, J., Jaitly, N., Goodfellow, I., Frey, B.: Adversarial autoencoders. arXiv preprint [arXiv:1511.05644](https://arxiv.org/abs/1511.05644) (2015)
5. Goodfellow, I., et al.: Generative adversarial nets. In: Conference and Workshop on Neural Information Processing Systems (2014)
6. Denton, E., Chintala, S., Szlam, A., Fergus, R.: Deep generative image models using a laplacian pyramid of adversarial networks. arXiv preprint [arXiv:1506.05751](https://arxiv.org/abs/1506.05751) (2015)
7. Radford, A., Metz, L., Chintala, S.: Unsupervised representation learning with deep convolutional generative adversarial networks. arXiv preprint [arXiv:1511.06434](https://arxiv.org/abs/1511.06434) (2015)
8. Im, D.J., Kim, C.D., Jiang, H., Memisevic, R.: Generating images with recurrent adversarial networks. arXiv preprint [arXiv:1602.05110](https://arxiv.org/abs/1602.05110) (2016)
9. Chen, X., Duan, Y., Houthoofd, R., Schulman, J., Sutskever, I., Abbeel, P.: Info-Gan: interpretable representation learning by information maximizing generative adversarial nets. arXiv preprint [arXiv:1606.03657](https://arxiv.org/abs/1606.03657) (2016)
10. Zhao, J.B., Mathieu, M., LeCun, Y.: Energy-based generative adversarial network. arXiv preprint [arXiv:1609.03126](https://arxiv.org/abs/1609.03126) (2016)
11. Hamid, E., Werner, Z., Gerhard, W.: Mixture density generative adversarial networks. In: IEEE Conference on Computer Vision and Pattern Recognition, pp. 5520–5829(2019)
12. Li, S.Q., Liu, Y.: Remote sensing sample generation method based on generative adversarial network. In: Bulletin of Surveying and Mapping (2019)
13. Hoang, T., Truyen, T., Svetha, V.: Improving generalization and stability of generative adversarial networks. In: International Conference on Learning Representations (2019)
14. Mirza, M., Osindero, S.: Conditional generative adversarial nets. arXiv preprint [arXiv:1411.1784](https://arxiv.org/abs/1411.1784) (2014)
15. Huang, S.W., Lin, C. T., Chen, S. P., Wu, Y.Y., Lai, S.H.: AugGAN: cross domain adaptation with GAN-based data augmentation. In: European Conference on Computer Vision (2018)
16. Zhong, Z., Zheng, L., Zheng, Z., Li, S., Yang, Y.: Camera style adaptation for person re-identification. In: IEEE Conference on Computer Vision and Pattern Recognition (2018)
17. Salimans, T., Goodfellow, I., Zaremba, W., Cheung, V., Radford, A., Chen, X.: Improved techniques for training GANs. arXiv preprint [arXiv:1606.03498](https://arxiv.org/abs/1606.03498) (2016)
18. Szegedy, C., et al.: Going deeper with convolutions. In: IEEE Conference on Computer Vision and Pattern Recognition (2014)
19. Zhu, Z., Ong, Y.S., Dash, M.: Markov blanket-embedded genetic algorithm for gene selection. *Pattern Recogn.* **49**(11), 3236–3248 (2007)
20. Bengio, Y., Courville, A., Vincent, P.: Representation learning: a review and new perspectives. *IEEE Trans. Pattern Anal. Mach. Intell.* **35**(8), 1798–1828 (2013)
21. Brodley, C.E., Utgoff, P.E.: Multivariate decision trees. *Mach. Learn.* **19**(1), 45–77 (1995)
22. Zhou, Z.H.: Machine Learning, 1st edn. Tsinghua University Press, Beijing (2016)



A Cognitive Model of Morphological Neural Network

Naiqin Feng^{1,2(✉)}, Lijuan Qin¹, and Bin Sun¹

¹ Zhengzhou University of Industrial Technology, Zhengzhou 451150, China
fengnaiqin@126.com

² Henan Normal University, Xinxiang 453007, China

Abstract. In this paper, a morphological neural network (MNN) cognitive tree model related to multi disciplines is proposed. The model has four layers: soil layer, primary layer, growth layer and presentation layer. Through the study of MNN at different levels, the cognitive function and mechanism of MNN are profoundly revealed, and the theoretical framework of MNN cognition is established. This paper can be seen as an example of multi-disciplinary cross-over and fusion research, which not only helps to improve the understanding of MNN itself, but also brings some inspirations to promote the interdisciplinary research and coordinated development of computer science, artificial intelligence, neurobiology, cognitive psychology and so on.

Keywords: Morphological neural network · Cognitive model · Multiple disciplines · Crossover and fusion

1 Introduction

Nowadays, the development of science and technology is changing with each passing day, and it is fruitful. Among them, many scientific and technological achievements come from interdisciplinary integration. For example, the world-famous AI was founded by 10 scientists in the fields of mathematics, psychology, neurophysiology, information theory and computer science. Researchers in the field of AI span many fields, such as neuroscience and psychology. As a result, they have brought about a high yield of academic research [1]. For example, building on the Parallel Distributed Processing movement's appeal to biological computation, current state-of-the-art convolutional neural networks (CNNs) incorporate several canonical hallmarks of neural computation, including nonlinear transduction, divisive normalization, and maximum-based pooling of inputs [2]. These operations were directly inspired by single-cell recordings from the mammalian visual cortex.

Recently, however, some scholars are worried. For example, researchers in the fields of neuroscience and AI argue that interactions between disciplines have become less common because of the enormous advances in complexity in both disciplines and the consolidation of disciplinary boundaries, making it more difficult to cross disciplines [3]. We believe that this concern is justified. Many high-level research results are the product of interdisciplinary research, which in turn promotes the coordinated development of multidisciplinary research. It can be seen that multi-disciplinary

interaction and cooperation is how important, which is the inevitable trend of the development of science and technology today [4, 5].

However, interdisciplinary research is challenging. At present, there is no unified theory and method to follow, and there are not many mature experiences and examples to refer to. This paper attempts to study interdisciplinary intersection and fusion and present a model and an example of interdisciplinary research involving AI, neurobiology, and cognitive psychology. In particular, we put the morphological neural network (MNN) as a cognitive neural network and proposed an MNN cognitive tree (MNNCT) model. It has four layers: the soil layer, the primary layer, the growth layer and the fruit layer. The morphological cognitive neural network is studied at these four levels. Jiao et al. pointed out that cognitive neural network is one of the important research directions in the future [6]. The paper aims to deeply reveal the cognitive function and cognitive mechanism of MNN and integrate the theoretical framework of MNN cognition by studying the psychological and neurobiological foundation of MNN cognition, the structure of neurons and networks, learning and memory methods, cognitive ability and performance level. We hope that the study of MNN cognitive tree can bring some enlightenment and help to the interdisciplinary crossing and integration, especially to the cross research of cognitive neural network.

2 MNNCT

Artificial neural network (ANN) is the product of human intelligence. Inspired by the nature and aiming at the cognitive problem of MNN, we proposed a cognitive framework of MNN, called morphological neural network cognitive tree, or MNNCT, as shown in Fig. 1.

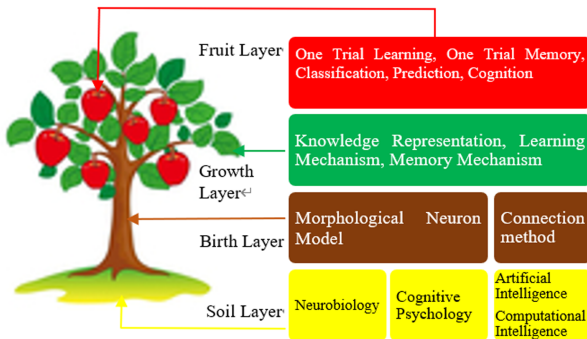


Fig. 1. Morphological neural network cognitive tree.

The MNNCT is divided into four levels, from the bottom to the top, which are the soil layer, the primary layer, the growth layer and the fruit layer. The soil layer is at the bottom of the theory model, mainly including basic neurobiological theory, basic theory of cognitive psychology, AI and computational intelligence theory. This layer

provides the necessary nutrients for the MNNCT, which is MNN's "culture medium". There are various elements in it. Some elements are large amounts and main elements, while others are small amounts, called micro-nutrient. It is important to note that micronutrients, although in small amounts, may be essential, otherwise they may cause neural network malnutrition and congenital deficiencies. Under the urging of various nutrients, the morphological neural network began to germinate, and some morphological neurons and an MNN constructed by connecting many neurons were born, thus entering the primary layer.

In the key next layer—the growth layer, under the guidance of the instructor and the "photosynthesis" of the environment, MNN began to receive "education" through effective learning (morphological neural computing). It remembered a lot of knowledge, and formed some memory matrices (W_{XY} , M_{XY} , A_{XY} , B_{XY} , V_{XY} , T_{XY} , etc.) in its neural network [7–10]. It learned associative memory and possessed some basic cognitive qualities and ability. Next, MNN began to show its cognitive abilities. It can discover connections and knowledge from the data, and quickly remember the learned knowledge in a unique work way (similar to "One-Trial Learning") that is different from traditional neural networks, thus in the association memory, pattern recognition, image processing, classification and prediction, evidence reasoning and other aspects it shows excellent cognitive abilities [11–13], resulting in "rich results".

3 Soil Layer

3.1 The Structure of the Soil Layer of Neural Network

Artificial neural network (ANN) is a simulation of the structure and function of biological neural network in brain. In other words, ANN was built on a model of the brain and its nervous system, and if that foundation wasn't strong, nothing would happen. Two of these disciplines cannot be ignored: neurobiology and cognitive psychology.

ANN is a mathematical model based on the basic principle of neural network in biology. After understanding and abstracting the structure of human brain and the response mechanism of external stimulus, using the topological knowledge of network as the theoretical basis, it simulates the processing mechanism of complex information of human brain's neural system. The idea of constructing neural networks is inspired by the operation of biological neural networks. It combines the knowledge of biological neural networks with mathematical statistical models and accurately describes and implements them with the help of mathematical statistical tools.

On the other hand, in the field of artificial perception in AI, we use mathematical statistics to enable neural networks to have human-like decision-making ability and simple judgment ability. This method is a further extension of traditional logic calculation. Neural network is a mathematical model that uses information processing mechanism similar to the connection structure of the brain's synapses. It is simulated on the basis of human understanding of its own brain tissue structure and thinking mechanism. It is rooted in neuroscience, Mathematics, thinking science, AI, statistics, physics, computer science, and engineering science. From this we can see the general appearance of the soil layer where an ANN is grown, which mainly includes

neurobiology, cognitive psychology, computational science, AI, as well as theories and methods of other disciplines [14, 15]. Figure 2 depicts the basic structure of the soil layer of ANNs.

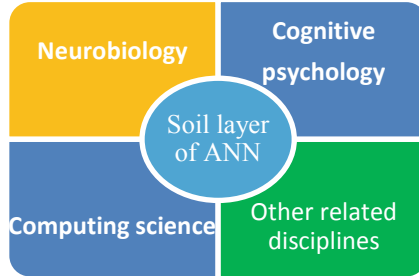


Fig. 2. Soil layer structure of ANN.

3.2 Inspiration from Neurobiology

Let us take a look at neurobiology [16], which directly inspired the birth of ANNs. Among them, the most important is the brain biological neuron model. Although the structure of biological neurons is well known, we must emphasize it because it is so important. A typical biological neuron is a single cell (as shown in Fig. 3), and each cell is composed of a cell body and many tendrils extending from the body. The body or somatic cells contain machines for maintaining basic cell functions and energy processing (for example, DNA-containing cell nuclei, and organelles for building proteins and processing sugar and oxygen). There are two types of tendrils: dendrites, which receive information from other neurons and bring them into the cell body; axons, which send information from the cell body to other neurons.

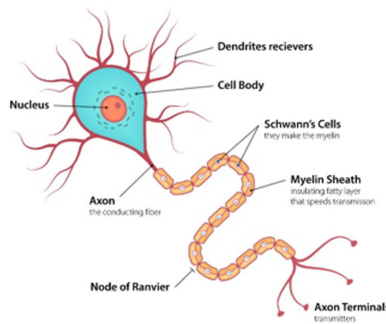


Fig. 3. Neuronal structure.

One can divide neurotransmitters and their receptors into excitatory and inhibitory classes [17]. In the case of excitatory neurotransmission, spikes (electrical pulses)

received from the transmitting neuron increase the likelihood that the receiving neuron may also have spikes. This is due to the special nature of activated receptors on receptor neurons. When inhibitory neurotransmitters bind to inhibitory receptors, the electrical energy received by dendrites in neurons decreases rather than increases. Generally, neurons have receptors for excitatory and inhibitory neurotransmitters, but can release (transmit) only one or another.

In mammalian cortex, there are more excitatory neurons (releasing neurotransmitter glutamate from each spike) than inhibitory neurons (releasing neurotransmitter GABA from each spike). However, these inhibitory neurons are very important to increase the information selectivity of receiving neurons, to turn off neurons for information routing and to prevent epileptic activities.

In deep learning networks, there is no difference between excitatory and inhibitory neurons (only neurons with excitatory or inhibitory neurotransmitters, respectively). The output activity of all neurons is greater than zero, which is a model inhibited synapse. The weight of the synapse is allowed to be negative, in which case the input from the transmitting neuron causes the output of the receiving neuron to decrease.

3.3 Inspiration from Cognitive Psychology

Cognitive psychology is one of the important nutrients in the soil layer of ANNs, providing indispensable nutrients such as attention, perception, memory, association, and thinking. Cognitive psychology regards the cognitive process as a system of information processing according to a certain program consisting of a series of consecutive cognitive operation stages such as information acquisition, coding, storage, extraction and use [18].

Atjason and Hiflynn first proposed a three-level processing model of memory information (see Fig. 4). They believed that after external information entered the memory system, it experienced three stages: sensory memory, short-term memory and long-term memory [19].

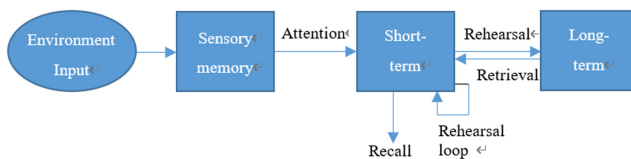


Fig. 4. Three-level processing model of memory information.

External information is input into sensory memory first, and sensory memory has rich information. It has some characteristics of each sensory channel. It can be divided into image memory, audio-visual memory, etc., but it will disappear soon. Some information will be re-encoded into short-term memory. The form of information encoding may be auditory, spoken or written language, and the information of short-term memory will also disappear quickly. The short-term memory can be regarded as a buffer, or it can be regarded as a processor where information enters the long-term

memory. Long-term memory is a real information library, where information can be aural, spoken, written, or visually encoded. The information in the long-term memory may not be extracted because of fading, interference, or reduced strength, but the storage of this information can be said to be permanent. In this model. The transfer of information from one memory stage to another is mostly controlled by people consciously or unconsciously. Retelling is the key to complete the transfer of information. Simply keeping the retelling does not work. Only accurate and integrated retelling can organize the retelling material and link it with other information. Processing at a deeper level can transfer information from short-term memory to long-term memory.

Researchers have proposed many new ANN models based on psychology. For example, network models based on episodic memory, ANN models based on dual memory [20], lattice associative memory models with dendritic structures [21] and so on. These new ANN models inspired by psychology have obtained better network performance and application effects.

4 Birth Layer

The pace of humans studying themselves and understanding themselves has never stopped. This curiosity and research motivation gave birth to ANN's original seeds. Different from the traditional neural network model, the basic calculations in the MNN model are based on the algebraic lattice structure ($\mathbf{R}, \wedge, \vee, +$), wherein the symbols \wedge and \vee represent the binary operations of minimum and maximum, respectively [7–13]. The nonlinear of MNN is stronger than that of traditional neural network. The basic computational model of MNNs is as follows:

$$\tau_i(t+1) = \wedge_{j=1}^n a_j(t) + w_{ij} \quad (1)$$

$$a_i(t+1) = f(\tau_i(t+1) - \theta_i) \quad (2)$$

or

$$\tau_i(t+1) = \vee_{j=1}^n a_j(t) + w_{ij} \quad (3)$$

$$a_i(t+1) = f(\tau_i(t+1) - \theta_i) \quad (4)$$

Where $a_j(t)$ denotes the value of the j th neuron at time t , n represents the number of neurons in the network, w_{ij} the synaptic connectivity value between the i th neuron and the j th neuron, $\tau_i(t+1)$ the next total input effect on the i th neuron, θ_i a threshold, and f the next state function which usually introduces a nonlinearity into the network.

MNN is a newer ANN. Its network structure and learning algorithm are essentially different from traditional ANNs. MNN is a two-layer network, namely the input layer and the output layer. The connection weight matrix between two layers of neurons (memory matrix $\mathbf{W}_{XY}/\mathbf{M}_{XY}$) is not obtained by dynamic learning or training, but by one calculation (“one trial learning”). Figure 5 shows a morphological neuron model.

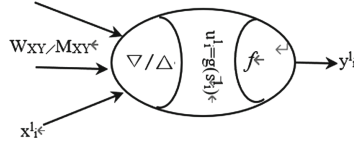


Fig. 5. A model of morphological neuron.

5 Growth Layer

The ANN cognitive tree after birth soon entered its growing period. Unlike trees in nature, ANN does not have natural learning ability, its learning ability is endowed by people. Researchers have designed various learning methods for ANN. For example, in 1949, in the book “Organization of Behavior”, psychologist Donald O. Hebb. analyzed the change rules of connection strength between neurons, and based on this, he proposed the famous Hebb learning rule. Here, we focus on the growth layer of morphological neural networks.

Let X and Y are a pair of associative memory matrices, the X is the input mode matrix of dimension $n \times p$, and the Y is the output mode matrix of dimension $m \times p$, using the unified framework of MAMs for the representation, then the minimal product associative memory that contacts X and Y is defined by

$$W_{XY} = Y \overset{\circ}{\wedge} X \tag{5}$$

W_{XY} is matrix of dimension $m \times n$, and its i, j th entry is defined by

$$w_{ij} = \overset{\circ}{\wedge}_{k=1}^p y_{ik} \circ x_{jk} = (y_{i1} \circ x_{j1}) \wedge \cdots \wedge (y_{ip} \circ x_{jp}). \tag{6}$$

The maximum product memory contacting X and Y is given by

$$M_{XY} = Y \overset{\circ}{\vee} X \tag{7}$$

M_{XY} is matrix of dimension $m \times n$, and its i, j th entry is defined by

$$m_{ij} = \overset{\circ}{\vee}_{k=1}^p y_{ik} \circ x_{jk} = (y_{i1} \circ x_{j1}) \vee \cdots \vee (y_{ip} \circ x_{jp}). \tag{8}$$

In the above equation, \circ represents an abstract operation symbol, which can be $+$, $-$, \times or $/$, namely four arithmetic operation symbols, or log and exp logarithmic and exponential transcendental operation symbols. After such neural calculations, MAM obtains the memory matrix W_{XY} and M_{XY} . The memory matrix is essentially the relationship matrix between input and output, which corresponds to the connection weights in a standard ANN.

When the input pattern matrix X is provided to the network, the associative memory output matrix Y_0 is calculated by

$$Y_0 = W_{XY} \overset{\ominus}{\vee} X \quad (9)$$

Y_0 is matrix of dimension $m \times p$, and the i, j th entry is defined by

$$y_{ij} = \overset{\vee}{\bigvee}_{k=1}^n w_{ik} \Theta x_{kj} = (w_{i1} \Theta x_{1j}) \vee \cdots \vee (w_{in} \Theta x_{nj}) \quad (10)$$

or

$$Y_0 = M_{XY} \overset{\ominus}{\wedge} X \quad (11)$$

and the i, j th entry is defined by

$$y_{ij} = \overset{\wedge}{\bigwedge}_{k=1}^n m_{ik} \Theta x_{kj} = (m_{i1} \Theta x_{1j}) \wedge \cdots \wedge (m_{in} \Theta x_{nj}). \quad (12)$$

When $Y_0 = Y$, W_{XY} and M_{XY} are called the complete recall memories for (X, Y) . In order to better simulate biological neurons and biological neural networks, Gerhard X. Ritter et al. also developed a morphological neuron and morphological neural network with dendritic structure [21].

6 Fruit Layer

The growth layer is the layer of development, learning and memory of ANN. Through specific training methods and effective learning, it has remembered a lot of knowledge, formed some memory matrices (W_{XY} , M_{XY} , etc.) in the network, and learned associative memory, with some cognitive abilities. It shows excellent performance in associative memory, pattern recognition, image processing, classification and prediction, evidence reasoning, etc., and bears “lots of fruit.”

6.1 Unlimited Storage Capacity

MNN has unlimited storage capacity. As mentioned above, after the morphological calculation between the output and input modes, the memory matrices W_{XY} , M_{XY} , etc. are established. The relationship between input and output modes or mode characteristics is stored in these matrices. From the previous formulas (5) to (12), we can see that these memory matrices are of $m \times n$ dimensions, where m is the dimension of the output mode and n is the dimension of the input mode. The size of the memory matrix is entirely determined by their product, regardless of the number of mode pairs involved in learning or memory. This means that in theory MNN has unlimited storage capacity. In practice, it is also possible to achieve unlimited storage capacity. We can take a step-by-step calculation and two-in-one synthetic calculation strategy, that is, first calculate the memory matrix of a part of the training mode, then calculate a sub-memory matrix of a new mode, and then combine it with the previously obtained memory matrix. With this strategy, no matter how large the training set is, as long as it

exists, then we can always achieve their memory matrix. The previous formula also illustrates the feasibility of achieving unlimited storage capacity of MNN.

6.2 The Ability of One Trial Learning

The convolutional neural network (CNN) is a typical representative of DNN (deep neural network), but Zhou, Jin and Dong pointed out that the success of CNN does not mean that various previous problems can be solved or improved [22]. In the analysis of financial data, it was found that CNN did not achieve the expected performance. Zhu, Li, Jiao, et al. pointed out that the depth of deep networks is currently hundreds or even thousands of layers, and increasingly complex network models have brought challenges to the timeliness of their applications [23]. The same challenge also comes from cognitive psychology, because traditional neural networks are not yet able to simulate the task of “one trial learning” [24].

The author’s research shows that MNN and MAM can solve the simulation problem of “one trial learning” [11]. The theoretical analysis of MAM can illustrate this point. From the previous formulas, we can know that we only need to perform a morphological calculation on matrix X and matrix Y to obtain the relationship matrix W_{XY} , M_{XY} , etc., that is to say, memories are stored in them. There is no iteration, and no convergence problem. It belongs to “one trial learning”. Obviously, there is a huge difference of the neural computing method between MNNs and traditional neural networks. This difference enables MNNs to solve the simulation problem.

6.3 Ability to Resist Noise

MNN has good noise robustness, especially the ability to resist single corrosion or expansion noise. Theorem 1 gives the noise boundary of memory W_{XY} and M_{XY} in MAM.

Theorem 1. Assume that \tilde{x}^γ denotes a distorted version of x^γ . $W_{XY} \overset{\odot}{\vee} \tilde{x}^\gamma = y^\gamma$, if and only if

$$\tilde{x}_j^\gamma \leq x_j^\gamma \vee \bigwedge_{i=1}^m \left[\bigvee_{\xi \neq \gamma} \left(y_i^\xi \odot y_i^\gamma \circ x_j^\xi \right) \right] \quad \forall j = 1, \dots, n \quad (13)$$

At the same time, for each row entry $i \in \{1, \dots, m\}$, there exists a column entry $j_i \in \{1, \dots, n\}$, such that

$$\tilde{x}_{j_i}^\gamma = x_{j_i}^\gamma \vee \left(\bigvee_{\xi \neq \gamma} \left[y_i^\xi \odot y_i^\gamma \circ x_{j_i}^\xi \right] \right). \quad (14)$$

Similarly, $W_{XY} \overset{\odot}{\vee} \tilde{x}^\gamma = y^\gamma$, if and only if

$$\tilde{x}_j^\gamma \geq x_j^\gamma \wedge \bigvee_{i=1}^m \left(\bigwedge_{\xi \neq \gamma} \left[y_i^\xi \odot y_i^\gamma \circ x_j^\xi \right] \right) \quad \forall j = 1, \dots, n \quad (15)$$

At the same time, for each row entry $i \in \{1, \dots, m\}$, there exists a column entry $j_i \in \{1, \dots, n\}$, such that

$$\tilde{x}_{j_i}^\gamma = x_{j_i}^\gamma \wedge \left(\bigwedge_{\xi \neq \gamma} \left[y_i^\xi \odot y_i^\gamma \circ x_{j_i}^\xi \right] \right). \quad (16)$$

Theorem 1 shows that W_{XY} has the ability to resist corrosion noise, while M_{XY} the ability to resist expansion noise. For more information, please refer to the literatures [7–10].

6.4 Implicit Learning Ability

Implicit learning has three characteristics, namely, automaticity, abstractness and comprehensibility [25]. Firstly, implicit learning is carried out automatically, generally there is no or little attention to participate; secondly, it is abstract, the knowledge acquired through implicit learning can be transferred to examples of other scenarios; Third, it is comprehensible, and what is learned implicitly is not a messy and incomprehensible thing, but something that can be explained.

MNN can not only simulate “one trial learning”, but also better simulate “implicit learning”. Compare the characteristics of MNN with the characteristics of “implicit learning” to know. First of all, MNN is “one trial learning”, there is no need to repeatedly train based on what “goals”, and “do not stop until the goal” does not exist on MNN. We only need to start the program, perform a neural calculation according to the formula, and get the corresponding memory matrix. This is compatible with the automaticity and unconsciousness of “implicit learning”. Secondly, MNN is highly abstract, and the results of learning can be applied to other related scenarios, which corresponds to the abstraction of “implicit learning”. Third, MNN is based on strict mathematical morphology. Its learning process is easy to track, and its learning results are also easy to interpret. We give an example of MAM network simulating implicit learning below.

In this experiment, it is assumed that the subjects are watching a sports program on TV. At the same time, the breast cancer data set D_1 is placed on the desk in front of them, which is easy to see. The data set has been desensitized and is therefore safe. When the sports program ends, the conclusion part of D_1 is covered and presented to the subjects at the same time. There are only two conclusions, benign or malignant, chosen by the subjects. Then, another data set D_2 in which its conclusions are hidden is provided to the subjects and let them try to write the classification information of the conclusions. Finally, the participants’ statistical data were classified and checked to see if they had learned implicit knowledge. After statistics, the accuracy rates of the participants’ learning and prediction accounted for a certain proportion. When the accuracy rate exceeds 50%, for example, greater than 60%, it can be considered that the subjects have learned “pro tacit knowledge”, that is, some knowledge about breast cancer classification are obtained by “implicit learning”.

The breast cancer data set started with 369 examples, and then gradually increased to 699. We chose the initial 369 samples for the experiment. We divided the 369 samples into two subsets D_1 and D_2 , which were used as training set and test set

respectively. D_1 has 200 samples (benign: 116, malignant: 84), and D_2 has 169 samples (benign: 85, malignant: 84). In this experiment, we selected the self-associative memory, that is, auto-MAM of $X \rightarrow X$. The experimental results are shown in Table 1.

Table 1. The experimental results for Breast Cancer Dataset D_1 & D_2

| Networks | Learning error | Prediction error | Net precision |
|----------------|-----------------|------------------|------------------|
| MAM W_{XY} | 0.0850 (17/200) | 0.0592 (10/169) | 0.9268 (342/369) |
| MAM M_{XY} | 0.0450 (9/200) | 0.1124 (19/169) | 0.9241 (341/369) |
| FMAM A_{XY} | 0.0850 (17/200) | 0.0533 (9/169) | 0.9295 (343/369) |
| FMAM B_{XY} | 0.0450 (9/200) | 0.1124 (19/169) | 0.9241 (341/369) |
| Average | 0.0650 | 0.0843 | 0.9261 |

The experimental results show that these MAM networks have a certain learning effect on the Breast Cancer Dataset. Among them, “subjects” MAM| W_{XY} , MAM| M_{XY} , FMAM| A_{XY} and FMAM| B_{XY} have better learning accuracy. The average accuracy of the 4 MAM networks reaches 0.9261. This experiment simulates implicit learning to a certain extent. With the help of MAMs and other MNNs, it can bring some inspiration to the research of cognitive psychology and neurobiology, thereby promoting the coordinated development of multiple disciplines.

7 Conclusions

From the perspective of interdisciplinary research, this paper proposes the model of MNNCT. Under the guidance of this research framework, MNN is studied in multi-level and multi-dimension. Through the research on cognitive psychology and neuroscience basic, neuron and network structure, learning and memory methods, cognitive ability and performance level of MNN, the paper deeply reveal the cognitive function and mechanism of MNN, and integrate the theory and practice of MNN cognition.

Cognitive neural network is one of the important research directions of the current ANN. This paper summarizes the author’s preliminary experience in study of MNN cognition and abstracts it into an MNNCT. We hope that this paper will bring some guidance and help to the coordinated development of multi-discipline.

Acknowledgements. This work is supported by the Henan Province’s Key R&D Project (Grant No. 192102310217), the science and technology research project of Zhengzhou city (Grant No. 153PKJGG153), the Key Research Project of Zhengzhou University of Industrial Technology (Grant No. JG-190101), the Key Scientific Research Projects of Higher Education Institutions of Henan Province (Grant No. 20A520039), and the Training Project of Young Backbone Teachers of Henan Province (Grant No. 2019GGJS279).

References

1. Hassabis, D., Kumaran, D., Summerfield, C., Botvinick, M.: Neuroscience-inspired AI. *Neuron* **95**(2), 245–258 (2017)
2. Yamins, D.L., DiCarlo, J.J.: Using goal-driven deep learning models to understand sensory cortex. *Nat. Neurosci.* **19**, 356–365 (2016)
3. Parisi, G.I., Kemker, R., Part, J.L., et al.: Continual lifelong learning with neural networks: a review. *Neural Netw.* **113**, 54–71 (2019). <https://doi.org/10.1016/j.neunet.2019.01.012>
4. Soltoggio, A., Stanley, K.O., Risi, S.: Born to learn: the inspiration, progress, and future of evolved plastic ANNs. *Neural Netw.* **108**, 48–67 (2018). <https://doi.org/10.1016/j.neunet.2018.07.013>
5. Prieto, A., et al.: Neural networks: an overview of early research, current frameworks and new challenges. *Neurocomputing* **214**, 242–268 (2016)
6. Jiao, L.C., Yang, S.Y., Liu, F., et al.: Seventy years beyond neural networks: retrospect and prospect. *Chin. J. Comput.* **39**(8), 1697–1717 (2016). <https://doi.org/10.11897/sp.j.1016.2016.01697>
7. Ritter, G.X., Sussner, P., Diaz-de-Leon, J.L.: Morphological associative memories. *IEEE Trans. Neural Netw.* **9**(2), 281–293 (1998). <https://doi.org/10.1109/72.661123>
8. Wang, M., Chen, S.C.: Enhanced FMAM based on empirical kernel map. *IEEE Trans. Neural Netw.* **16**(3), 557–564 (2005). <https://doi.org/10.1109/TNN.2005.847839>
9. Feng, N.Q., Liu, C.H., Zhang, C.P., et al.: Research on the framework of morphological associative memories. *Chin. J. Comput.* **33**(1), 157–166 (2010). (in Chinese with abstract in English). <https://doi.org/10.3724/sp.j.1016.2010.00157>. <http://cjc.ict.ac.cn/quanwenjiansuo/2010-1/fnq.pdf>
10. Feng, N.Q., Tian, Y., Wang, X.F., Song, L.M., Fan, H.J., Wang, S.X.: Logarithmic and exponential morphological associative memories. *Ruan Jian Xue Bao/J. Softw.* **26**(7), 1662–1674 (2015). (in Chinese with abstract in English). http://www.jos.org.cn/jos/ch/reader/view_abstract.aspx?file_no=4620&flag=1
11. Feng, N.Q., Sun, B.: On simulating one-trial learning using morphological neural networks. *Cogn. Syst. Res.* **53**, 61–70 (2019). <https://doi.org/10.1016/j.cogsys.2018.05.003>
12. Feng, N.Q., Wang, X.F., Mao, W.T., Ao, L.H.: Heteroassociative morphological memories based on four-dimensional storage. *Neurocomputing* **116**, 76–86 (2013). <https://doi.org/10.1016/j.neucom.2012.01.043>
13. Feng, N.Q., Yao, Y.L.: No rounding reverse fuzzy morphological associative memories. *Neural Netw. World* **6**, 571–587 (2016). <http://www.nnw.cz/doi/2016/NNW.2016.26.033.pdf>
14. Prieto, A., Prieto, B., Ortigosa, E.M., et al.: Neural networks: an overview of early research, current frameworks and new challenges. *Neurocomputing* **214**, 242–268 (2016). <https://doi.org/10.1016/j.neucom.2016.06.01410.1016/j.neucom.2016.06.014>
15. Mehrotra, K., Mohan, C.K., Ranka, S.: *Elements of Artificial Neural Networks*. MIT Press (1997)
16. Luo, L.: *Principles of Neurobiology*. Garland Science (2016)
17. Rudy, J.W.: *Neurobiology of Learning and Memory*, 2nd edn. Sinauer Associates, Inc. (2014)
18. McBride, D.M., Cutting, J.C.: *Cognitive Psychology: Theory, Process, and Methodology*. Sage Publications, Inc. (2018)
19. Anderson, J.: *Cognitive Psychology and its Implications*. Freeman/Worth (2015)

20. Zhang, H., Huang, B., Tian G.: Facial expression recognition based on deep convolution long short-term memory networks of double-channel weighted mixture. *Pattern Recogn. Lett.* **131**, 128–134 (2020)
21. Sossa, H., Guevara, E.: Efficient training for dendrite morphological neural networks. *Neurocomputing* **131**, 132–142 (2014). <https://doi.org/10.1016/j.neucom.2013.10.031>
22. Zhou, F.Y., Jin, L.P., Dong, J.: Review of convolutional neural network. *Chin. J. Comput.* **40**(6), 1229–1251 (2017). <https://doi.org/10.11897/sp.j.1016.2017.0122>
23. Zhu, H.M., Li, P., Jiao, L.C., et al.: Review of parallel deep neural network. *Chin. J. Comput.* **41**(8), 1861–1881 (2018). <https://doi.org/10.11897/sp.j.1016.2018.01861>
24. Yu, J.Y.: Cognitive psychology and neural networks. In: Cao, C.G., Zhou, Z.H. (eds.) *Neural Networks and their Applications*. Tsinghua University Press, Beijing, 2004, 406–445 (2004). <http://mylib.nlc.cn/web/guest/search/fangzheng/medaData>
25. Loonis, R.F., Brincat, S.L., Antzoulatos, E.G., Miller, E.K.: A meta-analysis suggests different neural correlates for implicit and explicit learning. *Neuron* **96**, 521–534 (2017)



SharedNet: A Novel Efficient Convolutional Architecture Based on Group Sharing Convolution

Jian-Xun Mi^{1,2}  and Jie Feng^{1,2} 

¹ Chongqing Key Laboratory of Image Cognition, Chongqing University of Posts and Telecommunications, Chongqing 400065, China

mijianxun@gmail.com

² College of Computer Science and Technology, Chongqing University of Posts and Telecommunications, Chongqing 400065, China

Abstract. We propose a novel efficient deep convolutional neural networks model for low-computational equipment, referred to as SharedNet. And on ImageNet, Our SharedNet has achieved the best accuracy and efficiency in similar convolutional neural networks. It is due to a new efficient convolution called group sharing convolution which applies parameter sharing to reduce computational cost. Referring to other efficient network design methods, we design our network units which called SharedNet unit by combining group convolution with group shared convolution. The experimental results show that the accuracy and efficiency of this unit are superior to the depthwise separable convolution. Interestingly, SharedNet also shows flexibility according to application requirements that the number of groups of a unit could be adjusted to balance accuracy and efficiency. Besides, for both neural architecture search and manually-designed CNNs, a model unit plays an import role and, therefore, we stack SharedNet units to build models referring to ResNet164 to test accuracy and efficiency of SharedNet units on CIFAR10 and CIFAR100.

Keywords: Efficient neural networks · Network compression · Deep learning

1 Introduction

Convolutional neural networks (CNNs) have been concerned by many researchers in computer vision from AlexNet [1] winning the ImageNet Challenge. For capturing more powerful features, building deeper and wider CNNs are a primary trend in many visual tasks [1–5], and at the same time, it leads to emerges the side-effect that more computing resources are needed, which might limit the large CNNs to be deployed on mobile phones, embedded devices and other equipment with low-computational resources and impede the spread of applications which are based on deep CNNs. Thus, in this study, we are motivated to explore efficient CNNs with high performance.

There are two ways to reduce computational resources in terms of FLOPs and memory. One is to prune and quantize the state-of-the-art models which have hundreds of layers and thousands of channels [6–10]. Generally, to pursue great saving of computational source, pruning and quantizing the state-of-the-art models result in

accuracy loss and require elaborate parameter re-training. Therefore, to improve the efficiency of models which has hundreds of layers and thousands of channels in this manner is utterly inadequate. Another way is to design a state-of-the-art model of efficiency. To this end, manual design and Neural Architecture Search (NAS) are two major modes. For making models efficient, the manually-designed model employs a more efficient convolution than standard convolution. For example, [11–14] achieve the significant improvement of efficiency and performance by redesigning convolution and model structure. Therefore, this mode makes CNNs to be easily deployed on low-computational equipment.

Depthwise separable convolution [11] uses depthwise convolution and pointwise convolution instead of traditional convolution, which reduces the computational cost. However, we argue that it is not the best option because the computational cost of depthwise convolution is much less than that of pointwise convolution. Therefore, there should be more balanced allocation schemes, and our group shared convolution and group convolution are one of them. In traditional manually-designed filters, different channels use the same filter to catch the same features, such as Gaussian filter or Sobel filter. Therefore, we use this idea to design group sharing convolution.

In this paper, we propose a new efficient convolution called group sharing convolution to build efficient model architecture called SharedNet. We apply the principle of parameter sharing to improve the efficiency of convolution, and combining other efficient convolutions to overcome the weakness of parameter sharing. In our experiment, we found that combining group sharing convolution and group convolution could obtain a better accuracy-efficiency rate (AER) than depthwise separation convolution. Besides, another contribution of this study is that we design a novel efficient network unit called SharedNet unit which is to benefit both NAS and manually-designed models. We explore some hyper-parameters of SharedNet unit in CIFAR10 and CIFAR100. Finally, SharedNet achieves the best results of manually-designed efficient model on ImageNet.

The paper is organized as follows: Sect. 2 reviews the developments of popular efficient convolutions. Section 3 describes group sharing convolution, SharedNet unit, and SharedNet architecture. Section 4 presents the influence of some hyper-parameters in our experiments and experimental results of comparing with other efficient models on ImageNet. Section 5 reviews our works and describes future studies.

2 Related Work

Efficient convolution is not only the core of manually-designed efficient networks such as MobileNets [11, 15, 16] ShuffleNets [12, 17], and IGCNets [18–20], but also the key of NAS efficient networks such as MnasNet [13], ProxylessNAS [14] and DARTS [21]. As an outstanding efficient convolution, group convolution first appeared in AlexNet [1]. It is composed of several small standard convolutions in parallel. And the input feature maps are divided into several groups as inputs of these small standard convolutions. However, features produced by group convolution is not as rich as that by standard convolution, because information communication of group convolution is limited to the same group rather than all channels. Fortunately, in the same

computational cost, group convolution performance was higher than standard convolution [22].

Depthwise separation convolution is one of the famous efficient convolutions, which is composed of a depthwise convolution and a pointwise convolution. It was concerned by many researchers and was applied in MobileNet firstly [11]. Depthwise convolution applied a single filter to each input channel. The pointwise convolution uses a 1×1 standard convolution to combine the outputs of depthwise convolution. Two convolutions play different roles that depthwise convolution captures local-features and pointwise convolution fuses these local-features. It is easy to see the computational cost of pointwise convolution is higher than that of depthwise convolution. By the way, depthwise convolution can be considered group convolution once groups equal to channels, and its ability to obtain rich local features is weaker standard convolution. Therefore, the further study proposed ShuffleNet which applied group convolution instead of pointwise convolution in depthwise separation convolution [12]. ShuffleNet operation cannot improve the ability to catch local-features with depthwise convolution. Thus, in MobileNet V2 [15], researchers proposed an inverted residuals bottleneck to increase channels of depthwise convolution so as to remedy this issue. [23] proposed EfficientNets based on NAS in which the searching space is contained inverted residuals bottleneck. It achieved the best accuracy on many famous datasets and the parameters of these models were less than the best model before.

As basic modules, both group convolution and depthwise separable convolution show the great potential of efficient convolution in the construction of state-of-the-art CNNs, and the efficiency of these CNNs is higher than that of standard ones. Therefore, efficient convolution will become an important component in the future development of CNNs.

3 SharedNet Architecture

In this section, we first describe our group sharing convolution which plays an important role in SharedNet. Then, we introduce SharedNet unit which overcomes the weakness of group sharing convolution. We finally describe the SharedNet model architecture.

3.1 Group Sharing Convolution

We propose a novel manual-designed efficient convolutional neural network, and it is built on group sharing convolution. The core idea of group sharing convolution is parameter sharing. In detail, group sharing convolution first divides the input feature maps into separate groups, and then it applies a filter to catch the same kind of features from each channel in an identical group. Benefitting from the parameters sharing, the efficiency of group sharing convolution could be improved.

For a standard 2D-convolution layer which has n convolution kernels, and each kernel contains $d \times k_1 \times k_2$ parameters. In Fig. 1(a), a $d \times h \times w$ input feature map X is computed to produce a single output feature map F_i by a convolution kernel \mathcal{K}_i ,

where d is the number of channels of the input feature map X (input depth) and also denote the depth of the convolution kernel \mathcal{K}_i :

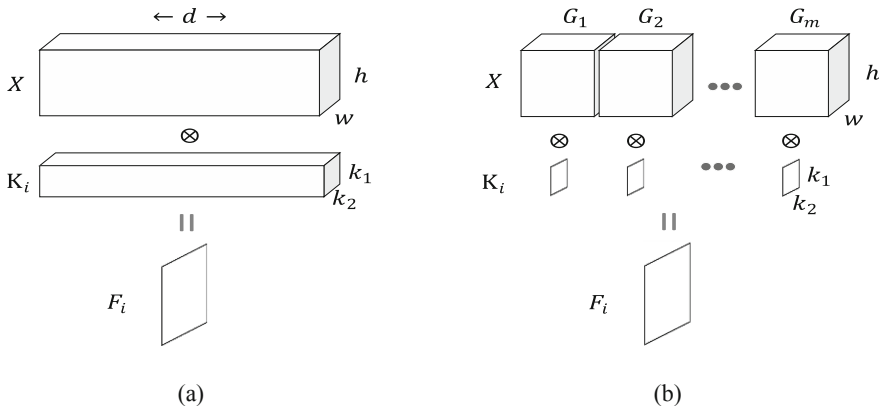


Fig. 1. Standard convolution vs. group sharing convolution. For a single output feature map, different channels catch different features in standard convolution (a), and different channels of the same group capture the same features in group sharing convolution (b).

$$F_i = X \otimes \mathcal{K}_i \tag{1}$$

When a standard 2D-convolution layer has n convolution kernels, and we set stride to one and let padding makes the width and height of an output feature map F_i consistent with the input feature map X . It is not hard to prove that the standard 2D-convolution layer has the computational cost of:

$$n \times d \times h \times w \times k_1 \times k_2 \tag{2}$$

where computational cost is influenced by four factors including the number of convolution kernels n , the input depth d , the size $h \times w$ of the input feature map X and the size $k_1 \times k_2$ of convolution kernels. Generally, the number of convolution kernels and the size of the input image are directly proportional to the amount of information in the output feature map, and the size of convolution kernels is directly related to the ability to catch local-features. Therefore, it is wise to reduce the input depth for efficiency improvement. Depthwise convolution and group convolution both reduce the input depth, and they are stacked to build state-of-the-art manually-designed CNNs [13, 15, 17, 23]. Reducing the input depth usually means that information communication is limited within several channels, which leads to incomplete information passing and low accuracy. To remedy this issue, information communication in full channels is realized by 1×1 standard convolutions in MobileNet V1 [11] and shuffling channels in ShuffleNet V1 [12]. However, the proposed group sharing convolutions can achieve approximate information communication in full channels only by a single operation. In other words, the 1×1 standard convolutions are not necessary anymore.

Figure 1(b) shows how an output feature map is computed by the input feature map and group sharing convolution. We divide the input feature map $\mathbf{X} = [\mathbf{G}_1, \mathbf{G}_2, \dots, \mathbf{G}_m]$ into m groups, and the j -th group $\mathbf{G}_j = [x_{j,1}, x_{j,2}, \dots, x_{j,g}]$ shares a single filter $\mathcal{K}_{i,j}$. The output feature map F_i is computed as:

$$F_i = \sum_{j=1}^m \mathcal{K}_{i,j} \otimes \sum_{l=1}^g x_{j,l} \quad (3)$$

Then, we define a compressed feature map $\mathcal{G}_j = \sum_{l=1}^g x_{j,l}$, and group sharing convolution can be further converted into:

$$F_i = \sum_{j=1}^m \mathcal{K}_{i,j} \otimes \mathcal{G}_j \quad (4)$$

where \mathcal{G}_j contains compressed information from the same feature in the same group. Information compression also appears in the bottleneck of ResNet where the shortcut is used to prevent information loss [4]. Therefore, SharedNet also applies bottleneck to ensure the completeness of the information.

Group sharing convolution has a computational cost of:

$$n \times m \times h \times w \times k_1 \times k_2 \quad (6)$$

where the computational cost depends on the numbers of groups m . Notice that there is different between this convolution and group convolution in terms of how m influences the computational cost. For group convolution, each output feature map is computed by the input feature maps of a group. It means the larger number of groups m , the fewer feature maps in a group (input depth). Thus, the richness and variety of features (parameters) are reduced when increasing m . In contrast, for our group sharing convolution, the computational cost and the richness and variety of features are proportional to m . In terms of feature capture, group convolution focuses on catching intra-group features, while group sharing convolution focuses on catching inter-group features, which reflects the opposite function of these two convolutions.

According to the definition, group sharing convolution obtains the same kind of local-features in the same group. Unfortunately, it cannot differ intra-group features, which leads to that intra-group features are homogenized. To build a model unit with a good intra-group and inter-group relationship, we combine the characteristics of group convolution and group sharing convolution. In Fig. 2, the input feature maps are first computed with group convolution to obtain intra-group feature maps, and then share group convolution is used to produce inter-group feature maps. Therefore, this combination seems somewhat similar to standard convolution. Besides, when the number of groups equals the input depth, group convolution transforms to depthwise convolution, and group sharing convolution transforms to pointwise convolution.

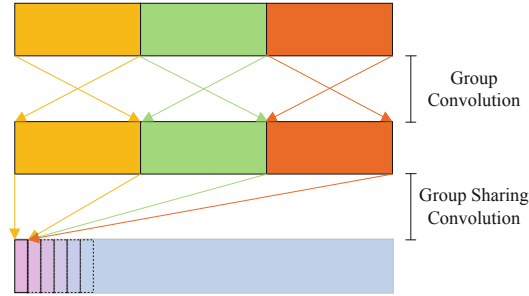


Fig. 2. Combination of group convolution and group sharing convolution. When groups equal to input channels, this combination becomes the depthwise separable convolution.

3.2 SharedNet Unit

We have noticed that model units can greatly improve both NAS and manually-designed models, especially manually-designed ones. Even, the state-of-the-art NAS models [13, 14, 16] have better performance than previous NAS models [21, 24], because the former ones exploit elaborate manually-designed model units. Therefore, how to design our model unit is significant.

As mentioned earlier, we apply shortcut to prevent the information loss of the compressed feature maps. And in order not to homogenize the intra-groups feature maps, we combine group convolution and group sharing convolution to build SharedNet unit. This is our main design principle of SharedNet Unit. Figure 3 shows two kinds of SharedNet Units respectively, i.e., a standard SharedNet Unit 3(a) and a down-sampling SharedNet Unit 3(b). According to the design principle, the information communication of feature maps has two ways. One is the original information transfer by shortcut. As a special case, we apply a 2×2 standard convolution in shortcut when feature maps are downsampled. Another is group information transfer by group convolution (which could be replaced by depthwise convolution) and group sharing convolution. In this way, we first apply channel weight which is initialized to 1 to differ intra-group information, then 1×1 group sharing convolution gains inter-group information as output. After that, we repeatedly realize the output feature maps segmentation and integration by applying a 3×3 group convolution and a 1×1 group sharing convolution. Besides, if one wants to improve the ability of group convolution to catch local-features, squeeze and excitation (SE) can be applied to group convolution.

3.3 Model Architecture

We build SharedNet architecture by stacking SharedNet unit, which is presented in Table 1. One can understand the architecture by roughly referring to MobileNet V2 [15]. We apply a standard convolution of size 3×3 with a stride equal to two in the first layer. Notice that we increase dimension twice in 14^2 feature maps. Compared with MobileNet V2 which increases the dimension of the first layers to 32 and reduces

to 16 in the following layer, we give up the expanding operation in 112^2 feature maps to reduce the computational cost and the recent MobileNet V3 [16] also abandons the expanding operation.

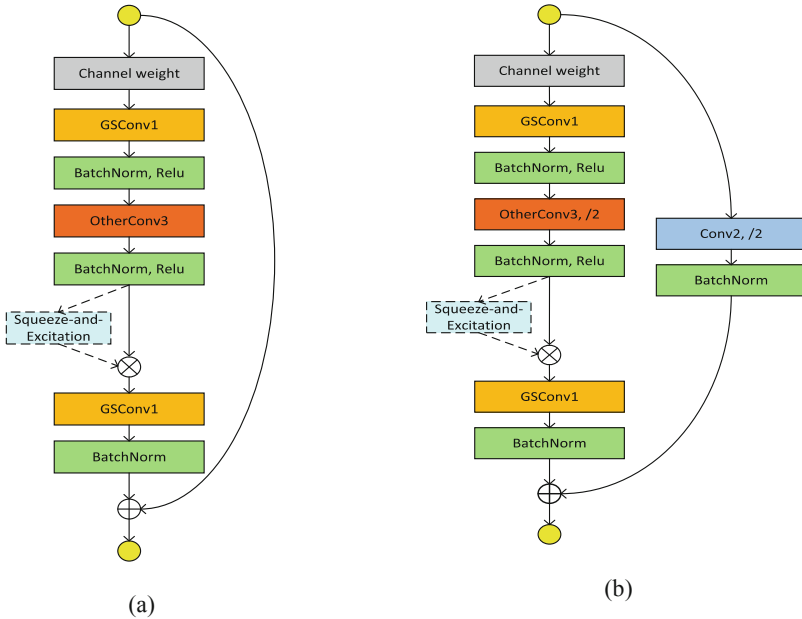


Fig. 3. Two kinds of SharedNet units. Both SharedNet units have two group sharing convolutions (GSConv) in front and end of the unit, and other convolution layer (OtherConv) utilizes depthwise convolution or group convolution alternatively. Besides, we apply a standard convolution as shortcut in down-sampling.

Due to the two group sharing convolutions in SharedNet unit, the number of groups is one of the hyper-parameters which balances accuracy and efficiency. In our experiment, we found that when groups were either too many or too small, the computational cost would increase. However, using more groups, the accuracy of SharedNet unit becomes better. More details are shown in Sect. 4.3. Therefore, for holding complete the input features, in SharedNet unit, the number of groups in the first group sharing convolution is consistent with that of input channels. Then the number of groups in the group convolution is consistent with that in the second group sharing convolution. In the second group sharing convolution, the groups are less than input channels. When the size of feature maps is between 112^2 and 14^2 , the groups are half of the input channels; when the size of feature maps are 7^2 , the groups are one-third of input channels.

Table 1. SharedNet architecture

| Input | Operator | Group1 | exp | Group2 | out size | Stride | n |
|-------------------|-----------------------|--------|------|--------|----------|--------|---|
| $224^2 \times 3$ | Conv, 3×3 | – | – | – | 16 | 2 | 1 |
| $112^2 \times 16$ | Unit, 3×3 | 16 | 16 | 8 | 16 | 1 | 1 |
| $112^2 \times 16$ | Unit, 3×3 | 16 | 48 | 24 | 24 | 2 | 1 |
| $56^2 \times 24$ | Unit, 3×3 | 24 | 48 | 24 | 24 | 1 | 2 |
| $56^2 \times 24$ | Unit, 3×3 | 24 | 112 | 56 | 48 | 2 | 1 |
| $28^2 \times 48$ | Unit, 3×3 | 48 | 112 | 56 | 48 | 1 | 2 |
| $28^2 \times 48$ | Unit, 3×3 | 48 | 384 | 192 | 144 | 2 | 1 |
| $14^2 \times 144$ | Unit, 3×3 | 144 | 384 | 192 | 144 | 1 | 2 |
| $14^2 \times 144$ | Unit, 3×3 | 144 | 480 | 240 | 160 | 1 | 1 |
| $14^2 \times 160$ | Unit, 3×3 | 160 | 480 | 240 | 160 | 1 | 1 |
| $14^2 \times 160$ | Unit, 3×3 | 160 | 1152 | 384 | 320 | 2 | 1 |
| $7^2 \times 320$ | Unit, 3×3 | 320 | 1152 | 384 | 320 | 1 | 2 |
| $7^2 \times 320$ | Conv, 1×1 | – | – | – | 1152 | 1 | 1 |
| $7^2 \times 1152$ | Avgpool, 7×7 | – | – | – | 1152 | 7 | 1 |
| $7^2 \times 1152$ | FC, Softmax | – | – | – | 1000 | – | 1 |

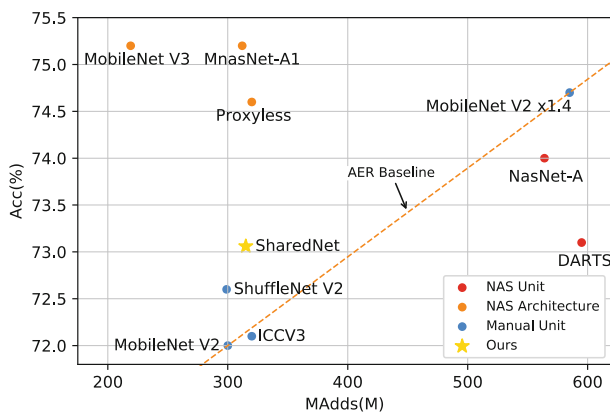


Fig. 4. ImageNet accuracy vs. efficiency. NAS models which are based on manual unit (NAS Architecture) have the best AER. The next is the manually-designed models (Manual Unit). The last is NAS models which are based on NAS Unit (NAS Unit).

4 Experiments

4.1 ImageNet Classification

Training parameters. SharedNet was trained by Pytorch. And following [15], we used the standard RMSProp with both alpha and momentum set to 0.9; the weight

decay was set to 0.00004, and eps was set to 1.0. Our learning rate was increased from 0 to 0.256 in the first 5 epochs and then decayed by 0.97 every 2.4 epochs; And batch norm was added after every convolution layer with momentum 0.99, which is referred to [13]. We used 2 T V100 asynchronous workers, a batch size of 512, image size of 224×224 and Dropout of 0.5 on ImageNet. All SharedNet unit used SE.

Multi-Adds (MAdd). MAdd is proposed in [11], Since almost all the multiplications and additions of the convolution neural network occur at the same time, the number of operations to measure the amount of calculation.

Table 2. Performance comparison on ImageNet. SharedNet achieves the best accuracy in manually-designed models, and has better AER than DARTS and NasNet-A.

| Model | Type | #Params | #Mult-Adds | Top1 Acc. (%) |
|----------------------------|--------|---------|------------|---------------|
| AlexNet | Manual | 61.1 M | 715 M | 62.5 |
| GoogleNet | Manual | 13.0 M | 1510 M | 69.8 |
| NasNet-A | Auto | 5.3 M | 564 M | 74.0 |
| DARTS | Auto | 4.9 M | 595 M | 73.1 |
| MnasNet-A1 | Auto | 3.9 M | 312 M | 75.2 |
| Proxyless | Auto | 4.0 M | 320 M | 74.6 |
| MobileNet V3 | Auto | 5.4 M | 219 M | 75.2 |
| MobileNet V2 | Manual | 3.4 M | 300 M | 72.0 |
| IGCV3 | Manual | 3.5 M | 320 M | 72.2 |
| ShuffleNet V2 1.5 \times | Manual | 3.5 M | 299 M | 72.6 |
| SharedNet | Manual | 7.3 M | 315 M | 73.06 |

Accuracy-Efficiency Rate (AER). This is a comprehensive evaluation index about efficiency and performance. And the calculation of AER is accuracy/computational-cost. With MobileNet V2 as a benchmark, we can easily see that SharedNet is better than MobileNet v2.

Results. We compared SharedNet with other state-of-the-art manual-designed efficient networks including MobileNet V2 [15], ShuffleNet V2 [17], and IGCV3 [20], and state-of-the-art NAS efficient networks including NasNet [24], DARTS, MnasNet [13], Proxyless [14], and MobileNet V3 [16]. The statistics of selected models is shown in Table 2, and the accuracy versus computational cost is shown in Fig. 4. Most networks which are built on NAS have better AER than the manual-designed networks, but the AER of SharedNet is higher than DARTS, NasNet, and other manual-designed efficient networks.

4.2 Performance of SharedNet Unit

Network. For showing the excellent performance of SharedNet unit, we applied ResNet164 as our basic architecture, and used SharedNet bottleneck or SharedNet unit

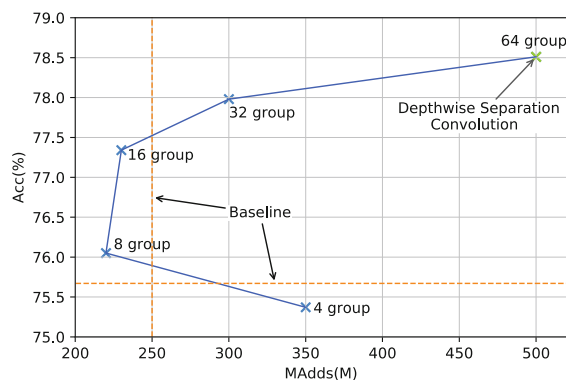
Table 3. Performance of SharedNet unit and influence of hyper-parameters.

| ResNet164 | MAdds | CIFAR10 | CIFAR100 |
|------------------------------------|-------|---------|----------|
| Pre-activation | 250 M | 94.54 | 75.67 |
| Swish | 250 M | 94.70 | 75.10 |
| SharedNet bottleneck | 100 M | 94.46 | 75.47 |
| SharedNet unit | 230 M | 95.12 | 77.34 |
| SharedNet unit + SE | 230 M | 95.49 | 78.33 |
| SharedNet unit + SE + Dropout(0.5) | 230 M | – | 78.78 |

instead of bottleneck in ResNet164, and added a 1×1 standard convolution layer before avgpool layer. The Channels of SharedNet bottleneck are consistent with the bottleneck in ResNet164. In detail, output channel of the first group sharing convolution is a quarter of input channel, and output channel of the second group sharing convolution is four times of the input channel. All channels of SharedNet unit are the same. When sizes of feature maps are 322, 162, and 82 respectively, the corresponding numbers of groups are 16, 32, and 64. Finally, we applied relu6 [15] before the second down-sampling, and applied hswish [16] after that.

Training parameters. In order to reduce the influence of training hyper-parameters, we strictly apply the same hyper-parameters of original ResNet paper. Thus, the standard SGD with momentum is set to 0.9, and weight decay is set to 0.0001. We started with a learning rate of 0.1, and then multiplied by 0.1 at 80-th and 120-th epochs. And we use a batch size of 128.

Results. Table 3 shows the accuracy of SharedNet unit with some hyper-parameters. When the accuracy is the same, SharedNet bottleneck is more efficient than bottleneck of ResNet164; On the other hand, when they have the same efficiency, SharedNet unit has higher accuracy than bottleneck of ResNet164. And if SharedNet used SE and utilized dropout of 0.5, the accuracy gained further improvement.

**Fig. 5.** Influence of the number of groups.

4.3 Number of Group in SharedNet Unit

Results. We experimented with five different numbers of groups on CIFAR100, and the results showed that the more groups SharedNet unit had, the higher accuracy is reached. In Fig. 5, when the number of groups is in the range between a quarter (16 groups) and a half (32 groups) of the input channels, SharedNet unit have a better AER. As mentioned above, when the input channels of SharedNet unit are consistent with the groups (64 groups), SharedNet unit can be converted into depthwise separable convolution. According to Fig. 5, the combination of group convolution and group sharing convolution has a better AER than depthwise separable convolution. Besides, the number of groups can balance accuracy and efficiency to meet different application requirements.

5 Conclusions and Future Work

We proposed an efficient convolution called group sharing convolution and a novel manual-designed efficient network called SharedNet built utilizing both groups sharing convolution and group convolution. And we manually designed the SharedNet unit to overcome the weakness of group sharing convolution. We carefully investigate the influence of the number of groups on accuracy and efficiency. Finally, by referring to the basic model architecture of MobileNet V2 we build SharedNet by the SharedNet unit to improve its efficiency.

SharedNet achieved the best result of manual-designed efficient models on ImageNet, and even the AER of our SharedNet is higher than some NAS models. Nevertheless, NAS models still show the advantage in model architecture design. However, as NAS models utilizing manually-designed efficient unit outperforms NAS models with NAS based efficient unit, the SharedNet shows great potential in NAS efficient networks. Therefore, our future works include using NAS to search a better architecture and further improve SharedNet to be adaptive to NAS manner.

Acknowledgement. This work was sponsored by Natural Science Foundation of Chongqing (Grant No. cstc2018jcyjAX0532).

References

1. Krizhevsky, A., Sutskever, I., Hinton, G.E.: ImageNet classification with deep convolutional neural networks. In: NIPS (2012)
2. Simonyan, K., Zisserman, A.: Very deep convolutional networks for large-scale image recognition. In: ICLR (2015)
3. Szegedy, C., et al.: Going deeper with convolutions. In: CVPR, vol. 07, pp. 1–9, 12 June 2015
4. He, K., Zhang, X., Ren, S., Sun, J.: Deep residual learning for image recognition. In: ICLR, CVPR, vol. 2016, pp. 770–778, December 2016

5. Huang, G., Liu, Z., Van Der Maaten, L., Weinberger, K.Q.: Densely connected convolutional networks. In: CVPR, vol. 2017, pp. 2261–2269, January 2017
6. Li, H., Samet, H., Kadav, A., Durdanovic, I., Graf, H.P.: Pruning filters for efficient convnets. In: ICLR. ICLR (2017)
7. Liu, Z., Li, J., Shen, Z., Huang, G., Yan, S., Zhang, C.-S.: Learning efficient convolutional networks through network slimming. In ICCV, pp. 2755–2763. IEEE Computer Society (2017)
8. He, Y., Liu, P., Wang, Z., Hu, Z., Yang, Y.: Filter pruning via geometric median for deep convolutional neural networks acceleration. In: CVPR, pp. 4340–4349. Computer Vision Foundation. IEEE (2019)
9. Courbariaux, M., Bengio, Y., David, J.P.: Binaryconnect: training deep neural networks with binary weights during propagations. In: NIPS, vol. 2015, pp. 3123–3131. Neural Information Processing Systems Foundation (2015)
10. Chen, S., Zhao, Q.: Shallowing deep networks: layer-wise pruning based on feature representations. IEEE Trans. Pattern Anal. Mach. Intell. **41**(12), 3048–3056 (2018)
11. Howard, A.G., et al.: MobileNets: efficient convolutional neural networks for mobile vision applications (2017)
12. Zhang, X., Zhou, X.Y., Lin, M.X., Sun, R.: ShuffleNet: an extremely efficient convolutional neural network for mobile devices. In: CVPR, pp. 6848–6856. IEEE, New York (2018)
13. Tan, M., et al.: MnasNet: platform-aware neural architecture search for mobile. In: CVPR, pp. 2820–2828. Computer Vision Foundation (2018)
14. Cai, H., Zhu, L., Han, S.: Proxylessnas: direct neural architecture search on target task and hardware. In: ICLR (2019)
15. Sandler, M., Howard, A., Zhu, M., Zhmoginov, A., Chen, L.C.: MobileNetV2: inverted residuals and linear bottlenecks. In: CVPR, pp. 4510–4520 (2018)
16. Howard, A., et al.: Searching for MobileNetV3. CoRR, abs/1905.0 (2019)
17. Ma, N., Zhang, X., Zheng, H.-T., Sun, J.: ShuffleNet V2: practical guidelines for efficient CNN architecture design. In: Ferrari, V., Hebert, M., Sminchisescu, C., Weiss, Y. (eds.) Computer Vision – ECCV 2018. LNCS, vol. 11218, pp. 122–138. Springer, Cham (2018). https://doi.org/10.1007/978-3-030-01264-9_8
18. Zhang, T., Qi, G.J., Xiao, B., Wang, J.: Interleaved group convolutions. In: CVPR, vol. 2017, pp. 4383–4392. Institute of Electrical and Electronics Engineers Inc., December 2017
19. Xie, G., Wang, J., Zhang, T., Lai, J., Hong, R., Qi, G.J.: Interleaved structured sparse convolutional neural networks. In: CVPR, pp. 8847–8856. IEEE Computer Society, December 2018
20. Sun, K., Li, M., Liu, D., Wang, J.: IGCv3: interleaved low-rank group convolutions for efficient deep neural networks. In BMVC. BMVA Press (2019)
21. Liu, H., Simonyan, K., Yang, Y.: DARTS: differentiable architecture search. In: ICLR (2019)
22. Xie, S., Girshick, R., Dollár, P., Tu, Z., He, K.: Aggregated residual transformations for deep neural networks. In: CVPR, vol. 2017, pp. 5987–5995, January 2017
23. Tan, M., Le, Q.V.: EfficientNet: rethinking model scaling for convolutional neural networks. In: Chaudhuri, K., Salakhutdinov, R. (eds.) ICML, Volume 97 of Proceedings of Machine Learning Research, PMLR, pp. 6105–6114 (2019)
24. Zoph, B., Le, Q.V.: Neural architecture search with reinforcement learning. In: ICLR (2017)



Paying Deep Attention to Both Neighbors and Multiple Tasks

Gaoyuan Liang¹, Haoran Mo^{2(✉)}, Ying Qiao³, Chuxin Wang⁴,
and Jing-Yan Wang⁵

¹ Heriot Watt University, Dubai Campus, Dubai International Academic City,
294345 Dubai, UAE

gaoyuanliang@outlook.com

² Innopolis University, Innopolis, Russia

m.haoran.cq@gmail.com

³ Microsoft Corporation, Redmond, WA, USA

qy01111@gmail.com

⁴ Hebei University of Environmental Engineering,

Qin Huang Dao 066000, China

⁵ New York University Abu Dhabi, Abu Dhabi, UAE

jimjywang@gmail.com

Abstract. In this paper, we propose a novel deep attention neural network. This network is designed for multi-task learning. The network is composed of multiple dual-attention layers of attention over neighbors and tasks. The neighbor attention layer represents each data point by paying attention over its neighboring data points, i.e., the output of this layer of a data point is the weighted average of its neighbors' inputs, and the weighting scores are calculated according to the similarity between the data point and its neighbors. The task attention layer takes the output of the neighbor attention layer as input, and transfer it to multiple task-specific representations for an input data point, and uses attention mechanism to calculate the outputs for different tasks. The output of the input data points for a task is calculated by a weighted average over all the task-specific representations, and the weighting scores are based on the similarity between the target task and the other tasks. The outputs of the neighbor attention layer and task attention layer are concatenated as the output of one dual-attention. To train the parameters of the network, we minimize the classification losses and encourage the correlation among different tasks. The experiments over the benchmark of multi-task learning show the advantage of the proposed method.

Keywords: Deep learning · Attention mechanism · Multi-task learning

1 Introduction

Attention mechanism has shown its effectiveness in many applications of machine learning, such as computer vision [8, 23], natural language processing [9, 13], and network analysis [6, 18, 19]. It explores a data point's contextual information to enhance its representation for various learning problems, by putting attentions over the

contextual data. Meanwhile, multi-task learning has been a popular learning problem for many machine learning applications. Instead of considering a single learning task, multi-task learning considers several learning problems simultaneously [5]. The motive is that in many real-world applications, for the same data, there may be different learning tasks, however, they are closely related. For example, in the face attribute annotation problem, the prediction of a face's gender is usually closely related to the prediction of long hair [27]. Since usually female has more possibility than male to have long hair, we can learn the gender and long hair predictor together to let them help each other. In this way, the accuracy of both prediction tasks is boosted. Recently, deep learning has been widely applied to multi-task learning [7, 10, 12, 21, 24, 25]. By using multiple layers of neural network as the prediction models of multi-learning problems, the features and the relations among the tasks are embedded to the hierarchical layers.

Recently, the attention mechanism has attracted much attention by the multi-task learning problems. Liu et al. [15] developed a multi-task learning method to learn the task-regarding attention of features. The proposed method is based on an attention neural network, which has a shared sub-network among tasks, and an attention layer for each task. By this design, the model can learn task-specific features from the shared features by paying different attention for different tasks. Meanwhile, since the common features are shared among all the tasks, it can somehow relate to different tasks. Moreover, the training of the parameters of the model is conducted in an end-to-end way. Lan et al. [11] proposed an attention neural network for multi-task learning. This model is used to solve the problem of both discourse relationship representation and identification through two types of representation. The attention-based neural network is designed for the learning of discourse relationship representation. It has two arguments and one multi-task framework so that the knowledge from both the annotated and unannotated data can be used for the training process. Zhao et al. [28] designed multi-task learning which avoids using pre-defined task relations. This method can learn task relations automatically and adaptively. Moreover, the learning process can learn the relations between features and tasks, and the relation between different features. The proposed model, named as a multi-relational attention network, explores three types of relations, which are learned by three attention-based models. They are the relations among tasks, relations among features, and relations between tasks and features. Dent et al. [2] developed a method to solve the problem of multi-task learning of both answer selection and knowledge base question answering. The method tries to learn from the rich correlation information between these two tasks. Firstly both tasks are treated as ranking problems so that they can share the same learning framework. But one task is a ranking problem at the text level, while the other is at the knowledge level. The internal relations between these two tasks are also learned by jointly learning the knowledge and answer contextual representation. A multi-task multi-view attention learning method is designed to make the tasks to interact with each other, and learn the representations of the question sentences.

In this paper, we explore the problem of learning effective multi-task prediction models by proposing a novel deep attention model. This model pays attention to a data point's neighbors and multiple tasks. We develop a novel deep learning model to use the neighborhood and multi-task information effectively for the purpose of multi-task learning. Our contributions are listed as follows. The deep model is composed of

multiple dual-attention layers. Each dual-attention layer is composed of a neighborhood attention layer and a task-attention layer. In the neighborhood layer, we represent the input data point as an attention-weighted combination of input features of its neighboring data points. In the attention layer over tasks, we first convert the input feature to task-wise features by task-wise representation function and then calculate the new task-wise feature by a weighted combination of the task-wise features. The attention scores over tasks are also calculated from the input task-wise features of the same data point. Then the outputs of the neighborhood attention layer and the task-wise representation layer are concatenated as the input of the next dual-attention layer. In this way, the output of the model can explore both the neighborhood with attention and tasks over attention. Moreover, since the output of both sub-layers is the input of the next dual-attention layer, the relations between neighborhood and tasks are embedded in the model. To train the model’s parameters, we minimize the objective of prediction errors and model complexity. We compare the proposed method against the state-of-the-art deep learning multi-task models with an attention mechanism. The experiments are conducted over four benchmark data sets. We also study how the performance changes according to the tradeoff parameters, and the iteration numbers to show the convergence of the algorithm.

2 Proposed Method

2.1 Network Structure

Suppose we have a set of n training data. To represent each data point, we explore its attention over its neighboring data points, and meanwhile, its attention over multiple tasks. To this end, we design a deep attention network of L layers, and each layer is composed of two attention layers and a concatenation layer. The two attention layers are of attentions over neighbors and tasks respectively, and the concatenation layer merges the outputs of these layers.

- **Attention layer over neighbors.** For an attention layer of neighbors, the input of a the i -th data point is denoted as \mathbf{x}_i , and its nearest neighbors is denoted as \mathcal{N}_i . To explore its attention over the data points in \mathcal{N}_i , we firstly calculate the similarity score between \mathbf{x}_i and a data point $\mathbf{x}_j \in \mathcal{N}_i$, which is denoted as ω_{ij} . We first concatenate \mathbf{x}_i and \mathbf{x}_j to a longer vector as the input, $\begin{bmatrix} \mathbf{x}_i \\ \mathbf{x}_j \end{bmatrix}$, and the input it to a full-connection layer with an activation function, f ,

$$\omega_{ij} = f\left(\begin{bmatrix} \mathbf{x}_i \\ \mathbf{x}_j \end{bmatrix}\right) = \sigma\left(\boldsymbol{\omega}^\top \begin{bmatrix} \mathbf{x}_i \\ \mathbf{x}_j \end{bmatrix} + b\right) \quad (1)$$

where $\sigma(x) = x^2$ is the activation function of f , and $(\boldsymbol{\omega}, b)$ is the parameter of the full-connection function. Then we employ a softmax function to normalize the similarity scores between \mathbf{x}_i and its neighbors to convert them to the attention scores of \mathbf{x}_j over the neighbors,

$$\alpha_{ij} = \frac{\exp(\omega_{ij})}{\sum_{j':x_{j'} \in \mathcal{N}_i} \exp(\omega_{ij'})}, \quad (2)$$

The output of this layer for \mathbf{x}_i , is the sum over the inputs of the its neighbors weighted by the corresponding attention scores,

$$\mathbf{z}_i \leftarrow \varpi(\mathbf{x}_i, \mathcal{N}_i) = \sum_{j':x_{j'} \in \mathcal{N}_i} \alpha_{ij} \mathbf{x}_j, \quad (3)$$

where ϖ is the overall function of this layer, and \mathbf{z}_i is the output vector of this layer.

- **Attention layer over tasks.** The next sub-layer is the layer to explore the attentions over multiple tasks. The input of the i -th data point is the output of last layer of neighbor attention, \mathbf{z}_i . Assuming we have m tasks in the multi-task learning problem, we first extract the task-wise features from \mathbf{z}_i for each task to represent the effective input for each specific task. For the k -th task, we design a full-connection layer with an activation layer as follows,

$$\mathbf{t}_i^k \leftarrow g_k(\mathbf{z}_i) = \varphi(V_k^\top \mathbf{z}_i + \mathbf{b}_k), t = 1, \dots, m, \quad (4)$$

where g_k is the task-wise feature extraction layer, and (V_k, \mathbf{f}_k) is the parameter of the full-connection layer, and $\varphi(x) = \tanh(x)$ is the activation layer. To explore the attentions of the k -th attention over the other tasks, we calculate the affinity score between the k -th task and the l -th task, regarding the i -th data point, as follows,

$$\theta_i^{kl} = h_{kl}(\mathbf{t}_i^k, \mathbf{t}_i^l) = \mathbf{t}_i^{k\top} A_{kl} \mathbf{t}_i^l, \quad (5)$$

where h_{kl} is the affinity function for the (k,l) -th task pair, and A_{kl} is its parameter matrix. For the i -th data point, the attention score of its k -th task over the l -th task is calculated by a softmax function,

$$\beta_i^{kl} = \frac{\exp(\theta_i^{kl})}{\sum_{l'=1}^m \exp(\theta_i^{kl'})}, \quad (6)$$

and its representation regarding the k -th task is the sum over the task-wise representations weighted by the attention scores,

$$\mathbf{v}_i^k \leftarrow \kappa_k(\mathbf{z}_i) = \sum_{l=1}^m \beta_i^{kl} \mathbf{t}_i^l, \quad (7)$$

where κ_k is the function for the k -th task of this layer, and \mathbf{v}_i^k is the task-wise representation of the i -th data point, which will be used for task-specific prediction problems.

- **Concatenation layer.** This layer concatenates the outputs of the last two layers of attentions, and the input vector of each data point, as the input of the next layer, \mathbf{x}_i^{next}

$$\mathbf{x}_i^{next} \leftarrow \zeta(\mathbf{x}_i, \mathbf{z}_i, \mathbf{v}_i^1, \dots, \mathbf{v}_i^m) = \begin{bmatrix} \mathbf{x}_i \\ \mathbf{z}_i \\ \mathbf{v}_i^1 \\ \vdots \\ \mathbf{v}_i^m \end{bmatrix}, \quad (8)$$

where ζ is the concatenation function.

With the above defined layer, we build the multi-layer neural network of dual attentions of neighbors and tasks. For the first layer, the input is the simple original vector of each data point, \mathbf{x}_i^1 . For the l -th layer, the processing is as follows,

$$\begin{aligned} \mathbf{z}_i^l &= \varpi_l(\mathbf{x}_i^l, \mathcal{N}_i^l), \\ \mathbf{v}_i^{k^l} &= \kappa_{kl}(\mathbf{z}_i^l), k = 1, \dots, m, \\ \mathbf{x}_i^{l+1} &= \xi(\mathbf{x}_i^l, \mathbf{z}_i^l, \mathbf{v}_i^{1^l}, \dots, \mathbf{v}_i^{m^l}). \end{aligned} \quad (9)$$

The output of the network are the outputs of the last layer, and the task-wise representations, $\mathbf{v}_i^{1^{L+1}}, \dots, \mathbf{v}_i^{m^{L+1}}$, are used to predict the task-wise labels. For the k -th task, we take the outputs of task-wise representations of all layers and concatenate them as the feature representation of this task. Thus, we define a network for each task accordingly, to convert a data point \mathbf{x}_i , and its neighbor \mathcal{N}_i , to a task-wise representation feature vector,

$$\vartheta_k(\mathbf{x}_i, \mathcal{N}_i; \Psi) = \begin{bmatrix} \mathbf{v}^{k^1} \\ \vdots \\ \mathbf{v}^{k^L} \end{bmatrix} \in \mathbb{R}^d, \quad (10)$$

where d is the dimension of the output, and Ψ is the parameter set of the network.

2.2 Training of the Network Parameters

We first consider the problem of learning multiple predictors for multiple tasks. For the k -th task, we denote a data point's task-wise representation as

$$\boldsymbol{\tau}^k = \vartheta_k(\mathbf{x}, \mathcal{N}; \Psi), \quad (11)$$

and use it as the input vector for the corresponding task. With this input vector for a data point, for the k -th task, we design a linear predictor to approximate the response from the task-wise output from the dual-attention network, τ^k ,

$$\psi_k(\tau^k) = W_k^\top \tau^k + \gamma_k \in \mathbb{R}^{c_k} \quad (12)$$

where ψ_k is the predictor of the k -th task, (W_k, γ_k) is the parameter of ψ_k , and $W_k \in \mathbb{R}^{d \times c_k}$.

To learn good quality predictor, we minimize the losses of the data points over the training set for all tasks,

$$\min_{\Psi, (W_k, \gamma_k)_{k=1}^m} \left\{ \sum_{k=1}^m \sum_{i \in \mathcal{X}_k} \|y_i^k - (W_k^\top \tau_i^k + \gamma_k)\|_2^2 + C \left(\|\Psi\|_2^2 + \sum_{k=1}^m \|W_k\|_2^2 \right) \right\}, \quad (13)$$

where \mathcal{X}_k is the training set of the k -th task, y_i^k is the ground truth (regression response, or class label vector) of the i -th data point of the k -th task, and Ψ is the set of trainable parameters of the network to generate the representations τ_i^k . The last term is the squared ℓ_2 norms of the parameters of the model, and C is its weight. To solve this problem, we employ the alternating direction method of multipliers (ADMM) [1] to update the parameters alternately in an iterative algorithm.

3 Experiments

In this section, we will experimentally evaluate the proposed method, called deep dual attention network (DDAN).

3.1 Benchmark Data Sets

In the experiments, we evaluate methods of multi-task learning for three benchmark data sets.

- **Penn Action** [26] data set is a video data set for tasks of action recognition and human pose estimation. In this data set, there are 2,326 videos captured for sportspeople. The action recognition tasks have 15 different action classes, thus it is a classification problem. Meanwhile, for the pose estimation problem, there are 13 body joints whose locations need to be predicted from each frame of a video. Thus the pose estimation task is a regression problem. The sub-tasks are 15 classification problems and 13 regression problems in total.
- **Multi-Attribute Facial Landmark** [27] data set is a data set of face images. It has 20,000 face images which are selected from the Celebrity face database [17]. For this data set, we have multi-task problems of 22 binary classification problems, and 5 regression problems. The 22 classification problems are the prediction of 22 face attributes, such as the right profile face, smiling face, etc. The 5 regression problems are the estimation of the locations of the 5 facial landmarks.

- **Dianping dataset** [28] is a data set collected from the Chinese online review website, www.dianping.com. This data set has the review data of 10,070 food chain stores and 456 shopping malls. The tasks of this data set are to predict the review number, ratings, quality score, environment score, and service score of each store, making it a 5-task learning problem. Each task is a business success measure.

3.2 Results

To conduct the experiment, we split the date set to ten folds according to the 10-fold cross-validation protocol. For the regression tasks, we use the mean squared error (MSE) to measure the performance, while for the classification tasks, we use the misclassification rate (MR) to measure the performance. As overall performance measures, we calculate an average MSE overall regression tasks and an average MR overall classification tasks. To evaluate the proposed method, we compare it to the state-of-the-art deep learning-based multi-task learning methods and study its performance with the change of the tradeoff parameters, and convergence.

Comparison to Other Methods

In our experiment, we compare our method to the methods proposed by Liu et al. [15], Lan et al. [11], Zhao et al. [28], and Dent et al. [2]. The results are shown in Fig. 1. From this figure, we can see that for all the cases of all data sets, our proposed method consistently outperforms the compared methods of multi-task learning based on attention mechanism. It is always giving the lowest error measures, either for the regression or for the classification tasks. For example, for the Dianping data set, it is the only method which achieves an MSE lower than 0.25, while all other methods can only obtain MSE higher than 0.30 or close to 0.30.

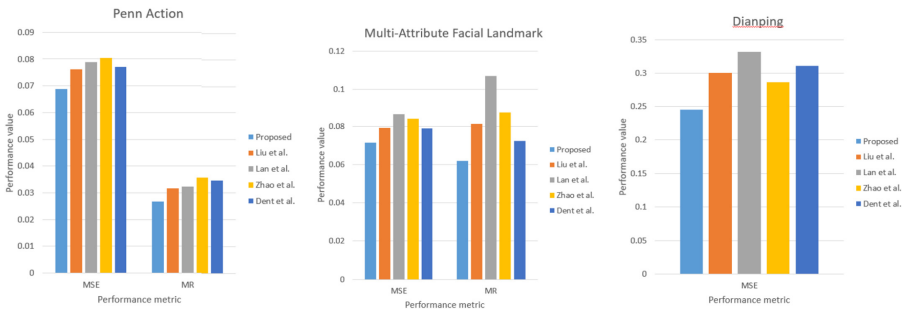


Fig. 1. Comparison results over benchmark data sets.

Sensitivity to C

We also explore the changes in the performance of our method regarding the changes in the tradeoff parameter C . The error metrics of both regression and classification regarding the changes in the value of C is reported in Fig. 2. In this figure, we can also see that a large value of C can reduce the error metrics. This indicates that a simpler

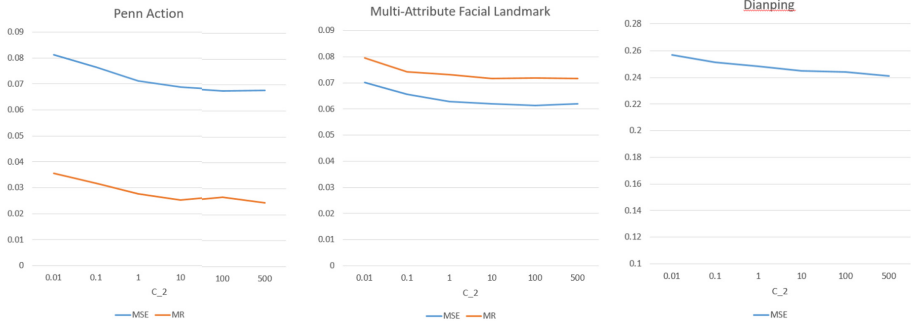


Fig. 2. Performance sensitivity to C .

model is also beneficial for the predictions over the test set since it can reduce the risk of the over-fitting problems.

4 Conclusion and Future Works

In this paper, we proposed a novel deep learning method for multi-task learning problems. Our model is based on dual-attentions. One attention is at the neighborhood level, and another one is at the level of tasks. The dual-attention layer can explore both the neighborhood and task attention and the relations between them. Moreover, the attention is optimized for each data point. Our deep model is composed of multiple such dual-attention layers. We design an iterative algorithm to learn the parameters of the model to reduce the training errors and the model complexity. The experiments over benchmark data sets show that our model outperforms the state-of-the-art deep learning models with an attention mechanism. In the future, we will extend our work to other applications, such as network analysis [3, 4, 16, 20, 22], recommendation system [14], etc.

References

1. Boyd, S., Parikh, N., Chu, E., Peleato, B., Eckstein, J.: Distributed optimization and statistical learning via the alternating direction method of multipliers. *Found. Trends Mach. Learn.* **3**(1), 1–122 (2011)
2. Deng, Y., et al.: Multi-task learning with multi-view attention for answer selection and knowledge base question answering. In: *Proceedings of the AAAI Conference on Artificial Intelligence*, vol. 33, pp. 6318–6325 (2019)
3. Du, H., Yang, S.J.: Discovering collaborative cyber attack patterns using social network analysis. In: Salerno, J., Yang, S.J., Nau, D., Chai, S.-K. (eds.) *SBP 2011. LNCS*, vol. 6589, pp. 129–136. Springer, Heidelberg (2011). https://doi.org/10.1007/978-3-642-19656-0_20
4. Du, H., Yang, S.J.: Probabilistic inference for obfuscated network attack sequences. In: *2014 44th Annual IEEE/IFIP International Conference on Dependable Systems and Networks*, pp. 57–67 (2014)

5. Evgeniou, T., Pontil, M.: Regularized multi-task learning. In: Proceedings of the Tenth ACM SIGKDD International Conference on Knowledge Discovery and Data Mining, pp. 109–117. ACM (2004)
6. Gao, H., Ji, S.: Graph representation learning via hard and channel-wise attention networks. In: Proceedings of the 25th ACM SIGKDD International Conference on Knowledge Discovery & Data Mining, pp. 741–749. ACM, New York (2019)
7. Geng, Y., et al.: Learning convolutional neural network to maximize pos@ top performance measure. In: ESANN 2017 - Proceedings, pp. 589–594 (2016)
8. Geng, Y., et al.: A novel image tag completion method based on convolutional neural transformation. In: Lintas, A., Rovetta, S., Verschure, P.F.M.J., Villa, A.E.P. (eds.) ICANN 2017. LNCS, vol. 10614, pp. 539–546. Springer, Cham (2017). https://doi.org/10.1007/978-3-319-68612-7_61
9. Hao, Y., et al.: An end-to-end model for question answering over knowledge base with cross-attention combining global knowledge. In: Proceedings of the 55th Annual Meeting of the Association for Computational Linguistics, vol. 1, pp. 221–231 (2017)
10. Jabi, M., Pedersoli, M., Mitiche, A., Ben Ayed, I.: Deep clustering: on the link between discriminative models and k-means. *IEEE Trans. Pattern Anal. Mach. Intell.* 1 (2019). <https://doi.org/10.1109/tpami.2019.2962683>
11. Lan, M., Wang, J., Wu, Y., Niu, Z.Y., Wang, H.: Multi-task attention-based neural networks for implicit discourse relationship representation and identification. In: Proceedings of the 2017 Conference on Empirical Methods in Natural Language Processing, pp. 1299–1308 (2017)
12. Li, S., et al.: Deep residual correction network for partial domain adaptation. *IEEE Trans. Pattern Anal. Mach. Intell.* 1 (2020). <https://doi.org/10.1109/tpami.2020.2964173>
13. Lin, Y., Liu, Z., Sun, M.: Neural relation extraction with multi-lingual attention. In: Proceedings of the 55th Annual Meeting of the Association for Computational Linguistics, vol. 1, pp. 34–43 (2017)
14. Liu, D., Lian, J., Qiao, Y., Chen, J.H., Sun, G., Xie, X.: Fast and accurate knowledge-aware document representation enhancement for news recommendations (2019)
15. Liu, S., Johns, E., Davison, A.J.: End-to-end multi-task learning with attention. In: Proceedings of the IEEE Conference on Computer Vision and Pattern Recognition, pp. 1871–1880 (2019)
16. Mo, H., Lee, J.: Spatial community search using pagerank vector. In: 2019 International Conference on Computing, Networking and Communications (ICNC), pp. 792–796. IEEE (2019)
17. Sun, Y., Wang, X., Tang, X.: Deep learning face representation from predicting 10,000 classes. In: Proceedings of the IEEE Conference on Computer Vision and Pattern Recognition, pp. 1891–1898 (2014)
18. Tang, X., Wang, T., Yang, H., Song, H.: AKUPM: attention-enhanced knowledge-aware user preference model for recommendation. In: Proceedings of the 25th ACM SIGKDD International Conference on Knowledge Discovery & Data Mining, KDD 19, pp. 1891–1899. ACM, New York (2019). <https://doi.org/10.1145/3292500.3330705>
19. Wang, X., He, X., Cao, Y., Liu, M., Chua, T.S.: KGAT: knowledge graph attention network for recommendation. In: Proceedings of the 25th ACM SIGKDD International Conference on Knowledge Discovery & Data Mining, pp. 950–958. ACM, New York (2019)
20. Wang, Z., He, Z., Shah, M., Zhang, T., Fan, D., Zhang, W.: Network-based multi-task learning models for biomarker selection and cancer outcome prediction. *Bioinformatics* 36 (6), 1814–1822 (2020)
21. Yu, T., Li, Y., Li, B.: Deep learning of determinantal point processes via proper spectral sub-gradient. In: International Conference on Learning Representations, ICLR, vol. 20 (2020)

22. Yu, T., Wang, R., Yan, J., Li, B.: Learning deep graph matching with channel independent embedding and hungarian attention. In: International Conference on Learning Representations, ICLR, vol. 20 (2020)
23. Zanca, D., Melacci, S., Gori, M.: Gravitational laws of focus of attention. *IEEE Trans. Pattern Anal. and Mach. Intell.* 1 (2019). <https://doi.org/10.1109/tpami.2019.2920636>
24. Zhang, G., et al.: Learning convolutional ranking-score function by query preference regularization. In: Yin, H., et al. (eds.) IDEAL 2017. LNCS, vol. 10585, pp. 1–8. Springer, Cham (2017). https://doi.org/10.1007/978-3-319-68935-7_1
25. Zhang, G., Liang, G., Su, F., Qu, F., Wang, J.-Y.: Cross-domain attribute representation based on convolutional neural network. In: Huang, D.-S., Gromiha, M.M., Han, K., Hussain, A. (eds.) ICIC 2018. LNCS (LNAI), vol. 10956, pp. 134–142. Springer, Cham (2018). https://doi.org/10.1007/978-3-319-95957-3_15
26. Zhang, W., Zhu, M., Derpanis, K.G.: From actemes to action: a strongly-supervised representation for detailed action understanding. In: Proceedings of the IEEE International Conference on Computer Vision, pp. 2248–2255 (2013)
27. Zhang, Z., Luo, P., Loy, C.C., Tang, X.: Learning deep representation for face alignment with auxiliary attributes. *IEEE Trans. Pattern Anal. Mach. Intell.* **38**(5), 918–930 (2015)
28. Zhao, J., Du, B., Sun, L., Zhuang, F., Lv, W., Xiong, H.: Multiple relational attention network for multi-task learning. In: Proceedings of the 25th ACM SIGKDD International Conference on Knowledge Discovery & Data Mining, KDD 19, pp. 1123–1131. ACM, New York (2019)



Image Classification Based on Deep Belief Network and YELM

ChengYong Zhang¹, Zhengwei Li^{2,3,4,5(✉)}, Ru Nie^{2,3(✉)}, Lei Wang⁶,
and Huan Zhao^{2,3}

¹ Jiangsu Vocational College of Information Technology, Wuxi 214153, China

² School of Computer Science and Technology, China University of Mining and Technology, Xuzhou 221116, China
{zwli, nr}@cumt.edu.cn

³ Engineering Research Center of Mine Digitalization of Ministry of Education, China University of Mining and Technology, Xuzhou 221116, China

⁴ Institute of Machine Learning and Systems Biology, College of Electronics and Information Engineering, Tongji University, Shanghai 201804, China

⁵ KUNPAND Communications (Kunshan) Co., Ltd, Suzhou 215300, China

⁶ School of Mechatronic Engineering, China University of Mining and Technology, Xuzhou 221116, China

Abstract. For a large amount of image data, an image classification method based on improved deep belief network (IDBN) and improved extreme learning machine (YELM) was proposed. Firstly, IDBN was used to simplify the complex high-dimensional data to lower dimensions space, and get the main inherent feature of the images with lower dimension. Then YELM was used to classify data after the dimension reduction. The proposed IDBN-YELM method has a significant improvement in classification accuracy. Extensive experiments were performed using challenging dataset and results were compared against the models such as DBN, YELM, IDBN-ELM. Though a lot of comparative experiments on the street view house numbers (SVHN) dataset, the results show that the IDBN-YELM has the high classification accuracy for the problem of large-scale image classification.

Keywords: Image classification · Improved Deep Belief Network · Extreme learning machines · YELM

1 Introduction

With the rapid development of information technology, a large amount of information can be obtained through the Internet. There are massive images on the Internet. In recent years, how to classify large-scale image data quickly and effectively has become a growing concern [1–4].

Image classification is the first attempt of deep learning in application field. In 1989, LeCun *et al.* published convolution neural networks (CNNs) [5]. CNNs have shown their huge potential of training on image data and could obtain high accuracy in image classification tasks. After that, Kussual *et al.* put forward a new neural network based on permutation encoding technology [6], which also has a good performance in

face recognition and other small object recognition task. The permutation coding technique makes it possible to take not only detected features, but also the position of each feature in the image into account. In 2006, Hinton *et al.* published an article [7] in the top academic journal “science”, and put forward the method of deep belief network, opening a new upsurge of deep learning. At present, DBN is widely used in image recognition, natural language processing, and other fields [8–12].

Extreme learning machine (ELM) was proposed by Huang *et al.* in 2004 [13]. It is a learning algorithm based on single-hidden-layer feed forward neural networks (SLFN) [14], in which the parameter iterative adjustment process of the traditional neural network is transformed into solving the minimum norm least-squares solution of a general linear system and putting the solution as the output weights of the network with Moore-Penrose generalized inverse matrix theory [15, 16]. The algorithm has the characteristics of easy realization and high efficiency.

In 2015, Zhang *et al.* proposed an improved ELM algorithm named P-ELM subject based on PCA (Principal Components Analysis) technique [17]. The proposed P-ELM algorithm can not only ensure the full column rank of newly generated hidden layer output matrix (H'), but also improve the learning speed by reducing the number of hidden nodes. Yong Peng *et al.* proposed a discriminative ELM with supervised sparsity preserving (SPELM) [18]. SPELM performs as a subspace learning method by considering the discriminative as well as sparsity information of data [19].

YELM is an improved algorithm of ELM proposed by Yuan [20] and its adjustments are carried out in the calculation method of the output weights. By discussing in cases of H is column full rank, row full rank, neither column nor row full rank, it not only proves that the output weights must have one solution, but also greatly improves the speed of the realization significantly. It is the reason why we chose YELM in this paper.

In this paper, we proposed a method of image classification based on improved deep belief network and YELM (IDBN-YELM), which mainly includes two stages:

- (1) Achieve the expression of the dimension reduction by the improved deep belief network. Because the image has a higher dimensionality, the dimensionality reduction of the high-dimensional vector is realized through the deep belief network, which could capture the inherent characteristics of the image with the low-dimensional vector.
- (2) Classify images with YELM. Use YELM to train reduced-dimension data. Through many comparative experiments, the results show that the proposed method has higher classification accuracy.

2 Method Research

2.1 DBN and IDBN

Deep belief network (DBN) is a generative graphical model consisting of stacked restricted Boltzmann machines (RBMs). Based on its deep structure DBN can capture hierarchical representation of input data. DBN is constructed layer by layer using

RBM [21], which includes a visible layer and several hidden layers, with a powerful ability of feature learning [22]. A DBN model is considered as a stack of several RBMs, in which top-down connections in the model can be used to generate low-level features of images from high-level representations, and bottom-up connections can be used to infer the high-level representations that would generate observed set of low-level features. We can train the data layer by layer: (1) the bottom of RBMs trains the original input data; (2) the lower layer of feature becomes the input of the next RBMs; (3) process (1) and (2) can be repeated as many times as desired. Given visible unit x and ℓ hidden layers the joint distribution is defined as

$$P(x, h^1, \dots, h^\ell) = p(h^{\ell-1}, h^\ell) \left(\prod_{k=1}^{\ell-2} p(h^k | h^{k+1}) \right) p(x | h^\ell) \quad (1)$$

Since each layer of DBN is constructed as RBM, training each layer of DBN is the same as training a RBM. Classification is conducted by initializing a network through DBN training. Given training dataset $D = \{(x_1, y_1), \dots, (x_{|D|}, y_{|D|})\}$ with input x and label y , the pretraining phase solves the following optimization problem at each layer k :

$$\min_{\theta_k} \frac{1}{|D|} \sum_{i=1}^{|D|} [-\log p(x_i^k; \theta_k)] \quad (2)$$

where $\theta_k = (W_k, b_k, c_k)$ is the RBMs model parameter that indicates weights, visible bias, and hidden bias in the energy function, and x_i^k is visible input to layer k corresponding to input x_i . Note that in layer-wise updating manner we need to solve ℓ of the problems from the bottom to the top hidden layer. For the fine-tuning phase we solve the following optimization problem:

$$\min_{\phi} \frac{1}{|D|} \sum_{i=1}^{|D|} [\mathcal{L}(\phi; y^i, h(x_i))] \quad (3)$$

where $\mathcal{L}()$ is a loss function, h is the final hidden features at layer ℓ , and ϕ is the parameters of the classifier. Here, $h(x_i^k)$ is simplified by $h(x_i)$.

In this article, we adopted an improved deep belief network (IDBN) model proposed by Koo et al., which is a supervised models based on DBN in order to improve this two-phase strategy. This model implement classification based on the corresponding hidden space. Owing to the minimization for the expected loss, it is more robust and thus could obtain higher precision than the basic DBN model. The problem solving can be transformed into the following minimization of expected loss function:

$$\min_{\theta_L, \theta_{DBN}} \mathbb{E}_{y, h|x} [\theta_L; y, h(\theta_{DBN}; x)] \quad (4)$$

Given training samples D , the mathematical form of the IDBN reads

$$\begin{cases} \min_{\theta_L, \theta_{DBN}} \frac{1}{|D|} \sum_{i=1}^{|D|} [p(h|x^i) \mathcal{L}(\theta_L; y_i, h(\theta_{DBN}; x_i))] \\ s.t. |\theta_{DBN} - \theta_{DBN}^*| \leq \delta \end{cases} \quad (5)$$

where θ_{DBN}^* are the optimal IDBN parameters and δ is a hyperparameter. With notation $h(\theta_{DBN}; x_i) = h(x_i)$, we explicitly show the dependency of h on θ_{DBN} . We modify the expected loss by introducing a constraint that sets bounds on DBN related parameters with respect to their optimal values. This model has two benefits. First, the model keeps a good representation of input by constraining parameters fitted in the unsupervised manner. Second, the constraint regularizes the model parameters by preventing them from blowing up while being updated.

2.2 ELM and YELM

Extreme learning machine is one of the most popular and important learning algorithms. It comes from single-hidden-layer feedforward neural networks (see Fig. 1). Compared with the traditional algorithm, extreme learning machine only need to set the number of hidden layer nodes, do not need to adjust the network’s input weights between input layer and hidden layer and bias parameters on hidden layers. The unique optimal solution needs to be learned only once.

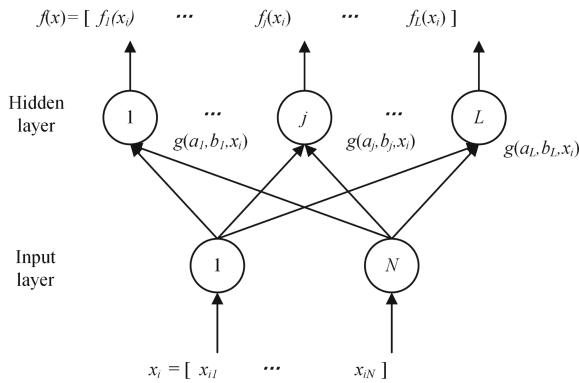


Fig. 1. The model of ELM

For given samples set $\{X, T\} = \{x_i, t_i\}_{i=1}^N$, where $x_i = (x_{i1}, x_{i2}, \dots, x_{in}) \in R^n$, $t_i \in R$. That standard SLFNs with L hidden nodes and an activation function can approximate these N samples, there exist β_j, w_i and b_j such that:

$$f_L(x_j) = \sum_{i=1}^L \beta_i g(w_i, b_i, x_j) = t_j, j = 1, 2, \dots, N \quad (6)$$

where $g(\cdot)$ is an activation function, β_i ($i = 1, \dots, L$) is the i -th coefficient vector, w_i denotes the weight vector connecting the i -th hidden node and the input layer, b_i is the bias of i -th hidden node. Equation (6) can be briefly denoted as:

$$H\beta = T \quad (7)$$

where

$$H = \begin{bmatrix} g(w_1, b_1, x_1) & g(w_2, b_2, x_2) & \cdots & g(w_L, b_L, x_1) \\ g(w_1, b_1, x_2) & g(w_2, b_2, x_2) & \cdots & g(w_L, b_L, x_2) \\ \vdots & \vdots & \vdots & \vdots \\ g(w_1, b_1, x_N) & g(w_2, b_2, x_N) & \cdots & g(w_L, b_L, x_N) \end{bmatrix}_{N \times L}$$

$$\beta = \begin{bmatrix} \beta_1^T \\ \beta_2^T \\ \vdots \\ \beta_N^T \end{bmatrix}_{L \times M}, T = \begin{bmatrix} t_1^T \\ t_2^T \\ \vdots \\ t_N^T \end{bmatrix}_{N \times M}$$

where H is called the hidden layer output matrix, the i -th column of H is the i -th hidden node output with respect to the input x_1, x_2, \dots, x_N . ELM is a very simple algorithm and has a high speed for learning the model. However, there is no solution for the equation $H\beta = T$ in many cases.

YELM is an extension of ELM, proposed by Yuan *et al.* in 2011. In YELM, Eq. (7) is equivalent to the following equation:

$$H^T H \beta = H^T T \quad (8)$$

Optimal approximation solution of YELM is discussed in cases of H is column full rank, row full rank, neither column nor row full rank. If H is column full rank, optimal approximation solution is solved by $\beta = (H^T H)^{-1} H^T T$; If H is row full rank, optimal approximation solution is solved by $\beta = H^T (H H^T)^{-1} T$; If H is neither column nor row full rank, the *rank-1* and *rank-2* approximation optimal methods are used to get optimal approximation solution. But in fact, the extra time spent in the third phase of the algorithm is $O(L^2)$, which is shorter in comparison with that spent in the third phase of the ELM algorithm used to compute the output weights. This improvement not only improves the generalization of the algorithm, but also greatly improves the speed of algorithm implementation.

3 Image Classification Based on IDBN and YELM

The training process of image classification based on IDBN and YELM includes two stages: IDBN training and YELM training. Achieving the feature of the dimension reduction by IDBN [23, 24], then, implementing image classification by YELM training. The whole training process of IDBN-YELM can be expressed in Fig. 2.

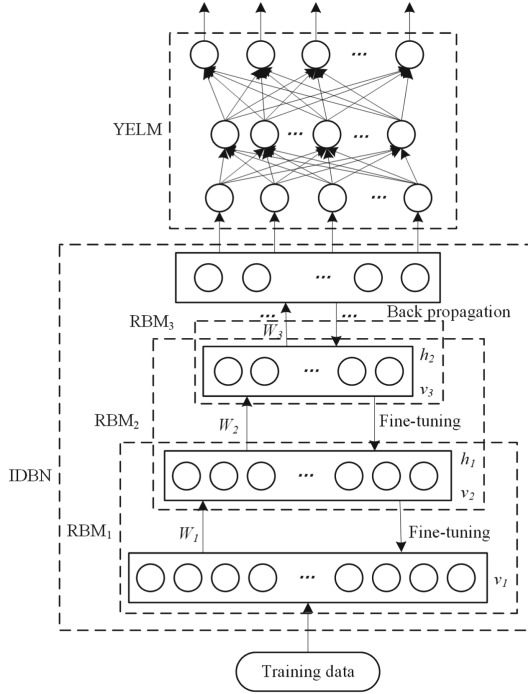


Fig. 2. Architecture of IDBN-YELM

3.1 The Training Process of IDBN

Restricted Boltzmann machine consists of two adjacent layers in the improved deep belief network, the adjustment of network weights uses the direction from the bottom up. Adjusting the weight leads to optimizing the energy functions as follows:

$$E(x, h) = -b'x - c'h - h'Wx - x'Ux - h'Vh \quad (9)$$

where h is a latent variable, x is an input vector, W, U, V are weight matrices;

To optimize the energy function, using the gradient descent method:

$$\frac{\partial \log p(v^0)}{\partial w_{ij}^\infty} = h_j^0 (v_i^0 - \bar{v}_i^0) \quad (10)$$

where v_i^0, \bar{v}_i^0 are the values of neurons status, w_{ij}^∞ is the weight.

After using gradient descent method to obtain minimum energy, symmetrical weight matrix W can be extracted. Finally, according to the input vector x , with the output of the restricted Boltzmann machine the latent variables can be extracted, namely the low dimensional feature.

3.2 The Training Process of YELM

After extracting low-dimensional data, YELM will be taken as a classifier for classification training. In training period, we adopted the dimension of the feature vector as the number of input layer neurons and used the number of the sample's categories to determine the number of output layer neurons. Given an activation function $g(x)$, and hidden node number L , the training process of YELM can be divided into three steps:

Step 1: Randomly assign hidden node parameters $w_i, b_i, i = 1, 2, \dots, L$

Step 2: Calculate the hidden layer output matrix H by equation (3), $r = \text{rank}(H)$

Step 3:

If $r=L$:

Compute the output weight by $\beta^+ = (H^T H)^{-1} H^T T$

If $r < L$:

Compute the output weight by $\beta^+ = H^T (H^T H)^{-1} T$;

Else:

let $M = H^T H, c = H^T T, \varepsilon = 10^{-4}$, solve optimal models $\min_{B \in \mathbb{R}^{L \times L}} \|M - B\|$ and $\min_{\beta \in \mathbb{R}^L} \|B^* \beta - c\|$;

Get the corresponding solutions B^*, β^* ;

If $\|c - B^* \beta^*\| > \varepsilon$:

Compute $B = B^* + \frac{(c - B^* \beta^*)(c - B^* \beta^*)^T}{(c - B^* \beta^*)^T \beta^*}$;

Else:

Compute $B = B^* + \frac{c c^T}{c^T \beta^*} - \frac{B^* \beta^* (\beta^*)^T B^*}{(\beta^*)^T B^* \beta^*}$;

Get the output weight by $\beta^+ = B^{-1} c$.

4 Experiments

The data set used in this article is the Street View House Numbers (SVHN) dataset provided by Google [25], which is mainly used for image recognition algorithms. It is similar to the MNIST data set, which consists of ten numbers from "0" to "9" and represents the corresponding digital label. The SVHN dataset provides two different formats to meet different testing needs, both of which include training set, test set and additional set. The second format is a cropped image with a single character in the center. These images are cropped from the original image and contain more than 600,000 images. All images are normalized to 32×32 , and the interference factors such as distortion, rotation, background noise are added to the image. The following four experiments were all trained on SVHN dataset.

- (1) IDBN-YELM experiment: Firstly, we reduced dimension of the samples with the improved deep belief network, then classified the reduced-dimension data with YELM, after all, the accuracy rate that we got is 94.57%. In this experiment, the pre-training part is unsupervised learning, and the fine-tuning part is supervised learning.

- (2) IDBN-ELM experiment: This process is like the IDBN-YELM experiment, just difference in that what model we chose. Finally, the accuracy rate that we got is 94.33%.
- (3) YELM experiment: We classified the image on SVHN with YELM by constantly changing the number of hidden layer neurons, and the accuracy rate is 60.49%.
- (4) IDBN experiment: We classified the image on SVHN with IDBN, the accuracy rate is 94.29%.

As can be seen from Fig. 3 and Fig. 4, the combination of IDBN and YELM is superior to one of them. For using the improved deep belief network, the interior structure of high-dimensional data is got, and the goal of reducing dimension is achieved. Then, classifying low-dimensional data with YELM, which greatly reduces the amount of calculation and improves the classification accuracy.

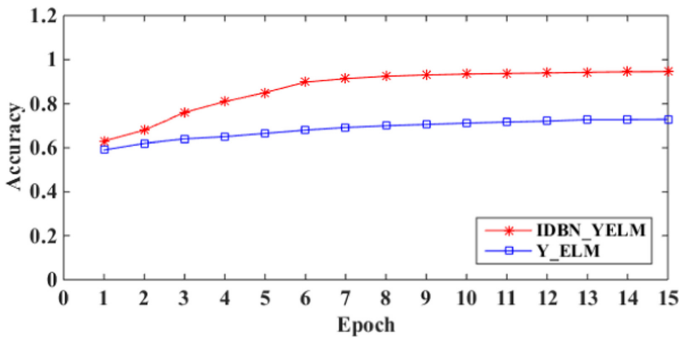


Fig. 3. Classification accuracies of IDBN-YELM and YELM on SVHN dataset

As can be seen from Fig. 5 that the performance of IDBN-YELM is slightly better than that of IDBN-ELM. The main reason of this result is that YELM classifier is introduced.

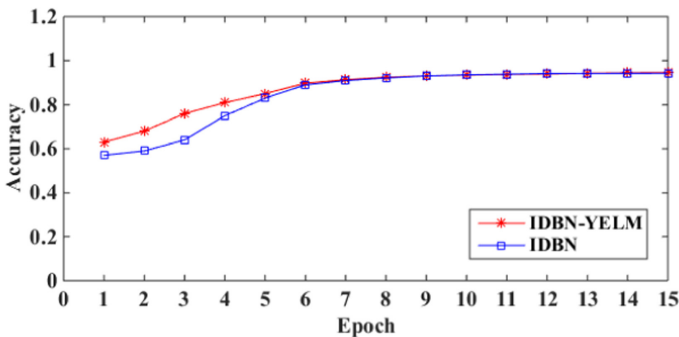


Fig. 4. Classification accuracies of IDBN-YELM and IDBN on SVHN dataset

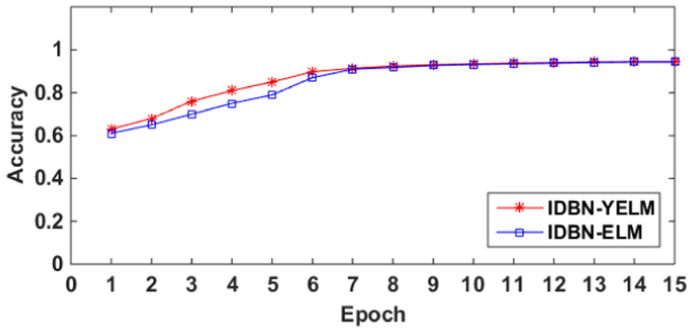


Fig. 5. Classification accuracies of IDBN-YELM and IDBN-ELM on SVHN dataset

5 Conclusions

In this paper, we proposed a method of image classification based on improved deep belief network and YELM to extend the traditional classification algorithms. Firstly, we achieved dimension reduction of high-dimensional data by improved deep belief network, then we used YELM to train reduced-dimension data. Experiment results showed that this novel method can achieve high accuracy of image classification. However, one drawback of this model is that one more training phase to the two-phase approach is necessary.





References

1. Kamusoko, C.: Image classification. In: Kamusoko, C. (ed.) Remote Sensing Image Classification in R. SG, pp. 81–153. Springer, Singapore (2019). https://doi.org/10.1007/978-981-13-8012-9_4
2. Li, C., Wang, K., Xu, N.: A survey for the applications of content-based microscopic image analysis in microorganism classification domains. *Artif. Intell. Rev.* **51**(4), 577–646 (2017). <https://doi.org/10.1007/s10462-017-9572-4>
3. Liu, X., Zhang, R., Meng, Z., Hong, R., Liu, G.: Correction to: on fusing the latent deep CNN feature for image classification. *World Wide Web* **22**, 1887 (2019)
4. Zheng, S., Zhang, Y., Liu, W., Zou, Y.: Improved image representation and sparse representation for image classification. *Appl. Intell.* **50**(6), 1687–1698 (2020). <https://doi.org/10.1007/s10489-019-01612-3>
5. Lecun, Y., et al.: Backpropagation applied to handwritten zip code recognition. *Neural Comput.* **1**, 541–551 (1989)
6. Kussul, E.M., Baidyk, T.N., Wunsch II, D.C., Makeyev, O., Martn, A.: Permutation coding technique for image recognition systems. *IEEE Trans. Neural Netw.* **17**, 1566–1579 (2006)
7. Hinton, G.E., Salakhutdinov, R.R.: Reducing the dimensionality of data with neural networks. *Science* **313**, 504 (2006)
8. Desai, S., Sinha, D., El-Sharkawy, M.: Image classification on NXP i.MX RT1060 using ultra-thin MobileNet DNN (2020)
9. Geng, Z., Li, Z., Han, Y.: A new deep belief network based on RBM with glial chains. *Inf. Sci.* **463–464**, 294–306 (2018)

10. Prasetio, M.D., Hayashida, T., Nishizaki, I., Sekizaki, S.: Deep belief network optimization in speech recognition. In: 2017 International Conference on Sustainable Information Engineering and Technology (SIET), pp. 138–143 (2017)
11. Wei, P., Li, Y., Zhang, Z., Hu, T., Li, Z., Liu, D.: An optimization method for intrusion detection classification model based on deep belief network. *IEEE Access* **7**, 87593–87605 (2019)
12. Zhang, Y., Li, P., Wang, X.: Intrusion detection for IoT based on improved genetic algorithm and deep belief network. *IEEE Access* **7**, 31711–31722 (2019)
13. Huang, G.B., Zhu, Q.Y., Siew, C.K.: Extreme learning machine: a new learning scheme of feedforward neural networks. In: 2004 IEEE International Joint Conference on Neural Networks (2004)
14. Kannoja, S.P., Jaiswal, G.: Ensemble of hybrid CNN-ELM model for image classification. In: 2018 5th International Conference on Signal Processing and Integrated Networks (SPIN), pp. 538–541 (2018)
15. Huang, G.B., Zhu, Q.Y., Siew, C.K.J.N.: Extreme learning machine: theory and applications. *Neurocomputing* **70**, 489–501 (2006)
16. Huang, G.B.J.C.C.: An insight into extreme learning machines random neurons, random features and kernels. *Cogn. Comput.* **6**, 1–15 (2014). <https://doi.org/10.1007/s12559-014-9255-2>
17. Zhang, H., Yin, Y., Zhang, S., Sun, C.: An improved ELM algorithm based on PCA technique. In: Cao, J., Mao, K., Cambria, E., Man, Z., Toh, K.-A. (eds.) *Proceedings of ELM-2014 Volume 2*. PALO, vol. 4, pp. 95–104. Springer, Cham (2015). https://doi.org/10.1007/978-3-319-14066-7_10
18. Peng, Y., Lu, B.L.J.N.: Discriminative extreme learning machine with supervised sparsity preserving for image classification. *Neurocomputing* **261**, 242–252 (2017)
19. Lendasse, A., Man, V.C., Miche, Y., Huang, G.B.: Advances in extreme learning machines (ELM2014). *Neurocomputing* **174**, 1–3 (2016)
20. Yuan, Y., Wang, Y., Cao, F.J.N.: Optimization approximation solution for regression problem based on extreme learning machine. *Neurocomputing* **74**, 2475–2482 (2011)
21. Barra, A., Genovese, G., Sollich, P., Tantari, D.J.P.R.E.: Phase diagram of restricted Boltzmann machines and generalized Hopfield networks with arbitrary priors. *Phys. Rev.* **97**, 022310 (2018)
22. Leng, B., Zhang, X., Yao, M., Xiong, Z.: 3D object classification using deep belief networks. In: Gurrin, C., Hopfgartner, F., Hurst, W., Johansen, H., Lee, H., O'Connor, N. (eds.) *MMM 2014*. LNCS, vol. 8326, pp. 128–139. Springer, Cham (2014). https://doi.org/10.1007/978-3-319-04117-9_12
23. Luo, X., Xu, S.: Forest mapping from hyperspectral image using deep belief network. In: 2019 15th International Conference on Mobile Ad-Hoc and Sensor Networks (MSN), pp. 395–398 (2019)
24. Ma, Y., Bao, C., Xia, BJJOTU: Speaker segmentation based on discriminative deep belief networks. *J. Tsinghua Univ. (Sci. Technol.)* **53**, 804–807 (2013)
25. Netzer, Y., Wang, T., Coates, A., Bissacco, A., Wu, B., Ng, A.: Reading digits in natural images with unsupervised feature learning. In: *NIPS* (2011)



Double Channel Neural Non Invasive Blood Pressure Prediction

Annunziata Paviglianiti¹ , Vincenzo Randazzo¹ ,
Giansalvo Cirrincione^{2,3} , and Eros Pasero¹ 

- ¹ DET - Department of Electronics and Telecommunications,
Politecnico di Torino, Turin, Italy
{annunziata.paviglianiti, vincenzo.randazzo,
eros.pasero}@polito.it
- ² Lab. LTI, Université de Picardie Jules Verne, Amiens, France
giansalvo.cirrincione@u-picardie.fr
- ³ University of South Pacific, Suva, Fiji

Abstract. Cardiovascular Diseases represent the leading cause of deaths in the world. Arterial Blood Pressure (ABP) is an important physiological parameter that should be properly monitored for the purposes of prevention. This work applies the neural network output-error (NNOE) model to ABP forecasting. Three input configurations are proposed based on ECG and PPG for estimating both systolic and diastolic blood pressures. The double channel configuration is the best performing one by means of the mean absolute error w.r.t the corresponding invasive blood pressure signal (IBP); indeed, it is also proven to be compliant with the ANSI/AAMI/ISO 81060-2:2013 regulation for non invasive ABP techniques. Both ECG and PPG correlations to IBP signal are further analyzed using Spearman's correlation coefficient. Despite it suggests PPG is more closely related to ABP, its regression performance is worse than ECG input configuration one. However, this behavior can be explained looking to human biology and ABP computation, which is based on peaks (systoles) and valleys (diastoles) extraction.

Keywords: Arterial blood pressure · Electrocardiogram · Machine learning · Neural networks output error · Photoplethysmogram · System identification

1 Introduction

Cardiovascular diseases (CVDs) represent the most meaningful worldwide health problem. Indeed, they generate a heavy impact on people's life expectancy, on sick's life quality and on the use of health resources. The definition of CVDs includes pathologies affecting both the heart and the blood vessels. The most frequent pathology affects the arterial blood pressure (ABP). Hypertension consists of a persistent increase in blood pressure that acts on the heart. This condition may cause serious complications to the heart and to other organs such as the kidneys, the brain and the eyes. Globally, hypertension kills roughly 8 million people per year [1, 2].

Blood pressure is determined by the set of forces acting on the wall of the vessels: on one hand, the hydrostatic pressure exerted by the blood; on the other side, the

resistance opposed by the vessel wall. The hydrostatic pressure depends on the strength and frequency with which the heart contracts by pumping the oxygenated blood, while the peripheral resistances depend on the extent of the blood flow, the elasticity and the diameter of the vessel wall: the smaller the vessel diameter, the higher the pressure inside them [3]. The complex physiological regulation system involves the autonomic nervous system (the part of the central nervous system responsible for controlling involuntary actions), some hormones and neuromodulators produced by the adrenal gland and the kidney that regulates the volume (total volume of blood) [4]. When one of these regulating elements is not able to respond appropriately to blood pressure variations, arterial hypertension may occur. The measurement of ABP consists of two quantities: the systole (SBP), determined by the peak pressure that is observed following the contraction of the left ventricle and the diastolic pressure (DBP), calculated during the relaxation phase. Due to ageing, diastolic blood pressure tends to decrease, while, at the same time, SBP increases; therefore, it is desirable to prevent the onset of the disease and report values out of the norm to ensure non-reversible damage. American Heart Association (AHA) classifies hypertension into four different stages, which characterize the individual's health status in relation to blood pressure values [5]. This is a great way to easily identify the severity level and find the most appropriate cure in a timely manner. Due to the importance of prevention, and to avoid the degeneration of hypertension, it is necessary to constantly keep both the pressure values under control [6].

Currently, there are two methodologies for ABP measurement. On one hand, an invasive method, based on an intra-arterial blood pressure (IBP) technique, which represents a direct measurement by inserting a cannula needle in a suitable artery. This method is employed in the Intensive Care Unit (ICU) and in the operating theatre and shows continuous patient monitoring of the arterial blood pressure together with its waveform visualization on a display. Unfortunately, this procedure may lead to pains and infections [7]. On the other hand, a non-invasive indirect method based on Korotkoff sounds. The most common device for indirect measurement is the sphygmomanometer, which returns the systolic and diastolic pressure values through the compression and decompression of a cuff, positioned around the patient's arm [8]; however, this procedure may lead to the misclassification of large numbers of patients because the model has inaccuracies. The non-invasive method proposed in this paper is based on the use of artificial neural networks (ANNs), which have been recently applied to medical problems, particularly in the fields of radiology, urology and cardiology. An ANN is a distributed network capable of identifying relationships in input data that are not easily evident with current common analytical techniques; in this sense, artificial neural networks can predict the relationships that exist between inputs and outputs [9]. In cardiology, artificial neural networks have been successfully applied to the diagnosis and treatment of coronary artery disease and myocardial infarction, in electrocardiographic interpretation and in arrhythmia detection and in image analysis in cardiac radiography [10]. Another application, related to blood, is a non-invasive practice for determining hemoglobin concentration [11]. The trained model can be embedded in wearable devices, such as the ECG Watch [12] and the VITAL-ECG [13–15], for providing an anytime, everywhere, unobtrusive blood pressure measurement feature. In the proposed work, the neural network output error (NNOE) model, a

recurrent neural network, has been implemented. NNOE is able to learn the physiological relation that exists between the inputs, the electrocardiographic (ECG) and the photoplethysmographic (PLETH/PPG) signals, and the output (the ABP value) [16]. The former represents the electrical signals in the heart, which are a consequence of cardiac muscle depolarization followed by repolarization during each cardiac cycle (heartbeat) [17]; PPG detects blood volume changes in the microvascular bed of tissue, in an optical way [18]. The rest of the paper is organized as follows: Sect. 2 carries out an analysis about the methodology for ABP estimation: the dataset used for the experiments is presented, the data pre-processing is detailed and the neural network architecture is accurately explained together with the chosen evaluation metrics. Sect. 3 details the experimental results, followed by the conclusions in Sect. 4.

2 Methodology

Figure 1 shows the proposed framework, which is made of four main processing units:

1. Dataset description: data are extracted from MIMIC Database [19], in particular ECG, PPG are chosen as input and the IBP as target.
2. Data pre-processing: all signals are filtered with a moving mean; ECG is also filtered with a high-pass filter to remove disturbances that characterize the signal.
3. Neural Network: NNOE Neural Network Output Error [20], a recurrent neural network used to predict the values of IBP, both systolic and diastolic blood pressure values.
4. Metrics: SSE (sum-squared error) for MLP training and MAE (mean absolute error) to evaluate the quality of the forecasting.

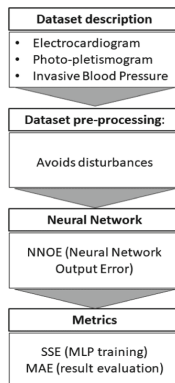


Fig. 1. Methodology of the proposed work

2.1 Dataset Description

The goal of the work is to obtain a neural network trained in a way that, given the ECG and PPG inputs, returns a sufficiently accurate estimation of the ABP signal.

Subsequently, the systolic and diastolic pressure is extracted from the peaks (SBP) and the valleys (DBP) of the ABP predicted signal.

The MIMIC (Multi-parameter Intelligent Monitoring for Intensive Care) Database is a collection of physiological signals from about 100 different patients, registered in the Intensive Care Units of medicine, surgery and cardiology of Boston's Beth Israel Hospital [19, 21]. The recordings include continuous signals and periodic measurements extracted from the patient monitors and clinical data obtained from the records of each patient. The length of the data can vary from 20 to 40 h, and the recordings from the patient monitors are divided into files of 10 min, which can be concatenated to obtain a single continuous signal. Figure 2 shows the extracted signals from the MIMIC Database of a single patient (ECG, PPG and IBP). ECG and PPG represent the input signals, while IBP is the output. In this study, twenty-nine patients are considered. The results are analyzed comparing three different neural network configurations:

- ECG signal as input;
- PPG signal as input;
- ECG/PPG synchronized as an input (double channel).

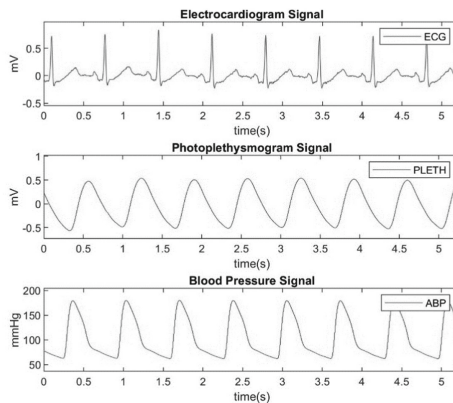


Fig. 2. Input signals (ECG and PPG) and output signal (IBP)

2.2 Data Pre-processing

The ECG signal can mainly contain three types of noise:

- *Baseline wander*: low frequency noise around 0.5–0.6 Hz, which results in an oscillation around the baseline; it may be due to the use of incorrect electrodes (electrode-skin impedance), patient movements or breathing.
- *Power line interference*: around 50–60 Hz due to the electrical network; it can be removed using a notch filter with a cutoff frequency of 50–60 Hz.
- *Electromyography disturbance*: a high frequency noise, above 100 Hz, removed using a low pass filter having an appropriate cutoff frequency.

By analyzing the signals in the database, a high-pass filter is applied to the ECG signal to remove the *baseline wander*. Figure 3 shows the signal improvement after the disturbance removal.

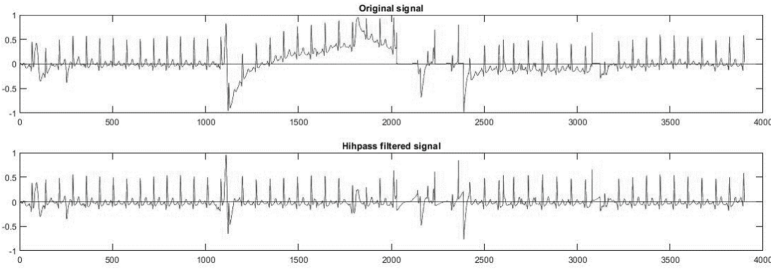


Fig. 3. Baseline wander removal from ECG signal

In addition, a moving mean filter is applied for removing the remaining noise in the three signals (ECG, PPG and ABP). The filter, with a window of 3 samples, represents the simplest form of a low-pass filter.

2.3 Neural Network Architecture – NNOE

There are basically two approaches to forecasting, which depend on the application [20]: the former uses the actual and previous values of the output in the regression vector (e.g. NARX and NARMAX), the latter uses only the previous predictions in the regression vector (e.g. NNOE). Obviously only the second case can be considered for ABP estimation, because the actual blood pressure information is not available.

The goal of the neural network output error (NNOE) is to implement a generic model structure for the identification of nonlinear dynamic systems in a stochastic environment. The basic structure of the neural network is a multilayer perceptron (MLP, [22]), which has the ability to model very complex continuous functional relationships.

Figure 4 shows the workflow of the dynamical system identification.

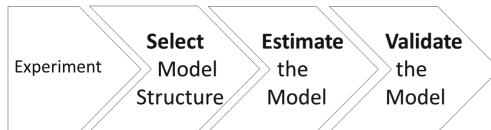


Fig. 4. Dynamical system identification

The experimental phase consists of the dataset collection, called Z^N , which describes the entire system with a sampling frequency:

$$Z^N = \{[u(t), y(t)|_{t=1, \dots, N}]\} \tag{1}$$

$u(t)$ and $y(t)$ represent the control signal and the measured output signal, respectively, where t specifies sampling instant.

For the selection of the model structure, a number of regressors is chosen based on the idea of a linear system identification, determining the network architecture optimization with the given regressors as inputs. For NNOE, the shape of the regression vector is given by:

$$\varphi(t) = [\hat{y}(t - 1|\theta) \dots \hat{y}(t - n|\theta) u(t - d) \dots u(t - d - m)]^T \tag{2}$$

where θ is a vector containing the weights, n is the y-predicted lag, m is the input lag and d the delay to obtain the prediction. The vector of prediction is given by:

$$\hat{y}(t|\theta) = g(\varphi(t), \theta) \tag{3}$$

where g is the function realized by the artificial neural network.

The most common method of validation is the investigation of the residuals (prediction errors) by cross-validation on a test set.

NNOE has a predictor with a feedback through the choice of regressors, which in the neural network terminology means that the networks become recurrent: future network inputs will depend on present and past network outputs (see Fig. 5).

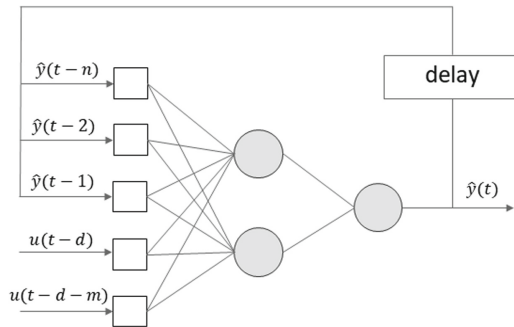


Fig. 5. Structure of NNOE model

2.4 Metrics

Two metrics are considered in this paper: the Sum of Squares Error (SSE) for the MLP training and the Mean Absolute Error (MAE) for the evaluation of the results. Both metrics express how much the network prediction is similar to the desired output (target).

The SSE metric quantifies how a dataset varies around a central number (like the mean). Generally, a lower residual sum of squares indicates that the regression model

can better explain the data while a higher residual sum of squares indicates that the model poorly explains the data [23, 24].

$$SSE = \sum_i^n (y_i - \tilde{y}_i)^2 \quad (4)$$

MAE, instead, measures the average magnitude of the errors in a set of predictions, without considering their direction. It represents the average over the test sample of the absolute differences between prediction and actual observation where all individual differences have equal weight [25].

$$MAE = \frac{1}{n} \sum_i^n |y_i - \tilde{y}_i| \quad (5)$$

3 Results

In the following, three NNOE configurations have been compared with regard to the inputs; as shown in Fig. 6, the first one uses only ECG, the second one only PPG, while the latter both ECG and PPG as inputs.

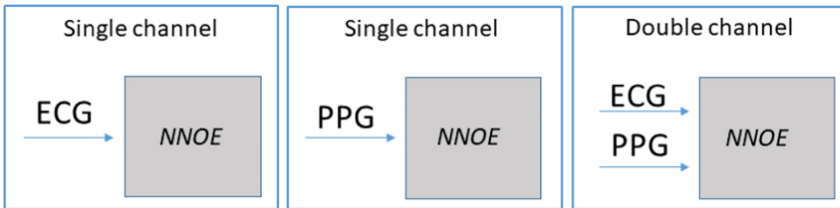


Fig. 6. NNOE input configurations. Single channel: ECG (left) or PPG (center); double channel: ECG and PPG (right).

The network optimal architecture is determined using a *trial-and-error* approach, where different numbers of hidden neurons and regressors were tested w.r.t. MAE. At the end, the chosen neural architecture consists of a multilayer perceptron (MLP) with fifty neurons and three regressors.

Figure 7 and Fig. 8 show the MAE for SBP and DBP, respectively; for each patient (x axis) the MAEs of the three input configurations are grouped:

- the blue bar represents the network error with the electrocardiogram signal as input;
- the orange bar gives the performances with photoplethysmogram as input signal;
- the yellow bar shows the network MAE with the double channel (ECG and PPG).

To evaluate each input configuration quality, the MAEs have been averaged for all patients (excluding the outliers) as shown in Table 1: the double channel configuration has the best performance, with an average value of 2.42 and 3.17 for SBP and DBP, respectively.

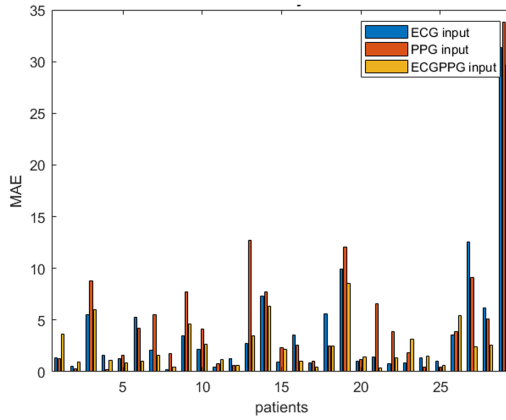


Fig. 7. Mean absolute error for SBP for every patient. (Color figure online)

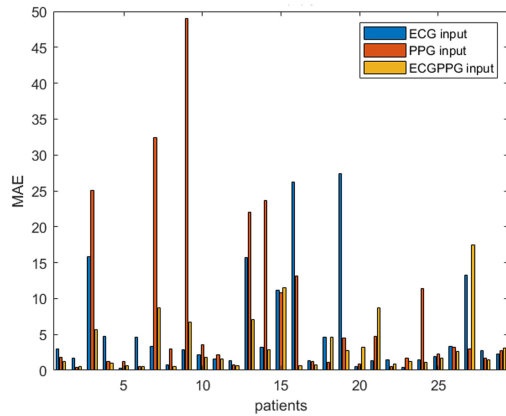


Fig. 8. Mean absolute error for DBP for every patient. (Color figure online)

Table 1. Systolic and diastolic blood pressure MAE (in mmHg) for the three different inputs.

| Inputs | MAE (SBP) | MAE (DBP) |
|---------|-------------|-------------|
| PPG | 3.03 | 5.72 |
| ECG | 3.94 | 5.49 |
| ECG/PPG | 2.42 | 3.17 |

Because the analysis based only on the MAE metric is not sufficient to assess the quality of the proposed method, a deeper comparison between the desired target (IBP) and the NNOE predicted signal is performed. Figure 9 shows the target-output signals plot for each input configuration for patient 2 (which has the lowest MAEs): the

blue solid line represents the desired output (target) while the red dashed line the prediction signals. As can be seen, the double channel (ECG/PPG) is the best performing one.

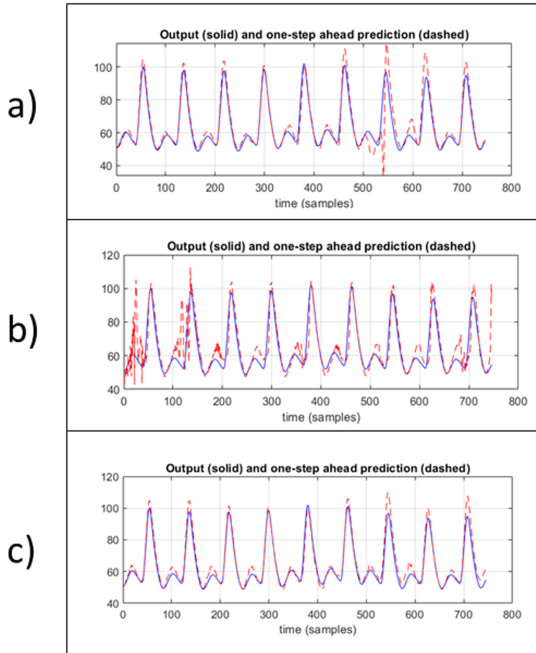


Fig. 9. Output vs. target signals for each input configuration: ECG (a), PPG (b), ECG/PPG (c). (Color figure online)

3.1 Discussion

Some considerations can be drawn just by considering one patient (here patient 2). The Spearman's rank correlation coefficient measures the non linear correlation between two variables. For ECG and ABP, it is equal to 0.17, while for PPG and ABP, it is equal to 0.37. Hence, PPG is more correlated to ABP than ECG. Furthermore, the test SSE for the NNOE model of the relationship between PPG and ABP is equal to 3.19×10^4 , and for the relationship between ECG and ABP is equal to 3.42×10^4 . All these estimates prove PPG is better related to ABP than ECG. So, why does ECG yield a better estimation of ABP? To answer this question, it must be considered that the goal of the algorithm is the accurate evaluation of SBP and DBP. As seen before, the most difficult evaluation is SBP, which depends on the slope of the signal, i.e. its derivative. This first order rate is proportional to the latency time of the phenomenon. ECG is immediately related to ABP, because the pressure depends on the heartbeat. On the contrary, PPG depends on the level of oxygen in blood, which in turn depends on the global cardio-circulatory apparatus: hence it requires a longer time to follow the blood

pressure rate of change. These considerations are also confirmed in Fig. 2, which shows that the PPG signal has a slower rate of change in the peaks than the other two signals. It can be deduced that the PPG inertia prevents from the accurate synchronous detection of the pressure peaks. Concluding, despite the fact that PPG better represents the ABP signal, ECG better estimates the ABP peaks. In the case of two channels, the pros of both ECG and PPG yield the best result.

4 Conclusion

In this paper, a non invasive blood pressure estimation technique is presented. To determine the best input among a single (ECG or PPG) and a double channel (synchronized ECG and PPG) configurations, a comparative analysis is carried out. Because the goal is the ABP forecasting, the NNOE method is used, which is a recurrent neural network, based on MLP, employing only the previous predictions in the regression vector. The algorithm is tested on twenty-nine subjects by always using the IBP as target signal for training. From each predicted signal, peaks and valleys have been extracted to compute the corresponding SBP and DBP values; then, they are compared with ABP ones in terms of MAE as required by ANSI/AAMI/ISO 81060-2:2013 regulation for non invasive ABP techniques. The double channel configuration yields the best results w.r.t. mean absolute error, which results to be, on average, 2.42 mmHg and 3.17 mmHg for SBP and DBP, respectively; in this sense, this configuration is compliant with the legislation because the estimated values are within ± 5 mmHg w.r.t. real invasive measurements. Among the single input configurations, ECG performs better than PPG w.r.t. MAE; on the contrary, the Spearman's coefficients between the ABP and the two inputs suggests an opposite relationship. This behavior is explained by the human biology and the SBP latency time: ECG is immediately related to ABP by means of the heartbeat, while PPG is related to the global cardio-circulatory apparatus, which requires a longer time to follow the blood pressure rate of change. In this sense, PPG inertia prevents from the accurate synchronous detection of the pressure peaks.

The proposed technique can be embedded in wearable portable devices to perform continuous monitoring of vital parameters to prevent the onset of cardiovascular diseases, such as hypertension; indeed, the neural approach can be exploited to fight CVDs and reduce the amount of people, who die for such pathologies.

Future work will deal with an extensive comparison with deep neural networks, e.g. convolution neural networks. It will be also further analyzed the use of the recurrent neural networks, already used in this experiment [26]. Furthermore, a deeper study of specificity and sensitivity w.r.t. the single patient will be conducted; an unsupervised patient clustering will be exploited for tuning supervised neural networks specific for each cluster, such an approach could be useful to improve the generalization capability of the proposed approach.





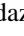
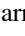

References

1. Kumar, C., Sagar, V., Kumar, M., Kiran, K.: Awareness about hypertension and its modifiable risk factors among adult population in a rural area of Ranchi district of Jharkhand, India. *Int. J. Community Med. Public Heal.* **3**(5), 1069–1073 (2016). <https://doi.org/10.18203/2394-6040.ijcmph20161359>
2. Leung, A.A., et al.: Hypertension Canada's 2017 guidelines for diagnosis, risk assessment, prevention, and treatment of hypertension in adults. *Can. J. Cardiol.* **33**(5), 557–576 (2017). <https://doi.org/10.1016/j.cjca.2017.03.005>
3. Järhult, J., Mellander, S.: Autoregulation of capillary hydrostatic pressure in skeletal muscle during regional arterial hypo- and hypertension. *Acta Physiol. Scand.* **91**(1), 32–41 (1974). <https://doi.org/10.1111/j.1748-1716.1974.tb05654.x>
4. James, P.A., et al.: 2014 evidence-based guideline for the management of high blood pressure in adults: report from the panel members appointed to the Eighth Joint National Committee (JNC 8). *JAMA – J. Am. Med. Assoc.* **311**(5), 507–520 (2014). <https://doi.org/10.1001/jama.2013.284427>
5. Understanding Blood Pressure Readings | American Heart Association. <https://www.heart.org/en/health-topics/high-blood-pressure/understanding-blood-pressure-readings>. Accessed 11 May 2020
6. Torlasco, C., et al.: [BP.03.03] cardiovascular risk and hypertension control in Italy. Data from the 2015 world hypertension day. *J. Hypertens.* **35**, e176–e177 (2017). <https://doi.org/10.1097/01.hjh.0000523480.78727.21>
7. Pellaton, C., et al.: Accuracy testing of a new optical device for noninvasive estimation of systolic and diastolic blood pressure compared to intra-arterial measurements. *Blood Press. Monit.* **25**(2), 105–109 (2020). <https://doi.org/10.1097/MBP.0000000000000421>
8. Pickering, T.G., et al.: Recommendations for blood pressure measurement in humans and experimental animals: part 1: blood pressure measurement in humans - a statement for professionals from the Subcommittee of Professional and Public Education of the American Heart Association Council on high blood pressure research. *Circulation* **111**(5), 697–716 (2005). <https://doi.org/10.1161/01.cir.0000154900.76284.f6>
9. Menolascina, F., et al.: Developing optimal input design strategies in cancer systems biology with applications to microfluidic device engineering. *BMC Bioinformatics* **10**(SUPPL. 12), S4 (2009). <https://doi.org/10.1186/1471-2105-10-S12-S4>
10. Itchhaporia, D., Snow, P.B., Almassy, R.J., Oetgen, W.J.: Artificial neural networks: Current status in cardiovascular medicine. *J. Am. Coll. Cardiol.* **28**(2), 515–521 (1996). [https://doi.org/10.1016/0735-1097\(96\)00174-x](https://doi.org/10.1016/0735-1097(96)00174-x)
11. Bevilacqua, V., et al.: A novel approach to evaluate blood parameters using computer vision techniques. In: 2016 IEEE International Symposium on Medical Measurements and Applications, MeMeA 2016 - Proceedings (2016). <https://doi.org/10.1109/memea.2016.7533760>
12. Randazzo, V., Ferretti, J., Pasero, E.: ECG WATCH: a real time wireless wearable ECG. In: Medical Measurements and Applications, MeMeA 2019 - Symposium Proceedings (2019). <https://doi.org/10.1109/memea.2019.8802210>
13. Randazzo, V., Ferretti, J., Pasero, E.: A wearable smart device to monitor multiple vital parameters—VITAL ECG. *Electronics* **9**(2), 300 (2020). <https://doi.org/10.3390/electronics9020300>
14. Randazzo, V., Pasero, E., Navaretti, S.: VITAL-ECG: a portable wearable hospital. In: 2018 IEEE Sensors Applications Symposium, SAS 2018 - Proceedings, January 2018, pp. 1–6 (2018). <https://doi.org/10.1109/sas.2018.8336776>

15. Paviglianiti, A., Pasero, E.: VITAL-ECG: a de-bias algorithm embedded in a gender-immune device. In: 2020 IEEE International Workshop on Metrology for Industry 4.0 & IoT, pp. 314–318 (2020). <https://doi.org/10.1109/metroind4.0iot48571.2020.9138291>
16. Paviglianiti, A., Randazzo, V., Pasero, E., Vallan, A.: Noninvasive arterial blood pressure estimation using ABPNet and VITAL-ECG. In: I2MTC 2020 - International Instrumentation and Measurement Technology Conference, Proceedings (2020). <https://doi.org/10.1109/i2mtc43012.2020.9129361>
17. Chua, C.P., Heneghan, C.: Continuous blood pressure monitoring using ECG and finger photoplethysmogram. In: Annual International Conference of the IEEE Engineering in Medicine and Biology - Proceedings, pp. 5117–5120 (2006). <https://doi.org/10.1109/iembs.2006.259612>
18. Chua, E.C.P., Redmond, S.J., McDarby, G., Heneghan, C.: Towards using photoplethysmogram amplitude to measure blood pressure during sleep. *Ann. Biomed. Eng.* **38**(3), 945–954 (2010). <https://doi.org/10.1007/s10439-009-9882-z>
19. Moody, G.B., Mark, R.G.: A database to support development and evaluation of intelligent intensive care monitoring. *Comput. Cardiol.* 657–660 (1996). <http://doi.org/10.1109/cic.1996.542622>
20. Nørgaard, M., Ravn, O., Poulsen, N.K., Hansen, L.K.: *Neural Networks for Modelling and Control of Dynamic Systems: A Practitioner's Handbook*. Springer, London (2000)
21. Goldberger, A.L., et al.: PhysioBank, PhysioToolkit, and PhysioNet: components of a new research resource for complex physiologic signals. *Circulation* **101**(23) (2000). <https://doi.org/10.1161/01.cir.101.23.e215>
22. Haykin, S.: *Neural Networks: A Comprehensive Foundation*, 3rd edn., vol. 13, no. 4. Prentice-Hall, Inc., Upper Saddle River ©2007 (1999)
23. Specht, D.F.: A general regression neural network. *IEEE Trans. Neural Netw.* **2**, 568–576 (1991)
24. Rawlings, J.O., Pantula, S.G., Dickey, D.A.: *Applied Regression Analysis: A Research Tool*, 2nd edn. Springer, New York (1998). <https://doi.org/10.1007/b98890>
25. Willmott, C., Matsuura, K.: Advantages of the mean absolute error (MAE) over the root mean square error (RMSE) in assessing average model performance. *Clim. Res.* **30**(1), 79–82 (2005). <https://doi.org/10.3354/cr030079>
26. Paviglianiti, A., Randazzo, V., Cirrincione, G., Pasero, E.: Neural recurrent approaches to noninvasive blood pressure estimation. In: 2020 International Joint Conference on Neural Networks (IJCNN) (2020)



Unsupervised Multi-omic Data Fusion: The Neural Graph Learning Network

Pietro Barbiero¹ , Marta Lovino² , Mattia Siviero² ,
Gabriele Ciravegna³ , Vincenzo Randazzo⁴ , Elisa Ficarra² ,
and Giansalvo Cirrincione^{5,6} 

¹ Department of Computer Science and Technology, Cambridge University,
Cambridge, UK

barbiero@tutanota.com

² DAUIN, Politecnico di Torino, Turin, Italy

³ DINFO, University of Florence, Florence, Italy

⁴ DET, Politecnico di Torino, Turin, Italy

⁵ University of Picardie Jules Verne, Amiens, France

⁶ University of South Pacific, Suva, Fiji

Abstract. In recent years, due to the high availability of omic data, data driven biology has greatly expanded. However, the analysis of different data sources is still an open challenge. A few multi-omic approaches have been proposed in literature. However, none of them take into consideration the intrinsic topology of each omic. In this work, an unsupervised learning method based on a deep neural network is proposed. For each omic, a separate network is trained, whose outputs are fused into a single graph; for this purpose, an innovative loss function has been designed to better represent the data cluster manifolds. A graph adjacency matrix is exploited to determine similarities among samples. With this approach, omics having a different number of features are merged into a unique representation. Quantitative and qualitative analyses show that the proposed method has results comparable to the state of the art. The method has a great intrinsic flexibility as it can be customized according to the complexity of the tasks and it has a lot of room for future improvements compared to more fine-tuned methods, opening the way for future research.

Keywords: mRNA · miRNA · Lung cancer · Multi-omics · SNF · Data fusion · Neural networks · MLP · Unsupervised learning · Competitive learning · Kamada-Kawai graph visualization

1 Introduction

In recent years, the development of high throughput techniques for biological data acquisition, like next generation sequencing for DNA and RNA, has significantly increased the availability of raw data, while decreasing the cost by orders of magnitude. For instance, the cost of sequencing a full human genome has fallen from 100 billion dollars to 1000 dollars in the last 20 years [23]. The availability of this kind of “omic data” (such as genomic, epigenomic and proteomic data) has remarkably speeded up

progress across of biology and medicine. This is also due to emerging cooperative efforts across institutions to build common standardized datasets.

The availability and standardization of data is opening avenues to data driven research, from statistical analysis to supervised and unsupervised machine learning. Supervised learning is limited to the fields where it is possible to obtain accurate labels. One example is the prediction of hard outcomes, like in survival studies [8]. Conversely, unsupervised learning and especially clustering analysis, can lead to the discovery of new classes that may have biological relevance. For instance, clustering of RNA expression data can lead to the discovery of cancer subtypes [12]. Applying machine learning to single-omic data has produced significant results. mRNA expression data has been successfully used for instance to perform clustering on cancer subtypes or classification based on known sub-types [13]. However, it is limited by the incomplete information carried by single omics. Thus, using multi-omic data integration is of fundamental importance in order to get more accurate analyses and predictions. However, the integration is not trivial and represents an open computational problem.

A solution can be attempted by merging all the features from different omics in a single feature space or performing a consensus clustering among the different input datasets. The former leads, however, to further increase the dimensionality, while the latter is limited in accuracy by the fact that the fusion process is not learnt from the topology of the input spaces. Indeed, multi-omic data integration does not consistently perform better than single omic analysis on the best performing omic [24].

The development of new data fusion techniques is an open research problem. Here the proposed method to address it is a deep learning approach called Neural Graph Learning Fusion (NGL-F).

The paper is organized as follows: Sect. 2 introduces the background, in particular concerning the problem of applying machine learning to the study of multi-omic data; Sect. 3 introduces and describes the NGL-F algorithm; Sect. 4 details the dataset and how the experiments have been performed, comparing the results with those obtained through the Similarity Network Fusion(SNF) algorithm [26], a well-established method for multi-omic data fusion; Sect. 5, at last, describes the conclusions and the future works.

One of the main contributions of this work is to propose an original neural approach for modeling multi-omic datasets. Compared to the state-of-the-art algorithms, this approach exploits the manifold topology of the input space. The main advantage of this approach is the possibility to extend the algorithm to the case of omics having a different number of samples; this is not possible using the existing techniques, which are not tailored to the problem at hand.

2 Background

Given the greater availability of omic data, thanks to high throughput techniques, data driven biology has greatly expanded with the help of the creation of open databases and the development and improvement of algorithms.

Cooperative effort has led to large scale projects aiming to provide a unified basis for omic data collection and study. Examples are the Ensembl Genome project and the Human Proteome Project, providing respectively a growing data set for the main eukaryotic genes and an attempt to create a map of the protein based molecular architecture of the cell [15, 20]. Similarly, in the medical field, several public databases combine multiple information like omic data, clinical data and histological images, providing the foundation for data driven medical research. Among such projects, the National Cancer Institute Genomic Data Commons (GDC) is a unified data sharing platform for multiple cancer genomic projects. It provides standards for data collection to minimize inconsistencies due to the procedures used. With more than 80'000 samples it constitutes a valuable resource for data driven medical research [18].

Projects like the aforementioned have opened several avenues for computational studies, from statistical analysis to machine learning. The typical problems to be solved are classification and clustering. Clustering problem are of great interest because they allow the discovery of new classes from data beyond human capability. For example, the discovery of new cancer subtypes plays an important role in designing effective therapies that account for resistances. Clustering is an unsupervised learning approach to partitioning sample sets so as to maximize a similarity score among samples in the same subset and minimize it between different subsets [17]. While different computational approaches have produced significant results even with single omics, [13], any omic taken by itself provides an incomplete picture. For example, greater gene expression values for protein coding genes correlate with higher protein counts for the protein they code for. However, there are regulatory mechanisms that inhibit the translation of mRNA into proteins. One such regulatory element is a small non-coding RNA molecule (miRNA). Thus, combining mRNA and miRNA data should provide a better insight into the cell activity. In general, combining the information from multiple omics is crucial to discover patterns and generate insights at a system level. However, there are significant difficulties to be overcome.

Focusing on multi-omic clustering, different approaches are available. One distinction is between early integration and late integration algorithms: the former unite the features from different omics in a single matrix then perform the clustering; the latter perform clustering separately on the omics then merge the information. Early integration might reveal problematic when the number of samples is much less than the number of features because it increases significantly the dimensionality of the feature space. Late integration is a complex theoretical and computational problem requiring the discovery of new and better algorithms to perform the fusion of the clustering results obtained from each and every omic individually. The difficulties in the use of multi omic data emerge when widely used techniques are benchmarked on real clinical cases as shown not to perform consistently better than single omic data, especially if the comparison is with the best performing omic [24].

One of the state of the art techniques is Similarity Network Fusion (SNF) [26], which starts from the similarity matrices of the original data and creates a consensus through an iterative algorithm: at each step the matrices from individual omics are updated accounting for relevant contributions from the others. This approach has outperformed single-omic studies in some problems such as identification of cancer subtypes and prediction of survival rates when combining mRNA expression, DNA

methylation and miRNA expression. The method is simple and fast however it has limitations like requiring to have the same samples across all omics. Although the proposed NGL-F method has been trained on datasets containing the same samples, in principle this is not a strict requirement. Neural networks offer an ample development space: not only they allow to effectively build weighed graphs through strategies such as competitive learning, which then can be merged by accounting for connection strength, but they have built-in tools such as backpropagation to allow each clustering to take into account the information from other omics by introducing a global loss function with coupling terms. An open problem is the determination of well-performing implementations of those coupling terms.

3 The NGL-F Neural Network

The Neural Graph Learning for data Fusion (NGL-F) is a gradient-based competitive neural network [6], which uncovers topological sample-to-sample relationships using multiple data sources. Given two or more types of data for the same set of samples (e.g., patients), NGL-F learns the mutual relationships among samples taking into account such heterogeneous information simultaneously. The output of NGL-F is a set of graphs. For each data set NGL-F aims at finding a graph where nodes represent cluster centroids while edges represent cluster topological properties. Thereafter, the learned topology described by such graphs is used to create the sample adjacency matrix (S). The information contained in the matrix represents all datasets and it can be used to uncover latent patterns among samples. In this sense, the sample adjacency matrix is used to build a unique graph (sample graph) in which nodes represents samples and the edges are derived from S .

NGL-F is composed of a set of dual multi-layer perceptrons (MLPs), one for each dataset, equipped with a final competitive layer. Weights are estimated by backpropagation [6]. The activation functions are ReLU for the hidden layers and linear for the output competitive units. The input of each network is a dataset represented as a matrix $X_Z \in \mathbb{R}^{d,n}$, where n is the number of samples and d the number of features. Each MLP provides as output a set of vectors $w \in \mathbb{R}^d$ representing cluster centroids for the input data. For each data source taken into consideration, a multi-layer neural network is instantiated. The architecture of each network can be customized according to the complexity of its own data set (see Fig. 1).

The loss function of NGL-F takes into account at the same time the quality of clusters found by each MLP and their underlying topology. The relationships among clusters are modeled using an adjacency matrix E , where $E(i, j)$ represents the number of samples for which w_i and w_j are the two closest centroids. The higher $E(i, j)$, the more their respective clusters are related. The matrix E represents a graph on the neural network, where the nodes are the neurons and the edges are inter-neuron connections. These links represent the topology of the input data. The loss function of each MLP is

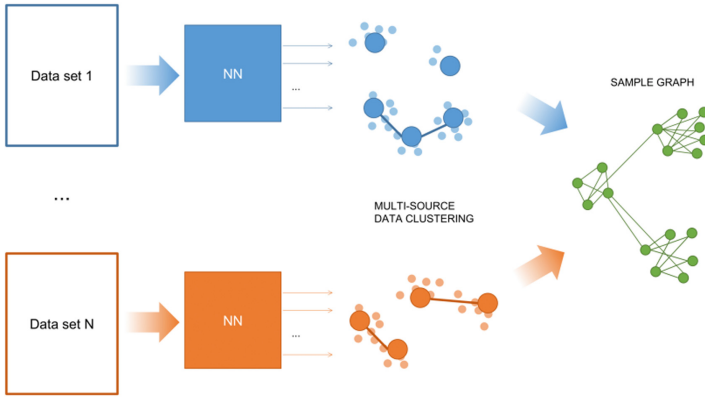


Fig. 1. NGL-F architecture: N datasets are fed in input to NGL-F. For each dataset, a multi-layer perceptron is employed and customized according to dataset complexity. Clustering outputs are at the end combined in order to create a sample graph built from the adjacency matrix S.

composed of four terms taking into account inter and intra-cluster distances, quantization error and parsimony in representing the underlying topology:

$$\mathcal{L} = \frac{\max_k d_{\{intra\}}(C_k)}{\max_{\{i,j\}} d_{\{inter\}}(C_i, C_j)} + Q + \|E\| \tag{1}$$

where $d_{\{intra\}}(C_k)$ is the intra-cluster distance, $d_{\{inter\}}(C_i, C_j)$ the inter-cluster distance, and Q the quantization error. The complete diameter distance is used as an intra-cluster quality index, representing the distance between the two remotest samples belonging to the same cluster:

$$d_{\{intra\}}(C_i) = \max_{x,y \in C_i} d(x,y) \tag{2}$$

The single linkage distance, representing the closest distance between two samples belonging to two different clusters, is used to model inter-cluster distance:

$$d_{\{inter\}}(C_i) = \min_{x \in C_i, y \in C_j} d(x,y) \tag{3}$$

The quantization error is computed as the norm of the distances between cluster centroids (w_i) and cluster points (C_i):

$$Q = \|d(w_i, x)\|_2 \quad \forall x \in C_i \tag{4}$$

The NGL-F loss function is the linear combination of MLPs' losses:

$$\mathcal{L} = \sum_z \mathcal{L}_z \quad (5)$$

Once all networks terminate the training procedure, the resulting clusters are analyzed. For each data set, two samples are considered near to each other in case they belong to the same cluster; far from each other in case they belong to different clusters. A sample adjacency matrix S is then computed as follow:

$$S(i, j) = \sum_{d=1}^n \text{near}_d(i, j) \quad (6)$$

where $\text{near}_d(i, j)$ is a boolean function calculating the proximity of the samples as previously explained and n is the number of data set taken into consideration. This matrix is the result of the fusion process. Its quality can be analyzed and compared to other methods in different ways, as it will be shown in the next section.

4 Experiments

Data are downloaded from the portal of the NIH Genomic Data Commons [22] and are collected in tabular form, resulting in a mRNA and a miRNA transcriptome profiling matrix.

The mRNA matrix consists in raw counts gene expression values [4]. A higher value represents, for protein coding genes, a greater amount of protein produced. This is true unless regulatory mechanisms inhibit the translation of the mRNA.

The miRNA matrix consists in raw counts miRNA values [9]. As miRNA inhibits the translation of mRNA, a higher expression value corresponds to a lower presence of the proteins related to that sequence.

The data was preprocessed as follows:

- For the mRNA matrix, the genes with an expression value equal to zero across all the samples were deleted. Then the normalization was performed through a variance stabilizing transformation [16] and only protein coding genes were selected. This resulted in 17682 genes for which the expression value is reported.
- For the miRNA matrix, the sequences with zero expression value across the samples were deleted and the matrix was normalized through DESeq2 [21]. The final values were obtained as $\log_2(\text{exprValue} + 1)$ [3].

The patients for which either the mRNA or the miRNA data was missing were deleted from the matrices. This resulted in 1248 miRNA and mRNA sequences for which the expression value is reported. This deletion is not a strict requirement in general for NGL-F but it is necessary to compare it with SNF and taken as requirement for this specific implementation.

Data samples come from either healthy or cancerous lung tissue belonging to two types: Lung Adenocarcinoma (LUAD) or Lung Squamous cells Carcinoma (LUSC). The healthy tissue has been taken from non-tumoral tissue samples usually close to the

position of the tumor. Data was acquired from three projects: TCGA-LUAD [25] and CPTAC-3, with samples from adenocarcinoma patients, and TCGA-LUSC, with samples from squamous cells carcinoma patients. Overall this resulted in six different annotations all reported as the name of the project followed by either the “tumoral” or “healthy” annotation.

All the code for the experiments has been implemented in Python 3, relying upon open-source libraries [1, 14]. All the experiments have been run on the same machine: Intel®Core™i7-8750H 6-Core Processor at 2.20 GHz equipped with 8 GB RAM.

The two datasets previously described are fed as input to the NGL-F algorithm. The structure of the networks employed in this paper is reported in Fig. 2. NGL-F is a single neural network that employs a set of dual multi-layer perceptrons, one for each analyzed omic. The use of dual networks is justified given the high-dimensionality of the data sources [2, 6, 7]. The number of features may vary between different omic and it is maintained through the layers, as dual networks are trained on the transposed matrix [6]. In this way, output nodes preserve input dimensionality and can be used as cluster centroids for each input matrix. In this implementation, the only requirement is on the number of samples (1248) that needs to be identical among the omics. As mentioned in Sect. 3, the fusion process consists in the creation of a unique sample adjacency matrix that takes into consideration the information extracted from every omic data. In order to compare the results of the proposed method, the experiment was repeated by using the SNF algorithm [26].

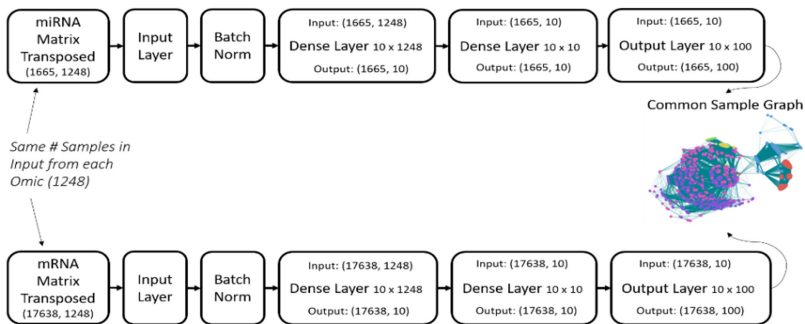


Fig. 2. NGL-F network architecture as used in the experiments. Between brackets the dimensionality of input/output data of each layer are reported. Regarding the matrices, the dimensions are defined as features \times samples since the matrix is transposed. Next to each dense and output layer, instead, is reported the dimensionality of the associated weight matrix. Also, it should be noticed the different dimensionality of the two input sources, miRNA (top) and mRNA (bottom) maintained through the layers.

The adjacency matrix built by both methods are depicted in Fig. 3. Observing the two plots, the results are pretty similar with both methods capable of identifying similarities among data. This is a first important result as it shows the quality of the fusion process carried out by the proposed method when compared to a state-of-the-art algorithm.

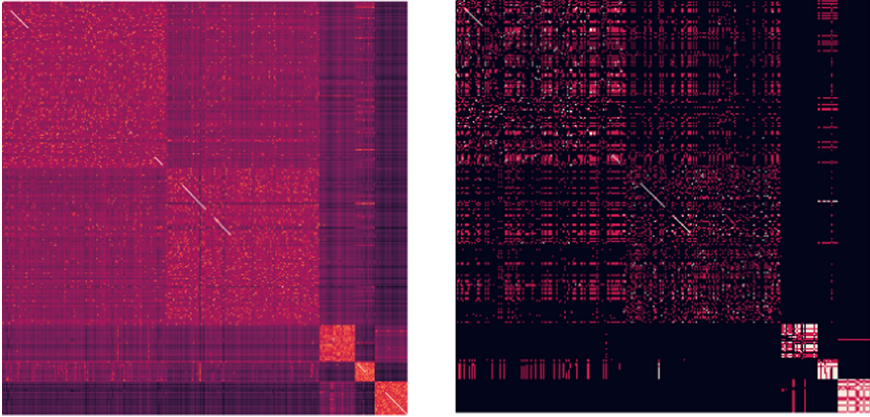


Fig. 3. Adjacency matrix of the sample using (left) SNF and (right) NGL-F algorithms

In order to better analyze this result, it was decided to plot the sample adjacency matrix through the Kamada-Kawai path-length algorithm [19]. This algorithm is a force-directed graph drawing method that can be used to visualize undirected graphs in a two-dimensional space. The main characteristics of this class of algorithms is that edges are displayed in such a way that the number of crossings is the lowest possible. In the two plots of Fig. 4, it is clear that the number of connections found by SNF is redundant: even isolated samples as the LUAD tumoral ones on the top and left edges are connected with many other samples. Conversely, NGL-F better identifies outliers as it can be seen with the tumoral CPTAC3 on the top right corner. However, the sample adjacency matrix plot produced by SNF, better separates LUAD from LUSC tumoral data, while in the plot concerning NGL-F the samples belonging to the two classes are quite confused.

At last, the quality of the proposed algorithm is validated through a comparison of the spectral clustering executed on the two adjacency matrices. In Fig. 5, the quality of the clusters of the grouped samples can be appreciated. More precisely, a harmonic mean of purity and efficiency of the clusters is computed according to the class of the samples belonging to each cluster. Both clustering techniques are capable to precisely identify CPTAC3 healthy samples, grouped in the C5 cluster. Also, CPTAC3 tumor samples are mostly collected in a single cluster, C4; however, the adjacency matrix produced by SNF seems to better separate these samples as the corresponding cluster quality is higher. Instead, samples belonging to LUAD and LUSC (both tumor and healthy) seem to be more difficult to identify. Indeed, for both tissues, tumor samples are collected together in the C0 and C2 clusters for SNF and C0 and C1 clusters for NGL-F. At last, the few LUAD and LUSC healthy samples are mostly placed in C3 cluster for NGL-F, while they are split among all the clusters in the case of SNF.

Summing up, the results produced by the two algorithms are very similar. It is worth pointing out the importance of this result, as NGL-F is a completely new algorithm and it is based on a recent neural theory [6]. Compared to state-of-the-art methods, the neural network structure of NGL-F shows a higher flexibility and can be

easily extended to omics with different number of samples. Future works may include the improvement of the loss function taking account cluster densities [11] and the development of incremental, hierarchical [10], and biclustering [5] versions of NGL-F.

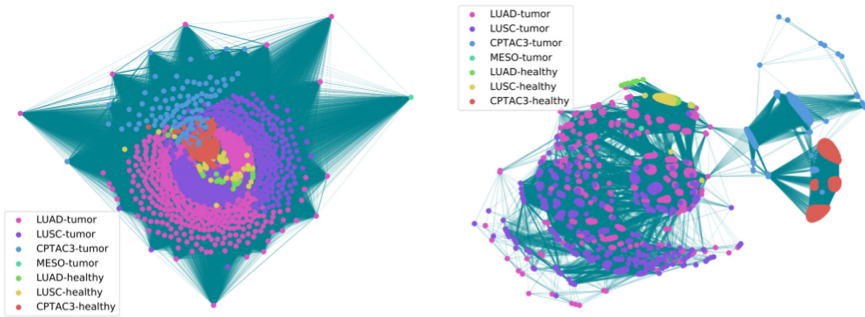


Fig. 4. Graph of the sample adjacency matrix through the Kamada-Kawai path-length algorithm.

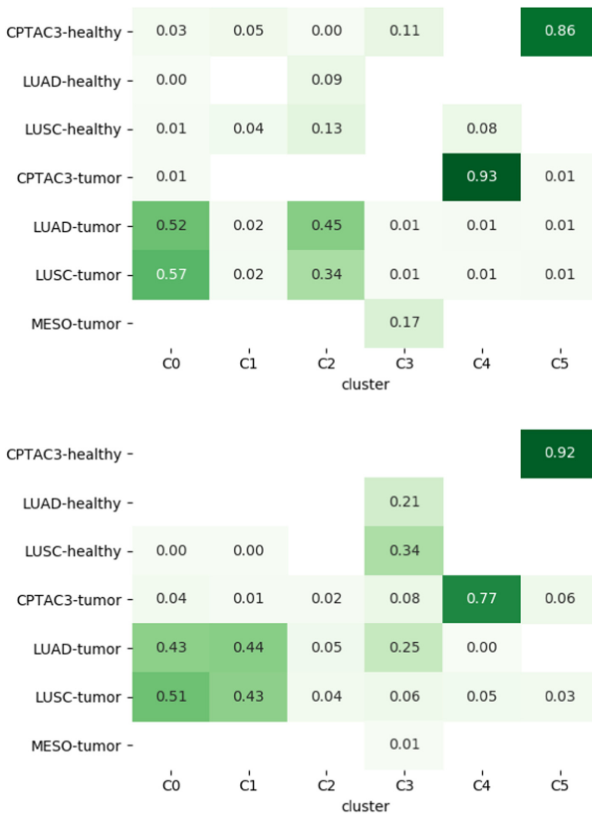


Fig. 5. Harmonic mean of cluster efficiency and purity computed on the spectral clusters, computed on the adjacency matrix produced by SNF (top) and NGL-F (bottom) algorithms

5 Conclusions

Since the interpretation of data coming from multiple data sources is still an open and challenging problem, some multi-omic approaches have been recently proposed. However, these methods do not take into account the intrinsic topology of each omic. Therefore, NGL-F has been designed to tackle this issue. It is an unsupervised deep learning neural network endowed with an original final layer which is competitive, because of the choice of the loss function. Indeed, it takes into account both the quantization and the clustering and the onset of the edges. The training procedure is repeated for all input datasets generating each a network of centroids to which the samples are assigned in a competitive fashion, with criteria for creating and decaying connections between the centroids themselves. The final outcome is a connected graph for each input which is merged to obtain the final graph from which the clusters are derived. Experimental results show its competitiveness with state-of-the-art algorithms; however, they are more flexible in the sense that several kinds of layers can be employed and more than two input sources can be fed simultaneously. Hence, the proposed algorithm is suitable for a wider range of applications.

Future work will deal with the implementation of convolutional layers into the neural architecture and with a deeper analysis of the loss function. A shallow version of the network, which underlines both the competitive aspect of the approach and the topology of the data by the edges, is under study. It will be applied not only to few omics and also to non-biological data.

References

1. Abadi, M., et al.: TensorFlow: a system for large-scale machine learning. In: 12th USENIX Symposium on Operating Systems Design and Implementation (OSDI 2016), pp. 265–283 (2016)
2. Altman, N., Krzywinski, M.: The curse (s) of dimensionality. *Nat. Methods* **15**(6), 399–400 (2018)
3. Anders, S., Huber, W.: Differential expression of RNA-Seq data at the gene level – the DESeq package. European Molecular Biology Laboratory (EMBL), Heidelberg, Germany, 10, f1000research (2012)
4. Anders, S., Pyl, P.T., Huber, W.: HTSeq—a Python framework to work with high-throughput sequencing data. *Bioinformatics* **31**(2), 166–169 (2015)
5. Barbiero, P., Bertotti, A., Ciravegna, G., Cirrincione, G., Cirrincione, M., Piccolo, E.: Neural biclustering in gene expression analysis. In: International Conference on Computational Science and Computational Intelligence (2017)
6. Barbiero, P., Ciravegna, G., Randazzo, V., Cirrincione, G.: Topological gradient-based competitive learning (2020)
7. Barbiero, P., Squillero, G., Tonda, A.: Modeling generalization in machine learning: a methodological and computational study (2020)
8. Chaudhary, K., Poirion, O.B., Lu, L., Garmire, L.X.: Deep learning-based multi-omics integration robustly predicts survival in liver cancer. *Clin. Cancer Res.* **24**(6), 1248–1259 (2018)

9. Chu, A., et al.: Large-scale profiling of microRNAs for the cancer genome atlas. *Nucleic Acids Res.* **44**(1), e3 (2016)
10. Cirrincione, G., Ciravegna, G., Barbiero, P., Randazzo, V., Pasero, E.: The GH-EXIN neural network for hierarchical clustering. *Neural Networks* **121**, 57–73 (2020)
11. Ester, M., Kriegel, H.P., Sander, J., Xu, X., et al.: A density-based algorithm for discovering clusters in large spatial databases with noise. In: *KDD*, vol. 96, pp. 226–231 (1996)
12. Gao, S., et al.: Unsupervised clustering reveals new prostate cancer subtypes. *Transl. Cancer Res.* **6**(3), 561–572 (2017)
13. Golub, T.R., et al.: Molecular classification of cancer: class discovery and class prediction by gene expression monitoring. *Science* **286**(5439), 531–537 (1999)
14. Hagberg, A., Swart, P., Chult, D.S.: Exploring network structure, dynamics, and function using NetworkX. Technical report, Los Alamos National Lab. (LANL), LosAlamos, NM (United States) (2008)
15. Hubbard, T., et al.: The ensembl genome database project. *Nucleic Acids Res.* **30**(1), 38–41 (2002)
16. Huber, W., Von Heydebreck, A., Sülthmann, H., Poustka, A., Vingron, M.: Variance stabilization applied to microarray data calibration and to the quantification of differential expression. *Bioinformatics* **18**(suppl1), S96–S104 (2002)
17. Jain, A.K., Murty, M.N., Flynn, P.J.: Data clustering: a review. *ACM Comput. Surv. (CSUR)* **31**(3), 264–323 (1999)
18. Jensen, M.A., Ferretti, V., Grossman, R.L., Staudt, L.M.: The NCI genomic data commons as an engine for precision medicine. *Blood J. Am. Soc. Hematol.* **130**(4), 453–459 (2017)
19. Kamada, T., Kawai, S.: An algorithm for drawing general undirected graphs. *Inf. Process. Lett.* **31**(1), 7–15 (1989). [https://doi.org/10.1016/0020-0190\(89\)90102-6](https://doi.org/10.1016/0020-0190(89)90102-6). <http://www.sciencedirect.com/science/article/pii/0020019089901026>
20. Legrain, P., et al.: The human proteome project: current state and future direction. *Mol. Cell. Proteomics* **10**(7) (2011)
21. Love, M.I., Huber, W., Anders, S.: Moderated estimation of fold change and dispersion for RNA-Seq data with DESeq2. *Genome Biol.* **15**(12), 550 (2014). <https://doi.org/10.1186/s13059-014-0550-8>
22. National Cancer Institute: GDC data portal. <https://portal.gdc.cancer.gov/>. Accessed 14 June 2020
23. National Human Genome Research Institute: The cost of sequencing a human genome. <https://www.genome.gov/about-genomics/fact-sheets/Sequencing-Human-Genome-cost>. Accessed 14 June 2020
24. Rappoport, N., Shamir, R.: Multi-omic and multi-view clustering algorithms: review and cancer benchmark. *Nucleic Acids Res.* **46**(20), 10546–10562 (2018)
25. Tomczak, K., Czerwinska, P., Wiznerowicz, M.: The cancer genome atlas (TCGA): an immeasurable source of knowledge. *Contemp. Oncol.* **19**(1A), A68 (2015)
26. Wang, B., et al.: Similarity network fusion for aggregating data types on a genomic scale. *Nat. Methods* **11**(3), 333 (2014)



Random Occlusion Recovery with Noise Channel for Person Re-identification

Kun Zhang^{1(✉)}, Di Wu¹, Changan Yuan², Xiao Qin³, Hongjie Wu^{4,5}, Xingming Zhao^{6,7}, Lijun Zhang⁸, Yuchuan Du⁹, and Hanli Wang¹⁰

- ¹ Institute of Machine Learning and Systems Biology, School of Electronics and Information Engineering, Tongji University, Shanghai, China
1830806@tongji.edu.cn
- ² Guangxi Academy of Science, Nanning 530025, China
- ³ School of Computer and Information Engineering, Nanning Normal University, Nanning 530299, China
- ⁴ School of Computer Science and Technology, Soochow University, Suzhou 215006, China
- ⁵ School of Electronic and Information Engineering, Suzhou University of Science and Technology, Suzhou 215009, China
- ⁶ Institute of Science and Technology for Brain Inspired Intelligence (ISTBI), Fudan University, Shanghai 200433, China
- ⁷ Key Laboratory of Computational Neuroscience and Brain-Inspired Intelligence, Ministry of Education, Shanghai, China
- ⁸ Collaborative Innovation Center of Intelligent New Energy Vehicle and School of Automotive Studies, Tongji University, Shanghai 201804, China
- ⁹ The Key Laboratory of Road and Traffic Engineering of the Ministry of Education, Department of Transportation Engineering, Tongji University, Shanghai 201804, China
- ¹⁰ Department of Computer Science and Technology, the Key Laboratory of Embedded System and Service Computing, and Shanghai Institute of Intelligent Science and Technology, Tongji University, Shanghai 200092, China

Abstract. Person re-identification, as the basic task of a multi-camera surveillance system, plays an important role in a variety of surveillance applications. However, the current mainstream person re-identification model based on deep learning requires a lot of labeled data, which takes a lot of time and manpower. In this study, we proposed a person re-identification method based on random occlusion recovery with noise channel. We add random occlusion blocks to the original image, use the GAN model for repair, and use the repaired image to expand the original training set. After that, the generated image is adjusted through the noise channel. Finally, we use the enhanced data set to train the baseline model. Our model achieves the state-of-the-art on Market-1501 dataset, proving that the method is effective.

Keywords: Generative adversarial network · Label noise · Person re-identification

1 Introduction

Person re-identification (ReID) refers to the process of matching the similarity of all people in the images taken by other candidate cameras given a person's captured image under a certain camera. The given camera and candidate camera usually have no overlapping area of view angle. A person re-identification system is generally divided into two parts: Person tracking and image capture, and Person identification and retrieval. Detection and recognition are regarded as two independent problems in computer vision research, so most of the research work on Person re-recognition is focused on the Person recognition and retrieval part.

At present, there are still many difficulties in the field of Person re-identification. First, because the database of Person recognition comes from ordinary surveillance cameras, the image resolution is low, and the Person images cut from it are often very blurred. Taking Market1501 of Tsinghua University as an example [1], the resolution of the image is only 64×128 . In addition, for the same Person target, factors such as angle of view, scene, lighting, scale, posture and occlusion at the time of shooting will lead to different cameras. The images below are quite different. For example, different angles of view will make the angle formed by the optical axis of the Person and the camera different, making the picture in the image different; and occlusion will cause some important features to be unrecognizable. In extreme cases, the image of the same person under two cameras is very different, but the images of two different people are very similar.

Besides, the available public ReID datasets are limited in size, especially the number of images per identity. For example, for large ReID datasets like CUHK03 [2], Market-1501 and DukeMTMC-ReID [3], the average number of images per identity is only 9.6, 17.2 and 23.5, respectively. Recently, several GAN based data enhancement methods have been introduced to alleviate this problem [4, 5]. However, because the appearance and background of the generated samples are far from their original identity, most of the above methods must assign new labels to the generated samples. In addition, if some methods are adopted to label the generated image, such as random selection of labels, label noise will inevitably be introduced, which will affect the effect of the model.

Therefore, the number of images per identity cannot be increased. In order to solve the above problems, our purpose is to generate enough similar but not identical samples with the original image, and add its original label to generated images. Finally, we introduce the Noise Label model, so that the original data and the generated data can be used simultaneously in training process.

2 Related Work

2.1 GAN-Based ReID Model

In recent years, in order to solve the scarcity of data, some people have tried to use the GAN model to expand the size of the person-ReID data set. Zheng et al. [4] proposed a generative adversarial network to generate unlabeled samples of the ReID dataset. They

introduced an outlier label smoothing regularization (LSRO) method to label the generated samples. To reduce the domain gap between different data sets, Wei et al. [6] introduced a transfer generation adversarial network to alleviate the field gap by transferring people in the data set to the B data set. The transferred Persons from A maintain the similar background, lighting and other styles as dataset B. A camera style adaptive model is proposed, which converts the image style captured by one camera to another camera [5]. They use label smoothing regularization (LSR) method to reduce the influence of noise introduced by pattern transfer samples. In [8], the normalized GAN model was introduced to reduce the impact of pose changes.

2.2 Label Noise Model

For the most common classification methods, such as logistic regression and support vector machines, robust noise variables are proposed [8, 9]. Then a general unbiased estimation method for binary classification with noise tags is proposed by Natarajan et al. [8]. They developed an agency cost function that can be represented by the weighted sum of the original cost functions, and provided an asymptotic bound on performance. Grandvalet and Bengio [11] solved the problem of label loss, which can be regarded as an extreme case of label data noise. They proposed a semi-supervised algorithm that encourages classifiers to predict label-free labels with high confidence by adding regularization terms to the cost function. Despite the great success of deep learning, few studies have explicitly attempted to solve the neural network (NN) training problem using unreliable label data [12, 13]. Besides, Inspired by the improvements shown in the noise labeling neural network [14], we can directly apply NLNN to the combined set of existing clean data and noise self-labeling data (Fig. 1).

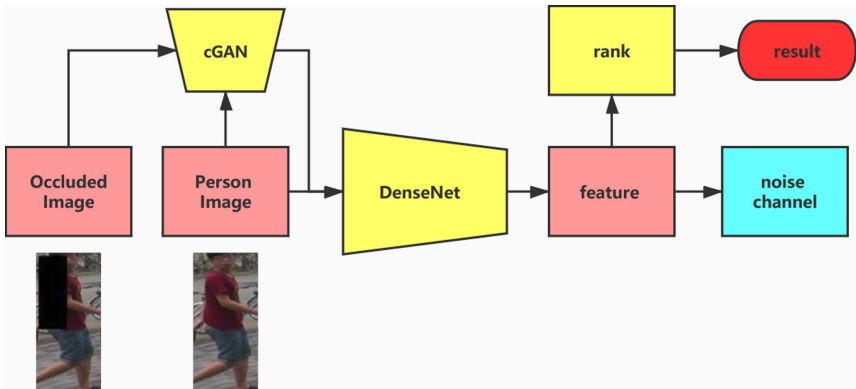


Fig. 1. The network architecture

3 The Proposed Method

3.1 Random Occlusion

For each target image, we randomly add a rectangular occlusion block on it, and randomly select the region length and width from 2 cm to 5 cm. In order to make the rectangle block the Person image as much as possible, we divide the image into three columns from left to right, and randomly select the center of the matrix in the middle column. The pixel values of R, G and B channels of the occlusion block are 0,255 and the average values on the dataset. On the Market-1501 dataset, the pixel average values are 89.3,102.5 and 98.7.

3.2 GAN Model

The generative adversary network (GAN) [14] adopts the idea of two person zero-sum game, which consists of two parts: generative network and discriminative network. GAN is used to learn the original data set and generate the image, while the discriminator network is used to determine whether the input image is real (original data set) or forged (generated by the generator network). Two networks are trained at the same time. The goal is to make the discrimination model unable to distinguish the authenticity of the generated image. In this paper, we used the conditional GAN [15], the mathematical expression of the optimization objective is as follows:

$$\min_{\theta_g} \max_{\theta_d} [\mathbb{E}_{x,y} \log D_{\theta_d}(x, y) + \mathbb{E}_{x,z} \log(1 - D_{\theta_d}(G_{\theta_g}(x, z)))]$$

Where x is the occluded image, y is the target image, D and G represent the discriminator network and generator network.

3.3 Noise Channel

For the generated image, we can not directly think that the original label is the true label. For the observed noise label z , we need to learn the transition probability before the noise label and the true label:

$$\theta(i, j) = p(z = j | y = i)$$

Using a similar idea from Bekker and Goldberger (2016), for a multi-classification network with softmax output,

$$p(y = i | x; w) = \frac{\exp(u_i^T h)}{\sum_{j=1}^k \exp(u_j^T h)}$$

Where k is the number of classes, x is the input feature, y is the true label, and w is the network weights.

For all training images, we think that the label of the original data is clean ($z \in C$), and the label of the generated data is noisy ($z \in N$). For the observation label z , we define the following distribution:

$$p(z = j|x, w, \theta) = \begin{cases} \sum_{i=1}^k p(z = j|y = i; \theta)p(y = i|x; w) & \text{if } z \in N \\ p(y = j|x; w) & \text{if } z \in C \text{ i.e. } z = y \end{cases}$$

Given the distribution, we need to use the EM algorithm to solve the hidden parameters. In E-step, fixed parameters θ, w predicting the true distribution probability c of each noise label z .

$$c_{ii} = p(y_t = i|x_t, z_t; w, \theta) = \frac{p(z_t|y_t = i, \theta)p(y_t = i|x_t; w)}{\sum_j p(z_t|y_t = j, \theta)p(y_t = j|x_t; w)} \quad \text{for } z_t \in N$$

In M-step, updating parameters θ :

$$\theta(i, j) = \frac{\sum_t c_{ti} 1_{z_t=j}}{\sum_t c_{ti}} \quad i, j \in \{1, \dots, k\}, z_t \in N$$

As describe above, the target function can be expressed as:

$$S(w) = \sum_{z_t \in C} \log p(z_t|x_t, w) + \sum_{z_t \in N} \sum_{i=1}^k \log p(y_t = i|x_t; w)$$

4 Experiments and Results

In this section, we present the experiment details to testify the effectiveness of the proposed method. The datasets and training details as well as the comparison results are also discussed.

4.1 Datasets

The Market-1501 dataset was collected by the team of Tsinghua University. The data comes from 6 cameras (5 high-resolution cameras and 1 low-resolution camera). The data set contains a total of 32668 images from 1501 pedestrians. The images of each pedestrian are from at least two cameras. The data set is randomly divided into three parts: train set, test set and query set. The train set contains 12936 images from 751 pedestrians, the test set contains 19732 images from 750 pedestrians, and the query set contains 3368 images from 750 pedestrians.

4.2 Implementation Details

We select the imagenet pre-trained DenseNet as CNN base model. The last FC layer are modified with 751 units. We set the dropout probability to 0.5. We use the stochastic gradient descent as the optimizer to update the network. The momentum and weight decay are set to 0.9 and $5e-4$, respectively. We set initial learning rate α to 0.01 and decrease it by dividing 0.1 after each 30 epochs. The total training epoch and mini-batch size are set to 60 and 32, respectively.

For the GAN model, we use the U-Net [16] as the generator network, Similar to the work of [17], we apply a five layers convolutional network that with PReLU and batch normalization operations for the discriminator. All the occluded and original images are resized into 256×256 pixels. The Adam is used to optimize the network. We set the momentum and initial learning rate to 0.5 and 0.0002, respectively.

4.3 Results

We compare our approach with the following approaches: BoW + KISSME [1], SL [18], DNS [19], Gated Siamese [20], Deep Transfer [21], CAN [22], CNN Embedding [23], SVD-Net [24], HydraPlus-Net [25], CNN+DCGAN [4], TriNet [26], CamStyle [27]. The experimental comparison results are shown in this section below (Table 1).

Table 1. Results (mAP, Rank1 and Rank5 matching accuracy in %) on the Market-1501

| Method | Single query | | | |
|--------------------|--------------|--------------|--------------|--------------|
| | mAP | Rank-1 | Rank-5 | Rank-10 |
| BoW + KISSME [1] | 20.76 | 44.42 | – | – |
| SL [18] | 26.35 | 51.90 | – | – |
| DNS [19] | 35.68 | 61.02 | – | – |
| Gated Siamese [20] | 39.55 | 65.88 | – | – |
| Deep Transfer [21] | 65.50 | 83.70 | – | – |
| CAN [22] | 35.90 | 60.30 | – | – |
| CNN Embedding [23] | 59.87 | 79.51 | 90.91 | – |
| SVD-Net [24] | 62.10 | 82.3 | 92.3 | 95.2 |
| HydraPlus-Net [25] | – | 76.9 | 91.30 | 94.5 |
| CNN+DCGAN [4] | 56.23 | 78.06 | – | – |
| TriNet [26] | 81.07 | 86.67 | 93.38 | – |
| CamStyle [27] | 71.55 | 89.49 | – | – |
| DesNet-Base | 73.58 | 89.67 | 96.61 | 98.16 |
| Ours | 80.86 | 91.48 | 97.45 | 98.52 |
| Ours+rerank | 90.42 | 93.35 | 96.87 | 97.92 |

5 Conclusions

In this study, a GAN-based data augmentation with noise channel method was proposed for person ReID. We generated images from occluded images and process label with noise channel. The original images and the generated images composed of the training set to train the baseline model. Our method enhancing the discriminative and robust of the feature representations. the experiment on Market-1501 dataset demonstrated that achieved state-of-the-art performance.

Acknowledgements. This work was supported by the grant of National Key R&D Program of China (No. 2018AAA0100100) and partly supported by National Natural Science Foundation of China (Grant nos. 61861146002, 61732012, 61932008, 61532008, 61672382, 61772357, and 61672203) and China Postdoctoral Science Foundation (Grant no. 2017M611619) and supported by “BAGUI Scholar” Program and the Scientific & Technological Base and Talent Special Program, GuiKe AD18126015 of the Guangxi Zhuang Autonomous Region of China and supported by Shanghai Municipal Science and Technology Major Project (No. 2018SHZDZX01), LCNBI and ZJLab.

References

1. Zheng, L., Shen, L., Tian, L., Wang, S., Wang, J., Tian, Q.: Scalable person re-identification: a benchmark. In: IEEE International Conference on Computer Vision, pp. 1116–1124 (2016)
2. Li, W., Zhao, R., Xiao, T., Wang, X.: DeepReID: deep filter pairing neural network for person re-identification. In: Computer Vision and Pattern Recognition, pp. 152–159 (2014)
3. Ristani, E., Solera, F., Zou, R., Cucchiara, R., Tomasi, C.: Performance measures and a data set for multi-target, multi-camera tracking. In: Hua, G., Jégou, H. (eds.) ECCV 2016. LNCS, vol. 9914, pp. 17–35. Springer, Cham (2016). https://doi.org/10.1007/978-3-319-48881-3_2
4. Zheng, Z., Zheng, L., Yang, Y.: Unlabeled samples generated by GAN improve the person re-identification baseline in vitro. In: IEEE International Conference on Computer Vision, pp. 3774–3782 (2017)
5. Zhong, Z., Zheng, L., Zheng, Z., Li, S., Yang, Y.: Camera style adaptation for person re-identification. In: Computer Vision and Pattern Recognition, pp. 5157–5166 (2018)
6. Wei, L., Zhang, S., Gao, W., Tian, Q.: Person transfer GAN to bridge domain gap for person re-identification. In: Computer Vision and Pattern Recognition, pp. 79–88 (2018)
7. Qian, X., Fu, Y., Wang, W., Xiang, T., Wu, Y., Jiang, Y., et al.: Pose-normalized image generation for person re-identification. arXiv: Computer Vision and Pattern Recognition (2017)
8. Frénay, B., Verleysen, M.: Classification in the presence of label noise: a survey. IEEE Trans. Neural Netw. Learn. Syst. **25**(5), 845–869 (2014)
9. Bootkrajang, J., Kabán, A.: Label-noise robust logistic regression and its applications. In: Flach, P.A., De Bie, T., Cristianini, N. (eds.) ECML PKDD 2012. LNCS (LNAI), vol. 7523, pp. 143–158. Springer, Heidelberg (2012). https://doi.org/10.1007/978-3-642-33460-3_15
10. Grandvalet, Y., Bengio, Y.: Semi-supervised learning by entropy minimization. In: Advances in Neural Information Processing Systems (NIPS) (2005)
11. Minh, V., Hinton, G.: Learning to label aerial images from noisy data. In: International Conference on Machine Learning (ICML) (2012)

12. Chen, T., et al.: ABD-NET: attentive but diverse person re-identification. In: Proceedings of the IEEE International Conference on Computer Vision, pp. 8351–8361 (2019)
13. Quan, R., Dong, X., Wu, Y., Zhu, L., Yang, Y.: Auto-ReID: searching for a part-aware ConvNet for person re-identification. arXiv preprint [arXiv:1903.09776](https://arxiv.org/abs/1903.09776) (2019)
14. Guo, J., Yuan, Y., Huang, L., Zhang, C., Yao, J.-G., Han, K.: Beyond human parts: dual part-aligned representations for person re-identification. In: Proceedings of the IEEE International Conference on Computer Vision, pp. 3642–3651 (2019)
15. Chen, B., Deng, W., Hu, J.: Mixed high-order attention network for person re-identification. In: Proceedings of the IEEE International Conference on Computer Vision, pp. 371–381 (2019)
16. Chang, X., Hospedales, T.M., Xiang, T.: Multi-level factorisation net for person re-identification. In: Proceedings of the IEEE Conference on Computer Vision and Pattern Recognition, pp. 2109–2118 (2018)
17. Wu, D., et al.: Omnidirectional feature learning for person re-identification. *IEEE Access* **7**, 28402–28411 (2019)
18. Wu, Y., Zhang, K., Wu, D., et al.: Person re-identification by multi-scale feature representation learning with random batch feature mask. *IEEE Trans. Cogn. Dev. Syst.* (2020). <https://doi.org/10.1109/tcds.2020.3003674>
19. Wan, X.F., Huang, D.S., Xu, H.: An efficient local Chan-Vese model for image segmentation. *Pattern Recogn.* **43**(3), 603–618 (2010)
20. Zhao, Z.Q., Glotin, H., Xie, Z., Gao, J., Wu, X.: Cooperative sparse representation in two opposite directions for semi supervised image annotation. *IEEE Trans. Image Process.* **21**(9), 4218–4231 (2012)
21. Li, B., Huang, D.S.: Locally linear discriminant embedding: an efficient method for face recognition. *Pattern Recogn.* **41**(12), 3813–3821 (2008)
22. Zhao, Z.Q., Glotin, H., Xie, Z., Gao, J., Wu, X.: Cooperative sparse representation in two opposite directions for semi-supervised image annotation. *IEEE Trans. Image Process. (TIP)* **21**(9), 4218–4231 (2012)
23. Huang, D.S.: *Systematic Theory of Neural Networks for Pattern Recognition* (in Chinese). Publishing House of Electronic Industry of China, Beijing (1996)
24. Huang, D.S., Du, J.-X.: A constructive hybrid structure optimization methodology for radial basis probabilistic neural networks. *IEEE Trans. Neural Netw.* **19**(12), 2099–2115 (2008)
25. Huang, D.S.: Radial basis probabilistic neural networks: model and application. *Int. J. Pattern Recogn. Artif. Intell.* **13**(7), 1083–1101 (1999)
26. Wang, X.-F., Huang, D.S.: A novel density-based clustering framework by using level set method. *IEEE Trans. Knowl. Data Eng.* **21**(11), 1515–1531 (2009)
27. Shang, L., Huang, D.S., Du, J.-X., Zheng, C.-H.: Palmprint recognition using Fast ICA algorithm and radial basis probabilistic neural network. *Neurocomputing* **69**(13–15), 1782–1786 (2006)
28. Zhao, Z.-Q., Huang, D.S., Sun, B.-Y.: Human face recognition based on multiple features using neural networks committee. *Pattern Recogn. Lett.* **25**(12), 1351–1358 (2004)
29. Huang, D.S., Ip, H.H.S., Chi, Z.-R.: A neural root finder of polynomials based on root moments. *Neural Comput.* **16**(8), 1721–1762 (2004)
30. Huang, D.S.: A constructive approach for finding arbitrary roots of polynomials by neural networks. *IEEE Trans. Neural Netw.* **15**(2), 477–491 (2004)
31. Huang, D.S., Chi, Z., Siu, W.-C.: A case study for constrained learning neural root finders. *Appl. Math. Comput.* **165**(3), 699–718 (2005)
32. Huang, D.S., Ip, H.H.S., Law, K.C.K., Chi, Z.: Zeroing polynomials using modified constrained neural network approach. *IEEE Trans. Neural Netw.* **16**(3), 721–732 (2005)

33. Huang, D.S., Ip, H.H.S., Law, K.C.K., Chi, Z., Wong, H.S.: A new partitioning neural network model for recursively finding arbitrary roots of higher order arbitrary polynomials. *Appl. Math. Comput.* **162**(3), 1183–1200 (2005)
34. Huang, D.S., Zhao, W.-B.: Determining the centers of radial basis probabilistic neural networks by recursive orthogonal least square algorithms. *Appl. Math. Comput.* **162**(1), 461–473 (2005)
35. Huang, D.S., Ip, H.H.S., Chi, Z., Wong, H.S.: Dilation method for finding close roots of polynomials based on constrained learning neural networks. *Phys. Lett. A* **309**(5–6), 443–451 (2003)
36. Huang, D.S.: Application of generalized radial basis function networks to recognition of radar targets. *Int. J. Pattern Recogn. Artif. Intell.* **13**(6), 945–962 (1999)
37. Huang, D.S.: The local minima free condition of feedforward neural networks for outer-supervised learning. *IEEE Trans. Syst. Man Cybern.* **28B**(3), 477–480 (1998)
38. Huang, D.S.: The united adaptive learning algorithm for the link weights and the shape parameters in RBFN for pattern recognition. *Int. J. Pattern Recogn. Artif. Intell.* **11**(6), 873–888 (1997)
39. Huang, D.S., Ma, S.D.: Linear and nonlinear feedforward neural network classifiers: a comprehensive understanding. *J. Intell. Syst.* **9**(1), 1–38 (1999)



Detection of Abnormal Behavior Based on the Scene of Anti-photographing

Wei Zhang and Fan Lin^(✉)

School of Informatics, Xiamen University, Xiamen 361005, China
iamafan@xmu.edu.cn

Abstract. In the era of increasingly prominent information security issues, Anti-Photographing is a subject worthy of study, which is based on the problem of camera equipment detection and camera behavior analysis. Although the current target detection algorithm is relatively mature, there are still problems in the accuracy of target detection in complex scenes. Resnet50 is a neural network framework with high learning efficiency based on the residual module, which is widely used in object recognition tasks. In this paper, we propose a new detection framework, which is based on the Gaussian skin color model combined with the Openpose method to improve the accuracy of hand region extraction. At the same time, the mobile phone recognition model based on the Resnet50 network is used to identify whether the hand holds a mobile phone. At last, the gestures of the person's hand and face are combined to complete the evaluation of whether there is a photographing behavior. The results of testing experiments on the photographing behavior in the video frame show that the framework has a good detection effect on photographing behavior.

Keywords: Gauss skin color model · Openpose · Hand region extracting
Resnet50 · Object detection · Behavior analyzing

1 Introduction

With the popularization and development of smartphones, information storage using photos as a medium has become extremely common. At the same time, the use of photos as an information carrier for leaks is increasing. In the confidentiality and information management work of national defense leaking units and confidential departments, key industries, and enterprise units, screen photo leaks have become a severely affected area for the control of leaks. Tracing back to the source is that on some important occasions, there is no monitoring and control of the photographing behavior. It can be seen that the monitoring and prevention of the candid camera behavior of the mobile phone have far-reaching significance, which can effectively prevent information leakage and avoid the occurrence of huge losses at the source. Now, most video surveillance back-ends still rely on manual monitoring for analysis and processing. Obviously, relying on humans will always have the drawbacks that people are tired and unable to perform real-time monitoring and analysis. Our goal is to propose a system that recognizes camera behaviors based on deep learning for video surveillance. It mainly includes two technologies, target detection and behavior recognition.

Analyzing behavior in video surveillance generally refers to detecting areas where pixels change in an image under an ordered time series, and extracting the changed areas from the background image for analysis. Target classification and behavior analysis are based on the extracted content of the target pixel area, so the quality of the target area extraction [1] directly affects the accuracy of subsequent algorithms. Among them, object detection is closely related to the feature expression of the image. There are two kinds of feature expressions. One is the manually designed feature expressions, such as gradient histogram feature (HOG) [2, 3], color space SIFT [4], and local self-similarity [5]. The other is the feature expression method of deep learning. This method is relatively abstract. It uses a convolutional neural network to extract various abstract features by highly abstracting the image. On a sufficient data set, deep learning is more accurate in extracting features from samples, but the disadvantage is that it is not yet possible to cognitively interpret the features extracted from deep learning.

The behavior recognition subject framework in the behavior analysis of video surveillance is divided into feature extraction and behavior classification. With the rise of deep learning, mainstream video behavior analysis algorithm frameworks include Two Stream [6–8], C3D [9], etc. where the main idea of the Two Stream method is to perform single-frame pictures and superimposed optical flow pictures, respectively. Network training detection, and then weight the two detection results to complete the behavior recognition. The C3D algorithm can be seen from the naming that it is a 3D convolution of the input video stream in time and space, extracting features and classifying to obtain behavior analysis results.

The research topic of this paper is mainly based on the deep learning in the surveillance scene of the camera behavior detection [10–12], the main part is to extract and analyze the information of the hand, so the perfect acquisition of the hand area is a key to behavior detection. The acquisition of the hand area is usually modeled using the skin color model [13, 14], and the hand area extraction is performed by setting the skin color and the range of the human torso interval range [15–17], which has a lot of noise. The interference has a great influence on the classification accuracy of the later classification model.

In this paper, we propose an algorithm based on the appearance of the human hand region and Resnet50 [18] framework algorithm to achieve the detection of camera behavior in video surveillance. This new algorithm uses a hand region extraction method based on the appearance of the human body to eliminate the noise as much as possible. It first uses the denoising algorithm to perform Gaussian denoising on the captured video frame images, and then uses Openpose to frame the human body rectangular frame and standard. The joint node of the hand defines the range of the hand extraction area; then to eliminate other noise interference in the rectangular frame of the human body, this paper proposes a second skin color screening algorithm to limit the human skin color to the color space to obtain the hand area. After acquiring the hand area, input it into the trained mobile phone recognition model to identify whether the hand area contains a mobile phone, and then combine the results of the behavior analysis of the video to obtain the final evaluation, and realize the function of video surveillance intelligent behavior analysis.

The rest of the paper is organized as follows. The second section briefly introduces the related work. The third section introduces our methods and experiment, the mobile

phone recognition algorithm based on the human hand surface extraction model combined with the resnet50 framework, and the description of the experimental part. Section 4 presents the experimental results and analysis. Section 5 gives conclusions and puts forward some prospects for future work.

2 Related Work

For the problem of anti-photographing behavior detection, there are two main aspects to be solved. One is the detection and extraction of the hand area, and the other is the detection of whether the camera device is held in the hand area. For the detection and extraction of hand regions, there are currently many solutions. Most of the traditional methods are based on skin color to obtain the hand and face area range, and then locate the hand area. These include RGB-based skin detection [19]; elliptical skin model-based skin detection [20]; YCrCb color space Cr component combined with Otsu threshold segmentation skin detection [21]; face detection algorithm based on improved YCrCb color space [22]; Adaptive skin color detection based on HSV color space [23], etc. We briefly introduce two methods, one is the skin color detection method based on RGB, which finds the pixels within the defined skin color range according to the RGB color model, and then sets the pixels outside the range to black to reach the extraction target The purpose of area extraction. However, because RGB is greatly affected by light, the robustness is too low, and the experimental effect is not ideal. Another method is skin detection based on an elliptical skin model. The principle of this method is to map skin information to YCrCb space. In the two-dimensional space of CrCb, these skin pixels approximate an ellipse distribution. According to this principle, we can use the skin color statistical information to obtain a CrCb ellipse, and filter the input image pixels to obtain the target skin color area. The experimental effect is relatively ideal. However, the traditional skin color-based area extraction method cannot directly and accurately extract the hand area, because the skin color includes not only the hand skin color but also the facial skin color, and even the leg skin color. The problem to be solved in this paper is that after determining the area close to the human skin color range, it can be further accurate to the hand area, and then accurately extract the target area. With the rise of deep learning, hand detection can also be detected by training models, but compared to skin color detection, the effect is not so ideal.

Target detection is based on target classification. In recent years, the target detection algorithm has made great progress. The more popular algorithms can be divided into two categories. The first category is based on Region Proposal's R-CNN series of algorithms, such as R-CNN [24], Fast R-CNN [25], Faster R-CNN [26], etc., they are two-stage, need to first generate the target candidate box by algorithm, locate the target position, and then classify and return the candidate box. The other type is a one-stage algorithm such as Yolo [27] and SSD [28], which only uses a convolutional neural network CNN to directly predict the category and position of different targets. The first type of method has a higher accuracy but is slower, and the second type is the opposite. However, most of these algorithms are based on classifying the content within the frame and then achieving the recognition effect, which is equivalent to traversing the entire image, which takes time. The problem to be solved in this article is

to use traditional methods to frame the exact location of the target, and then only need to classify the content in the frame to achieve the target detection effect, the speed will be faster.

3 Method and Experiment

In this work, we propose a new method for detecting camera behaviors in video surveillance. Its overall architecture is shown in Fig. 1. The method includes two parts, one is the hand region extraction based on the Openpose combined with the skin color selection model, and the other is the mobile phone recognition based on the ResNet50 neural network model.

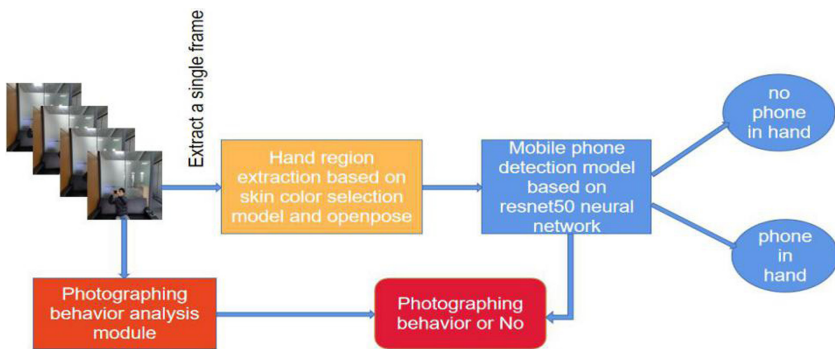


Fig. 1. Photographing detection framework

3.1 Hand Region Extraction

Using skin color to detect the hand region is a common method. The main reason is that the posture of the hand is changeable, and the shape and texture characteristics of the hand are different in different postures. Compared with the skin color, the detection of the hand region is more stable and accurate, and it will not be translated. And rotation effects. The RGB color space is the most common and common in life. Since the chromaticity space of RGB information does not have good separation, it is easily affected by light intensity to cause chromaticity changes, which affects the extraction of hand regions. However, after investigation, it was found that the YCbCr color space can separate the luminance Y information, and it can better represent the characteristics of skin color information in the chroma CrCb space. After a statistical analysis of the distribution of skin color under different brightnesses, it is finally concluded that for different brightnesses, the change in brightness range in YCbCr space is large (Y value), while the change in chromaticity range is small (CbCr value). Basically tends to be consistent, and approximates a two-dimensional Gaussian distribution. Therefore, the skin color can be modeled based on these to obtain a two-dimensional skin color Gaussian model $G = (M_{cr,cb}, C)$. Where $M_{cr,cb}$ is expressed as the mean value of skin

color in CbCr space, C represents its covariance. Let pixel $P_i = (Cr_i, Cb_i)$ be the pixel value of the skin color of the pixels in the sample set in the CbCr space, and N the number of sample sets, then the Gaussian model formula is:

$$M_{cr,cb} = E(P) = \frac{1}{N} \sum_{i=1}^N P_i \quad (1)$$

$$C = E\left[(P - M_{cr,cb})(P - M_{cr,cb})^T\right] \quad (2)$$

$$= \frac{1}{N} \sum_{i=1}^N (P_i - M_{cr,cb})(P_i - M_{cr,cb})^T$$

After the Gaussian skin color model is established, the skin color probability of each pixel on the graph, $P(I_{x,y})$, can be calculated according to the Gaussian model. The formula is:

$$I_{x,y} = (Cr_{x,y}, Cb_{x,y}) \quad (3)$$

$$P(I_{x,y}) = \exp\left[-0.5 * (I_{x,y} - M_{cr,cb})^T C^{-1} (I_{x,y} - M_{cr,cb})\right] \quad (4)$$

However, when directly using the YCbCr color space to detect human skin color, noise information is introduced. In order to solve this problem. This article uses openpose to help define the target area of the human body. Next is a brief introduction to openpose. Openpose is an open source library based on convolutional neural network and supervised learning and using caffe as the framework. It can realize the tracking of human facial expressions, torso, limbs and even fingers. It is not only suitable for single person but also for multiple people, and has a good Robustness. Enter a picture to be detected and get a Feature map through the vgg network. After 6 stages, each stage has two branches, one for key point detection and one for PAF detection. With heatmap and PAF, you can know all the key points in the picture, and then map the points to each person through PAFs to achieve the positioning of the joint points of the human body. The use of Openpose has a good positioning aid for human hands and faces, and provides strong support for accurately extracting the hand area.

Our paper proposes a new hand region extraction algorithm as follows: (1) The input image is converted from the original RGB color space to the YCbCr color space, which is used to reduce the impact of lighting on target recognition in the later hand. (2) The openpose framework is introduced to determine the position of the face and hand joints, and frame the approximate target area, which can effectively reduce the noise range generated by the image during processing. (3) Since the skin color distribution of the human face area and the human hand area belong to the same distribution, this paper uses the skin color range of the face to further frame the hand area

within the human body area range, and then combine the hand marked by openpose. The gateway node further extracts the range of the hand area more accurately. (4) Since the hand area and the face area overlap when taking pictures under the camera, you can first determine whether the hand area and the face area determined by the skin color selection model are connected. If it is connected, it means that the person is taking a picture Suspected. In order to more accurately determine whether a picture is being taken, a comprehensive judgment can be made in combination with the recognition result of the subsequent mobile phone.

Since this article is to detect the camera behavior in video surveillance, the object of this module is the mobile phone, the mobile phone itself is not large, if you want to learn more mobile phone features, you need to learn a deeper neural network, so this module is selected Residual network. The residual network ResNet aims to solve the problem of degradation of the network and the disappearance of gradients as the number of neural network layers increases. At this point, the number of layers of the neural network can exceed the previous constraints, reaching dozens, hundreds, or even thousands of layers, providing feasibility for advanced semantic feature extraction and classification. In this module, the residual network is used to extract the deep features of the mobile phone, which is helpful to improve the accuracy of mobile phone recognition.

3.2 Experiment

In this part, we will introduce the training of our model, and at the same time, we will verify the effectiveness of our trained Resnet50 model to recognize the mobile phone through the input picture. The specific experimental environment configuration is as follows:

Experimental Environment

Window10, 12G DDR3 1600 MHz, i7, Anaconda4.8, Python3.6, Opencv-python3.4, openpose.

Training Data

We train the model on a proprietary data set, which is a collection of photos of the poses of the person we took and then annotate them. The data set was taken by ourselves, which mainly includes yellow people, and there are two types of genders. The data set includes various poses for taking pictures, and also contains various handshaking techniques, many of which have hands. Block the phone's data set. It should be mentioned that the camera devices in the data set used in this article are mainly mobile phones. For model training, we divide the data into three parts, namely, 2288 camera poses with a mobile phone in the hand, 3600 camera poses without a mobile phone in the hand, and 2051 background pictures, the datasets are shown in Fig. 2. Train Resnet50 as a three-category.



Fig. 2. Datasets of training

Training Model

We set epoch to 15, batch to 16, and learning rate to 0.001. The loss function is the cross-entropy loss function.

4 Results and Analysis

In this module, we mainly introduce the experimental results. It includes the following parts:

- (1) Display and analysis of Renderings during the extraction of hand area

It can be clearly seen from the flow in Fig. 3 that before extracting the hand region, this article will first obtain the wrist joint point coordinates of the target person through Openpose, and then save the wrist joint point position, and at the same time intercept the approximate target area. Then the RGB to YCrCb processing is performed on the rough target area image, that is, the transition from (c) module to (d) module in Fig. 3. Then use the YCrCb threshold to define the skin color selection model to filter the approximate target area to obtain the target person’s hand and face area, select the center of the respective connected area in each connection area of the hand and face area, and then combine the wrist coordinates to frame an approximate Hand area, determine which center of each connected area falls in this area, and then you can get the final hand area extraction frame according to the intersection of the hand area obtained by skin color filtering and the hand area determined by the wrist node, that is, This is the expected result of the hand region extraction algorithm in this paper.

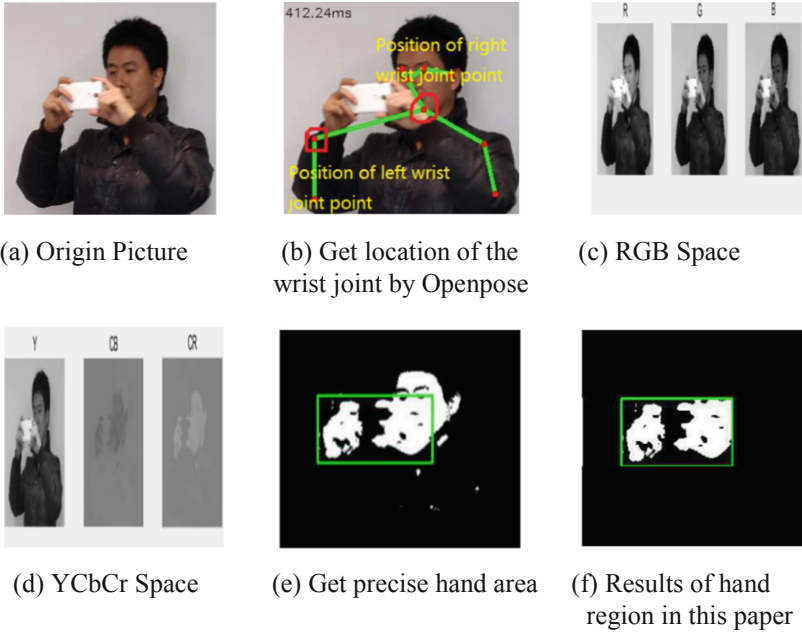


Fig. 3. Extract detail region by a novel skin color selection algorithm

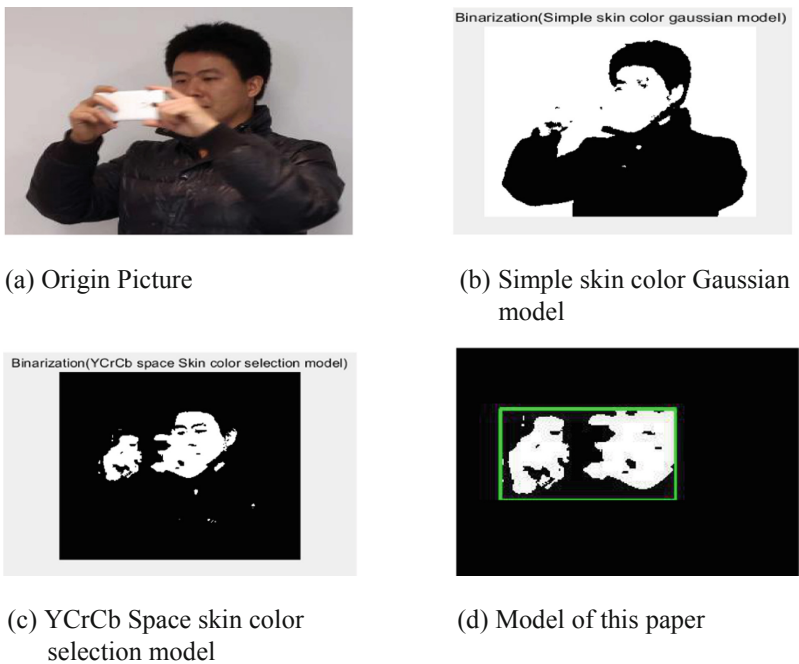


Fig. 4. Comparison of hand region extraction algorithms

- (2) Comparison and analysis of hand area extraction effects based on several skin color selection models.

It can be clearly seen from the experiment in Fig. 4 that the YCrCb color space is similar to the color space distribution obtained by the Gaussian model trained with a large number of skin samples, but the YCrCb color space selection model has a more accurate effect on skin color extraction. Most of the reasons for this difference come from the threshold setting. The two models are similar in that they cannot directly and accurately extract the hand area, but can be used as the first screening option. The algorithm in this article is based on them to first extract the main target area through Openpose, which to a large extent suppresses the generation of additional noise in the entire picture, and at the same time can obtain the approximate area of the hand based on the wrist joint coordinates obtained by Openpose Then, combined with the skin color region obtained by the skin color extraction model, the hand regions obtained by the two methods are properly fused to obtain a more accurate hand region. It can be seen from the (d) module in Fig. 4 that the algorithm proposed in this paper has a very good effect on the extraction of the hand region.

- (3) The effect of detecting mobile phones based on ResNet50 mobile phone identification model.

We extract a frame of the picture from video surveillance, use the hand area extraction algorithm proposed in this paper to frame the hand area in the video frame, and input the area into the trained mobile phone recognition model based on the Resnet50 network framework. The region performs deep feature extraction to determine whether the hand holds a mobile phone.



(a)Hand Region of Skin Color Mask without Mobile Phone in hand (b) Hand Region of origin picture without Mobile Phone in hand (c) no mobile phone:0.75 (True label:no mobile phone)

Fig. 5. Detect Mobile Phone without phone in hand



Fig. 6. Detect Mobile Phone with phone in hand

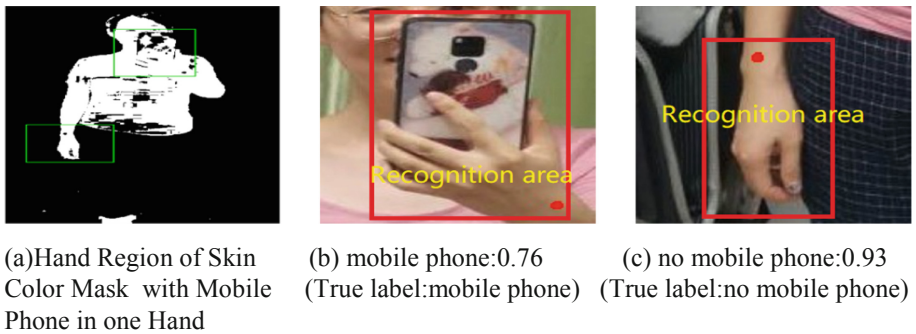


Fig. 7. Detect Mobile Phone with phone in one hand

From the detection effects of Fig. 5, Fig. 6 and Fig. 7, we can see that the mobile phone identification model based on the Resnet50 network is in line with the expected mobile phone detection effect in the hand area, which can effectively identify camera devices such as mobile phones, which can better combine photos behavior analysis for more accurate detection of photographing behavior.

In order to verify the feasibility of the algorithm framework of this article, this article also selected about 100 pictures in two videos for testing. In terms of hand positioning, compared with the ordinary Gaussian skin color model and the YCrCb threshold limit model, the hand area extraction algorithm proposed in this paper achieves 89.6% accuracy, which is significantly higher than the 75% based on the ordinary Gaussian model and the YCrCb threshold limit model. 84%. The main reason for this difference is on the one hand because of the light, on the other hand is the influence of the surrounding environment tone. In terms of mobile phone recognition model, this paper chose the deep model framework Resnet-50. Compared with the mobile phone recognition model based on vgg, the recognition accuracy rate has increased from 65% to 71%. The deep network is conducive to the picture. The extraction of deep-level features plays a key role in the identification of subsequent targets.

5 Conclusion

In the era of the rapid development of artificial intelligence, intelligent video surveillance has begun to gradually replace the traditional artificial-based video behavior analysis as the mainstream monitoring method. In real life, more and more business scenarios are also stimulating the intelligent video surveillance industry. Rapid development. This article is mainly based on solving the prevention and control of prohibited photography in secret scenes such as museums, company core meetings, military bases, etc., using human skin color Gaussian modeling combined with Openpose to obtain the hand area and relying on detection algorithms to complete the recognition of photographing behavior.

Although this article has achieved a certain effect on the detection of photographing behavior in a static background, it has not yet involved dynamic video detection. The algorithm we propose now is only for the analysis of single-frame pictures. Therefore, we need to further improve the detection dimension. In addition to the current feature extraction of space, we need to further study in the future work to extract some sequence features from the time dimension, combined with the time and space features to identify the camera action and improve the accuracy of intelligent video surveillance.

References

1. Chen, Z.L.: Research on Region of Interest Extraction. Central South University
2. Alhindi, T.J., Kalra, S., Ng, K.H.: Comparing LBP, HOG and Deep Features for Classification of Histopathology Images (2018)
3. Dalal, B.N.: Histogram of oriented gradients for human detection. In: Proceedings of the IEEE CVPR (2005)
4. Dou, J.F., Qin, Q., Tu, Z.M.: Robust image matching based on the information of SIFT. *Optik* **171**, 850–861 (2018). S0030402618309021
5. Zhai, F., Cai, X., Li, Y.M.: A method of pedestrian detection based on the local row color self-similarity. *Microcomput. Appl.* **000**(004), 4–7 (2015)
6. Simonyan, K., Zisserman, A.: Two-stream convolutional networks for action recognition in videos. In: Advances in Neural Information Processing Systems (2014)
7. Zhu, Y., Lan, Z.: Hidden Two-Stream Convolutional Networks for Action Recognition (2017)
8. Wang, L., Xiong, Y., Wang, Z.: Temporal Segment Networks: Towards Good Practices for Deep Action Recognition (2016)
9. Tran, D., Bourdev, L., Fergus, R.: Learning spatiotemporal features with 3D convolutional networks (2015)
10. Guo, C.S., Meng, Z.H.: Gesture recognition based on improved Hough transform algorithm. *Comput. Syst. Appl.* **027**(004), 243–248 (2018)
11. Abdallah, M.B., Kallel, M., Bouhleb, M.S.: An overview of gesture recognition. In: International Conference on Sciences of Electronics. IEEE (2012)
12. Lin, S.Q., Wu, Y.D., Chen, Y.H.: Gesture recognition based on geometric features. *Comput. Eng. Des.* **02**, 284–288 (2014)

13. Rogez, G., Khademi, M., Supančič III, J.S., Montiel, J.M.M., Ramanan, D.: 3D hand pose detection in egocentric RGB-D images. In: Agapito, L., Bronstein, M.M., Rother, C. (eds.) ECCV 2014. LNCS, vol. 8925, pp. 356–371. Springer, Cham (2015). https://doi.org/10.1007/978-3-319-16178-5_25
14. Ma, Y.Z.: Hand Detection Based on Skin Color and Block Feature
15. Huang, Z.C., Zhang, P., Zhao, H.R.: Face detection algorithm based on skin color information in intelligent video surveillance. *Mod. Electron. Tech.* **041**(007), 58–61 (2018)
16. Li, J., Xu, J., Tian, L.: Adaptive skin color segmentation method based on YcbCr space. *Public Commun. Sci. Technol.*, 235–236 (2010)
17. Fan, W.B., Zhu, L.J.: A gesture detection and recognition method based on skin color feature extraction. *Mod. Electron. Tech.* **497**(18), 85–88
18. He, K., Zhang, X., Ren, S.: Deep Residual Learning for Image Recognition (2015)
19. Jiang, F.B.: The study of skin detection algorithms based on the RGB-H-CbCr new color space. *Sci. Mosaic* **000**(009), 34–38 (2011)
20. Li, J., Hao, X.L.: Face detection using ellipse skin model. *Comput. Meas. Control* **14**(2), 170–171
21. Yang, X.F., Qi, Y.C., Li, T., Yuan, Q.: Eye localization optimization method based on YCb'Cr' skin color feature and Otsu algorithm. *J. Nanjing Univ. Posts Telecommun. (Nat. Sci.)* **1**, 99–102 (2014)
22. Wang, H.Q.: Face Detection Algorithm Based on Improved YCrCb Color Space (2010)
23. Tian, W., Zhuang, Z.Q.: Self-adaptive skin color detection based on HSV color space. *Comput. Eng. Appl.* **14**, 81–85 (2004)
24. Girshick, R., Donahue, J., Darrell, T.: Rich feature hierarchies for accurate object detection and semantic segmentation. In: IEEE 2014 IEEE Conference on Computer Vision and Pattern Recognition (CVPR), pp. 580–587 (2014)
25. Girshick, R.: Fast R-CNN. *Computer Science* (2015)
26. Ren, S., He, K., Girshick, R.: Faster R-CNN: towards real-time object detection with region proposal networks. *IEEE Trans. Pattern Anal. Mach. Intell.* **39**(6) (2015)
27. Redmon, J., Divvala, S., Girshick, R.: You Only Look Once: Unified, Real-Time Object Detection (2015)
28. Liu, W., Anguelov, D., Erhan, D.: SSD: Single Shot MultiBox Detector (2016)

Signal Processing



Emergency Siren Recognition in Urban Scenarios: Synthetic Dataset and Deep Learning Models

Michela Cantarini^(✉), Luca Serafini, Leonardo Gabrielli,
Emanuele Principi, and Stefano Squartini

Department of Information Engineering, Università Politecnica delle Marche,
Via Breccie Bianche, 60131 Ancona, AN, Italy
michela.cantarini@pm.univpm.it

Abstract. Emergency Siren Recognition (ESR) is an important issue for automotive safety. We are interested in the early recognition of ambulance sirens in urban scenarios, where noise can be produced by a wide variety of sources and represents an impediment to the perception of alarm sounds by drivers. In this paper, we propose a deep convolutional neural network based on the U-Net encoding path for the ESR task. To overcome the problem of audio acquisition, an algorithm has been implemented to generate a synthetic dataset that reproduces the sound of a siren in multiple urban traffic contexts. We perform emergency sound recognition to identify the presence of the alerting sound using spectrogram-like features. Our experimental evaluations demonstrate that our ESR approach has achieved excellent performance both in mono-scenarios and multi-scenarios at very low SNRs, also in conditions unseen during training thanks to a large amount of training data.

Keywords: Emergency siren recognition · Convolutional neural network · Synthetic dataset

1 Introduction

Nowadays, artificial intelligence in the automotive industry has found many applications to increase efficiency, performance, and safety. Research has achieved important results in the implementation of acoustic sensors, e.g., for automatic detection of road conditions [1].

Emergency Siren Recognition (ESR) is an important branch of sound recognition applied in intelligent car safety systems via devices called Emergency Vehicle Detection Systems (EVDS). They are used as safety systems both in conventional cars with warning lights and in autonomous driving with an automatic approach to the side of the road to allow emergency vehicles to pass undisturbed. Such devices have an important task because in some cases drivers do not have a clear perception of signals coming from outside. This is due to high soundproofing in passenger compartments, distractions, or driver hearing impairment. Besides, the noise level produced by urban traffic may mask the presence of emergency vehicle siren. The background noise level

varies on an hourly and daily basis due to different traffic flows, and it is influenced by exceptional events such as the passage of trains, planes, heavy vehicles, or weather conditions (thunderstorms, gusts of wind). Rapid identification of the approach of emergency vehicles is therefore essential so that precautions can be taken quickly.

The theme of ESR was developed several years ago with the implementation of radio waves detection systems emitted by emergency vehicles [2]. Later implementations are based on conventional adaptive filtering techniques applied to the signal received by microphones [3], or on the use of ultrasound signals [4]. In [5], the periodic siren signal is extracted from an aperiodic signal with a pitch detection algorithm; in [6], an approach based on Longest Common Subsequence (LCS) is applied for ambulance siren recognition. Recent realizations employ Machine Learning algorithms. In [7, 8], and [9], Mel-Frequency Cepstral Coefficients (MFCCs) are used as features to train neural networks. In [10], a method based on sinusoidal modeling where the sound is represented by a relatively low number of tones is compared with a method that uses PLP cepstral features to train a Multi-Layer Perceptron (MLP). In [11], different types of features are selected to train a Support Vector Machine classifier (SVM). The most recent studies use deep learning architectures with data augmentation techniques, combined features, and multi-task learning models. In [12], a multi-channel CNN architecture with mixup [13] augmentation is compared to a single-channel architecture without any augmentation to classify emergency and non-emergency signals. In [14], an exhaustive study for the classification of siren, horn, and noise sounds is illustrated. Three CNN-based neural network models are developed: the first combines MFCC and log-Mel features in a 2D-CNN (MLNet), the second develops a 1D-CNN (WaveNet) which automatically learns the features for classification from raw waveform, and at last, a CNN-based ensemble model (SirenNet) is designed from the combination of the two described networks. In [15], alerting acoustic event detection and sound source localization in an urban scenario are performed in a Multi-Task Learning (MTL) scheme, together with signal denoising. Two neural networks are used for this purpose. The first one is based on a U-Net [16] architecture to perform two tasks simultaneously, semantic segmentation of the input and classification. The second one is a CNN that uses the outputs of the segmentation to perform the localization, i.e., identification of the direction of arrival of the sound source. The features used in both neural networks are gammatone-like spectrograms, known as gammatonegrams [17].

1.1 Scope of the Work

This work aims to study and evaluate the performance of an automatic system based on deep learning algorithms for ESR in urban traffic scenarios. For this purpose, a synthetic dataset of audio files has been generated; it considers the Doppler effect due to the relative source-observer movement and simulates different acoustic scenarios in which the emergency vehicle siren is immersed. Two types of features have been extracted from the generated audio files: gammatonegrams and log-Mel spectrograms. The features have been input to two CNN networks whose structure is inspired by the U-Net encoding branch described in [15]. The CNNs were trained with a supervised approach and tested for a binary classification task: *Siren vs. Noise* (S/N). For the training of the CNNs two datasets and a third one obtained from the union of the

previous ones have been realized. The networks were then tested with three datasets at different Signal-to-Noise Ratio (SNR) values. At last, the performance in terms of accuracy was compared and analyzed.

The rest of this paper is organized as follows. Section 2 provides a detailed introduction of proposed methods. Section 3 presents the experiment settings on different datasets, and Sect. 4 gives experimental results. Finally, Sect. 5 concludes the paper.

2 Proposed Method

2.1 Synthetic Dataset Generation Algorithm

An important part of the ESR work is the dataset generation process. To overcome the problem of direct data acquisition, an algorithm has been implemented to generate audio files containing the sound of an ambulance siren according to the Italian law [18] within different contexts of background urban traffic noise.

First, an audio file of an Italian ambulance siren was found on the web. It consists of the alternation of two tones, respectively at 392 Hz and 660 Hz corresponding to the musical notes G4 and E5. The period is obtained by alternating two consecutive times of 392 Hz tone for the duration of $1/3$ period, 660 Hz tone for the duration of $1/18$ period, 392 Hz tone for the duration of $1/18$ period, and 660 Hz tone for the duration of $1/18$ period. It is supposed to last for (3 ± 0.5) s. A pause between two sound sequences is not supposed to last longer than 0.2 s. Ambulance alarm devices generate a two-tone siren from a square wave, so the emitted signal will be made up of a fundamental frequency plus other higher-order harmonics. A single period of the siren audio file has been isolated to repeat it until the desired duration.

Then a Doppler effect simulation algorithm was implemented using the delay line concept developed in [19]. The Doppler effect consists of a frequency shift or a continuously variable delay in time; the implementation was done emulating a variable-length delay line to be applied to every single sample. In case the delay to be implemented is an integer quantity, the sample of the signal affected by Doppler is given by a sample of the delayed input signal. Otherwise, in case the delay to be implemented is constituted by a fractional quantity, the output sample is generated starting from the linear interpolation between two adjacent samples of the second original input signal.

The simulation of the source motion to the receiver has also been implemented. It has been possible to simulate different situations of approach or alignment of the sound source to the receiver, assuming that the receiver is in quiet. The variables are source position and velocity, specifically: starting coordinate along the x -axis, starting coordinate along the y -axis, velocity along the x -axis, velocity along the y -axis, and the vector sum of the x and y velocity components to simulate motion at different angles. Different boundary conditions have been simulated, expressed in approaching and moving the source away from the receiver, evaluating different directions and distances; various background noise contexts of urban traffic and weather events; various SNRs to simulate a gradual reduction in siren warning perception (Fig. 1).

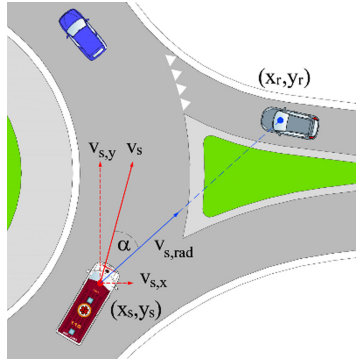


Fig. 1. Source in position (x_s, y_s) approaching the receiver in position (x_r, y_r) . Given velocity source v_s , the radial velocity $v_{s,rad}$ varies as a function of the angle α .

2.2 Features

Several studies have shown that different features work best for different types of acoustic scene or task. As mentioned in Sect. 1 and depicted in Fig. 4, we employ two types of spectrograms as features: gammatonegrams and log-Mel coefficients.

Gammatonegram: is the result of filtering a signal for a gammatone filter-bank. This type of filter-bank has been introduced to describe the impulsive response of the human auditory system and represent auditory perception; it emphasizes frequencies in the range of the audible. A gammatone filter-bank is composed of linear filters. The impulse response centered in a given frequency f_c takes the expression:

$$g(t, f_c) = \begin{cases} at^{n-1} e^{-2\pi bt} \cos(2\pi f_c t + \varphi) & \text{if } t \geq 0 \\ 0 & \text{otherwise} \end{cases} \quad (1)$$

where a controls the gain, n is the filter order, b is filter bandwidth, φ is the phase of the carrier, and f_c is central frequency.

Given $x(t)$ the waveform of the audio signal, the output response $y(t, f_c)$ of a filter characterized by a central frequency f_c can be calculated as:

$$y(t, f_c) = x(t) * g(t, f_c) \quad (2)$$

A gammatonegram consists of a two-dimensional representation of audio signal intensity, depending on time and frequency. If a spectrogram is composed of filters that all have the same spectral width, a gammatonegram is the result of filtering for a gammatone filter-bank in which each filter is characterized by a band whose amplitude increases with the central frequency f_c . The Equivalent Rectangular Bandwidth (ERB) scale is usually used to quantify the bandwidth of these filters.

log-Mel spectrogram: is widely used for acoustic scene classification tasks. It begins with a set of short-time Fourier transform (STFT) spectra, computed from an input

signal divided into frames lasting between 20 ÷ 40 ms since the signal is not subject to significant changes on a short-term scale. A Mel-filter bank, which simulates the overall frequency selectivity of the human auditory system using the frequency warping

$$Mel(f) = 2595 * \log_{10} \left(1 + \frac{f}{700} \right) \quad (3)$$

is then applied to the power spectra to generate a Mel spectrogram. Logarithmic scaling is then applied to all filterbank energies to obtain the log-Mel spectrogram. We use the Librosa toolbox [20] to extract log-Mel features used in our experiments.

2.3 Deep Learning Model

The proposed work uses a Convolutional Neural Network (CNN) as an ESR system model, inspired to the U-Net encoding path described in Sect. 1 to perform a *Siren/Noise* binary classification task.

In particular, the CNN structure is illustrated in Fig. 2 and Table 1.

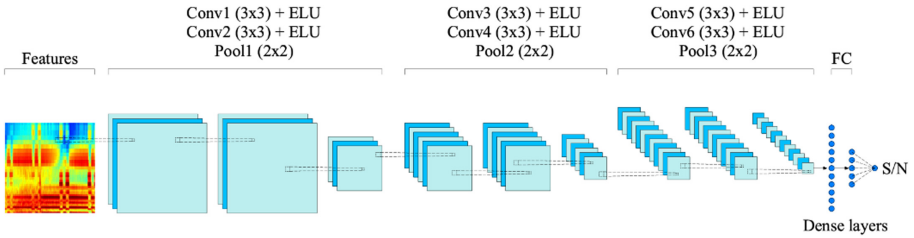


Fig. 2. CNN architecture for *Siren/Noise* classification.

Table 1. Configuration of proposed CNN.

| Layer | Ksize | Stride | Nums of filters |
|-------|--------|-----------------|-----------------|
| Input | – | – | – |
| Conv1 | (3, 3) | (1, 1) | 4 |
| Conv2 | (3, 3) | (1, 1) | 4 |
| Pool1 | (2, 2) | (2, 2) | – |
| Conv3 | (3, 3) | (1, 1) | 8 |
| Conv4 | (3, 3) | (1, 1) | 8 |
| Pool2 | (2, 2) | (2, 2) | – |
| Conv5 | (3, 3) | (1, 1) | 16 |
| Conv6 | (3, 3) | (1, 1) | 16 |
| Pool3 | (2, 2) | (2, 2) | – |
| FC1 | – | – | 10 |
| FC2 | – | Nums of classes | Nums of classes |

The proposed CNN architecture is composed of six convolutional layers and two fully connected layers. The first part has the task to perform a sub-sampling of the input through the application of three successive downsampling steps. The first two convolutional layers both use filter kernels of size (3×3) . An Exponential Linear Unit (ELU) activation function is applied to the output of each of them. The max pooling layers, placed as successive steps to the convolutional layers, use a square matrix of size (2×2) and a stride of 2. The number of feature channels doubles at each downsampling step, from 4 to 8 to 16. At the same time, the resolution (the spatial dimension of the feature maps) is halved after each max pooling operation. So, what you get at the end of the convolutional part of the network is a more compact representation of the input. The second part deals with classification and consists of two fully-connected consecutive layers. Finally, a sigmoid activation function has been applied in the last layer to obtain a binary classification.

3 Experiments

3.1 Dataset

Three datasets have been created for the training of the networks, called training datasets (A), (B), and (A + B). The training dataset (A) is composed of 64000 files, of which 32000 are urban traffic noise audio files and the remaining 32000 are siren audio files in an urban traffic context with spectral content mostly at frequencies below 2500 Hz. Also, the training dataset (B) consists of 64000 files with the siren/noise distribution equal to the training dataset (A); the only difference is that the traffic noise spectral content in the siren situation is mostly below 5500 Hz. The training dataset (A + B) is the sum of the previously described datasets. Siren audio files for training were generated with SNR values of 0, -5, -10, and -15 dB.

Three datasets have been created for the network test, called test datasets (a), (b), and (a + b). The test dataset (a) consists of 12000 files, of which 6000 are urban traffic noise audio files and 6000 are siren audio files mixed with noise with spectral content similar to siren files belonging to the training dataset (A). The same subdivision and characterization were assigned to the test dataset (b); the test dataset (a + b) is the sum of the previous ones. Siren audio files for testing were generated with SNR values of 0, -5, -10, -15, -20, -25, and -30 dB to evaluate the capability for recognition and generalization of the networks at decreasing SNRs.

Detailed information of the dataset files subdivision is shown in Table 2.

Table 2. Description of datasets.

| Dataset | Class (label) | Num of samples | SNR (dB) |
|---------------|---------------|----------------|--------------------------|
| Train (A) | Noise (0) | 32000 | – |
| | Siren (1) | 32000 | 0/–5/–10/–15 |
| Train (B) | Noise (0) | 32000 | – |
| | Siren (1) | 32000 | 0/–5/–10/–15 |
| Train (A + B) | Noise (0) | 64000 | – |
| | Siren (1) | 64000 | 0/–5/–10/–15 |
| Test (a) | Noise (0) | 6000 | – |
| | Siren (1) | 6000 | 0/–5/–10/–15/–20/–25/–30 |
| Test (b) | Noise (0) | 6000 | – |
| | Siren (1) | 6000 | 0/–5/–10/–15/–20/–25/–30 |
| Test (a + b) | Noise (0) | 12000 | – |
| | Siren (1) | 12000 | 0/–5/–10/–15/–20/–25/–30 |

The files used for network testing are different from the ones used for training. All the audio files from which the features have been extracted have a duration of 0.5 s with an overlap of 10 ms. A Hamming type window has been applied to the frames of both classes to avoid spectral leakage.

3.2 Preprocessing

All audio files have been downsampled to 16 kHz and normalized at -1 dB. We use two spectrogram-like representations: log-Mel spectrogram and gammatone spectrogram. Features are extracted from all recordings with a hamming window size of 1024, hop length of 512, 64 bands for gammatonegrams, and 40 bands for log-Mels. Then, the resulting spectrograms are converted into a logarithmic scale.

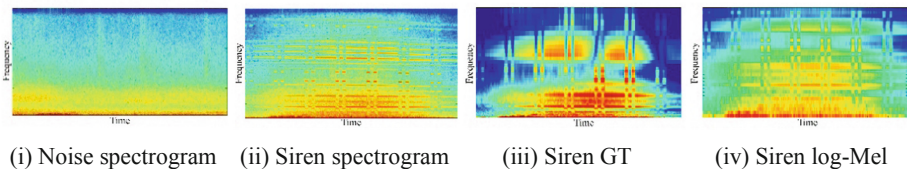


Fig. 3. Example of spectrogram representations of a sound frame of 10 s for the different acoustic classes considered (training dataset (A)). The frequency range is between 0 and 8 kHz. From left to right: (i) urban traffic noise spectrogram, (ii) siren spectrogram (SNR = 0 dB), (iii) siren gammatonegram (SNR = 0 dB), and (iv) siren log-Mel spectrogram (SNR = 0 dB).

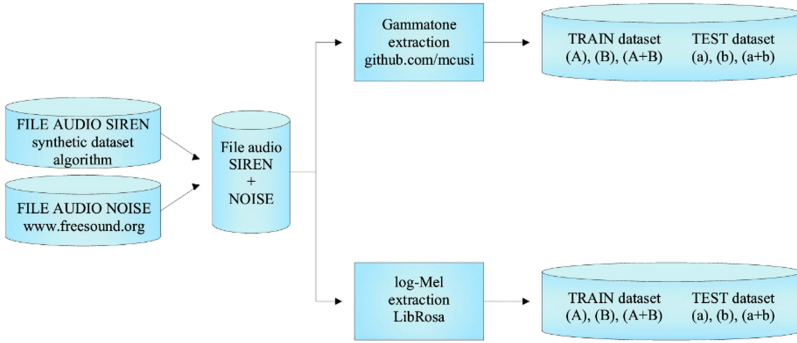


Fig. 4. Experiment overview: download urban traffic noise audio files from www.freesound.org [22], generation siren audio files and raw data organization; feature extraction using <https://github.com/mcusi> [17] and LibRosa [20]; train the networks with datasets (A), (B), and (A + B); test the networks using datasets (a), (b), and (a + b) at different SNRs.

3.3 Training Settings

The CNNs have been trained through a supervised learning task to perform binary classification. Splitting percentages of each dataset are about 70% for the training-set, 15% for the validation-set, and 15% for the test-set. The network input batch size is 32 samples, each with its label indicating its class. Training has been performed by using Adam [21] and binary cross-entropy loss. At the end of the training phase, the weights have been saved to be loaded for the test phase.

The networks have been trained on the three datasets generated (train (A), train (B), and train (A + B)), and tested for different SNRs. Training cases (A) and (B) have been tested with both test datasets (a) and (b); training case (A + B) has been tested with test dataset (a + b). Figure 4 shows the general scheme of the experiments.

We used the following metrics to evaluate the results of the classification:

$$Accuracy = \frac{TP + TN}{TP + FP + TN + FN} \text{ and } F_1score = 2 \times \frac{P \times R}{P + R} \quad (4)$$

where P and R represent precision and recall, respectively:

$$P = \frac{TP}{TP + FP} \text{ and } R = \frac{TP}{TP + FN} \quad (5)$$

where TP, FP, TN, and FN are the true positive, false positive, true negative, and false negative rate respectively.

The metrics are evaluated using scikit-learn¹ python library. Computer experiments were performed using Keras² with Tensorflow³ as backend. Parallel computing is performed using cuDNN⁴ libraries and Nvidia GeForce GTX 970.

4 Results

The following tables summarize the results of the CNNs performance trained and tested with the datasets described in Sect. 3.

In Table 3, we can observe that the CNNs trained with the dataset (A) and tested with the dataset (a) have excellent performance in the ESR task. Accuracy at SNR of -15 dB is 95.00% for GTs and 91.92% for log-Mels. On the other hand, the performance with test dataset (b) decreases at SNRs less than -5 dB for GTs and 0 dB for log-Mels, showing better results for GTs.

Table 3. Results obtained with training dataset (A) and test datasets (a), (b) at the same SNRs used in training.

| Train (A) | | | | | | | | |
|-----------|--------------|--------------------|----------|--------------------|----------|--------------------|----------|--------------------|
| SNR (dB) | Test (a) | | | | Test (b) | | | |
| | GTs | | log-Mels | | GTs | | log-Mels | |
| | Acc (%) | F ₁ (%) | Acc (%) | F ₁ (%) | Acc (%) | F ₁ (%) | Acc (%) | F ₁ (%) |
| 0 | 100 | 100 | 93.94 | 93.93 | 96.75 | 96.64 | 95.72 | 95.80 |
| -5 | 98.77 | 98.75 | 92.69 | 92.58 | 93.63 | 93.19 | 79.04 | 75.38 |
| -10 | 95.01 | 94.75 | 91.94 | 91.79 | 66.67 | 50.02 | 62.47 | 45.35 |
| -15 | 95.00 | 94.74 | 91.92 | 91.76 | 50.11 | 0.50 | 57.56 | 33.42 |

In Table 4, the same considerations apply to the experiments performed with the training dataset (B). Accuracy at SNR of -15 dB is 99.87% for GTs and 83.98% for log-Mels, considering the results obtained with the test dataset (b).

In Table 5, the networks trained with the dataset (A + B) and tested with the dataset (a + b) show excellent accuracy results (94.97% for GTs and 92.00% for log-Mels at SNR equal to -15 dB). In all cases, GTs perform better than log-Mels.

Finally, Table 6 shows the best results of the experiments for SNRs not used during the training. The CNNs trained and tested with the corresponding datasets have generalization capabilities even at low SNRs (-20 , -25 , and -30 dB).

¹ scikit-learn.org.

² keras.io.

³ www.tensorflow.org.

⁴ <https://developer.nvidia.com/cudnn>.

Table 4. Results obtained with training dataset (B) and test datasets (a), (b) at the same SNRs used in training.

| Train (B) | | | | | | | | |
|-----------|----------|--------------------|----------|--------------------|--------------|--------------------|----------|--------------------|
| SNR (dB) | Test (a) | | | | Test (b) | | | |
| | GTs | | log-Mels | | GTs | | log-Mels | |
| | Acc (%) | F ₁ (%) | Acc (%) | F ₁ (%) | Acc (%) | F ₁ (%) | Acc (%) | F ₁ (%) |
| 0 | 86.55 | 84.46 | 67.37 | 57.26 | 100 | 100 | 98.79 | 98.79 |
| -5 | 55.76 | 20.65 | 56.01 | 24.72 | 100 | 100 | 98.30 | 98.30 |
| -10 | 50.00 | 0.00 | 49.19 | 1.45 | 100 | 100 | 89.41 | 88.39 |
| -15 | 50.00 | 0.00 | 48.79 | 0.00 | 99.87 | 99.87 | 83.98 | 81.46 |

Table 5. Results obtained with training dataset (A + B) and test dataset (a + b) at the same SNRs used in training.

| Train (A + B) | | | | |
|---------------|--------------|--------------------|----------|--------------------|
| SNR (dB) | Test (a + b) | | | |
| | GTs | | log-Mels | |
| | Acc (%) | F ₁ (%) | Acc (%) | F ₁ (%) |
| 0 | 99.78 | 99.78 | 95.63 | 95.63 |
| -5 | 99.34 | 99.34 | 94.70 | 94.65 |
| -10 | 98.10 | 98.07 | 92.71 | 92.52 |
| -15 | 94.97 | 94.72 | 92.00 | 91.76 |

Table 6. Results obtained with the corresponding training and test datasets at SNRs not used in training.

| SNR (dB) | Train (A) | | Train (B) | | Train (A + B) | |
|----------|-----------|----------|-----------|----------|---------------|----------|
| | Test (a) | | Test (b) | | Test (a + b) | |
| | GTs | log-Mels | GTs | log-Mels | GTs | log-Mels |
| | Acc (%) | Acc (%) | Acc (%) | Acc (%) | Acc (%) | Acc (%) |
| -20 | 95.00 | 91.92 | 93.91 | 83.79 | 94.62 | 91.63 |
| -25 | 95.00 | 91.92 | 90.00 | 83.79 | 94.37 | 91.44 |
| -30 | 95.00 | 91.92 | 90.00 | 83.79 | 94.37 | 91.41 |

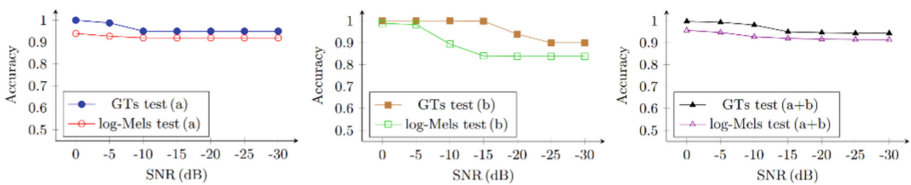
The following considerations can be drawn from the analysis of the results:

- the CNNs trained with frames that contain siren sounds in mono-scenario noise contexts show good performance even at low SNRs only when tested with frames characterized by similar noise spectral contents. In this case, the networks tested with siren frames in background noise conditions unseen during training have good performance only at high SNRs;

- the CNNs trained with frames that contain siren sounds in multi-background noise contexts give excellent results in the test even at SNRs not used in training, showing a good capability to generalize.

We have obtained the best results at low SNRs when the networks are trained with the dataset (A) both in the condition of a single spectral range and in multiple background noises. This consideration can be reasonably justified by the presence of harmonic components in the siren sound. In Fig. 3, we can observe that the low tone of the siren with fundamental at 392 Hz (G4) has harmonic components up to 6272 Hz and the high tone (E5) with fundamental at 660 Hz has visible harmonic components up to 7920 Hz. These frequency values are subject to slight variations due to the Doppler effect. A background noise characterized by a low-frequency spectral content does not mask the higher harmonic components, so siren frames are more easily recognizable even at low SNRs. The results also show that the network learns not only the siren sound but also the characteristics of background noise.

In Fig. 5, the best accuracy of the GTs and log-Mels is compared for each experiment. The results show that both GTs and log-Mels give very good results with cleaner datasets. In more complex urban traffic scenarios GTs have better performance at low SNRs.



(i) GTs and log-Mels accuracy with training (A) and test (a) datasets. (ii) GTs and log-Mels accuracy with training (B) and test (b) datasets. (iii) GTs and log-Mels accuracy with training (A+B) and test (a+b) datasets.

Fig. 5. GTs and log-Mels best test accuracy for (A), (B), and (A + B) training conditions at different SNRs.

At last, Table 7 compares our work with recent related CNN-based works for the ESR task. From the comparison with [15], we can observe that our network trained and tested with gammatonegrams achieves the same results obtained by the Mono network, from which our work was inspired. As in our work, the dataset consists of noises acquisitions, and the siren audio files were generated by mixing the target signal with the recorded background noise. However, we have no detailed information about the method of generating synthetic datasets and the number of samples used. On the other hand, the accuracy obtained in [14] shows that the recent techniques of feature combination achieve better performance than log-Mels only. In this case, the number of samples of the dataset is comparable to ours but all audio files are real-field recordings from online resources, public datasets, and direct acquisitions. No information is provided on the SNR values of the audio files for network training and testing.

Table 7. Comparison of the mean classification accuracy obtained with recent related CNN-based models (input data length of 0.5 s).

| Work | Dataset | Features | Model | Acc (%) |
|----------------------------------|--|-----------------------|----------------|---------|
| L. Marchegiani et al. [15], 2018 | Recordings, and synthetic $-35 \leq \text{SNR}_{\text{test}} \leq -5$ | GTs | SeC network | 94.00 |
| | | | FS network | 98.00 |
| | | | Mono network | 96.00 |
| V.-T. Tran et al. [14], 2020 | Recordings No SNR details | Raw data | WaveNet | 94.43 |
| | | MFCCs + log-Mels | MLNet | 95.37 |
| | | Raw, MFCCs + log-Mels | SirenNet | 97.42 |
| This work | Recordings, and synthetic $-15 \leq \text{SNR}_{\text{train}} \leq 0$ $-30 \leq \text{SNR}_{\text{test}} \leq 0$ | log-Mels | Mono-scenario | 90.58 |
| | | | Multi-scenario | 92.79 |
| This work | | GTs | Mono-scenario | 96.25 |
| | | | Multi-scenario | 96.51 |

In this paper, we want to show that the classification performance is closely related to the background noise of the training dataset. Therefore, it is essential to improve the ESR task as much as possible before correlating it with other tasks, such as the sound source localization. The accuracy obtained by aggregating raw data with combined MFCCs and log-Mels is not much higher than the performance of gammatonegrams, so they prove to be extremely useful features in audio classification tasks.

5 Conclusion

In this work, we proposed a deep learning approach for emergency siren recognition in urban scenarios. We used a convolutional neural network inspired by the U-Net encoding path for the *Siren vs. Noise* classification task. Given the difficulty of having a large number of siren audio recordings, a synthetic dataset that simulates the siren alarm in different background noises has been generated. We considered different relative source-observer positions and multiple speeds of the source to simulate the Doppler effect. The level of perception of the siren sound was obtained by generating audio files at different SNRs. Network performance in multi-condition training and testing with two types of features at different SNRs was compared. The classification accuracy obtained from the proposed method achieves excellent results since the generation of a synthetic dataset can provide a big number of data for the training. Our future work will focus on reducing background noise through filtering and denoising techniques.

Acknowledgement. This work is supported by Marche Region in implementation of the financial programme POR MARCHE FESR 2014–2020, project “Miracle” (Marche Innovation and Research Facilities for Connected and sustainable Living Environments), CUP B28I19000330007.

References

1. Pepe, G.: Detecting road surface wetness using microphones and convolutional neural networks. In: Audio Engineering Society Convention 146. Audio Engineering Society (2019)
2. Jackson, L.: Emergency vehicle detection device. U.S. Patent No. 5,235,329 (1993)
3. Fazenda, B.: Acoustic based safety emergency vehicle detection for intelligent transport systems. In: 2009 ICCAS-SICE. IEEE (2009)
4. Brill, W.E.: Emergency vehicle detection system. U.S. Patent No. 6,362,749 (2002)
5. Meucci, F.: A real-time siren detector to improve safety of guide in traffic environment. In: 2008 16th European Signal Processing Conference. IEEE (2008)
6. Liaw, J.J.: Recognition of the ambulance siren sound in Taiwan by the Longest Common Subsequence. In: 2013 IEEE International Conference on Systems, Man, and Cybernetics. IEEE (2013)
7. Tran, V.T., Yan, Y.C., Tsa, W.H.: Detection of ambulance and fire truck siren sounds using neural networks. *ARPN J. Eng. Appl. Sci.* **12**(5), 9–14 (2017)
8. Beritelli, F.: An automatic emergency signal recognition system for the hearing impaired. In: 2006 IEEE 12th Digital Signal Processing Workshop & 4th IEEE Signal Processing Education Workshop. IEEE (2006)
9. Salamon, J., Christopher, J., Juan, P.B.: A dataset and taxonomy for urban sound research. In: Proceedings of the 22nd ACM International Conference on Multimedia (2014)
10. Ellis, D.P.W.: Detecting alarm sounds, pp. 59–62 (2001)
11. Carmel, D., Ariel, Y., Yair, M.: Detection of alarm sounds in noisy environments. In: 2017 25th European Signal Processing Conference (EUSIPCO). IEEE (2017)
12. Padhy, S.: Emergency signal classification for the hearing impaired using multi-channel convolutional neural network architecture. In: 2019 IEEE Conference on Information and Communication Technology. IEEE (2019)
13. Zhang, H.Y.: mixup: Beyond empirical risk minimization. arXiv preprint [arXiv:1710.09412](https://arxiv.org/abs/1710.09412) (2017)
14. Tran, V.T., Tsai, W.H.: Acoustic-based emergency vehicle detection using convolutional neural networks. *IEEE Access* **8**, 75702–75713 (2020)
15. Marchegiani, L., Paul, N.: Listening for sirens: locating and classifying acoustic alarms in city scenes. arXiv preprint [arXiv:1810.04989](https://arxiv.org/abs/1810.04989) (2018)
16. Ronneberger, O., Fischer, P., Brox, T.: U-Net: convolutional networks for biomedical image segmentation. In: Navab, N., Hornegger, J., Wells, W.M., Frangi, A.F. (eds.) MICCAI 2015. LNCS, vol. 9351, pp. 234–241. Springer, Cham (2015). https://doi.org/10.1007/978-3-319-24574-4_28
17. Ellis, D.P.W.: Gammatone-like spectrograms (2009). <http://www.ee.columbia.edu/~dpwe/resources/matlab/gammatonegram>
18. Ministero dei Trasporti: D.M. 17.10.1980 (G.U. n.310 del 12.11.1980)
19. Smith, J.: Doppler simulation and the Leslie. In: Proceedings of the International Conference on Digital Audio Effects, Hamburg (2002)

20. McFee, B.: librosa: Audio and music signal analysis in python. In: Proceedings of the 14th Python in Science Conference, vol. 8 (2015)
21. Kingma, D.P., Jimmy, B.: Adam: a method for stochastic optimization. arXiv preprint [arXiv:1412.6980](https://arxiv.org/abs/1412.6980) (2014)
22. Font, F., Gerard, R., Xavier, S.: Freesound technical demo. In: Proceedings of the 21st ACM International Conference on Multimedia (2013)

Pattern Recognition



Cucumber Disease Recognition Based on Depthwise Separable Convolution

Xianfeng Wang, Zhen Wang, and Shanwen Zhang^(✉)

Department of Information Engineering, XiJing University, Xi'an 710123, China
wjdw716@163.com

Abstract. Cucumber disease seriously affects the yield and quality of cucumber planting, so quickly and accurately identifying the type of cucumber disease is the premise of cucumber disease control. In view of the complexity of feature extraction in existing cucumber disease recognition methods based on disease leaf image, and the vulnerability of extracted features to the diversity of disease leaf image, light and background, a cucumber disease recognition method based on depthwise separable convolutional network was proposed. This method can automatically obtain the classification features of the image of disease leaf, which overcomes the shortage of the existing crop disease recognition methods that need to extract the classification features manually, and the recognition rate has been greatly improved. The method was applied to the cucumber leaf disease data set and the average recognition accuracy reached 99.23%. The results show that this method has high recognition accuracy and can provide reference for other crops.

Keywords: Leaf image of disease · Cucumber disease identification · Convolutional neural networks (CNNs) · Depthwise separable convolution (DWSC)

1 Introduction

Cucumber is one of the most important vegetable crops in the world. Cucumber downy mildew, powdery mildew and fusarium wilt are the three major diseases of cucumber production in China. Timely and accurate identification of cucumber diseases is of great significance for reducing loss, stabilizing yield and ensuring quality. Studies have shown that many disease symptoms are usually found in disease leaves. Different kinds of cucumber diseased leaves have their own characteristics of color, texture and shape. The disease types can be determined by observing the image of cucumber disease leaves. The traditional methods of disease identification based on the image of disease leaf have achieved good results, but these methods need more complicated processing and recognition process of disease image [1, 2]. Under normal circumstances, cucumber leaves of different kinds will show different forms, and change with time, without fixed shape, so cucumber disease recognition based on disease leaf image is still a challenging research topic [3, 4].

With the continuous development of big data, machine learning, artificial intelligence and other technologies, people are more and more able to realize the value of big

data. The data-driven concept has also been gradually applied in various fields, and the use of data to drive decision-making and product intelligence has been continuously realized. In recent years, Convolutional Neural Networks (CNNs) has achieved great success in image recognition, semantic segmentation, target detection and other fields [5, 6]. Because of its strong ability to represent image features, more and more scholars have applied CNNs in the field of agriculture and achieved a high recognition rate [7, 8]. Brahimi [9] et al. used the improved convolutional neural network to identify the tomato leaf diseases, replaced the traditional convolutional neural network's Softmax classifier with an SVM classifier, and extracted the input image features in layers using the cascade network architecture during the training process, so as to obtain the deeper semantic features of the image. The average identification accuracy reached 98.6% in the tests of identifying different tomato diseases. Yang et al. [17] trained a regional convolutional neural network model by using images of rice disease in multiple natural scenes. During the construction of the model, the local receptive field of the original convolutional kernel is enlarged by using void convolution, and the full connection layer of the original convolutional neural network is replaced by the global pooling layer. The average identification accuracy of 10 common rice diseases was 95.48%. The experimental results show that it is effective and feasible to use CNNs for crop disease image classification. The network structure of CNNs is mainly constructed by alternating repetition of the convolutional layer and the lower sampling layer. The convolutional layer is used to extract the local features of the input neuron data, and the lower sampling layer is used to scale and map the data extracted from the upper layer to reduce the amount of training data, so that the extracted features have the invariability of scaling. Generally speaking, the convolution kernel of different scales can be selected to extract multi-scale features, so that the extracted features have the invariance of rotation and translation. The input image is convolved with the kernel that can be learned, and the data after the convolution is obtained through the activation function to obtain a feature graph. The feature graph of the convolutional layer can be obtained by combining multiple input graphs, but the convolution kernel parameters of the same input graph are consistent, which is also the significance of weight sharing. The initial value of the convolution kernel is not randomly set, but is pre-set through training or according to certain standards, such as preprocessing with Gabor filter according to biological visual features. The lower sampling layer enhances the scale invariance by reducing the spatial resolution of the network. It avoids the complicated feature extraction and image reconstruction in traditional recognition algorithms. The observation characteristics obtained by the local receptive field method are independent of translation, scaling and rotation. In the convolution phase, the weight sharing structure is used to reduce the number of weights and thus the complexity of the network model, which is more obvious when the input feature map is a high-resolution image. However, generally speaking, CNNs model has a large number of parameters, a large amount of computation, and a high requirement for the use of equipment, resulting in poor popularity. Instead of standard convolution, the method combining depthwise separable convolution and convolution can greatly reduce the number of parameters of the model, accelerate the convergence, improve the recognition accuracy, and obtain a device model with small number of parameters and calculation, which is suitable for mobile devices and resource-limited devices. Under normal circumstances,

cucumber leaves of different kinds will show different forms, and change with time, without fixed shape, so cucumber disease recognition based on disease leaf image is still a challenging research topic. In order to solve the problems of the existing cucumber disease identification methods, such as heavy computation and complex feature extraction, a cucumber disease identification method based on depthwise separable convolution was proposed, and the experimental verification was carried out on the database of six kinds of cucumber disease leaf images.

2 Depthwise Separable Convolution (DWSC)

The traditional CNN uses large-scale convolution kernel, such as the 11×11 convolution kernel in AlexNet. Although the receptive field is large, the parameters of the model are also greatly increased. In the GoogleNet model, several cascade structure of small size convolution kernel in 3×3 are used to keep the same receptive field to the original image, at the same time, the parameters of the model are greatly reduced, the depthwise of the network is increased, and the nonlinear expression ability of image features is enhanced. Since the traditional convolution kernel acts on each channel of the input eigengraph, the computation is still too large. Howard et al. [26] used DWSC to construct the CNN so that it can also operate efficiently at the mobile end. The idea of DWSC is to divide the traditional convolution operation into two steps: first, one-to-one two-dimensional convolution is carried out for each channel of the input eigengraph to reduce the parameter calculation, which is called depth-wise convolution; then the traditional convolution (three-dimensional convolution) operation is carried out with 1×1 size convolution kernel to combine the characteristics of each channel, also known as point-wise convolution. DWSC is refers to the standard convolution is decomposed into a deep convolution and a 1×1 standard convolution (point by point convolution). By deep convolution corresponds to the characteristic picture of each input channel, 1×1 point convolution is responsible for the fused characteristics were extracted by depth convolution. Separation by feature extraction and feature fusion can effectively reduce the computational complexity and capacity model. Figure 1 shows the standard convolution and depth of separable convolution structure. The structure of DWSC is shown in Fig. 1.

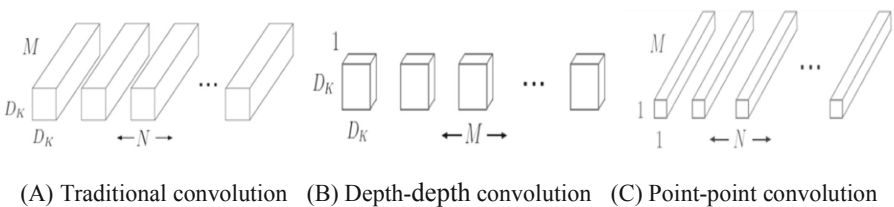


Fig. 1. The structures of standard convolution and DWSC

Assuming that the size of the input characteristic graph is $D_f \times D_f$, the number of channels is M , and the size of the convolution kernel is $D_k \times D_k$, N in total, then the calculation cost of the traditional convolution and DWSC is shown in Eq. (1) and Eq. (2), respectively.

$$D_f \times D_f \times M \times N \times D_k \times D_k \tag{1}$$

$$D_f \times D_f \times M \times D_k \times D_k + D_f \times D_f \times M \times N \tag{2}$$

Then, the ratio of computation cost of DWSC to the traditional convolution is

$$\frac{D_f \times D_f \times M \times D_k \times D_k + D_f \times D_f \times M \times N}{D_f \times D_f \times M \times N \times D_k \times D_k} = \frac{1}{N} + \frac{1}{D_k \times D_k} \tag{3}$$

It can be seen that the reduction of DWSC computation cost is related to the output channel N and the convolution kernel size $D_k \times D_k$ used. In practice, the 3×3 -size convolution kernel is generally used in the deep separable convolution. If the output channel is 64, the calculation cost of the deep separable convolution is only 0.126 times that of the traditional convolution parameters. The structure of the depthwise separable convolution is shown in Fig. 2C and D. Assume that the size of the input feature maps is $D_f \times D_f$, the number of channels is M , and the size of the convolution kernel is $D_M \times D_M$, which contain N convolution kernels.

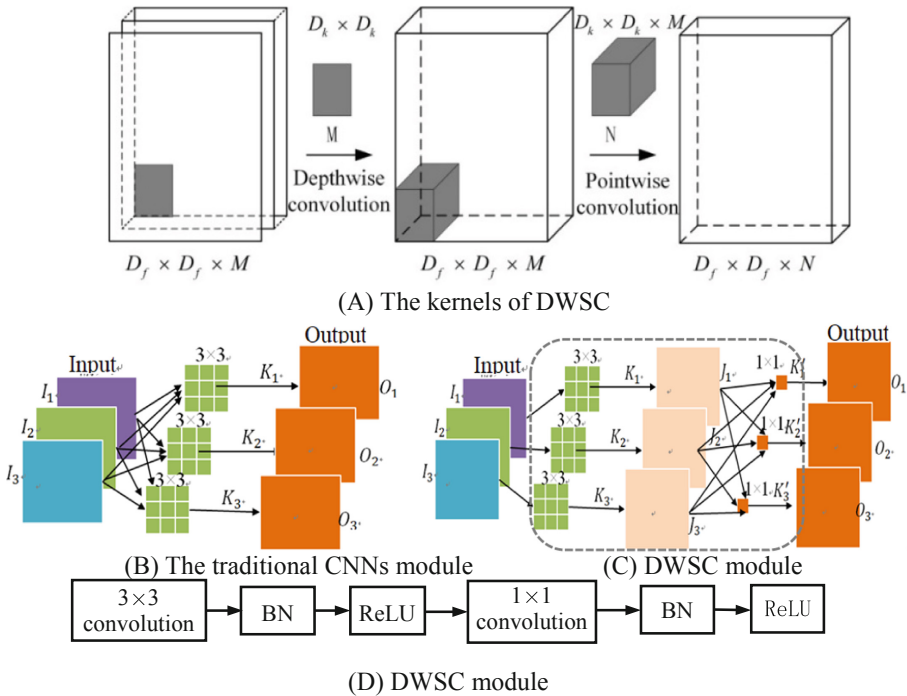


Fig. 2. The structures of traditional CNNs model and DSCNNs

Because the number of input channels is small, the expression ability of the model feature map to image features is weak, so this paper will expand the number of input channels in DWSC to enhance the nonlinear mapping ability of the model and improve the accuracy of the model.

The convolution of DWSC can be expressed as:

$$\text{Conv}_{\text{Deep}}(W, y)_{(i,j)} = \sum_{k,l}^{K,L} W_{(k,l)} \odot y_{(i+k,j+l)}, \text{Conv}_{\text{point}}(W, y)_{(i,j)} = \sum_m^M W_{(k,l)} \odot y_{(i,j,m)} \quad (4)$$

where \odot represents the multiplication of corresponding elements.

The separation convolution of DWSC is obtained by combining depth-by-depth convolution and point-by-point convolution:

$$\text{Conv}_{\text{DWSC}}(W_p, W_d, y)_{(i,j)} = \text{Conv}_{\text{point}(i,j)}(W_p, \text{Conv}_{\text{deep}(i,j)}(W_d, y)) \quad (5)$$

In DWSC, the fully connected layer is replaced with global average pooling layer. Global average pooling (GAP) layer enforces direct correspondences between feature maps and categories. In this way the feature maps can be intuitively interpreted as categories confidence maps. Furthermore, there is no parameter to optimize in GAP layer; thus overfitting is avoided. We can see that GAP layer takes the average value of each feature map which can be regarded as confidence value for each category, and the resulting vector is fed directly into the Softmax function to get the probability distribution among sentiment categories.

In DWSC, each layer is faced with the situation that the distribution of input changes with training, so each middle layer needs to constantly adapt to the changes of its input, resulting in the network becomes difficult to train. By standardizing the mean value and variance of the input, the normalized layer enables each layer to learn a more stable input distribution, ensuring that the network can use a larger learning rate, thus improving the training speed of the network and the network expression ability. Batch Normalization (BN) performs global normalization along the batch dimension N of the sample. When the input distribution changes, the previously calculated data distribution may also change, resulting in inconsistent weight training at each layer of the network.

3 Cucumber Disease Recognition Method

Taking the input image size 384×384 as an example, the specific parameters of each layer of the model structure shown in Fig. 2C are as follows: r is the width coefficient, and Depth-wise residuals layer is the residual block composed of depthwise separable convolutions. The Down sample layer is the lower sampling layer, which is composed of the Max pooling layer and the common convolution (Conv) layer. The step size is 2. The size of the pooling kernel of the Max pooling layer is 2×2 , and the size of the Conv kernel is 3×3 . The output of the lower sampling layer consists of the superposition of the characteristic graphs of the pooling layer and the convolution layer.

With the Down sample layer 1 as an example, the 32 output channels is composed of the superposition of the 3 channels with the pooling core of 2×2 and the 29 channels with the Conv kernel of 3×3 . Up sample layer is the upper sampling layer, using the 2×2 -size transposition convolution with step size of 2.

In general, CNNs uses Softmax as the optimization objection to train the network model. Softmax's loss function optimizes the difference between categories, but ignores the intra-class compactness, resulting in a larger classification error. To solve this problem, a central loss function is introduced to optimize class compactness to reduce class variation. Combining with the Softmax loss function and the center loss function, the training network model can simultaneously increase the inter-class difference and reduce the intra-class change, so that the model can learn the discriminative depth feature. Softmax loss function is defined as follows:

$$L_S = - \sum_{i=1}^m \log \exp(W_{y_i}^T x_i + b_{y_i}) / \sum_{j=1}^n \exp(W_j^T x_i + b_j) \quad (6)$$

where $x_i \in \mathbb{R}^d$ is the i -th depth feature belonging to the category y_i , d is the dimension of the feature, $W \in \mathbb{R}^{d \times n}$ is the weight of the last full connection layer, $b \in \mathbb{R}^n$ is the bias term, m and n represent the batch and category numbers, respectively.

Combined with Softmax loss function and center loss function, the training network model can effectively increase the inter-class difference and reduce the intra-class change, so that the model has higher robustness and recognition accuracy. The loss function L can be trained by Stochastic gradient descent (SGD). The model hyper-parameters of the model are trained to minimize the cost function.

4 Experiments and Analysis

In order to verify the performance of DWSC based cucumber disease identification method, we used the image database of cucumber disease leaves constructed by agricultural demonstration park in Yangling district, Shaanxi province for experiment. Using simple camera devices, the images were collected under several conditions depending on the time (e.g., illumination), season (e.g., temperature, humidity), and place where they were taken (e.g., greenhouse) with various types of data, including:

Leaf images with various resolutions. Leaf images at early, medium, and last infection status. Leaf images containing different infected areas in the plant (e.g., stem, leaves, fruits, etc.). Different cucumber leaf sizes. Leaf images surrounding the plant in the greenhouse, etc. The database contains 1,200 images of the leaves of the six common cucumber diseases of scab, powdery mildew, downy mildew, anthrax, keratinosis and bacterial keratinosis, 200 per class. DWSC is trained by A large number of images. So, we augmented the original by the transforms as follows.

Randomly select Crop Center on the original image of the 256×256 size, and use the 224×224 size window to capture it, then extend the screenshot to 256×256 so as to unify the image input size.

A 30% Gauss noise is added to the original image with an offset of 0.2 and a standard deviation of 0.3.

The original image RGB components are increased by 20%, the contrast is increased by 30%, the sharpness is decreased by 10%.

The original image is radially blurred by rotation blur and scaling blur respectively. The rotating fuzzy unit is 10, and the scaling fuzzy unit is 30. They are used to simulate the effects of quickly rotating or moving cameras to achieve radiation like functions.

From the above process, each original is augmented to produce 10 corresponding enhanced images respectively. Finally the imbalanced standard image set containing 12000 images, 2000 per disease.

The 6-fold cross validation method is selected for the experiment, that is, 10,000 samples were randomly selected as the training sample set and 2000 samples were selected as the test sample set. Through the input of color disease leaf images with the dimension of the three channels of $128 \times 128 \times 3$, the convolution template was selected as $9 \times 9 \times 3$, and the pooling layer was selected as 2×2 maximum pooling method for the down sampling. In the network construction, the linear correction unit (ReLU) is used as the output function of each convolutional layer. In the pooling layer, dropout method is adopted to randomly disconnect network nodes to prevent network overfitting. The random gradient drop method is used to calculate the DCNN parameters layer by layer. The number of neurons in the full connection layer is about 1000. In the output layer, Softmax excitation function was used to obtain 6 recognition results, corresponding to the prediction probability of 6 disease image categories; The momentum gradient descent method of adaptive learning rate was used to optimize the model. Parameter setting: learning rate is 0.01, learning rate is reduced to 0.001 after 1000 iterations, training target is 0.001, weight attenuation coefficient is 0.001, maximum training times is 3000.

In order to demonstrate the effectiveness of the proposed algorithm, the proposed method was compared with four existing methods for cucumber disease identification: Image Processing Technology (IPT) [1], global-local singular value decomposition (GLSVD) [3] and image processing (IP) [7]. The proposed method does not need to extract the disease spots from the image of disease leaf, and directly uses the color image of disease leaf to identify the disease. The other four methods firstly used histogram threshold segmentation to remove the background, then used the maximum inter-category variance method to segment the disease spots [4, 5], and finally used the disease spot image to identify the disease. All algorithms were simulated by MATLAB R2013a, and the experimental platform was a workstation based on Win7 operation system (Intel(R) Xeon(R) e5-2650 v2 CPU and 32 Gb memory). The recognition results are shown in Table 1.

Table 1. The recognition rates and variances on five methods

| Method | IPT | GLSVD | IP | DWSC |
|----------------------|------------------|------------------|------------------|------------------|
| Recognition rate (%) | 78.14 ± 1.84 | 87.31 ± 1.42 | 84.26 ± 2.06 | 96.12 ± 2.03 |
| Training time (h) | 0.25 | 1.5 | 17 | 62 |
| Recognition time (s) | 9.3 | 3.8 | 5.4 | 2.5 |

As can be seen from Table 1, the recognition rate of this method is very high. The reason is that the classification features extracted by the traditional disease identification method based on feature extraction are sensitive to the rotation and illumination changes of the image of disease leaves, so it is not easy to extract the best classification features. However, the deep learning model can be used to learn the invariable features of image rotation and illumination. Through experimental comparison, the cucumber disease classification model proposed in this paper has obvious advantages in large database and can be applied to the winter jujube disease identification system based on the Internet of things.

5 Conclusions

Aiming at the problem of cucumber disease identification based on disease leaf image, a cucumber disease identification method based on DWSC is proposed, and the experimental results showed the effectiveness of the method. Compared with traditional crop disease identification methods, this method can directly input a two-dimensional color disease leaf image into DWSC, and obtain the disease type identification results at the output end. Its advantage is that it does not need complicated spot segmentation and feature extraction process, and feature extraction and pattern recognition are completely put into a network. The core of this method is the structural design of DWSC and the solution of network. Therefore, how to reduce the training time and avoid the occurrence of over-fitting state is the direction of further research in the future.

References

1. Dong, P., Wang, X.: Recognition of greenhouse cucumber disease based on image processing technology. *Open J. Appl. Sci.* **3**(1), 27–31 (2013)
2. Gao, R., Wu, H.: Nearest neighbor recognition of cucumber disease images based on Kd-tree. *Inf. Technol. J.* **12**(23), 7385–7390 (2013)
3. Zhang, S., Wang, Z.: Cucumber disease recognition based on Global-Local Singular value decomposition. *Neurocomputing* **205**, 341–348 (2016)
4. Wei, Y., et al.: A study of image processing on identifying cucumber disease. In: Li, D., Chen, Y. (eds.) CCTA 2011. IAICT, vol. 370, pp. 201–209. Springer, Heidelberg (2012). https://doi.org/10.1007/978-3-642-27275-2_22
5. LeCun, Y., Bengio, Y., Hinton, G.: Deep learning. *Nature* **521**(7553), 436–444 (2015)
6. Schmidhuber, J.: Deep learning in neural networks: an overview. *Neural Networks* **61**, 85–117 (2015)
7. Zhong, G., Wang, L.-N., Ling, X., et al.: An overview on data representation learning: from traditional feature learning to recent deep learning. *J. Finan. Data Sci.* **2**(4), 265–278 (2016)
8. Lu, Y., Yi, S., Zeng, N.: Identification of rice diseases using deep convolutional neural networks. *Neurocomputing* **267**, 378–384 (2017)
9. Brahimi, M., Boukhalifa, K., Moussaoui, A.: Deep learning for tomato diseases: classification and symptoms visualization. *Appl. Artif. Intell.* **31**(4), 299–315 (2017)
10. Wu, Y., He, K.: Group normalization. *Int. J. Comput. Vis.* (2018). https://doi.org/10.1007/978-3-030-01261-8_1



Noise Robust Illumination Invariant Face Recognition via Contourlet Transform in Logarithm Domain

Guangyi Chen¹(✉) and Wenfang Xie²

¹ Department of Computer Science and Software Engineering,
Concordia University, Montreal, QC H3G 1M8, Canada
guangyi_chen@hotmail.com

² Department of Mechanical and Industrial Engineering,
Concordia University, Montreal, QC H3G 1M8, Canada
wfxie@me.concordia.ca

Abstract. Face recognition under varying lighting conditions is an important topic in many real-life applications. In this paper, we propose a novel algorithm for illumination invariant face recognition. We first convert the face images to the logarithm domain, which makes the dark regions brighter. We then use contourlet transform to generate face images that are approximately invariant to illumination change and use collaborative representation-based classifier (CRC) to classify the unknown faces to one known class. We set the approximation subband and a few highest frequency contourlet coefficient subbands to zero values, and then perform the inverse contourlet transform to generate illumination invariant face images. Experimental results show that our proposed algorithm outperforms two existing methods for the Extended Yale Face Database B for high noise levels. Nevertheless, our new method is not as good as existing methods for low noise levels. In addition, our new method is comparable to existing methods for the CMU-PIE face database.

Keywords: Face recognition · Contourlet transform · Collaborative Representation-based Classifier (CRC) · Invariant features · Pattern recognition · Computer vision

1 Introduction

Face recognition is an active research topic in such applications as commercial, military, and public security. We review a lot of existing face recognition algorithms here. Eigenfaces [1, 2] are a popular method for face recognition that computes the principal components of face images. This method creates a mathematical model that best describes a face by extracting the most relevant information contained in the face images. He et al. [3] proposed Laplacianfaces, where the face images are analysed by using locality-preserving projections. Wright et al. [4] proposed robust face recognition by means of sparse representation. They investigated the problem of automatically recognizing human faces from frontal views with varying expression, illumination, occlusion, and disguise. They treated the classification problem as recognizing among

multiple linear regression models, and their new theory from sparse signal representation offers the key to addressing this problem. Lee et al. [5] investigated face recognition in variable lighting conditions. They arranged physical lighting in such a way that the acquired images can be used as the basis vectors of a low-dimensional linear space. Du and Ward [6] studied a region-based image enhancement method for face classification. However, this method produces defects on the boundary between different image regions. Yang et al. [7] studied a new wavelet-based method for face recognition. They revealed that nonlinear approximation preserves more information in an image than linear approximation. Chen et al. [8] investigated illumination normalization for robust face classification by first performing logarithm transform to the face images and then performing discrete cosine transform (DCT) to the logarithm images (LOG-DCT). They set the low-resolution DCT coefficients to zero and then perform inverse DCT to obtain illumination invariant face maps for classification. Ruiz-Pinales et al. [9] proposed a translation-invariant support vector machines (SVM) for face image recognition. They presented a novel method for incorporating global translation invariance in SVM. Even though other methods incorporated a feature extraction stage, they scaled the image and then recognized it by using a modified SVM classifier. Translation invariance is obtained by replacing dot products between pattern images with the maximum cross-correlation value. Ahonen et al. [10] investigated face recognition with local binary patterns (LBP). In their paper, they proposed a novel and fast face image representation by means of LBP texture features. They divided the face images into several regions, extracted the LBP feature distributions, and then concatenated into a feature vector as a face descriptor. Xie et al. [11] investigated normalization of face illumination based on large and small-scale features. This method achieved particularly good recognition results for illumination invariant face recognition. Lai et al. [12] investigated a face classification method by means of multiscale logarithm difference edge-maps under varying lighting conditions. They used a logarithm difference model that eliminates light intensity from pixels in a neighbourhood. It is better than holistic image decomposition methods such as LOG-DCT and LTV. Zhang et al. [13] studied face classification by using gradient faces under varying illumination conditions. Nevertheless, these gradient faces are extremely sensitive to noise. Chen et al. [14] presented a log total variation model (LTV) for face recognition under variable lighting conditions. Nevertheless, it is more complex than other methods because it needs to solve differential equations. Chen et al. [15–17] also proposed several novel methods for illumination invariant face recognition by means of dual-tree complex wavelet transform (DTCWT) and novel filters. In addition, Chen et al. [18, 19] investigated hyperspectral face recognition by using log-polar Fourier features and other features. Both methods achieved particularly good classification results when compared to state-of-the-arts methods published in the literature.

In this paper, we develop a novel algorithm for face recognition by means of contourlet transform to generate illumination invariant face images, and by using collaborative representation-based classifier (CRC) to classify the faces. Our novel method improves upon existing methods in most testing cases for both the Extended Yale Face Database B and the CMU-PIE illumination face database. In addition, our proposed algorithm does not require any modelling, and they can be applied directly to any face image without any lighting assumption or any prior information on 3D face geometry.

2 The Proposed Method

We briefly introduce the Lambertian reflectance theory, the contourlet transform, and the CRC classifier here. Based on the Lambertian reflectance theory [20], the intensity image can be modeled as

$$I(x, y) = R(x, y)L(x, y) \quad (1)$$

where R is the reflectance and L is the illumination. Because R depends only on the surface material of the person, it is the intrinsic representation of a face image. The very convenient solution is to convert the face intensity image to the logarithm domain. As a result, the multiplication in the above equation becomes addition:

$$\log I(x, y) = \log R(x, y) + \log L(x, y) \quad (2)$$

Hence, the face recognition problem is easier than before.

Do and Vetterli [21] proposed contourlet transform for efficiently representing 2D images. We all know the major limitations of commonly used separable extensions of one-dimensional transforms, e.g., the Fourier and wavelet transforms, in capturing the geometry of image edges. Do and Vetterli introduced a 2D transform that can capture the intrinsic geometrical structure, which is a key in visual information. The important challenge to explore geometry in images is from the discrete nature of the data. As a result, unlike other methods, e.g., curvelets, that first develop a transform in the continuous domain and then discretize for sampled data, their method begins with a discrete-domain construction and then studies its convergence to an expansion in the continuous domain. Particularly, Do and Vetterli constructed a discrete-domain multiresolution and multidirection expansion using nonseparable filter banks, in much the same way that wavelets were derived from filter banks. This construction produces a flexible multiresolution, local, and directional image expansion using contour segments and it is called the contourlet transform. The discrete contourlet transform has a fast-iterated filter bank algorithm that requires $O(N)$ operations for N -pixel images. Furthermore, they generated a precise link between the developed filter bank and the associated continuous domain contourlet expansion by means of a directional multiresolution analysis framework. They demonstrated that with parabolic scaling and sufficiently directional vanishing moments, contourlets achieved the optimal approximation rate for piecewise smooth functions with discontinuities along twice continuously differentiable curves. Finally, they conducted some experiments to demonstrate the potential of contourlets in several image processing tasks.

It is believed that the l_1 - norm sparsity constraint on coding coefficients plays an important role in the success of sparse representation-based classifier (SRC), whereas the use of all training samples to collaboratively represent the query sample is ignored. In [22], the authors discussed how SRC works, and showed that the collaborative representation mechanism used in SRC is more important to its success of face classification. The SRC is a special case of the CRC, which has various instantiations by applying different norms to the coding residual and coding coefficients. Furthermore, the l_1 or l_2 norm characterization of coding residual is related to the robustness of CRC

to outlier facial pixels, and in the meantime the l_1 or l_2 norm characterization of coding coefficient is related to the degree of discrimination of facial features. Experiments were performed to show the accuracy and efficiency of the CRC for face recognition.

Motivated by LOG-DCT [8], we propose a new method for illumination invariant face recognition in this paper. Because of different illumination conditions, the acquired face images can be very dark, which makes existing face recognition methods perform worse. To increase recognition rate, we intend to elevate the dark region and suppress bright region by using the logarithm transform. We perform contourlet transform to these logarithm images and set the approximation subband, and a few highest frequency contourlet subbands to zero values. An inverse contourlet transform will generate our enhanced face images, which are approximately invariant to illumination. The reason why we choose contourlet transform is because this transform can represent edges more accurately. Figure 1 shows the different stages of our illumination invariant face recognition algorithm: (a) the input face image, (b) the logarithm of the input image, (c) the contourlet transform on the logarithm image, (d) the output illumination invariant face generated by inverse contourlet transform.

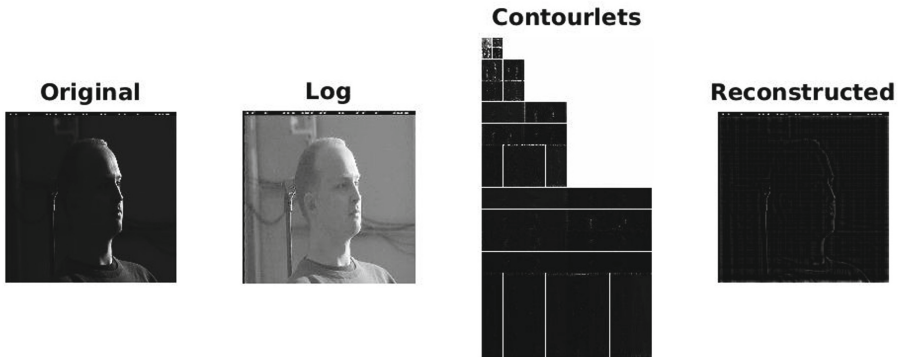


Fig. 1. The different steps of our new face recognition algorithm LOG-CONTOURLETS: (a) the input face image, (b) the logarithm of the input image, (c) the contourlet transform on the logarithm image, (d) the output illumination invariant face image generated by inverse contourlet transform.

We present the steps of our new algorithm LOG-CONTOURLETS for illumination invariant face recognition by using the contourlet transform. This algorithm can be described as follows:

Algorithm LOG-CONTOURLETS

- Step 1. Initialization: $J = [0, 2, 3, 4]$.
- Step 2. Take the logarithm transform of the intensity image $I(x, y)$ as Eq. (2).
- Step 3. Normalize image $\log I(x, y)$ to the range $[0., 255]$, denoted as IM .
- Step 4. Perform the forward contourlet transform to IM for J decomposition levels, denote it as $CIM = \text{CONTOURLETS}(IM, J)$.

- Step 5. Set the approximation subband and a few highest frequency contourlet coefficient subbands to zero values.
- Step 6. Conduct inverse contourlet transform to the output image from Step 5 to obtain face image D .
- Step 7. Normalize D so that it has zero mean and unit variance.
- Step 8. Set $E = D^k$, where $k = 0.69$ is a constant.
- Step 9. Use CRC to classify the resulting face image to one of the known classes.

The contributions of this paper can be summarized here. In our new algorithm, we perform logarithm transform to make dark regions brighter and we use contourlet transform to generate illumination invariant face images. This combination of logarithm transform with the contourlet transform is new to our best knowledge. Our method is easy to implement, and it yields higher recognition rates than two existing methods for most testing cases.

3 Experimental Results

In this paper, we perform experiments with the Extended Yale Face Database B [5] and the CMU-PIE illumination face database [23]. The Extended Yale B database contains face images of 38 subjects in 64 diverse lighting conditions: from normal to extremely badly illuminated. There exists only one ideal image for each person. There are 2414 available images in total. We cropped and fixed the face images to have 192×168 pixels. We take one well-lighted face image as the single reference and take all the rest available $2414 - 38 = 2376$ images as test samples. The faces are divided into 5 subsets according to angles between the light source direction and the camera axis (Table 1):

Table 1. The five subsets of the Extended Yale Face Database, their corresponding angles, and the number of faces in each subset.

| Subsets | Angles | Number of faces |
|----------|--|-----------------|
| Subset 1 | $1^\circ \leq \text{angle} \leq 12^\circ$ | 7×38 |
| Subset 2 | $13^\circ \leq \text{angle} \leq 25^\circ$ | 12×38 |
| Subset 3 | $26^\circ \leq \text{angle} \leq 50^\circ$ | 12×38 |
| Subset 4 | $51^\circ \leq \text{angle} \leq 77^\circ$ | 14×38 |
| Subset 5 | $78^\circ \leq \text{angle}$ | 19×38 |

The degree of variation gets higher from Subset 1 to Subset 5. Figure 2 shows the five subsets for one subject.

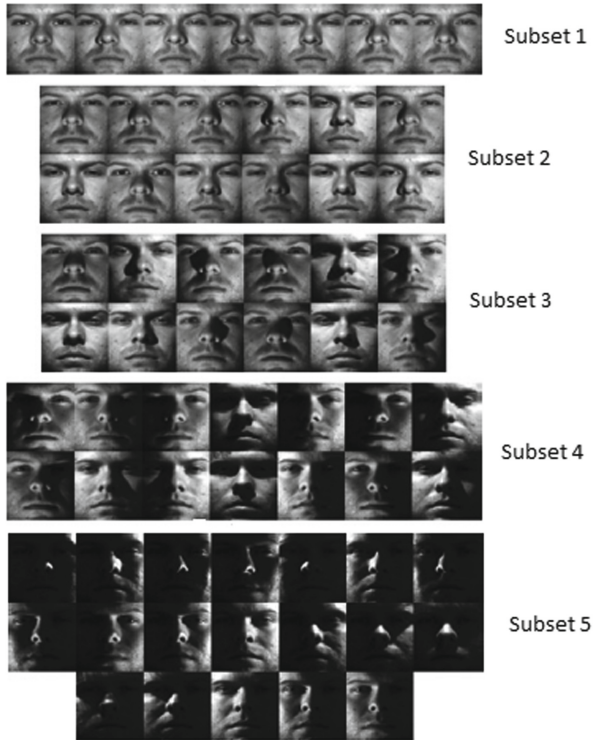


Fig. 2. The five subsets of the Extended Yale-B face database.

The CMU Pose, Illumination and Expression (PIE) database has 41368 face images from 68 persons. Every person contains images captured for 13 poses and 43 illumination conditions. We only select the images that focuses on illumination variations on light intensity and direction in frontal view. There exist 68 persons in each 43 images yielding a total of 2924 images. Figure 3 shows different original face images under different lighting condition in this database.

For both face databases, we select only one frontally lit face image in each class for training and the remaining face images for testing. We convert every face image to the logarithm domain and normalize it to have pixel values to fall in the range of $[0, 255]$. We then perform contourlet transform to these normalized face images for several scales and set the contourlet coefficients to zero for a few high frequency subbands and the approximation subband. An inverse contourlet transform will generate the enhanced faces, which are approximately invariant to illumination changes and hence are good for noisy face recognition.



Fig. 3. An example of the face images under different lighting condition of the CMU-PIE illumination face database.

We conduct experiments to test the performance of our proposed algorithm for different noise levels. In our experiments, the noise standard deviation σ_n ranges from 5 to 40. The noisy face images are generated by adding Gaussian white noise to the noise-free face images:

$$B = A + \sigma_n I, \quad (3)$$

where I obeys Gaussian distribution $N(0, 1)$ with 0 mean and unit variance. Figure 4 shows the noise-added face images for σ_n ranging from 5 to 40. We compare our proposed algorithm with LOG-Discrete Wavelet Transform (LOG-DWT) and LOG-DCT [8] for both extended Yale face database B and CMU-PIE face database. Table 2 shows the correct classification rates (%) of the proposed method LOG-CONTOURLETS, the LOG-DWT, and the LOG-DCT for face images corrupted by Gaussian white noise. The correct recognition rate is defined as the percentage of faces that are recognized correctly regarding their true class labels. For extended Yale face database B, our proposed algorithm outperforms both LOG-DWT and LOG-DCT for higher noise levels, but our new algorithm is not as good as LOG-DCT for low noise levels. For the CMU-PIE face database, all algorithms achieve perfect recognition results (100%). In conclusion, our new algorithm proposed in this paper is very robust to Gaussian white noise for illumination invariant face recognition.

For our proposed method LOG-CONTOURLETS, we consider four testing cases: (0*000), (0**00), (0***0), and (0****). We perform the contourlet transform to the Log face images and we obtain one approximation subband and four high frequency subbands. In the above notation, the '0' means to set the subband to 0 values and the '*' means to keep the subbands unchanged. For example, (0*000) means the approximation subband is set to 0 values, the next subband is unchanged, and the remaining three subbands are set to 0 values. The meanings of the other three testing cases can be understood easily.

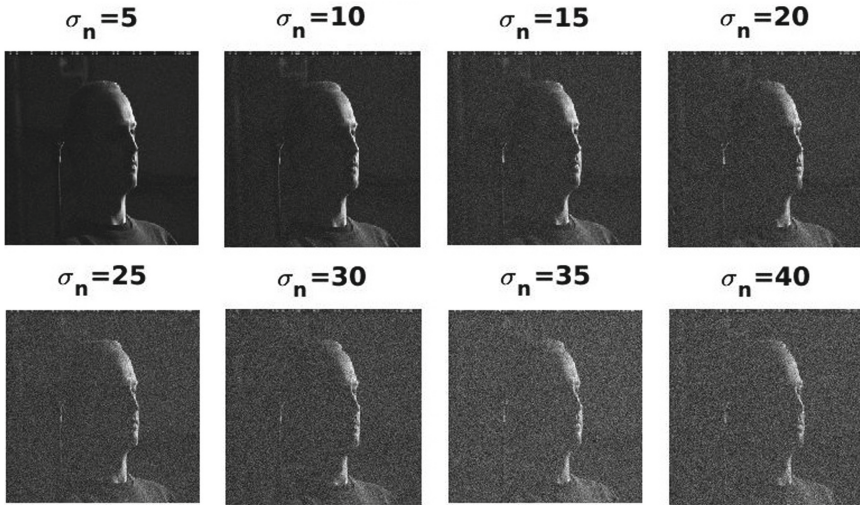


Fig. 4. An example of the noisy face images with different noise levels.

Table 2. The correct classification rates (%) of the proposed method LOG-CONTOURLETS, the LOG-DWT, and the LOG-DCT [8] for face images corrupted by Gaussian white noise. The best results are highlighted in bold font.

| Databases | Methods | Noise standard deviation (σ_n) | | | | | | | |
|-------------------------------|--------------------------|---|--------------|--------------|--------------|--------------|--------------|--------------|--------------|
| | | 5 | 10 | 15 | 20 | 25 | 30 | 35 | 40 |
| Extended Yale Face Database B | LOG-CONTOUR-LETS (0*000) | 80.65 | 75.98 | 73.68 | 71.84 | 71.04 | 69.95 | 69.18 | 68.54 |
| | LOG-CONTOUR-LETS (0**00) | 84.93 | 81.52 | 79.00 | 77.00 | 75.55 | 74.99 | 74.03 | 73.29 |
| | LOG-CONTOUR-LETS (0***0) | 84.55 | 80.51 | 78.53 | 77.18 | 75.92 | 74.87 | 74.26 | 73.54 |
| | LOG-CONTOUR-LETS (0****) | 84.20 | 80.63 | 78.62 | 77.40 | 76.17 | 75.26 | 74.76 | 74.15 |
| | LOG-DWT | 83.26 | 78.93 | 76.68 | 75.34 | 73.94 | 73.00 | 72.25 | 71.58 |
| | LOG-DCT [8] | 87.28 | 82.28 | 78.85 | 77.17 | 75.85 | 74.59 | 73.94 | 73.53 |
| CMU-PIE | LOG-CONTOUR-LETS (0*000) | 100 | 100 | 100 | 100 | 100 | 100 | 100 | 100 |
| | LOG-CONTOUR-LETS (0**00) | 100 | 100 | 100 | 100 | 100 | 100 | 100 | 100 |
| | LOG-CONTOUR-LETS (0***0) | 100 | 100 | 100 | 100 | 100 | 100 | 100 | 100 |
| | LOG-CONTOUR-LETS (0****) | 100 | 100 | 100 | 100 | 100 | 100 | 100 | 100 |
| | LOG-DWT | 100 | 100 | 100 | 100 | 100 | 100 | 100 | 100 |
| | LOG-DCT [8] | 100 | 100 | 100 | 100 | 100 | 100 | 100 | 100 |

4 Conclusions

In this paper, we have proposed a novel algorithm for face recognition by extracting contourlet faces in logarithm domain. Our new algorithm is relatively invariant to illumination changes in the face images. The CRC is used as a classifier in our algorithm. Our new algorithm is better than two existing algorithms in correct recognition rate for the Extended Yale Face Database B for high noise levels, but it is not as good

as existing methods for low noise levels. Our new algorithm is comparable to existing algorithms for the CMU-PIE illumination face database. Our proposed algorithm is more suitable for recognizing noisy face images with varying illumination.

References

1. Turk, K., Pentland, A.: Eigenfaces for recognition. *J. Cogn. Neurosci.* **3**, 71–86 (1991)
2. Turk, M., Pentland, A.: Face recognition using eigenfaces. In: *Proceedings of. IEEE Conference on Computer Vision and Pattern Recognition (CVPR)*, pp. 586–591 (1991)
3. He, X., Yan, S., Hu, Y., Niyogi, P., Zhang, H.J.: Face recognition using Laplacianfaces. *IEEE Trans. Pattern Anal. Mach. Intell.* **27**, 328–340 (2005)
4. Wright, J., Yang, A.Y., Ganesh, A., Sastry, S., Ma, Y.: Robust face recognition via sparse representation. *IEEE Trans. Pattern Anal. Mach. Intell.* **31**, 210–227 (2009)
5. Lee, K.C., Ho, J., Kriegman, D.: Acquiring linear subspaces for face recognition under variable lighting. *IEEE Trans. Pattern Anal. Mach. Intell.* **27**, 684–698 (2005)
6. Du, S., Ward, R.K.: Adaptive region-based image enhancement method for robust face recognition under variable illumination conditions. *IEEE Trans. Circ. Syst. Video Technol.* **20**, 1165–1175 (2010)
7. Yang, L.H., Bui, T.D., Suen, C.Y.: Image Recognition based on Nonlinear Wavelet Approximation. *Int. J. Wavelets Multiresolut. Inf. Process.* **1**, 151–162 (2003)
8. Chen, W., Er, M., Wu, S.: Illumination compensation and normalization for robust face recognition using discrete cosine transform in logarithm domain. *IEEE Trans. Syst. Man, Cybern. B, Cybern.* **36**, 458–466 (2006)
9. Ruiz-Pinales, J., Acosta-Reyes, J.J., Salazar-Garibay, A., Jaime-Rivas, R.: Shift invariant support vector machines face recognition system. *World Acad. Sci. Eng. Technol.* **16**, 947–951 (2008)
10. Ahonen, T., Hadid, A., Pietikainen, M.: Face description with local binary patterns: Application to face recognition. *IEEE Trans. Pattern Anal. Mach. Intell.* **28**, 2037–2041 (2006)
11. Xie, X., Zheng, W., Lai, J., Yuen, P.C., Suen, C.Y.: Normalization of face illumination based on large and small-scale features. *IEEE Trans. Image Process.* **20**, 1807–1821 (2011)
12. Lai, Z.R., Dai, D.Q., Ren, C.X., Huang, K.K.: Multiscale logarithm difference edge maps for face recognition against varying lighting conditions. *IEEE Trans. Image Process.* **24**, 1735–1747 (2015)
13. Zhang, T., Tang, Y.Y., Fang, B., Shang, Z., Liu, X.: Face recognition under varying illumination using gradient faces. *IEEE Trans. Image Process.* **18**, 2599–2606 (2009)
14. Chen, T., Yin, W., Zhou, X.S., Comaniciu, D., Huang, T.S.: Total variation models for variable lighting face recognition. *IEEE Trans. Pattern Anal. Mach. Intell.* **28**, 1519–1524 (2006)
15. Chen, G.Y.: An experimental study for the effects of noise on face recognition algorithms under varying illumination. *Multimedia Tools Appl.* **78**(18), 26615–26631 (2019). <https://doi.org/10.1007/s11042-019-07810-y>
16. Chen, G.Y., Bui, T.D., Krzyzak, A.: Illumination invariant face recognition using dual-tree complex wavelet transform in logarithm domain. *J. Electr. Eng.* **70**(2), 113–121 (2019)
17. Chen, G.Y., Bui, T.D., Krzyzak, A.: Filter-based face recognition under varying illumination. *IET Biometrics* **7**(6), 628–635 (2018)
18. Chen, G.Y., Li, C.J., Sun, W.: Hyperspectral face recognition via feature extraction and CRC-based classifier. *IET Image Process.* **11**(4), 266–272 (2017)

19. Chen, G.Y., Sun, W., Xie, W.F.: Hyperspectral face recognition using log-polar Fourier features and collaborative representation-based voting classifiers. *IET Biometrics* **6**(1), 36–42 (2017)
20. Horn, B.K.P.: *Robot Vision*. MIT Press, Cambridge (1997)
21. Do, M.N., Vetterli, M.: The contourlet transform: an efficient directional multiresolution image representation. *IEEE Trans. Image Process.* **14**(12), 2091–2106 (2005)
22. Zhang, L., Yang, M., Feng, X.: Sparse representation or collaborative representation: which helps face recognition? In: *IEEE International Conference on Computer Vision*, pp. 471–478 (2011)
23. Sim, T., Baker, S., Bsat, M.: The CMU pose, illumination, and expression database. *IEEE Trans. Pattern Anal. Mach. Intell.* **25**, 1615–1618 (2003)



License Plate Detection and Recognition Technology for Complex Real Scenarios

Zhipeng Li¹(✉), Fei Wang¹, Hamdan Taleb¹, Changan Yuan², Xiao Qin³, Hongjie Wu⁴, Xingming Zhao⁵, and Lijun Zhang⁶

¹ Institute of Machine Learning and Systems Biology, School of Electronics and Information Engineering, Tongji University, Shanghai 201804, China
lizhipengqilu@gmail.com

² Guangxi Academy of Science, Nanning 530025, China

³ School of Computer and Information Engineering,
Nanning Normal University, Nanning 530299, China

⁴ School of Electronic and Information
Engineering, Suzhou University of Science and Technology,
Suzhou 215009, China

⁵ Institute of Science and Technology for Brain Inspired Intelligence (ISTBI),
Fudan University, Shanghai 200433, China

⁶ Collaborative Innovation Center of Intelligent New Energy Vehicle and School
of Automotive Studies, Tongji University, Shanghai 201804, China

Abstract. At present, Automatic License Plate Recognition (ALPR) technology has been widely used in residential parking, high-speed intersection toll stations, roadside illegal parking, smart transportation and other fields. Although automatic license plate technology has been widely used in various fields, at present, whether it is commercial or academic methods, it is to explore the license plate recognition research of approximate frontal images in specific regions or specific countries (such as China, Brazil, and the United States). Aiming at real and complex scenarios, this paper builds a dataset for countries along the Belt and Road (such as Kenya, Nigeria, Togo, Ghana, etc.), called BR-ALPR dataset, designed to ALPR. We use yolov3 to complete the license plate detection. For license plate recognition, we use an improved Convolutional Recurrent Neural Network (CRNN) algorithm, which inserts the Spatial Transformation Network (STN) into the CRNN. In addition, we still use the method of template paste to complete the enhancement of the dataset. Experimental results show that our method is superior to advanced commercial methods for the detection and recognition of license plates in complex real Scenarios.

Keywords: License plate · CRNN · STN · BR-ALPR · Template paste

1 Introduction

Automatic License Plate Recognition (ALPR) has been greatly improved with the development of software and hardware, among which Deep Learning makes the greatest contribution on the software side. Deep learning networks based on Convolutional Neural Networks (CNNs) have been widely used in many fields [1–5]. Many

scholars have also done a lot of research on deep learning [6–9]. The introduction of CNNs has improved accuracy a lot on both image detection and recognition, making it possible for ALPR to be used in more scenarios [10–14]. Some popular CNN frameworks includes Yolo [15], a state-of-the-art, real-time object detection system, and CRNN [16], a Network for Image-based Sequence Recognition which is widely used in Optical Character Recognition (OCR). Combining these mature networks and machines of good configuration, some ALPR system has obtained a better result and been recognized commercially.

While these commercial ALPR perform well in most cases, they are not that good in complex scenarios like tilt, distortion, bad weather, uneven lighting and blurring. Additionally, these systems mainly focus on specific countries, their datasets are limited to specific characters and shape, which cannot cover other parts of the world.

Our system has good performance in most complex scenarios, moreover, it is dedicated to regions along the Belt and Road, which is not explored yet. Our first contribution is the datasets part, we collected huge amount of data from variety of real-time scenarios in different countries, we also generalized some artificially. By applying data augmentation technique to these images, the final datasets are more complete than others. The Second contribution is the integrating Spatial Transformer Networks (STN) [17] with CRNN in detection phase, making the network capable of learning invariance to translation, scale, rotation and more generic warping.

At the OCR stage, we also generalized some character datasets artificially, these characters are processed through affine transformation, perspective transformation and brightness transformation respectively, training on these datasets make the system more robust, achieving very high accuracy in the Belt and Road datasets.

The rest of the paper is organized as follows: Sect. 2 discusses some work related to our own. At the same time, the Sect. 3 presents our BR-ALPR dataset. we introduce the formulation and implementation of our ALPR system in Sect. 4, and finally give the results of experiments in Sect. 5. The last part is the analysis of experimental results and our further research work in the future.

2 Related Work

ALPR system is composed of two tasks, license plate detection and recognition, as our main contribution is the recognition phase and dataset part, we start this section by giving a brief introduction to previous work on detection, then we introduce complete ALPR solutions.

2.1 License Plate Detection

License plate detection is to localize the license plates in the image in the form of bounding boxes. Deep learning methods have been used in many fields to perform well [18–26]. There are also many license plate detection and recognition algorithms based on deep learning. Following is some existing methods. The Deformable Parts Models (DPM) [27] algorithm uses the sliding window technique to run the classifier at evenly spaced positions throughout the image, traversing each region of the image.

This algorithm performs poorly when it comes to calculation cost. DPM cuts out too many small squares in the picture, which convolutional network has to deal with one by one. The R-CNN [28] algorithm uses the idea of Region Proposal, first generating potential bounding boxes in the image, and then running classifiers on these bounding boxes. After classification, the boundary boxes are refined through post-processing to eliminate repeated detection, and the boundary boxes are reextracted according to other objects in the scene. These complex pipelines are slow and difficult to optimize because each individual component must be trained separately. Yolo uses the idea of grid, YOLOv3 [29] split input image into grids on 3 scales in order to achieve the prediction of large, middle and small objects. YOLOv3 adopts a new Darknet-53 structure. Darknet-53 borrows the ideas of Resnet and adds residual module to the network, which is conducive to solving the gradient problem of deep network.

In 1, the authors created a new CNN Network, Warped a Planar Object Detection Network, based on Yolov2 [30]. This network use STN to detect and adjust non-rectangular regions, making it easier to recognize in OCR phase, and Residual Network [31] is added in this network to improve the gradient problem and training speed, which is further improved due to the introduction of mini-batch gradient descent method and the use of ADAM [32] optimizer. As Residual Module is already integrated into Yolov3, this network can be enhanced using Yolov3.

[33] adopts a lightweight and high-performance multi-angle license plate recognition model based on YOLOv2 and makes the following improvements: (1) Increase the number of grids to achieve a good recall rate when recognizing small characters. (2) Increase the number of Anchor box to increase the recall rate. (3) Reduce the number of convolutional layers in YOLOv2 and change the size of the filter, so as to achieve a balance between recall rate and calculation amount. The effect of this literature on more complex scenes and real-time performance is not that good.

2.2 Complete ALPR Solutions

[34] introduces a new data set CCPD and a new RPNNet network for vehicle license plate recognition, implementing an end-to-end recognition system. According to this paper, CCPD is by far the largest and most diverse public data sets used for license plate recognition. RPNNet is divided into the detection and recognition module. Detection module is based on CNN, it integrates the dropout algorithm to improve the generalization ability of the algorithm; The recognition module is based on ROI, it implements the reuse of feature map from convolution layer, through sharing feature map in detection and recognition stage, license plate location and character recognition can be integrated in one network, the loss function can also be joint training, improve the efficiency of training and recognition This method needs to be optimized as follows: (1) The detection and recognition of multiple license plates in one picture is not supported. (2) For pictures without license plates, it still output result. (3) Rotation detection is not supported. (4) The recognition part does not support the recognition of Variable-length characters. (5) Using 7 different classifiers, resulting in too many model parameters.

Similar to [29], the network in [35] is also a single end to end network. This network use VGG-16 to extract feature map, simplifying the network architecture,

while, increasing the feature number to be trained. Region Proposal Network (RPN) [10] is used to select candidate box, RPN will generate a number of different scales and different aspect ratio candidate box for each feature point, these boxes will be filtered by non-maximum suppression(NMS) to give the final sample of 100 candidate box, through moving candidate box evenly, RPN can more quickly and accurately find the target frame. The recognition phase is regarded as a sequence labeled process, which uses a two-way RNN(BRNN) network with CTC loss [36], as well as a LSTM network to avoid gradient vanishing and exploding. The problem of this method is nearly half of the prediction time is spent on NMS part, which is a weakness in performance compared to our proposed method.

3 The BR-ALPR Dataset

The dataset contains 219 Kenyan national license plate data captured from intersection monitoring while driving through regular traffic in an urban environment, as well as 137 Ghanaian national license plate data collected from the Internet and 115 Brazilian license plate data.

The Kenyan license plate dataset we proposed is shown in Fig. 1. This data set is collected by vehicles passing through road intersections and monitoring equipment installed above the intersections. The data consists of two time periods, partly collected from 17:13:52, December 11, 2019 to 17:26:49, December 11, 2019, and partly collected at 17:13, December 01, 2019 :51 to 17:26:39 on December 01, 2019. The resolution of each picture collected is 4096×2160 . Each picture contains at least one car, and at least one car's license plate is clearly visible.

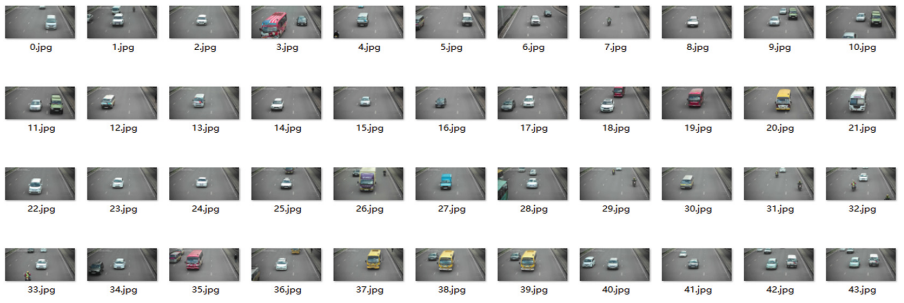


Fig. 1. Kenya license plate data in BR-ALPR

When we searched the national license plate information of Ghana, we found that Ghana is a special country with many foreign license plates. For example, it contains Nigeria, Togo and Burkina Faso national license plate data. The Burkina Faso license plates we collected include license plate information for ambassadors, public-private partnerships, government departments, private cars, international organizations, etc.

Table 1. Different license plate styles in different countries in the BR-ALPR dataset

| COUNTRY | TYPE | STYLE |
|--------------|---|---|
| Burkina Faso | Private(Personal and Comercial)(Long) |  |
| Burkina Faso | Private(Personal and Comercial) (Short) |  |
| Burkina Faso | Government(Type 1(Long)) |  |
| Burkina Faso | Government(Type 2) |  |
| Burkina Faso | Government(Type 3) |  |
| Burkina Faso | Public private partnership(Long) |  |
| Burkina Faso | Public private partnership(Short) |  |
| Burkina Faso | Public private partnership(Type 2) |  |
| Burkina Faso | Embassy(Long) |  |
| Burkina Faso | Embassy(Short) |  |
| Nigeria | Private |  |
| Nigeria | Commercial |  |
| Nigeria | Top public civil servant |  |
| Nigeria | Military and Paramilitary operatives |  |
| Nigeria | Diplomatic |  |

| | | |
|--------|---------|---|
| Brazil | Private |  |
| Kenya | Private |  |
| Togo | Type 1 |  |
| Togo | Type 2 |  |
| Togo | Type 3 |  |
| Togo | Type 4 |  |
| Togo | Type 5 |  |
| Togo | Type 6 |  |
| Togo | Type 7 |  |
| Togo | Type 8 |  |
| Togo | Type 9 |  |
| Togo | Type 10 |  |

The Nigerian license plates in current use were introduced in 1992 and revised in 2011. Nigeria and Liberia are the only two African countries that use the North American standard 6 × 12 inches (152 × 300 mm). The international code for Nigeria is “WAN” (West Africa Nigeria). The Nigerian license plates, with the exception of the plates for the diplomatic community and international organizations, all generally have a white background with the number and lettering imprinted in blue, red, green and black depending on the classification of the car. The upper left-hand corner usually carries the Flag of Nigeria with the national coat of arms on the right while the map of the country rests in the background. The state name and slogan are displayed at the top center of the plate with the “Federal Republic of Nigeria” written at the bottom. The

unique plate combination itself is in the format ABC-123DE. The first three letters indicate the Local Government Area in which the vehicle was registered, which are followed by three digits and two letters. The background consists of an outline of a map of Nigeria. Before 2011, the three letters indicating the Local Government Area were at the end, in the format AB123-CDE. Other types of Nigerian license plates are also in use. Commercial vehicles are written in red and government plates are in green. Diplomatic plates have a purple background with white lettering, and consist of up to three numbers, followed by CD or CMD and another number. Instead of the name of the state, they read CORPS DIPLOMATIQUE. Cars of the consular corps have the letters CORPS CONSULAIRE(CC). The national license plates of Togo are more complicated, with 10 types of license plates, different types of license plates, and different numbers of characters. The types of license plates are complex, and the type changes are varied. Some are simple license plates, some contain vehicles, some are inclined, some are not clear, and some license plates are two-line characters. The various license plate styles of various countries in BR-ALPR are shown in Table 1. Otherwise, more detailed introductions and downloads of the BR-ALPR dataset will be shared on www.yunyunai.cn.

The dataset of 115 Brazilian license plates collected from the Internet. Each picture contains a license plate information. Brazilian license plates are relatively simple. Each license plate consists of 7 characters. The first three digits are letters and the last four digits are Arabic numerals.

4 Proposed ALPR Approach

This section describes our proposed license plate detection and recognition method, which includes two stages of license plate detection and recognition. The first stage mainly completes the license plate detection, and the second stage mainly performs character recognition on the detected license plates. We use YOLO v3 for license plate detection. For the detected license plates, we use the improved Convolutional Recurrent Neural Network (CRNN) algorithm to complete character recognition.

4.1 License Plate Detection

The license plate detection stage is to find the license plate targets in the image and determine their positions. There are many related algorithms. The deformable parts models (DPM) algorithm uses a sliding window technique to run the classifier at evenly spaced positions on the entire image, traversing each area of the image. The sliding window algorithm has an obvious shortcoming, which is the calculation cost. The algorithm cuts out too many small squares in the picture, and the convolution network has to deal with each one. The R-CNN algorithm uses the idea of selection, first generating potential bounding boxes in the image, and then running classifiers on these bounding boxes. After classification, the bounding box is refined through post-processing to eliminate duplicate detection, and the bounding box is re-extracted according to other objects in the scene. These complex pipelines are slow and difficult to optimize because each individual component must be trained separately. Unlike

sliding window and candidate area-based technologies, Yolo uses a grid idea. YOLOv3 divides the input image into coarse, medium, and fine grids in order to predict large, medium, and small objects, respectively. Each grid corresponds to a ROI (region of interest). If the center of an object happens to fall in this grid, then this grid is responsible for predicting this object. If the size of the input picture is 416×416 , then the coarse, medium and fine grid sizes are 13×13 , 26×26 and 52×52 respectively. In this way, it is scaled by 32, 16 and 8 times in the length and width dimensions. In fact, these multiples are just the size of the ROI. This project uses Yolo's latest version of Yolo V3 algorithm to complete this task. The main improvement of YOLO V3 relative to yolo v2 is: adjusted the structure of the network, yolo v3 uses a new darknet-53 structure, darknet-53 borrows the idea of resnet, and adds a residual module to the network, which is helpful to solve the deep The gradient problem of the hierarchical network, each residual module consists of two convolutional layers and a shortcut connections. In the entire v3 structure, there is no pooling layer and fully connected layer. The downsampling of the network is by setting the convolution stride to 2. Achieved, the size of the image will be reduced to half every time through this convolutional layer; using multi-scale features for object detection, for the input $416 \times 416 \times 3$ images, three different scale prediction results are obtained through the darknet network Each scale corresponds to N channels, and contains prediction information; the object classification is replaced with softmax by Logistic, and softmax is not used when predicting the object category, and the logistic output is used for prediction, which can support multi-label objects.

For our proposed BR-ALPR data set. We use LabelImage to label the location information of the license plate, and then input the label data to YOLO v3 to complete the detection of the license plate. As shown in Fig. 2, the license plate detection result is framed by a green box. Figure 3 shows the BR-ALPR dataset license plate detection results.



Fig. 2. Using yolov3 for license plate detection



Fig. 3. License plate detection results of BR-ALPR dataset

4.2 License Plate Recognition

After we use YOLO v3 to complete the license plate detection, the character recognition of the next license plate needs to be performed for the detected license plate. We use the scene text recognition algorithm CRNN. The CRNN algorithm has shown great advantages in many scene text recognition. Compared with the previous scene text recognition system, CRNN has four significant characteristics: (1) It has end-to-end trainability, and most of the existing algorithm components are individually trained and adjusted. (2) Naturally process sequences of arbitrary length without involving character segmentation and horizontal scale normalization. (3) Not limited to any predefined vocabulary, and has achieved remarkable results in both non-vocabulary and vocabulary-based scene text recognition tasks. (4) An effective but much smaller model is generated, which is more practical for real application scenarios. The basic idea is: text recognition is a method for predicting sequences, so an RNN network for sequence prediction is used. After extracting the features of the picture through CNN, the RNN is used to predict the sequence, and finally the final result is obtained through a CTC translation layer. Simply put, it is the structure of CNN+RNN+CTC. We transplanted it to license plate character recognition, which can recognize characters of indefinite length, suitable for complex real scene character recognition. The network structure diagram of CRNN recognition of license plate characters is shown in the Fig. 4.

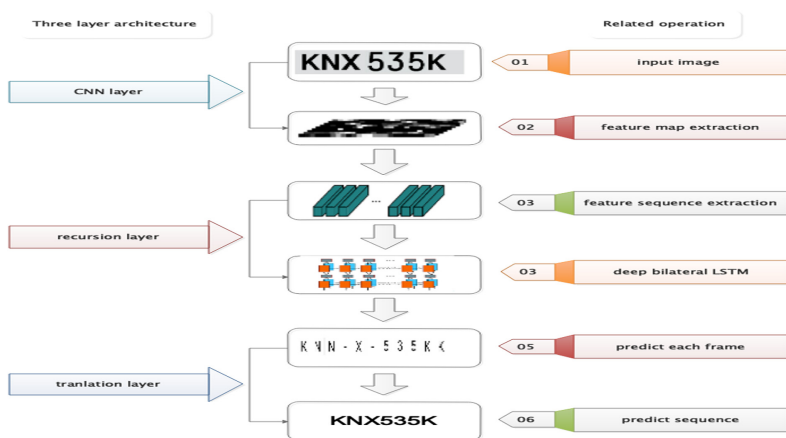


Fig. 4. Structure diagram of license plate character recognition using CRNN

Considering that our data set is more complicated (for example, the quality of Ghana national license plate data we collected from the Internet is relatively poor, and some license plates are not taken as front images). Real-world scenes like roadside mobile law enforcement shots are not necessarily approximate frontal images. Considering the locality, translation invariance, reduction invariance, rotation invariance, etc. of the input samples of the CRNN algorithm, it is necessary to transform the data to achieve better recognition. Based on the above ideas, we improve the CRNN algorithm. Before CNN extracts features, we insert a spatial transformation network. The STN network can adaptively transform and align the input license plate data transformation (including translation, scaling, rotation, and other geometry, etc.), the STN network structure is shown in Fig. 5. The STN network is mainly composed of three parts, Localisation net, Grid generator and Sampler. Localisation net is a network for regression transformation parameter θ . Its input feature image, after a series of convolution operations, the last regression layer outputs spatial transformation parameters. For our license plate data, we need to correct the inclined license plate, θ is a 6-dimensional (2×3) vector. θ can be expressed as

$$\theta = f_{Localisation\ net}(U) \tag{1}$$

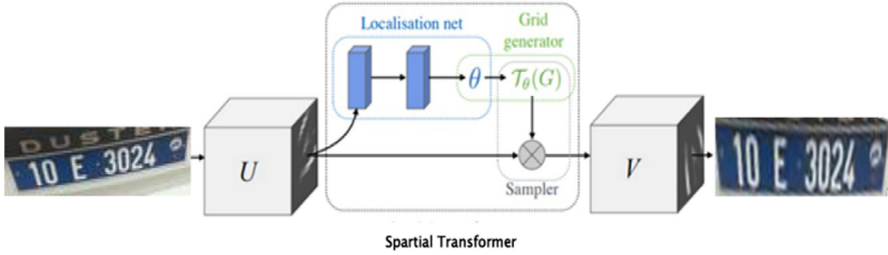


Fig. 5. The STN network structure

Grid Generator is to construct a sampling grid according to the parameters obtained by the affine transformation. It is the output of a set of points in the input image after sampling transformation. What the grid generator actually obtains is a mapping relationship θ . Assume that the coordinate of each pixel of the feature image U is (x_i^s, y_i^s) the coordinate of each pixel of V is (x_i^t, y_i^t) , and the spatial transformation function Γ_θ is a two-dimensional affine transformation function, Then the correspondence between (x_i^s, y_i^s) and (x_i^t, y_i^t) can be written as

$$\begin{pmatrix} x_i^s \\ y_i^s \end{pmatrix} = \Gamma_\theta(G_i) = A_\theta \begin{pmatrix} x_i^t \\ y_i^t \\ 1 \end{pmatrix} = \begin{bmatrix} \theta_{11} & \theta_{12} & \theta_{13} \\ \theta_{21} & \theta_{22} & \theta_{23} \end{bmatrix} \begin{pmatrix} x_i^t \\ y_i^t \\ 1 \end{pmatrix} \tag{2}$$

The sampler uses the sampling grid and the input feature map as input to generate output, and obtains the result of the feature map after transformation. After obtaining the changed feature map, use bilinear interpolation for sampling to complete the back propagation of the error, so that the network can learn the best θ . The loss of the entire improved CRNN consists of two parts. The first half is the loss generated by the training STN network part, and the second half is the loss generated by the CRNN recognition. The total loss is shown in the following formula:

$$L_{total} = \mathcal{L}_{STN} + \mathcal{L}_{CRNN} \quad (3)$$

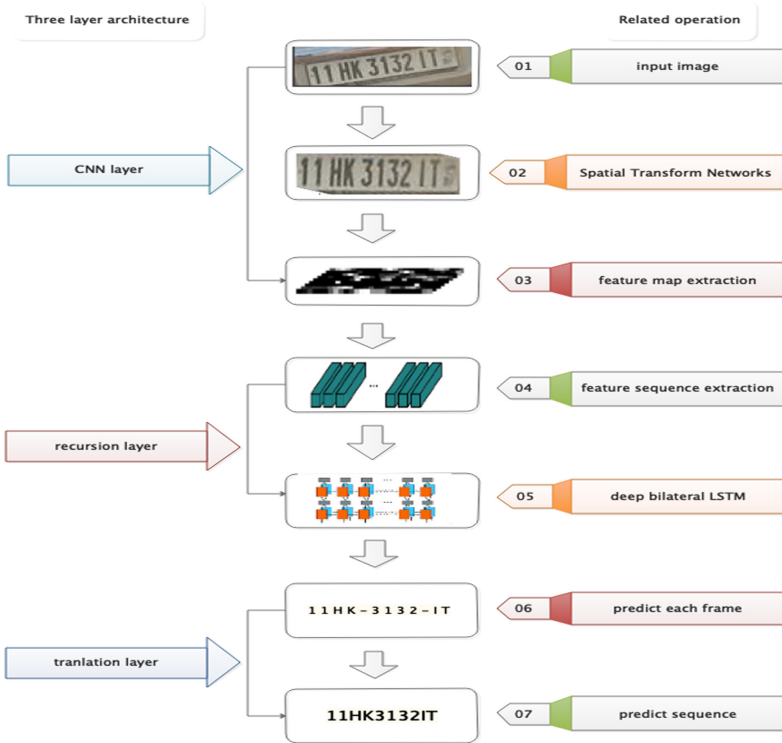


Fig. 6. The improved CRNN network structure

We insert the STN network into the CRNN to complete the BR-ALPR license plate recognition network structure as shown in the Fig. 6.

5 Experimental Results

In this section, we conduct experiments to verify the effectiveness of the proposed ALPR system. We conduct the test on the experimental machine with GPU NVIDIA GTX Titan Z. For the license plate detection, we complete the labeling of the labeling

of the BR-ALPR dataset, and use YOLOv3 built by the darknet network framework to complete the license plate detection. Since our BR-ALPR data set has real scene collection and online collection, the data set is relatively messy, but YOLOv3 has three scales, which can detect license plate targets of different sizes in the picture, so we use YOLOv3 directly detects the license plate on BR-ALPR.



Fig. 7. Enhanced data display effect of Kenyan license plates

Due to the relatively small amount of data, we use the method of template paste to generate some license plate data. We make the license plate base plate that is the same as the real scene. According to the Kenya license plate data format, we randomly generate numbers and paste them on the template, and add affine conversion and perspective conversion. A large number of license plate data is generated by specific scene techniques such as brightness conversion, affine conversion, etc., thereby completing the expansion of Kenyan license plate data in BR-ALPR. The generated license plate data is shown in Fig. 7. Data enhancement can further solve the shortage of data. In the experiment, we used this method to double the Kenyan license plate data in BR-ALPR dataset.

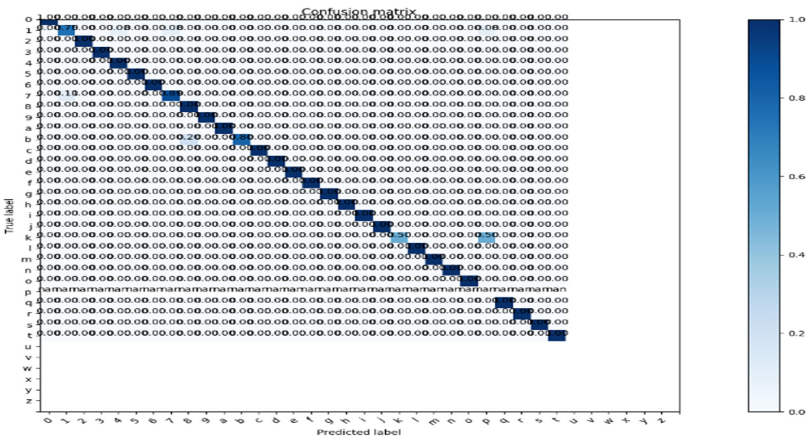


Fig. 8. Confusion matrix diagram of license plate character recognition

Table 2. Structural parameters of our improved CRNN

| Type | Configurations |
|------------------------------|--------------------------------|
| Input | (10,32,100,3) |
| STN(Localisation net) Conv2d | Kernel-size:3 stride:1 |
| MaxPooling | Pool_size:2 stride:2 |
| Fully_connected | |
| Fully_connected | |
| Conv2d | Kernel-size:3 stride:1 |
| Conv2d | Kernel-size:3 stride:1 |
| Conv2d | Kernel-size:3 stride:1 |
| MaxPooling | Kernel-size:2 × 1 stride:1 |
| Conv2d | Kernel-size:3 stride:1 |
| Conv2d | Kernel-size:3 stride:1 |
| MaxPooling | Kernel-size:2 × 1 stride:2 × 1 |
| Conv2d | Kernel-size:2 stride:2 × 1 |
| Map-to-Sequence | |
| Bidirectional-LSTM | Hidden units:256 |
| Bidirectional-LSTM | Hidden units:256 |
| Transcription | |
| character recognition | |

We resize the detected license plate image to (100,32), and then use the same protocol proposed by Goncalves et al. [37] to divide the detected license plate dataset as follows: 40% for training, 40% for testing, 20% Used for verification, and then input it into the improved CRNN network structure. Our improved CRNN layer network parameters are shown in Table 2. We use the improved CRNN for license plate character recognition. The experimental results show that the mean test per char accuracy is 0.96, and the test license plate sequence recognition rate is 0.8019. We have drawn a confusion matrix for improved CRNN for character recognition. The confusion matrix is shown in Fig. 8. It can be seen from the confusion matrix that due to the small number of samples, certain characters cause errors in the prediction of some characters. Our method is compared with the current commercial Sighthound [38] and OpenALPR [39] license plate recognition methods. The comparison results are shown in Table 3. Because our data set is special, these commercial methods are only suitable for specific countries and regions. For example, OpenALPR has a better recognition effect on Brazilian license plate data. Therefore, the method we proposed on this data set takes precedence over other commercial methods and can be very good. Realize the license plate recognition of the countries covered by this dataset.

Table 3. The accuracy of our proposed method and advanced commercial method in the BR-ALPR dataset for license plate recognition

| ALPR | Full sequence accuracy |
|-----------------|------------------------|
| Sighthound [21] | 46.36% |
| OpenALPR [22] | 43.64% |
| Ours | 80.19% |

6 Conclusions and Future Work

At present, most methods of license plate recognition are the license plate recognition of specific countries and similar frontal images. This paper proposes a complex data BR-ALPR for the license plate recognition of some underdeveloped countries in the Belt and Road Initiative. Part of the data set is collected by cameras on the road, and part is collected on the Internet. The license plates of these countries that we want to recognize are more complicated, have many styles, and are difficult to recognize. Since the current commercial methods and academic methods do not have these national data sets, there is little exploration of license plate recognition in these countries. This paper proposes this BR-ALPR data set, which is of great significance to promote license plate recognition in these countries. For the BR-ALPR data set, we propose a set of methods for the license plate detection and recognition of this data set. We use YOLO v3 to complete the license plate detection. For the license plates after detection, we use the improved CRNN for license plate character recognition. We insert the spatial transformation network into the CRNN to achieve the correction of inclined license plates to achieve better character recognition. Our experimental results are compared with existing commercial methods, and the results show the superiority of our proposed method.

Regarding future research, we will further improve the BR-ALPR dataset, and at the same time add more national license plate data along the Belt and Road. In addition, we will upgrade the license plate detection module and upgrade YOLO v3 to YOLO v4 [40]. In addition, we will continue to explore the impact of the state space network inserted into the CRNN's different network layers on license plate character recognition, or we continue to optimize the network and use the end-to-end network License plate detection and recognition.

Acknowledgments. This work was supported by the grant of National Key R&D Program of China (No. 2018AAA0100100) and partly supported by National Natural Science Foundation of China (Grant nos. 61520106006, 61861146002, 61772370, 61702371, 61732012, 61932008, 61532008, 61672382, 61772357, and 61672203) and China Postdoctoral Science Foundation (Grant no. 2017M611619) and supported by "BAGUI Scholar" Program and the Scientific & Technological Base and Talent Special Program, GuiKe AD18126015 of the Guangxi Zhuang Autonomous Region of China and supported by Shanghai Municipal Science and Technology Major Project (No.2018SHZDZX01), LCNBI and ZJLab.

References




1. Huang, D.S.: Systematic Theory of Neural Networks for Pattern Recognition. Publishing House of Electronic Industry of China, Beijing (1996)
2. Wu, D., Zheng, S., Yuan, C., Huang, D.S.: A deep model with combined losses for person re-identification. *Cogn. Syst. Res.* **54**, 74–82 (2019)
3. Huang, D.S.: Radial basis probabilistic neural networks: model and application. *Int. J. Pattern Recogn. Artif. Intell.* **13**(7), 1083–1101 (1999)
4. Wang, X.F., Huang, D.S.: A novel density-based clustering framework by using level set method. *Knowl. Data Eng.* **21**(11), 1515–1531 (2009)
5. Wu, Y.: Person re-identification by multi-scale feature representation learning with random batch feature mask. *IEEE Trans. Cogn. Develop. Syst.* (2020). <https://doi.org/10.1109/TCDS.2020.3003674>
6. Zhao, Z.Q., Huang, D.S., Sun, B.Y.: Human face recognition based on multiple features using neural networks committee. *Pattern Recogn. Lett.* **25**(12), 1351–1358 (2004)
7. Wu, D., Shen, Z., Yuan, C., Huang, D.S.: A deep model with combined losses for person re-identification. *Cogn. Syst. Res.* **54**, 74–82 (2018)
8. Li, B., Huang, D.S.: Locally linear discriminant embedding: An efficient method for face recognition. *Pattern Recogn.* **41**(12), 3813–3821 (2008)
9. Huang, D.S., Du, J.X.: A constructive hybrid structure optimization methodology for radial basis probabilistic neural networks. *Neural Netw.* **19**(12), 2099–2115 (2008)
10. Silva, S.M., Jung, C.R.: License Plate Detection and Recognition in Unconstrained Scenarios. In: Ferrari, V., Hebert, M., Sminchisescu, C., Weiss, Y. (eds.) *ECCV 2018*. LNCS, vol. 11216, pp. 593–609. Springer, Cham (2018). https://doi.org/10.1007/978-3-030-01258-8_36
11. Laroca, R., Severo, E., Zanlorensi, L.A.: A robust real-time automatic license plate recognition based on the YOLO detector. In: 2018 International Joint Conference on Neural Networks (IJCNN). IEEE, pp. 1–10 (2018)
12. Xu, Z., Yang, W., Meng, A.: Towards end-to-end license plate detection and recognition: a large dataset and baseline. In: Proceedings of the European Conference on Computer Vision (ECCV), pp. 255–271 (2018)
13. Li, H., Wang, P., Shen, C.: Toward end-to-end car license plate detection and recognition with deep neural networks. *IEEE Trans. Intell. Transp. Syst.* **20**(3), 1126–1136 (2018)
14. Lin, C., Wu, C.: A lightweight, high-performance multi-angle license plate recognition model. In: 2019 International Conference on Advanced Mechatronic Systems (ICAMechS), pp. 235–240 (2019)
15. Redmon, J., Divvala, S., Girshick, R.: You only look once: unified, real-time object detection. In: Proceedings of the IEEE Conference on Computer Vision and Pattern Recognition, pp. 779–788 (2016)
16. Shi, B., Bai, X., Yao, C.: An end-to-end trainable neural network for image-based sequence recognition and its application to scene text recognition. *IEEE Trans. Pattern Anal. Mach. Intell.* **39**(11), 2298–2304 (2016)
17. Jaderberg, M., Simonyan, K., Zisserman, A., Kavukcuoglu, K.: Spatial transformer networks (2015). <https://arxiv.org/abs/1506.02025>
18. Huang, D.S.: Application of generalized radial basis function networks to recognition of radar targets. *Int. J. Pattern Recogn. Artif. Intell.* **13**(6), 945–962 (1999)
19. Huang, D.S., Chi, Z.R., Siu, W.C.: A case study for constrained learning neural root finders. *Appl. Math. Comput.* **165**(3), 699–718 (2005)

20. Shang, L., Huang, D.S., Du, J.X., Zheng, C.H.: Palmprint recognition using Fast ICA algorithm and radial basis probabilistic neural network. *Neurocomputing* **69**(13–15), 1782–1786 (2006)
21. Huang, D.S., Zhao, W.B.: Determining the centers of radial basis probabilistic neural networks by recursive orthogonal least square algorithms. *Appl. Math. Comput.* **162**(1), 461–473 (2005)
22. Huang, D.S.: The local minima free condition of feedforward neural networks for outer-supervised learning. *IEEE Trans. Syst. Man Cybern.* **28**(3), 477–480 (1998)
23. Huang, D.S., Horace, H.S., Chi, Z.R., Wong, H.S.: Dilation method for finding close roots of polynomials based on constrained learning neural networks. *Phys. Lett.* **309**(5), 443–451 (2003)
24. Wang, X.F., Huang, D.S., Xu, H.: An efficient local Chan-Vese model for image segmentation. *Pattern Recogn.* **43**(3), 603–618 (2010)
25. Huang, D.S.: The united adaptive learning algorithm for the link weights and the shape parameters in RBFN for pattern recognition. *Int. J. Pattern Recogn. Artif. Intell.* **11**(6), 873–888 (1997)
26. Huang, D.S.: *Systematic Theory of Neural Networks for Pattern Recognition* (in Chinese). Publishing House of Electronic Industry of China (1996)
27. Felzenszwalb, P.F., Girshick, R.B., McAllester, D., Ramanan, D.: Object detection with discriminatively trained part-based models. *IEEE Trans. Pattern Anal. Mach. Intell.* **32**(9), 1627–1645 (2010). <https://doi.org/10.1109/TPAMI.2009.167>
28. Ren, S., He, K., Girshick, R.: Faster r-cnn: towards real-time object detection with region proposal networks. In: *Advances in Neural Information Processing Systems*, pp. 91–99 (2015)
29. Redmon, J., Farhadi, A.: YOLOv3: an incremental Improvement (2018)
30. Redmon, J., Farhadi, A.: YOLO9000: better, faster, stronger. In: *2017 IEEE Conference on Computer Vision and Pattern Recognition (CVPR)*, pp. 6517–6525. IEEE (2017). <http://dx.doi.org/10.1109/CVPR.2017.690>
31. He, K., Zhang, X., Ren, S.: Deep residual learning for image recognition. In: *Proceedings of the IEEE Conference on Computer Vision and Pattern Recognition*, pp. 770–778 (2016)
32. Kingma, D.P., Ba, J.: Adam: a method for stochastic optimization. *Computer Science* (2014)
33. Lin, C., Wu, C.: A lightweight, high-performance multi-angle license plate recognition model. In: *2019 International Conference on Advanced Mechatronic Systems (ICAMechS)*, pp. 235–240 (2019)
34. Xu, Z., et al.: Towards End-to-End License Plate Detection and Recognition: A Large Dataset and Baseline. In: Ferrari, V., Hebert, M., Sminchisescu, C., Weiss, Y. (eds.) *ECCV 2018*. LNCS, vol. 11217, pp. 261–277. Springer, Cham (2018). https://doi.org/10.1007/978-3-030-01261-8_16
35. Li, H., Wang, P., Shen, C.: Toward end-to-end car license plate detection and recognition with deep neural networks. *IEEE Trans. Intell. Transp. Syst.* **20**(3), 1126–1136 (2018)
36. Graves, A., Liwicki, M., Fernandez, S.: A novel connectionist system for unconstrained handwriting recognition. *IEEE Trans. Pattern Anal. Mach. Intell.* **31**(5), 855–868 (2009)
37. Gonçalves, G.R.: Errata: benchmark for license plate character segmentation. *J. Electron. Imaging.* **25**(6), 69801 (2016)
38. Masood, S.Z., Shu, G., Dehghan, A., Ortiz, E.G.: License plate detection and recognition using deeply learned convolutional neural networks. In: *2017 IEEE Conference on Computer Vision and Pattern Recognition (CVPR)*. IEEE (2017)
39. OpenALPR Cloud API. <http://www.openalpr.com/cloud-api.html>
40. Bochkovskiy, A., Wang, C.Y.: YOLOv4: optimal speed and accuracy of object detection, arxiv (2020)

Biometrics Recognition



Shallow Neural Network for Biometrics from the ECG-WATCH

Vincenzo Randazzo¹ , Giansalvo Cirrincione^{2,3} ,
and Eros Pasero¹ 

¹ DET, Politecnico di Torino, Turin, Italy

{vincenzo.randazzo, eros.pasero}@polito.it

² University of Picardie Jules Verne, Amiens, France

exin@u-picardie.fr

³ University of South Pacific, Suva, Fiji

Abstract. Applications such as surveillance, banking and healthcare deal with sensitive data whose confidentiality and integrity depends on accurate human recognition. In this sense, the crucial mechanism for performing an effective access control is *authentication*, which unequivocally yields user identity. In 2018, just in North America, around 445K identity thefts have been denounced. The most adopted strategy for automatic identity recognition uses a *secret* for encrypting and decrypting the authentication information. This approach works very well until the *secret* is kept safe. Electrocardiograms (ECGs) can be exploited for biometric purposes because both the physiological and geometrical differences in each human heart correspond to uniqueness in the ECG morphology. Compared with classical biometric techniques, e.g. fingerprints, ECG-based methods can definitely be considered a more reliable and safer way for user authentication due to ECG inherent robustness to circumvention, obfuscation and replay attacks. In this paper, the ECG WATCH, a non-expensive wristwatch for recording ECGs anytime, anywhere, in just 10 s, is proposed for user authentication. The ECG WATCH acquisitions have been used to train a shallow neural network, which has reached a 99% classification accuracy and 100% intruder recognition rate.

Keywords: Biometrics · CCA · ECG · EKG · ECG WATCH · Electrocardiogram · Intruder recognition · Multilayer perceptron · PCA · Supervised learning · Wearable device

1 Introduction

In the last decades, the increasing amount of information technologies, smartphones and wearables, has led to an exponential growth of the data shared on internet. Information is always travelling around, e.g. over Bluetooth. In such a scenario, each piece of information must be accessible only to its authorized users, aka *access control* [1]. Applications such as surveillance, banking and healthcare deal with sensitive data whose confidentiality and integrity depends on accurate human recognition [2]. In this

sense, the crucial mechanism for performing an effective access control is *authentication*, which unequivocally yields user identity.

Biometric-based techniques take advantage of intrinsic human properties, such as physiological and behavioural; the former are related to some characteristic of human body like fingerprints [3] and retinas [4], while the latter one relies on the subject behaviour, e.g. typing rhythm, gait, and voice. Since the authentication method needs to be robust to forgery, not every biological parameter can be employed for biometrics. In this sense, it can be used any physiological and/or behavioural feature that fulfils requirements such as universality, distinctiveness and permanence [5].

ECG Biometrics. Because of its inherent robustness to circumvention, obfuscation and replay attacks, a biosignals-based approach has been largely explored during the last decades [6]. The idea is to exploit vital signals typically employed for medical diagnoses - such as electroencephalogram (EEG) [6, 7], photoplethysmography [8] and electrocardiogram (ECG) [9, 10] - for biometric purposes. In particular, the latter is quite interesting because both the physiological and geometrical differences in each human heart correspond to uniqueness in the ECG morphology [11]. In this sense, ECG exhibits various meaningful properties - such as uniqueness, permanence, and ease of collection [9] - that make ECG a preferable choice over both PPG and EEG; compared with classical biometric techniques, e.g. fingerprints, ECG-based methods can definitely be considered a more reliable and safer way for user authentication [12] because:

- ECG is an internal signal and no traces remain after its acquisition, i.e. it is harder to be sniffed without the user noticing.
- The inherent inter-variability of each recording implies ECG is difficult to be fabricated.
- ECG acquisition is less prone to ambient noise than other methods, such as voice [13, 14] or face recognition [15], where ambient noise or lighting conditions can deeply affect the recognition process.
- The ECG signal can be acquired via various conductive materials and simple electronics, which can also be easily embedded in fabric or wearables.

Paper Outline. The rest of the paper is organized as follows. Section 2 presents the state of the art of ECG-based neural biometric techniques. In Sect. 3 the proposed approach, based on wearable devices, is detailed. Section 4 illustrates the experimental ECG dataset, whose manifold and intrinsic dimensionality is analysed in Sect. 5. The chosen shallow neural network for user authentication is described in Sect. 6. Finally, Sect. 7 yields the conclusions.

2 State of the Art

ECG based biometrics has proven to be robust to both emotional and mental state variations [16]. With respect to the nature of the considered features ECG-based biometric systems can be clustered into three groups: fiducial, non-fiducial and hybrid.

The former approach is based on the extraction of specific points on the ECG heartbeat, called *fiducials*, and their usage as input features, which may also involve their amplitude, angle, or duration. The fifteen fiducial features based on the R peaks used in [17] yield 82% and 79% heartbeat identification rates using two different ECG sites, neck and chest, respectively. The fiducial amplitude and duration, together with QRS and PR intervals, are exploited in [18]; the method reaches 79% and 85.3% of accuracy w.r.t. different lead configurations.

Non-fiducial methods are based on statistical attributes of the signal, in either the time or frequency domain, rather than specific points on the electrocardiogram curve. Autocorrelation and linear dimension reduction using kernel principal component analysis (kPCA) and SVM [19] is used in [20]. K-nearest neighbourhood classifier and Hadamard transform were exploited in [21]. 1-D convolutional neural networks were used in [22]. The discrete cosine transform and autocorrelation coefficients are employed in [23–25].

Finally, both fiducial and non-fiducial features are combined in the latter category [26, 27], which, in this sense, is called *hybrid*. For instance, [11] presents a technique where the fiducial features are the positions and amplitudes of the P, Q, R, S and T points, while the non-fiducial attributes are represented by the autocorrelation and discrete cosine transform coefficients.

3 The ECG WATCH Biometric System

Data breaches can be prevented by using biometric authentication devices for limiting the access to specific software and sites such as airport security areas or hospital neonatal wards. The identity and access management market is quickly increasing (today is bigger than \$4bn), with biometric hardware credentials being a key growth trend [28]; specifically, a rising amount of companies is working for using ECG biometrics in both consumer and enterprise applications, such as smart clothing, access control cards and wrist wearables [12].

In this contest, a perfect tool for ECG biometric authentication is the ECG-WATCH [29, 30], shown in Fig. 1. It is wearable and unobtrusive; it records, in only 10 s, a single-lead ECG, which will be shown into a smartphone or desktop app; acquisitions are stored in the smartphone in an open format; data can also be shared to physicians for deeper analysis. The device is as big as an everyday watch; thus, it can be constantly worn at wrist without any discomfort for the user; it is low cost (30 €) and, above all, wireless (no long cables are required). In this sense, the ECG-WATCH has been designed as a full-heart-monitoring too; indeed, the app is provided with an automatic silent atrial fibrillation detecting algorithm [31]. The ECG WATCH uses two dry electrodes (one on top and the other on the back) to measure the user electrical potential difference along one of the three peripheral leads (I, II, III) of the Einthoven’s triangle [32]: when it placed between user wrists, it acquires the lead I; when signal is recorded among the left leg and the right arm, the device measures the lead II; finally, if it is used between the left leg and arm, it gathers the lead III.

In [33] authors have proven device acquisition quality, which has been then exploited for pathology recognition through a neural system [34]. In this work, instead



Fig. 1. The ECG WATCH

of classifying heart diseases, an artificial neural network [35–42] is used for discriminating among different individuals. Due to the employment of wearable devices and mobile apps, and the need of a fast recognition algorithm, a shallow neural network [43–45] analogous to the one proposed in [46] is preferred to deeper models such the 1-D convolutional neural network of [47].

4 The Experimental Dataset

ECGs have been collected in the Neuronica Lab of Politecnico di Torino on six male volunteers: five healthy subjects and one cardiopathic (*Subject3*). All acquisitions were recorded between wrists at 1 kHz; heartbeats (HBs), whose length has been empirically set to twenty time-instants, have been extracted using autocorrelation and discrete cosine transform (DCT). For each volunteer, the number of acquired ECGs, together with the corresponding total amount of HBs, is detailed in Table 1. The final TS has 2331 rows (the cumulative sum of HBs) and 20 columns (the chosen heartbeat size).

Table 1. Dataset taxonomy

| | Age | Sex | No. of ECGs | No. of heartbeats |
|-----------|-----|-----|-------------|-------------------|
| Subject1 | 26 | M | 47 | 429 |
| Subject2 | 27 | M | 22 | 185 |
| Subject3* | 60 | M | 63 | 748 |
| Subject4 | 24 | M | 56 | 531 |
| Subject5 | 27 | M | 20 | 190 |
| Subject6 | 23 | M | 31 | 248 |

*Cardiopathic

Figure 2 does not exhibit a common pattern for all the subjects; R-peaks, i.e. the HBs, are somehow distinguishable but the plot is quite noisy. Figure 3 provides a deeper level of analysis; here, HBs are plotted into a separate subfigure for each subject:

- Subject2 and Subject5 subfigures are very well concentrated around their mean, i.e. the heartbeats are clearly distinguishable.
- Subject6 is thicker around the mean but the overall shape is still appreciable.

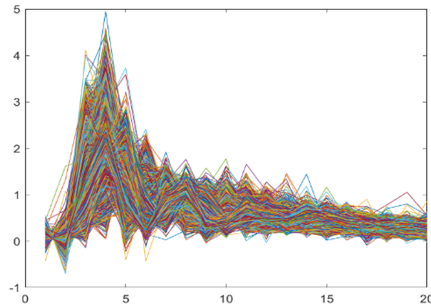


Fig. 2. Heartbeat visualization: whole dataset.

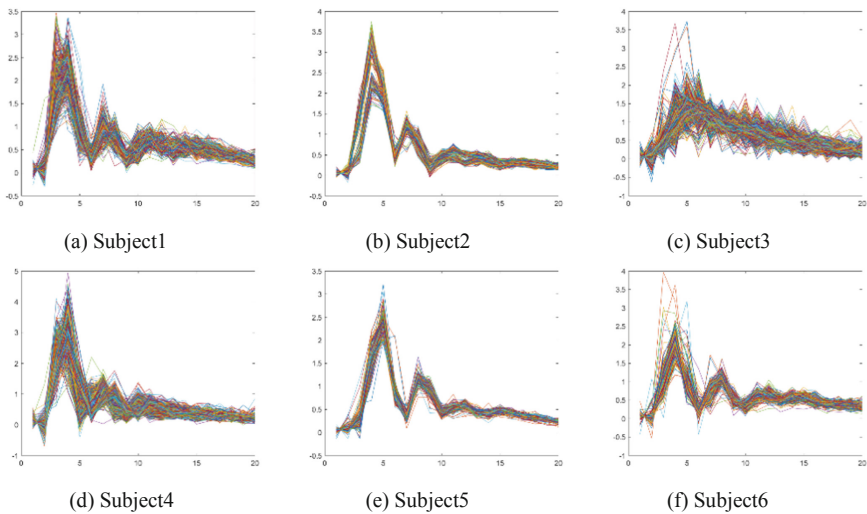


Fig. 3. Heartbeat visualization: single subject.

- Subject1 and Subject4 are quite noisy.
- Subject3 heartbeats are completely unrecognizable; it can be argued that the morphology loss is due to the cardiovascular disease.

5 Manifold Analysis

The database has been studied to determine its intrinsic dimensionality (ID). A preliminary linear analysis has been conducted using the Principal Component Analysis (PCA) [48]. Figure 4 shows the corresponding Pareto chart [49] computed on the whole dataset, where each column represents the amount of variance explained by the corresponding principal component (of course, the plot has a decreasing trend).

Assuming 90% is a significative threshold for the explained variance while ignoring noise, the intrinsic dimensionality can be estimated to 12.

Because of the differences depicted in Fig. 3, each subject samples have been analysed separately; Table 2 summarizes the results: despite the intrinsic dimensionality of the whole dataset is equal to 12, it varies a lot w.r.t. each volunteers, from a minimum of 8 up to 15. Interestingly, Subject3, whose plot is the less HB shaped, has also the higher intrinsic dimensionality w.r.t. the PCA linear analysis.

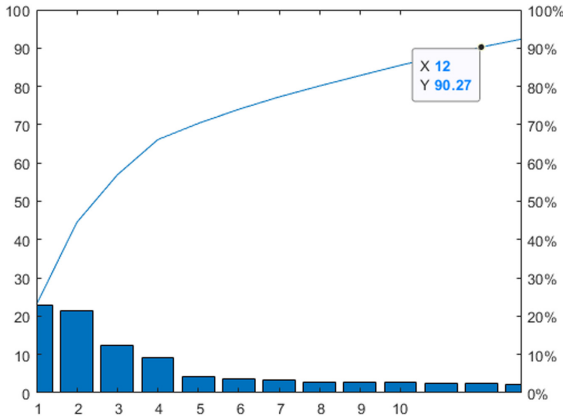


Fig. 4. Pareto chart: whole dataset.

Table 2. Intrinsic dimensionality

| | Whole DB | Subject1 | Subject2 | Subject3 | Subject4 | Subject5 | Subject6 |
|------|------------|------------|-----------|------------|------------|------------|------------|
| PCA* | 12 (90.27) | 14 (91.04) | 8 (90.12) | 15 (92.23) | 11 (90.45) | 14 (91.44) | 13 (91.92) |

*in brackets the percentage of explained variance.

6 MLP-Based Authentication

Although the previous analyses have demonstrated the input dataset is easy to be clustered in terms of healthy and sick subjects, it must be further deepened if it is possible also to recognize each volunteer. The wearable philosophy requires a simple algorithm with regard to both the computational complexity and the time needed for providing a result, i.e. the authorization token; at the same time, the most important constraint to be considered is the accuracy. At this purpose, a simple shallow neural network has been trained. The input layer is mapped one-to-one to the input features; thus, it is made of twenty units. The hidden layer is made of fifty neurons, and the output units are equipped with soft-max activation functions [49]. Due to the cross-entropy error function, the network yields the membership probabilities for each subject of the TS. To balance the overrepresentation (see Table 1) of Subject3 (~750

samples), the two youngest attendees (Subject4 and Subject6), were merged into as a single fifth class (~ 780 HBs), say *other*, which is also used for representing *external* people w.r.t. the authentication system. The shallow network has been trained by means of the Scaled Conjugated Gradient algorithm [49]. To preserve the input label distribution, in all the simulations, the input dataset was split into balanced training, validation and test subsets w.r.t. the five classes (*Subject1*, *Subject2*, *Subject3*, *Subject5*, *other*). Seventy percent of the TS was used for training, while the rest was divided in equal parts for test and validation sets, respectively.

The training and testing confusion matrices are shown in Fig. 5; in both cases, the overall accuracy exceeds 99%. More in detail, classes 2 and 4 precision and class 3 recall reach 100% for both training and testing, while class 3 precision and class 5 recall are higher in testing than in training.

Class 3 (the cardiopathic attendee) has confirmed to be the simplest to be recognized; however, both the overall and the single class performances are definitely impressive. In this sense, the proposed technique is suitable for the application at hand.

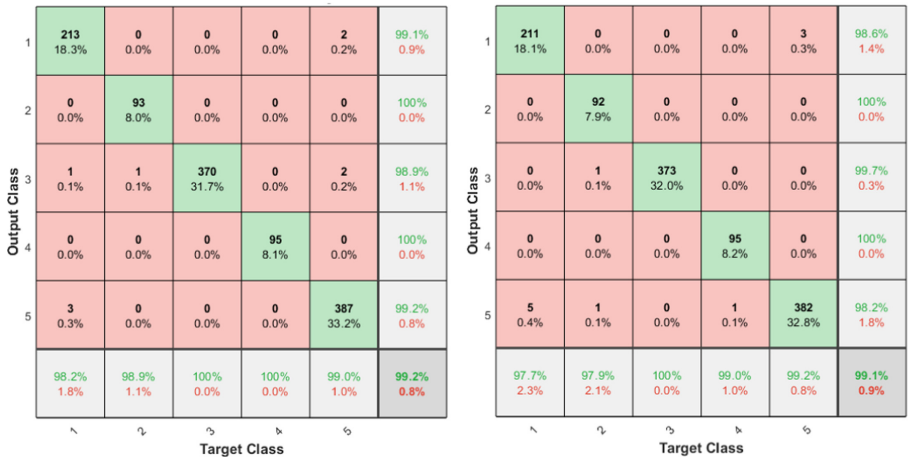


Fig. 5. Shallow neural network confusion matrices: training (left) and testing (right).

6.1 Unknown Subject

As a final test, the method robustness has been measured using a novel, additional subject never fed to the network, neither in training nor in test. The scope was simulating a real case scenario, where an intruder tries to deceive the system by means of a fake identity; here, it is modelled using the fifth class, which represent the non-authorized users, i.e. the rejected tokens.

The *intruder* is a ten-years old child, who kindly provided 128 heartbeats. Figure 6 yields the recall phase confusion matrix: the intruder is never misclassified, which proves the biometric model is robust and can be exploited for real authorization tasks.

| | | | | | | | |
|--------------|--------------|--------------|--------------|--------------|--------------|--------------|---------------|
| Output Class | 1 | 0 0.0% | 0 0.0% | 0 0.0% | 0 0.0% | 0 0.0% | NaN% NaN% |
| | 2 | 0 0.0% | 0 0.0% | 0 0.0% | 0 0.0% | 0 0.0% | NaN% NaN% |
| | 3 | 0 0.0% | 0 0.0% | 0 0.0% | 0 0.0% | 0 0.0% | NaN% NaN% |
| | 4 | 0 0.0% | 0 0.0% | 0 0.0% | 0 0.0% | 0 0.0% | NaN% NaN% |
| | 5 | 1 0.8% | 8 6.3% | 1 0.8% | 0 0.0% | 118 92.2% | 92.2% 7.8% |
| | | 0.0% 100% | 0.0% 100% | 0.0% 100% | NaN% NaN% | 100% 0.0% | 92.2% 7.8% |
| | Target Class | | | | | | |

Fig. 6. Shallow neural network confusion matrix: intruder simulation

7 Final Considerations

ECG-based authentication provides greater security and safety in a world of risk; if used together with other biometrics, it can yield the most powerful digital security strategy; indeed, such an approach may totally modify the security model, from external-based biometric to internal physiological data, which are almost impossible to forge. In this paper, a shallow neural network has demonstrated to be able to recognize subjects and, above all, to detect intrusion attempts. Its robustness has also been proven w.r.t. heart pathologies.

Finally, studying vital parameters signals could lead to extrapolate deeper human insights, which could have even more significant applications than authentication. For instance, ongoing researches have explored the usage of wearable devices to assess changes in the human nervous system w.r.t. external inputs [50]: pre-defined emotional states have been related to physiological data acquired with a wristband. In this sense, it can be thought as an advancement towards the understanding of the physiology underlying emotions.

References

1. Sandhu, R.S., Samarati, P.: Access control: principle and practice. *IEEE Commun. Mag.* **32** (9), 40–48 (1994)
2. Krawczyk, S., Jain, A.K.: Securing electronic medical records using biometric authentication. In: Kanade, T., Jain, A., Ratha, N.K. (eds.) *AVBPA 2005*. LNCS, vol. 3546, pp. 1110–1119. Springer, Heidelberg (2005). https://doi.org/10.1007/11527923_115
3. Gallo, V.: Performance assessment in fingerprinting and multi component quantitative NMR analyses. *Anal. Chem.* **87**(13), 6709–6717 (2015)

4. Bevilacqua, V., et al.: Retinal fundus biometric analysis for personal identifications. In: Huang, D.-S., Wunsch, D.C., Levine, D.S., Jo, K.-H. (eds.) ICIC 2008. LNCS (LNAI), vol. 5227, pp. 1229–1237. Springer, Heidelberg (2008). https://doi.org/10.1007/978-3-540-85984-0_147
5. Jain, A.K., Arun, R., Salil, P.: An introduction to biometric recognition. *IEEE Trans. Circuits Syst. Video Technol.* **14**(1), 4–20 (2004)
6. Riera, A.: STARFAST: a wireless wearable EEG/ECG biometric system based on the ENOBIO sensor. In: *Proceedings of the International Workshop on Wearable Micro and Nanosystems for Personalised Health* (2008)
7. Hu, J.F., Mu, Z.D.: EEG authentication system based on auto-regression coefficients. In: *2016 10th International Conference on Intelligent Systems and Control (ISCO)*. IEEE (2016)
8. Lee, A., Younghyun, K.: Photoplethysmography as a form of biometric authentication. In: *2015 IEEE SENSORS*. IEEE (2015)
9. Biel, L.: ECG analysis: a new approach in human identification. *IEEE Trans. Instrum. Meas.* **50**(3), 808–812 (2001)
10. Agrafioti, F.: Heart biometrics: theory, methods and applications. In: *Biometrics*, Shanghai, China, pp. 199–216. InTech (2011)
11. Wang, Y.J.: Analysis of human electrocardiogram for biometric recognition. *EURASIP J. Adv. Sig. Process.* **2008**(1), 148658 (2007)
12. Condon, A., Grace, W.: ECG biometrics: the heart of data-driven disruption? *Biom. Technol. Today* **2018**(1), 7–9 (2018)
13. Dimauro, G.: Assessment of speech intelligibility in Parkinson’s disease using a speech-to-text system. *IEEE Access* **5**, 22199–22208 (2017)
14. Ferrero, R.: Ubiquitous fridge with natural language interaction. In: *2019 IEEE International Conference on RFID Technology and Applications (RFID-TA)*. IEEE (2019)
15. Bevilacqua, V.: A new tool to support diagnosis of neurological disorders by means of facial expressions. In: *2011 IEEE International Symposium on Medical Measurements and Applications*. IEEE (2011)
16. Irvine, J.M.: A new biometric: human identification from circulatory function. In: *Joint Statistical Meetings of the American Statistical Association*, San Francisco (2003)
17. Israel, S.A.: ECG to identify individuals. *Pattern Recogn.* **38**(1), 133–142 (2005)
18. Zhang, Z.M., Wei, D.M.: A new ECG identification method using Bayes’ theorem. In: *TENCON 2006–2006 IEEE Region 10 Conference*. IEEE (2006)
19. Bevilacqua, V.: Comparison of data-merging methods with SVM attribute selection and classification in breast cancer gene expression. *BMC Bioinform.* **13**(7), 1–15 (2012)
20. Hejazi, M.: ECG biometric authentication based on non-fiducial approach using kernel methods. *Digit. Sig. Process.* **52**, 72–86 (2016)
21. Camara, C., Peris-Lopez, P., Tapiador, J.E.: Human identification using compressed ECG signals. *J. Med. Syst.* **39**(11), 1–10 (2015). <https://doi.org/10.1007/s10916-015-0323-2>
22. Zhang, Q.X., Zhou, D., Xuan, Z.: HeartID: a multiresolution convolutional neural network for ECG-based biometric human identification in smart health applications. *IEEE Access* **5**, 11805–11816 (2017)
23. Bassiouni, M.: A machine learning technique for person identification using ECG signals. *Int. J. Appl. Phys.* **1**, 37–41 (2016)
24. Hejazi, M.: Non-fiducial based ECG biometric authentication using one-class support vector machine. In: *2017 Signal Processing: Algorithms, Architectures, Arrangements, and Applications (SPA)*. IEEE (2017)
25. Tan, R., Marek, P.: Toward improving electrocardiogram (ECG) biometric verification using mobile sensors: a two-stage classifier approach. *Sensors* **17**(2), 410 (2017)

26. Silva, H., Gamboa, H., Fred, A.: One lead ECG based personal identification with feature subspace ensembles. In: Perner, P. (ed.) *MLDM 2007*. LNCS (LNAI), vol. 4571, pp. 770–783. Springer, Heidelberg (2007). https://doi.org/10.1007/978-3-540-73499-4_58
27. Sriram, J.C.: Activity-aware ECG-based patient authentication for remote health monitoring. In: *Proceedings of the 2009 International Conference on Multimodal Interfaces (2009)*
28. IHS Markit Predictions for 2017 - Electronic Access Control. <https://technology.informa.com/588015/electronic-access-control-ihs-markit-pre%ADdictions-for-2017>. Accessed 27 May 2020
29. Pasero, E., Eugenio, B., Federico, C.: Intruder recognition using ECG signal. In: *2015 International Joint Conference on Neural Networks (IJCNN)*. IEEE (2015)
30. Randazzo, V., Jacopo, F., Eros, P.: ECG WATCH: a real time wireless wearable ECG. In: *2019 IEEE International Symposium on Medical Measurements and Applications (MeMeA)*. IEEE (2019)
31. Randazzo, V., Eros, P., Silvio, N.: VITAL-ECG: a portable wearable hospital. In: *2018 IEEE Sensors Applications Symposium (SAS)*. IEEE (2018)
32. Einthoven's, T. (2020). <https://medical-dictionary.thefreedictionary.com/Einthoven%27s+triangle>
33. Randazzo, V., Jacopo, F., Eros, P.: A wearable smart device to monitor multiple vital parameters—VITAL ECG. *Electronics* **9**(2), 300 (2020)
34. Ferretti, J., Randazzo, V., Cirrincione, G., Pasero, E.: 1-D convolutional neural network for ECG arrhythmia classification. In: Esposito, A., Faundez-Zanuy, M., Morabito, F.C., Pasero, E. (eds.) *Progresses in Artificial Intelligence and Neural Systems*. SIST, vol. 184, pp. 269–279. Springer, Singapore (2021). https://doi.org/10.1007/978-981-15-5093-5_25
35. Bevilacqua, V., Mastronardi, G., Menolascina, F., Pannarale, P., Pedone, A.: A novel multi-objective genetic algorithm approach to artificial neural network topology optimisation: the breast cancer classification problem. In: *The 2006 IEEE International Joint Conference on Neural Network Proceedings*, Vancouver, BC, pp. 1958–1965 (2006). <https://doi.org/10.1109/ijcnn.2006.246940>
36. Randazzo, V., Cirrincione, G., Ciravegna, G., Pasero, E.: Nonstationary topological learning with bridges and convex polytopes: the G-EXIN neural network. In: *2018 International Joint Conference on Neural Networks (IJCNN)*, Rio de Janeiro, pp. 1–6 (2018). <https://doi.org/10.1109/ijcnn.2018.8489186>
37. Cirrincione, G.: The GH-EXIN neural network for hierarchical clustering. *Neural Networks* **121**, 57–73 (2020)
38. Cirrincione, G., Randazzo, V., Kumar, R.R., Cirrincione, M., Pasero, E.: Growing curvilinear component analysis (GCCA) for stator fault detection in induction machines. In: Esposito, A., Faundez-Zanuy, M., Morabito, F.C., Pasero, E. (eds.) *Neural Approaches to Dynamics of Signal Exchanges*. SIST, vol. 151, pp. 235–244. Springer, Singapore (2020). https://doi.org/10.1007/978-981-13-8950-4_22
39. Kumar, R.R., Randazzo, V., Cirrincione, G., Cirrincione, M., Pasero, E.: Analysis of stator faults in induction machines using growing curvilinear component analysis. In: *20th International Conference on Electrical Machines and Systems (ICEMS)*, Sydney, NSW, pp. 1–6 (2017). <https://doi.org/10.1109/icems.2017.8056240>
40. Cirrincione, G., Randazzo, V., Pasero, E.: Growing curvilinear component analysis (GCCA) for dimensionality reduction of nonstationary data. In: Esposito, A., Faundez-Zanuy, M., Morabito, F.C., Pasero, E. (eds.) *Multidisciplinary Approaches to Neural Computing*. SIST, vol. 69, pp. 151–160. Springer, Cham (2018). https://doi.org/10.1007/978-3-319-56904-8_15

41. Cirrincione, G., Hérault, J., Randazzo, V.: The on-line curvilinear component analysis (onCCA) for real-time data reduction. In: 2015 International Joint Conference on Neural Networks (IJCNN), Killarney, pp. 1–8 (2015). <https://doi.org/10.1109/ijcnn.2015.7280318>
42. Cirrincione, G., Vincenzo, R., Eros, P.: The growing curvilinear component analysis (GCCA) neural network. *Neural Networks* **103**, 108–117 (2018)
43. Paviglianiti, A., Randazzo, V., Pasero, E., Vallan, A.: Noninvasive arterial blood pressure estimation using ABPNet and VITAL-ECG. In: 2020 IEEE International Instrumentation and Measurement Technology Conference (I2MTC), Dubrovnik, Croatia, pp. 1–5 (2020). <https://doi.org/10.1109/i2mtc43012.2020.9129361>
44. Randazzo, V., Cirrincione, G., Paviglianiti, A., Pasero, E., Morabito, F.C.: Neural feature extraction for the analysis of Parkinsonian patient handwriting. In: Esposito, A., Faundez-Zanuy, M., Morabito, F.C., Pasero, E. (eds.) *Progresses in Artificial Intelligence and Neural Systems*. SIST, vol. 184, pp. 243–253. Springer, Singapore (2021). https://doi.org/10.1007/978-981-15-5093-5_23
45. Paviglianiti, A., Randazzo, V., Cirrincione, G., Pasero, E.: Neural recurrent approaches to noninvasive blood pressure estimation. In: 2020 International Joint Conference on Neural Networks (IJCNN), Glasgow, pp. 1–7. IEEE (2020)
46. Cirrincione, G., Randazzo, V., Pasero, E.: A neural based comparative analysis for feature extraction from ECG signals. In: Esposito, A., Faundez-Zanuy, M., Morabito, F.C., Pasero, E. (eds.) *Neural Approaches to Dynamics of Signal Exchanges*. SIST, vol. 151, pp. 247–256. Springer, Singapore (2020). https://doi.org/10.1007/978-981-13-8950-4_23
47. Ferretti, J.: Towards uncovering feature extraction from temporal signals in deep CNN: the ECG case study. In: 2020 International Joint Conference on Neural Networks (IJCNN), Glasgow, pp. 1–7. IEEE (2020)
48. Hotelling, H.: Analysis of a complex of statistical variables into principal components. *J. Educ. Psychol.* **24**(6), 417 (1933)
49. Bishop, C.M.: *Neural Networks for Pattern Recognition*. Oxford University Press, Oxford (1995)
50. Natarajan, A., Kevin, S.X., Brian, E.: Detecting divisions of the autonomic nervous system using wearables. In: 38th Annual International Conference of the IEEE Engineering in Medicine and Biology Society (EMBC). IEEE (2016)

Image Processing



Component Tree Computation of 2D Images

Rui Tao and Yuqing Song^(✉)

Tianjin University of Technology and Education, 1310 Dagu South Road,
Tianjin 300222, China
yqsong7@hotmail.com

Abstract. Level set methods are fruitful in computer vision, image coding, image processing, geographic information systems, and many other fields. The connected components of the level sets of an image, ordered by inclusion, are organized into a component tree. We present an algorithm to compute the component tree from image level lines. The running time is $O(m)$, where m is the number of image level lines. Experiments show that the new algorithm runs nearly 2 times faster than the existing method.

Keywords: Level line · Level set · Component tree · Image processing

1 Introduction

The component tree representation provides a unifying formalism for many applications, such as feature extraction [1, 2], image filtering [3, 4], segmentation [5, 6], classification [7], data visualization [8], and stream analysis [9]. The upper (resp. lower) level sets of an image are the pixel sets of level greater (resp. less) than or equal to a given level. The connected components of these level sets, ordered by inclusion, are organized into a component tree, where the component tree of upper (resp. lower) level sets are called a max-tree (resp. min-tree). Max and min-trees are contrast invariant representations of images. This representation is proven to be equivalent to some other popular morphological hierarchies: watersheds, quasi flat zones, and binary partition trees [10, 11]. A more general framework can be found in [12], which encompasses watersheds, graph cuts, random walker, and shortest path segmentation.

Traditional component computation can be classified into three classes: immersion algorithms, flooding algorithms, and merge-based algorithms [13]. Recent trends include parallel computation [14, 15] and extension to multivariate images, i.e., color or multispectral images [16]. Component algorithms generate components, not their boundaries. Monasse et al. argued that for human vision system the boundaries of the components are perceptually more important than the components themselves [17]. Their algorithm, FLLT (Fast Level Line Transform), computes a tree of level lines, where a shape is a level set component with holes filled, and the boundary of a shape is called a level line. FLLT takes a region growing approach to build the min and max-trees. The two trees are then fused to build a level line tree. An improved version, FLST (Fast Level Set Transform) [18], decomposes an image into a shape tree and computes the shape boundaries. The shape tree computation has been extended for the general

case of multidimensional images [19, 20]. Level lines of 2D images can also be computed by a top-down approach [21, 22], which takes the image boundary as the root level line and then processes the private region of each level line to extract its child level lines.

The relationship between the level line tree and the component tree was investigated, based on which an algorithm was proposed to build the component tree from the level lines [23]. The representation of the components by level lines can be used for computing contour-based shape attributes, examining and analyzing object inner structures, and investigating chiaroscuro patterns. In this paper we introduce a new components-from-level-lines algorithm, which visits the level line tree bottom-up, and matches the inner and outer boundaries of components to build the component tree. The algorithm takes $O(m)$ time, where m is the number of level lines. The time is optimal. Experiments show that the new algorithm runs nearly 2 times faster than the existing method in [23].

The rest of the paper is organized as follows. The algorithm is presented in Sect. 2. Section 3 is an experimental report. Section 4 concludes.

2 Proposed Method

2.1 Algorithm Overview

Given the image f on the domain Ω , we call upper level set X_λ of value λ and lower level set X^μ of value μ the subsets of Ω : $X_\lambda = \{x \in \Omega | f(x) \geq \lambda\}$, $X^\mu = \{x \in \Omega | f(x) \leq \mu\}$. The connected components of the upper/lower level sets are organized into an inclusion tree, called *the max/min-tree*. In this paper we elaborate on how *the max-tree* T is computed from the tree τ of the level lines (the boundaries of the upper level sets). The min-tree can be computed by flipping the image.

The algorithm computes the max-tree T from the level line tree τ . Each component $C \in T$ consists of an outer boundary (a positive level line in τ) and zero or more inner boundaries (negative level lines in τ). The computation is to match each positive line with the right negative lines at right levels. The basic idea is quite simple. We process the lines bottom-up, and maintain a tree-structured stack of unmatched negative lines during the process. At each negative line α , α is “pushed” to the stack and becomes the root. At each positive line β , the roots of the stack, if not empty, are “popped” to match β and build the components out-bounded by β . A brief trace of the algorithm is as follows, using the example in Fig. 1.

- (1) We process the level lines (Fig. 1b) in inverse depth first ordering: $\delta, \gamma, \beta, \alpha, \sigma,$ and η , where only the first 3 level lines are negative.
- (2) At δ , $\text{stack}(\delta) = \{\delta\}$
- (3) At γ , $\text{stack}(\gamma) = \{\gamma\}$.
- (4) At β , $\text{stack}(\beta) = \{\beta\} \cup \text{stack}(\gamma) = \{\beta, \gamma\}$, ordered by inclusion. β becomes the root.

- (5) At α , $\text{stack}(\alpha) = \text{stack}(\beta) \cup \text{stack}(\delta) = \{\beta, \gamma, \delta\}$, ordered by inclusion. See Fig. 1(f).
- α matches with β and δ at levels in $[k_2 + 1, k_1]$, making C_1 . See Fig. 1(d, e). β is popped from $\text{stack}(\alpha)$. Now $\text{stack}(\alpha) = \{\gamma, \delta\}$.
 - α matches with γ and δ at levels in $[k_3 + 1, k_2]$, making C_2 . δ is popped from $\text{stack}(\alpha)$. Now $\text{stack}(\alpha) = \{\gamma\}$.
 - α matches with γ at levels in $[k_4 + 1, k_3]$, making C_3 . Now $\text{stack}(\alpha) = \{\gamma\}$.
 - After the 3 components C_1 , C_2 , and C_3 are built, $\text{stack}(\alpha) = \{\gamma\}$. See Fig. 1(g).
- (6) At σ , $\text{stack}(\sigma) = \text{stack}(\alpha) = \{\gamma\}$.
- σ matches with γ at levels in $[k_5 + 1, k_4]$, making C_4 . γ is popped from $\text{stack}(\sigma)$. Now $\text{stack}(\sigma) = \{\}$.
- (7) At η , $\text{stack}(\eta) = \text{stack}(\sigma) = \{\}$.
- η does not match any negative line. So η solely makes C_5 with no holes. Now $\text{stack}(\eta) = \{\}$.

2.2 The Algorithm

The whole algorithm consists of 4 procedures, Algorithm 1–Algorithm 4, where Algorithm 4 is the main procedure. Algorithm 1 processes a negative line α : build $\text{stack}(\alpha)$ by merging $\{\alpha\}$ and the stacks at α 's child lines. Algorithm 2 processes a positive line α , building the component sequence Q of α , where Q consists of the components with α as their outer boundary. The last component in the sequence of each positive line α is recorded by a function $\Phi(\alpha)$. Algorithm 3 computes the child components of the components in a sequence Q . Algorithm 4 computes the component tree T from the level line tree τ . The procedure visits τ bottom-up and process all the lines to build T .

In the procedures, each level line is a node of τ with the following attributes:

- *pre*gion, the private region, i.e., the region inside the level line and outside its child level lines. In the private region, the image assumes a constant pixel value, which is called the private value.
- *p*value, the private value,
- *p*arent, the parent level line,
- *c*hildren, the set of the child level lines.

Each component, as a node of T , has the following attributes:

- *outb*, the out boundary,
- *inB*, the list of inner boundaries,
- *p*value, the private value, i.e., the pixel value in the region which is the subtraction of the component by its child components.
- *c*hildren, the set of the child components.

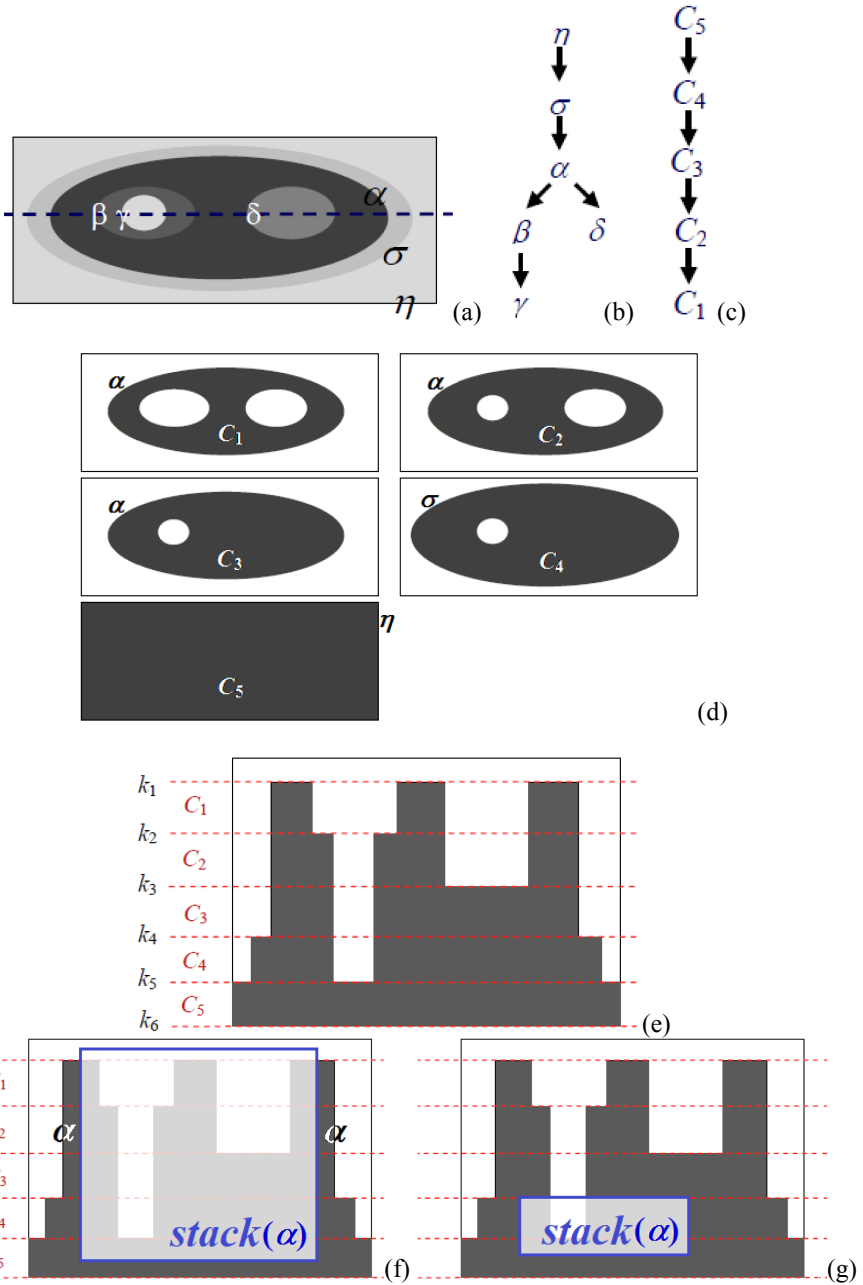


Fig. 1. (a) An image. (b) The level line tree τ . (c) The component tree T . (d) The components. (e) The intensity (of darkness) function along the blue dashed 1D slice in (a). In this figure we use red dash lines (whose levels are k_i 's, respectively) to separate the levels of the components. (f) $stack(\alpha)$ at the beginning of step (5). (g) $stack(\alpha)$ at the end of step (5).

Algorithm 1: *Process_Negative_Line* (α)

1. $stack(\alpha) \leftarrow \{\alpha\} \cup (\cup_{\beta \in \alpha.children} stack(\beta))$

Algorithm 2: *Process_Positive_Line* (α)

1. $Q \leftarrow$ Create an empty array of components

2. $i \leftarrow 1$

3. $k \leftarrow \alpha.pvalue$

4. $stack(\alpha) \leftarrow \cup_{\beta \in \alpha.children} stack(\beta)$

5. **do**

6. $Q[i].inB \leftarrow \{\text{the roots of } stack(\alpha)\}.$

7. $Q[i].outb \leftarrow \alpha$

8. $Q[i].pvalue \leftarrow k$

9. $k \leftarrow \max(\alpha.parent.pvalue, \max_{\gamma \in Q[i].inB} \gamma.pvalue)$

10. $stack(\alpha) \leftarrow stack(\alpha) - \{\gamma \in Q[i].inB \mid \gamma.pvalue = k\}$

11. $i \leftarrow i + 1$

12. **while** $k > \alpha.parent.pvalue$

13. $\Phi(\alpha) \leftarrow Q[i-1]$

14. **return** Q

Algorithm 3: *Compute_Child_Components* (Q)

1. **for** each $Q[i]$ in Q **do**

2. **if** $i \neq 1$ //not the first component

3. $\text{Add } Q[i-1]$ to $Q[i].children$

4. **else** **for** each positive child line β of $Q[i].outb$

5. $\text{Add } \Phi(\beta)$ to $Q[i].children$

6. **for** each D in $Q[i].children$ **do** //breadth first search

7. **for** each β in $D.inB$ **do**

8. **if** $\beta.pvalue \neq Q[i].pvalue$ **continue**

9. **for** each positive child level line γ of β **do**

10. $\text{Add } \Phi(\gamma)$ to $Q[i].children$

Algorithm 4: *Compute_Component_Tree* (τ)

1. **for** each $\alpha \in \tau$ **do** // in inverse depth first ordering
2. **if** α is positive
3. $Q \leftarrow \text{Process_Positive_Line}(\alpha)$
4. $\text{Compute_Child_Components}(Q)$
5. **else**
6. $\text{Process_Negative_Line}(\alpha)$
7. $T \leftarrow$ Create a component tree from $\Phi(\tau.\text{rootline})$
8. **return** T

A time analysis for the algorithm is straightforward. Let m be the number of level lines. Algorithm 1 requires $O(|\alpha.\text{children}|)$ time. Processing all negative lines takes $O(\sum_{\alpha \in \tau} |\alpha.\text{children}|) = O(m)$ time. Algorithm 2 takes $O(|\alpha.\text{children}| + \sum_{C \in Q(\alpha)} |Bd(C)|)$ time, where $Bd(C)$ is the boundary set of C . Processing all positive lines takes $O(\sum_{\alpha \in \tau} |\alpha.\text{children}| + \sum_{\alpha \in \tau} \sum_{C \in Q(\alpha)} |Bd(C)|) = O(m)$. In Algorithm 3, For each C in Q , we search the children (Lines 2–5, 9–10) in $O(\sum_{C \in Q(\alpha)} |C.\text{children}|)$ time. The subtotal time on all components is $O(\sum_{\alpha \in \tau} \sum_{C \in Q(\alpha)} |C.\text{children}|) = O(\sum_{C \in T} |C.\text{children}|) = O(|T|)$. For each C in Q , we access the inner boundaries of the children (Lines 7–8) in $O(\sum_{C \in Q(\alpha)} \sum_{D \in C.\text{children}} |Bd(D)|)$ time. The subtotal time is $O(\sum_{\alpha \in \tau} \sum_{C \in Q(\alpha)} \sum_{D \in C.\text{children}} |Bd(D)|) = O(\sum_{C \in T} \sum_{D \in C.\text{children}} |Bd(D)|) = O(\sum_{C \in T} |Bd(C)|) = O(m)$. The total time of the algorithm is $O(m)$.

3 Experiments

We implemented our algorithm in C++ and ran experiments on a Dell Precision T1600 workstation with 3.10 GHz E31225 CPU and 3.25 GB RAM. The test images, listed in Table 1, are natural images of different sizes and scenes. For each image, we ran the algorithm in [22] to build the level line trees and ran the algorithm in [23] and the proposed algorithm, respectively, to build the component trees. Experiment statistics are listed in Table 2. In the experiments, when measuring the computation time of an algorithm on an image, we ran the algorithm on the image 20 times and took the average execution time. We compared the computation times by the algorithm [23] and the proposed algorithm in Table 3. The proposed method is nearly 2 times faster in average (See the time ratio column in the table).

Table 1. The test images.**Table 2.** Statistics of the test images. For each image, we list the image size n (in pixels), the number m of the level lines, the number M of components in the max-tree.

| Image | n | m | M |
|-------|--------------------|---------|---------|
| 1 | 531×411 | 36882 | 16935 |
| 2 | 560×420 | 19765 | 9895 |
| 3 | 1414×971 | 191371 | 95284 |
| 4 | 1320×870 | 153667 | 79288 |
| 5 | 1600×1200 | 274944 | 138154 |
| 6 | 1600×1200 | 125552 | 60591 |
| 7 | 2592×1944 | 993808 | 505662 |
| 8 | 1912×2700 | 3133980 | 1569496 |

Table 3. Computation time in milliseconds by the proposed algorithm (T_{new}) and the algorithm in [23] (T_{old}), as well as the time ratio T_{old}/T_{new} .

| Image | T_{new} | T_{old} | T_{old}/T_{new} |
|---------|-----------|-----------|-------------------|
| 1 | 5 | 11 | 2.20 |
| 2 | 2 | 3 | 1.50 |
| 3 | 28 | 50 | 1.79 |
| 4 | 23 | 39 | 1.70 |
| 5 | 43 | 80 | 1.86 |
| 6 | 16 | 24 | 1.50 |
| 7 | 176 | 347 | 1.97 |
| 8 | 900 | 2829 | 3.14 |
| average | | | 1.96 |

4 Conclusion

We introduced a novel algorithm to compute level set components from level lines. The algorithm visits the level line tree bottom-up, and matches the positive level lines with the negative level lines at the proper levels to build the component tree. The running time of the algorithm is linear to the number of input level lines. Experiments show that the new algorithm runs nearly 2 times faster than the existing method. The algorithm represents the components by level lines. The new representation can be used for computing contour-based shape attributes, examining and analyzing object inner structures, and investigating chiaroscuro patterns.

Acknowledgment. This research was supported by Natural Science Foundation of China [61070112], Tianjin Science and Technology Innovation Platform Plan [16PTGCCX00150], and Tianjin Artificial Intelligence Science and Technology Major Project [17ZXRGGX00070].

References

1. Silva Dennis, J., Alves Wonder, A.L., Fumio, H.R.: Incremental bit-quads count in component trees: theory, algorithms, and optimization. *Pattern Recogn. Lett.* **129**, 33–40 (2020)
2. Serna, A., Marcotegui, B., et al.: Segmentation of elongated objects using attribute profiles and area stability: application to melanocyte segmentation in engineered skin. *Pattern Recogn. Lett.* **47**, 172–182 (2014)
3. Naegel, B., Passat, N.: Towards connected filtering based on component-graphs. In: Hendriks, Cris L.Luengo, Borgefors, G., Strand, R. (eds.) ISMM 2013. LNCS, vol. 7883, pp. 353–364. Springer, Heidelberg (2013). https://doi.org/10.1007/978-3-642-38294-9_30
4. Kurtz, C., Naegel, B., Passat, N.: Connected filtering based on multivalued component-trees. *IEEE Trans. Image Process.* **23**(12), 5152–5164 (2014)
5. Gloger, O., Tönnies, K.: Subject-Specific prior shape knowledge in feature-oriented probability maps for fully automatized liver segmentation in MR volume data. *Pattern Recogn.* **84**, 288–300 (2018)

6. Xu, Y., Carlinet, E., Géraud, T., et al.: Hierarchical segmentation using tree-based shape spaces. *IEEE Trans. Pattern Anal. Mach. Intell.* **39**(3), 457–469 (2017)
7. Pham, M.T., Aptoula, E., Lefevre, S.: Classification of remote sensing images using attribute profiles and feature profiles from different trees: a comparative study. In: *IEEE International Geoscience & Remote Sensing Symposium*. IEEE (2018)
8. Drapeau, J., Thierry, G., Mickaël, C., et al.: Extraction of ancient maps content by using trees of connected components. In: *International Conference on Document Analysis & Recognition*. IEEE (2018)
9. Çağlayan, T., Behzad, M., et al.: Component trees for image sequences and streams. *Pattern Recogn. Lett* **129** (2019) <https://doi.org/10.1016/j.patrec.2019.11.038>
10. Maia, D.S., Cousty, J., Najman, L., et al.: On the probabilities of hierarchical watersheds. In: *Mathematical Morphology and its Applications to Signal and Image Processing* (2019)
11. Najman, L., Cousty, J., Perret, B.: Playing with Kruskal: algorithms for morphological trees in edge-weighted graphs. In: Hendriks, C.L.L., Borgefors, G., Strand, R. (eds.) *ISMM 2013*. LNCS, vol. 7883, pp. 135–146. Springer, Heidelberg (2013). https://doi.org/10.1007/978-3-642-38294-9_12
12. Couprie, C., Grady, L., Najman, L., Talbot, H.: Power watershed: a unifying graph-based optimization framework. *IEEE Trans. Pattern Anal. Mach. Intell.* **33**(7), 1384–1399 (2011)
13. Carlinet, E., Géraud, T.: A comparison of many max-tree computation algorithms. In: Hendriks, C.L.L., Borgefors, G., Strand, R. (eds.) *ISMM 2013*. LNCS, vol. 7883, pp. 73–85. Springer, Heidelberg (2013). https://doi.org/10.1007/978-3-642-38294-9_7
14. Gotz, M., Cavallaro, G., Geraud, T., et al.: Parallel computation of component trees on distributed memory machines. *IEEE Trans. Parallel Distrib. Syst.* **29**(11), 2582–2598 (2018)
15. Gueunet, C., Fortin, P., Tierny, J., et al.: Task-based augmented contour trees with fibonacci heaps. *IEEE Trans. Parallel Distrib. Syst.* **30**(8), 1889–1905 (2019)
16. Carlinet, E., Geraud, T.: MToS: a tree of shapes for multivariate images. *IEEE Trans. Image Process.* **24**(12), 5330–5342 (2015)
17. Monasse, P., Guichard, F.: Fast computation of a contrast-invariant image representation. *IEEE Trans. Image Process.* **9**(5), 860–872 (2000)
18. Monasse, P.: Morphological representation of digital images and application of registration. PhD dissertation, University of Paris-Dauphine (2000)
19. Caselles, V., et al.: Constructing the tree of shapes of an image by fusion of the trees of connected components of upper and lower level sets. *Positivity* **12**(1), 55–73 (2008)
20. Géraud, T., Carlinet, E., Crozet, S., Najman, L.: A Quasi-linear algorithm to compute the tree of shapes of n D images. In: Hendriks, C.L.L., Borgefors, G., Strand, R. (eds.) *ISMM 2013*. LNCS, vol. 7883, pp. 98–110. Springer, Heidelberg (2013). https://doi.org/10.1007/978-3-642-38294-9_9
21. Song, Y.: A topdown algorithm for computation of level line trees. *IEEE Trans. Image Process.* **16**(8), 2107–2116 (2007)
22. Song, Y.: Computation of level lines of 4-/8-connectedness. *J. Vis. Commun. Image Represent.* **25**(2), 435–444 (2014)
23. Song, Y., et al.: Computation of level set components from level lines. *IEEE Trans. Image Process.* **20**(10), 2722–2729 (2011)



An Efficient Method for Computation of Entropy and Joint Entropy of Images

Debapriya Sengupta^{1,2(✉)}, Phalguni Gupta³, and Arindam Biswas¹

¹ Indian Institute of Engineering Science and Technology (IIEST),
Shibpur, Howrah, India

debapriya_20oct@yahoo.co.in

² National Institute of Technical Teachers' Training and Research (NITTTR),
Kolkata, India

³ GLA University, Mathura, India

Abstract. This paper proposes an efficient method to compute entropy and joint entropy of images. Entropy of images is used to determine its quality. It is defined as the randomness or uncertainty present in the image. Similarly, joint entropy is a measure of the uncertainty present in the overlapped region of two images. Entropy and joint entropy computations are vital in several image processing applications. Intensity based image registration is done by maximizing the mutual information between two images. Mutual information is nothing but the difference between sum of individual entropies and joint entropy of two images. Image registration has applications, especially in the medical field, e.g. diagnosis and treatment of diseases. The entropy and joint entropy computation methods proposed in this paper are computationally less expensive than the standard methods. Entropy computation takes 78.60% less time than the standard method while computational time of joint entropy is reduced by 83.59%. This increase in efficiency comes at the cost of an error of 1.52% in entropy and 4.54% in joint entropy.

Keywords: Entropy · Joint entropy · Image registration

1 Introduction

Entropy is a measure of information available in the image. Similarly, joint entropy is the amount of information contained within the overlapped portion of two images. Entropy and joint entropy computations are vital in image processing applications. One of the most common applications, where entropy and joint entropy are indispensable, is image registration. Registration is a process which makes the pixels in two images precisely coincide to the same points in the scene. Once registered, the images can be combined or fused in a way that improves information extraction.

Several algorithms are available to register two images. A few common ones are corresponding landmark based registration algorithms [1, 2, 5, 19] and surface based registration algorithms [3, 4, 9, 11, 13, 14]. But the recent and more accurate algorithms are based on pixel intensities [7, 8, 12, 21, 22]. Development and use of entropy and joint entropy have brought in a breakthrough in the field of image registration using

pixel intensities. Minimizing joint entropy was proposed in [15]. This was further improved and mutual information was used as a measure of registration [6, 20]. Mutual information is the difference between the sum of the entropies of the individual images at overlap and their joint entropy. Various modifications of the mutual information measure, like normalization, have proved to be robust, and have resulted in fully automatic 3D-3D image registration algorithms [16–18].

Medical images are big in size. Registering two medical images requires to maximize the mutual information of the two images. Automatic maximization of mutual information, therefore, is a time consuming process. It consists of computing entropies of two overlapped images and their joint entropy, at overlap. Computation time for mutual information can be reduced by a significant amount, if entropy and joint entropy can be computed efficiently. In this paper, we have attempted to develop an efficient computation method for entropy and joint entropy of images.

The rest of the paper is organized as follows. Section 2 gives definitions and mathematical expressions for entropy and joint entropy. Section 3 derives the proposed modified formulae. Section 4 calculates the gain in computation time. Section 5 discusses about the error or difference in entropy and joint entropy values computed by the standard and proposed methods. Finally, Sect. 6 concludes the paper.

2 Entropy and Joint Entropy

The term entropy is derived from information theory and it gives a measure of the information contained in an image. It can also be defined as a measure of randomness or uncertainty within the image. More randomness implies more information which in turn implies higher entropy. Joint entropy is the entropy of the combination of two images which are overlapped on each other. Joint entropy changes with the position of overlap.

2.1 Entropy

Given events $e_1, e_2 \dots e_m$ occurring with probabilities $p_1, p_2 \dots p_m$, the Shanon Entropy, is defined as,

$$H = \sum_i p_i \log\left(\frac{1}{p_i}\right) = - \sum_i p_i \log(p_i) \quad (1)$$

The term $\log\left(\frac{1}{p_i}\right)$ signifies that the amount of information gained from an event with probability p_i is inversely related to the probability of occurrence of the event. The rarer the event, the more meaning is assigned to occurrence of the event. The information per event is weighted by the probability of occurrence. The resulting entropy term is the average amount of information to be gained from a certain set of events.

In case of images, a probability distribution of intensities can be estimated by counting the number of times each intensity occurs in the image and dividing that number by the total number of occurrences. An image consisting of almost a single

intensity will have a low entropy value; it contains very little information. A high entropy value will be yielded by an image with more or less equal quantities of many different intensities, which is an image containing a lot of information. In this manner, the Shannon entropy is also a measure of dispersion of a probability distribution.

2.2 Joint Entropy

A joint histogram of two images, is a two-dimensional (2D) plot, showing the combination of intensities, in each of the two images, for all corresponding points [10]. Joint histogram changes as the alignment of the images change. A joint histogram of two images can be used to estimate a joint probability distribution of their intensities by dividing each entry in the histogram by the total number of entries. The Shannon entropy for a joint distribution i.e. joint entropy is defined as

$$H(A, B) = - \sum_{i,j} p_{(i,j)} \log(p_{(i,j)}) \quad (2)$$

When images are registered, corresponding structures overlap and joint histogram shows certain clusters for the intensities of those structures. As the images become misaligned, structures also start overlapping with structures that are not their counterparts in the other image.

3 Proposed Method

In this paper, we have made an attempt to improve the efficiency of computation of entropy and joint entropy. As it is evident from Eq. 1, the standard method for entropy computation takes each intensity i at a time, computes $p_i \log(p_i)$, then sums up for all i . In the proposed method, instead of considering each intensity i at a time, we consider intensities i and $i + 1$ together. Taking two consecutive intensities together, the modified equation becomes

$$H_1 = - \sum_{i=2r} (p_i + p_{i+1}) \log(p_i + p_{i+1}) \quad (3)$$

where r varies from 0 to $\frac{(L-1)}{2}$, L is the range of intensities. We compute the error introduced in H_1 .

Histogram of an image can be assumed to follow Gaussian distribution as frequency of occurrence vary smoothly with intensity. If $p_i = a$, p_{i+1} can be expressed as $a + c$, where c is a small real number, as it is unlikely that there should be a drastic change in probabilities, between two consecutive intensities. Hence, the first two terms in Eq. 3 can be written as

$$T_1 = a \log(a + a + c) + (a + c) \log(a + a + c) \quad (4)$$

which evaluates to

$$T_1 = a \log a + (a + c) \log(a + c) + (2a + c) \log(2) + a \log\left(1 + \frac{c}{2a}\right) + (a + c) \log\left\{1 - \frac{c}{2(a+c)}\right\} \tag{5}$$

It can be seen that the first two terms of Eq. 5 are same as those of Eq. 1, which is the standard equation of entropy. Thus,

$$(2a + c) \log 2 + a \log\left(1 + \frac{c}{2a}\right) + (a + c) \log\left\{1 - \frac{c}{2(a+c)}\right\} \tag{6}$$

denotes error. Since c is small,

$$\frac{c}{2a} < 1 \tag{7}$$

$$\frac{c}{2(a+c)} < 1 \tag{8}$$

Using Taylor series,

$$a \log\left(1 + \frac{c}{2a}\right) = a \left\{ \frac{c}{2a} - \frac{\left(\frac{c}{2a}\right)^2}{2} + \dots \right\} \tag{9}$$

Since $\frac{c}{2a} < 1$, higher order terms of the series get smaller and smaller, and can be neglected. Hence, Eq. 9 reduces to $\frac{c}{2}$.

Similarly, using Taylor series, we also get

$$(a + c) \log\left(1 - \frac{c}{2(a+c)}\right) = (a + c) \left\{ \frac{-c}{2(a+c)} - \frac{\left(\frac{-c}{2(a+c)}\right)^2}{2} + \dots \right\} \tag{10}$$

by neglecting square term onwards, Eq. 10 reduces to $-\frac{c}{2}$.

Using Eq. 9 and Eq. 10, Eq. 6 can be written as

$$(2a + c) \log 2 \tag{11}$$

Using the correction of Eq. 11, the modified equation of entropy becomes

$$H' = - \sum_{i=2r} (p_i + p_{i+1}) \log\left(\frac{p_i + p_{i+1}}{2}\right) \tag{12}$$

Going by similar intuition as for entropy, computation of joint entropy can also be modified. Instead of considering each intensity pair (i, j) of image pair (A, B) , we consider intensity pairs (i, j) , $((i + 1), j)$, $(i, (j + 1))$ and $((i + 1), (j + 1))$ together. Taking these four pairs together, the modified form of Eq. 2 becomes,

$$H_1(A, B) = - \sum_{i=2r_1, j=2r_2} P \log P \tag{13}$$

where $P = p_{(i,j)} + p_{(i,(j+1))} + p_{((i+1),j)} + p_{((i+1),(j+1))}$ and r_1 and r_2 vary from 0 to $\frac{(L_1-1)}{2}$ and 0 to $\frac{(L_2-1)}{2}$ respectively. L_1 and L_2 are intensity ranges of images A and B respectively. For a pair of values i and j , sum of four terms of Eq. 13 can be written as,

$$p_{(i,j)} \log P + p_{(i,(j+1))} \log P + p_{((i+1),j)} \log P + p_{((i+1),(j+1))} \log P \tag{14}$$

Like in case of entropy, joint probability of images (A, B) at any given orientation can be assumed to follow Gaussian distribution, i.e. drastic change in joint probability values between consecutive pair of intensities is unlikely. Hence, if $p_{(i,j)} = k$, $p_{(i,(j+1))}$, $p_{((i+1),j)}$ and $p_{((i+1),(j+1))}$ can be represented as $k + b_1$, $k + c_1$ and $k + d_1$ respectively, where b_1 , c_1 and d_1 are small real numbers. Substituting for $p_{(i,j)}$, $p_{(i,(j+1))}$, $p_{((i+1),j)}$ and $p_{((i+1),(j+1))}$, Eq. 14 can be written as,

$$k \log P + (k + b_1) \log P + (k + c_1) \log P + (k + d_1) \log P \tag{15}$$

Equation 15 evaluates to

$$\begin{aligned} &k \log(k) + (k + b_1) \log(k + b_1) + (k + c_1) \log(k + c_1) \\ &\quad + (k + d_1) \log(k + d_1) \\ &\quad + \log 4(4k + b_1 + c_1 + d_1) \\ &\quad + k \log \left\{ 1 + \frac{b_1 + c_1 + d_1}{4k} \right\} \\ &\quad + (k + b_1) \log \left\{ 1 + \frac{c_1 + d_1 - 3b_1}{4(k + b_1)} \right\} \\ &\quad + (k + c_1) \log \left\{ 1 + \frac{b_1 + d_1 - 3c_1}{4(k + c_1)} \right\} \\ &\quad + (k + d_1) \log \left\{ 1 + \frac{b_1 + c_1 - 3d_1}{4(k + d_1)} \right\} \end{aligned} \tag{16}$$

First four terms of Eq. 16 are four consecutive terms of the standard joint entropy equation (Eq. 2). Thus,

$$\begin{aligned}
 & \log 4(4k + b_1 + c_1 + d_1) + k \log \left\{ 1 + \frac{b_1 + c_1 + d_1}{4k} \right\} \\
 & + (k + b_1) \log \left\{ 1 + \frac{c_1 + d_1 - 3b_1}{4(k + b_1)} \right\} \\
 & + (k + c_1) \log \left\{ 1 + \frac{b_1 + d_1 - 3c_1}{4(k + c_1)} \right\} \\
 & + (k + d_1) \log \left\{ 1 + \frac{b_1 + c_1 - 3d_1}{4(k + d_1)} \right\}
 \end{aligned} \tag{17}$$

denotes error. Since b_1 , c_1 and d_1 are small real numbers,

$$\frac{b_1 + c_1 + d_1}{4k} < 1 \tag{18}$$

$$\frac{c_1 + d_1 - 3b_1}{4(k + b_1)} < 1 \tag{19}$$

$$\frac{b_1 + d_1 - 3c_1}{4(k + c_1)} < 1 \tag{20}$$

$$\frac{b_1 + c_1 - 3d_1}{4(k + d_1)} < 1 \tag{21}$$

Using Taylor series, neglecting second term onwards and summing up Eqs. 18, 19, 20 and 21, Eq. 17 reduces to

$$\log 4(4k + b_1 + c_1 + d_1) \tag{22}$$

Using this correction, the modified equation of joint entropy can be found out to be

$$H_1(A, B) = - \sum_{i=2r_1, j=2r_2} P \log \frac{P}{4} \tag{23}$$

4 Gain in Computation Time

The proposed formula of entropy considers two intensities at a time, as opposed to the standard formula, which considers one intensity. This results in reduction in computation. Similarly, the proposed formula of joint entropy considers four intensity combinations at a time, whereas the standard formula considers only one combination. This also results in decrease in computation by the proposed method.

4.1 Gain in Computation Time of Entropy

Two consecutive terms in entropy computation by the standard method are,

$$e_{std} = p_i \log(p_i) + p_{(i+1)} \log(p_{(i+1)}) \quad (24)$$

There are two logarithms, two multiplications and one addition in this computation. In the proposed method, p_i and $p_{(i+1)}$ are computed together.

$$e_{prp} = (p_i + p_{(i+1)}) \log\left(\frac{p_i + p_{(i+1)}}{2}\right) \quad (25)$$

This computation requires one logarithm, one multiplication, one addition and one division operations. So, compared to the standard method, the proposed method requires one logarithm and one multiplication less, but one extra division is required. We have noted the time required to do one logarithm and one multiplication operations and have compared that with the time required to do one division operation. The percentage reduction in computation time in the later, as compared to the former is calculated. This gives a measure of the gain in computation time. The time comparison has been done on a 64 bit Windows 10 Pro computer with 4 GB RAM and Intel(R) Core(TM) i7-4790, 3.60 GHz processor. The average gain in time is found to be 78.60%.

4.2 Gain in Computation Time of Joint Entropy

Joint entropy of intensities i and j by the standard method is,

$$p_{(i,j)} \log(p_{i,j}) + p_{((i+1),j)} \log(p_{((i+1),j)}) + p_{(i,(j+1))} \log(p_{(i,(j+1))}) \\ + p_{((i+1),(j+1))} \log(p_{((i+1),(j+1))}) \quad (26)$$

This computation requires four logarithms, four multiplications and three additions. In the proposed method, joint entropy of intensities i and j can be computed as

$$(p_{(i,j)} + p_{((i+1),j)} + p_{(i,(j+1))} + p_{((i+1),(j+1))}) \\ \log\left(\frac{p_{(i,j)} + p_{((i+1),j)} + p_{(i,(j+1))} + p_{((i+1),(j+1))}}{4}\right) \quad (27)$$

This computation requires three additions, one multiplication, one logarithm and one division. So, the proposed method needs three logarithms, and three multiplications less than the standard method, but one extra division is required. Like in the case of entropy, we have compared the time required to compute three logarithms and three multiplications with the time required to compute one division. Gain in computation time is given by the reduction in the time required by the later, as compared to the former. This computation, like in the case of entropy, has been done on a 64 bit Windows 10 Pro computer with 4 GB RAM and Intel(R) Core(TM) i7-4790, 3.60 GHz processor. The average time gain is found to be 83.59%.

5 Error Introduced by the Proposed Method

The proposed method assumes that histogram and joint histogram of images follow Gaussian distribution. This assumption is justified as abrupt change in frequencies between consecutive intensities is unlikely in images. However, in order to estimate the accuracy of our method, we compute the percentage error incurred. For this, we use a data-set of 9979 images collected randomly from six public image databases. We find out the average percentage difference in entropy values computed by the standard method and the proposed method. This difference comes out to be 1.52%. Similarly, we compute joint entropy of each image with itself rotated by 20°, on this data-set. Results show that there is an average of 4.54% difference between the values obtained by the standard and the proposed methods.

6 Conclusion

In this paper, we propose efficient methods for computation of entropy and joint entropy of images. The developed methods take 78.60% (entropy) and 83.59% (joint entropy) less time than the standard methods. This time efficiency can be of huge benefit in case of large size images, like medical images. Intensity based medical image registration requires to calculate entropies and joint entropy of two images. Mutual information, which is the difference between the sum of individual entropies and joint entropy, needs to be maximized. The proposed methods can improve time efficiency of medical image registration to a large extent. This time efficiency in entropy and joint entropy computations come at the cost of an error of 1.52% and 4.54% respectively.

References

1. Amit, Y., Kong, A.: Graphical templates for model registration. *IEEE Trans. Pattern Anal. Mach. Intell.* **18**(3), 225–236 (1996). <https://doi.org/10.1109/34.485529>
2. Arun, K., Huang, T., Blostein, S.: Least-squares fitting of two 3-D point sets. *IEEE Trans. Pattern Anal. Mach. Intell. PAMI* **9**(5), 698–700 (1987). <https://doi.org/10.1109/tpami.1987.4767965>
3. Besl, P., McKay, N.: A method for registration of 3-D shapes. *IEEE Trans. Pattern Anal. Mach. Intell.* **14**(2), 239–256 (1992). <https://doi.org/10.1109/34.121791>
4. Borgefors, G.: Distance transformations in digital images. *Comput. Vis., Graph. Image Process.* **34**(3), 344–371 (1986). [https://doi.org/10.1016/s0734-189x\(86\)80047-0](https://doi.org/10.1016/s0734-189x(86)80047-0)
5. Chua, C., Jarvis, R.: 3D free-form surface registration and object recognition. *Int. J. Comput. Vision* **17**(1), 77–99 (1996). <https://doi.org/10.1007/bf00127819>
6. Collingnon, A., Maes, F., Delaere, D., Vandermeulen, D., Suetens, P., Marchal, G.: Automated multi-modality image registration based on information theory. *Inf. Process. Med. Imaging* **3**, 263–274 (1995)
7. Elsen, P., Pol, E., Sumanaweera, T., Hemler, P., Napel, S., Adler, J.: Grey value correlation techniques used for automatic matching of CT and MR volume images of the head (1994)

8. Hajnal, J., Saeed, N., Oatridge, A., Williams, E., Young, I., Bydder, G.: Detection of subtle brain changes using subvoxel registration and subtraction of serial MR images. *J. Comput. Assist. Tomogr.* **19**(5), 677–691 (1995). <https://doi.org/10.1097/00004728-199509000-00001>
9. Hill, D., Hawkes, D.: Medical image registration using knowledge of adjacency of anatomical structures. *Image Vis. Comput.* **12**(3), 173–178 (1994). [https://doi.org/10.1016/0262-8856\(94\)90069-8](https://doi.org/10.1016/0262-8856(94)90069-8)
10. Hill, D.L.G., Hawkes, D.J., Harrison, N.A., Ruff, C.F.: A strategy for automated multimodality image registration incorporating anatomical knowledge and image characteristics. In: *Information Processing in Medical Imaging*, pp. 182–196 (1993)
11. Jiang, H., Robb, R., Tainter, K.: New approach to 3-D registration of multi-modality medical images by surface matching. *Vis. Biomed. Comput.* **1808** (1992)
12. Lemieux, L., Kitchen, N., Hughes, S., Thomas, D.: Voxel-based localization in frame-based and frameless stereotaxy and its accuracy. *Med. Phys.* **21**(8), 1301–1310 (1994). <https://doi.org/10.1118/1.597403>
13. Meyer, C., Leichtman, G., Brunberg, J., Wahl, R., Quint, L.: Simultaneous usage of homologous points, lines, and planes for optimal, 3-D, linear registration of multimodality imaging data. *IEEE Trans. Med. Imaging* **14**(1), 1–11 (1995). <https://doi.org/10.1109/42.370397>
14. Pelizzari, C., Chen, G., Spelbring, D., Weichselbaum, R., Chen, C.: Accurate three-dimensional registration of CT, PET, and/or MR images of the brain. *J. Comput. Assist. Tomogr.* **13**(1), 20–26 (1989). <https://doi.org/10.1097/00004728-198901000-00004>
15. Studholme, C., Derek, L., David, J.: Multiresolution voxel similarity measures for MR-PET registration. *Inf. Process. Med. Imaging* **3**, 287–298 (1995)
16. Studholme, C., Hill, D., Hawkes, D.: Automated 3-D registration of MR and CT images of the head. *Med. Image Anal.* **1**(2), 163–175 (1996). [https://doi.org/10.1016/s1361-8415\(96\)80011-9](https://doi.org/10.1016/s1361-8415(96)80011-9)
17. Studholme, C., Hill, D., Hawkes, D.: Automated three-dimensional registration of magnetic resonance and positron emission tomography brain images by multiresolution optimization of voxel similarity measures. *Med. Phys.* **24**(1), 25–35 (1997). <https://doi.org/10.1118/1.598130>
18. Studholme, C., Hill, D., Hawkes, D.: An overlap invariant entropy measure of 3D medical image alignment. *Pattern Recogn.* **32**(1), 71–86 (1999). [https://doi.org/10.1016/s0031-3203\(98\)00091-0](https://doi.org/10.1016/s0031-3203(98)00091-0)
19. Thirion, J.: New feature points based on geometric invariants for 3D image registration. *Int. J. Comput. Vision* **18**(2), 121–137 (1996). <https://doi.org/10.1007/bf00054999>
20. Wells, W., Viola, P., Atsumi, H., Nakajima, S., Kikinis, R.: Multi-modal volume registration by maximization of mutual information. *Med. Image Anal.* **1**(1), 35–51 (1996). [https://doi.org/10.1016/s1361-8415\(01\)80004-9](https://doi.org/10.1016/s1361-8415(01)80004-9)
21. Woods, R., Cherry, S., Mazziotta, J.: Rapid automated algorithm for aligning and reslicing PET images. *J. Comput. Assist. Tomogr.* **16**(4), 620–633 (1992). <https://doi.org/10.1097/00004728-199207000-00024>
22. Woods, R., Mazziotta, J., Cherry, A.R.: MRI-PET registration with automated algorithm. *J. Comput. Assist. Tomogr.* **17**(4), 536–546 (1993). <https://doi.org/10.1097/00004728-199307000-00004>



A Hybrid Convolutional Neural Network for Complex Leaves Identification

Daniel Ayala Niño^{1(✉)}, Jair Cervantes Canales¹,
Farid García Lamont¹, Joel Ayala de la Vega¹,
and Guillermo Calderón Zavala²

¹ UAEMEX (Universidad Autónoma del Estado de México), Jardín Zumpango
s/n, Fraccionamiento El Tejocote, 56259 Texcoco, CP, Mexico
{danielayalanio, joelayala2001}@yahoo.com.mx,
{jcervantesc, fgarcial}@uaemex.mx
² ColPos (Colegio de Postgraduados),
Km. 36.5, Montecillo, 56230 Texcoco, CP, Mexico
cazagu@colpos.mx

Abstract. The classification of leaves has gained popularity through the years, and a great variety of algorithms has been created to target these tasks, among those is the Deep Learning approach, which simplicity of learning from raw imputed data makes this task easy to target. However, not all methods are into the complex leaves classification task. In this work we propose a different approach in the way the leaf's pictures are used to train the models, this is done by using the front and back face of a leaf as one element of the dataset. These pairs will be inputted into two shared convolutional layers, making the models to learn from a complete leaf. The results obtained in this work overpassed the accuracy obtained in related works. For this, we created a new complex leaves dataset, that consists of 6 different kinds of peach varieties, the dataset is available in this link (<https://drive.google.com/drive/folders/1rWCr9DrknoK0HKFhNRavCVgZ5UKjU3hi>).

Keywords: Complex leaves identification · Convolutional Neural Networks · Computer vision

1 Introduction

Plants identification has always played an important role in different disciplines, such as medicine in the development of new drugs [1, 2, 15], botany [3], agriculture [4, 9, 32]. This last one is important for food production. It is known that by 2050, global food production will increase by 60%. Thus, knowing which variety of plant is better under certain conditions, will be a clue point to improve and increase the agricultural production [5].

Since the necessity of identifying plants has increased for different reasons exposed above, the techniques for classifying them have also improved. Botanists use different leaf's characteristics (features like texture, color, morphological, venation, among others) to identify the plants, they spend too much time studying a family of plant and its varieties, this is because most of these features are hand-crafted [3].

On the other hand, new technologies have targeted this aim, like machine learning and computer vision. This has been done by applying different techniques, such as extracting features from the leaves using different algorithms to get the more descriptors as possible from it [6–8, 10] and then using these features to feed a classifier. Nowadays with the increasing popularity of Deep Learning and Convolutional Neural Networks (CNN) due to its effectiveness with image classification, have demonstrated that it is not necessary to hand-engineer the features before its classification [11]. These kinds of models train using big datasets with millions of elements, and it is common knowledge that the bigger the dataset is the better the performance of the model will be [12].

Related papers have worked on big datasets classifying different kinds of plants [13, 14], but there are not too much-related papers focused on the classification of complex leaves using Deep Learning. In a previous work [7], we demonstrated that it is possible to classify complex leaves, using a Genetic Algorithm to select the features that better describe a plant, then this set of features were used to train a classifier, obtaining high rates of accuracy. Our purpose in this research is to create a model that could classify different varieties of peach and it will be able to learn from a complete leaf, not just from its back face or front face, by separate; thing that is not targeted yet in the state of the art. To accomplish this, we have created a new dataset in which these two leaf's faces are considered as one element of the dataset, and inputting these pairs into our new hybrid convolutional neural network models, which first convolutional layers are shared, this approach has overpassed our previous work's accuracy [7]. The CNN models used in this research were based on the models exposed in [16] and [24].

The paper is organized as follows. In Sect. 2 we give a brief review of the state of the art related to complex leaves classification. Then in Sect. 3, we describe the method used to classify the Peach leaves. We show the results obtained with the model described in Sect. 4. And finally, our conclusions related to the results obtained and future work is described in Sect. 5.

2 State of the Art

There are two main approaches that most of the literature used to classify plants by using leaves and computer vision. These basically are: Using hand-crafted features to feed a classifier [17], then we have the deep learning approach using CNN to automatically extract the main information from pictures and then classify them, in some cases it is necessary to pre-process the pictures to feed a CNN, something unusual, because in most of the cases CNN's are fed with raw pictures. We will give a glimpse of the state of the art related to the methods described above.

The hand-crafted extraction method has been broadly used for plant classification since every plant has unique physical characteristics that distinguish them from others [30, 31]. Like the morphological characteristics, which could be extracted using Fourier descriptors [18], where Aakif and Khan [13] used it together with a new feature called shape-defining, this final vector was used to feed an artificial neural network (ANN), obtaining an accuracy of 96%. Another way to do it is by the texture of the leaf, like

Backes et al. [19], who uses fractal theory to classify ten types of leaves achieving a precision of 90%. Caglayan et al. extracted shape and color features to classify them using algorithms like K-Nearest Neighbor, Support Vector Machines, Naïve Bayes and Random Forest, obtaining a 96% accuracy working along with the Flavia dataset [10]. Elneimr, proposed a system that consists of five steps, which are preprocessing the image, then the image segmentation is applied, after this, the features are extracted like curvelet transform descriptors, local binary pattern and gray level co-occurrence matrix texture, then the feature selection is carried using the Neighborhood Component Feature Selection (NCFS) technique, selecting the highly discriminative features, obtaining an accuracy of 98% [20]. The approaches described above are time-consuming since the process of pre-processing the image, extracting and selecting the features must be done with each element of the dataset, and for new leaves the same process must be carried. Most of the time all features extracted are used, but not all of them contribute significantly, so that means that other algorithms must be held to select the best features, this means more time spending selecting features [6, 7]. In contrast with the Deep Learning approach where all this is done automatically.

CNN's has become the most popular algorithm for computer vision tasks, due to its excellent performance in different fields like image classification, image recognition and image segmentation. And it has showed a great performance in the plant classification task. Like Guillermo et al. [11], where three different legume species were classified (white bean, red bean and soybean), here they highlight different levels of vein details, using vein segmentation, using two kinds of setups, reaching a 96.9% accuracy, in comparison with a similar approach, done by Larese et al. [21] where 95.1% accuracy was reached, here instead of CNN's some vein measures were extracted to feed a SVM, PDA or RF. Lee et al. [22], used CNN's to classify the plants from the MalayaKew (MK) Leaf Dataset, that consist of images of leaves from 44 species classes, and reusing a pre-trained CNN ILSVRC2012. Here they used deconvolutional networks (DN) to find out which part of the leaves the CNN is focusing on, obtaining a 99.5% accuracy. CNN's are also used to create new features like the work of Ramos et al. [23], where a convolutional autoencoder (CAE) is used as feature extractor from the leaf's pictures, and this final vector is used to feed a SVM, obtaining an accuracy of 94.74%. Bing Wang and Dian Wang, proposed a method of Few-Shot learning applying the Siamese Network [24], this to create a metric space for leaf classification, where similar samples are close to each other and dissimilar samples are far away, this is due to the small datasets that were used (Flavia, Swedish and Leafsnap) obtaining a 95.32% accuracy. Lee et al. [16], also used DN to find out what a CNN is learning from leaves, and proposed hybrid-CNN's models, these hybrid models have two inputs, one input is the leaf picture, and the second input is a patch from the same leaf, this with the aim to focus on the leaf's venation. Three different hybrid models were described on this work, obtaining a 96.3% accuracy using the hybrid model Early fusion (conv-sum).

Something to highlight about the state of the art described above is that the models were not focused to classify complex leaves, which are leaves that belong to the same species, but they are from different varieties. The leaves used in the state of the art did not meet this requirement, being this our target, which consists of classifying 6 varieties of peach. Also, most of the CNN's in the literature don't pay attention to which side of

the leaf they are learning from, both sides of the leaves are used as different samples of the dataset, in our approach we want the model to learn from a complete leaf, and that is its front and back face, and this is achieved by our hybrid CNN models.

3 CNN Proposal

Deep learning is a machine learning algorithm that consists of multiple layers, letting the representations of multiple data abstraction. Its main purpose is to extrapolate new features from raw input representations, this is done without telling the model which features to use and how to extract them. Being this the importance of using CNN, because of its ability to classify and extract the characteristics from images without needing to tell it how to do it, and the convolutional layer helps us to reach this purpose. After each convolution layer comes a pooling layer, this kernel is creating subsamples from the inputted image, in order to reduce the computational cost and space. At the end of these convolution and pooling layers, the full connected layer follows, this last layer works as a hidden layer of an ANN [7]. In this section, the architecture used for this work is discussed.

3.1 Models

The architectures exposed here follows the same principle proposed by Lee et al. [16] and Bing Wang [24], in this work, we decided that it is important for the model to train with a dataset divided into two components, the front face of the leaf and the backside of the same, and in contrast of [24], we use this principle of the Siamese network to create a function that learns the similarities among the front side and the backside of the same leaf, that is why the comparison of leaves belonging to a different variety is not held. Figure 1 shows a representation of the models applied, as it can be seen, we have two different models that use an early convolution fusion, applying a conv-sum [16]. The input (a) of the models consists of the front face of the leaf and the input (b) is the same leaf back face. Two different datasets were created to train the models, one model was trained with pictures of 224×224 pixels (Fig. 1a), and the second model with a higher resolution, 416×416 pixels (Fig. 1b). More details about the dataset will be drawn out in Sect. 4.

The early convolution fusion consists of two streams, these streams are sharing weights, that means its updating is not independent from each other. After the first 3 conv-layers, the resulting convolutional tensor from each stream will be added up, the result will be convolved across two more units, this for the first model, for the second model, the result will be convolved across 4 units, this is because the picture is bigger and it is possible to extract more information from it. More details about the models are described on Table 1 and 2. Dropout where used in the unit 4 and 5 of model (224×224), for unit 4 a dropout of 0.05 was used and for unit 5 a dropout 0.1 was used.

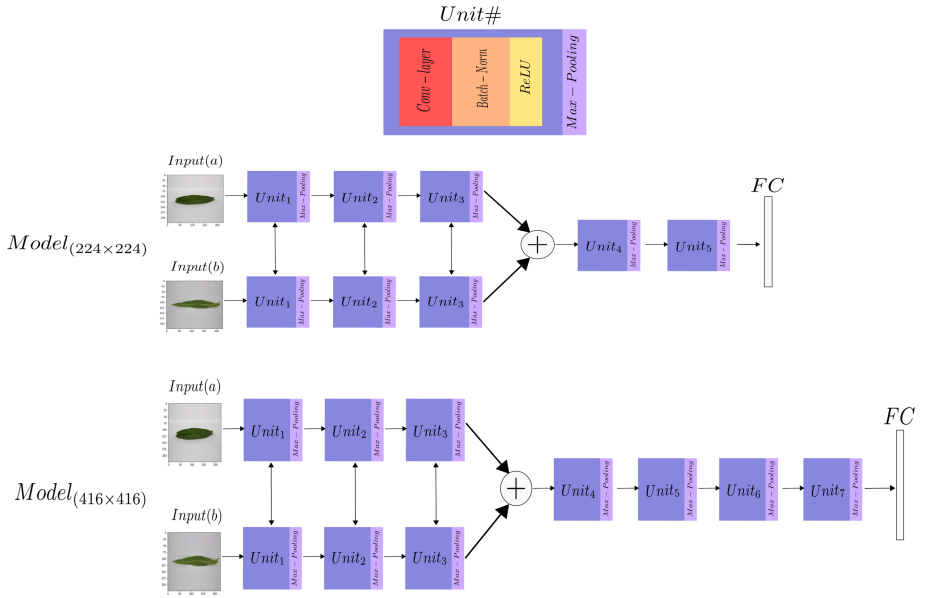


Fig. 1. a) Model (224 × 224). b) Model (224 × 224).

Table 1. Model (224 × 224)

| Unit1 ConvL1 | MaxPool 1 | Unit2 ConvL2 | MaxPool2 | Unit 3 ConvL3 | MaxPool3 | Unit4 ConvL4 | Max- Pool4 | Unit5 ConvL5 | Max- Pool5 | FC |
|-----------------|--------------|-----------------|----------|------------------|----------|-----------------|---------------|-----------------|---------------|-----|
| 5X5X18 | 3X3 | 5X5X30 | 3X3 | 5X5X60 | 3X3 | 5X5X100 | 2X2 | 5X5X90 | 2X2 | 720 |

Table 2. Model (416 × 416)

| Unit 1 Conv L1 | Max Pool 1 | Unit2 ConvL 2 | Max Pool 2 | Unit 3 ConvL 3 | Max Pool 3 | Unit4 ConvL4 | Max- Pool 4 | Unit5 ConvL 5 | Max- Pool 5 | Unit6 ConvL 6 | Max- Pool 6 | Unit6 ConvL7 | Max- Pool 7 | FC |
|-------------------------|------------------|---------------------|------------------|----------------------|------------------|-----------------|-------------------|---------------------|-------------------|---------------------|-------------------|-----------------|-------------------|-----|
| 5X5 X18 | 3X3 | 5X5X3 0 | 3X3 | 5X5X6 0 | 3X3 | 5X5X10 0 | 2X2 | 5X5X9 0 | 2X2 | 5X5X9 0 | 2X2 | 5X5X18 0 | 2X2 | 720 |

He initialization [25] were used for all the conv-layers, this is given that ReLU activation is applied [26]. For the FC layer, the Xavier initialization [27] were used, given that Softmax activation is applied on the FC. The He initializer is similar to the Xavier initializer, except that Xavier initialization uses a scaling factor for the weights, as it can be observed on Eq. 1 (He) and Eq. 2 (Xavier).

$$\text{Var}(w_i) = \text{sqr}t\left(\frac{2}{fan_{in}}\right) \quad (1)$$

$$\text{Var}(w_i) = \text{sqr}t\left(\frac{1}{fan_{in}}\right) \quad (2)$$

Where fan_{in} is the number of input units in the weight tensor.

Given that this is a multi-class classification objective, the objective function used was the Categorical Cross-Entropy, also called as Softmax loss. This is a Softmax activation, Eq. 3, plus a cross-entropy loss, Eq. 4, where s_i and t_i are the ground truth. The point is to train the CNN to output a probability over the C classes.

$$f(y_i) = \frac{e^{s_i}}{\sum_j e^{s_j}} \quad (3)$$

$$CE = - \sum_i^C t_i \log(f(s)_i) \quad (4)$$

The Categorical Cross-Entropy is given as follows.

$$CE = - \log\left(\frac{e^{s_p}}{\sum_j^C e^{s_j}}\right) \quad (5)$$

Where s_p is the CNN score for the positive class.

4 Experiments

The experiments held in this section were carried out to test the efficiency and precision of the models. Metrics like accuracy, ROC, F-measure, sensitivity, and specificity were used to evaluate the models, more details about the metrics will be described in Subject. 4.2. These models were implemented on Python 3.7, using TensorFlow 2.0.0, using a GPU to speed up the training process.

4.1 Data Set

For this work, a new dataset was created with the help of the Fruit Department of the Postgraduate School, Texcoco. As mentioned above, the dataset consists of two elements, the front face of the leaf and its back face, the pictures were taken under a controlled environment, with a white background and artificial light, Fig. 2. These leaves belong to 6 different kinds of experimental peaches hold by the institution. No image preprocessing was applied, and no data augmentation techniques were used. Every pair of leaf picture is pointing to the same side, as it can be appreciated in Fig. 2, intuitively, this would make easier the classification for the model. Different image size was used to train each model, one dataset consists of 224×224 pictures, and the second dataset of 416×416 pictures. The dataset distribution is described in Table 3,

for the training process, the dataset was divided 10% for testing and the rest for training. For the test, the same “two-input” models were used, both leaf’s faces are essential for the plant identification, in contrast of [24], where the model trained using two different pictures where both could be from the same plant or one from the positive target and the second from a negative target, to make the model find similarities of one class in different angles and to distinguish it from other classes. Thus, during the test only one picture is needed, to feed a one stream CNN and RNN, and this is possible because the weights were shared.

Table 3. Dataset distribution.

| Class and name | Number of pairs | Training | Test |
|-----------------|-----------------|----------|------|
| 1. CP-03-06 | 101 | 90 | 11 |
| 2. Oro Azteca | 207 | 186 | 21 |
| 3. Oro San Juan | 204 | 179 | 25 |
| 4. Cardenal | 229 | 209 | 20 |
| 5. Colegio | 205 | 190 | 15 |
| 6. Robin | 319 | 285 | 34 |
| Total | 1265 | 1139 | 126 |

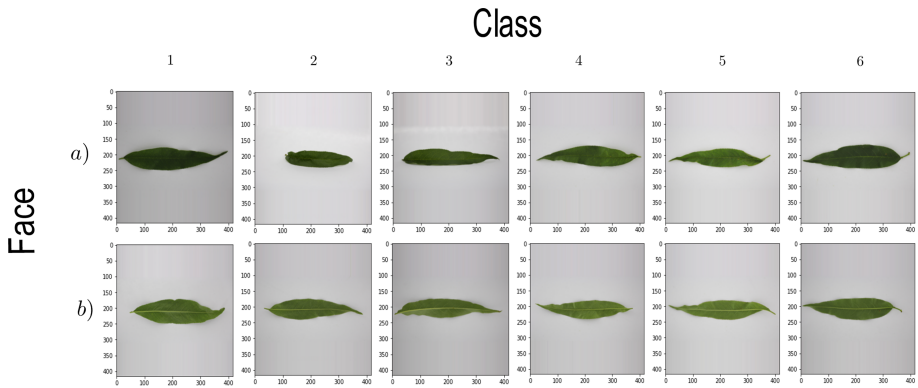


Fig. 2. Representation of the six different kinds of peach leaves. a) represents the front face of the leaf and b) its back face.

4.2 Results

As mentioned in the beginning of Sect. 4, the metrics used to test the model were accuracy, ROC, f-measure, recall and precision, here we are going to give a brief explanation about the metrics used. The accuracy is the number of correctly predicted data out of all the data points, that measure is obtained dividing the number of true positive and true negatives by the number of true positives, true negatives, false positives and false negatives. The F-measure is the harmonic mean of precision and

sensitivity, and it is obtained dividing 2 times the true positives by two times the true positives plus the false positives and the false negatives. The sensitivity is the true positive rate, and it is obtained dividing the true positives by the true positives and false negatives. The specificity is the true negative rate, and it is obtained dividing the true negative by the true negatives and false positives. The AUC-ROC curve is obtained plotting the sensitivity against the specificity and obtaining its area. For all the metrics, the closest to 1 they are the better the model performance is. Given that the number of elements on each class is not homogenous, every metric was obtained with a weighted average, that is, first each metric was obtained per class, that means it was a class versus all, after that, the weighted average was obtained as in Eq. 6.

$$weighted - avg = \frac{\sum_{n=1}^c M_n * C_n}{\sum_{n=1}^c C_n} \tag{6}$$

Where M_n is the metric obtained in class n , and C_n is the number of elements in class n . The results obtained were compared with the ones obtained in previous papers [6, 7] (Table 4, 5), in which 6 different kinds of peach were classified.

Table 4. Classification results with proposed approach and comparison with the previous work.

| | | Accuracy | ROC | F-measure | TP rate | FP rate |
|---|-------------------|----------|-------|-----------|---------|---------|
| Proposed models | Model (224 × 224) | 92.0635% | 0.990 | 0.920 | 0.920 | 0.978 |
| | Model (416 × 416) | 92.8571% | 0.992 | 0.927 | 0.928 | 0.983 |
| Complex leaves classification with features extractor [7] | Naïve Bayes | 76.165% | 0.922 | 0.761 | 0.762 | 0.050 |
| | SVM | 83.937% | 0.961 | 0.839 | 0.839 | 0.032 |
| | Logistic R. | 73.057% | 0.942 | 0.728 | 0.731 | 0.055 |
| | Decision tree | 72.020% | 0.852 | 0.718 | 0.720 | 0.058 |
| Complex identification of plants from leaves [6] | Bayes | 75.64% | – | – | – | – |
| | BP | 76.02% | – | – | – | – |
| | RL | 73.057% | – | – | – | – |
| | SVM _G | 83.97% | – | – | – | – |

In the previous work [7], two basic CNN’s were created, in order to find out how they handle the task. The models did not generalize well the data, and it was mentioned that more sophisticated models needed to be created to target this task. In Table 5, a comparison of our proposed model and the models in the previous work are shown.

Table 5. Comparison of models proposed with the models proposed in the previous work.

| | | Accuracy |
|-------------------|-----------------------|----------|
| Proposed models | Model (224 × 224) | 92.0635 |
| | Model (416 × 416) | 92.8571 |
| Previous work [7] | Convolutional model 1 | 62% |
| | Convolutional model 2 | 55% |

For [7], the dataset size was of 498 samples, smaller than the one used for this paper that sum up 1265 pairs, and their picture size used was 300×400 pixels for the feature extractor method, and 416×416 pixels for the one stream CNN. In the case of our hybrid-CNN approach the size used in [7] was like our second model (Model 416×416). In [6], the dataset was even smaller, consisting of 193 elements, being this one reason why the results were poor, the resolution of the images is not specified and only accuracy was considered.

Our proposed hybrid models obtained a high accuracy of 92.0635% for Model 224×224 , and a 92.8571% accuracy for Model 416×416 , overpassing the SVM approach from [6] and [7], where an accuracy of 83.97% and 83.937% was obtained. The difference is notable in the case of the one stream CNN approach [7], where the higher accuracy was of 62%. The performance of both hybrid models was slightly similar, being the model trained with higher resolution the one with better accuracy, with just a difference of 0.7936. The use of higher resolution pictures did not bring out better results in our approach.

5 Conclusions

Every species of plants has different kinds of varieties, and these varieties behave different under certain environments, given to the continuing development of better varieties. That is why it is important to identify the different varieties of plants a species has; this kind of leaves are called complex leaves. As seen in Fig. 2, the leaves by simple sight have the same color, texture, and morphology, this makes these kinds of leaves hard to classify. To target this task, two models were proposed to classify 6 different kinds of peach's leaves and a new dataset was created using leaves from the Fruit Department of the Postgraduate College, Texcoco. These pictures were taken under a controlled environment with white background. To train the proposed models, the dataset was divided into two parts, the front face of the leaf and its back face, this pair of samples represent one element of the dataset, for each model two datasets were used, one model trained with 224×224 pictures and the other with 416×416 . The proposed models significantly overpassed the models in [6] and [7]. The results demonstrated that it is important to consider both sides of a leaf as one. The Hybrid-CNN models gained more insights about how to classify a plant from a complete leaf, instead than learning from one single side.

Nowadays there are datasets available with thousands and millions of pictures available for training a model, but unfortunately, this is not always the case. Sometimes the data is not always available, and it is of common knowledge that the more data the

model train with the best its performance will be. But there is not an universal rule to state what amount of data is enough for the model to not overfit. In this work, not all classes were balanced, in Table 3, the number of elements of class 1 with which the model trained represents less than 10% of all the training set, and despite this drawback, we obtained a high accuracy. On the other hand, the Bayesian Neural Networks has demonstrated that they can handle small datasets, and avoid the overfitting, handling it as uncertainty [28, 29]. Being this our next step, by applying Bayesian CNN in combination of our proposed method, to increase the accuracy rate and see how this new approach can handle the complex leaves classification.

References

1. Zhang, Z., Sejdíć, E.: Radiological images and machine learning: trends, perspectives, and prospects. *Comput. Biol. Med.* **108**, 354–370 (2019)
2. Amador, J.D.J., Espejel Cabrera, J., Cervantes, J., Jalili, L.D., Ruiz Castilla, J.S.: Automatic calculation of body mass index using digital image processing. In: Figueroa-García, J.C., Villegas, J.G., Orozco-Arroyave, J.R., Maya Duque, P.A. (eds.) WEA 2018. CCIS, vol. 916, pp. 309–319. Springer, Cham (2018). https://doi.org/10.1007/978-3-030-00353-1_28
3. Wang, Z., Sun, X., Zhang, Y., Ying, Z., Ma, Y.: Leaf recognition based on PCNN. *Neural Comput. Appl.* **27**(4), 899–908 (2015). <https://doi.org/10.1007/s00521-015-1904-1>
4. Alishahi, A., Farahmand, H., Prieto, N., Cozzolino, D.: Identification of transgenic foods using NIR spectroscopy: a review. *Spectrochimica Acta Part A Mol. Biomol. Spectrosc.* **75** (1), 1–7 (2010)
5. FAO: Save and Grow (2011)
6. Cervantes, J., Garcia Lamont, F., Rodriguez Mazahua, L., Zarco Hidalgo, A., Ruiz Castilla, J.S.: Complex identification of plants from leaves. In: Huang, D.-S., Gromiha, M.M., Han, K., Hussain, A. (eds.) ICIC 2018. LNCS (LNAI), vol. 10956, pp. 376–387. Springer, Cham (2018). https://doi.org/10.1007/978-3-319-95957-3_41
7. Ayala Niño, D., Ruiz Castilla, J.S., Arévalo Zenteno, M.D., Jalili, L.D.: Complex leaves classification with features extractor. In: Huang, D.-S., Jo, K.-H., Huang, Z.-K. (eds.) ICIC 2019. LNCS, vol. 11644, pp. 758–769. Springer, Cham (2019). https://doi.org/10.1007/978-3-030-26969-2_72
8. Garcia, F., Cervantes, J., Lopez, A., Alvarado, M.: Fruit classification by extracting color chromaticity, shape and texture features: towards an application for supermarkets. *IEEE Latin Am. Trans.* **14**(7), 3434–3443 (2016)
9. Brahimi, M., Boukhalifa, K., Moussaoui, A.: Deep learning for tomato diseases: classification and symptoms visualization. *Appl. Artif. Intell.* **31**, 299–315 (2017)
10. Caglayan, A., Guclu, O., Can, A.B.: A plant recognition approach using shape and color features in leaf images. In: Petrosino, A. (ed.) ICIAP 2013. LNCS, vol. 8157, pp. 161–170. Springer, Heidelberg (2013). https://doi.org/10.1007/978-3-642-41184-7_17
11. Grinblat, G.L., Uzal, L.C., Larese, M.G., Granito, P.M.: Deep learning for plant identification using vein morphological patterns. *Comput. Electron. Agric.* **127**, 418–424 (2016)
12. Perez, L., Wang, J.: The effectiveness of data augmentation in image classification using deep learning. [arXiv:1712.04021](https://arxiv.org/abs/1712.04021) (2017)
13. AaKif, A., Khan, M.F.: Automatic classification of plants based on their leaves. *Biosyst. Eng.* **139**, 66–75 (2015)
14. Zhao, C., Chan, S.S.F., Cham, W.-K., Chu, L.M.: Plant identification using leaf shapes—a pattern counting approach. *Pattern Recogn.* **48**(10), 3203–3215 (2015)

15. Naresh, Y.G., Nagendraswamy, H.S.: Classification of medicinal plants: an approach using modified LBP with symbolic representation. *Neurocomputing* **173**(3), 1789–1797 (2016)
16. Lee, S.H., Chan, C.S., Mayo, S.J., Remagnino, P.: How deep learning extracts and learns leaf features for plant classification. *Pattern Recogn.* **71**, 1–12 (2017)
17. Yousefi, E., Baleghi, Y., Sakhaei, S.M.: Rotation invariant wavelet descriptors, a new set of features to enhance plant leaves classification. *Comput. Electron. Agric.* **140**, 70–76 (2017)
18. Neto, J.C., Meyer, G.E., Jones, D.D., Samal, A.K.: Plant species identification using Elliptic Fourier leaf shape analysis. *Comput. Electron. Agric.* **50**(2), 121–134 (2006)
19. Backes, A.R., Bruno, O.M.: Plant leaf identification using multi-scale fractal dimension. In: Foggia, P., Sansone, C., Vento, M. (eds.) *ICIAP 2009. LNCS*, vol. 5716, pp. 143–150. Springer, Heidelberg (2009). https://doi.org/10.1007/978-3-642-04146-4_17
20. Elnemr, H.A.: Feature selection for texture-based plant leaves classification. In: 2017 Intl Conf on Advanced Control Circuits Systems (ACCS) Systems & 2017 Intl Conf on New Paradigms in Electronics & Information Technology (PEIT), Alexandria, pp. 91–97 (2017)
21. Larese, M.G., Bayá, A.E., Craviotto, R.M., Arango, M.R., Gallo, C., Granitto, P.M.: Multiscale recognition of legume varieties based on leaf venation images. *Experts Syst. Appl.* **41**, 4638–4647 (2014)
22. Lee, S.H., Chan, C.S., Wilkin, P., Remagnino, P.: Deep-plant: plant identification with convolutional neural networks. In: 2015 IEEE International Conference on Image Processing (ICIP), Quebec City, QC, pp. 452–456 (2015)
23. Paco Ramos, M.M., Paco Ramos, V.M., Fabian, A.L., Osco Mamani, E.F.: A feature extraction method based on convolutional autoencoder for plant leaves classification. In: Orjuela-Cañón, A., Figueroa-García, J., Arias-Londoño, J. (eds.) *ColCACI 2019. Communications in Computer and Information Science*, vol. 1096. Springer, Cham (2019). https://doi.org/10.1007/978-3-030-36211-9_12
24. Wang, B., Wang, D.: Plant leaves classification: a few-shot learning method based on siamese network. *IEEE Access* **7**, 151754–151763 (2019)
25. He, K., Zhang, X., Ren, S., Sun, J.: Delving deep into rectifiers: surpassing human-level performance on ImageNet classification. [arXiv:1502.01852](https://arxiv.org/abs/1502.01852) (2015)
26. Hayou, S., Doucet, A., Rousseau, J.: On the selection of initialization and activation function for deep neural networks. [arXiv:1805.08266](https://arxiv.org/abs/1805.08266) (2018)
27. Glorot, X., Bengio, Y.: Understanding the difficulty of training deep feedforward neural networks. In: *Proceedings of the Thirteenth International Conference on Artificial Intelligence and Statistics, JMLR Workshop and Conference Proceedings*, vol. 9, pp. 249–256 (2010). [arXiv:1506.02158](https://arxiv.org/abs/1506.02158)
28. Gal, Y., Ghahramani, Z.: Bayesian convolutional neural networks with Bernoulli approximate variational inference. <http://proceedings.mlr.press/v9/glorot10a.html> (2015)
29. Kendall, A., Gal, Y.: What uncertainties do we need in Bayesian deep learning for computer vision? [arXiv:1703.04977](https://arxiv.org/abs/1703.04977) (2017)
30. Jalili, L.D., Morales, A., Cervantes, J., Ruiz-Castilla, J.S.: Improving the performance of leaves identification by features selection with genetic algorithms. In: Figueroa-García, J.C., López-Santana, E.R., Ferro-Escobar, R. (eds.) *WEA 2016. CCIS*, vol. 657, pp. 103–114. Springer, Cham (2016). https://doi.org/10.1007/978-3-319-50880-1_10
31. Cervantes, J., García-Lamont, F., Rodríguez-Mazahua, L., Rendon, A.Y., Chau, A.L.: Recognition of Mexican sign language from frames in video sequences. In: Huang, D.-S., Jo, K.-H. (eds.) *ICIC 2016. LNCS*, vol. 9772, pp. 353–362. Springer, Cham (2016). https://doi.org/10.1007/978-3-319-42294-7_31
32. Ip, R.H.L., Ang, L.-M., Seng, K.P., Broster, J.C., Pratley, J.E.: Big data and machine learning for crop protection. *Comput. Electron. Agric.* **151**, 376–383 (2018)



Low Contrast Chinese Rubbing Image Segmentation Based on Gradient Filtering

Zhi-Kai Huang^{1(✉)}, Huan Wang², Xian-Chang Xi², Yi-Ning Ning²,
and Ling-Ying Hou²

¹ School of Information Engineering, Nanchang Institute of Technology,
Nanchang 330099, Jiangxi, China
huangzhikai2001@163.com

² College of Mechanical and Electrical Engineering, Nanchang Institute
of Technology, Nanchang 330099, Jiangxi, China

Abstract. For more than 1,500 years, rubbing is one of the most perhaps the oldest of the techniques that have been used in printmaking. Despite the fact that image binarization has been a widely studied in the past decades, segmenting Chinese characters from badly degraded rubbing images is still a challenging task. In this paper, a low contrast Chinese rubbing image segmentation algorithm based on improved gradient filtering have been present. At first, the image is preprocessed by a median filter to eliminate impulse noise. After that, segmented rubbing image is obtained by a binary image using a locally adaptive threshold. At the same time, a comparative study had made to various binarization methods based on numerically investigate the segmentation results using Jaccard' Measure (JM), False Positive (FP), True Positive (TP), True Negative (TN), F-measure, and False Negative (FN). Compared with the existing edge extraction algorithm, this algorithm has a better effect and higher segmentation accuracy.

Keywords: Chinese rubbing image · Gradient filtering · Image binarization · Gaussian filter

1 Introduction

Most of the Chinese historical documents are written or hand-drawn by different writers in different periods [1]. The most common handwritten characters in ancient books are the regular script and cursive script. The strokes of the regular script are scattered, but the font size on the same page does not have a difference; the cursive script is relatively concentrated, but the font size is a disparity, as shown in Fig. 1.



Fig. 1. Historical handwritten document image with low contrast, a) Cursive script. b) Regular script

Due to the unique handwriting or depiction style of different writers, the characteristics of Chinese characters in ancient literature are unique and different, which brings great difficulties to character segmentation. Moreover, compared with Latin letters or numbers, Chinese characters have a more complex structure, which makes the Chinese character segmentation more difficult. How to improve the accuracy of the segmentation of regular script and cursive script in ancient Chinese rubbing image is still an important and difficult problem in the field of historic Chinese document image segmentation.

Due to the volume of noise in the Chinese rubbing image, details could be partially/completely eliminated or over-smoothed. Preserving these details from being either occluded by noise or deformed in the denoising process is a challenging task, which brings difficulties to the real character segmentation [2]. By the way, it is difficult to determine the segmentation threshold because of the different font sizes in the Chinese inscription image, and the Chinese characters are mainly represented by the combination of lines in various directions. The commonly used edge extraction algorithm is not ideal in the case of low contrast with a lot of noise.

In this paper, a segmentation algorithm of the Chinese rubbing image based on an improved gradient filter has been proposed. Firstly, the image is preprocessed by a median filter to eliminate impulse noise. Literature survey shows that the optimal filter can be closely approximated by the first-order derivatives of a Gaussian function which is a 2-D convolution operator that is used to blur images and remove detail and noise, then, find gradient magnitude and direction of a 2-D image.

Finally, the final segmented image is obtained by a binary image using a locally adaptive threshold. Compared with the existing edge extraction algorithm, this algorithm has a better effect and higher segmentation accuracy.

2 Background: Gaussian Filter and Thresholding Technique

2.1 Gaussian Filter

Ideally denoising is all about filtering noise from the degraded image while preserving the details of the edges unchanged for image analysis and processing. Gaussian filter is a kind of linear smoothing filter, which is suitable for eliminating Gaussian noise and widely used in image processing. Generally speaking, Gaussian filtering is the process of a weighted average of the whole image. The value of each pixel is obtained by the weighted average of itself and other pixel values in the neighborhood. The specific operation of Gaussian filtering is to scan every pixel in the image with a template (or convolution, mask), and replace the value of the central pixel of the template with the weighted average gray value of the pixel in the neighborhood determined by the template. Image gradients are used to highlight interesting features in images and are used in many feature detection algorithms like edge/corner detection [3].

In one dimension, the Gaussian function is:

$$G(x) = \frac{1}{\sqrt{2\pi\sigma^2}} e^{-\frac{x^2}{2\sigma^2}} \quad (1)$$

where σ is the standard deviation of the distribution. The distribution is assumed to have a mean of 0. When working with images we need to use the two dimensional Gaussian function. This is simply the product of two 1D Gaussian functions (one for each direction) and is given by:

$$G(x, y) = \frac{1}{2\pi\sigma^2} e^{-\frac{x^2+y^2}{2\sigma^2}} \quad (2)$$

The Gaussian filter works by using the 2D distribution as a point-spread function. This is achieved by convolving the 2D Gaussian distribution function with the image. We need to produce a discrete approximation to the Gaussian function [4]. An integer-valued 5 by 5 convolution kernel approximating a Gaussian with a σ of 1 is shown in Fig. 2.

| | | | | | |
|-----------------|---|----|----|----|---|
| | 1 | 4 | 7 | 4 | 1 |
| | 4 | 16 | 26 | 16 | 4 |
| $\frac{1}{273}$ | 7 | 26 | 41 | 26 | 7 |
| | 4 | 16 | 26 | 16 | 4 |
| | 1 | 4 | 7 | 4 | 1 |

Fig. 2. By 5 convolution kernel approximating a Gaussian

2.2 Thresholding Technique

In the application of image processing, a binary operation is a very common processing method, such as processing of zero device pictures, extracting characters from text pictures and verification code pictures, character segmentation in license plate recognition, foreground segmentation in moving object detection in video images, etc. The commonly used image binarization methods are 1) global fixed threshold; 2) local adaptive threshold; 3) Otsu. The global fixed threshold algorithm is easy to understand, that is, the whole image is binarized with a unified threshold; the local adaptive threshold is to determine the binarization threshold of the pixel location according to the pixel value distribution of the neighborhood block of the pixel [5]. The advantage of this is that the binarization threshold at each pixel position is not fixed, but determined by the distribution of neighboring pixels. The binarization threshold of the image area with higher brightness is usually higher, while the binarization threshold of the image area with a lower brightness is correspondingly smaller. Local image regions with different brightness, contrast, and texture will have a corresponding local binary threshold. The commonly used local adaptive thresholds are: 1) mean value of local neighborhood blocks; 2) Gaussian weighted sum of local neighborhood blocks.

Adaptive threshold, whose idea is not to calculate the global image threshold, but to calculate the local threshold according to the brightness distribution of different regions of the image, so for different regions of the image, it can calculate different thresholds adaptively, so it is called adaptive threshold method. Convert the image to a binary image using adaptive thresholding [6].

3 Proposed Method

In our proposed method, at first, median filtering have been performed in each R, G, B channel for the original image. Each output pixel contains the median value in a 3-by-3 neighborhood around the corresponding pixel in the input image. It is particularly effective at removing salt and pepper noise. To overcome effect of Gaussian noise, smooth the image using a Gaussian smoothing filter before computing image gradients. The chosen of standard deviation parameter σ is crucial to use Gaussian smoothing filter, the central or intermediate differencing gradient operators can be used. The variance in each R, G, B channel have been computed. The minimize variance found in each R, G, B channel had been used as Gaussian smoothing filter parameter σ . Finally, binarize image using locally adaptive thresholding for the filtering image. The architecture of the proposed compound binarization algorithm is illustrated in Fig. 3.

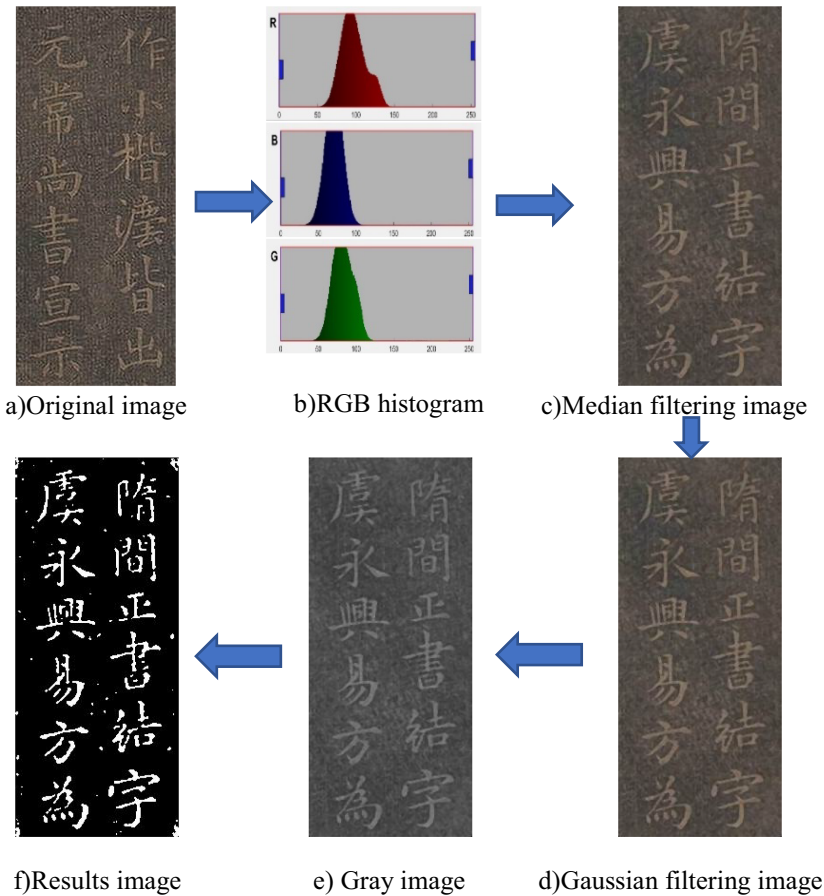


Fig. 3. The flowchart of proposed method.

4 Experimental Results and Discussion

In the experiments, we have used the test image samples come from the Chinese Stone Rubbing Collection in East Asian Library, University of California, Berkeley [7] with a resolution of $654 * 1352$ pixels and 256 intensity levels. A set of 48 low contrast document images, just like the two shown in Fig. 1, and the results were compared by visual inspection.

Some experimental results had been shown in Fig. 4. Here, Otsu’s global thresholding method had been employed as a comparison. The experimental results show that using our algorithm has outperformed global thresholding methods.

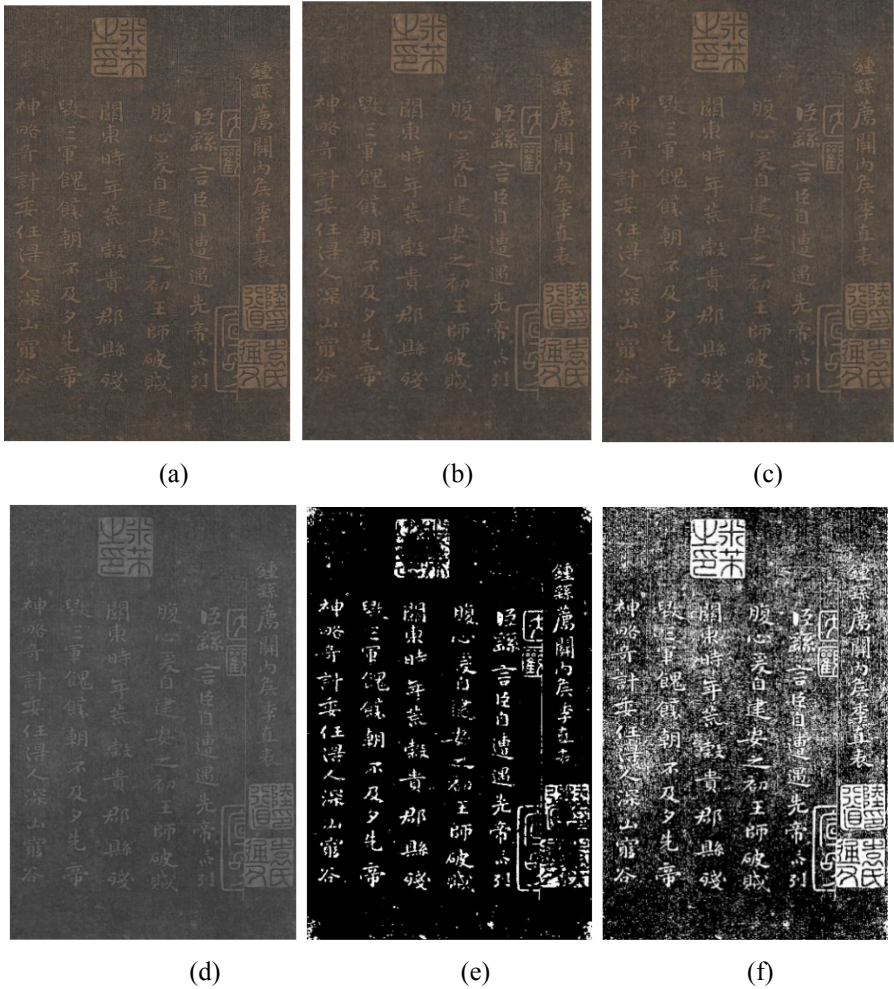


Fig. 4. Example of the segmentation results and process. (a) shows the original image before processing. (b) shows the median filtering of the original image. (c) shows the Gaussian filtering after the median filtering. (d) shows the gray image after filtering. (e) the segmentation result of our algorithm. (f) the result of Ostu's algorithm.

In order to performance comparisons, the segmentation results obtained using our algorithm, the images as shown in Fig. 3, which come from PHIBD 2012 datasets [16] were utilized as ground truth (GT) for the comparison, also. The measure is defined using Jaccard' Measure (JM), False Positive (FP), True Positive (TP), True Negative

(TN), F-measure, and False Negative (FN). Among that, JM is used to compute the percentage of pixel intersections between two segmentation images. Classifying text data as a background is considered an FP and classifying background data as a text is considered an FN. TP denotes true positive i.e. the pixels that are foreground in both ground truth and binarized image.

The definition of precision, recall, and F-measure is given as shown in the following four equations.

The definition of precision, recall, and JM is given as shown in the following three equations.

$$JM = \frac{S_1 \cap S_2}{S_1 \cup S_2} \quad (3)$$

Where S_1 represents the pixel by the GT and S_2 the pixel generated through the use of our segmentation algorithm (Figs. 5 and 6).

$$Fmeasure = \frac{2 \times TP}{2 \times TP + FP + FN} \quad (4)$$

$$Precision = \frac{TP}{TP + TN} \quad (5)$$

$$Recall = \frac{TP}{TP + FN} \quad (6)$$

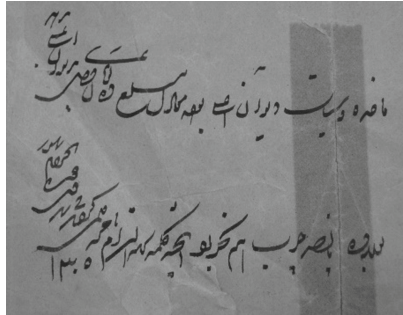


Fig. 5. A example shows an historical document image from PHIBD 2012 datasets (Image name: Persian06. Multi-degraded background, faded ink. Size: 1625 × 1269).



Fig. 6. (a) Median filtering image. (a) Gaussian filtering image. (b) The result of mean algorithm. (c) The result of the Otsu's algorithm. (d) The result of ours algorithm

Table 1. Results on the PHIBD 2012 dataset

| Method | F-measure | Precision | Recall | Jaccard | Accuracy |
|---------------|-----------|-----------|---------|---------|----------|
| Our algorithm | 99.72 | 0.9968 | 0.9975 | 0.9943 | 0.9947 |
| Ostu | 78.52 | 0.65705 | 0.97554 | 0.9753 | 0.97256 |
| Niblack | 99.36 | 0.9945 | 0.9947 | 0.9872 | 0.9047 |

The segmentation accuracy has been shown in Table 1 by using JM, Precision, Recall, Accuracy, and F-measure, which were calculated by comparing the ground truth image. For comparing the accuracy rate of the proposed approach against two well-known binarization algorithms: (1) the global thresholding algorithm Otsu [8] and our method. It has been found that global thresholding is not ideal for degraded historic images due to low contrast. Adaptive local thresholding methods well suited to local adaptive thresholding is in segmenting text from the image.

5 Conclusion

In this paper, low contrast Chinese rubbing image segmentation based on gradient filtering has been discussed. The visual inspection looked for errors in the separation of background and the foreground is proposed here. At the same time, a comparative study had made to various binarization methods based on numerically investigate the segmentation results. Experimental results reveal that the gradient edge detection method is perhaps the most elaborate edge detection method after the image has been denoising, which gives very good results. Although there is no image denoising algorithm beforehand, the Otsu's algorithm can complete segment the seal in the Chinese rubbing image. That will be a new question that can be studied carefully in the future.

Acknowledgement. This work was supported by the National Natural Science Foundation of China (Grant No. 61472173), the grants from the Educational Commission of Jiangxi province of China, No. GJJ151134.

References

1. Zhang, Y.-W., Chen, Y., Liu, H., Ji, Z., Zhang, C.: Modeling Chinese calligraphy reliefs from one image. *Comput. Graph.* **70**, 300–306 (2018)
2. Huang, Z.-K., et al.: Comparison of different image denoising algorithms for Chinese calligraphy images. *Neurocomputing* **188**, 102–112 (2016)
3. Ito, K., Xiong, K.: Gaussian filters for nonlinear filtering problems. *IEEE Trans. Autom. Control* **45**(5), 910–927 (2000)
4. Perona, P., Malik, J.: Scale-space and edge detection using anisotropic diffusion. *IEEE Trans. Pattern Anal. Mach. Intell.* **12**(7), 629–639 (1990)
5. Huang, Z., Chau, K.: A new image thresholding method based on Gaussian mixture model. *Appl. Math. Comput.* **205**(2), 899–907 (2008)
6. Huang, H., Huang, Z.-K., Ma, Y.-L., Hou, L.-Y.: An adaptive segmentation algorithm for degraded chinese rubbing image binarization based on background estimation. In: Huang, D.-S., Bevilacqua, V., Premaratne, P., Gupta, P. (eds.) *ICIC 2018. LNCS*, vol. 10954, pp. 15–24. Springer, Cham (2018). https://doi.org/10.1007/978-3-319-95930-6_3
7. <http://www.lib.berkeley.edu/EAL/stone/about.html>
8. http://www.iapr-tc11.org/mediawiki/index.php/Binarization_of_PHIBD_2012_dataset
9. Otsu, N.: A threshold selection method from gray-level histograms. *IEEE Trans. Syst. Man Cybern.* **9**(1), 62–66 (2007)
10. Gatos, B., Pratikakis, I., Perantonis, S., et al.: Adaptive degraded document image binarization. *Pattern Recogn.* **39**(3), 317–327 (2006)
11. Bataineh, B., Abdullah, S.N.H.S., Omar, K.: An adaptive local binarization method for document images based on a novel thresholding method and dynamic windows. *Pattern Recogn. Lett.* **32**(14), 1805–1813 (2011)



Industrial Smoke Image Segmentation Based on a New Algorithm of Cross-Entropy Model

Qian-Jing Huang¹, Le Zou², Zhi-Ze Wu³, Huan-Yi Li¹,
Xiao-Feng Wang²(✉), and Yan-Ping Chen²

¹ Department of Environmental Engineering, Hefei University, Hefei 230601, Anhui, China

² Anhui Provincial Engineering Laboratory of Big Data Technology Application for Urban Infrastructure, Department of Computer Science and Technology, Hefei University, Hefei 230601, China
xfwang@hfu.edu.cn

³ Institute of Applied Optimization, School of Artificial Intelligence and Big Data, Hefei University, Hefei 230601, Anhui, China

Abstract. Smoke segmentation from the industrial images is a key concern of environmental monitoring. As the similarities between the gray value of the background and the smoke, the existing segmentation algorithms are difficult to accurately segment the target smoke. In this paper, we construct a cross-entropy based industrial smoke image segmentation by integrating the iterative convolution-thresholding. Specially, we use the iterative convolution-thresholding to implicitly represent the interface of each image domain through a characteristic function. We further perform the combination of a regularization term and a fidelity term in the cross-entropy model. In the proposed algorithm, the fidelity term is first converted into the product of the characteristic function and the cross-entropy function. Then the functional of the characteristic function is used to obtain the regularization term by the approach of thermodynamic convolution approximation. The experimental results demonstrate that our proposal has a more accurate segmentation effect and higher segmentation efficiency.

Keywords: Image segmentation · Industrial smoke · Cross-entropy · Iterative convolution-thresholding

1 Introduction

With the development of industrial cities, the emission of industrial smoke continues to increase, which results in a series of environmental pollution problems such as ecological imbalance and environmental degradation [1]. According to the survey, industrial sources are still the main source of air pollution. Therefore, we need to monitor the emissions of industrial smoke. As a very critical part of the monitoring process, image segmentation is key concern.

In 1988, Osher and Sethian [2] put forward the level set method, which is a numerical method used to capture the shape and interface of objects. In this way, a zero level set of a high-dimensional function is used to represent the target contour, which is

called level set function. The image segmentation based on the level set method is mainly divided into two types: one is the level set image segmentation based on the edge model, and the other is the level set image segmentation based on the regional model. Mumford and Shah [3] proposed a region-based geometric active contour model in 1989, the biggest disadvantage of the model seems to be high computational complexity. Therefore, Chan and Vese [4] proposed the Chan-Vese (CV) model which is based on the Mumford-Shah (MS) model combined with the level set function, the CV model is an improvement of the energy function of the MS model. Based on the CV model, Li established a region-based binary level set segmentation method [5], which avoided the process of level set function re-initialization and reduced the complexity of the algorithm. Wang et al. [6] proposed a new local CV model based on level set method theory, curve evolution and local statistical functions, which can segment images with intensity inhomogeneity well. Zhang et al. [7] proposed a GAC-CV hybrid model, which merged the image edge and region information into the same energy functional, and adopted different segmentation strategies for different segmentation targets, which improves the capture ability of concave edges. Wang et al. [8] proposed an improved CV model. By adding shape template constraints and anchor point constraints, the shadow detection of single-frame color pictures was realized, and the problem of image segmentation with large differences in the brightness of the shadows was solved.

Industrial smoke segmentation is a relatively new direction. In recent years, some relevant scholars have conducted some research on the direction of industrial soot segmentation. Zhang et al. [9] proposed a region-based soot segmentation method to segment soot regions, which used threshold-based segmentation, regional growth, region splitting and merging methods for soot image segmentation. This method only considers the grayscale features of the smoke image, but does not consider other features. Hsu et al. [10] proposed a method for visual detection of industrial smoke, which combined smoke modeling, change detection and texture analysis to identify smoke emissions. This method can quickly divide the smoke area, but it was susceptible to fast moving wind and clouds. Wang et al. [11] proposed an industrial soot image segmentation method based on background modeling and feature matching, which has a good segmentation effect on moving interference and complex scene environments, but the segmentation accuracy needs to be improved. Chu [12] proposed a minimum error threshold smoke image segmentation algorithm based on improved Bayesian decision theory, which improved the shortcomings of the traditional threshold segmentation smoke image method. However, it does not take into account interference factors such as light changes and clouds in the monitoring process. Wang et al. [13] proposed a method for segmentation of industrial smoke in video by using the background subtraction method to obtain the edge motion area. The area growth algorithm is used to divide the smoke area in a uniform space, but this algorithm has a small hollow part of cloud image segmentation. In this paper, we combine the CV model and the cross-entropy model to construct an active contour model based on cross-entropy, and use an iterative convolution-thresholding algorithm to minimize the energy functional. Experiments prove the effectiveness and practicability of the proposed new algorithm for segmentation.

The rest of the article is organized as follows: In Sect. 2, the well-known active contour models are introduced. In Sect. 3, the image segmentation algorithm of the cross-entropy model based on iterative convolution-thresholding is presented. In Sect. 4, some examples of smoke image segmentation are given to demonstrate the performance and efficiency of the proposed algorithm. Finally, some conclusions are drawn in Sect. 5.

2 Related Models

The traditional CV [4] model objective function is composed of fidelity and regularization terms. The fidelity term measures the integral of the squared difference between the average value of the current segmented area and the grayscale of the original image in the current segmented area. When the objective function reaches the minimum value, the difference between the actual gray level of the target in the contour and the calculated gray level is the smallest. The cross-entropy model measures the probability distribution between the original image and the segmented image, and selects a threshold to minimize the distance. Affected by the above two models, Song [14] proposed an active contour model based on cross entropy. The energy functional is as follows:

$$\begin{aligned}
 F_c(c_1, c_2, C) = & \mu \int H'(\phi(x))|\nabla\phi|dx + \nu \int H(\phi(x))dx \\
 & + \lambda_1 \int I(x) \left| \log\left(\frac{I(x)}{c_1 + \sigma}\right) \right| H(\phi(x))dx \\
 & + \lambda_2 \int I(x) \left| \log\left(\frac{I(x)}{c_2 + \sigma}\right) \right| (1 - H(\phi(x)))dx
 \end{aligned} \tag{1}$$

In Eq. (1), to prevent the denominator from being zero leads to no solution, so a small constant σ is introduced. In this article, set $\sigma = 10^{-4}$, we consider only two-segment splits and not multi-segment splits. In order to simplify the calculation, the first two terms of the formula are merged into one term, and replaced by $\mu \sum_{i=1}^2 |\partial\Omega_i|$, $|\partial\Omega_i|$ represents the perimeter of the image domain Ω_i , μ is a positive parameter. When the image $I(x)$ is simplified to I , the above formula is simplified to:

$$F_c(c_1, c_2, \Omega_1, \Omega_2) = \mu \sum_{i=1}^2 |\partial\Omega_i| + \sum_{i=1}^2 \int_{\Omega_i} I \left| \log\left(\frac{I}{c_i + \sigma}\right) \right| dx \tag{2}$$

where

$$c_1 = \frac{\int_{\Omega} u I dx}{\int_{\Omega} u dx}, \quad c_2 = \frac{\int_{\Omega} (1 - u) I dx}{\int_{\Omega} (1 - u) dx} \tag{3}$$

The two items of the active contour model based on cross entropy are called regularization and fidelity terms. From the above formula, it can be seen that the fidelity terms for calculating variance in the CV model are replaced by the terms for calculating cross entropy. The main goal of this model is to minimize the cross entropy between a given image and the segmented image.

3 Iterative Convolution-Thresholding Algorithm to Minimize the Cross-Entropy Model

In the traditional CV model, the difference method is often used to minimize the energy functional. This method has been used by many scholars. However, this method is limited by the Courant Friedrichs Lew (CFL) condition. Because the convergence speed is slow, it is easy to fall into the local minimum, and the evolutionary process is time-consuming. In the model of this paper, an iterative convolution-thresholding (ICTM) segmentation algorithm based on cross-entropy active contour model is proposed. In this algorithm, the interface between every two divided regions is implicitly determined by its characteristic function, and the regularization term is written into the non-local approximation based on the characteristic function. Combining the coordinate descent method with sequential linear programming, an unconditional energy decomposition algorithm for solving the cross-entropy model is constructed. In the iterative convolution-thresholding, we set the first-stage characteristic function Ω_1 be:

$$u(x) = \begin{cases} 1, x \in \Omega_1 \\ 0, x \notin \Omega_1 \end{cases} \tag{4}$$

then the characteristic function of the second paragraph Ω_2 can be implicitly expressed as $1 - u(x)$.

From the articles of Esedoglu and Otto [15], $\tau \ll 1$, we can see that $|\partial\Omega_i|$ in Eq. (2) can be approximated as:

$$|\partial\Omega_1| \approx \sqrt{\frac{\pi}{\tau}} \int_{\Omega} u G_{\tau} * (1 - u) dx \tag{5}$$

In Eq. (5), * represents convolution. Among G_{τ} comes from the weight function in Li [16] article. The fidelity term in Eq. (2) can be multiplied by the cross-entropy function of each region by the characteristic function of the corresponding region, then it can be expressed in the form of integrals over the entire region Ω ,

$$\int_{\Omega_1} I \left| \log \left(\frac{I}{c_1 + \sigma} \right) \right| dx = \int_{\Omega} u I \left| \log \left(\frac{I}{c_1 + \sigma} \right) \right| dx \tag{6}$$

$$\int_{\Omega_2} I \left| \log \left(\frac{I}{c_2 + \sigma} \right) \right| dx = \int_{\Omega} (1 - u) I \left| \log \left(\frac{I}{c_2 + \sigma} \right) \right| dx \quad (7)$$

set $E_i(I, c_1, c_2) = I \left| \log \left(\frac{I}{c_i + \sigma} \right) \right|$, then Eq. (2) can be written as:

$$\varepsilon = F_c(c_1, c_2, \Omega_1, \Omega_2) = \mu \sum_{i=1}^2 |\partial\Omega_i| + \sum_{i=1}^2 \int_{\Omega_i} E_i(I, c_1, c_2) dx \quad (8)$$

then:

$$\varepsilon = \varepsilon(u, c) = \varepsilon_i(u, c) + \varepsilon^\tau(u, c) \quad (9)$$

Let $\beta := \{u \in BV(\Omega, R) | u = \{0, 1\}\}$, $BV(\Omega, R)$ denote the bounded variational function space, and then use the coordinate descent method to minimize $\varepsilon(u, c)$, we set the initial guess is u_0 , find the minimization factors in order. For fixed values u^k , usually:

$$c^k = \arg \min_{c \in S} \varepsilon(u^k, c) \quad (10)$$

where $S = S_1 \times S_2 \times \dots \times S_n$, S_i is the allowable set of c_i . For the cross-entropy model, the convex fidelity term is strictly used, and because ε^τ is independent of c , then c^k is the global minimum value of ε_i relative to c , that is:

$$c^k = \arg \min_{c \in S} \int_{\Omega} u^k E_1(I, c) + (1 - u^k) E_2(I, c) dx \quad (11)$$

when the value c^k is fixed, since $\varepsilon_i(u, c^k)$ is linear and $\varepsilon^\tau(u, c^k)$ is a concave function, then $\varepsilon(u, c^k)$ is a concave functional, then:

$$u^{k+1} = \arg \min_{u \in \beta} \varepsilon(u, c^k) = \arg \min_{u \in \kappa} \varepsilon^\tau(u, c^k) \quad (12)$$

where, κ is the convex set of β . Set

$$\phi = E_1(I, c_1) - E_2(I, c_2) + \mu \sqrt{\frac{\pi}{\tau}} G_\tau * (1 - 2u^k) \quad (13)$$

After relaxation and linearization, the linear functional minimization on the convex set is used to approximate the optimization Eq. (12). Because of $u(x) \geq 0$, it can be executed in point state. The minimum can be obtained by the following:

$$u^{k+1}(x) = \begin{cases} 1, & \phi(x) \leq 0 \\ 0, & \phi(x) > 0 \end{cases} \quad (14)$$

In the iterative convolution-thresholding algorithm, the condition to judge whether the algorithm converges is $\int_{\Omega} |u^k - u^{k-1}| dx > 10^{-12}$. The interface between two different image domains is implicitly represented by their characteristic functions. The fidelity term is expressed as the linear relationship between the characteristic function and the cross entropy function. Through the product of the characteristic function and the cross entropy function, and then iterate to obtain the minimum value c^k , so the minimum value of the linear approximation is found. The regularization term is approximated by the thermonuclear convolution function of the characteristic function, and fast Fourier transform (FFT) is used for thermonuclear convolution. Then calculate ϕ^k , then obtain u^{k+1} through the threshold, and finally obtain the minimized energy functional function u^s of Eq. (2) through the loop. In addition, since the functional ε^f is always lower than its linear approximation, the smallest element can be given a smaller value in Eq. (9). This speeds up the convergence speed of the iterative convolution-thresholding, the number of iterations to reach a steady state is reduced.

4 Experiments

In order to verify the effectiveness of the algorithm proposed in this paper for industrial smoke segmentation, experiments were conducted on three types of industrial smoke images, such as grayscale inequality, natural scenes and complex backgrounds. In this paper, a new algorithm was constructed based on the iterative convolution-thresholding to solve the energy functional of the cross-entropy model, which is referred to as the ICTM-CEACM model. Compared with the traditional CV model [4], LIF model [17], LIC model [18], ICV model [19], LCVSR model [20], SPF model [21], and the cross-entropy model for minimizing energy functional based on difference method [14] (referred to as FD-CEACM model), the experiment was conducted, mainly from the two aspects of segmentation effect and segmentation efficiency. The experimental environment of this paper was CPU model Intel Core i5-4210U, main frequency 2.40 GHz, 8 GB RAM, simulation software Matlab R2018b, operating system was Windows 10. The sizes of the six industrial smoke images were 358×208 , 400×241 , 678×432 , 282×169 , 481×274 , and 470×310 , respectively. The parameters of all methods were set to the optimal, and the experimental results of six images are now presented.

In Fig. 1, it showed two industrial smoke images of intensity inhomogeneity, including target smoke and other interference. For windy conditions, soot was affected, and areas with low concentrations of soot caused by wind conditions was ignored. According to the experimental results, only FD-CEACM and ICTM-CEACM segments did not have interference chimneys, and all other models had interference, so it can be seen that CEACM has a good segmentation effect on interference. FD-CEACM and ICTM-CEACM were different from the segmentation algorithm. The former was the difference method, while the latter was the iterative convolution-thresholding. The time

step size of the difference method was set artificially, so it was difficult to find a reasonable value, resulting in the incomplete segmentation of the contour. The iterative convolution-thresholding implicitly expresses the interface of the two segmentation regions through the characteristic function, the fidelity term was constructed by the linear function of the characteristic function, and the regularization term was approximated by the thermonuclear convolution function, so as to obtain a relatively complete smoke segmentation contour. The symbolic distance function of SPF model can effectively prevent the contour from moving in the weak edge or the fuzzy edge, so it had a good effect on the smoke segmentation. LIF model is an active contour model based on the local gray information of the image. It was sensitive to the initial contour and had a poor effect on smoke segmentation. The CV model and the ICV model are based on the global information of the image. The image is composed of two regions that are close to the constant value. Therefore, the segmentation effect of the intensity inhomogeneity image was poor. Based on the gradient information of the image, LIC model has a good edge processing, which not only separated the object, but also separated the interference. The significant detection of the LCVSR model can provided a rough outline of the object, and it was impossible to distinguish the object from the interference, so the two objects were separated.

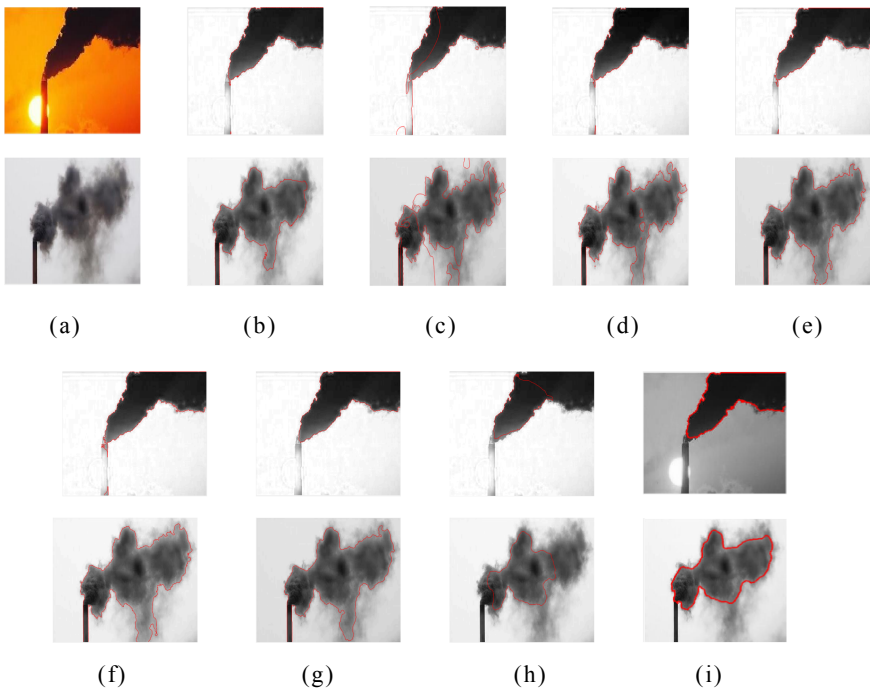


Fig. 1. Segmentation results of industrial smoke image with intensity inhomogeneity (a) the original image (b) CV model segmentation results (c) LIF model segmentation results (d) LIC model segmentation results (e) ICV model segmentation results (f) LCVSR model segmentation results (g) SPF model segmentation results (h) FD-CEACM model segmentation results (i) ICTM-CEACM model segmentation results

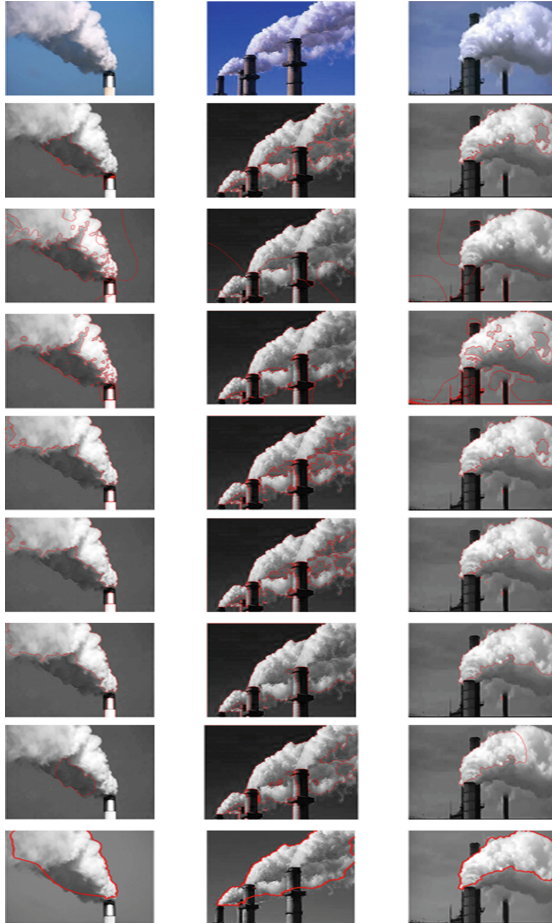


Fig. 2. Segmentation results of three industrial smoke images in natural background Line 1: original image line 2: CV model segmentation result line 3: LIF model segmentation result line 4: LIC model segmentation result line 5: ICV model segmentation result line 6: LCVSR model segmentation result line 7: SPF model segmentation result line 8: FD-CEACM model segmentation result line 9: ICTM-CEACM model segmentation result

From Fig. 2, it can be seen that this is the image of industrial smoke in the natural background. Compared with the intensity inhomogeneity image and the complex background image, the industrial smoke image under the natural background is relatively simple. In the image, there are mainly objects, interference and backgrounds. From the experimental results, it can be seen that the complete segmentation of the target object contour was the SPF model and the ICTM-CEACM model. The SPF model mainly had a great effect on the contour edge. For weak edge and fuzzy edge, it can effectively prevent the movement, so as not to segment the interference. ICTM-CEACM model, by combining the cross entropy model with the CV model, can be

used to segment the model with interference, and the ICTM algorithm can be used to minimize the energy functional, so as to achieve a better effect in smoke image segmentation. Due to their own limitations, other models had segmented the distraction or the target object region with missing parts.

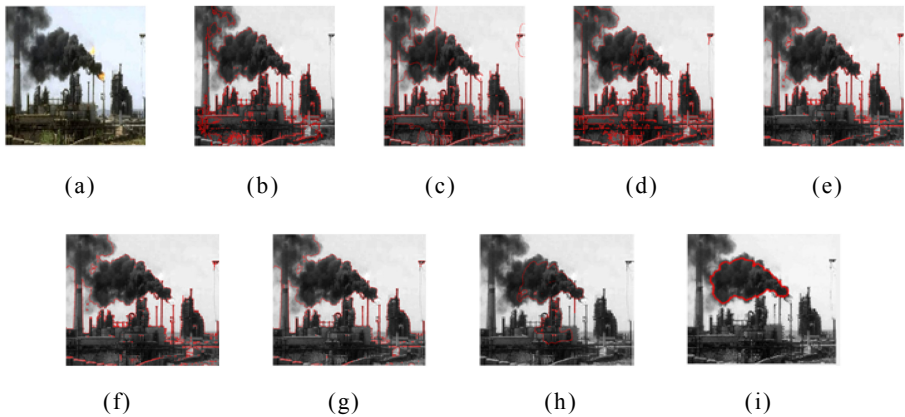


Fig. 3. Segmentation results of three industrial smoke images in natural background (a) original image (b) CV model segmentation results (c) LIF model segmentation results (d) LIC model segmentation results (e) ICV model segmentation results (f) LCVSR model segmentation results (g) SPF model segmentation results (h) FD-CEACM model segmentation results (i) ICTM-CEACM model segmentation results

Table 1. JSC of each algorithm for images with intensity inhomogeneity

| Model | Figure 1 (1) | Figure 1 (2) |
|------------|--------------|--------------|
| CV | 0.9532 | 0.9321 |
| LIF | 0.7005 | 0.6953 |
| LIC | 0.9056 | 0.7441 |
| ICV | 0.9102 | 0.8021 |
| LCVSR | 0.9010 | 0.8152 |
| SPF | 0.9710 | 0.8932 |
| FD-CEACM | 0.7123 | 0.7021 |
| ICTM-CEACM | 0.9817 | 0.9501 |

As we can see from Fig. 3, the background of this image of industrial smoke is very complex, including chimneys, buildings and some green environment. In addition, in the case of wind, we chose the region with high concentration of smoke as the segmentation target, while ignoring the part with low concentration caused by wind. As can be seen from the experimental results, the (b)–(h) images were not well processed to the complex background, and they all appeared in the segmentation results. Only in (i), the ICTM algorithm did not segment all the background objects, but only the smoke

Table 2. Comparison of iteration times of each segmentation algorithm

| Model | Figure1(1) | Figure1(2) | Figure2(1) | Figure2(2) | Figure2(3) | Figure3 |
|------------|------------|------------|------------|------------|------------|---------|
| CV | 1000 | 500 | 1500 | 1200 | 1500 | 1000 |
| LIF | 3200 | 4520 | 3000 | 3000 | 2400 | 1520 |
| LIC | 200 | 50 | 20 | 200 | 200 | 60 |
| ICV | 10 | 30 | 35 | 40 | 100 | 15 |
| LCVSR | 150 | 30 | 50 | 100 | 200 | 100 |
| SPF | 150 | 150 | 160 | 120 | 150 | 200 |
| FD-CEACM | 2500 | 2000 | 1500 | 2500 | 1500 | 2000 |
| ICTM-CEACM | 56 | 38 | 115 | 122 | 62 | 50 |

Table 3. Comparison of running time of each segmentation algorithm

| Model | Figure1(1) | Figure1(2) | Figure2(1) | Figure2(2) | Figure2(3) | Figure3 |
|------------|------------|------------|------------|------------|------------|----------|
| CV | 47.8529 | 23.7277 | 249.1348 | 48.3928 | 134.0759 | 97.0670 |
| LIF | 80.7304 | 137.6130 | 334.0627 | 55.5809 | 101.0496 | 68.3632 |
| LIC | 38.6675 | 14.1927 | 23.7552 | 27.5027 | 107.3623 | 36.0189 |
| ICV | 2.7051 | 5.3667 | 10.1911 | 5.3634 | 16.6867 | 5.1091 |
| LCVSR | 5.4778 | 1.9016 | 8.8801 | 3.4624 | 16.2903 | 9.9007 |
| SPF | 2.5116 | 3.0116 | 8.4744 | 3.3720 | 4.4812 | 7.0634 |
| FD-CEACM | 177.1977 | 144.6341 | 292.0068 | 155.4888 | 143.0658 | 235.0075 |
| ICTM-CEACM | 14.2528 | 10.2742 | 65.6235 | 21.2814 | 27.7081 | 21.7371 |

objects. CEACM model combined the two models of CV and cross entropy, based on the global information of the image, and improved the algorithm of the model, used ICTM to minimize the energy functional, so as to achieve a better segmentation of industrial smoke image with complex background.

Table 1 lists the Jaccard similarity coefficient (JSC) of each segmentation algorithm to images with intensity inhomogeneity. Table 2 and Table 3 list the iteration times and running time of each segmentation algorithm. We can see that the running time was approximately positively correlated with the number of iterations. When the number of iterations was relatively large, the running time correspondingly increased. From the table can be found that CV model, LIF and FD-CEACM iteration times and operation time compared to other models were larger, the traditional CV model was a driving force curve of the computational complexity is higher, LIF model is to calculate the image area information thus increased the amount of calculation model, FD-CEACM fidelity for further model is calculated by the logarithm, which is relatively slow. Compared with the running time, the number of iterations of ICV model and LCVSR model is less. The ICV model is a level set function without initialization, and the level set equation does not contain curvature and other complex difference terms. The LCVSR model extracts the initial contour through significant detection, and then carries out segmentation. Both models are susceptible to interference from interference,

and the segmentation effect is poor. SPF model has the characteristics of global and local, the iteration time is relatively short, but the iteration times are more. Based on the CEACM model of ICTM, it has some applicability to industrial smoke in a variety of scenarios and achieves a relatively good segmentation effect. Under the same segmentation effect, the iteration time and number of divisions are better than other models.

5 Conclusion

Considering the little difference between the background of industrial smoke image and the target object in gray value, interference and kinds of images, a new algorithm based on cross-entropy model is proposed to realize the accurate segmentation of industrial smoke images. Through the combination of CV model and cross-entropy model, a cross-entropy model is obtained, and an iterative convolution-thresholding algorithm is used to minimize the energy functional, which speeds up the convergence speed. The experimental results with several other models show that the improved algorithm based on the cross-entropy model in this paper has better segmentation results for industrial smoke, and the segmentation efficiency is high. Although this paper has advantages in both segmentation effect and iteration time, the use of convolution in the segmentation process increases the computational complexity and the segmentation time is relatively long. In the subsequent research, the computational complexity of convolution will be optimized to further improve the segmentation efficiency of the algorithm.

Acknowledgements. The authors would like to express their thanks to the referees for their valuable suggestions. This work was supported by the grant of the National Natural Science Foundation of China, Nos. 61672204, 61806068, the grant of Anhui Provincial Natural Science Foundation, 1908085MF184, 1908085QF285, the grant of Key Technologies R&D Program of Anhui Province, No. 1804a09020058, the grant of Teaching Team of Anhui Province, No. 2016jxtd101.

References

1. Lin, M.: Analysis on the promoting effect of environmental monitoring on environmental governance. *China New Telecommun.* **021**(012), 231 (2019)
2. Osher, S., Sethian, J.A.: Fronts propagating with curvature-dependent speed: algorithms based on Hamilton-Jacobi formulations. *J. Comput. Phys.* **79**(1), 12–49 (1988)
3. Mumford, D., Shah, J.: Boundary detection by minimizing functionals. In: *Image Understanding*, pp. 19–43 (1985)
4. Chan, T.F., Vese, L.A.: Active contours without edges. *IEEE Trans. Image Process.* **10**(2), 266–277 (2001)
5. Li, C., Xu, C., Gui, C.: Level set evolution without re-initialization: a new variational formulation. In: *IEEE Computer Society Conference on Computer Vision and Pattern Recognition*, vol. 1, pp. 430–436 (2005)
6. Wang, X.F., Huang, D.S., Xu, H.: An efficient local Chan-Vese model for image segmentation. *Pattern Recogn.* **43**(3), 603–618 (2010)

7. Zhang, G.D., Wang, F., Wen, D.Y.: Research on hydrophobic image segmentation algorithm based on GAC-CV hybrid model. *Comput. Technol. Autom.* **38**(03), 96–102 (2019)
8. Wang, C.: Improved edge detection of single frame image shadow in CV model. *Mod. Comput.* **2020**(10), 59–62–68 (2020)
9. Zhang, X.M., Wang, C.M., Hu, H.: A region-based smoke image segmentation method. *Comput. Eng. Appl.* **2008**(13), 193–196 (2008)
10. Hsu, Y.C., Dille, P.S., Randy, S.: *Industrial smoke detection and visualization*. Carnegie Mellon University, Pittsburgh (2016)
11. Wang, W.Z., Liu, H., Wang, B.: Image segmentation of industrial smoke and dust based on background modeling and feature matching. *Transducer Micro Syst. Technol.* **037**(008), 37–39,42 (2018)
12. Chu, Y.: *Study on smoke monitoring system based on video image processing*. Jiangsu University, Zhenjiang (2012)
13. Wang, Y.N., Liu, H., Chen, F.G.: The utility model provides a method to segment industrial emission smoke in video. *Inf. Technol.* **2018**(11), 142–146 (2018)
14. Song, Y., Wu, Y., Dai, Y.: A new active contour remote sensing river image segmentation algorithm inspired from the cross entropy. *Digit. Signal Proc.* **48**, 322–332 (2016)
15. Esedoglu, S., Otto, F.: Threshold dynamics for networks with arbitrary surface tensions. *Commun. Pure Appl. Math.* **68**(5), 808–864 (2015)
16. Li, C., Kao, C.Y., Gore, J.C.: Implicit active contours driven by local binary fitting energy. In: *IEEE Conference on Computer Vision and Pattern Recognition*. IEEE (2007)
17. Zhang, K.H., Song, H.H., Zhang, L.: Active contours driven by local image fitting energy. *Pattern Recogn.* **43**(4), 1199–1206 (2010)
18. Li, C.M., Huang, R., Ding, Z.H., Gatenby, J.C., Metaxas, D.N., Gore, J.C.: A level set method for image segmentation in the presence of intensity inhomogeneities with application to MRI. *IEEE Trans. Image Process.* **20**(7), 2007–2016 (2011)
19. Zhang, K.H., Zhou, W.G., Zhang, Z.: An improved CV active contour model. *Optoelectron. Compon.* **35**(12), 112–116 (2008)
20. Zou, L., Song, L.T., Wang, X.F., Chen, Y.P., Tang, C., Zhang, C.: Image segmentation based on local Chan-Vese model combined with fractional order derivative. In: Huang, D.-S., Bevilacqua, V., Premaratne, P. (eds.) *ICIC 2019*. LNCS, vol. 11643, pp. 326–336. Springer, Cham (2019). https://doi.org/10.1007/978-3-030-26763-6_32
21. Zhang, K.H., Zhang, L., Song, H.H., Zhou, W.G.: Active contours with selective local or global segmentation: a new formulation and level set method. *Image Vis. Comput.* **28**(4), 668–676 (2010)



Efficient Segmentation Using Gamma Correction with Complement Image of Chinese Rubbing Image

Han Huang¹(✉) and Yong-Li Ma²

¹ City University of Hong Kong, Kowloon Tong, Hong Kong
hanhuang9-c@my.cityu.edu.hk

² Nanchang Institute of Technology, Nanchang 330099, Jiangxi, China
Whitefox1966@163.com

Abstract. For Chinese rubbing image under the complex background, to against its characteristic of low contrast and large noise, we develop a gamma correction enhancement algorithm in which the grayscale space is being conducted before the Otsu's binarization, experiments on multiple pictures show the superiority of the algorithm. At first, the global contrast is enhanced based on the gamma correct algorithm for the complement image of the Chinese rubbing image. After that, we have implemented optimum global thresholding using Otsu's method for image segmentation. The experimental results show that our algorithm could correct the background noise of the image and enhance the stroke in the low contrast Chinese rubbing image, and there is no need to denoise in advance. The performance of the algorithm is simple, fast, and produces very good segmentation.

Keywords: Chinese rubbing image · Gamma correction · Contrast enhancement · Image segmentation · Thresholding image

1 Introduction

It is of great significance for the research and protection of ancient Chinese inscriptions. However, due to the reasons of some stele materials, natural weathering corrosion and man-made damage, the visual effect of the obtained image is poor, which is mainly manifested in the overall image being partial bright or partial dark, at the same time, there are uneven and irregular light and dark distribution, or there are patches and uneven light and dark noise, which brings difficulties to subsequent image processing such as text recognition [1].

Image enhancement is a method that refers to highlight some important information in an image and to weaken or remove some secondary information, which aims to improve the quality of human perception and interpretability of information in the next process [2]. In general, image enhancement techniques can be divided into three categories: spatial-domain methods, frequency-domain methods, combinational methods. The frequency-domain method is to transform the image to the transform domain for processing, and then transform back the result to the spatial domain [3]. The spatial

domain method is to directly change the pixel of the image. The frequency-domain method includes low-pass filtering, homomorphic filtering, etc. The spatial domain method includes image binarization, histogram equalization, contrast enhancement, fuzzy contrast enhancement, etc. [4, 5].

Contrast enhancement refers to the enhancement of the contrast and sharpness of the image and the better visual effect of the image. Contrast enhancements improve the perceptibility of objects in the scene by enhancing the brightness difference between objects and their backgrounds. The purpose is to make the objective images more suitable for a application than the original images, and the results of processing the image are more in line with the characteristics of the human visual recognition system or the requirements of the computers.

In practical application, processing speed is an important factor that should be considered. The gamma correct method does not need to transform the domain, so it has obvious advantages in processing speed compare to frequency-domain methods.

In this paper, the gamma correction algorithm based on the complement image of the Chinese rubbing image has been used for preprocessing, after that, binary segmentation is carried out based on gamma correction complement image, finally, a clear text image is obtained. This adaptive algorithm has low complexity and does not need human intervention. It can significantly improve the quality of Chinese rubbing image segmentation. Compared to the recently developed deep learning-based segmentation techniques, the main advantage of those classical approaches is they are unsupervised and thus no need for manually created training data.

2 Gamma Correction Techniques

Contrast is the local change in brightness and is defined as the ratio between average brightness, of an object about the background. The human visual system is logarithmically sensitive to brightness, that is to say, higher brightness requires higher contrast for the same perception.

Contrast enhancement processes adjust the relative brightness and darkness of objects in the scene to improve their visibility. The contrast and tone of the image can be changed by mapping the gray levels in the image to new values through a gray-level transform. The mapping function reassigns the current gray level GL to a new gray level GL' .

Gamma correction technique is used to enhance the image, which improves the details of the dark part in the image. In short, it is used to make the linear response of the image from the exposure intensity closer to the response of the human eye through non-linear transformation, that is, to correct the bleached (camera exposure) or over dark (under exposure) image.

The relationship between the gray value of the input and output image after gamma transformation is shown in Fig. 1: the abscissa is the input gray value, the ordinate is the output gray value, the blue curve is the input-output relationship when the gamma value is equal to 0.2, and the red curve is the input-output relationship of the corresponding negative image when the gamma value is equal to 0.2. It can be observed that when the gamma value is less than 1 (red curve), the overall brightness value of the

image is rapidly improved, and the contrast at the low gray level is increased, which is more conducive to distinguish the details of the image at the low gray level. A gamma value somewhere between provides a compromise between increase and decrease tendencies of the pixel value in the image [6].

The general form of the exponential function used for image processing is defined as

$$y = be^{ax+1} \tag{1}$$

Here again, $a (> 0)$ controls the curvature of the exponential function while b is a scaling factor.

Suppose an 8-bit image of size $m \times n$ pixels as $I(x, y)$, then the gamma intensity correction transforms the pixel intensity values at each spatial position (x, y) , for $x = 1, 2, \dots, m$ and $y = 1, 2, \dots, n$ in accordance with the following expression [7]

$$I_{gamma} = I(x, y)^\gamma \tag{2}$$

Where I_{gamma} represents the gamma intensity corrected form of the image $I(x, y)$, and γ represents for the different gamma values that controls the type of mapping. When γ is set to a value of $\gamma > 1$, dark regions in the original image become lighter in the gamma corrected one. Similarly, when γ is set to a value $\gamma < 1$ the light regions in the original image become darker in the gamma intensity corrected one.

In this paper, before using Gamma correction to enhance the image illumination, in which a new image $g'(x, y)$ is created from the image $g(x, y)$ by the transform

$$g'(x, y) = 255 - g(x, y) \tag{3}$$

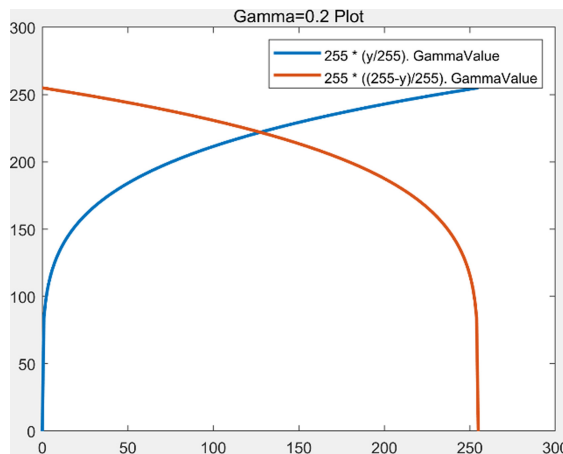


Fig. 1. Shows the function of the relationship between output and input signals by gamma correction. (Color figure online)

3 Proposed Method and Experimental Results

The suggested method comprises of three steps. Initially, the complement of the original image had been computed and returns the result. Then the contrast enhance is done by gamma correct. Afterwards, segmentation is done by using Otsu's algorithm [8]. A schematic overview of the recommended approach is shown in Fig. 2.

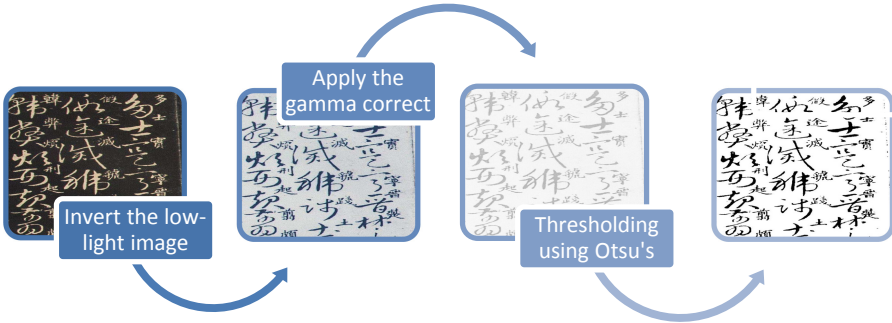
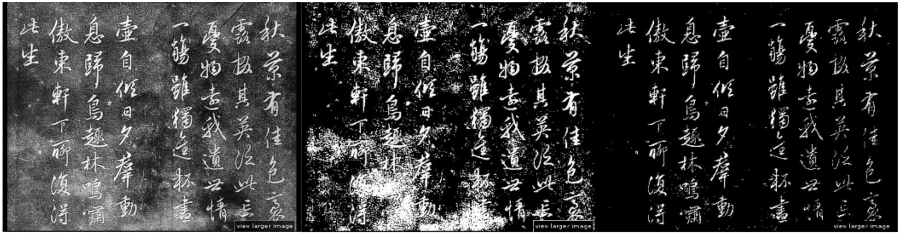


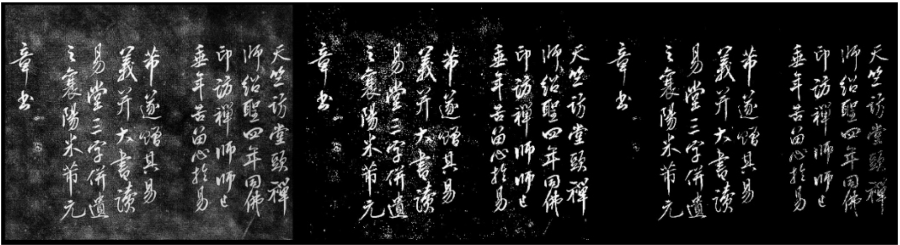
Fig. 2. Schematic overview of the recommended approach.

The dataset used in this paper, obtained from Field Museum online [9]. Some experimental results had been shown in Fig. 3. Here, Otsu's global thresholding method had been employed as a comparison. The experimental results show that using our algorithm has outperformed global thresholding methods.

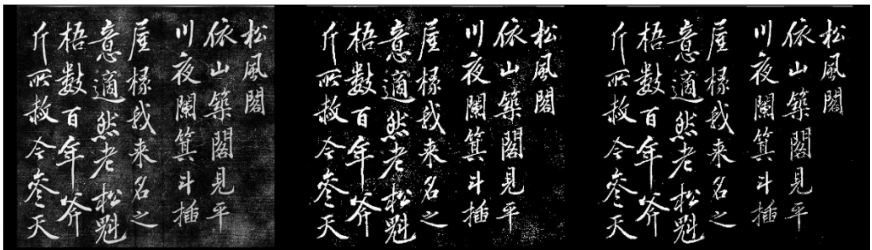
A visual assessment was performed for grayscale images as well as for color images. From the above segmentation images, it is clear that ours method are producing very good segmentation results, although we didn't take any denoising algorithm for the original image in advance. The proposed method can be implemented in a real-time optical character recognition system with limited resources.



(a)



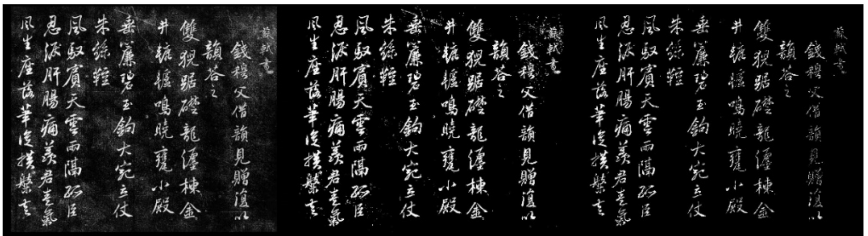
(b)



(c)



(d)



(e)

Fig. 3. Some results of experiments, from (a)–(e), left is the original rubbing image, middle is the segmentation using Otsu’s algorithm, right is binarization image using our method.

4 Conclusion

In this paper, a Chinese rubbing image binarization algorithm is developed to use gamma correct enhancement algorithm in the grayscale space with complement image. It is computationally simple, fast and has a high degree of detail preservation with less noise. We tested our algorithm on many different Chinese rubbing, and obtained encouraging results. Future work will also involve segmenting characters from Chinese rubbing images. Meanwhile, the techniques used in this paper are mostly classical image processing techniques. A combination of classical image processing techniques and recently developed deep learning techniques may further boost our segmentation performance, which will also be one of our future research directions.

Acknowledgements. This work was supported by the grants from the Educational Commission of Jiangxi province of China, No. GJJ151134.

References

1. Huang, Z.K., Li, Z.H., Huang, H., et al.: Comparison of different image denoising algorithms for Chinese calligraphy images. *Neurocomputing* **188**, 102–112 (2016)
2. Panetta, K.A., Wharton, E.J., Agaian, S.S.: Human visual system-based image enhancement and logarithmic contrast measure. *IEEE Trans. Syst. Man Cybern. B* **38**(1), 174–188 (2008)
3. Welfer, D., Scharcanski, J., Kitamura, C.M., et al.: Segmentation of the optic disk in color eye fundus images using an adaptive morphological approach. *Comput. Biol. Med.* **40**(2), 124–137 (2010)
4. Guo, X., Li, Y., Ling, H.: LIME: low-light image enhancement via illumination map estimation. *IEEE Trans. Image Process.* **26**(2), 982–993 (2017). <https://doi.org/10.1109/TIP.2016.2639450>
5. Dong, C., Loy, C.C., He, K., Tang, X.: Image super-resolution using deep convolutional networks. *IEEE Trans. Pattern Anal. Mach. Intell.* **38**(2), 295–307 (2016). <https://doi.org/10.1109/tpami.2015.2439281>
6. Singh, G., Mittal, A.: Various image enhancement techniques-a critical review. *Int. J. Innov. Sci. Res.* **10**(2), 267–274 (2014)
7. Chaudhuri, S., Chatterjee, S., Katz, N., Nelson, M., Goldbaum, M.: Detection of blood vessels in retinal images using two-dimensional matched filters. *IEEE Trans. Med. Imaging* **8**, 263–269 (1989)
8. Otsu, N.: A threshold selection method from gray-level histograms. *IEEE Trans. Syst. Man Cybern.* **9**(1), 62–66 (2007)
9. http://archive.fieldmuseum.org/chineserubbings/introduction_1.asp



State Spatial Selectivity and Its Impacts on Urban Sprawl: Insights from Remote Sensing Images of Zhuhai

Lingyue Li¹, Zhixin Qi², and Shi Xian³(✉)

¹ Department of Urban Planning, College of Architecture and Urban Planning, Tongji University, Shanghai, People's Republic of China

lilingyue929@gmail.com

² School of Geography and Planning, Sun Yat-Sen University, Guangzhou, People's Republic of China

³ School of Geographical Sciences, Guangzhou University, Guangzhou, People's Republic of China

geoshixian@gzhu.edu.cn

Abstract. This research unfolds a fuller picture of how state spatial selectivity (SSS) impacts Chinese urban growth through a case study of Zhuhai. Processing remote date image, three stages of Zhuhai's urban sprawl were identified: from germinal, gradualist increase under neoliberal decentralization and sustainable orientation, to expansion surge with amplified scalar restructuring and garden city ideology, to fluctuant growth shaped by multiscalar restructuring and urban livability. There are two main contributions. First, using remote sensing and GIS, this study quantifies the interdigitated spatial effects of SSS. Second, it enriches our understanding towards SSS and green growth by disentangling their relations and unraveling their evolving modalities in urban sprawl. We argue that SSS is crucial impetus touching off periodic, multiscalar rescaling to spur the increment of urban land while sustainability idea regulates the pace and intensity of urban growth and has nurtured out a livable Zhuhai. In this regard, urban growth in Zhuhai is modest compared with its peers in Pearl River Delta (PRD) region and displays periodic, multiscale characteristics. The main growth area in Zhuhai is oscillatory between east and west that a polycentric structure starts to emerge. The research also suggests that while SSS in China is mostly growth-oriented, a shrink-oriented SSS in the West has started to emerge.

Keywords: State spatial selectivity · Remote sensing image processing · Rescaling · Urban growth · Zhuhai

The research was funded by the National Natural Science Foundation of China (Grant No. 51808391, 41601445, 41701189), National Key R&D Program of China (Grant No. 2017YFA0604403) and the Pearl River Talent Recruitment Program (Grant No. 20170142).

© Springer Nature Switzerland AG 2020

D.-S. Huang et al. (Eds.): ICIC 2020, LNCS 12463, pp. 329–341, 2020.

https://doi.org/10.1007/978-3-030-60799-9_29

List of Abbreviations

| | |
|------|---------------------------|
| SSS | State spatial selectivity |
| PRD | Pearl River Delta |
| SEZs | Special economic zones |
| LEI | Landscape Expansion Index |

1 Introduction

China's urban territory has expanded exponentially since economic reform, receiving substantial scholarly attention. Although urban expansion created plenitudinous wealth, facilitated human (re)production, and extended living communities, concomitant issues such as environmental degradation, traffic congestion, and the greenhouse effect, emerged. These (un)favourable consequences have rendered urban expansion a double-edged sword that finds the driving force and mechanism behind bulks large in urban China (Wang et al. 2012). In hyper growth China, remote sensing images are valid data displaying the spatiotemporal evolution of urban expansion (e.g., Wang et al. 2012) whereas policy factors and impetus especially the contextualised politics behind are discussed insufficiently.

SSS is a form of regulation over spaces (Jones 1997); one that unceasingly breaks extant spatial orders for (re)equilibrium and intervenes. An in-depth evaluation on how SSS alters and associates with urban expansion rates and patterns can be interpreted as nuanced, and extended knowledge of the intrinsic mechanisms behind urbanisation. The concept of SSS originates from the crisis of Atlantic Fordism, but travelled to China, then evolved and variegated (Brenner 2004; Wu 2016). SSS rebuilds central-local relations and enhances policy intensity that leads to geospatial difference in expansion rate and modality and temporality of spatial selectivity adds complexity in examining the impacts of SSS. Given all these, some research questions are raised: How does SSS evolve along the capricious orientation/politics from central and local in post-reform China? What are the spatio-temporal patterns of urban expansion under an evolving SSS contingent on specific histories and geographies? In what ways does SSS transform an urban landscape?

Zhuhai is selected, not only because it is located in once the fastest growing and most urbanised PRD region but also because the city has benefitted from sustainable ideology. The Zhuhai case is intriguing as it reveals how a forefront city competes for spatial selectivity strategies in the fragmented PRD and how specific topography, geography, and sustainability idea affect SSS growth. This research contributes to the present studies in two main respects: first, it advances China's urban expansion from an SSS perspective, which significantly comprehends state intervention on the spatial process; second, it quantifies the impact of SSS on urban growth to describe the spatial manifestation of state action in detail.

2 Three Stages of SSS in Post-reform China

Arising in the transition from the Keynesian welfare state to a neoliberal Schumpeterian workfare state, SSS originates from a key mid-level notion of strategic selectivity, assumes material and ideological forms (Jessop 1993; Jones 1997), then travelled to China interpreting how decision making over space impacts fast territorial urbanization. Yet, applying it to China shall first note the dissimilarities of SSS in different context. First, shrink-oriented SSS started to emerge in the west whereas China remained expands fast, incorporating “Green GDP” to balance environmental protection. Second, private sectors play significant role in the west while government sectors dominate the growth in China. Third, with no Fordist–Keynesianism or the like to begin with, China’s SSS aims to enhances accumulation efficiency but SSS in the west targets to ease inherent capitalism crisis (Li and Chan 2017). Though rural hollowing shrank villages in China, this is a passive process rather than a proactive choice. Three stages of SSS in China’s rapid urbanization are generally identified.

2.1 Southeast Areas as the Pioneers Between 1978 and Early 1990s

Since 1978, insulated China has embarked on (re)introducing market-like rules, in which state power was, horizontally, unleashed to the market and, vertically, reshuffled within the state system. Synchronically, spatial selectivity first privileged remote south China, where central control was considerably weak. After the economic reform, four special economic zones (SEZs) were authorised to lodge transnational circulatory capital. The inspirational saying, “Crossing the river by feeling the stones”, was obtained by reform pioneers from cross-fertilisation with “foreign” ideas (Gabriel 1998). The acquisition of management knowledge, capital, and technology from overseas facilitated SEZs development at incredible, albeit uneven, rates. This phenomenon encouraged reformists to expand their zone experiment to another 14 coastal cities with unladen preferential tax incentives, flexibly regulated foreign exchange, and relaxed transfer of land use rights. In south China, extensive business connections with foreign capital were established in cross-border zones of industrialisation de facto and in situ urbanised rural area (Shen and Ma 2005). From 1980 to 1990, although the presumable growth in central state sectors was, paradoxically, much less than that outside the bureaucratic system (Harvey 2006), incipient urbanism is considered a state masterpiece achieved through scalar restructuring.

2.2 The Hinterland Region Starts to Gain Favour Since Early 1990s

When the nationwide large-scale urban growth commenced in early 1990s, the interior region was favoured. Fiscal decentralization and market reform in land, housing, and public services accelerated the growth. The time-lag of preferential policies led to regional inequality between the east and west, but the comparative advantages of the coast diminished. Two rounds of urban land increases were observed from 1990 to 2000: a surge during the first half of the decade and a slowing down in the latter half (Li and Yeh 2004). The sluggishness was partly affected by the “Ordinance for the Protection of Primary Agricultural Land” (Decree [No. 162] of the State Council), after

which many cities grew compactly, as opposed to the former “extensive sprawl” (Xiao et al. 2006). In the inner city, public and private sectors preferred value-added expansion in the form of micro infilling (He and Wu 2005, 2009). In the peri-urban interface or suburbs, new towns were popularised and promoted by either administrative relocation or population decentralisation.

2.3 An Era of City-Regionalization Since 2000

A form of SSS infused with multiple levels of power intervention diversified after 2000. In addition, tax redistribution transited a streamlined decentralisation towards hybrid power de/recentralisation, which scholars have regarded as “regionally decentralised authoritarianism”. City-regions, new zones, and bay area agglomerations burgeoned for scale production. Accordingly, land expansion was state-led and market-leaning but was, not surprisingly, characterised by scant participation, ubiquitous elite control, and local discretion. Thus, informal growth occasionally occurred. Market-oriented expansion is committed to maximising profits in rent-gap seeking, whereas the benefits of state-led growth largely accrue to reigning leaders. As Chinese officials are transferred, promoted, and dismissed frequently, the floating cadre network destabilised political ambiances for SSS-led expansion.

3 Research Method

Zhuhai sits at the southwest of Guangdong (Fig. 1). This region is among the rapidly growing regions in China where cities are densely populated. Over the past decades, the urban sprawl in Zhuhai has not been as intense as has that of its aggressive neighbours, but it has remained striking. Despite rapid urbanisation, a liveable environment benefitted from seashore climate and natural geography has long been a well-known city brand for Zhuhai. At the end of 2015, Zhuhai had 1,732 km² land surface area and 1.63 million resident population. Zhuhai city consists of three main districts: Xiangzhou (consisting of High-Technology Development Zone, Xiangzhou, and Hengqin) (553.31 km², 946.3 thousand inhabitants), Doumen (613.88 km², 428.4 thousand inhabitants), and Jinwan Districts (565.14 km², 259.4 thousand inhabitants). Zhuhai’s expansion pathway is invaluable in showcasing how a liveable city is shaped under cycles of SSS and how the produced rescaling (re)configures the spatiotemporal patterns of the city. A study mapping the expansion path in Zhuhai broadens the literature on urban expansion in west PRD and enriches our understanding on how SSS influences urban growth trajectory.

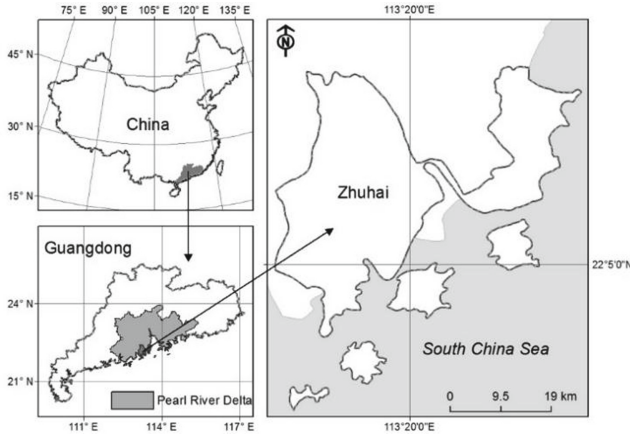


Fig. 1. PRD and Zhuhai

This research collates and processes remote sensing images to indicate the spatiotemporal changes and growth patterns of urban land in Zhuhai. Three episodes of growth are roughly identified, based on major shifts of SSS, data availability from Landsat image and growth rate of urban construction land in Zhuhai. Overall, three expansion phases with variant growth pace, rate, and patterns were roughly identified. The Landscape Expansion Index (LEI) (Liu et al. 2010) was applied to identify three types of its buffer zone: infill, edge-expansion, and outlying growth. Results quantified the impact of SSS on Zhuhai and contributed to an in-depth understanding of the politics of scale in Chinese cities (Fig. 2).

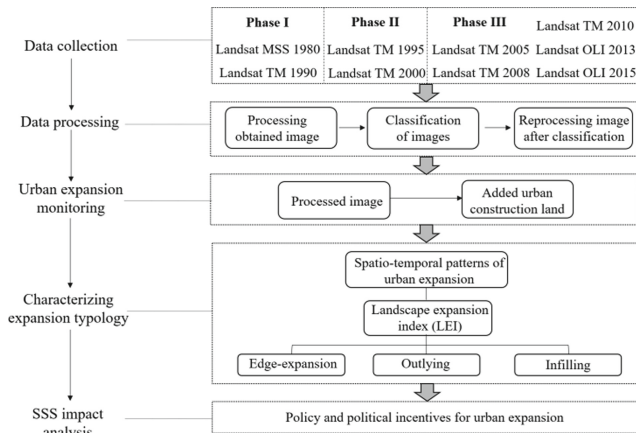


Fig. 2. Flow chart of remote sensing image processing

4 Urban Sprawl Under Multi-scalar SSS in Zhuhai

The inherited socialist landscape of urban China was profoundly reshaped after the market-oriented reform, wherein emergent and evolving scalar restructuring played an important role. Facing the South China Sea, Zhuhai is a forerunner of market reform modestly grew 212.49 km² from 1980 to 2015, less than one-third of its outstanding peer, Shenzhen (Fig. 3).

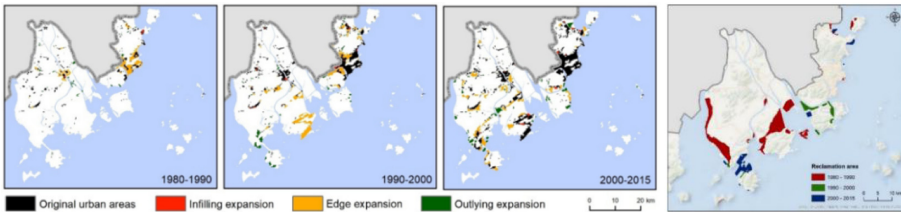


Fig. 3. Expansion, reclamation and scalar restructuring in Zhuhai (1980–2015)

4.1 Germinal Expansion Under Neoliberal Decentralisation (1980–1990)

Zhuhai was a precursor in economic reform and began its urban expansion around a policy-privileged zone. The incipient expansion was exploratory and gradual, driven by two remarkable scalar restructuring events: 1) the upscaling of Zhuhai from a county to a city in 1979 and 2) the upscaling of the Zhuhai SEZ in 1980. Zhuhai upgraded from a county to a city in 1979 by annexing former Zhuhai and Doumen counties. This administrative adjustment was part of Guangdong's power rescaling, wherein prefecture-level cities replacing autonomous states and districts became predominantly administrative units and counties became directly administered by cities. By the end of 1991, 12 more prefecture-level cities emerged under this provincial-led rescaling, in which Shenzhen and Zhuhai stood out, as entitled by the SEZ policy.

Officially unveiled as an SEZ in 1980, Zhuhai spearheaded the open-door policy and market reform and ventured on urban expansion near Macau. Zhuhai's early growth was exploratory, prudently expanding over authorised policy zones and developed centres. In its first 10 years, Zhuhai SEZ expanded in two rounds: initially from a small area (6.8 km²) adjoining Macau to a large area (15.16 km²) encompassing Xiangzhou main city proper in 1983 in the first round, and then to an augmented area (121 km²) consisting of entire Xiangzhou and the High-Technology Development Zone in 1988 in the second round. Urban construction land expanded along with this enlargement from 35.19 km² to 83.98 km², in which edge expansion represented 77.7%, outlying 19.2%, and infilling only 3.1% of the total. The SEZ policy was the prime incentive that triggered large-scale land growth in Xiangzhou bordering Macau. History also plays a role: Xiangzhou and Doumen districts, the ex-centres of Xiangzhou and Doumen counties, developed the most, with astonishingly high edge expansion, but infilling was almost negligible. From 1980 to 1990, urban land area in Xiangzhou increased to 29.02 km², of which 26.79 km² (i.e., 92.3%) was edge

expansion; Doumen grew less but still visible as its urban land area increased by 14.10 km², with 8.91 km² (i.e. 63.2%) from edge expansion. Infilling expansions rarely happened. In early stage, sufficient land taking advantage of traditional centre resources allowed rapid edge expansion. However, such growth was unsustainably extensive, and slowed down in late 1980s as available land shrank and infilling emerged.

Ten years of growth corresponded the first version of Zhuhai Master Plan, implemented in 1980. Expansion considerably varied in different areas. Sprawl within SEZ, particularly in Xiangzhou, was contiguous, but beyond the SEZ, in Doumen and Tangjiawan, was fractional. In north Xiangzhou, informal expansion occasionally exceeded planning redlines, implying that market forces were occasionally not subject to planning control. Compared with Shenzhen incredibly increased to 62 km² urban area within 10 years, Zhuhai's modest growth (by 48 km² in the same period) is inseparable from its sustainable mentality towards urban development. As perceived by the local government, a beautiful natural environment is a great asset that should be protected. Moreover, Macau did not achieve economies of scale, as Hong Kong did; thus, Zhuhai hardly economically benefitted. Shenzhen outperformed all other SEZs, because of its cross-border location advantage. Although economically backward, Zhuhai refused to sacrifice the environment for economic growth. Massive industrialisation was suppressed at the beginning of Zhuhai's urbanisation to avoid environmental deterioration. In the master plans approved in 1980 and 1988, the development objectives of Zhuhai were "coastal garden city" and "modern garden harbour city", indicating that a pro-environment mentality was always prioritised.

4.2 Expansion Surge with Amplified Scalar Restructuring (1990–2000)

Zhuhai's comparative advantage as a reform forerunner has been weakened since the 1990s because of central and provincial policy changes. In Guangdong, county-level cities burgeoned; from none in 1991 to 33 in 1996. All were upgraded from former counties. Most city-administering-county structures transformed to province-administering-county-level-city setups; hence, the provincial power decentralised to county-level to reduce the support for prefecture-level cities. In addition, the nationwide decentralisation of political power and the amplified open-door policy freed most interior regions replicating the SEZ model. In 1992, after Deng's Southern Tour Speech, Chinese Communist Party and the State Council launch new around of zone policy that nominated cities enjoyed favourable policies akin to that of SEZs. The homogeneity of policy zones intensified inter-urban competition, in which inward rescaling became the main impetus for urban development.

Zhuhai nonetheless grew in the second decade empowered by the municipal. Financed or managed by municipal state-owned enterprises, most significant projects completed during this period. For instance, Zhuhai Airport, the primary project in the 1990s, was operated by Zhuhai Airport Management Co., Ltd. Urban land expanded along these significant transportation, infrastructure, and development zones, increasing by 94.24 km², of which outlying growth represented 42.5%, edge expansion 44.7%, and infilling 12.8%. As Zhuhai Avenue and Zhuhai Airport were opened to the public, land parcels neighbouring the traffic corridor in Sanzao town and Gaolan Port

Economic and Technology Development Zone rapidly urbanised, thereby directing Zhuhai's main growth area westward in the early 1990s. From 1990 to 1995, Jinwan District expanded the most. Out of 65.97 km² urban land growth, Jinwan increased by 36.42 km². Edge expansion occurred in Nanping town in Xiangzhou and the High-Technology Development Zone. Between 1995 and 2000, the urban growth rate decreased significantly, with only 28.27 km² added urban land and outlying expansion shrank remarkably. Return of Hong Kong and Macau fostered industrial development in the less developed mainland that numerous industrial development zones emerged in Zhuhai. This development propelled urban expansion in North Zhuhai, in which growth in Xiangzhou and the High-Technology Development Zone accounted for 60% (17.00 km²) of the total from 1995 to 2000. Urban land expanded around thriving industrial parks as industrialisation-driven urbanisation prevailed. After the overbearing growth from 1990 to 1995, only a small proportion of land was infilled in Zhuhai Airport and Sanzao. Zhuhai's urban expansion surged in the West first, advanced by municipal financed large-scale infrastructures. As various development zones flourished in the north, urban growth then accelerated on the north side. In the second decade, the urban expansion rate and pattern varied in different regions. Urban expansion in Xiangzhou and Doumen continued, but the rate slowed down, supplemented by infilling. Growth in Tangjiawan, Zhuhai Airport, and West Doumen exceeded the planning scope; however, Hebao and the Damang islands of Gaolan Port lagged far behind in achieving the planning goal, especially in the industrial land use.

Industrial parks thrived, and arable land rapidly shrank, thereby adversely affecting the ecological environment, calling for protection approaches. The year 1992 became far-reaching as the "Eight Prohibitions for Environmental Protection" was legislated, making detailed rules and regulations to preserve the natural landscape in Zhuhai. Deng Xiaoping made the remarkable southern tour speech in 1992 and proclaimed that Singapore, the well-known garden country, was worth learning and emulating. Deng's advice inspired Zhuhai officials to imitate the Singaporean model, increasing Zhuhai's green coverage to 40%, and a green belt materialised along the Lover's Road. In 1996, the General Administration of Environmental Protection (later reorganised as the Ministry of Environmental Protection) recognised Zhuhai as the pilot area of a national eco-representative area. Zhuhai has begun to look for its own means of achieving sustainable development. In 1998, Zhuhai became the first Chinese city to obtain the "Best Practice for Improvement of Living Environment" award, which was granted by the United Nations for its beautiful living environment.

4.3 Fluctuant Expansion Shaped by Multiscalar Restructuring (2000–2015)

Scalar restructuring evolved sophisticated after China joined the World Trade Organisation in 2000, involved power recentralisation over the land leasing and upscaling strategies of Hengqin and Hong Kong-Zhuhai-Macau Bridge. In Guangdong province, transforming either counties or county-level cities into districts became mainstream administrative adjustment. A city-administering-district model matured, thereby enhancing the role of prefecture-level and vice-provincial-level cities, such as Zhuhai. Spatiotemporal expansion in Zhuhai fluctuated as rescaling strategies became complex.

Before 2010, west Zhuhai expanded much faster than did the east, but such difference was notably reduced after 2010, when both areas grew conspicuously. Growth in the east area prevailed in Xiangzhou adjacent to Macau, predominately in the form of edge expansion supplemented by infilling. However, the expansion in the west was sporadic, transport-oriented, and polycentric. Jinwan, for example, experienced fast outlying growth from 2010 to 2013, mainly expanding along Zhuhai Avenue. Growth in the High-Technology Development Zone was enduring; infilling prevailed between 2000 and 2005, whereas edge expansion and outlying reigned for the rest of the period. Hengqin, as the new zoning initiative, expanded rapidly after 2010, with the main growth pattern evolving from outlying to edge expansion. Doumen district underwent rapid urbanisation in two periods, with upsurges between 1980 and 1990 and 2000 and 2005; both stages were characterised by edge expansion.

From 2000 to 2015, urban land area in Zhuhai increased by 97.45 km², of which edge expansion accounted for 61.7%, outlying growth 26.6%, and infilling 11.7%. In the first 10 years, such growth continued but moved westward; until 2005, urban land increments were 34.1 km². Widespread edge expansion (23.1 km²) occurred in downtown Doumen, Xinqing Industrial Park, the Zhuhai Free Trade Zone, Gaolan Port Economic and Technology Development Zone, and also along Zhuhai Avenue, with one-third of the growth from outlying (5.7 km²) and infilling (5.3 km²). The expansion between 2005 and 2008 was 25.9 km², comparable to that from 2000 to 2005. Urban growth mostly occurred in west Zhuhai, for example, in downtown Jinwan, Hongqi town, Pingsha town, and Sanzao town, whereas increments in the east were lean and limited to the High-Technology Development Zone. In 2008, an impactful “Notice of the State Council on Promoting the Land Saving and Intensive Use (No. 3 [2008] of the State Council)” was issued to guarantee the 1.8 billion mu redline. Land expansion shrank significantly from 2008 to 2010, with only small portions of outlying (3.0 km²) and edge-expansion (6.9 km²) observable in Doumen, Pingsha, and Gao Langang. This low tide expansion resulted from the nationwide power recentralisation which coped with land resource constraints; however, the subsequent upscaling of Hengqin New Area re-exceptionalised Zhuhai, reinvented its scalar position, and revived its urban growth. From 2010 to 2013, Zhuhai embarked on a small climax of expansion: externally, construction of Hong Kong-Zhuhai-Macao Bridge and the opening of Guangzhou-Zhuhai inter-city extension line reinforced Zhuhai’s connection to the metropolitan kernel of PRD; internally, the preferential SEZ policy was geographically amplified to all of Zhuhai, and the approval of the Hengqin Master Plan essentially augmented Zhuhai’s constructed area. The “key action plan of the Pearl River Estuary Liveable Bay” favoured Zhuhai, where the coastal ambience, mountain backdrop, and affluent natural resources were pleasant; however, the added built-up area from the construction plans meant more under the land-centred accumulation logic. All three types of expansion captured Hengqin and Gaolan Port, with a small amount of edge expansion in the Zhuhai Free Trade Zone and the High-Technology Development Zone. The expansion decreased after 2013.

Well-preserved natural landscapes brought honours to Zhuhai, a model diffusing its sustainable development experiences for other cities. In the 2016 Chinese city competitiveness ranking, Zhuhai ranked first in the liveable city category. Zhuhai's environmental advantages became apparent under new city-regionalism. In the "Reform and Development Plan of PRD", approved by the State Council in 2009, leaders from Hong Kong, Macau, and Guangdong province reached a consensus to co-construct a high-quality living circle. As one of the most liveable cities in China, Zhuhai has the demonstrative sense in constructing quality life in a bay area. Recently, Zhuhai has shifted from its protection-oriented sustainable pathway to proactive strategic selectivity. The Europe–China Eco Cities Link programme is an attempt to cooperate with experiential international institutions to advance the development of ecological civilisation and pioneer a novel type of urbanisation.

5 Discussion and Conclusion

This study is one of the first endeavours to illustrate how SSS drives urban expansion in Zhuhai – the kernel of western PRD in China. The expansion of most of Zhuhai has followed an oscillatory pattern, starting in east Xiangzhou near Macau throughout the 1980s, moving to the west with the opening of Zhuhai Avenue in the early 1990s, returning to the east under thriving industrial parks in the late 1990s, backtracking to the west when infrastructure required completion after 2000, and being distributed across the entire municipality after 2010. Urban clusters gradually developed, and a polycentric structure emerged. In the first decade after Zhuhai formally upgraded to a city, the SSS of SEZ in the early 1980s unpacked tax preferences, flexible customs, trading regulations, and quotas, which fostered primitive capital accumulation and urban expansion. Nevertheless, Zhuhai's germinal growth was restrained by its sustainable ideology that natural environments should be protected and not sacrificed for economic development. The second decade witnessed an expansion surge that almost doubled the urban area. However, the impetus for growth from both the national or provincial level was much less than was that in the first phase, because SSS moved from the east coasts to the hinterland regions at the national level and trickled down to counties at the provincial level. The municipal-led infrastructural projects induced profound rescaling and expanded urban land. To balance the environment and development, Zhuhai learned Singapore's garden city model and established an ecological representative area to qualify expansion. From 2000 to 2015, Zhuhai's expansion fluctuated with the frequent changes in policy orientations. An upscaling of SSS towards city-regions underscored the city-to-city cooperation that diversified the expansion impetus. The long-standing adherence to sustainability was credited to Zhuhai, whose case became a model for liveable city development. Local sustainability fix, for instance the narrative of sustainable development, helped regulate the pace and scale of urban expansion and nurtured one of the most liveable metropolises in China.

The extant literature on China's SSS is echoed (Li et al. 2014; Sun and Chan 2016; Wu 2016). First, the periodisation of Chinese SSS engendered the periodic expansion in Zhuhai: from exploratory and gradualist expansion in early reform, incentivised by relaxation of state power, to expansion surges amid the rising urban entrepreneurialism and thriving localism, to fluctuating expansion co-influenced by power rescaling downwards to locality and upwards towards city-regions. The nascent growth along the coasts was exploratory and sporadic, partly because the Chinese government inherited a population control strategy to limit large cities and develop small- and medium-sized cities (Zhao and Zhang 1995). Second, multiscale restructuring shaped the rescaling-induced expansion in Zhuhai. In this research, the state is both an ideological ensemble and a material force of political structures that encompass national, provincial, municipal, and low-level governments (Li 2015). Thus, SSS speaks for multiscale and multi-level strategic actions over prerogative space. National rescaling strategies, such as the establishment of SEZ and the upgrading of Hengqin, have repositioned Zhuhai as the core city in west PRD. Provincial rescaling strategies, such as the construction of the Hong Kong-Zhuhai-Macau Bridge, have transited inter-city competition to city-to-city cooperation. Municipal rescaling strategies, such as the completion of the airport and Zhuhai Avenue, have reiterated the spatial layout within Zhuhai city. Third, contradictions caused by SSS have necessitated a spatial fix to sustain the expansion-based accumulation in Zhuhai. Race-to-bottom competition results in environment degradation and social inequality, to reconcile which Zhuhai has repressed industrialisation and implemented a sustainability fix.

Though there is notable difference, SSS-led transformation in this research shares some similarities to that in the west. In both contexts, SSS creates various growth poles that lead to uneven geography. In Zhuhai, past selectivity strategy intensifies the development differences between the east and west, which has restrained the integration strategy. The "soft" and "fuzzy" boundaries created by SSS are universal. Neither the four-step amplification of SEZ from 1980 to 2010, nor the changing strategy towards Hengqin, nor those ever-ongoing projects are fixed entities that accommodate political contestation. In addition, history and geo-context influence SSS and its subsequent expansion. The ex-centres of Xiangzhou and Doumen counties expanded most during the early reform period. Cross-border governance is important for the power realignment among national government, core city, and large market investors in peripheral development. How central government addresses the "One Country, Two System" issue would be central to Zhuhai's cross-border expansion. Similar issue is also observed in inner periphery of Amsterdam, Paris, and Milan metropolises, differentiated spatial outcomes are attributed to the articulation of the changing relationships among three sources of power (Savini et al. 2015). In short, cross-border regions add geographical heterogeneity to nation-state spaces because the frontiers are both sensitive and apt to receive investment (Table 1).

Table 1. Expansion patterns and scalar restructuring in Zhuhai

| | Expansion area (km ²) | | Characteristics of expansion | Reclamation (km ²) | Form of state spatial selectivity | Power flow |
|-----------------------|-----------------------------------|-------|---|---|---|--|
| Stage I (1980–1990) | Outlying: | 9.31 | City proper and cross-border expansion | 108.37 Large-scale reclamation for paddy fields, fish ponds and cropland | Guangdong up scaled Zhuhai from a county to a city; Central State up scaled Zhuhai SEZ as a forerunner of market reform; | Decentralization of provincial and central state power to Zhuhai (in coastal cities) |
| | Edge: | 38.07 | | | | |
| | Infilling: | 1.41 | | | | |
| Stage II (1990–2000) | Outlying: | 40.08 | Transportation, infrastructure, and development zone oriented expansion | 18.62 A small amount of reclamation in Hengqing and west Jinwan | Zhuhai rescaled itself through transportation, infrastructure, and development zones; | Amplified decentralization (to the interior and counties) that impairs Zhuhai's comparative advantages |
| | Edge: | 42.13 | | | | |
| | Infilling: | 12.03 | | | | |
| Stage III (2000–2015) | Outlying: | 25.91 | Fluctuating and sporadic expansion in entire Zhuhai | 29.14 Sporadic reclamation in Gaolan Port and Hengqin | Central State up scaled Hengqin as national new area and enlarged SEZ to entire Zhuhai; Multiscale restructuring at regional, provincial, and municipal level; | De/recentralization concurs and leads to multiscale restructuring |
| | Edge: | 60.12 | | | | |
| | Infilling: | 11.42 | | | | |

References

- Brenner, N.: Urban governance and the production of new state spaces in Western Europe, 1960–2000. *Rev. Int. Polit. Econ.* **11**(3), 447–488 (2004)
- Gabriel, S.J.: Economic liberalization in post-Mao China: crossing the river by feeling for stones. *China Essay Ser.* **7**, 1–9 (1998)
- Harvey, D.: *Spaces of Global Capitalism: Towards a Theory of Uneven Development*. Verso Books, London (2006)
- He, S., Wu, F.: Property-led redevelopment in post-reform China: a case study of Xintiandi redevelopment project in Shanghai. *J. Urban Aff.* **27**(1), 1–23 (2005)
- He, S., Wu, F.: China's emerging neoliberal urbanism: perspectives from urban redevelopment. *Antipode* **41**(2), 282–304 (2009)
- Jessop, B.: Towards a Schumpeterian workfare state? Preliminary remarks on post-Fordist political economy. *Stud. Polit. Econ.* **40**, 7–39 (1993)
- Jones, M.R.: Spatial selectivity of the state? The regulationist enigma and local struggles over economic governance. *Environ. Plann. A* **29**(5), 831–864 (1997)
- Li, L.: State rescaling and national new area development in China: the case of Chongqing Liangjiang. *Habitat Int.* **50**, 80–89 (2015)
- Li, L., Chan, R.C.: Contesting China's engagement with neoliberal urbanism: an overview of the evolving policy and mismatches in urban China. *Asian Educ. Dev. Stud.* **6**(1), 44–56 (2017)
- Li, X., Yeh, A.G.: Analyzing spatial restructuring of land use patterns in a fast growing region using remote sensing and GIS. *Landscape Urban Plann.* **69**(4), 335–354 (2004)

- Li, Z., Xu, J., Yeh, A.G.O.: State rescaling and the making of city-regions in the Pearl River Delta. *Environ. Plann. C* **32**(1), 129–143 (2014)
- Liu, X., Li, X.Y., Chen, Y., Tan, Z., Li, S., Ai, B.: A new landscape index for quantifying urban expansion using multi-temporal remotely sensed data. *Landscape Ecol.* **25**(5), 671–682 (2010)
- Savini, F., Majoor, S., Salet, W.: Urban peripheries: reflecting on politics and projects in Amsterdam, Milan, and Paris. *Environ. Plann. C* **33**(3), 457–474 (2015)
- Shen, X., Ma, L.J.C.: Privatization of rural industry and de facto urbanization from below in southern Jiangsu, China. *Geoforum* **36**(6), 761–777 (2005)
- Sun, Y., Chan, R.C.: Planning discourses, local state commitment, and the making of a new state space (NSS) for China: evidence from regional strategic development plans in the Pearl River Delta. *Urban Stud.* **54**(14), 3281–3298 (2016)
- Wang, L., et al.: China's urban expansion from 1990 to 2010 determined with satellite remote sensing. *Chin. Sci. Bull.* **57**(22), 2802–2812 (2012)
- Wu, F.: China's emergent city-region governance: a new form of state spatial selectivity through state-orchestrated rescaling. *Int. J. Urban Reg. Res.* **40**(6), 1134–1151 (2016)
- Xiao, J., et al.: Evaluating urban expansion and land use change in Shijiazhuang, China, by using GIS and remote sensing. *Landscape Urban Plann.* **75**(1), 69–80 (2006)
- Zhao, X., Zhang, L.: Urban performance and the control of urban size in China. *Urban Stud.* **32**(4–5), 813–846 (1995)



A Tversky Loss-Based Convolutional Neural Network for Liver Vessels Segmentation

Nicola Altini¹(✉), Berardino Prencipe¹, Antonio Brunetti^{1,2},
Gioacchino Brunetti³, Vito Triggiani³, Leonarda Carnimeo¹,
Francescomaria Marino¹, Andrea Guerriero¹, Laura Villani⁴,
Arnaldo Scardapane⁴, and Giacomo Donato Cascarano^{1,2}

¹ Polytechnic University of Bari, 70126 Bari, Italy

nicola.altini@poliba.it

² Apulian Bioengineering srl, Via delle Violette, 14, 70026 Modugno, BA, Italy

³ Masmec Biomed SpA, Via delle Violette, 14, 70026 Modugno, BA, Italy

⁴ Bari Medical School, Bari, Italy

Abstract. The volumetric estimation of organs is a crucial issue both for the diagnosis or assessment of pathologies and for surgical planning. Three-dimensional imaging techniques, e.g. Computed Tomography (CT), are widely used for this task, allowing to perform 3D analysis based on the segmentation of each bi-dimensional slice. In this paper, we considered a fully automatic setup based on Convolutional Neural Networks (CNNs) for the semantic segmentation of human liver parenchyma and vessels in CT scans. Vessels segmentation is also crucial for surgical planning as it allows separating the liver into anatomical segments, each with its own vascularization.

The CNN model proposed for liver segmentation has been trained by minimizing the Dice loss function, whereas a Tversky loss-based function has been exploited in designing the CNN model for liver vessels segmentation, aiming at penalizing the false negatives more than the false positives. In this work, the training set from the Liver Tumor Segmentation (LiTS) Challenge, composed of 131 CT scans, was considered for training and tuning the architectural hyperparameters of the liver parenchyma segmentation model; 20 CT scans of the SLIVER07 dataset, instead, were used as the test set for a final estimation of the proposed method. Moreover, 20 CT scans from the 3D-IRCADb were considered as a training set for the liver vessels segmentation model and four CT scans from Polyclinic of Bari were used as an independent test set.

Obtained results are promising, being the determined Dice Coefficient higher than 96% for the liver parenchyma model on the considered test set, and Accuracy higher than 99% for the suggested liver vessels model.

Keywords: Convolutional Neural Network · Dice · Tversky · Liver segmentation · Vessels segmentation

1 Introduction

The volume quantification of organs is of fundamental importance in the clinical field, for diagnosing pathologies and monitoring their progression over time. Imaging techniques offer fast and accurate methods for performing this task in a non-invasive way. In fact, starting from volumetric imaging acquisitions, such as Computed Tomography (CT) or Magnetic Resonance (MR), it is possible to perform the three-dimensional segmentation of organs, thus obtaining their volumetric information. This task, however, revealed to be time-consuming, although needed expert medical doctors to manually accomplish it by labelling each bi-dimensional slice in the volumetric acquisition. This procedure was also susceptible to differences inter- and intra-operator [1]. Taking into account these premises, researchers made considerable efforts in developing semi-automatic or automatic segmentation methods, especially for those body areas containing organs whose morphology could physiologically vary over time, or due to pathologies, such as kidneys or liver. Recent works investigated the use of Convolutional Neural Networks (CNNs), and Deep Learning (DL) strategies, in order to design and implement automatic clinical decision support systems based on medical images [2–4] or medical signals, as ECG [5, 6]. The main advantage of CNNs is that they do not require the extraction of handcrafted features, which is a time-consuming and challenging process as it involves an in-depth domain knowledge [7, 8]. Neural Networks are also useful for hierarchical clustering [9] and nonstationary topological learning [10]. Artificial Intelligence techniques are also widely used in other medical domain contexts, such as speech-to-text for the assessment of Parkinson’s Disease [11, 12], attribute selection and classification in gene expression [13, 14], human force estimation [15], or in cancer systems biology [16].

Medical decision support systems also include the segmentation of organs from volumetric imaging acquisitions [17–19]. For example, De Vos *et al.* made an effort for localizing anatomical structures in 3D medical images using CNNs, with the purpose to ease tasks such as image analysis and segmentation [20]. Regarding the abdominal area, there has been a growing interest in CT scan analysis for diagnosis purposes and therapy planning. In fact, the segmentation of organs is crucial for several clinical procedures, including radiotherapy, volume measurement and computer-assisted surgery [21]. Rafiei *et al.* developed a 3D to 2D Fully Convolutional Network (3D-2D-FCN) to perform automatic liver segmentation for accelerating the detection of trauma areas in emergencies [22]. Lu *et al.* developed and validated an automatic approach integrating multi-dimensional features into graph cut refinement for the liver segmentation task [21]. Kim *et al.* proposed a 3D patch-based U-Net, followed by a graph-cut post-processing, for the multi-organ segmentation of liver, stomach, duodenum and right/left kidneys. The authors employed a Multi-Class Cross-Entropy loss function with six classes. Their proposed method outperforms atlas-based approaches, whilst shows comparable results with the inter-observer delineations of organs [23].

A further application of the segmentation task applied to liver regards the vessels identification. According to Couinaud model [24], hepatic vessels represent the anatomic borders of hepatic segments and, consequently, segmentectomies, based on the precise identifications of these vascular landmarks, are crucial in the modern hepatic

surgery because they avoid unnecessary removal of healthy liver parenchyma and reduce the complications of most extensive resections [25]. In literature, there are different approaches for liver vessels segmentation. Oliveira *et al.* proposed a segmentation method exploiting a region-based approach [26], where a gaussian mixture model was used to identify the threshold to be selected for adequately separating parenchyma from hepatic veins. Yang *et al.* proposed a semi-automatic method for vessels extraction. They used a connected-threshold region-growing method from the ITK library [27] to initially segment the veins. To find the threshold, they exploited the histogram of the masked liver. However, this process has to be supervised by an expert user through a graphic interface [28]. Goceri *et al.* proposed a method called Adaptive Vein Segmentation (AVS): they exploited k -means clustering for initial mask generation; then they applied post-processing procedures for mask refinement, followed by morphological operations to reconstruct the vessels [29]. Chi *et al.* used a context-based voting algorithm to conduct a full vessels segmentation and recognition of multiple vasculatures. Their approach considered context information of voxels related to vessels intensity, saliency, direction, and connectivity [30]. Zeng *et al.*, instead, proposed a liver-vessels segmentation and identification approach, based on the combination of oriented flux symmetry and graph cuts [31]. Vessels segmentation is a crucial task for many other applications too. For instance, reliable biometric analysis systems for personal identification can be realized with a proper analysis of the bifurcations of the vessels in the retinal fundus [32].

In this work, a Deep Learning approach is proposed aiming at a proper image segmentation of liver parenchyma and vessels. The suggested implementation is based on the V-Net architecture, a CNN widely used in volumetric medical image segmentation [33]. In particular, for the CNN model of liver parenchyma, the Dice loss function is herein optimized. The proposed image segmentation model of liver parenchyma poses the basis for a subsequent vessels segmentation, allowing to exclude those ones which are outside the liver region. Moreover, the penalization of false negatives (i.e., vessels voxels classified as background) over false positives (i.e., background voxels classified as vessels) is herein investigated to highlight how its value could speed up the network convergence and the overall segmentation performance. For this purpose, the Tversky loss-based function is herein exploited in designing the CNN model for liver vessels segmentation. Instead, for liver parenchyma segmentation, the Tversky loss does not lead to significant improvements. Note that the unbalancing is lesser compared to the problem of vessels segmentation.

2 Materials

2.1 Liver Parenchyma Segmentation

In order to design and implement the proposed automatic liver parenchyma segmentation approach, we considered the training set of the Liver Tumor Segmentation (LiTS) Challenge, containing CT abdominal acquisitions of 131 subjects [34]. Regarding the test set, we evaluated the results of our experiments with a different independent set, composed of 20 scans from the SLIVER07 dataset [35].

In the CT scans of LiTS Challenge, pixel spacing belongs to range 0.56 mm to 1.0 mm in x/y -direction, whilst slice distance ranges between 0.45 mm and 6.0 mm, with the number of slices varying from 42 to 1026 [34]. In the CT scans of SLIVER07, pixel spacing is included in the range 0.55 mm to 0.8 mm in the x/y -direction, and slice distance belongs to range 1 mm to 3 mm, depending on the used machine and protocol [35]. We pre-processed all the images by windowing the HU values into the range $[-150, 350]$. For the CNN model, the values were then scaled into the range $[0, 1]$.

2.2 Liver Vessels Segmentation

We used the 20 CT scans of 3D-IRCADb for training and internally cross-validating our CNN model, and a dataset of the Polyclinic of Bari composed of 4 CT scans as an independent test set for external validation. The 3D-IRCADb dataset contains CT scans whose axial-plane resolution varies from 0.56 mm to 0.81 mm, whilst resolution along the z -axis spans from 1 mm to 4 mm. The number of slices ranges between 74 and 260. The 20 CT scans of 3D-IRCADb come from 10 women and 10 men; the number of patients with hepatic tumours is 75% of the overall dataset [36].

The dataset from the Polyclinic of Bari contains 4 CT scans with an axial plane resolution varying from 0.76 mm to 0.86 mm, and a z -axis resolution spanning from 0.7 mm to 0.8 mm. The number of slices is between 563 and 694. Pre-processing adopted for liver vessels segmentation was the same used for liver parenchyma segmentation.

3 Methods

In the biomedical image segmentation area, a well-known and widely used semantic segmentation CNN architecture is U-Net [37], whose model is based on an encoder-decoder architecture and performs the segmentation of bi-dimensional images. Later, a 3D implementation of U-Net has been proposed by Çiçek *et al.* [38].

Milletari *et al.* proposed a variation of the standard U-Net, called V-Net, for the 3D medical image segmentation [33]. Among the peculiarities of V-Net, we note the use of down-convolutions, with stride $2 \times 2 \times 2$ and kernel-size $2 \times 2 \times 2$, instead of $2 \times 2 \times 2$ max-pooling, the use of PReLU [39] non-linearities and the adoption of residual connections. A 2.5D variant of the V-Net architecture is depicted in Fig. 1, where all the 3D layers are replaced by the corresponding 2D ones, with a first layer which processes 5 slices as 5 channels.

In the adopted architecture, “down” convolutional layers have stride 2×2 and kernel-size 2×2 ; normal convolutional layers have kernel-size 5×5 , and transposed convolutional layers used as “up” convolutions have 2×2 kernels. Moreover, we added a Batch-Normalization (BN) layer after each convolutional layer. The use of BN layers has been taken into consideration by the same authors of the original V-Net [40]. Instead of PReLU non-linearities, we adopted the standard ReLu ones.

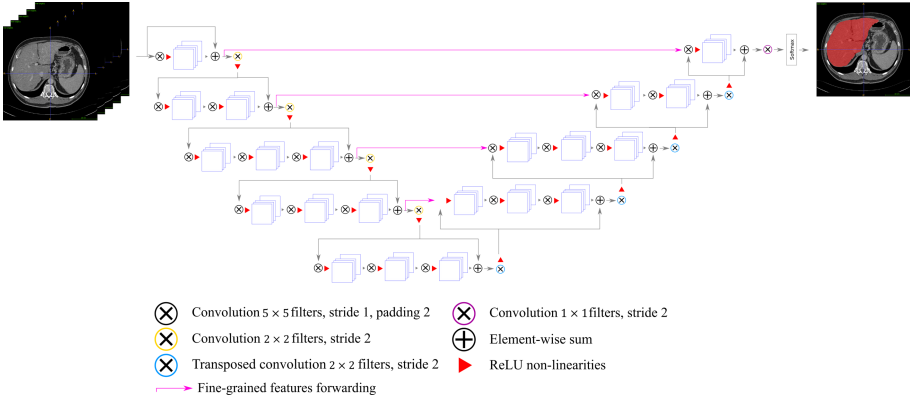


Fig. 1. The proposed 2.5D V-Net architecture.

For both the considered tasks, we trained our 2.5D V-Net by taking random patches of 5 slices from the training set, assigning a higher probability to take a patch containing at least one voxel belonging to the liver or to the vessels. The optimizer for the training process was Adam [41], with a starting learning rate of 0.01. We trained the network for 2001 epochs, reducing the learning rate by 10 every 333 epochs. 200 samples were processed per each epoch. The batch size has been set to 4.

In order to ensure low convergence time, it is crucial to select a proper loss function, such as Binary Cross-Entropy (BCE) loss function, as in Eq. (1), or the Weighted BCE (WBCE), as in Eq. (2). For the following definitions, let $p_i \in P$ be the probability of the i^{th} voxel to belong to the liver and $g_i \in G$ its binary label with $i = 1, \dots, N$; P and G respectively being the predicted segmented volume and the ground truth volume.

$$BCE = -\frac{1}{N} \sum_{i=1}^N (g_i \cdot \log(p_i) + (1 - g_i) \cdot \log(1 - p_i)) \quad (1)$$

$$WBCE = -\frac{1}{N} \sum_{i=1}^N (\omega_1 \cdot g_i \cdot \log(p_i) + \omega_0 \cdot (1 - g_i) \cdot \log(1 - p_i)) \quad (2)$$

In Eq. (2), ω_1 and ω_0 are introduced to give a different weight for positives and negatives. These functions act as a proxy for the optimization of the true measures used later for the evaluation, which usually include the Dice Coefficient D , as in Eq. (3). Thus, another plausible choice for the optimization function consisted of directly adopting an objective function based on the Dice Coefficient [33], or, more generally, the Tversky index. Salehi *et al.* exploited the Tversky Loss function for lesion segmentation by means of 3D CNNs [42]. The used implementation is reported in Eq. (4), where p_{0i} is the probability of the i^{th} voxel to be positive, g_{0i} its binary label (i.e., 1 for positives and 0 for negatives), p_{1i} its probability of being a negative, g_{1i} its negated binary label, directly obtained by logical NOT applied to g_{0i} (i.e., 0 for positives and 1 for negatives).

$$D = \frac{2 \cdot \sum_{i=1}^N p_i g_i}{\sum_{i=1}^N p_i + \sum_{i=1}^N g_i} \quad (3)$$

$$T_{\alpha, \beta} = \frac{2 \cdot \sum_{i=1}^N p_{0i} g_{0i}}{\sum_{i=1}^N p_{0i} g_{0i} + \alpha \sum_{i=1}^N p_{0i} g_{1i} + \beta \sum_{i=1}^N p_{1i} g_{0i}} \quad (4)$$

We decided to employ a Tversky index-based loss function due to the unbalanced voxels problem. In fact, the voxels belonging to the liver region are only a fraction of the whole CT scan. In the LiTS dataset, the unbalancing ratio is approximately 40:1 in favour of negative voxels, becoming more relevant for the vessels segmentation (about 200:1 in favour of negative voxels). Dice Loss does not give different weights to False Positives (FPs) and False Negatives (FNs), thus it does not focus the learning on the maximization of the recall of the voxels of interest. With a Tversky Loss, thanks to the α and β coefficients, it is possible to give a major weight on FNs.

We considered different data augmentation techniques, as slice-wise right-left flipping of volume patches, gaussian blur, elastic transform with $\alpha = 2$ and $\sigma = 3$, multiplicative noise, random rotations in the range $[-10^\circ, 10^\circ]$, random brightness and contrast perturbations.

In the inference phase, we processed the volumetric images in a 3D sliding window fashion, processing sub-volumes of $512 \times 512 \times 5$ voxels. Since we adopted a 2.5D approach, the five processed slices were used for predicting the central one only. In order to create patches of five slices also at the begin and at the end of the CT scans, the first and last slices were replicated. The first step of post-processing consisted in applying morphological opening operator, in order to separate, if needed, the liver and the spleen. In fact, due to the similarity between spleen and liver intensity values and texture, the two organs could be misclassified. Then, we applied connected components labelling, retaining only the largest one, since the liver is the largest organ in the abdomen. Finally, we applied morphological closing and morphological hole-filling to the segmented masks. A similar procedure has been carried out for the vessels segmentation, without the morphological and connected components labelling post-processing. In Sect. 4, we report the segmentation results for both the liver parenchyma and the liver vessels.

4 Experimental Results

4.1 Segmentation Quality Measures

To evaluate the performance of the implemented segmentation algorithms, we refer to the indexes adopted in the SLIVER07 and LiTS challenges [34, 35]. It is possible to make a distinction between quality measures based on the volumetric overlap and those based on surface distances.

Relevant quality measures based on volumetric overlap are the Volumetric Overlap Error (*VOE*), defined in Eq. (5) and the Sørensen–Dice Coefficient (*DSC*), defined in Eq. (6). The *VOE* definition depends on the ratio between intersection and union, namely the Jaccard Index *J*. In all the definitions involved in the quality measures, we denote *B* as the binarized predicted segmented volume (obtained by thresholding *P*) and *G* as the ground truth volume; the cardinality operator for a set is denoted as $|\cdot|$.

$$VOE(B, G) = 1 - J(B, G), \text{ where } J(B, G) = \frac{|B \cap G|}{|B \cup G|} \quad (5)$$

$$DSC(B, G) = \frac{|B \cap G|}{|B| + |G|} \quad (6)$$

A more general formulation of both the *DSC* and Jaccard Index is the Tversky Index $T_{\alpha, \beta}(B, G)$, defined as:

$$T_{\alpha, \beta}(B, G) = \frac{|B \cap G|}{|B \cup G| + \alpha|B - G| + \beta|G - B|} \quad (7)$$

We note that $T_{0.5, 0.5}(B, G)$ corresponds to *DSC*(*B*, *G*), while $T_{1, 1}(B, G)$ corresponds to *J*(*B*, *G*). Besides calculating the overlap error, it is also possible to quantify the Relative Volume Difference (*RVD*), defined as:

$$RVD(B, G) = \frac{|B| - |G|}{|G|} \quad (8)$$

Interesting quality measures based on external surface distances are the Maximum Symmetric Surface Distance (*MSSD*, or Symmetric Hausdorff Distance) and the Average Symmetric Surface Distance (*ASSD*) [35]. These measures are particularly useful for applications like surgical planning, where to make a suitable prediction of the mesh of the organs is vital. We also evaluated performances in terms of Accuracy, Recall and Specificity, as in Bevilacqua *et al.* [2], considering Positives the voxels belonging to the liver or vessels (depending on the segmentation task), Negatives the others.

4.2 Results and Discussion

The results obtained for the liver parenchyma segmentation and liver vessels segmentation are reported in Table 1 and Table 2, respectively.

The 2.5D V-Net trained with the Dice loss allowed us to obtain a mean Dice Coefficient of 96.13% and a mean MSSD of 140.42 mm for the liver parenchyma segmentation task. Since in a surgical planning setup is crucial to reduce the Hausdorff distance, we note that the adoption of the post-processing is very beneficial.

It permitted us to reduce the mean MSSD to 31.50 mm, and its standard deviation from 86.96 mm to 12.05 mm. A so large reduction of the MSSD can be explained by the fact that sometimes the liver CNN model also segments the spleen region, as previously stated. The proposed approach outperforms other methods proposed in the literature, as reported in Table 1. Note that, since the liver segmentation task is not too unbalanced, the V-Net trained with Tversky loss with $\alpha = 0.3$, $\beta = 0.7$ leads to results comparable with the network trained with the Dice Loss, whereas the V-Net trained with the Tversky loss with $\alpha = 0.1$, $\beta = 0.9$ leads to worse overall results, since the coefficients penalize too much the false negatives.

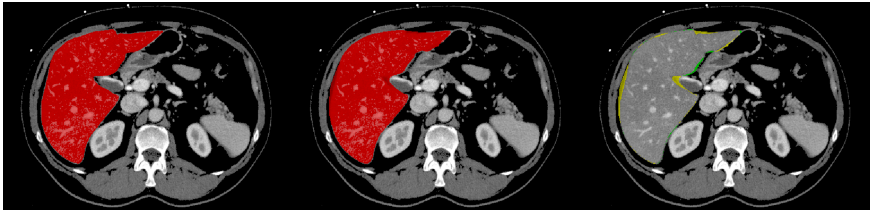
Regarding the vessels segmentation task, the proposed method shows high Accuracy, also compared to other approaches proposed in the literature, as can be seen in Table 2. The adoption of the Tversky loss to penalize false negatives more than false positives yields to progressively higher recall values when α is decreased and β is increased, with a best recall of 68.92 in the configuration with $\alpha = 0.1$, $\beta = 0.9$. Thus, in case of extremely unbalanced dataset, we appreciated the use of the Tversky loss function. However, we have to note that our test set is very small, and the results suffer from high variability. Examples of liver segmentation results obtained with the proposed method are depicted in Fig. 2, whereas examples of vessels segmentation results are reported in Fig. 3 and Fig. 4.

Table 1. Liver parenchyma segmentation results, expressed as “mean \pm standard deviation”. D-L stands for Dice Loss, whereas T-L stands for Tversky Loss. PP stands for post-processing.

| Model | DSC [%] | VOE [%] | RVD [%] | ASSD [mm] | MSSD [mm] |
|--|------------------|------------------|------------------|-----------------|--------------------|
| 2.5D V-Net, D-L | 96.13 \pm 2.45 | 7.35 \pm 4.31 | 1.13 \pm 6.24 | 4.18 \pm 7.95 | 140.42 \pm 86.96 |
| 2.5D V-Net, D-L, PP | 96.52 \pm 1.84 | 6.66 \pm 3.32 | 4.26 \pm 3.95 | 1.44 \pm 0.89 | 31.50 \pm 12.05 |
| 2.5D V-Net, T-L ($\alpha = 0.3, \beta = 0.7$) | 96.27 \pm 1.57 | 7.16 \pm 2.86 | 1.24 \pm 4.03 | 3.56 \pm 7.48 | 141.04 \pm 84.54 |
| 2.5D V-Net, T-L, PP ($\alpha = 0.3, \beta = 0.7$) | 96.26 \pm 1.18 | 7.19 \pm 2.18 | 5.11 \pm 3.24 | 1.50 \pm 0.61 | 31.26 \pm 12.18 |
| 2.5D V-Net, T-L ($\alpha = 0.1, \beta = 0.9$) | 94.21 \pm 3.01 | 10.81 \pm 5.16 | 7.05 \pm 5.90 | 6.03 \pm 8.56 | 158.37 \pm 65.09 |
| 2.5D V-Net, T-L, PP ($\alpha = 0.1, \beta = 0.9$) | 93.88 \pm 2.40 | 11.45 \pm 4.12 | 10.99 \pm 6.15 | 2.43 \pm 1.11 | 33.95 \pm 13.01 |
| Lu <i>et al.</i> [21] | N/A | 9.21 \pm 2.64 | 1.27 \pm 3.85 | 1.75 \pm 1.41 | 36.17 \pm 15.90 |
| Rafiei <i>et al.</i> [22] 3D-2D-FCN + CRF | 93.52 | N/A | N/A | N/A | N/A |
| Kim <i>et al.</i> [23] 3D U-Net | 95.9 \pm 1.8 | N/A | N/A | 0.71 \pm 0.30 | 8.93 \pm 6.30 |

Table 2. Liver vessels segmentation results, expressed as “mean \pm standard deviation”.

| Model | Accuracy [%] | Recall [%] | Specificity [%] | ASSD [mm] |
|--|------------------|-------------------|------------------|------------------|
| 2.5D V-Net, Dice loss | 99.94 \pm 0.02 | 56.67 \pm 20.13 | 99.96 \pm 0.03 | 9.51 \pm 0.52 |
| 2.5D V-Net, Tversky loss ($\alpha = 0.3, \beta = 0.7$) | 99.93 \pm 0.03 | 62.62 \pm 17.01 | 99.94 \pm 0.03 | 14.84 \pm 2.93 |
| 2.5D V-Net, Tversky loss ($\alpha = 0.1, \beta = 0.9$) | 99.91 \pm 0.04 | 68.92 \pm 19.13 | 99.92 \pm 0.05 | 15.79 \pm 2.21 |
| Goceri <i>et al.</i> [29] AVS | 89.57 \pm 0.57 | N/A | N/A | 23.1 \pm 16.4 |
| Chi <i>et al.</i> [30] Context-based voting | 98 \pm 1 | 70 \pm 1 | 99 \pm 1 | 2.28 \pm 1.38 |
| Zeng <i>et al.</i> [31] Oriented flux symmetry and graph cuts | 97.7 | 79.8 | 98.6 | N/A |

**Fig. 2.** A slice of the liver segmentation task: (left) ground truth; (center) Dice Loss-based 2.5D V-Net prediction; (right) difference between ground truth and prediction, where false negatives and false positives are respectively evidenced in green and in yellow. (Color figure online)**Fig. 3.** A slice of the vessels segmentation task: (left) ground truth; (center) Tversky Loss-based 2.5D V-Net prediction; (right) difference between ground truth and prediction where false negatives and false positives are respectively evidenced in green and in blue. (Color figure online)

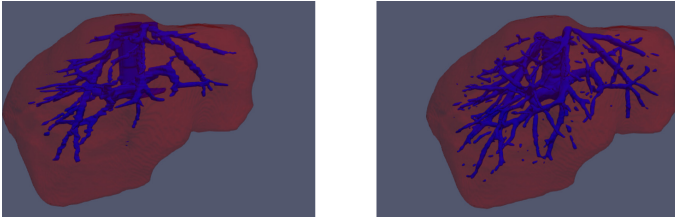


Fig. 4. View of a mesh of the vessels segmentation task: (left) ground truth; (right) Tversky Loss-based 2.5D V-Net prediction.

5 Conclusion and Future Works

In this work, we proposed a fully-automatic CNNs-based approach for the segmentation of liver parenchyma and vessels in CT scans.

The liver parenchyma segmentation has been evaluated on CT abdominal scans of 20 subjects considering different metrics. The proposed CNN approach allowed us to obtain high voxel-level performances, with Dice Coefficient greater than 96% on the test set. For a surgical planning setup, it is crucial to have a small Hausdorff distance, and we note that the employment of proper post-processing procedures can yield to the reduction of MSSD from 140.42 mm to 31.50 mm.

The model adopted for the liver vessels segmentation has been evaluated on an independent test set of 4 CT scans, with Accuracy higher than 99%. The obtained results show that the 2.5D V-Net, trained with a Tversky Loss, is a very promising approach for the vessels segmentation in CT scans, allowing to obtain accurate volumetric reconstructions of the segmented region.

The proposed system will help the radiologists in accomplishing the laborious task of segmenting liver and vessels from a CT scan, laying the foundation for further image analysis algorithm on the segmented region.

Future works will include further validation on datasets coming from different cohorts of subjects, and investigation on novel analysis of the segmented liver region, targeted to obtain the Couinaud hepatic segments classification.

References

1. Hoyte, L., et al.: Segmentations of MRI images of the female pelvic floor: a study of inter- and intra-reader reliability. *J. Magn. Reson. Imaging* **33**, 684–691 (2011). <https://doi.org/10.1002/jmri.22478>
2. Brunetti, A., Carnimeo, L., Trotta, G.F., Bevilacqua, V.: Computer-assisted frameworks for classification of liver, breast and blood neoplasias via neural networks: a survey based on medical images. *Neurocomputing* **335**, 274–298 (2019). <https://doi.org/10.1016/j.neucom.2018.06.080>
3. Altini, N., et al.: Semantic segmentation framework for glomeruli detection and classification in kidney histological sections. *Electronics* **9**, 503 (2020). <https://doi.org/10.3390/electronics9030503>

4. Bevilacqua, V., et al.: A novel deep learning approach in haematology for classification of leucocytes. In: Esposito, A., Faundez-Zanuy, M., Morabito, F.C., Pasero, E. (eds.) WIRN 2017 2017. SIST, vol. 103, pp. 265–274. Springer, Cham (2019). https://doi.org/10.1007/978-3-319-95095-2_25
5. Randazzo, V., Ferretti, J., Pasero, E.: ECG WATCH: a real time wireless wearable ECG. In: 2019 IEEE International Symposium on Medical Measurements and Applications (MeMeA), pp. 1–6. IEEE (2019). <https://doi.org/10.1109/memea.2019.8802210>
6. Ferretti, J., Randazzo, V., Cirrincione, G., Pasero, E.: 1-D convolutional neural network for ECG arrhythmia classification. In: Esposito, A., Faundez-Zanuy, M., Morabito, F.C., Pasero, E. (eds.) Progresses in Artificial Intelligence and Neural Systems. SIST, vol. 184, pp. 269–279. Springer, Singapore (2021). https://doi.org/10.1007/978-981-15-5093-5_25
7. Bevilacqua, V., et al.: A novel approach to evaluate blood parameters using computer vision techniques. In: 2016 IEEE International Symposium on Medical Measurements and Applications (MeMeA), pp. 1–6 (2016). <https://doi.org/10.1109/memea.2016.7533760>
8. Bevilacqua, V., D’Ambruoso, D., Mandolino, G., Suma, M.: A new tool to support diagnosis of neurological disorders by means of facial expressions. In: MeMeA 2011 – 2011 IEEE International Symposium on Medical Measurements and Applications, Proceedings (2011). <https://doi.org/10.1109/memea.2011.5966766>
9. Cirrincione, G., Ciravegna, G., Barbiero, P., Randazzo, V., Pasero, E.: The GH-EXIN neural network for hierarchical clustering. *Neural Networks* **121**, 57–73 (2020). <https://doi.org/10.1016/j.neunet.2019.07.018>
10. Randazzo, V., Cirrincione, G., Ciravegna, G., Pasero, E.: Nonstationary topological learning with bridges and convex polytopes: the G-EXIN neural network. In: 2018 International Joint Conference on Neural Networks (IJCNN), pp. 1–6. IEEE (2018). <https://doi.org/10.1109/ijcnn.2018.8489186>
11. Dimauro, G., Di Nicola, V., Bevilacqua, V., Caivano, D., Girardi, F.: Assessment of speech intelligibility in Parkinson’s disease using a speech-to-text system. *IEEE Access* **5**, 22199–22208 (2017). <https://doi.org/10.1109/ACCESS.2017.2762475>
12. Randazzo, V., Cirrincione, G., Paviglianiti, A., Pasero, E., Morabito, F.C.: Neural feature extraction for the analysis of Parkinsonian patient handwriting. In: Esposito, A., Faundez-Zanuy, M., Morabito, F.C., Pasero, E. (eds.) Progresses in Artificial Intelligence and Neural Systems. SIST, vol. 184, pp. 243–253. Springer, Singapore (2021). https://doi.org/10.1007/978-981-15-5093-5_23
13. Bevilacqua, V., Pannarale, P., Abbrescia, M., Cava, C., Paradiso, A., Tommasi, S.: Comparison of data-merging methods with SVM attribute selection and classification in breast cancer gene expression. *BMC Bioinformatics* **13**, S9 (2012). <https://doi.org/10.1186/1471-2105-13-S7-S9>
14. Cilia, N.D., De Stefano, C., Fontanella, F., Raimondo, S., di Freca, A.: An experimental comparison of feature-selection and classification methods for microarray datasets. *Information* **10**, 109 (2019)
15. Solazzi, M., Abbrescia, M., Vertechy, R., Loconsole, C., Bevilacqua, V., Frisoli, A.: An interaction torque control improving human force estimation of the rehab-exos exoskeleton. In: 2014 IEEE Haptics Symposium (HAPTICS), pp. 187–193. IEEE (2014). <https://doi.org/10.1109/haptics.2014.6775453>
16. Menolascina, F., et al.: Developing optimal input design strategies in cancer systems biology with applications to microfluidic device engineering. *BMC Bioinformatics* **10**, S4 (2009). <https://doi.org/10.1186/1471-2105-10-S12-S4>

17. Bevilacqua, V., Brunetti, A., Cascarano, G.D., Palmieri, F., Guerriero, A., Moschetta, M.: A deep learning approach for the automatic detection and segmentation in autosomal dominant polycystic kidney disease based on magnetic resonance images. In: Huang, D.-S., Jo, K.-H., Zhang, X.-L. (eds.) ICIC 2018. LNCS, vol. 10955, pp. 643–649. Springer, Cham (2018). https://doi.org/10.1007/978-3-319-95933-7_73
18. Bevilacqua, V., et al.: A comparison between two semantic deep learning frameworks for the autosomal dominant polycystic kidney disease segmentation based on magnetic resonance images. *BMC Med. Inform. Decis. Mak.* **19**(9), 1–12 (2019)
19. Litjens, G., et al.: A Survey on Deep Learning in Medical Image Analysis (2017). <https://doi.org/10.1016/j.media.2017.07.005>
20. de Vos, B.D., Wolterink, J.M., de Jong, P.A., Leiner, T., Viergever, M.A., Isgum, I.: ConvNet-based localization of anatomical structures in 3-D medical images. *IEEE Trans. Med. Imaging* **36**, 1470–1481 (2017). <https://doi.org/10.1109/TMI.2017.2673121>
21. Lu, X., Xie, Q., Zha, Y., Wang, D.: Fully automatic liver segmentation combining multi-dimensional graph cut with shape information in 3D CT images. *Sci. Rep.* **8**, 10700 (2018). <https://doi.org/10.1038/s41598-018-28787-y>
22. Rafiei, S., Nasr-Esfahani, E., Najarian, K., Karimi, N., Samavi, S., Soroushmehr, S.M.R.: Liver segmentation in CT images using three dimensional to two dimensional fully convolutional network. In: 2018 25th IEEE International Conference on Image Processing (ICIP), pp. 2067–2071. IEEE (2018). <https://doi.org/10.1109/icip.2018.8451238>
23. Kim, H., et al.: Abdominal multi-organ auto-segmentation using 3D-patch-based deep convolutional neural network. *Sci. Rep.* **10**, 1–9 (2020). <https://doi.org/10.1038/s41598-020-63285-0>
24. Couinaud, C.: Liver lobes and segments: notes on the anatomical architecture and surgery of the liver. *Presse Med.* **62**, 709–712 (1954)
25. Helling, T.S., Blondeau, B.: Anatomic segmental resection compared to major hepatectomy in the treatment of liver neoplasms. *HPB* **7**, 222–225 (2005). <https://doi.org/10.1080/13651820510028828>
26. Oliveira, D.A.B., Feitosa, R.Q., Correia, M.M.: Segmentation of liver, its vessels and lesions from CT images for surgical planning. *Biomed. Eng. Online* **10**, 1–23 (2011). <https://doi.org/10.1186/1475-925X-10-30>
27. Yoo, T.S., et al.: Engineering and algorithm design for an image processing API: a technical report on ITK—the Insight Toolkit. *Stud. Health Technol. Inform.* **85**, 586–592 (2002)
28. Yang, X., et al.: Segmentation of liver and vessels from CT images and classification of liver segments for preoperative liver surgical planning in living donor liver transplantation. *Comput. Methods Programs Biomed.* **158**, 41–52 (2018). <https://doi.org/10.1016/j.cmpb.2017.12.008>
29. Goceri, E., Shah, Z.K., Gurcan, M.N.: Vessel segmentation from abdominal magnetic resonance images: adaptive and reconstructive approach. *Int. J. Numer. Method. Biomed. Eng.* **33**, e2811 (2017). <https://doi.org/10.1002/cnm.2811>
30. Chi, Y., et al.: Segmentation of liver vasculature from contrast enhanced CT images using context-based voting. *IEEE Trans. Biomed. Eng.* **58**, 2144–2153 (2011). <https://doi.org/10.1109/tbme.2010.2093523>
31. Zeng, Y., et al.: Liver vessel segmentation and identification based on oriented flux symmetry and graph cuts. *Comput. Methods Programs Biomed.* **150**, 31–39 (2017). <https://doi.org/10.1016/j.cmpb.2017.07.002>
32. Bevilacqua, V., et al.: Retinal fundus biometric analysis for personal identifications. In: Huang, D.-S., Wunsch, D.C., Levine, D.S., Jo, K.-H. (eds.) ICIC 2008. LNCS (LNAI), vol. 5227, pp. 1229–1237. Springer, Heidelberg (2008). https://doi.org/10.1007/978-3-540-85984-0_147

33. Milletari, F., Navab, N., Ahmadi, S.A.: V-Net: fully convolutional neural networks for volumetric medical image segmentation. In: Proceedings of the 2016 4th International Conference on 3D Vision, 3DV 2016, pp. 565–571 (2016). <https://doi.org/10.1109/3dv.2016.79>
34. Bilic, P., et al.: The Liver Tumor Segmentation Benchmark (LiTS), pp. 1–43 (2019)
35. Heimann, T., et al.: Comparison and evaluation of methods for liver segmentation from CT datasets. *IEEE Trans. Med. Imaging* **28**, 1251–1265 (2009). <https://doi.org/10.1109/TMI.2009.2013851>
36. IRCAD France - Research Institute against Digestive Cancer: 3D-IRCADb (3D Image Reconstruction for Comparison of Algorithm Database) (2012). <https://www.ircad.fr/research/3dircadb/>. Accessed Apr 2020
37. Ronneberger, O., Fischer, P., Brox, T.: U-Net: convolutional networks for biomedical image segmentation. In: Navab, N., Hornegger, J., Wells, W.M., Frangi, A.F. (eds.) MICCAI 2015. LNCS, vol. 9351, pp. 234–241. Springer, Cham (2015). https://doi.org/10.1007/978-3-319-24574-4_28
38. Çiçek, Ö., Abdulkadir, A., Lienkamp, S.S., Brox, T., Ronneberger, O.: 3D U-Net: learning dense volumetric segmentation from sparse annotation. In: Ourselin, S., Joskowicz, L., Sabuncu, M.R., Unal, G., Wells, W. (eds.) MICCAI 2016. LNCS, vol. 9901, pp. 424–432. Springer, Cham (2016). https://doi.org/10.1007/978-3-319-46723-8_49
39. He, K., Zhang, X., Ren, S., Sun, J.: Delving deep into rectifiers: surpassing human-level performance on ImageNet classification. In: 2015 IEEE International Conference on Computer Vision (ICCV), pp. 1026–1034. IEEE (2015). <https://doi.org/10.1109/iccv.2015.123>
40. Shen, C., et al.: Improving V-Nets for multi-class abdominal organ segmentation. In: Angelini, E.D., Landman, B.A. (eds.) Medical Imaging 2019: Image Processing, p. 10. SPIE (2019). <https://doi.org/10.1117/12.2512790>
41. Kingma, D.P., Ba, J.: Adam: a method for stochastic optimization. CoRR abs/1412.6 (2014)
42. Salehi, S.S.M., Erdogmus, D., Gholipour, A.: Tversky loss function for image segmentation using 3D fully convolutional deep networks (2017)



A Classification Algorithm for Real Collar Images

Xiao Qin¹, Chengcheng Huang¹, Junhua Wu²,
and Changan Yuan²(✉)

¹ Nanning Normal University, Nanning 530299, China

² Guangxi Academy of Science, Nanning 530025, China
yuanchangan@126.com

Abstract. With the increasing development of e-commerce platforms, it has become a growing demand to use collar types to retrieve clothing on shopping websites. However, due to the lack of image training data sets for collar classification, the task of collar image classification faces many challenges such as multiple poses, multiple noises, and small detection areas. There is currently no specific collar image classification research report. The existing image classification algorithms are not ideal in the actual collar classification task. To this end, this paper collected 39248 images of network collars, constructed a small collar image data set with four categories called Collar-Four, and proposed a classification algorithm called SqueezeCNet. The algorithm is improved by adding a CBAM block to the Fire module in SqueezeNet. The improved module is called FireC. In the experimental part, the initialization model and transfer model of SqueezeCNet are compared with the random initialization model and transfer model of traditional convolutional neural networks on the Collar-Four dataset. The initialization model of SqueezeCNet obtains an accuracy of 76.66%, and the classification effect is better than random initialization model and transfer model of traditional convolutional neural networks. The transfer model of SqueezeCNet has an accuracy of 79.74%, which is the best among all experimental models. In addition, an ablation experiment was performed on the classification algorithm proposed in this paper, which further proved the effectiveness of the method in this paper. Experiments show that the application of SqueezeCNet on the Collar-Four dataset is feasible, and this algorithm can effectively solve the real-world collar image classification problem with noisy background.

Keywords: Collar classification · Collar-Four · SqueezeCNet · CBAM · Transfer learning

1 Introduction

With the development of the clothing industry, the clothing design field and the clothing sales field have put forward higher requirements on the management, classification and retrieval of clothing pictures, especially the clothing attribute classification, such as clothing collar type and clothing color. As a part of clothing, the collar not only protects the neck and decorate the clothing but also is an important feature to distinguish clothing styles. Therefore, it is very important for clothing information

management, release and retrieval that to classify clothing based on collars. At present, the research on clothing classification mainly focuses on the clothing itself. The opened clothing datasets include DeepFashion [1], DeepFashion2 [2], Street2shop [3], etc. Unfortunately, there is no public dataset available for classification of clothing attributes (such as collar), and no researchers pay attention to noisy collar images and conduct relevant image classification research. Therefore, no network for collar classification has been designed.

Compared with the noiseless collar image classification, there are the following problems for collar classification based on the clothing images that are on the e-commerce website: Firstly, the collar in the image is affected by occlusion, deformation, clothing ornaments, shooting distance, angle and background, which have different degrees of impact on the classification accuracy; Secondly, there usually are multiple people, multiple clothing types in the image of advertising, which brings difficult to conduct image recognize task. In a word, there are always many regions that are not related to the collar classification in this type of collar image.

The main works of this article are as follow:

- (1) A clothing collar classification image dataset named Collar-Four is established. The dataset includes four categories: round collar, lapel collar, stand collar and hooded collar, with a total of 39248 pictures, of which 70% are pictures with complex background.
- (2) An algorithm for the classification of collar images is called SqueezeCNet. In this paper, the initialization model and transfer model of this model are compared with the random initialization model and transfer model of neural network, and the ablation experiment of SqueezeCNet is carried out. Two sets of experiments prove that SqueezeCNet can effectively solve the noisy collar image data in the real world, and verify the effectiveness of Collar-Four in the deep learning classification algorithm. It shows that the dataset is suitable for the collar classification of clothing. Meaningful and contributing.

2 Related Work

2.1 Transfer Learning

Deep learning [4] was originally proposed by Hinton et al. in 2006. It is the internal law and representation level of learning sample data. The information obtained in the learning process is of great help to the interpretation of image data. Therefore, deep learning is currently used in various image recognition tasks [5–11]. Convolutional neural network is one of the representative algorithms of deep learning [12, 13]. However, the direct use of neural network models for image classification, no detailed optimization parameters and careful network design for specific tasks cannot achieve good classification results. With the emergence of more and more practical application scenarios, it is a hugely expensive task to obtain a large enough amount of data immediately, so transfer learning has attracted more and more attention. Therefore, for a classification problem in a new field, transfer learning [14] has become a good choice.

In the field of image classification, ImageNet dataset [15] is often used as a pre-training dataset. The parameters of the trained model are transferred, and then a certain number of target datasets are used to fine-tune the network and optimize the parameters, so that the model can start training and optimization at a good starting point. And the features extracted from the bottom layer in the pre-training model are universal, and can extract basic features such as the edge and texture of the image. Figure 1 shows the transfer learning process based on convolutional neural networks.

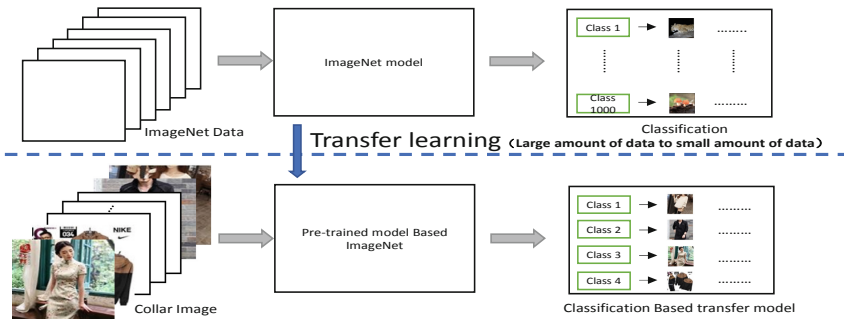


Fig. 1. Transfer learning based on convolutional neural network.

In recent years, transfer learning methods have been widely used to solve many challenging problems. Wu et al. [16] used transfer learning to perform classification task in Oxford flower dataset, and reach the accuracy of 95.29%, prove that transfer learning has better robustness and generalization ability in flower recognition; Seo et al. [17] used the pre-trained GoogLeNet model to learn features of more than 1,000 pieces of manually labeled clothing images, and then obtained a good clothing classification effect on this dataset, which proved the effectiveness of transfer learning on small clothing dataset.

2.2 Convolutional Block Attention Module (CBAM)

The basic idea of the attention mechanism in computer vision is to allow the neural network to ignore irrelevant information and focus on key information, thereby improving the performance of the model. There is currently a wealth of relevant research [18–21]. Convolutional Block Attention Module (CBAM) [22] is an attention mechanism module that combines space and channel. It multiplies the input features and adaptively refinement for features to enhance the expression ability of features. The CBAM block is shown in Fig. 2. First, the channel attention map is element-wise multiplication by the input feature map to obtain F1, and then the spatial attention map of F1 is calculated, and the two are element-wise multiplication to obtain the final output Refined Feature. Channel attention mainly focuses on what is meaningful in the input image. The channel attention module mainly uses global average pooling and global max pooling. Then, the correlation between channels is modeled by two full connection layers and corresponding activation functions, and the weights of each

feature channel are obtained by merge the two output. Spatial attention is mainly focused on location information. It also uses global average pooling and global max pooling to get two different feature descriptions, and then uses concatenation to merge the two feature descriptions, and uses convolution to generate spatial feature map.

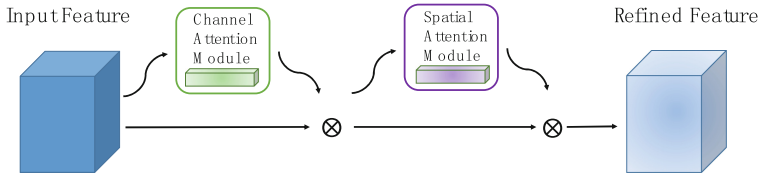


Fig. 2. CBAM module

2.3 SqueezeNet

SqueezeNet [23] is a network model that does not focus on improving classification accuracy, but focuses on reducing model parameters and reducing network calculations. Therefore, the network proposed a network unit structure similar to inception, named Fire module, it is the core module of SqueezeNet. A Fire module contains a squeeze convolutional layer (only 1×1 convolution kernel) and an expand convolutional layer (1×1 and 3×3 convolution kernels). Among them, the squeeze layer draws on the idea of Inception. The input layer first compresses the dimensionality through the squeeze convolution layer, and then expands the dimensionality through the expand convolution layer (convolution and convolution mixture). If the network uses too many 1×1 convolution kernels, the feature area of the image extracted by the convolution kernel is too small, which will cause the feature extraction ability of the network to decrease. Therefore, in the expand layer, the 1×1 convolution kernel only replaces part of the 3×3 convolution kernel. The structure diagram of Fire module is shown in Fig. 3.

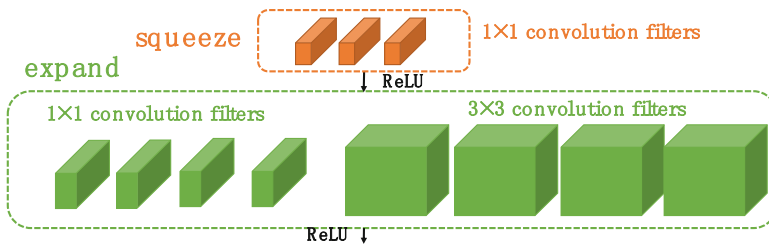


Fig. 3. Fire module.

3 Collar Classification Algorithm-SqueezeCNet

Aiming at the classification task of real collar images, this paper proposes a new classification algorithm-SqueezeCNet. The network is too deep, the parameter will be too large, which will affect the classification performance of the network. Therefore, this article chooses the lightweight SqueezeNet as the basic network to improve. In the Collar-Four dataset, the collar image contains too much noise information, and the collar only appears in a small area of the image. Although the convolutional neural network has strong feature representation ability, but due to the influence of the collar image perspective, background, occlusion and other factors, the network cannot focus on the features of the collar well. Therefore, this article borrows the CBAM block proposed in [22] and adds it to the Fire module in SqueezeNet, so that the network can pay attention to the distinctive area, and then carefully compare and identify the area to improve the classification performance. The improved Fire module is called FireC, and the improved algorithm is called SqueezeCNet. Table 1 lists the main parameter settings of the algorithm. Figure 4 shows the structure of SqueezeCNet.

Table 1. SqueezeCNet parameter settings

| Name | SqueezeCNet |
|---|---|
| Conv | 3×3 , 64, stride =2 |
| ReLU | 64 |
| Maxpool | 3×3 , stride =2 |
| FireC2 | squeeze $1 \times 1,16$; CBAM, 16; expend $1 \times 1,64$; expend $3 \times 3,64$ |
| FireC3 | squeeze $1 \times 1,16$; CBAM, 16; expend $1 \times 1,64$; expend $3 \times 3,64$ |
| Maxpool | 3×3 , stride = 2 |
| FireC4 | squeeze $1 \times 1,32$; CBAM, 32; expend $1 \times 1,128$; expend $3 \times 3,128$ |
| FireC5 | squeeze $1 \times 1,32$; CBAM, 32; expend $1 \times 1,128$; expend $3 \times 3,128$ |
| Maxpol | 3×3 , stride = 2 |
| FireC6 | squeeze $1 \times 1,48$; CBAM, 48; expend $1 \times 1,192$; expend $3 \times 3,192$ |
| FireC7 | squeeze $1 \times 1,48$; CBAM, 48; expend $1 \times 1,192$; expend $3 \times 3,192$ |
| FireC8 | squeeze $1 \times 1,64$; CBAM, 64; expend $1 \times 1,256$; expend $3 \times 3,256$ |
| FireC9 | squeeze $1 \times 1,64$; CBAM, 64; expend $1 \times 1,256$; expend $3 \times 3,256$ |
| Conv | 1×1 |
| num_calss, ReLU, AdaptiveAvgPool, softmax | |

FireC is shown in Fig. 5, the feature map s ($H \times W \times M$) is input to the squeeze operation and ReLU, and the feature map S ($H \times W \times n_1$) is obtained, where n_1 represents the number of channels of the 1×1 convolutional layer of the squeeze part. Then, S is input to the CBAM module. In CBAM, S first passes the channel attention block to obtain the weight coefficient W_c , where σ refers to the sigmoid function. S will go through average pooling and max pooling on the channel respectively in the channel attention block, and then go through MLP respectively. Perform

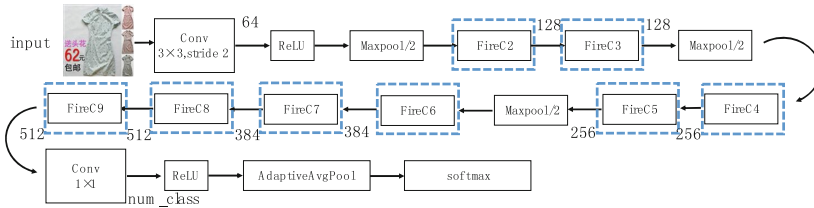


Fig. 4. The structure of SqueezeCNet.

an elementwise-based addition operation on the features output by the MLP, and then pass the sigmoid activation operation to obtain W_c . The new feature F_c can be obtained by elementwise multiplication of W_c and S . F_c is used as the input of the spatial attention block in CBAM, and finally the weight coefficient W_s is obtained, where f refers to the convolution operation. F_c will get two results through average pooling and max pooling in spatial attention block. After these two results are based on concat operation, W_s is obtained through convolution operation and sigmoid activation operation. The new feature F_s can be obtained by elementwise multiplication of F_c and W_s . Input F_s to expand and then perform ReLU, and final output of the entire FireC module is S_2 . The expand part includes 1×1 convolution and 3×3 convolution. F_s is input to 1×1 convolution to get a feature map size of $H \times W \times n_2$, F_s is input to 3×3 convolution to get a feature map size of $H \times W \times n_3$, n_2 represents the number of channels of the 1×1 convolution layer of the expand part, and n_3 represents the number of channels of the 3×3 convolution layer of the expand part. The results of two different core sizes are output through the concat operation, and the number of output channels is n_2+n_3 . The process description of FireC processing image is shown in Table 2:

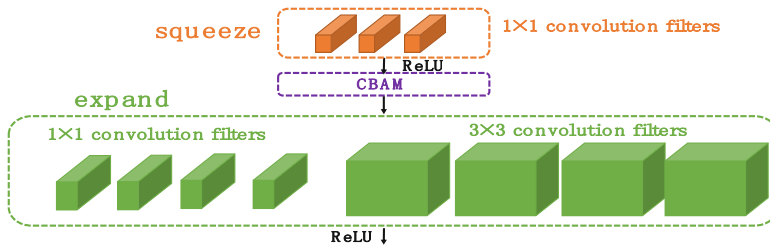


Fig. 5. FireC module

Table 2. FireC processes the image

| |
|---|
| FireC processes the image |
| input: feature map s |
| output: feature map S_2 |
| 1: $S = ReLU(squeeze(s))$ |
| 2: $W_c(S) = \sigma(MLP(Avgpool(S)) + MLP(Maxpool(S)))$ |
| 3: $F_c = S \otimes W_c(S)$ |
| 4: $W_s(F_c) = \sigma(f([Avgpool(F_c); Maxpool(F_c)]))$ |
| 5: $F_s = F_c \otimes W_s(F_c)$ |
| 6: $S_2 = ReLU(expand(F_s))$ |
| return S_2 |

4 Experiment

4.1 Experimental Environment and Parameter Settings

All the experiments are done on Collar-Four. The experimental environment includes Intel i7-7700 processor, 1T SSD solid state drive, 32 memory, NVIDIA GTX1080Ti GPU. In transfer learning model, the learning rate is set to $1e-4$, the weight attenuation is set to $1e-6$, the momentum factor is set to 0.9, and the SGD function is used to update the network weight. All experimental iterations are set to 300 generations.

4.2 Experimental Dataset

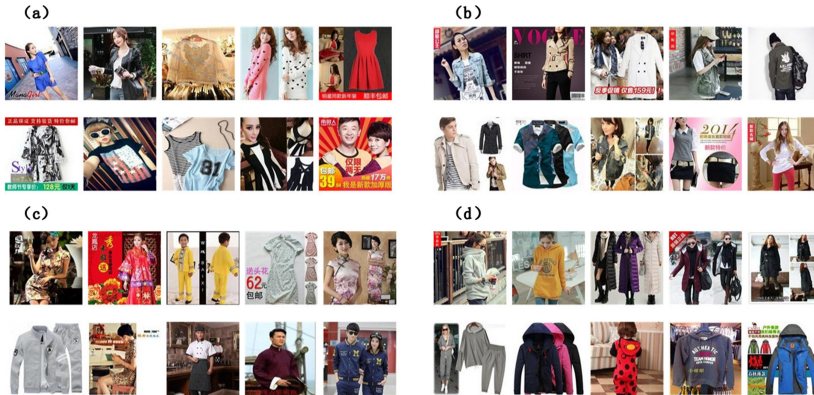
In view of the fact that there is no public collar image dataset at present, this paper constructs a collar type data set named Collar-Four. The images are from Taobao, tmall and clothing brand websites and other major e-commerce platforms. Pictures are collected by manually and crawlers. The pictures are for experimental use only, not for commercial use.

The images of the Collar-Four include images that only contain clothing, and images of models and models wearing them. In addition, the image has the characteristics of different landmarks, multi angle, multi pose, multiple objects of the same type in a single image, and different degrees of occlusion. The collar only exists in a small area of the image, and the rest of the image belongs to the classification independent noise. Therefore, the dataset has strong expression ability and rich diversity, which is helpful to learn the characteristics of collar and meet the requirements of the real world.

The dataset contains 39248 pictures with four categories of round collar, lapel collar, stand collar and hooded collar, each category contains 9600 to 10,000 three-channel RGB pictures. The datasets are divided into training sets and test sets, and the ratio of training data and test data is about 7: 3. Table 3 shows the total number of each collar category images, and the size of training set and test set of each collar category. Figure 6 shows partial images of four types of collars.

Table 3. Total number of images in each category and number of images in training sets and test sets.

| Collar type | Training set | Test set | Total |
|---------------|--------------|----------|-------|
| Round collar | 7014 | 3007 | 10021 |
| Lapel collar | 7000 | 3000 | 10000 |
| Stand collar | 6721 | 2881 | 9602 |
| Hooded collar | 6740 | 2885 | 9625 |

**Fig. 6.** Example images showing different categories are (a) round collar (b) lapel collar (c) stand collar (d) hooded collar.

4.3 Experimental Results and Analysis

Contrast Experiment. In order to solve the classification problem of real and noisy collar data, ResNet50 [24], VGG16 [25], VGG19 [25], ResNext [26], Res2Net-50 [27], SE-Res2Net-50 [27], SKNet [28], SqueezeCNet's random initialization model and transfer learning model to predict the category in Collar-Four. Table 4 shows the experimental results. The transfer model of SqueezeCNet has the best classification effect, followed by the initialization model of SqueezeCNet. The structure of the randomly initialized network and the parameters of the model start from random guessing. As a result, during the training process, the network may not be able to quickly and accurately find the optimal value, but it is easy to fall into a local optimum or even overfitting. Convolutional neural network itself has a large number of neurons, numerous weight information, complex structure, and the deeper the network, the greater the amount of parameters, the generalization ability of the model cannot reach the optimal, which affects the ability of the model to finally distinguish the image category. The random initialization network of ResNet50, VGG16, VGG19, ResNext-50, SKNet, Res2Net-50, SE-Res2Net-50 has a deep number of layers and a large amount of parameters, and it is not well trained to obtain good semantic parameters on a small amount of collar image data, the accuracy rates of 61.29%, 55.00%, 52.99%,

68.98%, 73.12%, 73.27 and 73.76% were obtained respectively. After randomly initializing the network using the transfer learning method, the network can learn from a good initial point and avoid training a complex model with millions of parameters, thereby improving the performance of the deep learning model, including improving the generalization ability of the model and enhancing the robustness. The classification effect of the transfer model of ResNet50, VGG16, and VGG19 is better than the random initialization model, and the accuracy rates of 73.98%, 75.18%, and 75.47% are obtained respectively. However, if you want to fundamentally improve the effect of network classification, you must improve from the basic network. Collar-Four is a collar image dataset in the real world. The image background contains a lot of noise, and the collar area occupies a relatively small portion of the image. If the network can accurately extract the collar itself, it needs to be more strong distinguishing ability. SqueezeCNet is based on SqueezeNet and adds CBAM module. After adding the CBAM module, the neural network pays more attention to the collar itself, enhancing beneficial features and suppressing useless features according to the importance of features. Therefore, SqueezeCNet obtains an accuracy rate of 76.66%, which is better than the random initialization model and transfer model of other networks. In order to further improve the effect of the model on collar image classification, we try to add the transfer learning method, and the effect is further improved. The classification accuracy of SqueezeCNet's transfer model in the collar four dataset reaches 79.74%, which is the best among all the methods.

Table 4. Comparison of accuracy between SqueezeCNet and other models.

| Method | Test set accuracy |
|----------------------|-------------------|
| ResNet50 | 61.29% |
| VGG16 | 55.00% |
| VGG19 | 52.99% |
| SKNet | 73.12% |
| SE-Res2Net-50 | 73.76% |
| Res2Net-50 | 73.27% |
| ResNext-50 | 68.98% |
| ResNet50+Transfer | 73.98% |
| VGG16+Transfer | 75.18% |
| VGG19+Transfer | 75.47% |
| SqueezeCNet | 76.66% |
| SqueezeCNet+Transfer | 79.74% |

SqueezeCNet's ablation experiment. Table 5 shows the ablation experiment results of SqueezeCNet. The CBAM module can improve the feature extraction capability of the basic network from the perspective of channel and space. Compared with SqueezeNet, the classification results of SqueezeCNet are improved by 10.49%, indicating that CBAM can effectively increase the feature extraction capabilities of the network,

thereby improving network performance; The pre-training model in the transfer learning method not only learns low-level features such as color and texture, but also learns high-level semantic features that help the classification of the target data set, thereby optimizing the target task and improving the classification performance of the model. After SqueezeCNet is added to the transfer learning method, the classification result is 11.89% higher than that of SqueezeNet, indicating that the transfer learning method can make the network have a better classification effect. The experimental results fully verify that the method proposed in this paper has good classification performance on the challenging noisy collar image on the Collar-Four dataset.

Table 5. SqueezeCNet’s ablation experimen.

| Method | Test set accuracy |
|----------------------|-------------------|
| SqueezeNet | 66.17% |
| SqueezeCNet | 76.66% |
| SqueezeNet+Transfer | 78.06% |
| SqueezeCNet+Transfer | 79.74% |

5 Conclusion

In the context of Internet shopping, efficient and accurate collar classification is helpful for merchants to describe clothing information, so that users can retrieve their favorite clothing styles through collar categories, and promote the development of the clothing sales industry. In the absence of relevant research, this paper constructs a collar dataset named Collar-Four, and the image contains a lot of noise. In addition, for real-world collar image data, a SqueezeCNet algorithm based on SqueezeNet is proposed. In SqueezeCNet, by introducing the CBAM module and transfer learning method, the feature extraction ability of the network is strengthened and training is started from a good start, which effectively solves the problem of difficulty in classifying collar images with a lot of noise in the real world. All experiments in this paper are based on Collar-Four. Specifically, the transfer models of SqueezeCNet and SqueezeCNet are compared with the random initialization models of ResNet50, VGG16, VGG19, ResNext, Res2Net-50, SKNet and the transfer models of ResNet50, VGG16, and VGG19. The experimental results show that the results obtained by the transfer models of SqueezeCNet and SqueezeCNet are better than the random initialization model and transfer model of traditional neural networks, which proves that the SqueezeCNet algorithm can be effectively applied to collar image classification. In addition, the classification algorithm proposed in this paper is verified by model ablation experiments, which further proves the effectiveness of this method. Therefore, the distribution of Collar-Four collar image data proposed in this paper is reasonable, can support the construction of classification models, and can be used as training set data for collar classification tasks in the real world. The Collar-Four dataset and SqueezeCNet algorithm have practical significance for carrying out research on the classification and retrieval of clothing collars.

Acknowledgment. This work is partially supported by the National Natural Science Foundation of China under Grant Nos. 61962006, 61802035, 61772091; the Project of Science Research and Technology Development in Guangxi under Grant Nos. AA18118047, AD18126015, AB16380272; thanks to the support by the BAGUI Scholar Program of Guangxi Zhuang Autonomous Region of China (2016 [21], 2019 [79]); the National Natural Science Foundation of Guangxi under Grant Nos. 2018GXNSFAA138005.

References

1. Liu, Z., Luo, P., Qiu, S., et al.: DeepFashion: powering robust clothes recognition and retrieval with rich annotations. In: Proceedings of the IEEE Conference on Computer Vision and Pattern Recognition, pp. 1096–1104 (2016)
2. Ge, Y., Zhang, R., Wang, X., et al.: DeepFashion2: a versatile benchmark for detection, pose estimation, segmentation and re-identification of clothing images. In: Proceedings of the IEEE Conference on Computer Vision and Pattern Recognition, pp. 5337–5345 (2019)
3. Kiapour, M.H., Han, X., Lazebnik, S., Berg, A.C., Berg, T.L.: Where to buy it: matching street clothing photos in online shops. In: ICCV, pp. 3343–3351. IEEE Computer Society (2015)
4. Hinton, G., Salakhutdinov, R.R.: Reducing the dimensionality of data with neural networks. *Science* **313**(5786), 504–507 (2006)
5. Zoran, D., Chrzanowski, M., Huang, P., et al.: Towards robust image classification using sequential attention models. arXiv: Computer Vision and Pattern Recognition (2019)
6. Xie, Q., Hovy, E., Luong, M., et al.: Self-training with Noisy student improves ImageNet classification. arXiv: Learning (2019)
7. Bertinetto, L., Muller, R., Tertikas, K., et al.: Making better mistakes: leveraging class hierarchies with deep networks. arXiv: Computer Vision and Pattern Recognition (2019)
8. Wu, Y., Zhang, K., Wu, D., et al.: Person re-identification by multi-scale feature representation learning with random batch feature mask. *IEEE Trans. Cogn. Dev. Syst.* (2020)
9. Chen, Z., Wei, X., Wang, P., et al.: Multi-label image recognition with graph convolutional networks. In: Proceedings of the IEEE Conference on Computer Vision and Pattern Recognition, pp. 5177–5186 (2019)
10. Wang, G., Wang, K., Lin, L., et al.: Adaptively connected neural networks. In: Proceedings of the IEEE/CVF Conference on Computer Vision and Pattern Recognition, pp. 1781–1790 (2019)
11. Yuan, C., et al.: An effective image classification method for shallow densely connected convolution networks through squeezing and splitting techniques. *Appl. Intell.* **49**(10), 3570–3586 (2019). <https://doi.org/10.1007/s10489-019-01468-7>
12. Goodfellow, I., Bengio, Y., Courville, A.: *Deep Learning*, vol. 1, pp. 326–366. MIT press, Cambridge (2016)
13. Gu, J., et al.: Recent advances in convolutional neural networks. arXiv preprint [arXiv:1512.07108](https://arxiv.org/abs/1512.07108) (2015)
14. Pan, S.J., Yang, Q.: A survey on transfer learning. *IEEE Trans. Knowl. Data Eng.* **22**(10), 1345–1359 (2010)
15. Deng, J., Dong, W., Socher, R., et al.: ImageNet: a large-scale hierarchical image database. In: 2009 IEEE Conference on Computer Vision and Pattern Recognition, pp. 248–255. IEEE (2009)

16. Wu, Y., Qin, X., Pan, Y., et al.: Convolution neural network based transfer learning for classification of flowers. In: 2018 IEEE 3rd International Conference on Signal and Image Processing (ICSIP), pp. 562–566. IEEE (2018)
17. Seo, Y., Shin, K.S.: Image classification of fine-grained fashion image based on style using pre-trained convolutional neural network. In: 2018 IEEE 3rd International Conference on Big Data Analysis, pp. 387–390. IEEE (2018)
18. Xiao, T., Xu, Y., Yang, K., et al.: The application of two-level attention models in deep convolutional neural network for fine-grained image classification. In: Proceedings of the IEEE Conference on Computer Vision and Pattern Recognition, pp. 842–850 (2015)
19. Hu, J., Shen, L., Albanie, S., et al.: Squeeze-and-excitation networks. *IEEE Trans. Pattern Anal. Mach. Intell.* 1 (2019)
20. Wang, X., Girshick, R., Gupta, A., et al.: Non-local neural networks. In: Proceedings of the IEEE Conference on Computer Vision and Pattern Recognition, pp. 7794–7803 (2018)
21. Fu, J., Liu, J., Tian, H., et al.: Dual attention network for scene segmentation. In: Proceedings of the IEEE/CVF Conference on Computer Vision Pattern Recognition, pp. 3146–3154 (2019)
22. Woo, S., Park, J., Lee, J., et al.: CBAM: convolutional block attention module. In: Proceedings of the European Conference on Computer Vision, pp. 3–19 (2018)
23. Iandola, F., Han, S., Moskewicz, M.W., et al.: SqueezeNet: AlexNet-level accuracy with 50x fewer parameters and <0.5 MB model size. *arXiv: Computer Vision and Pattern Recognition* (2017)
24. He, K., Zhang, X., Ren, S., Sun, J.: Deep residual learning for image recognition. In: Proceedings of the IEEE Conference on Computer Vision and Pattern Recognition, Las Vegas, USA, pp. 770–778 (2016)
25. Simonyan, K., Zisserman, A.: Very deep convolutional networks for large-scale image recognition. *arXiv preprint [arXiv:1409.1556](https://arxiv.org/abs/1409.1556)* (2014)
26. Saining, X., et al.: Aggregated residual transformations for deep neural networks. In: Proceedings of the IEEE Conference on Computer Vision and Pattern Recognition (2017)
27. Gao, S.H., Cheng, M.M., Zhao, K., et al.: Res2Net: a new multi-scale backbone architecture. *arXiv preprint [arXiv:1904.01169](https://arxiv.org/abs/1904.01169)* (2019)
28. Li, Xiang, et al.: Selective Kernel networks. In: Proceedings of the IEEE Conference on Computer Vision and Pattern Recognition (2019)



Accurate and Efficient Traffic Sign Detection with a Guided Region Enlarging Algorithm

Qing Tang, Ge Cao, and Kanghyun Jo^(✉)

University of Ulsan, Ulsan 44610, Korea
{tangqing, caoge}@islab.ulsan.ac.kr, acejo@ulsan.ac.kr

Abstract. Traffic signs detection is a hot and important topic in the research field of computer vision and lots of applications, e.g., driver assistance system and autonomous vehicle, etc. Thanks to the development of the convolutional neural network, object detection has achieved promising results in recent years. Nevertheless, traffic sign detection still faces two difficulties due to the characteristics of traffic signs. The first difficulty is the detection of small and blurred traffic signs. The second difficulty is that training samples are sparse and imbalanced. For tackling these two difficulties, Guided Region Enlarging Algorithm (GREA) is proposed in the paper. The GREA consists of two sub-modules, Potential region estimation network (PREN) and NMS-Cropping. The PREN obtains a potential object region of each input image first. Then, the potential object region is enlarged by the NMS-Cropping algorithm for subsequent augmenting training. The GREA makes use of features of a small and blurred traffic sign to enhance the performance of a traffic sign detector. To comprehensively evaluate the proposed approach, two traffic sign datasets include the Swedish traffic sign data set and the Tsinghua-Tencent 100k data set are utilized in the experiment. Experimental results demonstrate the efficiency of the proposed GREA, and our approach is comparable to the state-of-the-art approaches.

Keywords: Deep learning · Data augmentation · Intelligent transportation system · Traffic sign detection

1 Introduction

With the development of the driver-assistance system and autonomous vehicle, the traffic sign recognition (TSR) system has been heavily studied over the past decade. A good traffic sign detection mechanism helps vehicles perceiving the surrounding environment. In the Advanced Driver Assistance System (ADAS), the traffic sign detection mechanisms can remind the driver of traffic constraints if drivers ignore them. In Automated Driving System (ADS), A traffic sign detection mechanism can also provide traffic sign class and location information to the vehicle navigation system. This information can be used as distinct landmarks for generating High Definition Map (HD Map).

The appearance of traffic signs is designed to easily attract humans attention. Firstly, the main color of most of the traffic signs is high saturated colors, such as red,

blue, and white text on it. Secondly, the shape of the traffic sign is regular shapes, such as round, square, and triangle. Thirdly, the information that the traffic sign carried is brief and comprehensible. Three points above are the advantage of traffic signs for detecting. However, the uncontrolled environmental factors including weather conditions, variable illumination, and complex road conditions increase the difficulty of detection. These appearance characteristics of traffic signs are an important feature to distinguish it from the surrounding environment.

Traditional traffic sign detection approaches include a variety of classification or clustering algorithms. These clustering algorithms, such as the AdaBoost [1] train a binary classifier that classifies the sliding window of the image or specific region. The high classified score windows are treated as traffic sign locations. The other algorithm like SVM detects the traffic sign locations by using HoG features of sliding windows. Same to these two algorithms above, most of the traditional detection approaches use color, shape, edge, and other hand-craft features. However, the color values of traffic signs easily affected by illumination conditions. Also, objects such as trees and pedestrians which may occlude the traffic sign, so the shape of the traffic sign in an image is changed. It is hard for hand-craft features to provide the general characteristics of traffic signs.

Thanks to the development of deep learning algorithms, object detection using the Convolution Neural Network (CNN) made remarkable achievements recently. In the traffic sign detection task, CNN-based architectures such as Faster RCNN [2], FCN [3], and SSD [4] become mainstream detectors too. Although CNN-based detectors achieve higher accuracy than traditional traffic sign detectors, traffic sign detection still faces two difficulties that are different from general object detection.

The first difficulty is that most of the traffic signs are small. Traffic signs occupy relatively small areas in an image. Due to the characteristic of CNN, CNN-based object detection networks always get worse results for small objects than big objects. The CNN extracts various depth features by using multilevel convolution and pooling operation. For obtaining deeper semantic features, more convolution and pooling operation are needed. Because of these repeating operations, features of small objects may only exist in the shadow layer which cannot extract deep semantic features. A popular solution to this problem is to combine shadow and deep feature maps by concatenation or other mathematic operation, then the detector can be trained using these combined feature maps which include object information and its rich semantic features both [5]. [6] proposed a Perceptual Generative Adversarial Network (p-GAN) that generates a corresponding large feature of a small traffic sign.

The second difficulty is that training samples are sparse. From the statistical data of data sets that are presented in Sect. 5. The average number of traffic signs in an image less than 2. The TT100k data set provides more traffic signs per image than STSD. The details of the three datasets are presented in Sect. 4. With the number of training samples increasing, the generalization ability of CNN-based detector increases. Because of the small sizes and quantities of traffic signs, the training samples are not heterogeneous enough, although the size of data sets is large. This is a reason that the traffic sign classification task achieves almost 100% accuracy, but the traffic sign detection still has much room for improvement.

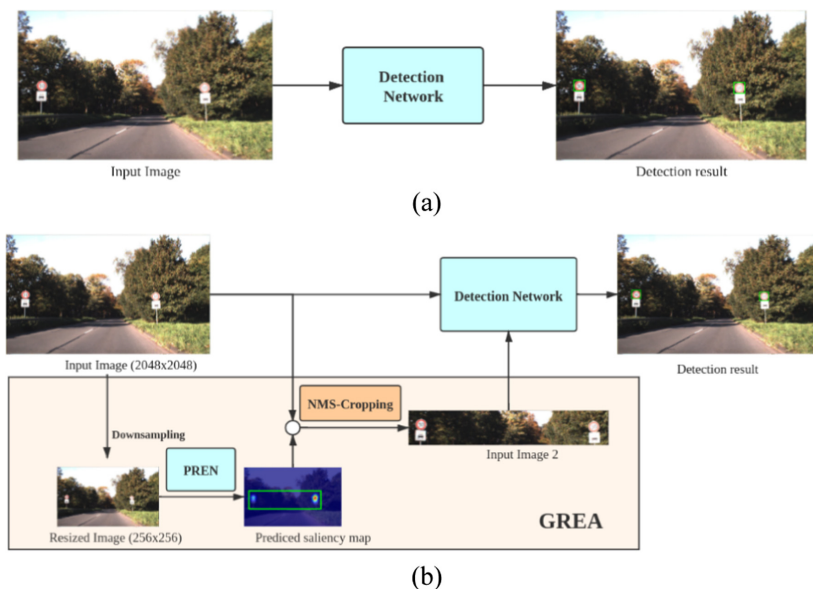


Fig. 1. The detection network architecture. (a) the original detection network. (b) the proposed network architecture with the GREA.

To tackle the above two difficulties, an efficient traffic sign detection mechanism is introduced in the paper. The training pipeline of the detection mechanism is shown in Fig. 1(b). Compared with the common detection network, a Guided Region Enlarging Algorithm (GREA) is attached for obtaining the potential traffic sign region. The GREA is only used in the training, therefore our approach enhances the performance without costing extra time.

The contributions of this work are summarized as follows:

- 1) An effective traffic sign detection mechanism had been introduced in the paper. The proposed detector achieves state-of-the-art performance on two mainstream traffic sign detection data sets that are STSD [7], and TT100k [8].
- 2) To alleviate the two difficulties that introduced above, the GREA is proposed in the paper. The experimental results prove the efficiency of GREA. Also, GREA improves the detection network's performance without costing extra time in inference.

2 Proposed Method

The proposed traffic sign detection mechanism is presented in this section. The framework is shown in Fig. 1(b). Compared with the common detection approach, the proposed approach adds a GREA module before the detection network. GREA consists of two parts. The first part is the potential region estimation network (PREN).

The PREN generates a saliency map of which the highlight region represents the potential traffic sign region of a corresponding down-sampling input image. According to the generated saliency map, the NMS Cropping Algorithm obtains a cropping region. The last step of GREA is to enlarge the cropping region. Both of the input image and its corresponding enlarging region are used to train the detection network. In this section, the TT100k data set is used for explanation, and the experiment configuration of the STSD data set will be described in detail in Sect. 3.

2.1 Overall Structure

Figure 1(b) is an illustration of the overall structure of the proposed traffic sign detection mechanism. It consists of two parts, the GREA and the detection network.

The GREA consists of two parts, the potential region estimation network (PREN) and the NMS-cropping algorithm. The input of PREN is a down-sampled original input image because large input consumes calculation time. First, The PREN generates a saliency map of a down-sampled image. Then, the NMS Cropping Algorithm obtains the cropping region based on the generated saliency map. The last step is to enlarge the cropping region for generating large size traffic signs.

The detection network consists of three parts which are Feature Pyramid Network (FPN) backbone, Region Proposal Network (RPN), and the classification and boxes regression branches. The architecture of the detection network is shown in Fig. 1. Both of the input image and its corresponding enlarging region are used to train the detection network.

2.2 The Guided Region Enlarge Algorithm

The small objects are hardly detected and classified. We summarized that there are mainly two reasons. The first reason is the convolution and pooling operations of CNN. These operations lead to bad performance in small object detection because the feature maps corresponding to small objects are easily omitted than the feature maps corresponding to large objects. The second reason is that blurred signs take a large proportion of small signs. The blurred signs are harder to detect than visible signs. Also, the poor quality of training samples leads to low testing performance.

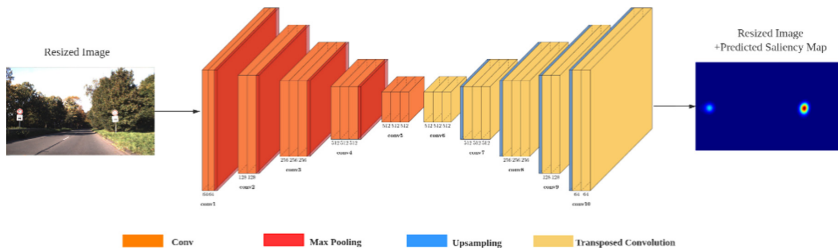


Fig. 2. The architecture of the potential region estimation network (PREN)



Fig. 3. The example of the image and its corresponding ground-truth saliency map.

GREA was designed to tackle these two difficulties above. The solution to the first difficulty is enlarging the potential traffic sign region for extracting more useful small traffic sign features. Moreover, GREA can create a lot of large-and-blurred traffic signs which balance the distribution of traffic signs.

The ground-truth saliency maps (SM) are generated using the ground-truth bounding boxes. Figure 5 shows three examples of predicted saliency map by PREN. The subfigure at the bottom left corner is zoomed in from the rectangular area of each image. It can be seen that PREN can predict traffic sign region accurately. data set. The ground-truth saliency maps are generated based on Gaussian distribution. The mean of the gaussian distribution is the center of a ground-truth bounding box. The σ is the standard deviation of the Gaussian distribution. The w and h are the width and height of the ground-truth bounding box. The example of the ground-truth saliency map is shown in Fig. 3.

$$3\sigma = (3\sigma_x, 3\sigma_y) = \left(\frac{w}{2}, \frac{h}{2}\right)$$

PREN is an encoder-decoder architecture that is shown in Fig. 2. The size of the input image is $256 \times 256 \times 3$ that is the 0.2 times down-sampling image of the TT100k data set image with $2048 \times 2048 \times 3$. The size of the output probability map is $256 \times 256 \times 1$. The encoder includes 13 convolution layers and 4 max-pooling layers. The decoder includes 13 transposed convolution layers and 4 up-sampling layers. The size of kernels is 3×3 with stride 1. The ReLU activations are used after each convolution layer except the last layer of decoder, which uses a sigmoid activation function to range the pixel value in $[0, 1]$. The binary cross entropies (BCE) loss is used in PREN. Figure 5 shows three sets of the predicted saliency map.

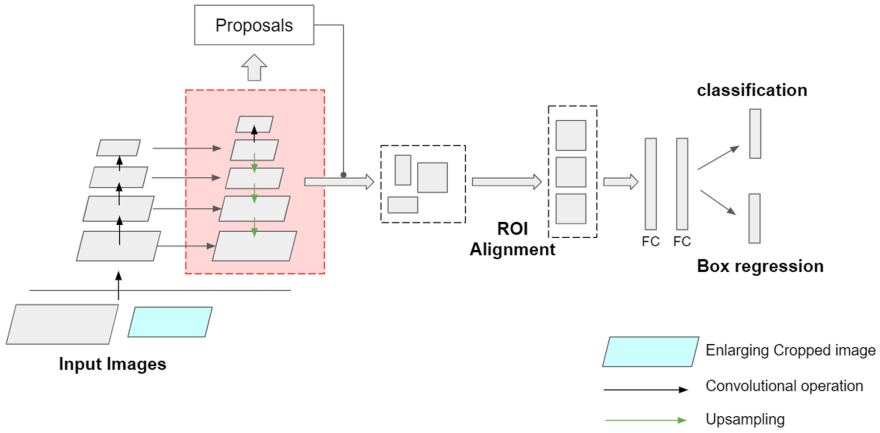


Fig. 4. The architecture of the detection network.

2.3 Non-maximum Suppression Cropping Algorithm

Non-maximum Suppression Cropping Algorithm (NMS-cropping) is proposed in the paper. Based on the predicted SM, NMS-cropping is used to crop the input image with 2048×2048 resolution. The first step is finding all local maximum points (LMP) of a predicted SM. If a pixel value is equal or larger than its neighbors, the pixel is considered as a local maximum point. The set of LMPs is denoted as C . Among all these points in C , there are some of them are noise points. As we observed, the values of the noise points are relatively small. If a point value less than the threshold t , the point is considered as a noise point.

$$t = k \times [\max(C) + \min(C)]$$

k is a hyperparameter that we use $k = 0.2$ in this paper. After the noise removal step, only satisfied points are saved in C .

Then, the edges of the cropping region are computed based on C . The four extreme points (most-top, most-down, most-left, and most-right) of C are chosen as cropping edges. Because most of the local maximum points correspond to the center of a traffic sign, a value e is padded to each edge for cropping a full traffic sign region. e is a random value from 5 to 15. Finally, the cropping region is enlarged by ratio r . The r is a random value from 1 to 3.

3 Detection Network

Based on the predicted probability map by Attention Network, Guided Region Enlarging Algorithm (GREA) generates an enlarged image of various sizes. And, the input image size of the two-stages detector is not fixed, which is an essential character in our proposed system. After comparing the characters of one-stage and two-stages

detector, the two-stages detector with FPN is used in this paper. The architecture of the detection network is shown in Fig. 4.

The Detection Network detects traffic signs in the original image (Input Image 1) and the cropped image (Input Image 2). The backbone of faster RCNN is ResNext-50 that was pre-trained on the coco 2017 train set. FPN is used to combine different semantic level features and predict proposals of different scale objects. The proposed detection network is a two-stages network with a region proposal process, which can be trained in an end-to-end manner.

4 Experiments Setting

4.1 Data Sets

The proposed traffic sign detection mechanism is evaluated over two data sets, the Sweden Traffic Sign Detection (STSD) Data Set [6] and the Tsinghua-Tencent 100k (TT-100k) Data Set [7]. STSD provides two sets (set1 and set2) images with 1280×960 resolution. Each set contains 5 parts. Part 0 is annotated while the other 4 parts are not annotated. Set1Part 0 contains 3,169 images that are used for training. Set2Part0 contains 3,481 images that are used for testing. STSD includes 20 classes in total.

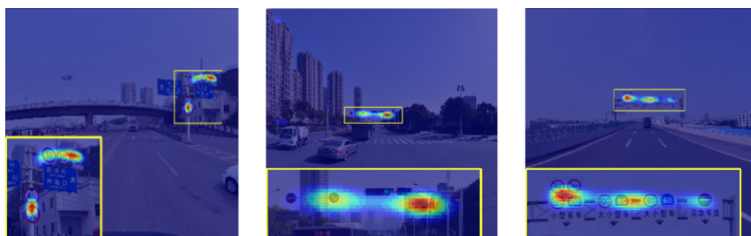


Fig. 5. An illustration of the predicted performance of PREN. The subfigure at the bottom left corner is zoomed in from the rectangular area of each image. It can be seen that PREN can predict traffic sign region accurately.

TT100k provides 6,105 training images and 3,071 test images with 2048×2048 resolution, and it includes 200 classes in total. [4] found that the instance sum of 155 classes is considerable. [4] divided 155 classes into three sub-classes, i.e. mandatory (i), prohibitory (p), and warning (s). To compare with the latest work, this work follows the procedure in [4] and considers also 48 traffic sign classes.

Table 1. The number of traffic signs for different size groups.

| Data set | | Small | Medium | Large | Total |
|----------|-------|-------|--------|-------|-------|
| STSD | Train | 1805 | 1228 | 135 | 3169 |
| | Test | 2327 | 1027 | 128 | 3482 |
| TT100k | Train | 6448 | 8869 | 1167 | 16527 |
| | Test | 3246 | 4284 | 625 | 8190 |

4.2 Implementation Detail

Open MMLab Detection Toolbox and Benchmark (MMDetection) is used to implement our proposed mechanism. The experimental environment is equipped with Intel Core i5-660 @3.30 GHz 4 and 1 Nvidia GeForce Titan 1080Ti GPU with 11 GB memory.

In the training step, PREN and the detection network are trained separately. PREN has been pre-trained on SALICON [12] data set for extracting saliency features better. Then, PREN is trained at pixel-level to predict the saliency map. The AdaGrad optimization algorithm with 0.0003 initial learning rate is employed to train the PREN. The batch size is set to 32. The detection network uses ResNeXt50 as the backbone network, which has been pre-trained on COCO [13]. Then, the network is trained in 20 epochs. The original images set is trained in the first epoch, then the partial enlarging images set is trained in the second epoch. The network is trained by the original images set and the partial enlarging images set alternately. Five anchor scales [16, 32, 64, 128, 256] for P2–P6 are used. Three anchor ratios [0.5, 1, 2] are used. Positive labels are assigned to the anchors with the Intersection-over-Union (IoU) large than 0.7. Negative labels are assigned to the anchors with IoU smaller than 0.3. The initial learning rate is 0.001, and it is decreased at the 15th epoch to 1/10 of the initial learning rate. The Stochastic Gradient Descent (SGD) optimization algorithm with 0.9 momentum is employed. The batch size is set to 2 during training STSD, and the batch size is set to 1 in TT100k because of the limited memory of GPU. In the evaluation step, a threshold of 0.6 is used for the confidence score. The Non-Maximum Suppression (NMS) is used to reduce the redundancy of predicted boxes. Because several traffic signs are overlapping is rare in the real world, a low IOU threshold of 0.2 of NMS is used in our work.

Table 2. Performance comparison of STSD dataset.

| Model | Metric (%) | Small | Medium | Large | Total |
|------------------------------|------------|-------------|-------------|-------------|-------------|
| Faster RCNN + FPN (baseline) | Recall | 57.1 | 83.9 | 76.6 | 69.5 |
| | Precision | 78.6 | 94.9 | 87.7 | 85 |
| | F1 score | 66.2 | 89 | 81.8 | 76.5 |
| | mAP | 41.1 | 83.1 | 90.8 | 57.6 |
| Baseline + GREa (ours) | Recall | 58.0 | 87.5 | 81.0 | 70.4 |
| | Precision | 83.3 | 95.4 | 90.8 | 88.2 |
| | F1 score | 68.4 | 91.2 | 85.6 | 78.3 |
| | mAP | 44.3 | 86.0 | 93.9 | 61.7 |

5 Experimental Result and Analysis

This section presents the experimental results of the proposed detector on two data sets. Previous works [6] use two regular matrices (Precision and Recall) and [9] only provided the graph of Area-under-Curve (AUC) to evaluate the performance of a traffic sign detector. We found out that these 3 regular matrices cannot comprehensively evaluate the performance of a detector. Therefore, except for 3 regular matrices, we also use mean Average Precision (mAP) to evaluate the proposed detector.

To prove the effectiveness of our proposed GREA in different scales, traffic signs are divided into three size groups: small (0, 32), medium (32, 96), and large (96, 200).

This section presents the experimental results of the proposed detector on two data sets. Several previous works generally use 3 regular matrices to evaluate the performance of a traffic sign detector, including precision, recall, F1 score. We found out that these 3 regular matrices cannot comprehensively evaluate the performance of a detector. Therefore, except for 3 regular matrices, we also use mean Average Precision (mAP) to evaluate the proposed detector.

To prove the effectiveness of our proposed GREA in different scales, traffic signs are divided into three size groups: small (0, 32), medium (32, 96), and large (96, 200).

Table 3. Performance comparison of TT100k dataset.

| Model | Metric (%) | Small | Medium | Large | Total |
|------------------------------|------------|-------------|-------------|-------------|-------------|
| Faster RCNN + FPN (baseline) | Recall | 84.6 | 91.3 | 89.3 | 92.9 |
| | Precision | 82.4 | 92.9 | 90.8 | 89 |
| | F1 score | 83.5 | 92.1 | 90 | 90.9 |
| | mAP | 74.3 | 95.2 | 95.2 | 89.5 |
| Baseline + GREA (ours) | Recall | 83.6 | 92.3 | 91.9 | 93.1 |
| | Precision | 85.1 | 94.4 | 93.7 | 91 |
| | F1 score | 84.3 | 93.3 | 92.8 | 92.1 |
| | mAP | 76.3 | 96.5 | 96.5 | 90.4 |

5.1 Performance on STSD Data Set

Table 2 summarizes the detector performance on STSD by comparing 4 evaluation matrices for 3 different size groups. Compared with the baseline model with 10 epochs, adding 10 epoch GREA module improves the mAP of the baseline model by 4.0 and 2.9 in terms of the small and medium group. Compared with the baseline model with 20 epochs, replacing 10 epochs by the GREA module also improves the mAP of the baseline model by 3.2 and 2.9 in terms of the small and medium group. Also, all evaluation matrices of the baseline model are increased by using the GREA module in terms of total traffic signs. Table 2 demonstrates that the GREA module can enhance the performance of the baseline detector. Compared to baseline with 10 epochs, the small group precision and the large group mAP decrease 0.2 and 1.5, respectively. The value of decreasing precision is minor. As shown in Table 1, there are 150 traffic signs

in large groups on STSD. We doubt that there are not sufficient samples to prove the efficiency of GREA in the large group. Also, three other matrices are improved significantly by 2.5, 2.9, and 2.7 in terms of precision, recall, and F1-measure. To further demonstrate the adaptability of the GREA in large traffic signs, the experimental results of a larger data set TT100k are provided in Table 3.

5.2 Performance on TT100k Data Set

As shown in Table 1, TT100k is larger and more balance than STSD. Table 3 summarizes the detector performance on TT100k. All of the evaluation matrices are improved significantly. The recall values of our approach outperform the baseline model by 1.1, 0.4, and 1.5 in small, medium, and large groups, respectively, and by 0.9 in total. It proves that our approach increases the proportion of ground truth traffic signs being detected. The precision values of our approach outperform the baseline model by 1.1, 0.8, and 2.7 in small, medium, and large groups, respectively, and by 1.0 in total. It proves that our approach increases the proportion of all the detected examples that are positive ground truth. Different from the experimental result on STSD, even the precision of the small group and the mAP of the large group achieve 1.1 and 2.2 improvement. It shows that the GREA module also helps detector learn features of large traffic signs. The experimental result of TT100k demonstrates the superior performance of the proposed method. The efficiency of our approach is discussed in Table 4. Because GREA is only used in the training step, the computation time is not increased during the test. Also, the proposed method is faster than [6] and [10].

Table 4. Efficiency comparison on the TT100k dataset.

| Method | Time (ms) |
|--|-----------|
| TrafficSign & light detection [9] | 15 |
| TT-100k Benchmark [6] | 4081 |
| Multi-scale recurrent attention network [10] | 600 |
| Faster RCNN + FPN (ours) | 345 |
| Faster RCNN + FPN + GREA (ours) | 345 |

6 Conclusion

Focus on the two main difficulties of traffic sign detection, an accurate and efficient traffic sign detection architecture is proposed in the paper. The proposed GREA can be served as a data augmentation algorithm for traffic sign detection. Therefore, the proposed architecture only used in the training step, the computation time in the test step is not increased. Experimental results demonstrate the efficiency of the proposed GREA module.

References

1. Chen, T., Lu, S.: Accurate and efficient traffic sign detection using discriminative AdaBoost and support vector regression. *IEEE Trans. Veh. Technol.* **65**(6), 4006–4015 (2016)
2. Ren, S., He, K., Girshick, R., Sun, J.: Faster R-CNN: towards real-time object detection with region proposal networks. In: *Proceedings of the NIPS*, pp. 91–99 (2015)
3. Dai, J., Li, Y., He, K., Sun, J.: R-FCN: object detection via region-based fully convolutional networks. In: *Proceedings of the NIPS*, pp. 379–387 (2016)
4. Liu, W., et al.: SSD: single shot multibox detector. In: Leibe, B., Matas, J., Sebe, N., Welling, M. (eds.) *ECCV 2016*. LNCS, vol. 9905, pp. 21–37. Springer, Cham (2016). https://doi.org/10.1007/978-3-319-46448-0_2
5. Lin, T., Dollar, P., Girshick, R., He, K., Hariharan, B., Belongie, S.: Feature pyramid networks for object detection. In: *Proceedings of the CVPR*, pp. 2117–2125 (2017)
6. Li, J., Liang, X., Wei, Y., Xu, T., Feng, J., Yan, S.: Perceptual generative adversarial networks for small object detection. In: *Proceedings of the CVPR*, pp. 1951–1959 (2017)
7. Larsson, F., Felsberg, M.: Using Fourier descriptors and spatial models for traffic sign recognition. In: Heyden, A., Kahl, F. (eds.) *SCIA 2011*. LNCS, vol. 6688, pp. 238–249. Springer, Heidelberg (2011). https://doi.org/10.1007/978-3-642-21227-7_23
8. Zhu, Z., Liang, D., Zhang, S., Huang, X., Li, B., Hu, S.: Traffic sign detection and classification in the wild. In: *Proceedings of the CVPR* (2016)
9. Pon, A., Andrienko, O., Haraken, A., Waslander, S.: A hierarchical deep architecture and mini-batch selection method for joint traffic sign and light detection. In: *Proceedings of the CRV*, pp. 122–130 (2018)
10. Tian, Y., Gelenter, J., Wang, X., Li, J., Yu, Y.: Traffic sign detection using a multi-scale recurrent attention network. *IEEE Trans. Intell. Transp. Syst.* **20**(12), 4466–4475 (2019)
11. Ou, Z., Xiao, F., Xiong, B., Shi, S., Song, M.: FAMN: feature aggregation multipath network for small traffic sign detection. *IEEE Access* **7**, 178798–178810 (2020)
12. Jiang, M., Huang, S., Duan, J., Zhao, Q.: SALICON: saliency in context (2015)
13. Lin, T.-Y., et al.: Microsoft COCO: common objects in context. In: Fleet, D., Pajdla, T., Schiele, B., Tuytelaars, T. (eds.) *ECCV 2014*. LNCS, vol. 8693, pp. 740–755. Springer, Cham (2014). https://doi.org/10.1007/978-3-319-10602-1_48



Plant Leaf Recognition Network Based on Feature Learning and Metric Learning

Hongwei Yang^{1(✉)}, Di Wu^{1(✉)}, Changan Yuan², Xiao Qin³,
Hongjie Wu^{4,5}, Xingming Zhao^{6,7}, and Zhongqiu Zhao⁸

¹ Institute of Machine Learning and Systems Biology, School of Electronics and Information Engineering, Tongji University, Shanghai, China
1830805@tongji.edu.cn

² Guangxi Academy of Science, Nanning 530025, China

³ School of Computer and Information Engineering,
Nanning Normal University, Nanning 530299, China

⁴ School of Computer Science and Technology, Soochow University,
Suzhou 215006, China

⁵ School of Electronic and Information Engineering, Suzhou University
of Science and Technology, Suzhou 215009, China

⁶ Institute of Science and Technology for Brain Inspired Intelligence (ISTBI),
Fudan University, Shanghai 200433, China

⁷ Key Laboratory of Computational Neuro-Science and Brain-Inspired
Intelligence, Ministry of Education, Shanghai, China

⁸ College of Computer Science and Information Engineering,
Hefei University of Technology, Hefei 230009, China

Abstract. Plant image recognition is an important thing for protecting plants, protecting the environment, and protecting nature. Recently, most models in the field of plant leaf recognition make classification after extracting global features. In this paper, we propose a plant leaf recognition model based on metric learning. Metric learning calculates the similarity of the extracted feature vectors to obtain the distance between different sample features, so as to determine whether similar pictures belong to the same category, and then achieve the classification effect. In this study, feature triplet are used for metric learning, and the loss function we used is triplet-loss.

Keywords: ResNet · Triplet-loss · Metric-learning · Global feature · Multi-task

1 Introduction

In the traditional plant identification industry, it is manual identification, which is a very difficult thing for the relevant operators, and the huge identification workload will lead to the decline of recognition accuracy. For the staff, it is very difficult to maintain the recognition accuracy at a certain level. At this time, the development of computer vision technology has brought great benefits to plant recognition. Using deep learning to recognize the plant image, only need to collect the relevant plant leaf image data, carry out the corresponding processing, put it into the built neural network for training,

after reaching a certain recognition accuracy, the trained network can be used for plant image recognition, and the recognition accuracy can always be kept at a very high level. This is a great innovation for the traditional plant image recognition method. Using computer technology can solve many problems in recognition. With the development of technology, even some recognition technology using deep learning can surpass the accuracy of human beings, so the popularization of plant image recognition technology will be around the corner.

Because of the particularity of the plant leaf data set, the number of pictures in each category is too small. It is not appropriate to use the general CNN to extract the global features and classify them. Therefore, we propose a method based on metric learning for plant leaf recognition.

Metric learning is a traditional machine learning method commonly used in face recognition, which is proposed by Eric Xing in nips 2002. It can be divided into two kinds: one is metric learning through linear transformation, the other is metric learning through nonlinear change. Its basic principle is to learn the metric distance function for a specific task according to different tasks. Later, metric learning was transferred to the field of text classification, especially for the text processing of high-dimensional data.

2 Dataset

We use ICL plant leaf data set. The ICL plant leaf data set was organized by the Institute of machine learning and systems biology, Tongji University, and was established in cooperation with Hefei botanical garden. The data set contains 407 kinds of plant leaf images, and each kind of plant contains 60–90 pictures, as shown in Fig. 1:

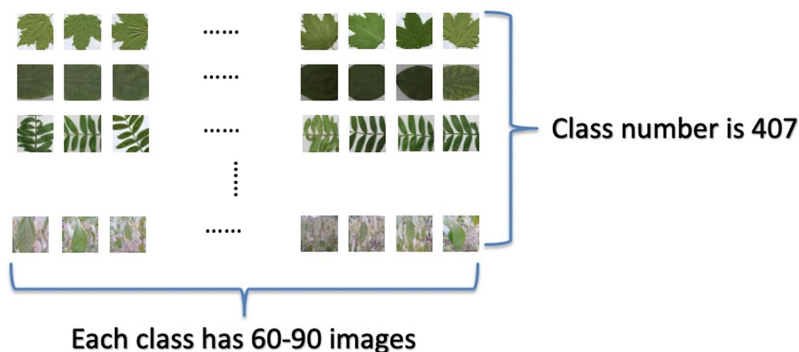


Fig. 1. The ICL dataset

The amount of single category data in the data set is very small. If the data is classified directly, the training effect will be very poor or over fitted due to the small amount of training data. Therefore, data preprocessing is needed. At the same time, because the image size in the data set is not uniform, if not, there is no way to train.

The image size in the original data set cannot be unified due to the environment and other factors during the shooting process. Therefore, before the training, the image size needs to be unified in advance. The method of times is to scale the image, the shortest side of the image to 224 pixel length, and the other side to scale according to the same scale. After all the images in the dataset are operated above, the image size has not been unified, but one of the edges is unified to 224. Next, carry out the clipping operation. After the previous operation, the edge length of the image is $224 * X$. in the top left, top right, bottom left, bottom right and the middle five positions of the image, respectively, intercept $160 * 160$ size pictures. After such interception, five $160 * 160$ size pictures are obtained, so that the work of unified picture format is completed. And in the subsequent operation, if you need the corresponding size of the plant picture, you can directly operate the $160 * 160$ size picture.

3 Triplet-Loss

The purpose of metric learning is to reduce the ternary loss as much as possible in the training iteration, that is to say, the closer anchor and positive are, the better anchor and negative are [4]. When the margin value is smaller, the loss tends to 0, so anchor and positive do not need to pull too close, anchor and negative do not need to pull too far, which can make the loss quickly approach 0. The result of this training can not distinguish the similar images very well. When the anchor is larger, it is necessary to make the network parameters desperately close the distance between anchor and positive, and the distance between anchor and negative. If the margin value is set too large, it is likely that the last loss will remain a large value, which is difficult to approach 0. Therefore, it is very important to set a reasonable margin value, which is an important index to measure the similarity. In short, the smaller the margin value is, the closer the loss tends to be to 0, but it is difficult to distinguish similar images. The larger the margin value is, the more difficult the loss value is to approach 0, even leading to network non convergence, but it can be more confident to distinguish more similar images. The loss function expression of triplet loss is as follows:

$$\sum_i^N [\|f(x_i^a) - f(x_i^p)\|_2^2 - \|f(x_i^a) - f(x_i^n)\|_2^2 + \alpha]_+ \quad (1)$$

Where $\|f(x_i^a) - f(x_i^p)\|_2^2$ is the Euclidean distance between positive samples and anchor, and $\|f(x_i^a) - f(x_i^n)\|_2^2$ is the Euclidean distance between negative samples and anchor. α means that there is a minimum gap between the distance between x-a and x-n and between x-a and x-p. In addition, the distance here is measured by Euclidean distance, $+$ means that when the value in $[\]$ is greater than zero, the value is taken as loss, and when it is less than zero, the loss is zero. When the distance between x-a and x-n is less than the distance between x-a and x-p Plus, the value in $[\]$ is greater than zero, resulting in loss. When the distance between x-a and x-n is \geq the distance between x-a and x-p Plus, the loss is zero.

4 Architecture of Deep Fusion Model

The proposed model focuses on two aspects: feature representation and feature learning [3]. It is based on two complementary designs, as follows: 1) global representation and metric representation; 2) recognition branch based on softmax and sorting branch with triplet loss.

In common multi classification tasks, softmax can achieve a certain classification effect. However, if softmax is used in the case of a large number of categories, but a single category has a small number of samples, the effect will be very poor, because the parameter update of the classification matrix is actually learning the central vector representation of each category, and the insufficient number of samples will lead to a medium. The result shows that the learning is not enough, the distance between different categories is not obvious, and the classification effect is greatly reduced. Recently, it is proposed to add a temperature (t) parameter to softmax, as follows:

$$\alpha(z)_j = \frac{e^{\frac{z_j}{t}}}{\sum_i^N e^{\frac{z_i}{t}}} \quad j = 1, 2, 3, \dots, N \quad (2)$$

The parameter t controls the degree of aggregation of softmax loss function. The larger the parameter t is, the more decentralized the output of softmax will be, and the output of dimensions corresponding to the target category will be allocated to other dimensions to achieve a smooth effect. The smaller the parameter t is, the output of dimensions corresponding to the target category will be more aggregated, and the output of dimensions corresponding to other categories will be smaller, So as to achieve the effect of expanding the distance between classes.

By setting the t parameter, it can effectively alleviate the phenomenon of poor classification effect caused by too small space between classes. However, in the extreme case of data set, the t parameter can't effectively control the space between classes, so it can't achieve good classification effect. In this case, it is necessary to use metric learning to control the distance between different classes.

In recent years, most of the plant leaf recognition models focus on the classification method based on softmax. However, most of the plant leaves have very high similarity. It is difficult to use softmax directly to separate the distance between different categories, which leads to the phenomenon of poor effect in the actual classification process [2]. The model proposed in this paper uses global features to directly classify, at the same time, it introduces metric learning to pull the distance between the positive samples in the data set and the anchor closer and closer, and between the negative samples and the anchor farther and farther, so that in the actual classification, the model can better distinguish the differences between different categories [19]. The model structure is as follows (Fig. 2):

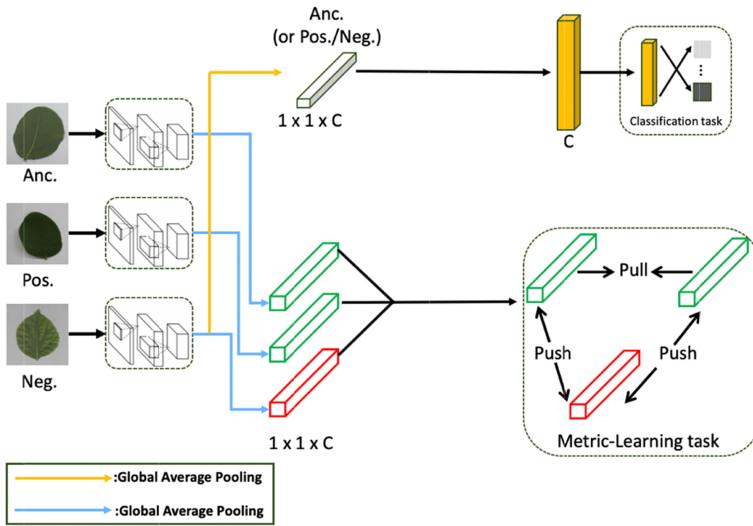


Fig. 2. The architecture of our new model

5 Experiment

5.1 Implementation Details

The model is built on the PyTorch framework. The backbone network is a ResNet-50 model pre-trained on ImageNet, where the global average pool and fully connected layers are discarded. The basic feature extractor is as follows (Fig. 3):

In order to avoid gradient explosion, we use gradient clamping. Adam with fault hyperparameters ($\epsilon = 10^{-8}$, $\beta_1 = 0.9$, $\beta_2 = 0.999$) is used to minimize the loss function [10]. The margin m in Eq. (1) is set to 0.5. Following the general practice of the learning rate attenuation table in [14], we set the initial learning rate to $3e10^{-4}$ and apply the attenuation table to the 100th epoch. The total number of training sessions for all experiments that have been conducted is set to 150.

In the process of training, aiming at the characteristics of metric learning, we adjust the data division during training. Because we use the triplet loss function, the purpose is to reduce the distance between the positive samples and the anchor, and enlarge the distance between the negative samples and the anchor. If we directly randomly select the input pictures to construct the triples, the difficulty of measuring the distance between features will be very small. In order to maximize the difficulty of measuring the distance between features and speed up the network training, in each epoch, we select the most difficult positive sample pair and the most difficult negative sample pair, construct a set of feature triples, and input the triplet loss function to calculate the loss. In this way, the distance between the positive sample and the anchor is the furthest, the distance between the negative sample and the anchor is the closest, and the trained network has the best effect of distinguishing the positive and negative samples, so as to achieve the purpose of improving the classification effect.

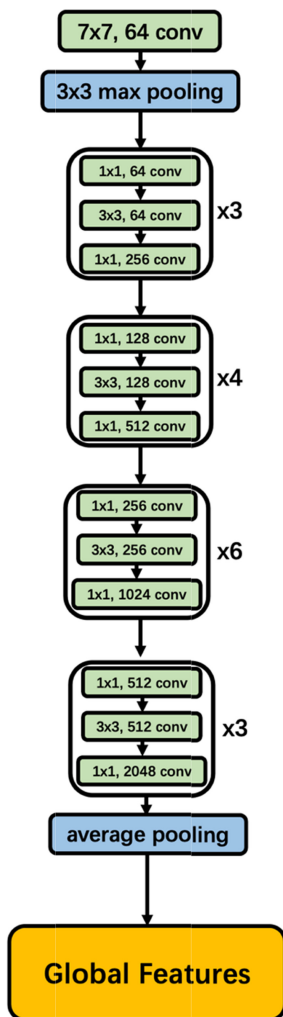


Fig. 3. The feature extractor of our network

5.2 Result

From the table, we can see that the accuracy of traditional CNN plus softmax classification can reach 85%–89%, and after using metric learning, the recognition accuracy is improved by 3%–7%, and the improvement effect is still very obvious as shown in the Table 1. In the test phase, we use the ternary loss branch as the feature descriptor.

Through the experiment results, we can see that the accuracy of using the strategy of basic feature extraction network plus softmax to classify is far lower than using the strategy of feature extraction plus metric learning. Metric learning is often used in face detection and pedestrian detection scenarios. Because there are a large number of similar input images in this kind of data set, simple feature extraction and classification

Table 1. Experimental results on the ICL dataset

| Method | Params (M) | Acc (%) |
|-------------------------------------|------------|---------|
| VGG + SoftMax | 134 | 85.24 |
| DenseNet (k = 12) [6] + SoftMax | 7.0 | 87.30 |
| DenseNet (k = 24) [6] + SoftMax | 27.2 | 89.21 |
| VGG + Metric-Learning | 134 | 90.02 |
| DenseNet (k = 12) + Metric-Learning | 7.0 | 91 |
| DenseNet (k = 24) + Metric-Learning | 27.2 | 92.24 |

can't distinguish the similar and different categories of images. With the addition of metric learning, the distance between the features of different categories is greatly extended, so that the feature distance of similar pictures is small, and that of different categories is large, achieving good classification effect (Table 2).

Table 2. Effectiveness of two branch

| Branch we use | Acc (%) |
|-------------------------------|---------|
| Global feature branch | 85.24 |
| Triplet loss branch | 65.33 |
| Global feature + triplet loss | 89.2 |

Then we carried out ablation experiments on the two branches respectively, including three groups of experiments: using CNN alone for classification, using metric learning classification alone, and using CNN classification and metric learning fusion. From the experimental results, we can see that using CNN alone for classification can achieve a basic accuracy, but the accuracy of using metric learning alone is very low, mainly because metric learning in our model is mainly used to assist CNN for classification, and the effect of using it alone for classification is not good. Therefore, we also choose CNN as the final feature descriptor in the test. The final method of metric learning and CNN fusion achieves the best results.

6 Conclusion

We propose a new type of plant leaf recognition model, which uses global features to directly classify plant leaves, and at the same time, we add a method of metric learning to jointly supervise the network learning of plant leaf features. Through the joint supervision of ternary loss and CNN, when the network parameters are updated, the global features and the distance between the global features will be taken into account, so as to better distinguish the similar plant leaves and achieve better classification effect. Experiments show that our method can improve the recognition accuracy.

Acknowledgements. This work was supported by the grant of National Key R&D Program of China (No. 2018AAA0100100) and partly supported by National Natural Science Foundation of China (Grant nos. 61861146002, 61520106006, 61732012, 61772370, 61702371, 61932008, 61532008, 61672382, 61772357, and 61672203) and China Postdoctoral Science Foundation (Grant no. 2017M611619) and supported by “BAGUI Scholar” Program and the Scientific & Technological Base and Talent Special Program, GuiKe AD18126015 of the Guangxi Zhuang Autonomous Region of China and supported by Shanghai Municipal Science and Technology Major Project (No. 2018SHZDZX01), LCNBI and ZJLab.

References

1. Varior, R.R., Shuai, B., Lu, J., Xu, D., Wang, G.: A siamese long short-term memory architecture for human re-identification. In: Leibe, B., Matas, J., Sebe, N., Welling, M. (eds.) ECCV 2016. LNCS, vol. 9911, pp. 135–153. Springer, Cham (2016). https://doi.org/10.1007/978-3-319-46478-7_9
2. Bai, X., Yang, M., Huang, T., Dou, Z., Yu, R., Xu, Y.: Deep-person: learning discriminative deep features for person re-identification. arXiv: Computer Vision and Pattern Recognition (2017)
3. Xiao, T., Li, S., Wang, B., Lin, L., Wang, X.: Joint detection and identification feature learning for person search. In: Computer Vision and Pattern Recognition, pp. 3376–3385 (2017)
4. Wu, D., Zheng, S., Yuan, C., Huang, D.: A deep model with combined losses for person re-identification. *Cogn. Syst. Res.* **54**, 74–82 (2018)
5. Wang, X.F., Huang, D.S., Xu, H.: An efficient local Chan-Vese model for image segmentation. *Pattern Recogn.* **43**(3), 603–618 (2010)
6. Huang, G., Liu, Z., et al.: Densely connected convolutional networks. In: Proceedings of the IEEE Conference on Computer Vision and Pattern Recognition, vol. 1, no. 2 (2017)
7. Li, B., Huang, D.S.: Locally linear discriminant embedding: an efficient method for face recognition. *Pattern Recogn.* **41**(12), 3813–3821 (2008)
8. Huang, D.S.: Systematic Theory of Neural Networks for Pattern Recognition. Publishing House of Electronic Industry of China, Beijing (1996)
9. Huang, D.S., Du, J.-X.: A constructive hybrid structure optimization methodology for radial basis probabilistic neural networks. *IEEE Trans. Neural Netw.* **19**(12), 2099–2115 (2008)
10. Hinton, G.E., Salakhutdinov, R.R.: Reducing the dimensionality of data with neural network. *Science* **313**(5786), 504–507 (2006)
11. Won, Y., Gader, P.D., Coffield, P.C.: Morphological shared-weight networks with applications to automatic target recognition. *IEEE Trans. Neural Netw.* **8**(5), 1195–1203 (1997)
12. Serre, T., Riesenhuber, M., Louie, J., Poggio, T.: On the role of object-specific features for real world object recognition in biological vision. In: Bühlhoff, H.H., Wallraven, C., Lee, S.-W., Poggio, T.A. (eds.) BMCV 2002. LNCS, vol. 2525, pp. 387–397. Springer, Heidelberg (2002). https://doi.org/10.1007/3-540-36181-2_39
13. Huang, D.S.: Radial basis probabilistic neural networks: model and application. *Int. J. Pattern Recogn. Artif. Intell.* **13**(7), 1083–1101 (1999)
14. Wang, X.-F., Huang, D.S.: A novel density-based clustering framework by using level set method. *IEEE Trans. Knowl. Data Eng.* **21**(11), 1515–1531 (2009)

15. Shang, L., Huang, D.S., Du, J.-X., Zheng, C.-H.: Palmprint recognition using Fast ICA algorithm and radial basis probabilistic neural network. *Neurocomputing* **69**(13–15), 1782–1786 (2006)
16. Zhao, Z.-Q., Huang, D.S., Sun, B.-Y.: Human face recognition based on multiple features using neural networks committee. *Pattern Recogn. Lett.* **25**(12), 1351–1358 (2004)
17. Simonyan, K., Zisserman, A.: Very deep convolutional networks for large-scale image recognition. arXiv preprint [arXiv:1409.1556](https://arxiv.org/abs/1409.1556) (2014)
18. Srivastava, R.K., Greff, K., Schmidhuber, J.: Training very deep networks. In: *Advances in Neural Information Processing Systems* (2015)
19. He, K., et al.: Deep residual learning for image recognition. In: *Proceedings of the IEEE Conference on Computer Vision and Pattern Recognition* (2016)
20. Huang, D.S., Zhao, W.-B.: Determining the centers of radial basis probabilistic neural networks by recursive orthogonal least square algorithms. *Appl. Math. Comput.* **162**(1), 461–473 (2005)
21. Huang, D.S.: Application of generalized radial basis function networks to recognition of radar targets. *Int. J. Pattern Recognit. Artif. Intell.* **13**(6), 945–962 (1999)
22. Huang, D.S., Ma, S.D.: Linear and nonlinear feedforward neural network classifiers: a comprehensive understanding. *J. Intell. Syst.* **9**(1), 1–38 (1999)



Position Attention-Guided Learning for Infrared-Visible Person Re-identification

Yong Wu¹, Sizhe Wan¹(✉), Di Wu¹, Chao Wang¹, Changan Yuan²,
Xiao Qin³, Hongjie Wu⁴, and Xingming Zhao⁵

¹ Institute of Machine Learning and Systems Biology, School of Electronics
and Information Engineering, Tongji University, Shanghai 201804, China

wuyong_tj@163.com, wsz9781@163.com

² Guangxi Academy of Science, Nanning 530025, China

³ School of Computer and Information Engineering,
Nanning Normal University, Nanning 530299, China

⁴ School of Electronic and Information Engineering, Suzhou University
of Science and Technology, Suzhou 215009, China

⁵ Institute of Science and Technology for Brain Inspired Intelligence (ISTBI),
Fudan University, Shanghai 200433, China

Abstract. Infrared-Visible person re-identification is a challenging and fundamental task of associating the same person across visible and thermal cameras. Most of the studies focus on improving the global features to address the cross-modality issue, thus, some discriminative local and salient features are ignored by the deep models. A novel deep architecture named Dual-path Local Information Structure (DLIS) with Position Attention-guided Learning Module (PALM) is proposed to address the cross-modality issue for Infrared-Visible PREID task. The DLIS has two individual branches which contains a visible stream and an infrared stream to extract modality sharable features. The PALM can capture long-range dependencies and enhance the discriminative local feature representations to form the final feature descriptors. To supervise the network extracting discriminative features to shrink the margin of different modalities, the proposed model is conducted the joint supervision of cross-entropy loss function and hetero-center loss function. Compared with the recent studies, the proposed methods achieve the state-of-the-art on the two benchmark datasets including SYSU-MM01 and RegDB dataset.

Keywords: Deep learning · Infrared-visible person re-identification · Cross-modality · Dual-path structure · Position attention-guided

1 Introduction

Person re-identification (PREID) is the core technology of multi-target tracking in disjoint cameras, is widely used in public security and intelligent video surveillance [1, 2]. With the rapid development of deep learning and neural network technology [3–6, 10–12, 16, 17, 20–22, 26, 27, 41, 42, 46, 47], most of current works pay more attention to identify the specific pedestrian on visible camera module [7–9, 13–15]. However, the pedestrian images captured by the cameras are single-channel infrared modality which

lose rich color features under low lighting conditions. Due to the huge gap between RGB images and infrared images, the traditional methods of matching RGB images can not address the problem effectively. In addition, the channel and spectrum between RGB and infrared images have large differences, making the cross-modality PReID to be a challenging task.

To meet these challenges, some methods have been proposed for the cross-modality PReID community. Wu et al. [18] contributed a cross-modality PReID dataset called SYSU-MM01 and proposed a deep zero-padding model to address the cross-modality issue. A generative adversarial network (GAN) training method proposed by Dai et al. [19] named cmGAN by jointed of triplet loss and cross-entropy loss which tries to learn discriminative feature representations for different modalities matching. Ye et al. [23] proposed a deep model called TONE by two-stream CNN architecture and hierarchical cross-modality metric learning (HCML) to learn discriminative features in a hierarchical manner. Based on the hierarchical feature representations learning strategy, Ye et al. [24] proposed a two-stream deep model for feature extracting with a bi-directional dual constrained top-ranking (DCTR) loss for similarity metric to ensure the learnt feature representations.

However, most of the current methods focus on improving the global features to address the above-mentioned issues. Some discriminative local feature representations are ignored by most deep models, such as the type of clothes or the style of the shoes. The local feature representations have significant discriminability and are not affected by the cross-modality modes. In addition, attention mechanism [30–32] is widely used in many computer vision tasks such as PReID. Li et al. [33] introduced a framework called Harmonious Attention CNN (HA-CNN), which jointed the soft pixel and hard regional attentions to ensure the feature representation learning. A Mask-Guided Contrastive Attention Model (MGCAM) is proposed in [34], eliminating the impact of background and training with a triplet loss by Multi-Scale Context-Aware Network (MSCAN).

Based on these observations, in this work, we propose a deep model called Dual-path Local Information Structure (DLIS) which learns the share specific feature representations to address the issues. The dual path network has two individual branches which contains a visible stream and an infrared stream to extract modality sharable features. The ResNet50 [46] model is adopted as the backbone network in each branch, which extracts the global features of the pedestrians. Besides, we propose a Position Attention-guided Learning Module (PALM) to enhance the discriminative local feature representations and achieve excellent recognition performance. The attention mechanism we proposed can force the model extracting the local feature representations rather than the global information only from the cross-modality images to form the final feature descriptors. We split the feature maps learned by the two branches into several stripes for local information learning. Extensive experiments demonstrate that our method achieves state of the art performance on two public and challenging datasets including SYSU-MM01 and RegDB.

The main contributions can be summarized as follows:

- (1) We present an architecture called Dual-path Local Information Structure (DLIS) to learn share specific feature representations. The experiments demonstrate that DLIS achieves excellent performance for Infrared-Visible PReID community.
- (2) We propose a novel attention mechanism named Position Attention-guided Learning Module (PALM) to capture long-range dependencies and enhance the discriminative local feature representations of heterogenous modality. The module can capture specific position information and extract modality local features to form discriminative feature descriptors.
- (3) Compared with the recent studies, the proposed model achieves the state-of-the-art on the two benchmark and challenging datasets including SYSU-MM01 and RegDB dataset.

2 Related Work

Most of current studies present a cross-modality matching deep model in RGB domains. Due to the large gap between RGB domains and infrared domains, many works have been proposed to address the cross-modality matching problem.

Wu et al. [18] firstly provided the cross-modality PReID dataset named SYSU-MM01 and proposed a deep zero-padding architecture for the cross-modality retrieval issue. A GAN model termed as cmGAN proposed by [19] which contained a generator and a discriminator. The purpose of the generator in cmGAN was to extract features of the two modalities, then feed the extracted features into the discriminator to distinguish the input modality. Ye et al. [23] proposed a deep two-stream CNN architecture termed as TONE. The TONE model trained by jointed supervision of cross-entropy loss and contrastive loss for reducing the cross-modality variations. Based on the TONE model trained with hierarchical metric learning, Ye et al. [24] proposed a dual path end-to-end deep model trained with a dual-constrained top-ranking (DCTR) loss to learn the final discriminative feature representations. A dual-level discrepancy reduction learning (D^2RL) method proposed by [25] to deal with the modality and appearance discrepancies separately. The model firstly unified the image representations by using the image-level conversion. The appearance discrepancy is then reduced by the feature-level dual-path network.

The part-level information may contain more fine-grained and discriminative features in PReID studies. To name just a few, for Part-based Convolution Baseline (PCB) [28], it divided the feature map into several stripes equally, aimed to learn the part-level local representations features for PReID task. Wang et al. [29] proposed a stripe-based model called Multiple Granularities Network (MGN), which divided the input image into multiple stripes for extracting discriminative local feature representations in multiple granularities manner.

3 Proposed Method

We will introduce the model of our proposed framework and methods for infrared-visible PREID task in this section, as shown in Fig. 1. The proposed model mainly composed of three components: (1) Dual-path local information structure (DLIS), (2) Position attention-guided learning module (PALM), (3) Cross-entropy loss and Hetero-center loss.

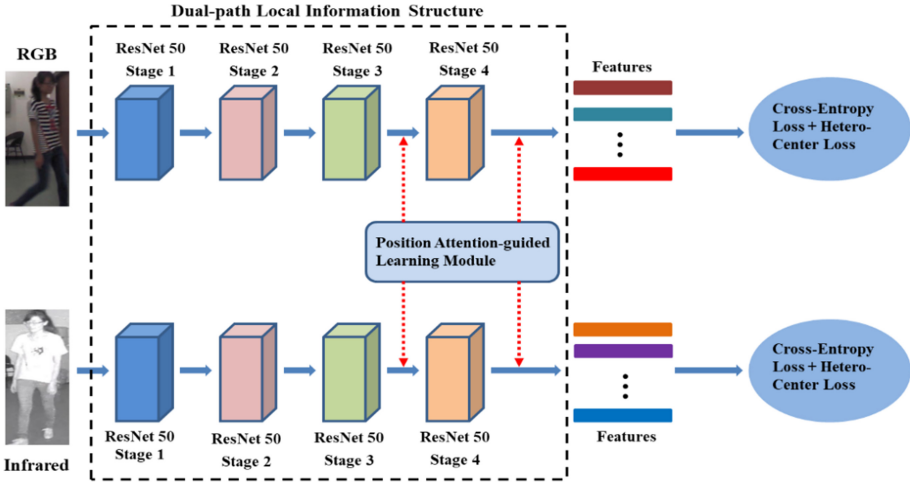


Fig. 1. The overall architecture for the proposed model. We adopt ResNet50 network as the backbone. The Dual-path Local Information Structure (DLIS) is composed of two shared ResNet50 networks, used to extract modality sharable features. The Position attention-guided learning module force the model to extract specific position information and capture modality local features. The proposed model is trained by cross-entropy loss and hetero-center loss.

3.1 Dual-Path Local Information Structure

We adopt a dual-path local information structure to extract the cross-modality person features, including a visible path and an infrared path. It can be observed that ResNets can achieve competitive performance in many visual tasks, thus, we adopt two ResNet50 networks as the backbone in each path respectively, which extract the modality-specific person features independently. As shown in Fig. 1, ResNet50 pre-trained model is mainly composed of four res-convolution modules which named Stage1, Stage2, Stage3 and Stage4. The res-convolution modules are independent in the dual-path structure for extracting the modality-specific person features, addressing the cross-modality variations issue.

Global feature representation learning is the primary choice which extracted the global information for each person. However, these methods may cause the salient and informative features losing issue. Inspired by [28, 35], we adopted the method of

dividing the feature map into multiple stripes to ensure the local feature representations corresponding to the body parts.

3.2 Position Attention-Guided Learning Module (PALM)

Inspired by [36, 37], we design a novel attention learning block which named Position Attention-guided Learning Module (PALM). The PALM can capture long-range dependencies and enhance the local representation capability for Infrared-Visible PReID task. The details of PALM as shown in Fig. 2. In the convolutional layer, the feature map which the number of channels, height and width are C , H , W , respectively. We first feed the feature map into the convolution layers with 1×1 convolution operator to generate new feature maps θ , ϕ , g , respectively, where $\{\theta, \phi, g\} \in \mathbb{R}^{\frac{C}{2} \times H \times W}$. Then we flatten the new three feature maps. Then we multiply the tensor θ and the tensor ϕ to obtain the feature F by a matrix multiplication operation. Analogously, the feature Y is obtained by a matrix multiplication between the tensor F and g . Finally, we perform an element-wise addition with the input feature to obtain the output feature.

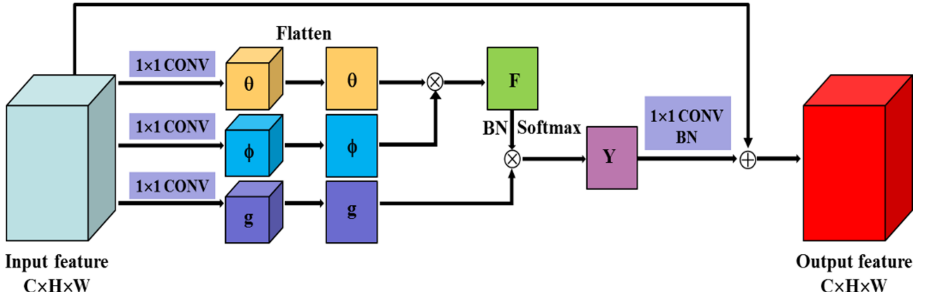


Fig. 2. The details of Position Attention-guided Learning Module (PALM). \otimes is matrix multiplication. \oplus represents element-wise addition. 1×1 CONV and BN represents the feature extraction layer with 1×1 convolution operator and Batch normalization, respectively.

3.3 Loss Functions

Since cross-modality PReID task can be considered as an image retrieval problem, we focus on the similarity of features learned by the dual-path structure to extract the modality-shared features. Thus, the purpose of the model in the training phase are to bridge the cross-modality and intra-modality gaps to capture the modality-shared features and improve the cross-modality similarity. However, most of the loss functions cannot perform the model to learn the modality-shared features. The cross-entropy loss (CE loss) is adopted for each path to learn the modality-specific features for classification. The CE loss function can be formulated as:

$$L_{CE} = - \sum_{n=1}^N \log \frac{e^{W_{y_n}^T x_n + b_{y_n}}}{\sum_{i=1}^I e^{W_i^T x_n + b_i}} \quad (1)$$

where N represent the batch size and W_i represent the i^{th} column of the weights, and b denote the bias term. I denote the number of identities. x_n denotes the n th visible and infrared features belonging to the y th class.

However, to further shrink the margin of different modalities in each class, the Hetero-Center (HC) loss [35] is used for supervising the model to extract discriminative feature representation to improve the cross-modality similarity. Hetero-Center (HC) loss can penalize the center distance and constrain the gap between two modality feature distributions. Hetero-Center (HC) loss is formulated as:

$$L_{HC} = \sum_{m=1}^M \left[\|C_{m,1} - C_{m,2}\|_2^2 \right] \quad (2)$$

where $C_{m,1} = \frac{1}{V} \sum_{n=1}^V X_{m,1,n}$ and $C_{m,2} = \frac{1}{I} \sum_{n=1}^I X_{m,2,n}$ represent the centers of feature representations of visible images and infrared images in the i th class. V and I denote the numbers of visible images and infrared images belonging to the i th class. M is the number of classes.

4 Experiments

4.1 Dataset Description

SYSU-MM01 [18] is the first large-scale dataset which consisting of four visible cameras and two infrared cameras in the field of Infrared-Visible PReID task. The images are collected from the indoor and outdoor environments. It contains a total of 287,628 RGB images and 15,792 infrared images. There are 395 identities which includes 22,258 RGB images and 11,909 infrared images in the training set. The test set contains 96 identities with 3,803 infrared images as the query set and 301 RGB images for the gallery. RegDB is captured by dual-camera systems [47]. It contains 8,240 images in total and 412 identities which 206 identities for training and 206 identities for testing. Each identity contains 10 different RGB images and 10 different infrared images. Two evaluation modes are adopted in the RegDB dataset, one is Visible to Thermal and the other is Thermal to Visible search mode. The evaluation metrics which including Cumulative Matching Characteristics (CMC) and mean Average Precisions (mAP) are applied in all experiments. Examples of two benchmark datasets are shown in Fig. 3.

4.2 Implementation Details

All experiments are performed based on Pytorch with two TITAN XP GPUs. We adopt the ResNet50 pre-trained network as the backbone. All the images are resized to 288×144 . Random erasing and horizontal random flipping methods are used for data augmentation. The initial learning rate is set to 0.01 and the momentum is set to 0.9. The learning rate is decreased by 0.1 at the 30th epoch and 60th epoch. The batch size is set to 64 and the feature map is equally split into six stripes. The quantity of identity set to four in a batch which each identity includes eight RGB images and eight infrared images.



Fig. 3. Examples from the SYSU-MM01 and RegDB benchmarks.

4.3 Comparison with State-of-the-Art Methods

We compare the proposed model with other state of-the-art methods, including HOG [38], LOMO [39], Two-stream [18], Zero-Padding [18], TONE [23], TONE+HCML [23], BCTR [24], BDTR [24], cmGAN [19], D²RL [25], AlignGAN [40], CMGN [43], HC Loss [35], JSIA-ReID [44], XIV [45].

Table 1. State-of-the-art comparisons on SYSU-MM01 under all-search single-shot mode

| Methods | Publication | Rank-1 | Rank-10 | Rank-20 | mAP |
|------------------------|---------------|--------------|--------------|--------------|--------------|
| HOG [38] | CVPR 2005 | 2.76 | 18.25 | 31.91 | 4.24 |
| LOMO [39] | CVPR 2015 | 3.64 | 23.18 | 37.28 | 4.53 |
| Two-stream [18] | ICCV 2017 | 11.65 | 47.99 | 65.50 | 12.85 |
| Zero-Padding [18] | ICCV 2017 | 14.80 | 54.12 | 71.33 | 15.95 |
| TONE [23] | AAAI 2018 | 12.52 | 50.72 | 68.60 | 14.42 |
| TONE+HCML [23] | AAAI 2018 | 14.32 | 53.16 | 69.17 | 16.16 |
| BCTR [24] | IJCAI 2018 | 16.12 | 54.90 | 71.47 | 19.15 |
| BDTR [24] | IJCAI 2018 | 17.01 | 55.43 | 71.96 | 19.66 |
| cmGAN [19] | IJCAI 2018 | 26.97 | 67.51 | 80.56 | 27.80 |
| D ² RL [25] | CVPR 2019 | 28.90 | 70.60 | 82.40 | 29.20 |
| AlignGAN [40] | ICCV 2019 | 42.40 | 85.00 | 93.70 | 40.70 |
| CMGN [43] | Neurocom 2020 | 27.21 | 68.19 | 81.76 | 27.91 |
| HC Loss [35] | Neurocom 2019 | 56.96 | 91.50 | 96.82 | 54.95 |
| JSIA-ReID [44] | AAAI 2020 | 38.10 | 80.70 | 89.90 | 36.90 |
| XIV [45] | AAAI 2020 | 49.92 | 89.79 | 95.96 | 50.73 |
| Ours | – | 59.03 | 93.03 | 97.77 | 57.21 |

We evaluate our proposed model on SYSU-MM01 dataset under all-search single-shot mode. The comparative results on Rank- n ($n = 1, 10, 20$) accuracy and mAP of our model against other methods on SYSU-MM01 are shown in Table 1. It can be seen that the proposed model can achieve Rank-1 accuracy 59.03%, Rank-10 accuracy 93.03%, Rank-20 accuracy 97.7%, and mAP 57.21% performance. Moreover, compared with the XIV [45] network, which adopted a two-stream deep model to extract discriminative features, we improve the performance from 49.92% to 59.03% in Rank-1 accuracy. Similarly, compared with the HC Loss [35], our proposed architecture improves mAP accuracy from 54.95% to 57.21%.

Table 2. State-of-the-art comparisons on RegDB with Visible to Thermal mode

| Methods | Publication | Rank-1 | Rank-10 | mAP |
|------------------------|---------------|--------------|--------------|--------------|
| HOG [38] | CVPR 2005 | 13.49 | 33.22 | 10.31 |
| LOMO [39] | CVPR 2015 | 0.85 | 2.47 | 2.28 |
| Two-stream [18] | ICCV 2017 | 12.43 | 30.36 | 13.42 |
| Zero-Padding [18] | ICCV 2017 | 17.75 | 34.21 | 18.90 |
| TONE [23] | AAAI 2018 | 16.87 | 34.03 | 14.92 |
| TONE+HCML [23] | AAAI 2018 | 24.44 | 47.53 | 20.80 |
| BCTR [24] | IJCAI 2018 | 32.67 | 57.64 | 30.99 |
| BDTR [24] | IJCAI 2018 | 33.47 | 58.42 | 31.83 |
| D ² RL [25] | CVPR 2019 | 43.40 | 66.10 | 44.10 |
| AlignGAN [40] | ICCV 2019 | 57.90 | – | 53.60 |
| CMGN [43] | Neurocom 2020 | 35.13 | 61.07 | 32.14 |
| HC Loss [35] | Neurocom 2019 | 83.00 | – | 72.00 |
| JSIA-ReID [44] | AAAI 2020 | 48.50 | – | 49.30 |
| XIV [45] | AAAI 2020 | 62.21 | 83.13 | 60.18 |
| Ours | – | 86.36 | 96.12 | 76.10 |

We further evaluate our model on RegDB dataset with visible to thermal training mode. As shown in Table 2, we achieve Rank-1 accuracy 86.36%, Rank-10 accuracy 96.12%, and mAP 76.10% performance. Compared with the HC Loss [35] model which used part-level method with the jointed supervision of CE loss and HC loss, our proposed model improves the Rank-1 accuracy from 83% to 86.36% and mAP accuracy from 72% to 76.10%, which further demonstrates the effectiveness of the proposed model.

5 Conclusion

In this work, we propose a novel Dual-path Local Information Structure with the Position Attention-guided Learning Module to learn share specific feature representations and enhance the discriminative local feature representations of heterogenous

modality for cross-modality PReID task. The DLIS has two individual branches which contains a visible stream and an infrared stream to extract modality sharable features. The PALM can extract the discriminative local features and achieve superior performance to form the final feature descriptors. To supervise the network extracting discriminative features to shrink the margin of different modalities, we conduct the joint supervision of cross-entropy loss and hetero-center loss. The proposed methods achieve the state-of-the-art on the two benchmark datasets including SYSU-MM01 and RegDB dataset.

Acknowledgements. This work was supported by the grant of National Key R&D Program of China (No. 2018AAA0100100) and partly supported by National Natural Science Foundation of China (Grant nos. 61861146002, 61520106006, 61772370, 61702371, 61732012, 61932008, 61532008, 61672382, 61672203, and 61772357) and China Postdoctoral Science Foundation (Grant no. 2017M611619) and supported by “BAGUI Scholar” Program and the Scientific & Technological Base and Talent Special Program, GuiKe AD18126015 of the Guangxi Zhuang Autonomous Region of China and supported by Shanghai Municipal Science and Technology Major Project (No.2018SHZDZX01), LCNBI and ZJLab.

References

1. Ye, M.: Deep learning for person re-identification: a survey and outlook (2020)
2. Wu, D.: Deep learning-based methods for person re-identification: a comprehensive review. *Neurocomputing* **337**, 354–371 (2019)
3. Wang, X.F., Huang, D.S., Xu, H.: An efficient local Chan-Vese model for image segmentation. *Pattern Recogn.* **43**(3), 603–618 (2010)
4. Li, B., Huang, D.S.: Locally linear discriminant embedding: an efficient method for face recognition. *Pattern Recogn.* **41**(12), 3813–3821 (2008)
5. Zhao, Z.Q., Glotin, H., Xie, Z., Gao, J., Wu, X.: Cooperative sparse representation in two opposite directions for semi-supervised image annotation. *IEEE Trans. Image Process. (TIP)* **21**(9), 4218–4231 (2012)
6. Huang, D.S., Du, J.-X.: A constructive hybrid structure optimization methodology for radial basis probabilistic neural networks. *IEEE Trans. Neural Netw.* **19**(12), 2099–2115 (2008)
7. Qian, X., Fu, Y., Xiang, T., Jiang, Y.-G., Xue, X.: Leader-based multi-scale attention deep architecture for person re-identification. *IEEE Trans. Pattern Anal. Mach. Intell.* **42**, 371–385 (2019)
8. Wu, Y., Zhang, K., Wu, D.: Person re-identification by multi-scale feature representation learning with random batch feature mask. *IEEE Trans. Cogn. Dev. Syst.* (2020). <https://doi.org/10.1109/tcds.2020.3003674>
9. Wu, D.: Omnidirectional feature learning for person re-identification. *IEEE Access* **7**, 28402–28411 (2019)
10. Wang, X.F., Huang, D.S.: A novel density-based clustering framework by using level set method. *IEEE Trans. Knowl. Data Eng.* **21**(11), 1515–1531 (2009)
11. Shang, L., Huang, D.S., Du, J.-X., Zheng, C.-H.: Palmprint recognition using fast ICA algorithm and radial basis probabilistic neural network. *Neurocomputing* **69**(13–15), 1782–1786 (2006)
12. Zhao, Z.Q., Huang, D.S., Sun, B.-Y.: Human face recognition based on multiple features using neural networks committee. *Pattern Recogn. Lett.* **25**(12), 1351–1358 (2004)

13. Dai, Z.: Batch DropBlock network for person re-identification and beyond. In: Proceedings of the IEEE International Conference on Computer Vision (2019)
14. Wu, D., Zheng, S., Yuan, C., Huang, D.: A deep model with combined losses for person re-identification. *Cogn. Syst. Res.* **54**, 74–82 (2018)
15. Wu, D., Zheng, S.J., Bao, W.Z.: A novel deep model with multi-loss and efficient training for person re-identification. *Neurocomputing* **324**(9), 69–75 (2018)
16. Huang, D.S., Ip, H.H.S., Chi, Z.-R.: A neural root finder of polynomials based on root moments. *Neural Comput.* **16**(8), 1721–1762 (2004)
17. Huang, D.S.: A constructive approach for finding arbitrary roots of polynomials by neural networks. *IEEE Trans. Neural Netw.* **15**(2), 477–491 (2004)
18. Wu, A.: RGB infrared cross modality person re identification. In: Proceedings of the IEEE International Conference on Computer Vision, pp. 5380–5389 (2017)
19. Dai, P., Ji, R.: Cross modality person re identification with generative adversarial training. In: Proceedings of International Joint Conference on Artificial Intelligence, pp. 677–683 (2018)
20. Huang, D.S., Ip, H.H.S., Law, K.C.K., Chi, Z.: Zeroing polynomials using modified constrained neural network approach. *IEEE Trans. Neural Netw.* **16**(3), 721–732 (2005)
21. Huang, D.S., Ip, H.H.S., Law, K.C.K., Chi, Z., Wong, H.S.: A new partitioning neural network model for recursively finding arbitrary roots of higher order arbitrary polynomials. *Appl. Math. Comput.* **162**(3), 1183–1200 (2005)
22. Huang, D.S., Zhao, W.-B.: Determining the centers of radial basis probabilistic neural networks by recursive orthogonal least square algorithms. *Appl. Math. Comput.* **162**(1), 461–473 (2005)
23. Ye, M., Lan, X., Li, J.: Hierarchical discriminative learning for visible thermal person re identification. In: Thirty Second AAAI Conference on Artificial Intelligence (2018)
24. Ye, M., Wang, Z., Lan, X., Yuen, P.C.: Visible thermal person re-identification via dual-constrained top-ranking. In: Proceedings of International Joint Conference on Artificial Intelligence, pp. 1092–1099 (2018)
25. Wang, Z., Wang, Z., Zheng, Y.: Learning to reduce dual level discrepancy for infrared visible person re identification. In: Proceedings of the IEEE Conference on Computer Vision and Pattern Recognition, pp. 618–626 (2019)
26. Huang, D.S., Chi, Z., Siu, W.-C.: A case study for constrained learning neural root finders. *Appl. Math. Comput.* **165**(3), 699–718 (2005)
27. Huang, D.S., Ip, H.H.S., Chi, Z., Wong, H.S.: Dilation method for finding close roots of polynomials based on constrained learning neural networks. *Phys. Lett. A* **309**(5–6), 443–451 (2003)
28. Sun, Y., Zheng, L., Yang, Y., Tian, Q., Wang, S.: Beyond part models: person retrieval with refined part pooling (and a strong convolutional baseline). In: Ferrari, V., Hebert, M., Sminchisescu, C., Weiss, Y. (eds.) ECCV 2018. LNCS, vol. 11208, pp. 501–518. Springer, Cham (2018). https://doi.org/10.1007/978-3-030-01225-0_30
29. Wang, G., Yuan, Y., Chen, X., Li, J., Zhou, X.: Learning discriminative features with multiple granularities for person re-identification. In: 2018 ACM Multimedia Conference on Multimedia Conference, pp. 274–282. ACM (2018)
30. Park, J., Woo, S., Lee, J., Kweon, I.S.: BAM: bottleneck attention module, arXiv: Computer Vision and Pattern Recognition (2018)
31. Woo, S., Park, J., Lee, J.-Y., Kweon, I.S.: CBAM: convolutional block attention module. In: Ferrari, V., Hebert, M., Sminchisescu, C., Weiss, Y. (eds.) ECCV 2018. LNCS, vol. 11211, pp. 3–19. Springer, Cham (2018). https://doi.org/10.1007/978-3-030-01234-2_1
32. Hu, J., Shen, L., Sun, G.: Squeeze-and-excitation networks. In: Proceedings of the IEEE Conference on Computer Vision and Pattern Recognition (CVPR), pp. 7132–7141 (2018)

33. Li, W., Zhu, X., Gong, S.: Harmonious attention network for person re-identification. In: Proceedings of the IEEE Conference on Computer Vision and Pattern Recognition, pp. 2285–2294 (2018)
34. Song, C., Huang, Y., Ouyang, W., Wang, L.: Mask-guided contrastive attention model for person re-identification. In: Proceedings of the IEEE Conference on Computer Vision and Pattern Recognition, pp. 1179–1188 (2018)
35. Zhu, Y., Yang, Z., Wang, L.: Hetero-center loss for cross-modality person re-identification. *Neurocomputing* **386**, 97–109 (2019)
36. Wang, X., Girshick, R., Gupta, A.: Non-local neural networks. In: Proceedings of the IEEE Conference on Computer Vision and Pattern Recognition (2018)
37. Zhu, Z., Xu, M., Bai, S., Huang, T., Bai, X.: Asymmetric non-local neural networks for semantic segmentation. In: Proceedings of the IEEE International Conference on Computer Vision (2019)
38. Dalal, N., Triggs, B.: Histograms of oriented gradients for human detection. In: Proceedings of the IEEE Conference on Computer Vision and Pattern Recognition, pp. 886–893 (2005)
39. Liao, S., Hu, Y., Zhu, X.: Person re-identification by local maximal occurrence representation and metric learning. In: Proceedings of the IEEE Conference on Computer Vision and Pattern Recognition, pp. 2197–2206 (2015)
40. Wang, G., Zhang, T., Cheng, J.: RGB-infrared cross-modality person re-identification via joint pixel and feature alignment. In: Proceedings of the IEEE International Conference on Computer Vision, pp. 3623–3632 (2019)
41. Huang, D.S.: Application of generalized radial basis function networks to recognition of radar targets. *Int. J. Pattern Recogn. Artif. Intell.* **13**(6), 945–962 (1999)
42. Huang, D.S., Ma, S.D.: Linear and nonlinear feedforward neural network classifiers: a comprehensive understanding. *J. Intell. Syst.* **9**(1), 1–38 (1999)
43. Jiang, J., Jin, K., Qi, M., Wang, Q., Wu, J., Chen, C.: A cross-modal multi-granularity attention network for RGB-IR person re-identification. *Neurocomputing* **406**, 59–67 (2020)
44. Wang, G.-A., Zhang, T., Yang, Y.: Cross-modality paired images generation for RGB-infrared person re-identification. In: Thirty-Fourth AAAI Conference on Artificial Intelligence (2020)
45. Li, D., Wei, X., Hong, X., Gong, Y.: Infrared-visible cross-modal person re-identification with an X modality. In: Thirty-Fourth AAAI Conference on Artificial Intelligence (2020)
46. He, K., Zhang, X.: Deep residual learning for image recognition. In: Proceedings of the IEEE Conference on Computer Vision and Pattern Recognition, pp. 770–778 (2016)
47. Nguyen, D.T., Hong, H.G., Kim, K.W.: Person recognition system based on a combination of body images from visible light and thermal cameras. *Sensors* **17**(3), 605 (2017)



A Novel Approach Based on Region Growing Algorithm for Liver and Spleen Segmentation from CT Scans

Berardino Prencipe¹, Nicola Altini¹, Giacomo Donato Cascarano^{1,2},
Andrea Guerriero¹, and Antonio Brunetti^{1,2} (✉)

¹ Polytechnic University of Bari, 70126 Bari, Italy
antonio.brunetti@poliba.it

² Apulian Bioengineering srl, Via delle Violette 14, 70026 Modugno, BA, Italy

Abstract. In this paper, we propose a novel approach to adapt 2D region growing algorithms to volumetric segmentation of liver and spleen from Computed Tomography (CT) scans. Abdominal organ segmentation is an essential and time-consuming task in clinical radiology. The possibility to implement a semi-automatic segmentation system could speed up the time required to label the images and to improve the delineation results, minimizing both intra- and inter-operator variability.

The proposed region growing algorithm exploits an initial seed point to perform the first slice-wise segmentation. Then, starting from this area, all other seeds are automatically discovered taking advantage of two data structures that we called Moving Average Seed Heatmap (MASH) and Area Union Map (AUM). The implemented mechanism avoids the choice of unsuitable seeds and the exclusion of irrelevant organs and tissues from the CT scan.

We assessed the validity of the proposed liver and spleen segmentation method on two publicly available datasets: SLIVER07 and Medical Segmentation Decathlon Task 09 (MSD 09), respectively.

The proposed method allowed us to obtain promising results for both liver and spleen segmentation, with a Dice Coefficient higher than 93% for the liver segmentation task and a Dice Coefficient greater than 92% for the spleen segmentation task on the designated validation sets.

Keywords: Liver segmentation · Spleen segmentation · Region growing

1 Introduction

Computed Tomography (CT) is one of the most important imaging techniques; it is fundamental for surgical planning and for the development of Computer-Aided Diagnosis systems that can support the physicians in the classification of neoplasia [1]. The human abdominal area presents different tissues and organs, like spleen, liver, stomach or kidneys, showing similar intensity values, making their segmentation a complex task. Traditional image processing approaches for biomedical image segmentation involve thresholding algorithms, *i.e.* methods that allow the segmentation of Regions of Interest (ROIs) using different thresholds that can be found through several

techniques, and Region Growing (RG) segmentation techniques, *i.e.* methods that start building the segmentation mask from a set of initial points, called seeds, then adding neighbouring points which are compliant to some homogeneity criteria.

In literature, there is a realm of region growing algorithms suited for the liver segmentation task, including approaches for both 2D and 3D segmentation. Choosing the right inclusion criteria for neighbouring pixels is crucial for obtaining acceptable segmentation performances. Most of the algorithms focus on the definition of proper homogeneity criteria. Gambino *et al.* presented an automatic 3D segmentation method that provides the seed's choice by minimizing an objective function and a homogeneity criterion based on Euclidean distance between the texture features associated to the voxels [2]. Other authors used a homogeneity criterion based on the difference between the already segmented area intensity and the pixel gradient [3, 4] or the pixel intensity [5–7]. Other approaches based on homogeneity criteria can be found in [8, 9]. Other authors focused on the pre-processing phase. In the attempt to resolve the region isolation problem in region growing algorithm, Lakshmipriya *et al.* employed a Non Sub-sampled Contourlet Transform (NSCT) to enhance the liver's edges and a bidirectional region growing algorithm [10]. Rafiei *et al.* focused on the pre-processing phase by using a contrast stretch algorithm and an atlas intensity distribution to create voxel probability maps [11]. Zhou *et al.* developed a semi-automatic liver segmentation algorithm exploiting intensity separation, region growing techniques and the morphological hole-filling operator to refine the segmentation results [12]. Other pre-processing methods can be found in [13, 14]. Elmorsy *et al.* focused on the post-processing phase, where they took advantage of an entropy filter to choose the best structural element to use [15]. Czipczer *et al.* combined a region growing algorithm and the results of a Convolutional Neural Network (CNN) model. To find the seed, they exploited an active contour model, whereas the masks generated by the CNN are refined through the GrowCut algorithm [16]. These two masks are then fused with a logical AND operation to obtain the final mask [17]. Bevilacqua *et al.* applied a pre-processing consisting of contrast enhancement and cropping, followed by local thresholding, extraction of the largest connected component and morphological operators, before of propagating the obtained mask in both directions to reach all the slices [18]. Other approaches including image processing procedures both prior and after the region growing could be found in [19, 20].

Different approaches have been tried in literature for spleen segmentation. Mihaylova *et al.* used the Chan-Vese active contour model to realize an automatic segmentation algorithm. To select the initial contour, they used template matching. After having segmented the area in the first slice, they used this area as initial contour for the following slice [21]. Subsequently, Mihaylova *et al.* presented a multistage approach based on segmentation methods, such as active contours without edges and *k*-means clustering. To define the initial contour, they created two atlas models [22]. Behrad *et al.* combined the features extracted from a neural network with those extracted from the image partitioned with a watershed transform. This process is repeated, varying the parameters of the segmentation algorithm, until the error between the features extracted from the two approaches is very small [23]. Jiang *et al.* used the ISO algorithm to segment the spleen. This algorithm can cause over-segmentation, so they used Principal Component Analysis algorithm to eliminate the muscles that can

cause misclassification [24]. Gauriau *et al.* adopted a multi-object template deformation framework to segment liver, kidneys, spleen and gallbladder, and used a random forest regression algorithm with shape priors to obtain confidence maps for each organ. The shape of each organ is then included in an energy optimization technique that also considers image-derived forces [25]. Reza Soroushmehr *et al.* proposed a slice-wise segmentation algorithm based on the position of ribs and vertebrae to determine the ROI of the spleen. After determining the area in the first slice, its centroid is used as initial spleen location for the following slice [26].

In this work, we propose a novel region growing algorithm to segment the liver and the spleen parenchyma from CT scans. For each of these two organs, the proposed approach requires the manual selection of a seed point; then, all the other seeds are discovered in a fully automatic way for the remaining slices, minimizing the user interaction. We also propose a robust approach for the seed selection phase, by exploiting two utility data structures that we called Moving Average Seed Heatmap (MASH) and Area Union Map (AUM), which also allow preventing the choice of seeds from undesired regions of the CT scan.

Requiring the minimum user interaction as possible, consisting only in the selection of a seed point, and eventually, in the tuning of some parameters, this approach could also be made fully automatic in future works by employing optimization algorithms. For instance, genetic algorithms have proven useful for optimization of Artificial Neural Networks topology [27], treatment planning for radiation therapy [28] and portfolio optimization [29], and can be employed for tuning the parameters of this RG method. Other approaches may be based on the Bayesian framework, for instance, Pan *et al.* proposed a Bayes-Based Region-Growing Algorithm for Medical Image Segmentation [30], whereas other applications for Pattern Recognition can be found in [31–34].

2 Materials and Methods

2.1 Materials

To segment liver parenchyma and to tune the parameters of the region growing algorithm, we exploited the SLIVER07 dataset. It presents a pixel spacing range in x/y -direction varying from 0.55 mm to 0.8 mm and a slice distance varying from 1 mm to 3 mm, depending on the acquisition protocol adopted [35].

For the spleen parenchyma segmentation task, we used the Medical Segmentation Decathlon Task 09 (MSD 09) dataset [36]. The x/y -direction spacing varies from 0.67 mm to 0.97 mm, and the z -direction ranges from 1.6 mm to 8 mm. Since we are mainly interested in applications related to surgical planning, we only considered CT scans with slice distance lesser or equal than 3 mm.

2.2 Region Growing Algorithm

The developed RG algorithm requires the user choosing an initial slice and a seed belonging to the organ region. The initial slice must be chosen among those showing

the largest liver (or spleen) area. Then, the centroid of the segmented area is used as seed for the segmentation of both the previous and the following slices (as done by Chen *et al.* [13]). Pre- and post-processing procedures were performed to filter the input data and to improve the segmentation algorithm, respectively. The algorithm workflow is detailed in the following paragraphs.

Pre-processing. This phase consists of two operations: first, we window the Hounsfield Unit (HU) values of the images in the range $[-150, 350]$ to exclude the irrelevant organs and tissues. Then, we filter the image via a median filter with a 3×3 kernel to reduce the noise.

Segmentation Algorithm. This phase consists of three sub-steps, here detailed, namely: (i) Pre-RG; (ii) Region Growing algorithm; (iii) Post-RG.

Pre-RG. Before launching the segmentation algorithm, we mask the slice with an Area Union Map (AUM) structure. The AUM is initialized with the segmented area of the first segmented slice; then, it is computed as the union of the last ten segmented slices. If there are less than ten slices, AUM is calculated with the available ones only. The AUM allows us to exclude the components having the same intensities range of the considered organ (liver or spleen) but that are not spatially near.

Region Growing Algorithm. We investigated the approach proposed by Edman *et al.*, consisting in the creation of a grey-scale map where the pixels with higher values are closer to the seed from the intensity and spatial distance point of view [37]. The algorithm searches for structures containing the seed with grey-level in the range reported in Eq. (1), where I_{seed} is the intensity of the seed and D is the maximum interval amplitude. The pseudocode for the grey-scale map generation algorithm is reported in Algorithm 1, whereas examples of the ongoing process are shown in Fig. 1.

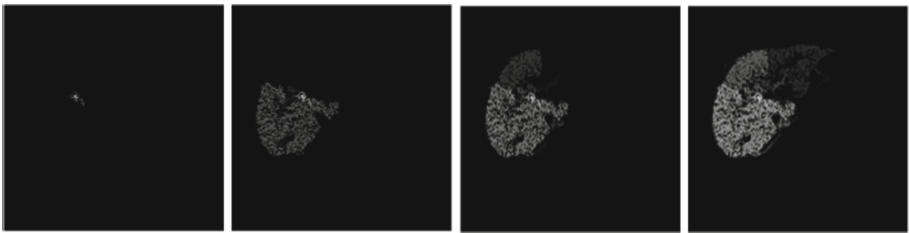


Fig. 1. Grey-scale map algorithm generation: a graphical representation.

$$[I_{seed} - i, I_{seed} + i] \quad \forall i = 1, 2, 3, \dots, D \quad (1)$$

Post-RG. The image obtained from the previous step is a gray-scale map. To obtain the binary mask, we applied the Otsu thresholding. An example is shown in Fig. 2.

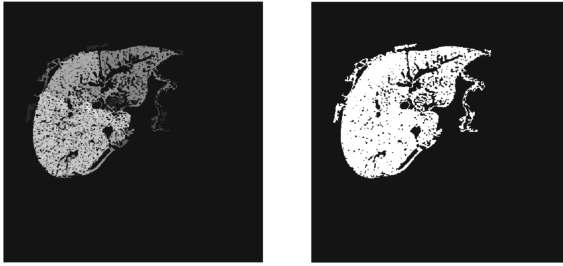


Fig. 2. Example of the application of the Otsu thresholding algorithm to process the grey-scale map (left) to obtain a binary mask (right).

```

function GreyScaleMap(image, seed, D)
Mask = Zeros-Matrix(size(image))
SeedGrayLevel = image(seed(1), seed(2))
for i from 0 to D do
    MaskI = Threshold-Image(image, SeedGrayLevel - D) AND
                NOT(Threshold-Image(image, SeedGrayLevel + D))
    MaskILabel = Label-Connected-Components(MaskI)
    for j from 1 to Max(MaskILabel) do
        ConnectedComponent = Extract-ConnectedComponent(MaskILabel, j)
        if ConnectedComponent(seed(1), seed(2)) == 1 then
            Mask = Mask + ConnectedComponent
        end
    end
end
return Mask

```

Algorithm 1. Grey-scale map generation algorithm pseudocode.

Post-processing. To refine the obtained mask, we applied morphological operators as post-processing. We used a morphological closing with a sphere structuring element with a radius of 4 voxels, a hole filling and a morphological opening with a sphere structuring element with a radius of 5 voxels. Figure 3 shows an example of post-processing results.



Fig. 3. Example of three consecutive slices before and after the post-processing step: (a) images before the post-processing; (b) images after the post-processing. This operation helps to recover from errors during the segmentation phase.

Due to the liver and spleen shape variability among the slices, the generated centroids could fall outside the organ region or, rather, in other undesirable parts (e.g. vessels). We faced this problem by computing the Intersection over Union (IoU), or Jaccard Index, defined in Eq. (2), between the current and the previous slice. A new seed is generated if the IoU is lesser than a threshold IoU_{th} ; otherwise, the seed is accepted. With empirical tests, we discovered that a good value for the IoU_{th} was 0.3.

$$IoU(A, B) = \frac{|A \cap B|}{|A \cup B|} \quad (2)$$

To choose an appropriate seed, we introduced a data structure that we called Moving Average Seed Heatmap (MASH), which allows the determination of the most probable areas where to place the new seed, as shown in Fig. 4. We initialized the MASH with the area of the first segmented slice; then we calculated the following ones according to Eq. (3), where we set $\gamma = 0.6$.

$$MASH_i = \begin{cases} Mask_1 & \text{if } i = 1 \\ \gamma MASH_{i-1} + (1 - \gamma)Mask_i & \text{if } i > 1 \end{cases} \quad (3)$$

The MASH must be updated for all the correctly segmented slices in the volume (N_{slices}), thus $i = 1, \dots, N_{slices}$. A correct segmentation is obtained if $IoU > IoU_{th}$. Otherwise, the MASH is exploited for generating the new seed.



Fig. 4. Example of a MASH. Pixel intensities are correlated with the probability of the corresponding pixel to be selected as seed point for the corresponding slice.

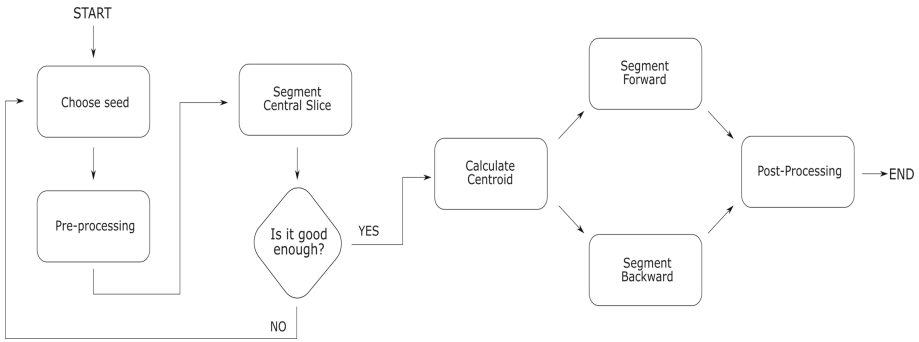


Fig. 5. Algorithm workflow.

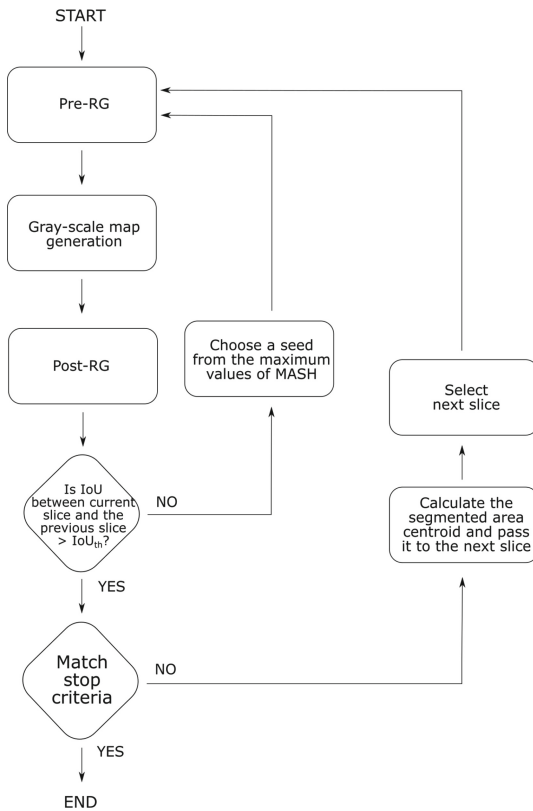


Fig. 6. Slice-wise segmentation flow chart.

The new seed is chosen among the pixels corresponding to the maximum value in the MASH and whose grey-level deviates at most 0.01% from the mean value of the area segmented in the previous slice. This process is repeated up to 200 times and stops

when the IoU between the considered slices reaches at least IoU_{th} . If this condition is not met, the seed is chosen among those pixels which allowed to obtain the highest value of IoU.

The Region Growing stops when the IoU between the area of the slice and the mean of the five previous segmented ones is below IoU_{th} or the current segmented area is lesser than a certain threshold, $Area_{th}$. In the liver case $Area_{th}$ has been set to 2500 pixels, whereas for the spleen it has been set to 1000 pixels. These two values have been found by performing empirical tests. The difference in the threshold areas is due to the different sizes of the two organs. The steps of the previous algorithm for selecting the seed points are represented in the flow-charts reported in Fig. 5 and Fig. 6, respectively.

3 Experimental Evaluation

To evaluate the performance of the presented algorithm, we refer to the metrics defined in the SLIVER07 challenge [35], namely the Volumetric Overlap Error (VOE), the Sørensen–Dice coefficient (DSC), the Relative Volume Difference (RVD), and the measures based on the external surface distance: the Maximum Symmetric Surface Distance (MSSD), also known as Hausdorff distance, and the Average Symmetric Surface Distance (ASSD).

Table 1. Proposed method for liver parenchyma segmentation. Results are expressed as “mean \pm standard deviation”.

| Model | VOE [%] | DSC [%] | RVD [%] | MSSD [mm] | ASSD [mm] |
|-----------------|------------------|------------------|--------------------|-------------------|-----------------|
| RG ($D = 20$) | 16.16 \pm 9.20 | 90.91 \pm 5.91 | -12.18 \pm 11.16 | 48.94 \pm 20.70 | 2.97 \pm 1.83 |
| RG ($D = 25$) | 11.32 \pm 4.10 | 93.95 \pm 2.37 | -3.97 \pm 6.86 | 40.13 \pm 17.83 | 1.95 \pm 0.94 |
| RG ($D = 30$) | 12.56 \pm 7.30 | 93.13 \pm 4.48 | -1.12 \pm 10.94 | 39.26 \pm 17.05 | 2.17 \pm 1.46 |

Table 2. Literature overview for liver parenchyma segmentation. Results are expressed as “mean \pm standard deviation” (when available).

| Model | VOE [%] | DSC [%] | RVD [%] | MSSD [mm] | ASSD [mm] |
|---------------------------------|-----------------|------------------|-----------------|-----------------|-----------------|
| Arjun <i>et al.</i> [3] | N/A | 86.5 | N/A | N/A | N/A |
| Bevilacqua <i>et al.</i> [18] | N/A | 90.6 \pm 2.6 | N/A | N/A | N/A |
| Rafei <i>et al.</i> [11] | N/A | 92.56 | N/A | N/A | N/A |
| Czipczer <i>et al.</i> [17] | 9.51 | 95 | 0.50 | 23.94 | 1.85 |
| Mostafa <i>et al.</i> [5] | N/A | 96.04 | N/A | N/A | N/A |
| LakshmiPriya <i>et al.</i> [10] | 6.11 | 97.04 | N/A | N/A | N/A |
| Kumar <i>et al.</i> [7] | N/A | 97.58 \pm 0.50 | N/A | N/A | N/A |
| Xu <i>et al.</i> [20] | 2.05 \pm 1.30 | N/A | 0.66 \pm 2.04 | 6.88 \pm 6.13 | 0.94 \pm 0.48 |

In Table 1 and Table 3 are reported the results for liver and spleen parenchyma segmentation, respectively. Table 2 and Table 4, instead, report the results from existing literature. We used two CT scans from the SLIVER07 dataset and one CT scan from the MSD 09 dataset to tune the parameters of the algorithm. Then, we used 18 CT scans from the SLIVER07 dataset for assessing the performances for the liver segmentation task, and 9 CT scans from the MSD 09 dataset for assessing the performances for the spleen segmentation task.

Table 3. Proposed method for spleen parenchyma segmentation. Results are expressed as “mean \pm standard deviation”.

| Model | VOE [%] | DSC [%] | RVD [%] | MSSD [mm] | ASSD [mm] |
|-----------------|------------------|------------------|-------------------|------------------|-----------------|
| RG ($D = 20$) | 16.94 \pm 3.98 | 90.69 \pm 2.30 | -14.54 \pm 4.40 | 11.93 \pm 4.76 | 1.27 \pm 0.49 |
| RG ($D = 25$) | 14.95 \pm 3.60 | 91.88 \pm 2.10 | -11.33 \pm 3.89 | 9.79 \pm 2.99 | 1.02 \pm 0.37 |
| RG ($D = 30$) | 14.50 \pm 3.60 | 92.14 \pm 2.09 | -8.70 \pm 3.97 | 11.75 \pm 5.54 | 1.05 \pm 0.43 |

Table 4. Literature overview for spleen parenchyma segmentation. Results are expressed as “mean \pm standard deviation” (when available).

| Model | DSC [%] | ASSD [mm] |
|-------------------------------------|------------------|-------------|
| Mihaylova <i>et al.</i> [21] | 79.83 | N/A |
| Behrad <i>et al.</i> [23] | 93.97 \pm 2.27 | N/A |
| Gauriau <i>et al.</i> [25] | 87 \pm 15 | 2.6 \pm 3 |
| Reza Soroushmehr <i>et al.</i> [26] | 97.3 | N/A |

For the liver parenchyma segmentation, the proposed algorithm reached the best performance with $D = 25$ obtaining the best DSC, VOE, MSSD and ASSD results. For the spleen parenchyma segmentation, we note that the best configuration among those proposed is that with $D = 30$, which has a mean DSC value greater than 92%. In both cases, the results are comparable with the literature, some of which present a more complex segmentation process. For the spleen parenchyma segmentation, we note that the proposed approach consents to improve the existing results for ASSD, by obtaining a mean ASSD of 1.02 mm, with a standard deviation of 0.37 mm. Figure 7 shows some examples for both liver parenchyma segmentation and spleen parenchyma segmentation task.

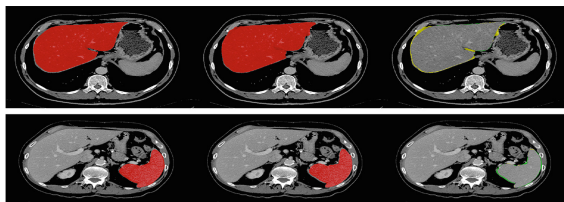


Fig. 7. Example of liver (top) and spleen (bottom) parenchyma segmentation: (left) ground truth; (center) prediction; (right) difference between prediction and ground truth, where the green label indicates the false negatives and the yellow label indicates the false positives. (Color figure online)

4 Conclusion

In this paper, we proposed a novel approach to adapt 2D Region growing algorithms to volumetric segmentation of liver and spleen. We introduced two data structures which have proven to be useful for our approach: the Moving Average Seed Heatmap (MASH) and the Area Union Map (AUM). These data structures, taking into account information from the slices previously segmented, allowed us to find an appropriate seed even when the centroid of the previous segmented slice is not appropriate, and to prevent the choice of the seed from undesired parts of the CT scan.

We validated the proposed algorithm on the SLIVER07 dataset and on the Medical Segmentation Decathlon Task 09 dataset, obtaining a Dice coefficient greater than 93% and 92% for liver and spleen segmentation, respectively. The obtained results are comparable with those attained in literature with more sophisticated methods.

To summarize, the proposed method, compared to the existing literature has many advantages. It could be applied extended to any 3D continuous and homogeneous region segmentation. In this paper, we analyze two applications: liver and spleen segmentation from CT scans, but there could be many other scenarios in which such an algorithm can be useful. It introduces useful bookkeeping data structures, which allows performing a 3D segmentation in a 2D slice-wise fashion. The possibility to break up a computationally complex problem as 3D segmentation into 2D segmentation is very important to permit the application of the algorithm also on large 3D images as abdominal CT scans. The proposed method is semi-automatic, involving the manual selection of a slice and a seed point from which starting the segmentation process. Future studies could focus on turning the method into a fully automatic one, by implementing an automatic seed selection algorithm, and the analysis of the slice-wise region growing segmentation also in the other axes.

References

1. Brunetti, A., Carnimeo, L., Trotta, G.F., Bevilacqua, V.: Computer-assisted frameworks for classification of liver, breast and blood neoplasias via neural networks: a survey based on medical images. *Neurocomputing* **335**, 274–298 (2019). <https://doi.org/10.1016/j.neucom.2018.06.080>
2. Gambino, O., Vitabile, S., Lo Re, G., La Tona, G., Librizzi, S., Pirrone, R., et al.: Automatic volumetric liver segmentation using texture based region growing. In: *CISIS 2010 - 4th International Conference on Complex, Intelligent and Software Intensive Systems*, pp. 146–152 (2010). <https://doi.org/10.1109/cisis.2010.118>
3. Arjun, P., Monisha, M.K., Mullaiyarasi, A., Kavitha, G.: Analysis of the liver in CT images using an improved region growing technique. In: *2015 International Conference on Industrial Instrumentation and Control (ICIC)*, pp. 1561–1566 (2015)
4. Lu, X., Wu, J., Ren, X., Zhang, B., Li, Y.: The study and application of the improved region growing algorithm for liver segmentation. *Optik (Stuttg)* **125**, 2142–2147 (2014)
5. Mostafa, A., Elfattah, M.A., Fouad, A., Hassanien, A.E., Hefny, H., Kim, T.H.: Region growing segmentation with iterative K-means for CT liver images. In: *Proceedings - 2015 4th International Conference on Advanced Information Technology and Sensor Application, AITS 2015*, pp. 88–91 (2016). <https://doi.org/10.1109/aits.2015.31>
6. Arica, S., Avşar, T.S., Erbay, G.: A plain segmentation algorithm utilizing region growing technique for automatic partitioning of computed tomography liver images. In: *2018 Medical Technologies National Congress TIPTEKNO 2018*, pp. 8–11 (2018). <https://doi.org/10.1109/tiptekno.2018.8597108>
7. Kumar, S.S., Moni, R.S., Rajeesh, J.: Automatic segmentation of liver and tumor for CAD of liver. *J. Adv. Inf. Technol.* **2**, 63–70 (2011)
8. Yan, Z., Wang, W., Yu, H., Huang, J.: Based on pre-treatment and region growing segmentation method of liver. In: *2010 3rd International Congress on Image and Signal Processing*, pp. 1338–1341 (2010)
9. Huang, J., Qu, W., Meng, L., Wang, C.: Based on statistical analysis and 3D region growing segmentation method of liver. In: *2011 3rd International Conference on Advanced Computer Control*, pp. 478–482 (2011)
10. LakshmiPriya, B., Jayanthi, K., Pottakkat, B., Ramkumar, G.: Liver segmentation using bidirectional region growing with edge enhancement in NSCT domain. In: *2018 IEEE International Conference on System, Computation, Automation and Networking (ICSCA)*, pp. 1–5 (2018)
11. Rafiei, S., Karimi, N., Mirmahboub, B., Najarian, K., Felfeliyan, B., Samavi, S., et al.: Liver segmentation in abdominal CT images using probabilistic atlas and adaptive 3D region growing. In: *2019 41st Annual International Conference of the IEEE Engineering in Medicine and Biology Society (EMBC)*, pp. 6310–6313 (2019)
12. Zhou, Z., Xue-Chang, Z., Si-Ming, Z., Hua-Fei, X., Yue-Ding, S.: Semi-automatic liver segmentation in CT images through intensity separation and region growing. *Procedia Comput. Sci.* **131**, 220–225 (2018). <https://doi.org/10.1016/j.procs.2018.04.206>
13. Chen, Y., Wang, Z., Zhao, W., Yang, X.: Liver segmentation from CT images based on region growing method. In: *2009 3rd International Conference on Bioinformatics and Biomedical Engineering*, pp. 1–4 (2009)
14. Gaber, T., Hassanien, A.E., El-Bendary, N., Dey, N. (eds.): *The 1st International Conference on Advanced Intelligent System and Informatics (AISIS 2015)*, November 28–30, 2015, Beni Suef, Egypt. AISC, vol. 407. Springer, Cham (2016). <https://doi.org/10.1007/978-3-319-26690-9>

15. Elmorsy, S.A., Abdou, M.A., Hassan, Y.F., Elsayed, A.: K3. A region growing liver segmentation method with advanced morphological enhancement. In: 2015 32nd National Radio Science Conference (NRSC), pp. 418–425 (2015)
16. Vezhnevets, V., Konouchine, V.: GrowCut- interactive multi-label N-D image segmentation by cellular automata. In: GraphiCon 2005 - International Conference on Computer Graphics and Vision, Proceedings (2005)
17. Czipczer, V., Manno-Kovacs, A.: Automatic liver segmentation on CT images combining region-based techniques and convolutional features. In: 2019 International Conference on Content-Based Multimedia Indexing (CBMI), pp. 1–6 (2019)
18. Bevilacqua, V., Brunetti, A., Trotta, G.F., Dimauro, G., Elez, K., Alberotanza, V., et al.: A novel approach for Hepatocellular Carcinoma detection and classification based on triphasic CT Protocol. In: 2017 IEEE Congress on Evolutionary Computation, CEC 2017 - Proceedings (2017). <https://doi.org/10.1109/cec.2017.7969527>
19. Bevilacqua, V., et al.: Synthesis of a neural network classifier for hepatocellular carcinoma grading based on triphasic CT images. In: Santosh, K.C., Hangarge, M., Bevilacqua, V., Negi, A. (eds.) RTIP2R 2016. CCIS, vol. 709, pp. 356–368. Springer, Singapore (2017). https://doi.org/10.1007/978-981-10-4859-3_32
20. Xu, L., Zhu, Y., Zhang, Y., Yang, H.: Liver segmentation based on region growing and level set active contour model with new signed pressure force function. *Optik (Stuttg)* **202**, 163 (2020). <https://doi.org/10.1016/j.ijleo.2019.163705>
21. Mihaylova, A., Georgieva, V.: Spleen segmentation in MRI sequence images using template matching and active contours. *Procedia Comput. Sci.* **131**, 15–22 (2018)
22. Mihaylova, A., Georgieva, V., Petrov, P.: Multistage approach for automatic spleen segmentation in MRI sequences. *Int. J. Reason. Intell. Syst.* **12**, 128 (2020). <https://doi.org/10.1504/IJRIS.2020.106806>
23. Behrad, A., Masoumi, H.: Automatic spleen segmentation in MRI images using a combined neural network and recursive watershed transform. In: 10th Symposium on Neural Network Applications in Electrical Engineering, pp. 63–67 (2010)
24. Jiang, H., Ma, Z., Zhang, B., Zhang, Y.: A spleen segmentation method based on PCA-ISO. In: 2011 6th International Conference on Computer Sciences and Convergence Information Technology (ICCIT), pp. 928–933 (2011)
25. Gauriau, R., Ardori, R., Lesage, D., Bloch, I.: Multiple template deformation application to abdominal organ segmentation. In: 2015 IEEE 12th International Symposium on Biomedical Imaging (ISBI), pp. 359–362 (2015)
26. Sorousmehr, S.M.R., Davuluri, P., Molaei, S., Hargraves, R.H., Tang, Y., Cockrell, C.H., et al.: Spleen segmentation and assessment in CT images for traumatic abdominal injuries. *J. Med. Syst.* **39**, 87 (2015)
27. Bevilacqua, V., Mastronardi, G., Menolascina, F., Pannarale, P., Pedone, A.: A novel multi-objective genetic algorithm approach to artificial neural network topology optimisation: the breast cancer classification problem. In: The 2006 IEEE International Joint Conference on Neural Network Proceedings, pp. 1958–1965. IEEE (2006). <https://doi.org/10.1109/ijcnn.2006.246940>
28. Bevilacqua, V., Mastronardi, G., Piscopo, G.: Evolutionary approach to inverse planning in coplanar radiotherapy. *Image Vis. Comput.* **25**, 196–203 (2007). <https://doi.org/10.1016/j.imavis.2006.01.027>
29. Bevilacqua, V., Pacelli, V., Saladino, S.: A novel multi objective genetic algorithm for the portfolio optimization. In: Huang, D.-S., Gan, Y., Bevilacqua, V., Figueroa, J.C. (eds.) ICIC 2011. LNCS, vol. 6838, pp. 186–193. Springer, Heidelberg (2011). https://doi.org/10.1007/978-3-642-24728-6_25

30. Pan, Z., Lu, J.: A Bayes-based region-growing algorithm for medical image segmentation. *Comput. Sci. Eng.* **9**, 32–38 (2007). <https://doi.org/10.1109/MCSE.2007.67>
31. Cordella, L.P., De Stefano, C., Fontanella, F., Scotto di Freca, A.: A weighted majority vote strategy using Bayesian networks. In: Petrosino, A. (ed.) *ICIAP 2013*. LNCS, vol. 8157, pp. 219–228. Springer, Heidelberg (2013). https://doi.org/10.1007/978-3-642-41184-7_23
32. De Stefano, C., Fontanella, F., Scotto di Freca, A.: A novel Naive Bayes voting strategy for combining classifiers. In: *2012 International Conference on Frontiers in Handwriting Recognition*, pp. 467–472. IEEE (2012). <https://doi.org/10.1109/icfhr.2012.166>
33. De Stefano, C., Fontanella, F., Marrocco, C., di Freca, A.S.: A hybrid evolutionary algorithm for Bayesian networks learning: an application to classifier combination. In: Di Chio, C., et al. (eds.) *EvoApplications 2010*. LNCS, vol. 6024, pp. 221–230. Springer, Heidelberg (2010). https://doi.org/10.1007/978-3-642-12239-2_23
34. Paviglianiti, A., Randazzo, V., Pasero, E., Vallan, A.: Noninvasive arterial blood pressure estimation using ABPNet and VITAL-ECG. In: *2020 IEEE International Instrumentation and Measurement Technology Conference (I2MTC)*, pp. 1–5 (2020)
35. Heimann, T., Van Ginneken, B., Styner, M.A., Arzhaeva, Y., Aurich, V., Bauer, C., et al.: Comparison and evaluation of methods for liver segmentation from CT datasets. *IEEE Trans. Med. Imaging* **28**, 1251–1265 (2009). <https://doi.org/10.1109/TMI.2009.2013851>
36. Simpson, A.L., Antonelli, M., Bakas, S., Bilello, M., Farahani, K., van Ginneken, B., et al.: A large annotated medical image dataset for the development and evaluation of segmentation algorithms (2019)
37. Edman, M.: Segmentation using a region growing algorithm. *Insight J.* 5672, 0–2 (2007)

Information Security



A Novel Approach of Steganalysis to Deal with Steganographic Algorithm Mismatch

Pengfei Shi^(✉), Donghui Hu^(✉), Yuchen Li^(✉), Shuli Zheng^(✉),
and Zhongqiu Zhao^(✉)

College of Computer Science and Information Engineering,
Hefei University of Technology, Hefei 230009, China
s624166801@126.com, {hudh, z.zhao}@hfut.edu.cn,
lyc4481341888@gmail.com, zsl251@163.com

Abstract. Steganalysis is the art to detect the hiding information introduced by the algorithm of steganography. When steganalysis model is trained on the image set with stego images produced by a certain type of steganographic algorithm, it may be hard to accurately detect another type of steganographic algorithm, we call this phenomena as steganographic algorithm mismatch in steganalysis, which greatly prevent the laatory steganalysis model from being put into the real-world applications. To solve this problem, researchers have proposed two widely-used approaches, *i.e.*, Spatial Rich Models (SRM) + Ensemble Classifier (EC), and Convolutional Neural Network (CNN) + Transfer Learning (TL). In this paper, we propose a different approach by constructing the “similar” or close training images that more suitable for fine-tune the steganalysis networks. We use an advanced steganalysis CNN to extract steganographic features, then use the features to match a “similar” image set which may be produced by one or several “similar” steganographic algorithms, and finally use the matched “similar” image set to fine-tune a specific advanced steganalysis networks. Experimental result on three types of spatial steganographic algorithms prove that the proposed method can improve the detection accuracy in the scenario of steganographic algorithm mismatch.

Keywords: Blind image steganalysis · Steganography mismatch · Convolutional Neural Network · Distance matching · Transfer Learning

1 Introduction

Steganography is a technique to achieve covert communication by embedding secret information into the carrier (audio, video, image, text, and etc.), defending being detected by the warder of steganalysis. As the most common media used in the internet, and also due to its redundancy, digital image become the most commonly used carriers of steganography. Digital image steganography can be divided into two classes, *i.e.*, spatial domain and frequency domain. Digital image steganography also can be classified as traditional steganography and the adaptive steganography. The former usually uses relative simple skill to hide information into the least significant bits, whereas the latter uses more advanced skill to hide information into the texture complex space of an

image to resisting steganalysis. The adaptive spatial domain steganographic methods includes WOW [1], S-UNIWARD [2] and HILL [2]. The adaptive frequency domain steganographic methods includes J-UNIWARD [3] and UED [4].

Steganalysis is the opposite art of steganography, which can decide whether an image is hiding secret information or not. With the development of machine learning, including the recently rapidly developing deep learning, the steganalysis algorithms are also developing rapidly. Fridrich *et al.* [5, 6] proposed the spatial domain rich model (SRM), which improves the detection accuracy of steganalysis by increasing feature diversity and dimensions. Xu *et al.* [7, 8] proposed a deep learning-based steganalysis, where the designed neural networks are characterized with embedded absolute layers and activation function ReLU, and achieved better detection performance than SRM. Ye *et al.* [9] proposed a more advanced deep learning-based approach, where the designed CNNs have a new activation function called truncated linear unit (TLU) and use more diverse high-pass filters in the first layer. More recently, Fridrich's team proposed the SRNet [10], which can automatically "compute noise residuals" without using of high-pass filters in the first layer, and can be applied into both spatial and frequency domains with excellent detection performance. However, in the real environment, owing to the mismatch between the (unknown) target steganographic algorithm and the (already known) steganographic algorithm used in the training phase, the performance of steganalysis decreases significantly.

Traditional approach of blind steganalysis to deal with steganographic algorithm mismatch is to train on a binary cover-versus-all-stego classifier [11, 12], where the training set contains the stego images embedded by a variety of known (existing) steganographic algorithms. This approach works well when the steganographic algorithms are already known, but it has the problems of long training time and large feature dimensions. Literature [13] combines the idea of CNN + TL to solve the problem of blind steganalysis by optimizing the study rate of CNN network, but transfer learning used in this method is somewhat rough and the steganalysis ability of the initial CNN (network without transfer learning) is low, which affects the improvement of the final detection performance of blind steganalysis.

In this paper, we present a different approach. We first use the CNN as a steganographic feature extractor to obtain more representative and lower-dimensional steganographic features; and then construct a training set by selecting "similar" images with steganographic features close to the images embedded with one or several existing steganographic algorithms; and finally use the constructed training set for transfer learning of steganalysis. We conduct experiments on several classical spatial domain adaptive steganographic algorithms. The experimental results show that the proposed method improves the detection accuracy of steganalysis in case of steganographic algorithm mismatch.

Section 2 describes the details of the proposed method. Section 3 presents the experimental results, and Sect. 4 draws the conclusion of this paper.

2 Proposed Approaches

Our main idea is an off-line approach, which first matches the steganographic algorithm, and then uses the training set embedded with the matched steganographic algorithms to detect the test image. We think that the closer the training images to the test images in terms of steganographic features, the higher the possibility we can successfully detect the test images. Figure 1 shows the framework of the proposed blind steganalysis method. We first build a steganographic algorithm feature library of some known steganographic algorithms, and then extract the steganographic features of the test images. By comparing the similarity between the steganographic feature of test images and the steganographic feature database, we construct a prediction table to record the ratio of features in the database embedded by each steganographic algorithm being similar with features of the test images. The ratios are then used to guide the construction of a training data set for transfer learning. Finally, the steganalysis model corresponding to the prediction algorithm is fine-tuned by the constructed data set, and the detection performance of the steganalysis model for the test images in the case of algorithm mismatch is improved.

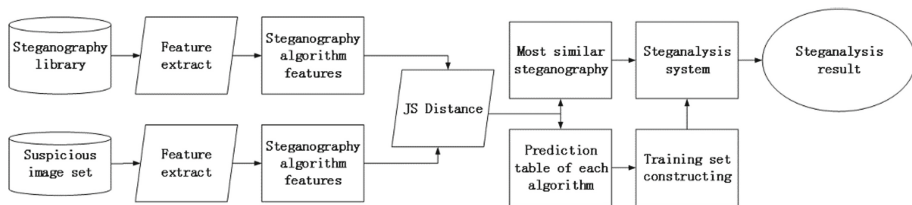


Fig. 1. The main framework of the proposed new blind steganalysis system

2.1 Steganographic Algorithm Sub-feature Extraction and Its Combination

Without the loss of generality, this paper uses the SRNet [10] as a steganographic algorithm feature extractor. Unlike the SRNet network directly inputs the feature map of the eleventh layer into the next layer of CNNs, we intercept the feature map of the eleventh layer as raw steganographic features. The steganographic feature map of this layer is a 3-dimensional tensor of $512 \times 16 \times 1 = 8192$ features, which causes a heavy time consumption for the subsequent calculation of similar distances. In order to obtain more representative and low-dimensional features, we use the method of axis dimensionality reduction to reduce the dimensions of features. The axis dimensionality reduction is achieved by selecting the representative values (such as maximal, minimal and mean values, which are calculated by the operations of *max*, *min* and *mean*, respectively) of features to represent the original features. For a 2-dimensional tensor, X-axis and Y-axis dimensionality reductions means to reduce the features along a row and a column of the feature map respectively. For example, the Y-axis dimensionality reduction with *max* operation can be expressed as follows:

$$\begin{pmatrix} a_{11} & \cdots & a_{1n} \\ \vdots & \ddots & \vdots \\ a_{m1} & \cdots & a_{mn} \end{pmatrix} \xrightarrow[\text{axis}]{y} [\max(A_1) \quad \max(A_2) \quad \cdots \quad \max(A_n)], \quad (1)$$

where $a_{ij}(1 \leq i \leq m, 1 \leq j \leq n)$ is the element of the i th row and j th column of the feature map, and $A_j(1 \leq j \leq n)$ represents the value of the j th column of the feature map.

We denotes the features obtained by the *min*, *max* and *mean* operations as F_{\min} , F_{\max} and F_{mean} , respectively. By combining sub-features, we then have new types of steganographic feature such as F_{\min_max} , F_{\min_mean} , F_{\max_mean} and $F_{\min_max_mean}$. We conduct experiments to determine which combination is more efficient and effective, which will be presented in Sect. 3.

2.2 Steganography Algorithm Matching and Construction of Fine-Tuning Training Set

Next, we design method to measure the similarity between two images, with the sub-features combination.

KL distance is a commonly used method to compare the similarity between two sets:

$$KL(P||Q) = \sum_i P(i) \frac{P(i)}{Q(i)}, \quad (2)$$

where P and Q represent two distributions for comparison. However, the KL distance lacks symmetry and has a certain degree of limitation. For example, $KL(P||Q)$ is not equal to $KL(Q||P)$. Therefore, we consider using JS algorithm, which is more comprehensive and valid in describing the similarity between two distributions. The formulation of JS distance is as follows:

$$JS(P \parallel Q) = \frac{1}{2}KL(P \parallel M) + \frac{1}{2}KL(Q \parallel M), \quad (3)$$

where $M = \frac{(P+Q)}{2}$.

In order to determine the most possible (or similar) steganographic algorithm used in the test images, we calculate the JS distance between the steganographic features of test image and the features in the steganographic feature database. The process be expressed as follows:

$$S_{\text{test}_i} = \text{Rank}(JS(\text{test}_i \parallel \text{lib}_1), JS(\text{test}_i \parallel \text{lib}_2), \dots, JS(\text{test}_i \parallel \text{lib}_n)), \quad (4)$$

where test_i and S_{test_i} represent the i th test image and its similarity value, respectively; *Rank* is a method of descending order of scores, lib_j represents the steganographic features of the j th image, and n is the total number of steganographic features in the library.

Then, we use the similarities to build a prediction table recording the ratio of features in the database being similar with features of the test images. The process is described in Algorithm 1, where table T records the ratio of each algorithm close to the algorithm used in the test set, and $Algo$ records the most possible (or similar) steganographic algorithm used in the test images.

Algorithm 1 The process of building prediction table of similar algorithms

Input: The test images $Test$; the steganographic images library Lib ; the total number of steganographic algorithms N .

Output: Prediction table T ; the most similarity steganographic algorithms $Algo$.

$T[1..N] = 0$;

for $i = 0$; $i < \text{length}(Test)$; $i ++$ **do**

 Extracts the steganographic feature of $Test_i$, denoting as $p(i)$;

for $j = 0$; $j < \text{length}(Lib)$; $j ++$ **do**

 Extracts the steganographic feature of Lib_j , denoting as $q(j)$;

 Calculates the similarity of $D[j] = JS(p(i), q(j))$;

end for

 Obtains the location of the minimum value of array D as $MinLoca$;

 Finds the steganographic algorithm used in the image with $MinLoca$ and record it as k th algorithm;

$T[k] += 1/\text{length}(Test)$;

end for

Obtains the $Algo$ by maximum value of the T ;

Finally, we use the ratios record in the prediction table T to build a training set for the test images. For example, if we want to build a M size of training set (actually, M pairs of stego-cover images), for k th steganographic algorithm, we select $M \times T[k]$ pairs of stego and cover with stego generated by the k th steganographic algorithm.

2.3 Transfer Learning

After the construction of training set for the test set, it is easy to apply the transfer learning for the algorithm mismatch of steganalysis.

First, we select the steganalysis model which has already been trained on the most possible steganographic algorithm ($Algo$ in Algorithm 1) as the initial CNN-based steganalysis model. Then, using the training set constructed in Sect. 2.2 to fine-tune the initial CNN-based steganalysis model. Considering that the higher the convolutional layer of the CNN network is, the higher the semantic level of features the convolutional

layer maps, we remain the first 11 layers of SRNet, and fine-tune the remainder layers. The detailed structure is shown in Fig. 2.

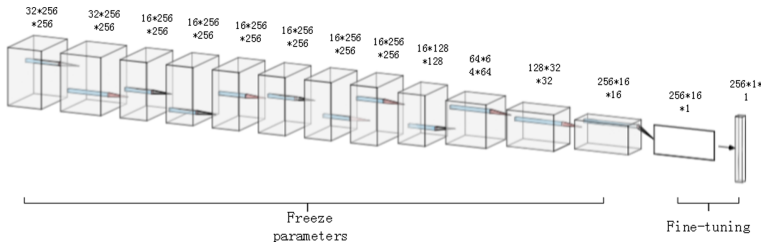


Fig. 2. The process of transfer learning

Because the initial CNN-based steganalysis model has a certain degree of steganalysis performance, we just retrain the initial CNN-based steganalysis model with a tiny learning rate of 0.0001 for 100k iterations.

3 Experiment

3.1 Experimental Setup

All experiments reported in this section were conducted on 10000 grayscale images with dimensions of 512×512 downloaded from BOSSbase 1.01 [14]. For all the experiments, the dataset (10000 images) is split as follows, 60% as a training set (6000 images), 20% as a validation set (2000 images), and the remainder 20% as a test set (2000 images). For the training set, we used three types of steganographic algorithms, WOW [1], SUNI [2], and HILL [2]. The embedding rates are set to 0.4 bpp. The steganographic algorithm feature library is composed of three types of steganographic algorithm features. Totally, there are $6000 \times 3 = 18000$ stego images to construct steganographic algorithm feature library. The Graphics card used in the experiments is RTX2080 TI with 11G memory.

3.2 Optimal Sub-feature Combination

Since the sub-features extracted by the SRNet steganalysis network are primitive and high-dimensional features, which are neither efficiency nor effective. To find the balance between efficiency and effectiveness of features, we conducted experiments to compare the time cost and the performance of different combinations of sub-features.

We first compare the time cost on the steganographic matching algorithm using different combination of sub-features, including only a single type, a combination of two types, and a combination of all types. In this experiment, the image set contains of 2000 images being used as test image. Table 1 shows the time consumption, where the first row records the total time of 2000 test images matched in the steganographic algorithm, and the second row records the average time of each image cost in the

matching. We can see clearly that the time cost increases with the increasing number of features being used (note that more sub-features means more number of features).

Table 1. Time consumption for combination of features in each dimension.

| | Single | Double | ALL |
|---------|-----------|-----------|-----------|
| Total | 2058.62 s | 3618.17 s | 4700.80 s |
| Average | 1.03 s | 1.80 s | 2.35 s |

We then conducted experiments to further compare the performance of steganographic algorithm matching by using different combinations of sub-features. We take the test set embedded by WOW algorithm with 0.4 embedding rate as an example. The three sub-features are F_{\min} , F_{\max} and F_{mean} . We randomly selected 200 images from the stego set of 2000 images embedded with WOW algorithm. Table 2 shows the average matching results of 5 experiments, where the first column represents steganographic algorithm, and the second to the last column show the matching results by using different combination of sub-features. As can be seen from the table, in the three types of combinations of sub-features, the performance of only a sub-feature is worse than multiple sub-features. Among the multiple sub-feature combinations, the combination of *min_max* has the best performance, which is even better than the combination of three sub-features (*Min_Max_Mean*). Thus, we choose the combination of *min_max* sub-features in the following steganographic algorithm matching experiments.

3.3 Steganography Matching Results

In this section, we conducted the experiment to verify the effectiveness of the steganographic algorithm matching method and tested the accuracy of the new blind steganalysis model proposed in this paper. In detail, for each of the three steganography algorithm, WOW, SUNI and HILL, we randomly selected 200 pairs of stego and cover images from 2000 pairs of images with cover images coming from the aforementioned test set. Thus we have three test image sets. Each test image set is then input into each steganalysis model (pre-trained with three steganography algorithms, WOW, SUNI and HILL on corresponding 3×2000 validation set), and the steganographic features are extracted for similarity calculating and algorithm matching. Table 3 shows the matching results of the three spatial steganographic algorithms. The data in the table are the average results from 5 experiments.

Table 2. Matching accuracy of each sub-feature combination.

| | Min | Max | Mean | Min_Max | Min_Mean | Max_Mean | Min_Max_Mean |
|------|--------|--------|--------|---------|----------|----------|--------------|
| HILL | 0.0321 | 0.0298 | 0.0795 | 0.0260 | 0.0398 | 0.0313 | 0.0300 |
| SUNI | 0.0860 | 0.1023 | 0.0235 | 0.0680 | 0.0590 | 0.0860 | 0.0660 |
| WOW | 0.8891 | 0.8697 | 0.8970 | 0.9060 | 0.9012 | 0.8827 | 0.9040 |

In Table 3, the first column represents the steganographic algorithm used on test images, the second column represents the steganographic algorithm to be predicted, the third to fifth columns represent the steganographic algorithm base on which to pre-train steganographic steganalysis model for extracting steganographic features, and the last column *Pred* gives the final predicted probability by calculating the average value of each row, which is a comprehensive result that takes into account the predictions of the steganographic algorithm under each model. We select the item with the largest proportion in the prediction table as the output of the predictive steganographic algorithm. From the table, we can see that for test images of unknown steganographic algorithms, the matching method can accurately match the steganography used by them. However, for HILL algorithm, the matching method outputs a wrong prediction. The main reason is HILL's steganographic features are very difficult to be captured by SRNet networks, which can be clarified by literature [10] that the SRNet's detection performance on HILL is approximately 4% lower than that on WOW and SUNI. However, there is no obvious gap between the matching result of WOW and SUNI with the same embedding rates.

3.4 Blind Steganalysis Results

In this sub-section, we evaluated the detection accuracy of the blind steganalysis method proposed in this paper, by comparing it with the blind steganalysis method proposed in [13]. Meanwhile, the test results of the laboratory environment of the SRNet network is used as a reference for the proposed method. Each test image set consists of 2000 pairs of stego-cover images.

In the table, the first row is the detection error rate of the SRNet steganalysis network when the steganographic algorithm is adapted; the second row is the detection error rate of steganalysis of the SRNet network in the case of algorithm mismatch. The third and fourth rows are the detection error rate obtained by the method proposed by [13] and proposed in this paper, respectively. We can see that, for the algorithms WOW

Table 3. Similarity matching table for each steganographic algorithm.

| Test algorithm | Algorithm to be predicted | Steganographic features extract on | | | Pred |
|----------------|---------------------------|------------------------------------|------------|------------|--------|
| | | WOW model | SUNI model | HILL model | |
| WOW | WOW | 0.8970 | 0.1602 | 0.1893 | 0.4155 |
| | SUNI | 0.0231 | 0.7622 | 0.3423 | 0.3759 |
| | HILL | 0.0799 | 0.0776 | 0.4684 | 0.2086 |
| SUNI | WOW | 0.7214 | 0.1848 | 0.1817 | 0.3626 |
| | SUNI | 0.1992 | 0.7328 | 0.3201 | 0.4174 |
| | HILL | 0.0794 | 0.0824 | 0.4982 | 0.2200 |
| HILL | WOW | 0.6291 | 0.2545 | 0.1962 | 0.3599 |
| | SUNI | 0.2702 | 0.6470 | 0.3437 | 0.4203 |
| | HILL | 0.1007 | 0.0985 | 0.4601 | 0.2198 |

and SUNI, our method has 6.72% and 8.66% improvement over the method proposed by [13], respectively (note that literature [13] did not detect HILL). For HILL, our method has a 5.44% improvement over the detection of the SRNet with algorithm mismatch [10]. And for WOW and SUNI, our method can achieve a very close detection performance comparing with SRNet in the case of algorithm adapted, that is a very ideal result achieved in laboratory environment where the detection algorithm is the algorithm used for training (Table 4).

Table 4. The detection error from different steganalysis system with the payload 0.4 bpp

| | WOW | SUNI | HILL |
|-------------------------------|--------|--------|--------|
| SRNet with algorithm adapted | 8.93% | 10.23% | 14.14% |
| SRNet with algorithm mismatch | 14.22% | 21.47% | 28.56% |
| Method proposed in [13] | 18.05% | 19.12% | – |
| Our method | 11.33% | 10.46% | 23.12% |

4 Conclusion and Future Work

In this paper we proposed a new model to solve the steganalysis in case of algorithm mismatch. Steganographic features with low feature dimensions and representativeness were designed to match similar steganographic algorithm and generate the matching table. The matching table is then used to guide the selecting of training images. Finally, the training images are used to fine-tune a CNN-based steganalysis and improve the detection performance in the scenario of algorithm mismatch. Experimental results show that the proposed approach outperformed [13] and [10] significantly. In the future research, we will design more advanced steganographic algorithm feature extraction networks, as well as more advanced transfer learning method for steganalysis in case of algorithm mismatch.

Acknowledgement. This work was supported by the National Natural Science Foundation of China (NSFC) under grant Nos. U1836102, 61672203 & 61976079, and Anhui Science and Technology Key Special Program under the grant No. 201903a05020016.

References

1. Holub, V., Fridrich, J.: Designing steganographic distortion using directional filters. In: IEEE Workshop on Information Forensic and Security. IEEE (2012)
2. Fridrich, J., Goljan, M.: Digital image steganography using stochastic modulation. Proc. SPIE – Int. Soc. Opt. Eng. **5020**(4), 191–202 (2003)
3. Holub, V., Fridrich, J.: Digital image steganography using universal distortion. In: IH and MMSEC 2013 - Proceedings of the 2013 ACM Information Hiding and Multimedia Security Workshop. <https://doi.org/10.1145/2482513.2482514>
4. Guo, L., Ni, J., Shi, Y.Q.: Uniform embedding for efficient JPEG steganography. IEEE Trans. Inf. Forensics Secur. **9**(5), 814–825 (2014)

5. Fridrich, J., Goljan, M.: Steganalysis of content-adaptive steganography in spatial domain (2011)
6. Fridrich, J., Kodovsky, J.: Rich models for steganalysis of digital images. *IEEE Trans. Inf. Forensics Secur.* **7**(3), 868–882 (2012)
7. Xu, G., Wu, H.Z., Shi, Y.Q.: Ensemble of CNNs for steganalysis: an empirical study. In: *The 4th ACM Workshop*. ACM (2016)
8. Xu, G., Wu, H.Z., Shi, Y.Q.: Structural design of convolutional neural networks for steganalysis. *IEEE Signal Process. Lett.* **23**, 708–712 (2016)
9. Ye, J., Ni, J., Yi, Y.: Deep learning hierarchical representations for image steganalysis. *IEEE Trans. Inf. Forensics Secur.* **12**, 2545–2557 (2017)
10. Boroumand, M., Chen, M., Fridrich, J.: Deep residual network for steganalysis of digital images. *IEEE Trans. Inf. Forensics Secur.* **14**, 1181–1193 (2018)
11. Pevny, T., Fridrich, J.J.: Novelty detection in blind steganalysis. In: *Workshop on Multimedia and Security*. ACM (2008)
12. Fridrich, J.: *Steganography in Digital Media (Principles, Algorithms, and Applications)*. Preface (2009). <https://doi.org/10.1017/cbo9781139192903.xv-xxii>
13. Mustafa, E.M., Elshafey, M.A., Fouad, M.M.: Accuracy enhancement of a blind image steganalysis approach using dynamic learning rate-based CNN on GPUs. In: *2019 10th IEEE International Conference on Intelligent Data Acquisition and Advanced Computing Systems: Technology and Applications (IDAACS)*, Metz, France, pp. 28–33 (2019)
14. Bas, P., Filler, T., Pevný, T.: “Break our steganographic system”: the ins and outs of organizing BOSS. In: Filler, T., Pevný, T., Craver, S., Ker, A. (eds.) *IH 2011*. LNCS, vol. 6958, pp. 59–70. Springer, Heidelberg (2011). https://doi.org/10.1007/978-3-642-24178-9_5



Research on User Information Security in the Context of New Media

Haiyu Wang^{1,2}(✉)

¹ School of Economics and Management, Zhengzhou Normal University,
Zhengzhou, China

wanghaiyu0830@163.com

² School of Journalism and Communication, Zhengzhou University,
Zhengzhou, China

Abstract. New media technology has reshaped the network communication mode, and every netizen has a great right of expression. At the same time, Internet users are also facing information security risks such as information disclosure, false information, hacker attacks, etc. Through the method of questionnaire survey, the author analyzes the information security problems faced by Internet users in the use of new media, and puts forward measures to improve Internet users' new media literacy, strengthen the industry self-discipline of platforms and enterprises, and improve laws and regulations.

Keywords: New media · Information security · New media literacy

1 Introduction

Information security refers to protecting the information space, information carrier and information resources of the state, institutions and individuals from all kinds of dangers, threats, infringements and misleading external states, ways and internal subjective feelings. In the era of big data, the information fusion line is online and offline, across software and hardware, including human body and objects. The nature, time, space, content and form of information security are reconstructed, presenting new features such as large networking, large concentration, large flow and large penetration. Information security management presents unprecedented complexity, interweaving, dynamic and comprehensive. The new media represented by digital technology breaks the barriers between the media, dissolves the boundaries between the media, between the region, between the administration, even between the disseminator and the receiver.

A total of 1000 questionnaires and 840 valid questionnaires were distributed in this survey.

Table 1 shows the proportion of personal information exposed when using new media platform. Nearly 60% of netizens said they occasionally exposed their personal information through new media platforms. Only 9.52% never exposed their personal information.

Table 1. Proportion of personal information exposed when using new media platform.

| options | subtotal | Proportion (%) |
|-----------|----------|----------------|
| never | 100 | 11.9 |
| no | 160 | 19.05 |
| sometimes | 500 | 59.52 |
| often | 80 | 9.52 |

New media provides a new communication space for netizens. In this virtual space, Internet users can get any information they want, at the same time, they also expose their living conditions without reservation, so their information security is greatly threatened. On the one hand, many new media platforms require users to register in real name and obtain users' location information, photo albums, address books and other contents, which makes users' privacy leak. On the other hand, it is the problem of information security caused by excessive presentation of their personal information and mass forwarding of unconfirmed information. This paper uses the methods of questionnaire and interview to study the user information security under the background of new media. Based on the analysis of 840 valid questionnaires, the author puts forward the countermeasures to protect the user's personal information security from individual, enterprise and national level. The innovation of the paper lies in the uniqueness of the method, the scientificity of the data and the feasibility of the countermeasures.

2 Analysis of Information Security

2.1 Disclosure of Personal Information

According to China new media industry security report, China's personal information is in a state of serious abuse. One of the major reasons is that there is no operational legal provisions for the protection of personal information. Due to personal information leakage, spam information, fraud information and other reasons, the loss of Internet users is serious. Generally speaking, personal information disclosure is mainly reflected in the following four aspects:

- 1) Active submission of user information: Internet applications such as social networking, shopping, games, payment, job hunting, house purchasing, etc. all require users to register their personal information at the time of registration.

A very typical example is that when we apply for a credit card on the Internet, we need to provide a complete set of personal data. These data include our personal

credit information, family member information, personal income, personal assets and other detailed information. These are personal information that we voluntarily submit.

- 2) Access to “cloud services”: cloud storage, cloud video, etc., usually storage and calculation are on the server side, so its server records a lot of data related to the user’s personal information.
Baidu disk, QQ album, which are widely used by us, store a lot of personal information. This information is stored on the servers of some companies.
- 3) The tracking record of the Internet service provider to the user’s behavior: the user browsing the website, using the search engine, online shopping, online social networking or instant messaging tools will generate a large number of online behavior data, which will usually be recorded by the service provider.

A large number of shopping websites record the consumption history of consumers and predict the future purchase demand of consumers based on big data. If we buy a book in Dangdang, the seller will record our browsing and purchasing history, and obtain the consumer’s email and telephone information. When the seller has relevant books on the shelves, they will send information to consumers through email or telephone, informing them of the relevant information of the new book.

Table 2 shows that about 10% of respondents said they had experienced personal information theft.

Table 2. Proportion of personal information stolen.

| options | subtotal | Proportion(%) |
|---------|----------|---------------|
| yes | 80 | 9.52 |
| no | 760 | 90.48 |

- (4) Access to mobile app software: many applications can access sensitive information such as contacts, call records, photo albums and location information on mobile phones.

Table 3 shows that about 17% of respondents have experienced personal information fraud in the past.

Table 3. Proportion of personal information fraud.

| options | subtotal | Proportion(%) |
|---------|----------|---------------|
| yes | 140 | 16.67 |
| no | 700 | 83.33 |

2.2 Dissemination of False Information

Relying on Internet technology, new media has the advantages of fast, efficient and wide spread in information dissemination, but at the same time, new media has become a new field of producing and disseminating false information. Every user can participate in the creation of information at any time, which provides tools and platforms for people with ulterior motives. At the same time, under the condition of high media integration, the same false information can be “copied” in many platforms, such as website, client, microblog, wechat, etc., and there is interaction effect.

A large number of false information spread viral on the Internet, some netizens cannot distinguish the true and false information, and waste too much time and energy on the false information. These information may mislead netizens’ emotion and behavior, incite netizens’ emotions, deceive Internet users to disclose personal information, and even use Internet users’ information to conduct bank transfer and other telecom fraud Terrible social consequences.

2.3 Hacker Virus Invasion

The external threats of network new media information security mainly focus on hacker invasion and computer virus. Because of the characteristics of computer virus, such as concealment, latency, infectivity, etc., once the computer virus is started, it may lead to system crash, data files are maliciously tampered with or lost, etc.

One of the common ways that viruses destroy network media is to send poisonous e-mails and hyperlinks containing virus web addresses to users. If users open them carelessly, they will bring viruses into the Internet devices, thus threatening the information security of users. In addition, hackers use a lot of software to decipher passwords, so as to destroy the system of network media or disturb the database, so as to collapse the attacked network media and even paralyze the whole network.

3 Countermeasures

For a long time, the means to ensure information security in our country have focused on technology, such as encryption technology, data backup, anti-virus, firewall, intrusion detection, identity authentication and so on, to a certain extent, to ensure the

security of information. However, in fact, it is not foolproof to rely on technology and products only to ensure information security. Many complex and changeable security risks cannot be eliminated. People’s shallow awareness of protecting personal information and lax system supervision will lead to information security risks. Therefore, the following information security measures are proposed in this paper.

Table 4 shows that all respondents believed that information protection for online shopping platforms, take-out platforms and other software is not good enough. Public awareness of prevention is not strong enough and the information protection mechanism of express company is blank or imperfect, that is in second place.

Table 4. Main reasons for personal information disclosure.

| options | subtotal | Proportion(%) |
|--|----------|---------------|
| Public awareness of prevention is not strong enough | 660 | 78.57 |
| Information protection for online shopping platforms, take-out platforms and other software is not good enough | 840 | 100 |
| Third party payment platform (WeChat, Alipay, etc.) information protection work is not good enough | 620 | 73.81 |
| The information protection mechanism of express company is blank or imperfect | 660 | 78.57 |
| The crackdown on lawbreakers is inadequate | 580 | 69.05 |
| Other (please indicate) | 0 | 0 |

3.1 Improve Netizens New Media Literacy

According to China new media industry security report, China’s personal information is in a state of serious abuse. One of the major reasons is that there is no operational legal provision for the protection of personal information. Due to personal information leakage, spam information, fraud information and other reasons, the loss of Internet users is serious. Generally speaking, personal information disclosure is mainly reflected in the following four aspects:

While people enjoy the convenience brought by new media, they will reduce the prevention of personal information security, which also leads to the frequent occurrence of neglecting their own information security and disclosing other people’s information at will. For example, wechat’s “shake and shake” function can check nearby people, broaden the social scope in the mode of delivery, but if these functions are used by lawbreakers, there will be moral and ethical problems and even illegal cases.

Netizens need to improve their new media literacy, grasp the scale of the use of new media, and know what information can be disclosed and what can not. At the same time, the uncertain information, the information without basis, do not comment, do not spread, reduce junk information, reduce the risk of information security. Therefore, to enhance personal new media literacy is the basic quality that every netizen should have for information security.

3.2 Strengthen Platform and Industry Self-discipline

New media platforms and industries need to further strengthen their responsibilities and obligations as social citizens, formulate industry norms, restrict their own business behavior, do not use or abuse the personal information of Internet users in violation of regulations, and effectively protect the privacy of Internet users' personal information. The platform needs to monitor the information released by Internet users in real time and take the responsibility of information gatekeeper. We should filter and eliminate information such as violence, yellow and violation of national security, and strive to build a safe, efficient and clear cyberspace.

3.3 Improve the Law

The state needs to further strengthen and accelerate the construction of laws and regulations on new media platform and industry, improve the legal system, supervise and manage the content and operation mode of new media, and make sure there are laws to abide by. Clearly stipulate the responsibility and obligation of new media platform to protect the user's personal information security, standardize its collection, use, dissemination and confidentiality of user information, formulate effective laws and regulations, continuously supervise the platform, timely and effectively solve the problems reflected by Internet users, and put an end to the events and disputes that violate the citizen's information security in the process of new media dissemination. Let our legal construction play a greater role in the Internet era.

4 Conclusion

New media endows grassroots netizens with great media access right, knowledge acquisition right, expression right, etc. at the same time, due to the openness and interactivity of the network environment, network security problems continue to emerge. Through the questionnaire survey, the author found that the Internet users' awareness of information security needs to be improved. The new media platform needs to strengthen self-discipline and protect the privacy of Internet users. At the same time, it needs the construction and improvement of national laws and regulations. Only by the coordinated development of the three can the information security be improved and a safe and clear cyberspace full of trust is jointly constructed.

References

1. Beck, U.: From industrial society to the risk society: questions of survival, social structure and ecological enlightenment. *Theory Cult. Soc.* **9**(1), 97–123 (1992)
2. Abdul Kader, H., El Abd, E., Ead, W.: Protecting online social networks profiles by hiding sensitive data attributes. *Procedia Comput. Sci.* **82**, 20–27 (2016)
3. Singh, A.K., Kumar, B., Singh, S.K., Ghrera, S.P., Mohan, A.: Multiple water marking technique for securing online social network contents using back propagation neural network. *Future Gener. Comput. Syst.* (2016)
4. Chang, W.Y., Liu, W.: Users divulge personal information based on the reliability analysis of empirical research - Sina Blog. *Intell. Mag.* (34-8) (2015)
5. Humerick, M.: Taking AI personally: how the E.U. Must learn to balance the interests of personal data privacy & artificial intelligence. *Santa Clara High Technol. Law J.* **34**(4), 393–418 (2018)
6. Frik, A., Mittone, L.: Factor influencing the perceived websites' privacy trustworthiness and users' purchase intentions. *J. Theoret. Appl. Electron. Commer. Res.* **14**(3), 1234–1239 (2019)
7. Hong-Youl, H., Huifeng, P., Christy, C.: The evolution of perceived security: the temporal role of SNS information perceptions. *Internet Res.* **28**(4), 1055–1078 (2018)
8. Mohammadi, A., Hamidi, H.: Analysis and evaluation of privacy protection behavior and information disclosure concerns in online social networks. *Internet J. Eng.* **31**(8), 1055–1078 (2018)
9. Silic, M., Back, A.: The dark side of social networking sites: understanding phishing risks. *Comput. Hum. Behav.* **60**, 35–43 (2016)



Research on Software Community Division Method Based on Inter-node Dependency

Jun Dong^{1,2}(✉), Chengqian Hao, Jiadong Ren^{1,2}, and Haitao Lu^{1,2}

¹ College of Information Science and Engineering, Yanshan University,
Qinhuangdao 066000, China
donycosmos@163.com

² The Key Computer Virtual Technology and System Integration Laboratory
of Hebei Province, Qinhuangdao 066000, China

Abstract. The mining of software community structure is of great significance in identifying software design pattern, software maintenance, software security and optimizing software structure. To improve the accuracy of description of software execution status model, A new method to construct merge software execute graph is proposed that based on the software execution network model. And then to get the software execution path through the software execution sequence analysis, The ND (Node Dependence) was proposed to measure the tightness of inter-node dependencies based on the design principle of “high cohesion, low coupling” of software. At last, depends on the software execution path, the SLCA (Software Label Communities Algorithm) community division algorithm is proposed to improve stability of community partition algorithm and validity of software module partition.

Keywords: Software community structure · Software executive network · Complex network · Inter-node dependency

1 Introduction

In recent years, the number and scale of software systems have shown exponential growth. It has become increasingly difficult to study software systems in the traditional way. In order to reduce the complexity of software systems, a large number of researchers abstract complex software systems into software network models.

In 2002, Valverde and other researchers [1] map the software system to the network structure model by combined the complex network method with the software network structure. From this time on, a large number of researchers have devoted themselves to the research work in this field. Liu B et al. [2] studied the internal logic of software with the method of UML class diagram in software engineering in 2005. Cai K Y et al. [3] proposed that software execution process should be regarded as an evolving complex network, the concept of software mirroring is introduced into a new model of complex networks and incorporate dynamic information about software behavior. Ma J et al. [4] modeled a software package as a network which nodes are represented by functions and edges are represented by dependencies between functions. Šubelj, Lovro et al. [5] had studied the different software system developed by

Java from the view of network science. Especially the research work [6, 7] in recent years shows that complex network theory can provide important technical support for exploratory analysis of large-scale complex software systems.

In solving the problem of community division in complex networks, a large number of algorithms have emerged correspondingly. According to the solving strategy, it can be divided into three categories: based on optimization, heuristic and similarity. The main idea of the algorithm based on optimization is turn the problem of finding community structure into the problem of optimization. Spectral clustering algorithm, Fast Newman algorithm [8] and Guimera-amarai algorithm [9] are typical representatives. The main idea of the algorithm based on heuristic is turn the problem into heuristic rules. Although this kind of algorithm can quickly obtain feasible solutions in a reasonable space range, the solution is not necessarily the optimal solution. Such as Label Propagation algorithm is typical representatives. The similarity-based algorithm measures the similarity between nodes according to their properties and topological relation, then the community structure is divided based on similarity. This kind of algorithm include based on node dependence and node clustering center degree [10]. Ruan J et al. [11] proposed an effective heuristic algorithm, which combines spectral division and local search to optimize Q. Wang Y et al. [12] proposed a method based on block vertex and degree entropy.

This paper studies the software community division method based on inter-node dependency. The Method divided the software network into modules by use the theory of complex network and the inherent characteristics and characteristics of the software itself. A method to calculate the dependency between software network nodes is proposed and the SLCA (Software Label Communities Algorithm) algorithm to divided the community structure in Software is bring forward as well.

2 Construction of Merge Software Execute Graph

In order to fully show the internal features of the software in operation, the same software will generate multiple software execution sequences based on different inputs, and each software execution sequence corresponds to a software execution diagram. Due to different inputs, the number of calls between the same two functions in different software execution diagrams will vary greatly, so these diagrams need to be integrated. Since the weights of software execution diagrams vary greatly, some values may be on the high side collectively. The high value of one group may obscure the characteristics of the others if the weights are simply superimposed. So a new approach is needed to proposed to deal with the problem.

The software execution sequence data set S which contains n sequences: $S = \{s_1, s_2, s_3, s_4, \dots, \dots, s_n\}$, each of these sequences has a different input. These sequences are converted into software execution diagrams respectively according to the corresponding method. Generate the software execution graph data set G : $G = \{g_1, g_2, g_3, g_4, \dots, \dots, g_n\}$.

Definition 2.1. Combined Weight. It is Integration of weights in software execution diagrams.

$$W_{ij} = \sum_i^n \frac{\log(1 + N_{ij})}{\sum_j^m \log(1 + N_{ij})} \quad (1)$$

W_{ij} represents the combined weight from node i to node j , N_{ij} represents the number of calls from node i to node j . There are n sets of networks for different inputs, the values of i and j in n groups of software execution diagrams are calculated respectively and then summed. The number of functions that called by i is m .

Definition 2.2. MSEG (merge software execute graph), integrated from multiple software execution diagrams. The functions in the software represent the nodes in the diagram. Call relationships as the edges of the graph. W_{ij} is weight.

$$MESG = \{Node_i, Node_j, W_{ij}\} \quad (2)$$

$Node_i$ and $Node_j$ are the relationship between the call and the called, it is $Node_i \rightarrow Node_j$. So, In the case presented above, multiple software execution diagrams need to be merged.

Algorithm 1 Generation algorithm of MSEG

Input: $G = \{g_1, g_2, g_3, g_4, \dots, \dots, g_n\}$

Output: MSEG

```

(01) Initialize mGraph
(02) for ( each gadj from G )
(03)   for ( each edgeSet from gadj )
(04)     allvalue = 0
(05)     for ( each edge from edgeSet )
(06)       allvalue += log( edge.value + 1 )
(07)     end for
(08)   for( each edge from edgeSet )
(09)     if( mGraph.containt( edge ) )
(10)       mGraph.get( edge ).value += log( edge.value + 1 ) / allvalue
(11)     else
(12)       mGraph.add( edge )
(13)     end for
(14)   end for
(15) end for
(16) return mGraph

```

In line 1, mGraph stores the final composite structure and adopts adjacency list. Lines 2 through 15 traverse multiple diagrams, lines 3 through 14 of which traverse the edges corresponding to each node in the diagram, allvalue is used to store the corresponding weight of each node. Lines 5 through 7 calculate allvalue. Lines 8 through 12 store the sum of weight in the mGraph.

3 Inter-node Dependency

3.1 Definitions of Inter-node Dependency

In order to improve the cohesion of modules in the division of software network modules, the degree of association between nodes needs to be calculated. In this paper, inter-node dependency is used to represent the degree of association between nodes, and the inter-node dependency is analyzed from the perspective of software execution path.

Definition 3.1. Software execute trace. The sequence of function calls during the execution of the software represents the path of function calls. The sequence from left to right is the relationship between the call and the called. The starting node of the sequence is the software running function, and the ending node of the sequence is the function that does not call other functions at run time.

In the software execution process, the software depending on each software execution path to complete the execution, the completion of each software execution path depends on each node in the path, the execution completion of each node depends on the completion of its subsequent nodes, in other words, the execution of the node depends on the node dependency set of the node.

Definition 3.2. NDS(Node Dependence Set). A node in all software execution paths that contain that node which subsequent node directly or indirectly called. The set of all these nodes is the node dependency set for that node.

$$NDS(N) = \{C|N \rightarrow C\}, C \in NDS \quad (3)$$

Where C , N represent a node in the software network. C is a node in the N node dependency set. $N \rightarrow C$ represents the existence of a software execution path, and C node is on the right of N node, that is, N function node calls C function node directly or indirectly. So, NDS is the dependency set of node N , It is written as $NDS(N)$.

When the dependency set of the node is obtained, the dependency degree of the two nodes can be judged according to the node dependency set of the two nodes. Of course, two nodes can calculate the dependency on the premise that two nodes must be reachable, that is, there is a path between two nodes, and they are a neighbor nodes.

When the node dependency set of a node is highly similar to that of an adjacency node, which indicates that the execution of the node will largely depend on the execution of the adjacency node.

Definition 3.3. ND (Node Dependence) represents the degree of dependency between two nodes.

$$ND_{ij} = \frac{\text{size}(NDS(i) \cap NDS(j) \cup j)}{\text{size}(NDS(i))} \times W_{ij} \quad (4)$$

$\text{size}()$ represents the size of the collection, that is, the number of nodes in the collection. W_{ij} represents the weight from node i to node j . Because j is a child of i , when take the intersection of two dependent sets need to add j nodes, and it prevents ND from being zero.

After obtaining the inter-node dependency, the software network can be divided into modules based on the dependency.

3.2 Calculation Procedure and Algorithm of Inter-node Dependency

Calculation procedure of inter-node dependency:

1. Get the software execution path according to the software execution sequence analysis.
2. The node dependency set of each node is calculated based on the software execution path.
3. The inter-node dependency is calculated and stored.

In this paper, prefix tree (trie) structure is used to store the execution path of software for save storage space. From the root node of the prefix tree to the leaf node of the tree is a software execution path.

The node structure of trie tree is designed as triples: (NodeId, Call, Children). Where NodeId represents the id of the tree node, that is, the name of the function. Call represents the number of times the parent node calls the function. Children represents the index of the function node directly called by the function under this path. Algorithm 2 parses the software execution sequence and obtains the prefix tree.

Algorithm 2 The trace of software execution mining

Input: Collection of software execution sequences: $S = \{S_1, S_2, S_3, \dots, S_n\}$

Output: Prefix tree of software execution trace

```

(01)   Initialize TriRootNode
(02)   for ( each s from S)
(03)       Initialize index=0
(04)       call Procedure MakeTree( s, TriRootNode )
(05)   end for
(06)   return TrieRootNode;

```

Function: **MakeTree**

Input: Software Sequence s, Node

```

(07)   index++
(08)   While( index < s.size && s.get( index ).startWith("E"))
(09)       name = s.get( index ).substring( 1 )
(10)       if ( Node.Children.contains( name ) )
(11)           NewNode = Node.get( s.get( index ).substring( 1 ) )
(12)           NewNode.getCall ++
(13)       else
(14)           NewNode = NewNode( name )
(15)           Node.addChildren( s, NewNode )
(16)       end if
(17)       call Procedure MakeTree( NewNode )
(18)   While end

```

Index++

Line 1 initializes the root node of the prefix tree. Line 2 loops through all the sequences in the database, mining out all the included paths and save to prefix tree. Line 3, index, represents the sequence position index and records the current position of the sequence. Line 4 calls the MakeTree function to construct the prefix tree. Lines 7 through 19 are the contents of the MakeTree function, in which the recursive algorithm is used to construct the prefix tree.

Postorder traversal of the prefix tree by follow the software execution path from step 1, and to establish a one-to-one correspondence between each node and its dependency set with dictionary structure. Save collection of dependencies for each node. Then, follow is the algorithm to calculate ND value of inter-node dependence.

Algorithm 3 Node dependency calculation algorithm

Input: Node Node_i, Node Node_j, Node dependency set Set, Prefix Tree TrieRootNode

Output: dependent value between nodes i and j

```

(01)   Initialize DSmap
(02)   call procedure MakeDS( TrieRootNode )
(03)   Initialize ND,unSet,interSet
(04)   for ( each Node from DSmap.get( Nodei ))
(05)       unSet.add( Node )
(06)       if ( map.get( Nodej ).contain( Node ))
(07)           interSet.add( Node )
(08)   end for
(09)   ND = interSet.size() + 1 / unSet.get( I ).size*wij
(10)   return ND

```

Function:**MakeDS**

Input:TreeNode

Output:Set

```

(11)   Initialize Set
(12)   for ( each treenode from TreeNode.children )
(13)       Set.addAll( MakeDS( treenode ))
(14)       Set.add( treenode )
(15)   end for
(16)   if ( DSmap.containsKey( TreeNode ))
(17)       DSmap.get( TreeNode ).addAll( Set )
(18)   else
(19)       DSmap.put( TreeNode,Set )

```

return Set

In line 1, the DSmap is initialized to store the node's dependency set, that's the structure in the second step. The second line calls the MakeDS function, the function iterates through the prefix tree recursively and computes the set of dependencies for the nodes. The 3 line initializes the dependency value ND, interSet that is the intersection of i and j and unSet that is the and set. Lines 4 through 8 traverse the node dependency set of the node i and add to unSet. Add to interSet when exists on dependency set of node j. Line 9 computes the ND value. Lines 11 through 20 are for MakeDS. Line 11 initializes the Set, which is used to store the child nodes of the node in the current path. Lines 12 through 15 traverse the child nodes of the tree nodes. Add a dependency set of child nodes and child nodes itself to the Set. Lines 16 through 19 merge the dependency set for the node into the DSmap.

4 Software Community Division Algorithm Based on Inter-node Dependency

The algorithm based on basic thought of Label Propagation Algorithm [13–15]. Since each propagation of the algorithm selects nodes randomly, So, depending on the dependency, a sequence is provided for the propagation of its nodes, The larger the ND value is, the more likely the two nodes are in a community, and the later the label propagation needs to be. The label of the node is updated sequentially according to the ND value. At the same time, when selecting the label of neighbor node, nodes with high inter-node dependence can be divided into a module as far as possible. This improves the cohesion of the modules.

According to algorithm 3, the ND value between nodes is calculated and saved. By the different ND values between nodes, the label propagation between nodes is carried out, and the label of nodes is constantly updated. This can improve the accuracy of module division. Divide different community modules in accordance with different labels.

In Algorithm 4, the SLCA (Software Label Communities Algorithm) Algorithm is described. Node structure, mainly used to store all kinds of information of the node, include $\langle nid, label, neighbours \rangle$, where *nid* is the id number of the node and *label* is the constantly updated label. The label is initialized to *nid* during the initialization phase. *Neighbours* is adjacency node set of the node directing, include $\langle node, weight, ND \rangle$, where *node* represents the reference to the adjacency node, *weight* represents the weight value between the node and the adjacency node, and *ND* represents the dependence value of the node on the adjacency node.

Algorithm 4 Software Label Communities Algorithm

*Input: merge software execute graph: finalList, iterations**Output: collection of community*

```

(01)   Initialize resultSet
(02)   sort(finalList)
(03)   for( t ← 0 to iterations)
(04)     for ( each node from finalList )
(05)       Initialize labelSet categorylabel
(06)       for ( each neighb from node.neighbhours() )
(07)         if ( labelSet.contain( neighb.label ))
(08)           labelSet.get( neighb.label ) += neighb.ND;
(09)         else
(10)           labelSet.add( neighb.label,neighb.ND )
(11)         end if
(12)       end for
(13)     for ( each label from lableSet )
(14)       if ( label.value> categorylabel.value )
(15)         categorylabel = labels
(16)       end if
(17)     end for
(18)     node.label = categorylabel;
(19)     resultSet.add( node.label,nodeId )
(20)   end for
(21) end for
(22) return resultSet

```

First initialize each node in the network with a unique label. In line 2, the ND value is used as the standard to sort finalList decreasing. Lines 3 through 22 are iterated according to the specified number of iterations. Lines 4 through 20 are the label propagation process. Lines 6 through 12, according to the dependence value between the node and its neighbor node, statistical accumulate it's value against label carried by the neighbor node of each node and saved to labelSet. Lines 13 through 18 traverse the labels contained in labelSet, compared the ND values of each node, assign the label of the maximum ND value to the node, and last, overwrite the original label. Iterate repeatedly until the community division reaches a plateau or iterates to a specified number of times.

5 Experiment

5.1 Experiment Setup

Two software systems in the open source software library are selected in the experiment, that is, software tar and cflow respectively. Use different files and different

commands to run the two programs, at the end of the run, even if it is the same version of the same software, the generated software execution sequence is also very different. Some data information is given below.

Table 1. Partial execution sequence data of cflow

| Version | File number | Node of sequence |
|---------|-------------|------------------|
| 1.0 | 10 | 5859704 |
| 1.0 | 04 | 6668 |
| 1.1 | 10 | 7027194 |
| 1.1 | 04 | 6824 |
| 1.5 | 10 | 1538914 |
| 1.5 | 04 | 5964 |

Table 2. Partial execution sequence data of tar

| Version | File number | Node of sequence |
|---------|-------------|------------------|
| 1.23 | 01 | 3562 |
| 1.23 | 12 | 82220 |
| 1.25 | 01 | 4678 |
| 1.25 | 12 | 164130 |
| 1.29 | 01 | 4668 |
| 1.29 | 12 | 106200 |

Table 1 and Table 2 above are the partial data of the execution sequence of the two software, respectively. And three of these versions are shown. The result data of two executions in each version is different from the input data of each execution, so there is a big difference in the number of execution sequence nodes. Take the number of sequence nodes, more and less for comparison, it can be seen that the number of large differences. Different versions of the same input data, the resulting sequence is also very different.

Table 3. Merge software execute graph of cflow

| Version | Amount of node | Amount of edge |
|---------|----------------|----------------|
| 1.0 | 101 | 175 |
| 1.1 | 105 | 185 |
| 1.2 | 106 | 186 |
| 1.3 | 106 | 189 |
| 1.4 | 116 | 206 |
| 1.5 | 119 | 211 |

Table 4. Merge software execute graph of tar

| Version | Amount of node | Amount of edge |
|---------|----------------|----------------|
| 1.23 | 117 | 168 |
| 1.24 | 124 | 177 |
| 1.20 | 151 | 213 |
| 1.21 | 150 | 212 |
| 1.28 | 183 | 247 |
| 1.29 | 192 | 256 |

Table 3 and Table 4 respectively show the information of merge software execute graph generated by different versions of cflow and tar. We can see in different versions of the same software, although the inputs are the same, there are differences in the number of nodes and the number of edges in the generated graph. In particular, the tar software, as the number of versions increases, it becomes apparent that the software itself is becoming more and more complex.

Table 5. Partial data of Merge software execute graph of cflow

| Version | Node number | Node number | Weight | ND |
|---------|-------------|-------------|--------|------|
| 1.0 | 8 | 10 | 5.1 | 0.3 |
| 1.1 | 85 | 36 | 16 | 1 |
| 1.4 | 53 | 24 | 15.5 | 0.97 |
| 1.5 | 15 | 17 | 2.7 | 0.17 |

Table 6. Partial data of Merge software execute graph of tar

| Version | Node number | Node number | Weight | ND |
|---------|-------------|-------------|--------|------|
| 1.23 | 20 | 24 | 1.6 | 0.3 |
| 1.24 | 15 | 78 | 0.12 | 0.15 |
| 1.27 | 123 | 125 | 4.5 | 0.23 |
| 1.29 | 13 | 124 | 8.6 | 0.4 |

Table 5 and Table 6 respectively show the edge’s information of merge software execute graph, which contains parent and child nodes and the weight between two nodes and the calculated dependency value. It is represents how dependent the parent node is on its children.

5.2 Experiment Result

In order to measure the quality of network model community division, modularity is adopted to measure the quality after module division. The calculation formula of modularity in weighted directed graph is as follows.

$$Q = \frac{1}{w} \sum_i \sum_j \left(w_{ij} - \frac{w_i^{out} w_j^{in}}{w} \right) \times \delta(i, j) \tag{5}$$

$\delta(i, j)$ indicates whether nodes i and j are in the same community, in a community, the return value is 1, whereas it is 0. w is the sum of all the weights in the entire network, w_{ij} represents the weight between node i and node j . w_i^{out} represents the weight sum of all out-degree edges of node i . w_j^{in} represents the weight sum of all in-degree edges of node j .

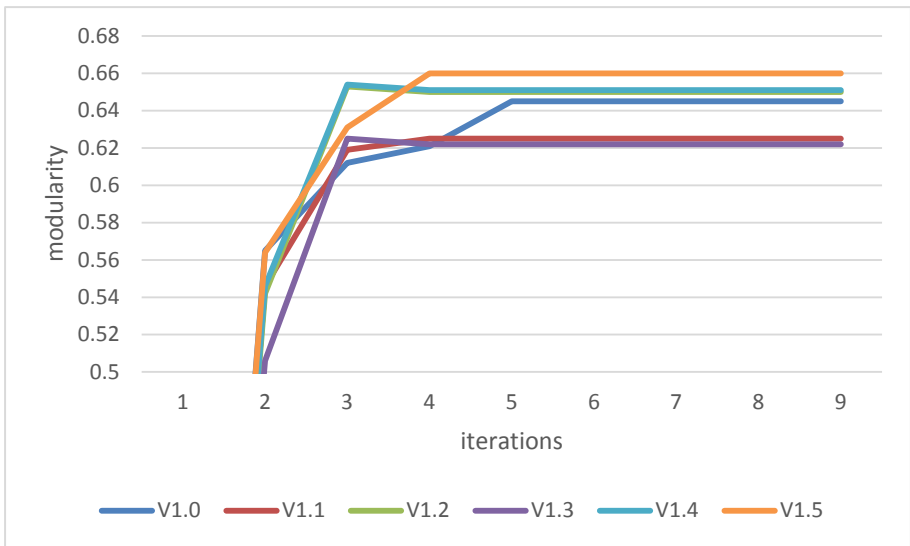


Fig. 1. Modularity curve of cflow

Figure 1 and Fig. 2 respectively show the module rate change of SLCA algorithm in the cflow and tar iterative process. And the variation trend of modularity between different versions of the same software is compared. It can be seen that with the increase of iteration times, the module rate increases rapidly and tends to be stable.

SLCA algorithm's performance is presented in Fig. 3 and 4 below, which is compared with OPSN algorithm and LPA algorithm with modularity as the standard. The three algorithms respectively analyze six different versions of cflow and divide modules. This can be seen in the figure below, the module rate of SLCA algorithm is higher than the other two algorithms. The LPA algorithm partition module process is very unstable, and corresponding module rate also varies greatly. SLCA algorithm is

very stable in module division. Each module division is almost the same, and the module rate is basically unchanged.

In Fig. 3, according to the version of tar is constantly updated, it's module rate is also increasing. This indicates that in terms of software modules, it has been continuously optimized to increase the module rate of the software. This is consistent with the idea of “low coupling, high cohesion” in software develop. The cflow in Fig. 4 is not an increasing trend, but the module rate has been high, this indicates that they have been doing well in the aspect of “high cohesion, low coupling”.

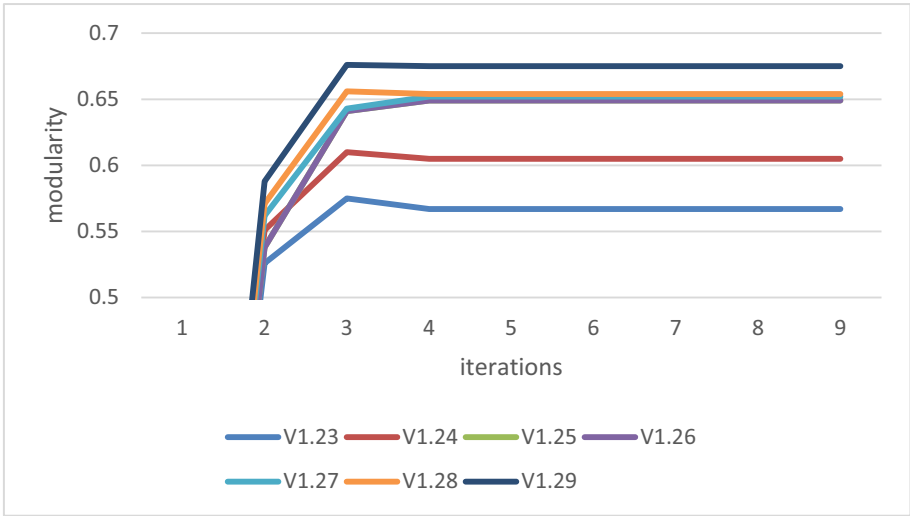


Fig. 2. Modularity curve of tar

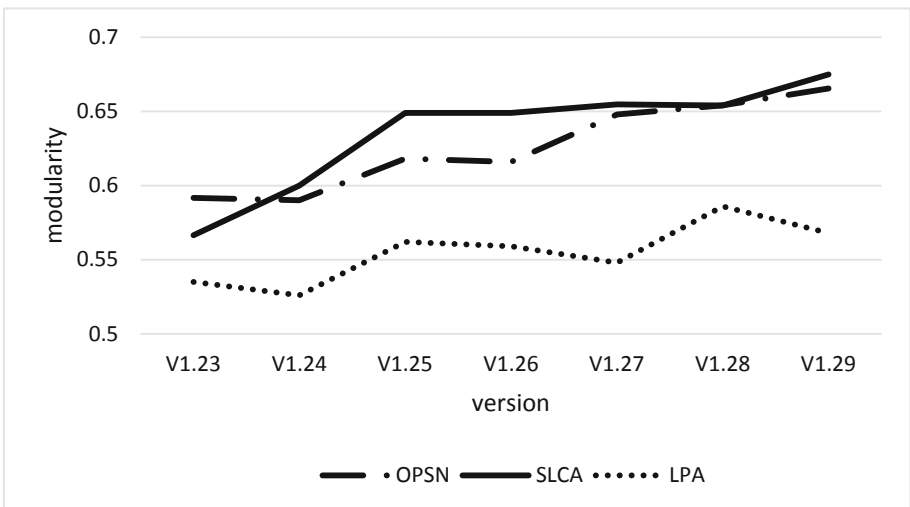


Fig. 3. Distribution of modularity of tar

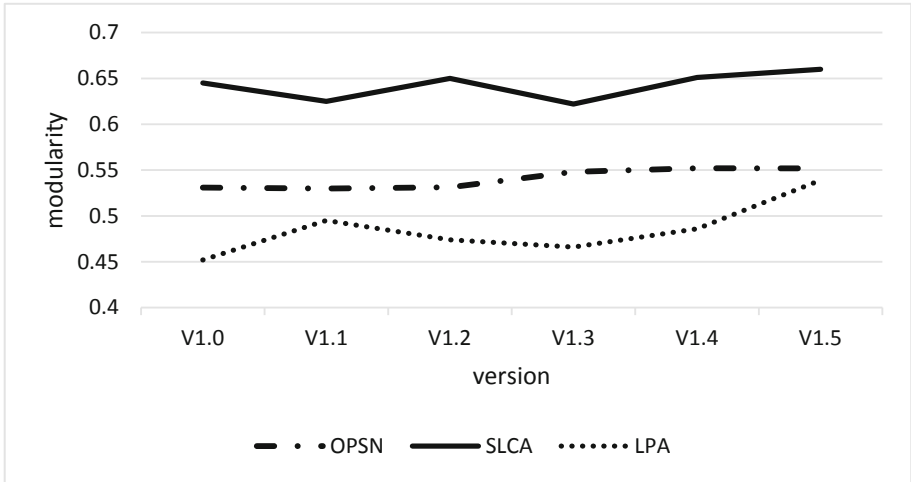


Fig. 4. Distribution of modularity of cflow

6 Conclusions

Based on tracing the software execution process to get the software execution sequence, this paper constructs the software execution path and the software execution network model. According to different input data and parameters, the software execution process is tracked several times. A more suitable software network model is constructed by integrating multiple software networks in a reasonable way. In the software network model that make the function into the network node and the number of calls between functions into the edge. From the point of view of functions calling each other and depending on each other, and combined with the software execution path of the run-time, paper build a collection of dependencies for function nodes. At the same time, a method to calculate the ND dependence between function nodes is proposed. This is used to describe the relationship between nodes. Label propagation algorithm combined with the dependence between nodes, the software network community is divided and the module structure of the software is mined. Module degree is used to analyze the effect of module partition between different algorithms and the different modules between different versions of the same software.

It is not rigorous that to evaluate software module division by module degree we found. In the future work, it is necessary to propose a new measurement method to measure the effect of software module division.

Acknowledgment. This work is supported by the National Key R&D Program of China (2016YFB0800700), the National Natural Science Foundation of China under Grants no. 61472341, no. 61572420, and no. 61772449, the Natural Science Foundation of Hebei Province of China under Grants no. F2015203326 and no. F2016203330.

References

1. Valverde, S., Cancho, R.F.I., Sole, R.V.: Scale-free networks from optimal design. *Eurphys. Lett.* **60**(4), 512–517 (2002)
2. Liu, B., Li, D., Liu, J., He, F.: Classifying class and finding community in UML metamodel network. In: Li, X., Wang, S., Dong, Z.Y. (eds.) *ADMA 2005*. LNCS (LNAI), vol. 3584, pp. 690–695. Springer, Heidelberg (2005). https://doi.org/10.1007/11527503_81
3. Cai, K.Y., Yin, B.B.: *Software Execution Processes as an Evolving Complex Network*. Elsevier Science Inc. (2009)
4. Ma, J., Zeng, D., Zhao, H.: *Modeling the Growth of Complex Software Function Dependency Networks*. Kluwer Academic Publishers (2012)
5. Šubelj, L., Bajec M. *Software systems through complex networks science*, pp. 9–16 (2012)
6. Liu, C.: Automatic discovery of behavioral models from software execution data. *IEEE Trans. Autom. Sci. Eng.* **15**(4), 1897–1908 (2018)
7. Phan, A.V.C., Nguyen, M.L., Bui, L.T.: Convolutional neural networks over control flow graphs for software defect prediction. In: *Proceedings of IEEE 29th ICTAI*, November 2017, pp. 45–52 (2017)
8. Newman, M.E.J.: Equivalence between modularity optimization and maximum likelihood methods for community detection. *Phys. Rev. E* **94**(5), 052315 (2016)
9. Guimerà, R., Nunes Amaral, L.A.: Functional cartography of complex metabolic networks. *Nature* **433**(7028), 895 (2005)
10. Yang, B., Liu, J.: Discovering global network communities based on local centralities[J]. *ACM Trans. Web* **2**(1), 1–32 (2008)
11. Ruan, J., Zhang, W.: Identifying network communities with a high resolution. *Phys. Rev. E Stat. Nonlinear Soft Matter. Phys.* **77**(1), 016104 (2008)
12. Yiwen, W., Min, Y.: A novel method for community detection in complex network using new representation for communities. In: Cao, L., Huang, J.Z., Bailey, J., Koh, Y.S., Luo, J. (eds.) *PAKDD 2011*. LNCS (LNAI), vol. 7104, pp. 89–99. Springer, Heidelberg (2012). https://doi.org/10.1007/978-3-642-28320-8_8
13. Huang, G., Zhang, P., Zhang, B., et al.: The optimal community detection of software based on complex networks. *Int. J. Mod. Phys. C* **27**(08), 1650085 (2016)
14. Zhao, Z., Yu, H., Zhu, Z.: Analysis of node communication influence based on network community structure. *Chin. J. Comput.* **37**(04), 753–766 (2014)
15. Dong, Z., Yin, P., He, C.: Overlapping community discovery algorithm based on link label propagation[J]. *Comput. Eng. Design* **10**, 3380–3385 (2014)



Blockchain-Based Group Key Management Scheme in IoT

Haiying Ma and Guorong Sun^(✉)

School of Information Science and Technology,
Nantong University, Nantong, Jiangsu, China
1930320011@stmail.ntu.edu.cn

Abstract. Group key management is an important method to protect privacy information in the IoT. However, the existing group key management scheme follows the hierarchical structure and highly depends on central authentication, which cannot be adapted to the distributed Internet of Things environment. Blockchain, a distributed ledger technology with the characteristics of being transparent, non-tamperable, and traceable, is a promising candidate for strengthening the security of group key management in IoT. This paper proposes a blockchain-based group key management scheme in IoT. This scheme uses blockchain technology to ensure that resources are shared securely in the decentralized domain administrator network, realize the dynamic security management of user information and keys, and improve the efficiency of the group key update for the dynamic group members. In this way, the user's activity and key update can be recorded in blocks, which is convenient for retrieval and audit work of other domain administrators.

Keywords: Internet of Things · Blockchain · Group key management

1 Introduction

Internet of Things (IoT) is a global network infrastructure that consists of numerous connected devices, and bridges the physical and digital worlds. IoT technology has a positive influence on all areas of our daily life including transportation, digital supply chain, industrial automation, healthcare, and so on. IoT devices collect a large amount of information from the surrounding environment and communicate with each other through embedded software systems. However, because the information transmitted by the connected devices contains user-sensitive data, data security and privacy leakage problems still exist in today's IoT environment.

Group key management is one of the effective ways to solve the problems of user data security and privacy leakage. Nowadays, Logical Key Hierarchy (LKH) [1] and One-way Function Key Tree (OFT) [2] are widely used in group key management schemes. However, the existing group key management schemes adopt a central authority, which may result in a single point of failure, large cross-domain key transmission delay, low efficiency, and complex key management, etc. Thus, it is difficult to adapt to the dynamic distributed IoT environment. Attribute-based encryption is also an effective method to ensure data security [3, 4]. However, the calculation for encryption

and decryption is large, so it is difficult for lightweight IoT devices to complete it in a short time. Blockchain can solve the security problems of group key management in IoT due to its nice characteristics of being decentralized, transparent, non-tamperable, and traceable.

In recent years, many researchers have studied the security mechanism of IoT based on blockchain. Krishnan et al. [5] proposed an IoT security framework suitable for resource-constrained environments such as smart cities, which uses blockchain technology and a secure hashing algorithm. It can guarantee the secure communication and authentication of data on various networks and devices. Pajooh et al. [6] proposed a multi-layer security network model for IoT network based on blockchain technology, which can address the problems associated with the actual deployment of the blockchain by dividing the IoT network into a multi-layer decentralized system. Mohanty et al. [7] proposed an efficient lightweight integrated blockchain (ELIB) model and applied it to a smart home environment, proving that the model can improve the security and privacy of IoT. Ge et al. [8] proposed a decentralized secure mechanism based on blockchain to store the important data generated in the IoT system. This mechanism effectively solves the data reliability, security and privacy issues that may be encountered in the conventional IoT-cloud system. Ma et al. [9] proposed a blockchain-based mechanism for fine-grained authorization in data crowdsourcing. It employs Ciphertext-Policy Attribute-Based Encryption (CP-ABE) to pre-process the complex encryption workload, and generates the attribute private key for data requester to achieve the fine-grained authorization. Pal et al. [10] discussed the need of key management for blockchain which includes the key management for bitcoin currency wallet and blockchain Public Key Infrastructure, and proposed a group key management scheme for secure group communication to improve the confidentiality of sensitive records over the blockchain network. Lei et al. [11] proposed a new key management scheme for key transfer among short messages in heterogeneous vehicular communication systems, which used blockchain technology to optimize the performance in dynamic transaction collection periods. Kung et al. [12] discussed the group key management problem in dynamic IoT environments, and proposed a two-tier Group Key Management (GKM) architecture called GROUPIT, which can accommodate multiple devices to handle frequent membership and device number changes. These works only focus on the use of blockchain and group key management to solve some security problems of IoT. Our scheme differs from the above works and focuses on using blockchain to solve the group key management problems in the IoT environment.

In this paper, we propose a blockchain-based group key management scheme in IoT. In this scheme, blockchain technology is deployed to guarantee that users can securely share resources in the decentralized domain administrator network, where domain administrators take over majority work of system administrator in the traditional structure. After user joins or leaves the user group, the hash value of the user's identity information and updated group keys will be added to the block as a transaction, which enables the domain administrators to verify information. Meanwhile, the group key will be automatically updated according to the hash value of the current block header. This not only improves the efficiency of group key update, simplifies key management, but also ensures forward and backward security and prevents collusion

attacks. Our scheme realizes the dynamic secure management of user information and keys, and improves the efficiency of the group key update for the dynamic group members.

2 Preliminaries

2.1 Blockchain

Blockchain is a kind of chain structure that uses blocks to store sequential transaction data. It has the characteristics of being decentralized, transparent, non-tamperable, and traceable. Since there is no trusted third-party authority, all consensus nodes are involved in maintaining the blockchain. The high redundancy of the block data reduces the risk of a single point of failure. In addition, the irreversibility of the hash function, the security of the consensus mechanism and the automatic execution of smart contracts guarantee the security of transaction data.

In this paper, the hash value of the block will be treated as a pseudo-random number generator (PRNG). It can be used to establish PRNG with time series, which is beneficial for generating and updating keys. For example, group key can be set to $Hash(BlockHashValue || MasterGroupKey)$, where $BlockHashValue$ is the hash value of the current block and the $MasterGroupKey$ is the group key for the group. Meanwhile, the hash value of the user's identity information and updated group keys will be added to the block as a transaction. This allows the domain administrator to retrieve data quickly, therefore it improves the efficiency of the system.

2.2 One-Way Function Tree Key Management Scheme

In our scheme, the OFT key management scheme is introduced to a user group. $f(a, b)$ is a mixing function, $g(\cdot)$ is a one-way hash function. The value of $g(\cdot)$ is called blinded node key. The details of these functions are as follows:

Mixing Function $f(a, b)$: This function connects two entities a and b , and users can calculate the required key k_i by the following formula, k_{left} and k_{right} represent left and right children of the node key k_i respectively.

$$k_i = f(g(k_{left}), g(k_{right})) \quad (1)$$

One-Way Hash Function $g(\cdot)$: A one-way hash function can be used to hide the contents of the original keys. The generated "blinded" keys can be securely shared with the corresponding users.

Key Transfer Function: $u_i \leftarrow enc(g(\cdot), k_i)$. It means that $g(\cdot)$ is encrypted with key k_i and transmitted to the user u_i .

The group key is determined by each user's blinded node key. All users know their brother's blinded node key as well as their ancestors' brother's blinded node key. As shown in Fig. 1, user u_1 not only stores its own key k_1 , but also stores $g(k_2)$ and $g(k_{34})$. It is convenient for u_1 to calculate the group key k .

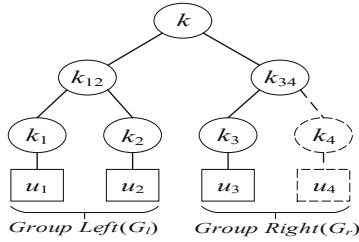


Fig. 1. An OFT key tree with height $h = 2$.

3 System Model of Blockchain-Based Group Key Management

In our system, there are three kinds of roles: a system administrator, domain administrators and users. When a user firstly joins the system, the system administrator will authenticate his/her identity information and register a unique ID for him/her. Then domain administrators take over majority work of system administrator. The user chooses a domain administrator to join the user group, and can obtain the corresponding keys and the group information. The hash value of the user’s identity information and updated group keys will be added to the block as a transaction. Meanwhile, the group key will be updated when users join or leave the user group. Besides, the group key will be updated at intervals. This can guarantee forward and backward safety, and prevent collusion attacks effectively.

3.1 System Model

The blockchain-based IoT group key management system model is show in Fig. 2.

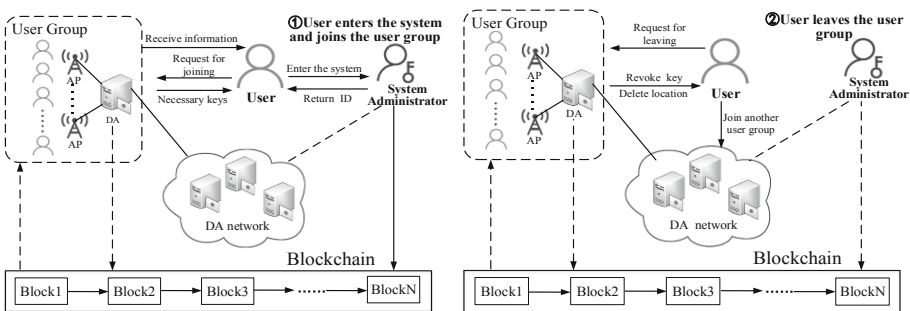


Fig. 2. System model.

System Administrator. Although the majority work of the system administrator has been taken over by domain administrators. However, in order to protect individual

privacy, the system administrator secretly stores the identity IDs of all users and provides services for initial registration, information change and identity revocation.

Domain Administrator. Domain administrator (DA) is a trusted server that provides key management services for users. DA manages a range of user domains, where one or more user groups exist in a user domain. All DAs form a blockchain network, and they verify the identities of users who apply to join the user group by retrieving user information in the block. When a user joins or leaves the group, the hash value of the user's identity information and updated group keys will be added to the block as a transaction. It is convenient for retrieval and audit work of other DAs.

User. User can join and leave each user group with the ID registered by the system administrator. After the user passes the verification and joins the user group, the DA will allocate a location and send corresponding keys for him/her. Then the user can calculate group key and receive the information in the group.

3.2 Block Format and Transaction Format

A block contains a block header and a block body. The block header consists of block version number (Version), the hash value of previous block (Prev Hash), the hash value of Merkle root (Merkle Root), the generation time of block (Timestamp), the difficulty of a hash puzzle (Target Value) and a nonce (Nonce). The Prev Hash links current block to the previous block and forms a chain structure. All transactions are stored through Merkle tree and Merkle Root ensures the integrity of the transactions. The selection of Nonce must ensure that the output of hash function is smaller than the Target Value.

The block body is composed of a list of transactions. The transaction consists of Transaction ID, Transaction Information, Transaction Type, Digital Signature, Public Key and Timestamp. Transaction information is the hash value of information which needs to be added to the block. Digital Signature can be used to verify whether the transaction has been tampered.

There are four types of transactions in our system, as shown below:

- (1) **User registering.** The corresponding identifier is *Register*, transaction information contains the hash value of user's identity ID and the time of joining the system.
- (2) **User joining.** The corresponding identifier is *Join*, transaction information contains the hash value of user's identity ID and the time of joining the user group. It also contains the user group where the user joins.
- (3) **User leaving.** The corresponding identifier is *Leave*, transaction information contains the hash value of user's identity ID and the time of leaving the user group. It also contains the user group where the user leaves.
- (4) **Key updating.** The corresponding identifier is *Update*, transaction information contains the hash value of the updated group key and updated time. It also contains the user group where key updates.

3.3 The Improved PoW Consensus Protocol

Proof-of-Work (PoW) consensus algorithm is the key to ensure the consistency of distributed nodes in Bitcoin network, which requires nodes to solve a hash puzzle to strive for accounting rights. Each node takes the block header as the input of double *SHA256* and controls the output of hash function by changing the nonce value. Only when the output value is smaller than the target, the hash puzzle is solved successfully. In given time, only the longest chain can be added to the main chain. The calculation method of hash puzzle is as follows:

$$SHA\ 256(SHA\ 256(Version \parallel PrevHash \parallel \dots \parallel Nonce)) < Target\ Value \quad (2)$$

In our scheme, because the DAs are trusted servers, so we make the DAs become the miners. In addition, there are numerous transactions in the IoT, so it is necessary to improve the consensus efficiency of blockchain. Since the users who join the system must be authenticated, and unauthorized users are not allowed to perform any operations, so the operating environment can be assumed to be semi-honest. This paper proposes an improved algorithm based on PoW algorithm, which makes miners solve the problem faster by increasing the target value and reducing the difficulty of the hash puzzle. According to the computing power of the miners, we plan to control the generation time of each block at about 2 min. In an ideal situation, the target value of this scheme should be 5 times bigger than the target value of Bitcoin.

Due to the difficulty of hash puzzle is reduced, it may exist that multiple nodes broadcast the result at the same time. In this situation, we use the longest chain and smallest nonce mechanism to reduce the workload of miners and improve the efficiency of the blockchain. In a certain period of time, the system gets the chain of different nodes (*thischain*, *otherchain*), and compares the length of two chains. The longest chain will be added to the main chain. If the chains have the same chain length, the system will get their last block (*thisblock*, *otherblock*), and compare the nonce value in their block header (*thisnonce*, *othernonce*). The chain in which the block has the smallest nonce value will be added to the main chain. In a rare case, chains have the same length and nonce value, then the consensus will fail and each node will wait for the next round of consensus.

4 Blockchain-Based Group Key Management Scheme in IoT

4.1 System Initialization

As the system starts, the following information will be initialized (Table 1):

- (1) **divide user domain:** system administrator divides multiple user domains according to different information classification, and users who need to obtain the same or similar information are allocated to the same user domain.
- (2) **set up domain administrators:** set up a domain administrator DA for each user domain and a DA manages multiple user groups.

- (3) **create user groups:** in order to better manage user keys, new user groups are created in the user domain. The user group is defined by a binary tree structure, where its leaf node is the encryption-key of each user, and the root node is the group key.

Table 1. Notations.

| Notations | Description |
|-----------|--|
| ID | The ID registered for user by the system administrator |
| U_i | The i th user in the current user group |
| k_i | The encryption-key of U_i in the user group |
| UG_i | The i th user group |
| G_k | The group key of the current user group |

4.2 User Register

As shown in Algorithm 1, when a user firstly joins the system, the system administrator *Admin* will register ID for him/her. Meanwhile, the hash value of the ID and the time of joining the system will be added to the block as a transaction, as shown below:

$$Register + h_1_tx + Sign(h_1_tx, SK_{Admin}), \text{ where } h_1_tx = h(ID, Time).$$

Then, the block will wait to be added to the main chain. It is convenient for other DAs to verify. After that, users can join or leave each user group with their ID s.

Algorithm 1. User Register

1. $Admin \rightarrow U_i : ID$
 2. $Admin \rightarrow Block : h_1_tx, Sign(h_1_tx, SK_{Admin}), \text{ where } h_1_tx = h(ID, Time)$
-

4.3 User Join

When a user applies to join a user group, he/she first sends a request to the DA. The request information includes his/her ID , UG_i and time of joining the system. DA will retrieve the blockchain according to the user's request information. The detailed process of user joining a user group is shown in Algorithm 2.

After the user passes the verification, DA will broadcast directly in the group to remind other users: "As the user joins, the group key will be updated". Then, DA will assign the location in the group and provide the necessary keys to the user. Besides, it will generate a transaction recording the hash value of the user's ID and the user's joining time, as well as the group where user joins and the signature made by current DA. The specific transaction is:

$Join + h_{1_tx} + UG_i + Sign(h_{1_tx}, SK_{DA_this}),$ where $h_{1_tx} = h(ID, Time)$.

Finally, DA will add the hash value of the updated G_k and the update time to the block as a transaction, as well as the group where key updates and the signature made by current DA. Then, the block will wait to be added to the main chain. The specific transaction is:

$Update + h_{2_tx} + UG_i + Sign(h_{2_tx}, SK_{DA_this}),$ where $h_{2_tx} = h(G_k, Time)$.

Algorithm 2. User Join

1. $U_i \rightarrow DA: ID, UG_i, Time$
 2. $DA \xrightarrow{Retrieve} Block$
 3. $DA \xrightarrow{Broadcast} Users: "As the user joins, the groupkey will be updated."$
 4. $DA \rightarrow U_i: k_i, necessaryblind keys$
 5. $G_k \xrightarrow{Update} h(BlockHashValue, k')$
 6. $DA \rightarrow Block: h_{1_tx}, UG_i, Sign(h_{1_tx}, SK_{DA_this}),$ where $h_{1_tx} = h(ID, Time)$
 7. $DA \rightarrow Block: h_{2_tx}, UG_i, Sign(h_{2_tx}, SK_{DA_this}),$ where $h_{2_tx} = h(G_k, Time)$
-

The new user u_4 joining the user group is shown in Fig. 1. Firstly, DA generates encryption-key k_4 for u_4 and then distributes his brother's blinded node key $g(k_3)$ and his ancestor's brother's blinded node key $g(k_{12})$ to u_4 , $g(k_3)$ and $g(k_{12})$ are encrypted by k_4 . Since u_4 joins the user group, the node keys k_{34} and k will be updated to k'_{34} and k' . u_4 calculates k'_{34} , k' and G_k using the following formulas:

$$k'_{34} = f(g(k_3), g(k_4)) \tag{3}$$

$$k' = f(g(k_{12}), g(k'_{34})) \tag{4}$$

$$G_k = h(BlockHashValue, k') \tag{5}$$

The blinded node keys which are calculated will be encrypted with corresponding keys and transmitted to the existing group members through multicast, as shown below:

$$u_3 \leftarrow enc(g(k_4), k_3) \tag{6}$$

$$u_1, u_2 \leftarrow enc(g(k'_{34}), k_{12}) \tag{7}$$

4.4 User Leave

When a user leaves the current user group, DA revokes the user's encryption-key and deletes his/her location from the key tree. As shown in Algorithm 3, DA broadcasts the

following message in the group to remind other users: “As a user leaves, the group key will be updated”, and add the hash value of the user’s ID and the time of leaving the group to the block as a transaction, as well as the group where user leaves and the signature made by current DA. The specific transaction is:

$$Leave + h_{1_tx} + UG_i + Sign(h_{1_tx}, SK_{DA_this}), \text{ where } h_{1_tx} = h(ID, Time).$$

To prevent collusion attacks, DA will generate a random number to participate in group key updating. Similarly, DA will add the hash value of the updated G_k and the update time to the block as a transaction, as well as the group where key updates and the signature made by current DA. Then, the block will wait to be added to the main chain. The specific transaction is:

$$Update + h_{2_tx} + UG_i + Sign(h_{2_tx}, SK_{DA_this}), \text{ where } h_{2_tx} = h(G_k, Time).$$

Algorithm 3. User Leave

1. $DA \xrightarrow{\text{Broadcast}} Users: "As a user leaves, the group key will be updated."$
 2. $DA \rightarrow Users: a \text{ random numbers for updating}$
 3. $DA \rightarrow Users: necessary \text{ blind keys}$
 4. $G_k \xrightarrow{\text{Update}} h(\text{BlockHashValue}, k')$
 5. $DA \rightarrow Block: h_{1_tx}, UG_i, Sign(h_{1_tx}, SK_{DA_this}), \text{ where } h_{1_tx} = h(ID, Time)$
 6. $DA \rightarrow Block: h_{2_tx}, UG_i, Sign(h_{2_tx}, SK_{DA_this}), \text{ where } h_{2_tx} = h(G_k, Time)$
-

As shown in Fig. 1, u_4 leaves the right subgroup G_r and the group key is generated by the blinded node keys of the subgroups G_r and G_l . Our scheme would change these two subgroup keys to prevent collusion attacks.

- (1) After u_4 leaves the user group, the structure of key tree will change. u_3 will be allocated a new encryption-key k'_{34} and it moves up to his parent’s node. The new blinded node key $g(k'_{34})$ is encrypted by k_{12} and shared with the left subgroups G_l :

$$G_l \leftarrow enc(g(k'_{34}), k_{12}) \quad (8)$$

- (2) As for the left subgroup G_l , DA generates a random number r_n , which is shared as $G_l \leftarrow enc(r_n, k_{12})$ among all current users of the subgroup.
- (3) The blinded node key $g(k_{12})$ will change to be $g(k'_{12})$ by using r_n .

$$g(k'_{12}) \rightarrow g(g(k_{12}) \oplus r_n) \quad (9)$$

- (4) The generated left subgroup key $g(k'_{12})$ is shared with the right subgroup:

$$G_r \leftarrow enc(g(k'_{12}), k'_3) \quad (10)$$

(5) The new group key G_k can be calculated by k'_{12}, k'_3 :

$$k' = f(g(k'_{12}), g(k'_3)) \tag{11}$$

$$G_k = h(BlockHashValue, k') \tag{12}$$

4.5 Update User Keys Regularly

As shown in Algorithm 4, in order to ensure the security of the user’s key, the key will be updated automatically at intervals. The update method is that concatenate the key with the current block hash value *BlockHashValue*. Then DA distributes the new blinded key of each node to the corresponding user. Finally, DA adds the hash value of the updated G_k and the update time to the block as a transaction, as well as the group where key updates and the signature made by current DA. Then, the block will wait to be added to the main chain. The specific transaction is:

$$Update + h_{2_tx} + UG_i + Sign(h_{2_tx}, SK_{DA_this}), \text{ where } h_{2_tx} = h(G_k, Time).$$

Algorithm 4.Update User Keys

1. $k_i \xrightarrow{Update} f(k_i, BlockHashValue)$
 2. $DA \rightarrow Users: necessaryblind\ keys$
 3. $DA \rightarrow Block: h_{2_tx}, UG_i, Sign(h_{2_tx}, SK_{DA_this}), \text{ where } h_{2_tx} = h(G_k, Time)$
-

5 Security Analysis and Performance Analysis

In the original OFT scheme, the blinded node keys known by the user who has left user group is kept unchanged, and the user can share the available blinded node key with other users, which may lead to collusion attacks and serious privacy disclosure. Our scheme fixes this vulnerability by generating random number to change blinded node keys and establishing the PRNG with time series. Assuming that DA is completely reliable, cryptography algorithm and consensus mechanism are secure, our scheme can guarantee forward and backward safety, and prevent collusion attacks.

Since our scheme involves the *BlockHashValue* in updating the group key, the group key is guaranteed to be updated with time series, basically preventing the possibility of collusion attacks. However, considering the hash value of the block header may not change for a certain period of time, in this case we discuss the security of the scheme. Here is a case: Alice leaves the subgroup G_l , Bob and Cindy join the subgroup G_l or G_r . Alice knows the initial group key k_{G_0} , which is calculated by $g(k_{G_l})$ and $g(k_{G_r})$.

Case 1 : consider the case where Bob and Cindy join the same subgroup G_r . Then we can calculate the group key k_G in different cases.

- (1) Alice leaves G_l : $k_{G1} = f(g(k'_{Gl}), g(k'_{Gr}))$
- (2) Bob joins G_r : $k_{G2} = f(g(k'_{Gl}), g(k''_{Gr}))$
- (3) Cindy joins G_r : $k_{G3} = f(g(k'_{Gl}), g(k''_{Gr}))$

In this case, Alice cannot collude with any existing user to obtain the illegal group key.

Case 2 : consider the case where Bob joins the subgroup G_l and Cindy joins the subgroup G_r . Similarly, we can calculate the group key k_G in different cases.

- (1) Alice leaves G_l : $k_{G1} = f(g(k'_{Gl}), g(k'_{Gr}))$
- (2) Bob joins G_l : $k_{G2} = f(g(k''_{Gl}), g(k'_{Gr}))$
- (3) Cindy joins G_r : $k_{G3} = f(g(k'_{Gl}), g(k''_{Gr}))$

In this case, Alice cannot collude with any existing user to obtain the illegal group key either. Therefore, our scheme guarantees forward and backward security, and prevents any collusion attacks. Table 2 shows the security comparison of some existing key management schemes, it indicates that our scheme has better security.

Table 2. Security comparison of key management schemes.

| Schemes | Forward security | Backward security | Prevent collusion attacks |
|------------|------------------|-------------------|---------------------------|
| [13] | Y | Y | Y |
| [14] | N | N | N |
| [15] | Y | Y | Y |
| Our scheme | Y | Y | Y |

Based on the Intel (R) Core (TM) i5-7300HQ environment, IntelliJ IDEA 2019.2.4 and the Go language, this scheme is implemented to analyze the performance efficiency, storage consumption and time consumption. In paper [15] and our scheme, the broadcast costs of user leaving the user group are $(\log_2(n))^2 + \log_2(n)$ and 5 respectively. So, compared to the paper [15], our scheme reduces the broadcast costs for user leave.

Considering the security of this scheme, we use 256-bit ECDSA digital signature algorithm and SHA256. A transaction which is stored in the block contains the type of transaction, the transaction data, the public key and digital signature. So, the storage consumption of a transaction is about 110B.

In our scheme, we conduct the consensus every 1 min. In this minute, miners will add all the transactions in the network to the block after verification. And the time for miners to solve the hash puzzle is about 2 min. This means that every 3 min a new block will be added to the main chain. Therefore, we conduct time-consuming tests and write performance tests on the process that blocks are added to the chain. We assume that a transaction will be generated every second. Figure 3 shows the time consumption

of adding 100 to 1000 pieces of transaction to the main chain. It has been proved through experiments that time consumption has no influence on normal key management processes.

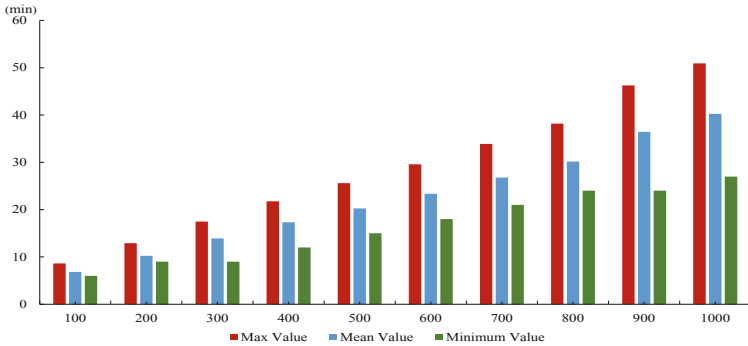


Fig. 3. Time consumption of adding transactions to the main chain.

6 Conclusion

This paper proposes a blockchain-based group key management scheme in IoT. In this scheme, blockchain technology is deployed to guarantee that users can securely share resources in the decentralized domain administrator network. After users join or leave user group, the hash value of the user's identity information and updated group keys will be added to the block as a transaction, which enables the domain administrators to verify information rapidly and improves the efficiency of the group key update for the dynamic group members. However, in order to facilitate the retrieval and audit work of other domain administrators, the user's activity and key update are recorded on the blockchain, which will increase the storage and computing overhead of the system. Meanwhile, this scheme does not consider the effective storage of keys. In our future work, we will focus on studying the blockchain-based efficient key storage scheme and improving the efficiency of the blockchain.

References

1. Harney, H., Harder, E.: Logical key hierarchy protocol. Draft-harney sparta-lkhp-sec-00.txt, IETF Internet Draft (1999)
2. Balenson, D., McGrew, D., Sherman, A.: Key management for large dynamic groups: one-way functions trees and amortized initialization. IETF Internet Draft (1999)
3. Ma, H., Wang, Z., Wang, J., Guan, Z.: Multi-authority attribute-based encryption resilient against auxiliary-input leakage. *J. Comput.* **31**(1), 134–147 (2020)
4. Ma, H., Wang, Z., Guan, Z.: Efficient ciphertext-policy attribute-based online/offline encryption with user revocation. *Secur. Commun. Netw.* **2019** (2019)

5. Krishnan, K., Jenu, R., Joseph, T., Silpa, M.: Blockchain based security framework for IoT implementations. In: 2018 International CET Conference on Control, Communication, and Computing (IC4), pp. 425–429. IEEE (2018)
6. Pajoo, H., Rashid, M.: A security framework for IoT authentication and authorization based on blockchain technology. In: 2019 18th IEEE International Conference on Trust, Security and Privacy in Computing and Communications/13th IEEE International Conference on Big Data Science and Engineering (TrustCom/BigDataSE). IEEE (2019)
7. Mohanty, S., Ramya, K., Rani, S.: An efficient lightweight integrated blockchain (ELIB) model for IoT security and privacy. *Future Gener. Comput. Syst.* **102**, 1027–1037 (2020)
8. Ge, C., Liu, Z., Fang, L.: A blockchain based decentralized data security mechanism for the Internet of Things. *J. Parallel Distrib. Comput.* **141**, 1–9 (2020)
9. Ma, H., Huang, E.X., Lam, K.Y.: Blockchain-based mechanism for fine-grained authorization in data crowdsourcing. *Future Gener. Comput. Syst.* **106**, 121–134 (2020)
10. Pal, O., Alam, B., Thakur, V., Singh, S.: Key management for blockchain technology. *ICT Express* (2019). <https://doi.org/10.1016/j.icte.2019.08.002>
11. Lei, A., Cruickshank, H., Cao, Y., Asuquo, P., Ogah, C.P.A., Sun, Z.: Blockchain-based dynamic key management for heterogeneous intelligent transportation systems. *IEEE Internet Things J.* **4**(6), 1832–1843 (2017)
12. Kung, Y.H., Hsiao, H.C.: GroupIt: lightweight group key management for dynamic IoT environments. *IEEE Internet Things J.* **5**(6), 5155–5165 (2018)
13. Wallner, D., Harder, E., Agee, R.: Key management for multicast: issues and architectures. IETF, RFC2627 (1999)
14. Sherman, A.T., McGrew, D.A.: Key establishment in large dynamic groups using one-way function trees. *IEEE Trans. Softw. Eng.* **29**(5), 444–458 (2003)
15. Ku, W.C., Chen, S.M.: An improved key management scheme for large dynamic groups using one-way function trees. In: 2003 International Conference on Parallel Processing Workshops, pp. 391–396. IEEE (2003)



Research on Ideological and Political Education of College Students Based on Network Information Security

Xiao-yu Liu^{1,2}(✉), Yu-hang Zhu¹, Yan Ma¹, Pan Zhou¹,
and Guang-yue Tian¹

¹ Zhengzhou Normal University, No. 6 Ying-cai Street, Hui-ji District,
Zhengzhou, Henan, China
zzsy_lxy@126.com

² Wuhan University of Technology, No. 122 Luo-shi Road, Hong-Shan District,
Wuhan, Hubei, China

Abstract. With the rapid development of Internet and instant messaging tools, college students' study and life, the respect such as communication, profound changes have taken place, ecological network public opinion is bound to profound influence on college students and college students' ideological and political education to bring trouble. Therefore, the ideological and political education based on network information security work is becoming more and more important. This article introduces the Problems existing of ideological and Political Education of College Students based on Network Information Security and Innovate the practical path of ideological and political education for college students based on Network Information Security.

Keywords: University students · Network information security · Ideological and political education · Strategy

1 Introduction

With the rapid popularization and application of the Internet in major cities of China, college students account for a very large proportion of Internet users. The advantages such as the rapidity and convenience of the Network provide convenience for college students' study, life and entertainment. However, due to the unsafe factors of the network itself and the undefined values of college students, college students unfortunately become victims in the process of using the network. It is necessary to educate college students about network information security. It is of great theoretical significance and practical value to study the problems existing in college students' network information security education (Table 1).

Table 1. The use of Internet by college students was investigated

| | Learning | Playing the game | Chat | Entertainment | Shopping | Posting a micro-blog |
|--------|----------|------------------|-------|---------------|----------|----------------------|
| Male | 13.2% | 24.6% | 20.4% | 17.4% | 10.2% | 14.2% |
| Female | 17.9% | 8.7% | 24.2% | 18.5% | 15.2% | 15.5% |

2 Literature Review

The popularization and application of network in China is relatively late, so the research on network information security in China is not sufficient compared with that in foreign countries. The research on network information security education in China mainly focuses on the following aspects:

2.1 The Necessity of Network Information Security Education in Colleges and Universities

Chinese scholar Guan Xiao-quan emphasized the necessity and importance of information security education for college students to reduce the injury suffered by college students in the network. Ren Zhan-juan analyzed the characteristics of college students and concluded that the network is a double-edged sword. She emphasized college students should improve their self-protection ability when surfing the Internet. Through the analysis of the research results on the necessity of network information security education, it can be seen that China's academic community has a profound understanding of the unsafe factors of network information security and the particularity of college students, and believes that colleges and universities need to strengthen the network information security education for college students.

2.2 The Current Situation of Network Information Security Education in Colleges and Universities

Many Chinese scholars have studied the current situation of the network information security education in colleges and universities because of the difficulties in the network information security education of Chinese college students. Wu Zi-guo and Tian Xiu-yun discussed the current situation of network information security education in colleges and universities at different levels. They believed that Chinese colleges and universities offered few courses on network information security for college students, and that the education intensity in network information security education in colleges and universities was insufficient, with low attention degree, and the educational effect was not obvious. Zhou Tao pointed out that colleges and universities currently pay insufficient attention to network information security education, in the capital, financial resources and other aspects of investment is insufficient, have not fully realized the dangers of ignoring network information security education. Dong Ya-ping thought that the courses of the ideological and political education network information security no matter in terms of types and the existing teaching materials, did not follow the era,

and affected the improvement of college students' knowledge and ability in network information security. In a word, there are big problems in network information security education in Chinese universities. The main manifestations are as follows: insufficient attention, imperfect course setting and arrangement and poor-timeliness textbook.

2.3 The System and Norms of Network Information Security Education in Colleges and Universities

Some scholars have studied the legislation and system of network information security education for college students. Lu Wei discussed the legislation and system formulation of network security for college students in China, combed through the legal system, and believed that the legal system specially formulated for network security in China is still not perfect, lacking relevant legislation and norms. It is believed that there will be a lack of theoretical basis for colleges and universities to carry out relevant educational activities.

2.4 The Strategy of Network Information Security Education in Colleges and Universities

Wei Qiao-yuan, a Chinese scholar, put forward strategies and suggestions from the five aspects of constructing network security operation mechanism, college curriculum setting, perfecting relevant legal system, perfecting education and teaching methods. Chen Lian-jiao and Wen Jin-ying thought that it is necessary to build a network security supervision system, which can be technically controlled by using some high-tech software in order to strengthen the network information security education of college students. Pei Jin-song and Gao Yan pointed out that the network information security education for college students only depends on the strength of colleges and universities is not enough. It is necessary for colleges and universities to learn from the experience of western countries, build cooperative relations between governments, institutions and social organizations, make full use of various social forces to improve the school network information security education, form a standardized network information security management system, and provide a safe and clean network environment for college students. Huang Ying-ping proposed that the values and world outlook of most college students are easily affected after the coming of the network era, and the education on network information security should be strengthened in colleges and universities from the aspects of curriculum reform and setting.

Therefore, it can be seen that in the studies of institutes, although China has studied many aspects in the study of college students' network information security education, the research contents are scattered, not concentrated, not deep enough, especially the research of college students' ideological and political education based on network information security are relatively lacking. In terms of research methods, the research on network information security education in china mainly focus on the theoretical research level, lacking of empirical investigation and the use of quantitative methods. In terms of research perspective, the research on network information security education in china is relatively single and localized.

3 Problems Existing of Ideological and Political Education of College Students Based on Network Information Security

3.1 Hysteresis of College Students' Cognition of Network Information Security

Previous studies have found that college students' cognition of network information security is not comprehensive enough and lags behind. The main reasons for the lagging cognition of college students on network information security are as follows: First, college students, who have little contact with the society and a low degree of cognition and understanding of the society, do not form a correct view of society and are not strong in discrimination and self-protection against some behaviors such as network fraud. Secondly, at the present stage, the strength of setting up network information security courses in Chinese university campuses cannot keep pace with the rapid development of network information technology and universities do not provide enough education and guidance on ideological and Political Education of College Students based on Network Information Security. Third, the ideological and political education courses are not comprehensive enough in terms of network information security knowledge, rules and regulations, laws and regulations, etc., leading to college students paying less attention on the knowledge of network information security.

3.2 The Supervisory Role of College Teachers in Network Information Security Education Needs to Be Strengthened

The diversity of network equipment, the flexibility of Internet access and the extensiveness of Internet access time make it more difficult for teachers to supervise students' Internet access. At present, colleges and universities have not worked out relevant systems on network information security, and the supervision role of college teachers on students cannot be brought into full play. A teacher is not only the impetrator of knowledge, but also the helper who helps students to solve their difficulties. A teacher is the main guide and guide in students' study and life. With the rapid development of network technology, the mass of network resources and the rapidity of solving problems have gradually replaced the position and role of teachers. When college students encounter difficulties in study or unsatisfactory things in life, they can solve them through the Internet. The appearance of network impinges on the original status and use of teachers. In the eyes of students, the guidance role of teachers is also reduced. At the same time, facing the emergence of new media and technology, most teachers have a low degree of cognition of the Internet. In the aspect of network information security, teachers cannot give students enough guidance and instructions.

3.3 Lack of Network Information Security Education Assessment System

The imperfect evaluation system of safety related knowledge and ability will directly affect college students' mastery of network information security knowledge and ability. Therefore, in order to improve college students' awareness, discrimination and

self-control of network information security, it is necessary to establish and improve the curriculum system of network information security education, especially the evaluation system of network information security education. The main ways of explaining network information security knowledge in colleges and universities are lectures related to ideological and political courses, blackboard newspapers and network publicity, etc., and colleges and universities have not yet formed a scientific and reasonable network information security education curriculum system (Table 2).

Table 2. The degree of college students' identification with the current network moral anomia

| Recognition degree of network moral anomie | The number of people | The percentage |
|--|----------------------|----------------|
| Very serious | 98 | 24.5% |
| Widespread | 182 | 45.5% |
| Individual phenomenon | 94 | 23.5% |
| Inexistence | 26 | 6.5% |
| The total | 400 | 100% |

4 Innovating the Practical Path of Ideological and Political Education for College Students Based on Network Information Security

To better innovate the practical path of ideological and political education for college students based on Network Information Security, three effective measures will be proposed below.

4.1 Innovating the Idea of Ideological and Political Education for College Students

From the perspective of network information security, it is beneficial to improve the effectiveness of college students' ideological and political education in network information security ecology through innovative educational concepts. The innovations of ideological and political education concept for college students from the perspective of network information security are as follows:

4.1.1 Setting up the Idea of Subject Equality

Subject equality means that under the network information security ecology, college students and ideological and political educators of college students have equal status in the network, and they can equally obtain relevant public opinion information and use the network media. At the same time, in real life, the equality of citizenship, personality and other aspects is only different between college students and educators in terms of knowledge and experience. With the rapid development of network information and the acceleration of the upgrading of network media, college students have more opportunities to obtain network public opinion information and have more ways to express their opinions. It is even easier than some educators to grasp the discourse expression

right of network media. Therefore, the subjectivity of college students' ideological and political educators is balanced, and the discourse authority is weakened. Educators need to strike a balance between acknowledging and accepting the facts that are being challenged by the object of their education. Educators should set up the idea of equality in carrying out ideological and political education for college students and promote the smooth development of ideological and political education for college students.

4.1.2 Fostering the Concept of Inclusiveness

In the era of network information, multi-cultural exchanges are increasingly deepened, which makes the information of network public opinion diversified and the network language diversified. The appearance of various opinions, attitudes and network language on the Internet is a kind of network normality, and college students are bound to be affected by this phenomenon. College students' ideological and political educators should focus on the objective facts behind the network public opinion rather than the expression of the network public opinion. Therefore, from the perspective of network information security, ideological and political educators of college students should establish the concept of tolerance, tolerance of college students' diverse choices, not only to promote the main theme, but also to embrace the multi-network culture.

4.1.3 Establishing the Concept of Resultant Force

Network information security ecology is the structure state of interactive and dynamic development between network information security subject, network information security carrier, network information security environment and network information security laws and norms. Network information security through its own four elements of the resultant force to promote its development. To be specific, in this ecology, as long as any one of the four elements changes, the other three elements will be corresponding force, or promote or inhibit, therefore, it is of great significance to make the network information security ecology in a state of dynamic balance and benign development. From the perspective of network information security, ideological and political education of college students should establish the concept of joint forces, so as to deal with the dilemma of ideological and political education of college students caused by the ecology of network public opinion and maximize the effectiveness of ideological and political education.

4.2 To Enrich the Ideological and Political Education of College Students

4.2.1 Online Legal Education of Public Opinion and Online Information Security Education

The virtual, free and open nature of the network space enables college students to have more independent choices in the network. Some false and irrational online public opinion information fills the cyberspace, and some college students' comments are reproduced without confirmation, posing a threat to universities and even the social security order. Therefore, it is necessary to strengthen the legal education of network public opinion in the ideological and political education of college students. In terms of content, strengthen legal knowledge education of online public opinion, and explain to students that the freedom of online speech is the freedom under the law, and any

freedom in the world is the freedom under the constraint of relevant laws. Students are warned to abide by national laws and regulations at any time and place (including their speech in cyberspace), or they will pay the price for their words and deeds. In addition, there are security risks and vulnerabilities in the Internet, enabling those with ulterior motives to take advantage of these vulnerabilities to steal national and individual information and harm national and individual interests. Therefore, strengthen the network information security education, to safeguard the interests of the country and the people is crucial. To strengthen college students' network information security education, in addition to strengthen the network information security laws and regulations education, also deal with computer password technology and application, the understanding to the virus and the prevention and control, anti-virus technology, hacker intrusion detection technology, firewall technology, intrusion detection techniques such as education, make students know the importance of the network information security, jointly participate in the maintenance of the network information security in our country.

4.2.2 The Traditional Virtue and Network Moral Education

“The country does not prosper without virtue, people do not stand without virtue”. Therefore, the ideological and political education of college students should strengthen the traditional Chinese virtue education and network moral education from the ecological perspective of network public opinion. With the advent of the network society, it has become normal for people to browse information and exchange information online. The traditional Chinese virtues of “benevolence, justice, propriety, wisdom and faithfulness” are also applicable in the network society. For example, people should not read other people's Internet emails and chat messages without their consent, which is the embodiment of “letter”. People should not spread online public opinions without verification, which is the embodiment of “wisdom” to distinguish right from wrong. In ideological and political education content at the same time, strengthen the education of network morality is good for college students to cultivate network moral consciousness, let college students in the case of anonymous also not to manufacture, spread false and irrational network public opinion, and realize that even in the network must abide by the moral, otherwise will be subject to the relevant laws and inner condemnation.

4.2.3 The Education of “Three Views” for College Students

“Three views” is the world outlook, outlook on life, values. “Three views” has an important guiding role for college students to realize life value and social value. However, the terror, pornography, violence, false information, entertaining, interesting and even vulgar contents in the Internet, as well as the decadent values in the West and the West on the Internet have a huge negative impact on the growth and development of college students. Therefore, it is necessary to strengthen the education of college students' world outlook, outlook on life and values, so that they can set up the correct “three outlook”, consciously resist individualism, money worship and hedonism, resist bad information of network public opinion, and form good behavior habits.

4.3 Innovating Ideological and Political Education Methods for College Students

4.3.1 Educator Initiative Dialogue

Educators should organize forces to take the initiative to understand the situation in relevant online speech and behavior. The team should be composed of counselors, student cadres and student tutors to monitor and investigate the thoughts and behaviors of college students. College students' ideological and political educators should have an equal dialogue with relevant students when they find their behaviors misbehaving in the network. Equal dialogue requires educators to keep a low profile, be tolerant and considerate of students, and realize understanding by feeling and reasoning. In addition, it should be noted that the equal dialogue should be conducted in private rather than in public, which is conducive to the students concerned to open up and tell the truth, so as to promote the solution of problems.

4.3.2 Setting up Internet Public Opinion Issues

Setting corresponding topics before the outbreak of public opinion can guide the direction of public opinion and avoid the outbreak of public opinion out of control. In the guidance of college students' network public opinion, colleges and universities can implement the topic setting, which can lead the attention of college students to the set target of network public opinion center. For example, can put the college students pay attention to the social politics, relationship problems, employment problems in campus network or zone on the campus BBS subject setting, when the relevant section of network public opinion, face-to-face announcement in the first place, on college students' network public opinion toward areas, helps control the disorder of college students' network public opinion extension.

4.3.3 Innovating Network Public Opinion Carrier

With the advent of new media era, college students prefer to use simple and fast ways to record social changes and their own growth. In the eyes of college students, websites or campus networks are less attractive than new media with instant messaging function, and new media are more easily accepted by college students. For example, weibo and WeChat are most widely used among college students. Therefore, the ideological and political education of college students can develop a new carrier platform to effectively monitor and guide the network public opinion of college students, and promote the ideological and political education of college students to improve the traditional methods. For example, universities can set up two types of WeChat public accounts, one is the WeChat public account that party members and league members must pay attention to, and the other is the WeChat public account for students on campus. The purpose of WeChat is to guide party members to consciously abide by party discipline and school related system, and play a vanguard and exemplary role. At the same time, the school student public account for daily information updates, content is closely related to college students' life, study and employment issues. This is conducive to the guidance of college students' network public opinion and the improvement of college students' ideological and political education methods. At the same time, it also enhances the discourse power of college students' ideological and political educators.

5 Conclusion

In summary, facing the huge impact of network informatization on college students' thoughts and concepts, network information security education is an urgent problem to be solved on campus. Therefore, the network information security education of college students should be included in the content of college education as soon as possible, to provide college students with the help of network information security awareness, behavior, technology and other aspects, so as to minimize the harm of college students in network information.

Acknowledgement. This research was financially supported by Zhengzhou Normal University 2019 Innovative Experimental Plan for College Students Project: DCY2019029.

References

1. zheng, C.: Try to analyze how to use big data thinking to carry out ideological and political education in universities. *Party Build. Ideological Educ. Schools* **18**, 45–46(2015)
2. Chen, H.D.: Thoughts on network ideological and political education in universities under the internet thinking mode. *Guide Ideological Theor. Educ.* **8**, 116–118 (2016)
3. Qu, B.K., Shi, L.F. (eds.): *Outlook on International Education*. People's Education Press, Beijing (1993)
4. Qiu, Q.Z., Sun, P.: Opportunities and challenges of ideological and political education in universities in the era of big data. *Educ. Theory Pract.* **36**(9), 35–37 (2016)
5. Qiu, Q.Z.: Ideological leadership construction in the era of big data. *J. Fujian Provincial Party School* **11**, 101–103 (2016)
6. Victor, M.S., Kenneth, C.: *The Age of Big Data: The Revolution of life, Work and Thinking*. Translated by Yang Yan sheng and Tao Zhou. Zhejiang People's Press, Hangzhou (2013)
7. Qi, P.C.: Research on the main problems and countermeasures of network information security education for college students. 2016 Master's thesis of Guangxi Normal University (2016)
8. Chen, H.M.: Research on existing problems and countermeasures of network security education for college students. 2019 Master's thesis of Central China Normal University (2019)
9. Zhang, Y.X., Kang, X.L.: Research on social network personal information security in the era of big data. *Lantai World* **5**, 24–25 (2015)
10. Su, G.H., Li, M.: Big data thinking in ideological and political education in Colleges and Universities. *J. Hun. Univ. Technol. (Soc. Sci. Edn.)* **03**, 60–64 (2018)
11. Zhang, B., Xia, X.: Research on ideological and political education response of college students from the perspective of new media. *Heilongjiang High. Educ. Res.* **02**, 125–126 (2017)
12. Ren, S.X., Wang, X.Y., Du, C.S.: Practice of innovative ideological and political education in colleges and universities. *Beijing Educ. Moral Educ.* **06**, 51–52 (2015)
13. Cui, H.H., Zhang, Y.I.: Ideological and political education discourse and its Modern Transformation. *Theor. Explor.* **1**, 70–74 (2016)
14. Kang, L.C.: *A Book to Understand the Big Data Era*. Democracy and Construction Press, Beijing (2015). 6

15. Tu, Z.P.: *Big Data: The Coming Data Revolution and How It Is Changing Government, Business and Our Lives*. Guangxi Normal University Press, Guilin (2012). 67
16. Yang, G.L., Liu, L., Yan, Z.H.: Application research of big data thinking in college students' ideological and political education. *Guide Ideological Polit. Educ.* **11**, 144–148 (2016)
17. Li, H.J., Wu, S., Xia, H.: Research on the construction of college network ideology in the era of big data. *Res. Ideological Educ.* **5**, 75–79 (2016)

Artificial Intelligence in Biological and Medical Information Procession



A Novel Plastic Neural Model with Dendritic Computation for Classification Problems

Junkai Ji¹(✉), Minhui Dong¹, Cheng Tang², Jiajun Zhao¹,
and Shuangbao Song³

¹ College of Computer Science and Software Engineering, Shenzhen University,
Shenzhen 518060, China

jjjunkai@szu.edu.cn,

{1910273042, 1910272062}@email.szu.edu.cn

² Faculty of Engineering, University of Toyama, Toyama-shi 930-8555, Japan
d2072006@ems.u-toyama.ac.jp

³ Aliyun School of Big Data, Changzhou University, Changzhou 213164, China
leadingsong@outlook.com

Abstract. This paper proposes a novel plastic neural model (PNM) at the single neuron level and a specified learning algorithm to train it. The dendritic structure of PNM presents its diversity to fulfill each particular task. During the training process, PNM divides the Euclidean space of the training instances into several appropriate hypercubes, which have the same dimensional number. And then, each hypercube is transformed into a corresponding dendritic branch in PNM. A suitable dendritic structure of PNM has been proved to have powerful computational capabilities to solve the classification problems. Both theoretical analysis and empirical study of the proposed model are demonstrated in this paper. Five benchmark problems are employed to verify the effectiveness of PNM in our experiment. The results have verified that PNM can provide competitive classification performance compared with several widely-used classifiers.

Keywords: Neural network · Dendrite · Plastic · Hypercube · Classification

1 Introduction

Artificial Neural Networks (ANN) are one kind of the most significant inventions in the field of soft computing [8, 27]. The rudimentary concepts of the neural network were first mathematically modeled by McCulloch and Pitts, which are inspired by biological neurons in our brain [26]. The well-known universal estimation proficiencies make Feedforward Neural Networks (FNN) most widely used over the last decade among numerous ANNs [13, 36]. Actually, there are two types of FNNs, namely Single Layer Perceptron (SLP) [33] and Multi-Layer Perceptron (MLP) [15]. MLPs have been proved to be capable of approximating any continuous and discontinuous function [7, 18]. Whereas, there is only one single perceptron in the SLP, which makes it unable to solve a non-linear problem [28].

Latest development in neurobiology have verified the importance of dendrites in neural computation [2, 10, 23, 24], that is the dendritic structure has greatly expanded the neural computational capacities. A single neuron with a dendritic structure has shown to be able to enhance the capacities of direction selectivity [31, 35], feature storage [32], computation of binocular disparity [3], and generalization [16, 17]. These enhancements provide us a hypothesis that such SLP might be able to be adopted to compute linearly non-separable functions [4].

Recently, Legenstein and Maass have introduced an integrated model with synaptic plasticity and branch-strength potentiation [22]. They have applied the model to solve a simple feature binding problem successfully, for justifying linearly nonseparable functions of single neurons. However, the Legenstein and Maass model is proved to be unable to solve the Exclusive-OR problem [6]. The ability of single neurons to perform non-linear pattern separation remains an open question [37].

In our previous papers, we have proposed an approximate logic neural model (ALNM) based on the interaction of dendrites [19], which has a neural-pruning function to form a unique dendritic topology for a particular task by screening out useless synapses and unnecessary dendrites. The model has been proved to be capable of solving non-linearly separated problems effectively by single-neuron computation. In addition, we have modified the neural model and trained it by adopting a generalized delta-rule-like unsupervised learning algorithm [38]. The new modified model has been applied to solve a two-dimension multi-directional selectivity problem successfully without an external teacher signal.

However, the learning algorithms of both approximate logic neuron model and unsupervised learnable neuron model are based on Error Back Propagation (EBP) algorithm. Because of the slow convergence property [11] and inherent local optima trapping problem of EBP [21, 25], the models are usually unable to find a suitable topological architecture easily. In this paper, a plastic neural model (PNM) with dendritic computation is proposed. The neural model is named ‘plastic’, because PNM is capable of constructing a specified dendritic structure for each classification problem. PNM has three layers, including a synaptic layer, a dendritic layer and a soma layer. Specifically, terminal axons of former neurons have two types of synapses connecting to each dendritic branch, namely direct synapse and inverse synapse. That makes each branch of the dendritic layer correspond to a hypercube in a multidimensional coordinate. Due to this distinctive property of the new model, we develop a novel learning algorithm to train PNM, which has no convergence problem and is effective in avoiding the disadvantages of EBP during the training process. To verify the effectiveness of PNM and its learning algorithm, five benchmark classification problems are utilized in our experiment.

The rest of the paper is organized as follows: Sect. 1 presents a detailed description of PNM; In Sect. 2, three examples are used to demonstrate the properties of PNM. Section 3 describes the learning algorithm and presents an application; Sect. 4 presents the comparative experiments and the discussion of the results; lastly, concluding remarks are given in Sect. 5.

2 Plastic Neural Model with Dendritic Computation

Inspired by biological neurons, PNM has a realistic neural model structure, which has shown in Fig. 1. It can be observed that PNM is composed of three layers: a synaptic layer, a dendritic layer, and a soma body.

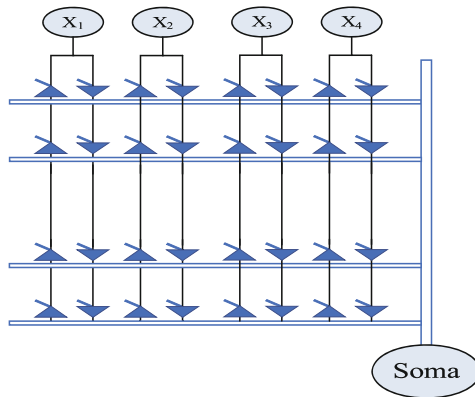


Fig. 1. Schematic diagram of PNM. Direct and inverse synapses (triangle and inverted triangle) process signals from terminal axons of the front neurons (vertical lines) and transmit them to independent branches of dendrites (horizontal lines) through dendritic computation. Then branch signals are collected in the soma body (black sphere).

2.1 Synaptic Layer

The synaptic layer is a specialized structure that is an information transfer medium for signal communication. If the input signal excites the synaptic layer, an excitatory postsynaptic potential (EPSP) will be generated to depolarize the potential of the soma body. It contributes to the fire of the neuron. On the contrary, if the input signal inhibits the synaptic layer, an inhibitory postsynaptic potential (IPSP) will occur to hyperpolarize the potential of the soma body. It prevents the neuron from firing [12]. In PNM, two types of synapses are defined, namely the direct synapse and the inverse synapse. Each synapse has its own threshold value. By comparing the signal inputs with the threshold, the outputs of the two kinds of synapses can be expressed by the following equation:

Direct synapse:

$$Y_{i,m}(\text{Direct}) = \frac{1}{1 + e^{-k(x_i - \theta_{i,m}(\text{Direct}))}} \quad (1)$$

Inverse synapse:

$$Y_{i,m}(\text{Inverse}) = \frac{1}{1 + e^{k(x_i - \theta_{i,m}(\text{Inverse}))}} \quad (2)$$

where k is a positive constant, x_i denotes the input signal from the i -th ($i = 1, 2, 3, \dots, I$) neuron, $Y_{i,m}$ denotes the synaptic computation result of x_i on the m -th ($m = 1, 2, 3, \dots, M$) branch of dendrite; $\theta_{i,m}(\text{Direct})$ and $\theta_{i,m}(\text{Inverse})$ correspond to the thresholds of the direct synapse and inverse synapse respectively, which need to be trained by a certain learning algorithm.

2.2 Dendritic Layer

In the biological neural networks, dendrites interact with synaptic signals on each branch nonlinearly. Biological experimental evidence reveals that neurons with multiplicative responses are extremely powerful computational elements in neural computation. A range of visual and auditory processes are implemented by the multiplication operation [34]. Inspired by these phenomena, multiplication operation is also adopted in the dendritic layer of PNM. The equation of the dendritic layer can be described as follows:

$$Z_m = \prod_{i=1}^I Y_{i,m}(\text{Direct}) * Y_{i,m}(\text{Inverse}) \quad (3)$$

2.3 Soma Layer

Soma body accumulates sublinear summation of the signals of each independent dendritic branch. It fires depending on the result of summation exceeds the soma's threshold. It is shown mathematically as:

$$O_{soma} = \frac{\sum_m Z_m e^{vZ_m}}{\sum_m e^{vZ_m}} \quad (4)$$

where v is a positive constant. It can be observed that a soft-maximum function are used in the equation. It will produce the same result as the maximum operation ($\lim_{v \rightarrow \infty} O_{soma} = \max(Z_1, Z_2, \dots, Z_M)$) within the limit.

3 Motivation

Based on the above mathematical description of PNM, the model's properties are introduced in this section. Specifically, the synaptic layer works as an analog-to-digital converter, since an extremely large k can make direct synapse and inverse synapse act as segmented functions. The direct synapse produces '1' only when the input is larger than the threshold. It provides the input with a lower boundary in this dimension.

However, the inverse synapse generates ‘1’ when the input is less than the threshold. Thus it offers an upper boundary in the dimension. Because the operation of the dendritic layer is multiplication, on each branch of dendrites, only when the input signal satisfies the lower and upper boundary restriction simultaneously, the dendritic layer can produce ‘1’ signal in this dimension. Similarly, only when all the inputs in different dimensions produce ‘1’, the branch of dendrite can produce a ‘1’ signal finally. In this way, a branch of dendrite will correspond to a N-dimensional hypercube. When an input point falls into the hypercube in the coordinate, the output of the dendritic branch is ‘1’. Otherwise, it outputs ‘0’. Since the soma layer works like the maximum operation, it means that the input signal only needs to fall into one of the hypercubes, the soma body produces ‘1’. Otherwise, it will output ‘0’. In order to illustrate the basic property of PNM, three examples with different dimensional number of input signals are demonstrated as follows.

Example 1: The first and simplest example is illustrated in Fig. 2(a). There are two intervals $[-1, 1]$ and $[3.5, 8]$ in the coordinate. The corresponding neural model, which can separate the two intervals, is shown in Fig. 2(b). It can be seen that one terminal axon has two synapses connecting to each branch of the dendritic layer. The two branches correspond to two intervals in the coordinate, respectively. In accordance with the above mathematical form of the neuron model, the soma body can be found to produce ‘1’ if and only if the input signal falls in these two intervals. Otherwise, it will produce ‘0’. It is easy to conclude that as long as there are enough branches of dendrites, the neural model is capable of identifying any finite interval in a direction.

Example 2: Fig. 2(b) provides a geometrical representation of the second example whose dimensional number becomes 2. Each branch of the dendritic layer represents a rectangle in a two-dimensional coordinate. To separate the blue part, it needs to be partitioned into four smaller rectangles. Hence, four branches of the dendritic layer have been designed to represent the four rectangles. The model structure is presented in Fig. 2(e). However, it needs to be noted that there are various ways to partition the blue part, so the neural model of PNM is not unique. We can infer that the plastic model is also powerful enough to simulate any two-dimensional geometrical figure in principle.

Example 3: The third case occurs when the neural model receives three-dimensional input signals. The signals fall into the parts, which are shown in Fig. 2(c). Similar to the above-mentioned examples, it needs to be divided into five smaller cubes. Each cube corresponds to one branch of dendrites in the neural structure, which has been presented in Fig. 2(f). When the dimension of the input signals exceeds 3, a branch of the dendritic layer corresponds to one hypercube in the coordinate. In general, it is difficult to realize the visualization of a multi-dimensional hypercube.

Based on the above examples, it is obvious that PNM is capable of representing the figures with different dimension numbers and arbitrary shapes. To solve the classification problems, suitable hypercubes need to be figured out to contain all the elements of each category. In the next section, we will introduce the specific learning algorithm of PNM.

4 Learning Algorithm

Based on the unique structural property of PNM, a novel learning algorithm is proposed. For the classification problem, the pattern has n classes, and each sample has k attributes. The main procedure of the learning algorithm can be described in Algorithm 1.

In order to further explain the training process of the learning algorithm, it is used to solve a simple classification problem, which has been illustrated in Fig. 3. It can be observed that, in order to classify the elements which have two attributes (x_1, x_2) into two categories represented by dots and stars, we draw a black rectangle to contain all the elements in Fig. 3(a) firstly. According to the learning algorithm, the rectangle is divided into 4 smaller ones, as shown in Fig. 3(b). Then, we assess these rectangles. Since there is no element in Rectangle ③, it needs to be discarded. Rectangle ② contains only stars and Rectangle ④ has dots merely. These two rectangles should be outputted directly. While both starts and dots fall into Rectangle ①, it will be kept and continued to be divided to generate four much smaller rectangles in the next separation. As shown in Fig. 3(c), Rectangle B is abandoned, Rectangle C is outputted, and Rectangles A and D are reserved to the next generation simultaneously. It can be observed that 10 rectangles are left in Fig. 3(d), each rectangle has only one type of elements. Finally, we transform these rectangles into a neural model with 10 branches of dendrites, and the training process is stopped.

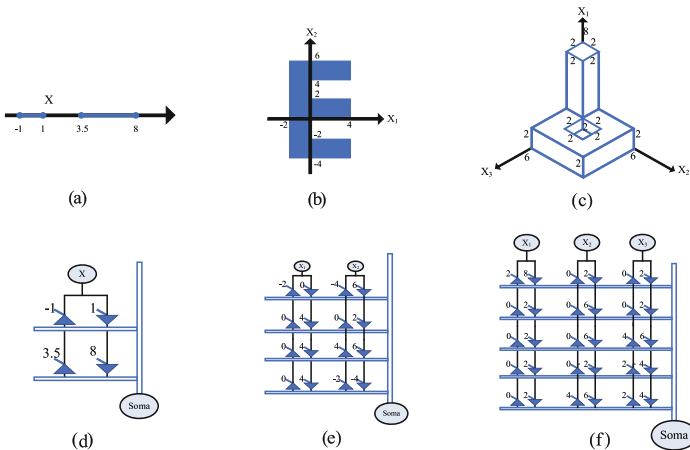


Fig. 2. The first example and its corresponding neural model. (Color figure online)

 Algorithm 1 The learning algorithm of PNM

- 1: Input: the training dataset with n classes and k attributes.
 - 2: Output: the parameters of PNM.
 - 3: Build a n -dimensional hypercube which contains all the elements,
 - 4: repeat
 - 5: Divide each remaining hypercube into $2k$ smaller ones by splitting each dimension right along the median.
 - 6: Assess each hypercube:
 - 7: If no element is in a hypercube, discard this hypercube directly;
 - 8: If only one class of the elements is left in a hypercube, output the hypercube;
 - 9: If more than one class of the elements fall into a hypercube, keep the hypercube;
 - 10: until (No hypercube is remaining.)
 - 11: Transform the output hypercubes into the dendritic structure of PNM; one hypercube corresponds to a branch of dendrites.
-

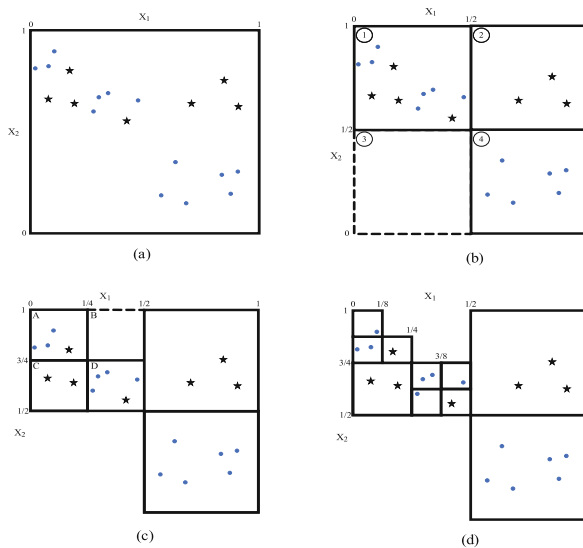


Fig. 3. Training demonstration of PNM.

5 Simulation

5.1 Benchmark Classification Problems

To evaluate the classification performance of PNM, five benchmark classification problems, which are obtained from the UCI Machine Learning Repository [30], are employed in our experiments. Table 1 summarizes the main characteristics of these datasets.

5.2 Experimental Setup

To provide an overall comparison, we compare the classification performance of PNM with those of several other famous classifiers, such as k-nearest neighbor algorithm (KNN) [20], Radial Basis Network (RBF) [5], Multilayer Perceptron (MLP) [15], Support Vector Machine (SVM) [1], and our previous model (ALNM) [19]. The initial parameter values of the classifiers are summarized in Table 2 in detail, while fine-tuning of classifiers is beyond the scope of this paper.

To estimate the classifiers' prediction error effectively, a well-known 10-fold cross-validation procedure [39] is applied to the benchmark datasets except for the XOR problem. Each dataset is partitioned into ten subsets. Every subset is used as the testing set for one time, and the remaining 9 subsets are grouped together to build a training set. Average error (AVE) and standard deviation (S TD) of the misclassified testing pattern are displayed in the tables of results. As the XOR dataset is too small, it cannot be divided into training and testing sets. Performance metrics of this problem are obtained by evaluating ten independent executions of the algorithm on the same training and testing subsets.

According to [9], comparing the algorithms based on AVE and S TD only is not sufficient. Thus, a statistical test is required to prove that the newly proposed algorithm has a significant improvement over other existing classifiers [14]. In the experiment, a Wilcoxon's rank-sum test [29], which is a non-parametric statistical test, is applied. The corresponding p-values of Wilcoxon's rank-sum test are presented in the result as well and the significance level is set to be 0.05. Conventionally, a p-value, which is less than 0.05, can be considered as strong evidence to reject the null hypothesis.

Table 1. Main characteristics of the datasets

| Dataset | Instances | Attributes | Classes |
|---------|-----------|------------|---------|
| XOR | 4 | 4 | 2 |
| Iris | 150 | 4 | 3 |
| Glass | 214 | 9 | 2 |
| Cancer | 699 | 9 | 2 |
| Pima | 768 | 6 | 2 |

Table 2. Initial parameters of different classifiers

| Classifier | Parameter | Value |
|------------|---------------------------------|-------------------|
| KNN | k | 5 |
| RBF | Spread of radial basis function | 1.0 |
| MLP | Hidden layer | 12 |
| | Learning rate | 0.1 |
| | Maximum iteration | 1000 |
| SVM | Function | Polynomial kernel |
| | Order | 2 |
| ALNM | Dendritic branch number | 26 |
| | Learning rate | 0.1 |
| | Maximum iteration | 1000 |

Table 3. Experimental results of the XOR problem

| Algorithm | Success time |
|-----------|--------------|
| KNN | 0/10 |
| RBF | 10/10 |
| MLP | 7/10 |
| SVM | 10/10 |
| ALNM | 9/10 |
| PNM | 10/10 |

5.3 Performance Comparisons

The classification performances of the classifiers on the XOR benchmark problem are summarized in Table 3. Success means that the after-learning outputs of the algorithm for the patterns are the same as their teacher signals. It can be observed that for the simplest nonlinear classification problem, KNN failed all the 10 running times. It means that KNN cannot solve the linearly inseparable problems. Since the MLP and ALNM's training algorithms are an EBP algorithm, they are easy to trap into the local minimum, and the success times are 7 and 9, respectively. They are smaller than those of RBF, SVM and PNM. These three classifiers are capable of solving the problem effectively. For the Iris benchmark problem, the incorrect classification rate of each classifier is presented in Table 4. It can be seen that PNM has the lowest AVE of the incorrect classification rate than those of the other five classifiers.

Table 4. Experimental results of the Iris dataset

| Algorithm | Test error rate | | p-value |
|-----------|-----------------|--------|----------|
| | AVE | STD | |
| KNN | 4.6667 | 5.4885 | 0.0246 |
| RBF | 16.6667 | 9.0267 | 8.47e-04 |
| MLP | 7.3333 | 5.8373 | 0.0068 |
| SVM | 2.6667 | 3.4427 | 0.0553 |
| ALNM | 4.6667 | 5.4885 | 0.0246 |
| PNM | 2.3168 | 1.7410 | \ |

Table 5. Experimental results of the Glass dataset

| Algorithm | Test error rate | | p-value |
|-----------|-----------------|--------|----------|
| | AVE | STD | |
| KNN | 8.4952 | 5.4708 | 0.0169 |
| RBF | 16.0381 | 7.3408 | 5.73e-04 |
| MLP | 10.4000 | 6.3506 | 0.0022 |
| SVM | 5.6381 | 3.9403 | 0.0821 |
| ALNM | 6.6667 | 4.0156 | 0.0257 |
| PNM | 4.6945 | 1.8113 | \ |

Besides, the p-values of KNN, RBF, MLP and ALNM are smaller than the significance level. It means that the performance of PNM is significantly better than those of the four classifiers. However, the p-value of SVM, which is larger than 0.05, implies that there is no significant difference between the performances of SVM and PNM. Considering the Glass benchmark problem, based on the values of AVE and S TD in Table 5, PNM can be thought to be the most powerful classifier. Similarly, the p-values suggest that PNM is significantly better than KNN, RBF, MLP and ALNM, but it cannot be thought to be significantly better than SVM. As to the Cancer benchmark problem, PNM performs better than all the other classifiers in terms of AVE and S TD, which are shown in Table 6. According to the p-values of the Wilcoxon’s rank-sum test, PNM is considered to have significantly better performance than RBF, MLP and ALNM, but it cannot be considered to be significantly better than KNN and SVM. For the Pima classification problem, the results in Table 7 indicate that PNM has a significant better performance than all the other classifiers obviously. In conclusion, according to the above results, it is clear that PNM is capable of presenting a competitive classification performance on the five benchmark classification problems when compared with several other widely-used classifiers.

Table 6. Experimental results of the Cancer dataset

| Algorithm | Test error rate | | p-value |
|-----------|-----------------|--------|----------|
| | AVE | STD | |
| KNN | 3.2999 | 1.9496 | 0.1040 |
| RBF | 11.2821 | 3.7186 | 1.15e-04 |
| MLP | 4.1527 | 2.3137 | 8.87E-03 |
| SVM | 3.3779 | 2.5493 | 0.1821 |
| ALNM | 3.5897 | 1.9788 | 0.0152 |
| PNM | 3.0623 | 1.2438 | \ |

Table 7. Experimental results of the Pima dataset

| Algorithm | Test error rate | | p-value |
|-----------|-----------------|---------|----------|
| | AVE | STD | |
| KNN | 29.3045 | 3.6786 | 0.0018 |
| RBF | 39.4612 | 13.5036 | 6.55e-04 |
| MLP | 27.2494 | 5.2190 | 0.0085 |
| SVM | 34.8246 | 5.2436 | 3.81E-04 |
| ALNM | 34.8997 | 5.4484 | 2.89E-04 |
| PNM | 21.5870 | 5.5942 | \ |

6 Conclusions

This paper proposes a novel plastic neural model with dendritic computation and a specific learning algorithm is adopted to train it. The learning algorithm is able to figure out suitable geometrical hypercubes in the coordinate for the elements of each category. Each hypercube represents a branch of dendrite in the topological structure of the model. Through training, PNM can provide a unique dendritic topology for each particular task. To evaluate the performance of PNM, five benchmark datasets are adopted in our experiment. Compared with five other widely-used classifiers, the statistical results demonstrate that PNM is able to provide convincing classification performance. It reveals that PNM including its learning algorithm has the following features: firstly, none of the parameters needs any fine-tuning in our model; secondly, unlike MLP and ALNM, there is no convergence problem in PNM because it can converge in finite steps efficiently; thirdly, the learning algorithm partitions the pattern space into smaller regions which will not overlap, and it can satisfactorily separate the training instances according to their category labels. In the meantime, the main drawback of PNM is also analyzed in our paper, and it will be focused on in our future research.

References

1. Adankon, M.M., Cheriet, M.: Support vector machine. *Encycl. Biometrics*, 1303–1308 (2009)
2. Anderson, J., Binzegger, T., Kahana, O., Martin, K., Segev, I.: Dendritic asymmetry cannot account for directional responses of neurons in visual cortex. *Nat. Neurosci.* **2**(9), 820–824 (1999)
3. Archie, K.A., Mel, B.W.: A model for intradendritic computation of binocular disparity. *Nat. Neurosci.* **3**(1), 54–63 (2000)
4. Cazé, R.D., Humphries, M., Gutkin, B.: Passive dendrites enable single neurons to compute linearly non-separable functions. *PLoS Comput. Biol.* **9**(2), 867 (2013)
5. Chen, S., Cowan, C.F., Grant, P.M.: Orthogonal least squares learning algorithm for radial basis function networks. *IEEE Trans. Neural Netw.* **2**(2), 302–309 (1991)
6. Costa, R.P., Sjöström, P.J.: One cell to rule them all, and in the dendrites bind them. *Front. Synaptic Neurosci.* **3** (2011)
7. Csáji, B.C.: Approximation with artificial neural networks. Faculty of Sciences, Eötvös Loránd University, Hungary 24, 48 (2001)
8. Dayhoff, J.E.: *Neural network architectures: an introduction*. Van Nostrand Reinhold Co. (1990)
9. Derrac, J., García, S., Molina, D., Herrera, F.: A practical tutorial on the use of nonparametric statistical tests as a methodology for comparing evolutionary and swarm intelligence algorithms. *Swarm Evol. Comput.* **1**(1), 3–18 (2011)
10. Euler, T., Detwiler, P.B., Denk, W.: Directionally selective calcium signals in dendrites of starburst amacrine cells. *Nature* **418**(6900), 845–852 (2002)
11. Fahlman, S.E.: *An empirical study of learning speed in back-propagation networks* (1988)
12. Ferster, D., Jagadeesh, B.: Eps-ipsip interactions in cat visual cortex studied with in vivo whole-cell patch recording. *J. Neurosci.* **12**(4), 1262–1274 (1992)
13. Fine, T.L.: *Feedforward Neural Network Methodology*. Springer, New York (2006). <https://doi.org/10.1007/b97705>
14. García, S., Molina, D., Lozano, M., Herrera, F.: A study on the use of non-parametric tests for analyzing the evolutionary algorithms behaviour: a case study on the cec2005 special session on real parameter optimization. *J. Heuristics* **15**(6), 617–644 (2009)
15. Gardner, M.W., Dorling, S.: Artificial neural networks (the multilayer perceptron) a review of applications in the atmospheric sciences. *Atmos. Environ.* **32**(14–15), 2627–2636 (1998)
16. Gurney, K.N.: Information processing in dendrites: I. input pattern generalization. *Neural Netw.* **14**(8), 991–1004 (2001)
17. Gurney, K.N.: Information processing in dendrites: II. information theoretic complexity. *Neural Netw.* **14**(8), 1005–1022 (2001)
18. Hornik, K., Stinchcombe, M., White, H.: Multilayer feedforward networks are universal approximators. *Neural Netw.* **2**(5), 359–366 (1989)
19. Ji, J., Gao, S., Cheng, J., Tang, Z., Todo, Y.: An approximate logic neuron model with a dendritic structure. *Neurocomputing* **173**, 1775–1783 (2016)
20. Larose, D.T.: k-nearest neighbor algorithm. In: *Discovering Knowledge in Data: An Introduction to Data Mining*, pp. 90–106 (2005)
21. Lee, Y., Oh, S.H., Kim, M.W.: An analysis of premature saturation in back propagation learning. *Neural Netw.* **6**(5), 719–728 (1993)
22. Legenstein, R., Maass, W.: Branch-specific plasticity enables self-organization of nonlinear computation in single neurons. *J. Neurosci.* **31**(30), 10787–10802 (2011)

23. Magee, J.C.: Dendritic integration of excitatory synaptic input. *Nat. Rev. Neurosci.* **1**(3), 181–190 (2000)
24. Magee, J.C.: Dendritic voltage-gated ion channels. *Dendrites*, 225–251 (2008)
25. Magoulas, G., Vrahatis, M., Androulakis, G.: On the alleviation of the problem of local minima in back-propagation. *Nonlinear Anal. Theor. Methods Appl.* **30**(7), 4545–4550 (1997)
26. McCulloch, W.S., Pitts, W.: A logical calculus of the ideas immanent in nervous activity. *Bull. Math. Biophys.* **5**(4), 115–133 (1943)
27. Mehrotra, K., Mohan, C.K., Ranka, S.: *Elements of Artificial Neural Networks*. MIT Press, Cambridge (1997)
28. Minsky, M., Papert, S.: *Perceptrons* (1969)
29. Mirjalili, S., Lewis, A.: S-shaped versus v-shaped transfer functions for binary particle swarm optimization. *Swarm Evol. Comput.* **9**, 1–14 (2013)
30. Newman, A.A.D.: *UCI repository of machine learning database (school of information and computer science)*, University of California, Irvine (2007)
31. Oesch, N., Euler, T., Taylor, W.R.: Direction-selective dendritic action potentials in rabbit retina. *Neuron* **47**(5), 739–750 (2005)
32. Poirazi, P., Mel, B.W.: Impact of active dendrites and structural plasticity on the memory capacity of neural tissue. *Neuron* **29**(3), 779–796 (2001)
33. Rosenblatt, F.: *The perceptron, a perceiving and recognizing automaton Project Para*. Cornell Aeronautical Laboratory (1957)
34. Salinas, E., Abbott, L.: A model of multiplicative neural responses in parietal cortex. *Proc. Natl. Acad. Sci.* **93**(21), 11956–11961 (1996)
35. Schachter, M.J., Oesch, N., Smith, R.G., Taylor, W.R.: Dendritic spikes amplify the synaptic signal to enhance detection of motion in a simulation of the direction-selective ganglion cell. *PLoS Comput. Biol.* **6**(8), e1000, 899 (2010)
36. Simon, H.: *Neural Networks, A Comprehensive Foundation*. Prentice-Hall, Englewood Cliffs (1999)
37. Sjöström, P.J., Rancz, E.A., Roth, A., Häusser, M.: Dendritic excitability and synaptic plasticity. *Physiol. Rev.* **88**(2), 769–840 (2008)
38. Todo, Y., Tamura, H., Yamashita, K., Tang, Z.: Unsupervised learnable neuron model with nonlinear interaction on dendrites. *Neural Networks* **60**, 96–103 (2014)
39. Varma, S., Simon, R.: Bias in error estimation when using cross-validation for model selection. *BMC Bioinf.* **7**(1), 91 (2006)



Improving Approximate Logic Neuron Model by Means of a Novel Learning Algorithm

Jiajun Zhao¹, Minhui Dong¹, Cheng Tang², Junkai Ji¹(✉),
and Ying He¹

¹ College of Computer Science and Software Engineering, Shenzhen University,
Shenzhen 518060, China

{1910272062, 1910273042}@email.szu.edu.cn,
{jijunkai, heying}@szu.edu.cn

² Faculty of Engineering, University of Toyama, Toyama-shi 930-8555, Japan
d2072006@ems.u-toyama.ac.jp

Abstract. Inspired by the dynamic dendritic architecture of biological neurons, the approximate logic neuron model (ALNM) is a novel model recently proposed by us. ALNM owns four layers, namely, the synaptic layer, the dendritic layer, the membrane layer, and the cell body. Through neural pruning function, the model can omit useless synapses and unnecessary branches of dendrites after the training process. In other words, it will form a unique and simplified dendritic structure for each particular classification task. Further, the simplified dendritic structure can be completely substituted by logic circuits, which makes ALNM be capable of running in hardware. However, although it has satisfactory performances to solve classification problems, it still suffers from some disadvantages owing to its learning algorithm, named batch gradient descent (BGD) algorithm. It is because that, using all the training data for each iteration is time-consuming and it is unsuitable for large scale problems. In addition, BGD cannot adaptively adjust the learning rate during the whole training process, which will converge slowly in the neighborhood of saddle points, and oscillate in the steep region of gradient space. To settle the above issues, we propose a novel stochastic adaptive gradient descent (SAGD) algorithm, which uses stochastic gradient descent information and adaptively adjusts the learning rate, to improve the classification performances of ALNM. In our experiments, ALNM trained by the new algorithm is evaluated on three benchmark classification datasets, and experimental results demonstrate that it performs significantly better than the original model in terms of accuracy and convergence rate.

Keywords: Neural network · Dendrite · Learning algorithm · Classification · Logic circuit

1 Introduction

In the last two decades, artificial neural networks have been applied to various tasks, such as classification [3], regression [26], vision [4] and control systems [2]. In 1943, McCulloch and Pitts proposed the first neuron model, and it has been widely employed as a fundamental unit for modern research of neural networks [18]. However, it has

been criticized for not considering the nonlinear mechanisms of dendrites, which occupies the vast majority space of the brain *in vivo*. And a single layer of McCullochPitts neuron model could not settle some fairly elementary nonlinear functions, such as the XOR problem, according to the theoretical and empirical evidence of Papert and Minsky in [19].

Koch, Poggio and Torre suggest that the behavior of interaction between branches and synapses could be considered from the perspective of logic operations [13, 14]. Coincidence detection in the auditory system [22] and direction selectivity in retinal ganglion cells [25] have verified their hypothesis. However, for a specific complex task, it is often difficult for Koch's model to construct diverse dendrite morphology [5]. To resolve this crisis, a variety of plasticity mechanisms in pyramidal neurons were proposed [6, 8, 15, 20, 23]. Meanwhile, biological evidence also supports structural synaptic plasticity, which involves synapse formation and elimination [9].

Recent progress in neurobiology has brought to the foreground of the importance of neuron pruning, a process by which unnecessary dendrites are selectively removed without causing cell death, during an early stage of neurogenesis [17]. Dendritic pruning [11] and axon pruning [16] were observed in dendritic arborization neurons and the *drosophila* mushroom body, respectively. According to these biophysical phenomena, we proposed an approximate logic neuron model (ALNM). The main architecture of ALNM has four types of layers, such as the synaptic layer, the dendritic layer, the membrane layer, and the cell body. To be specific, the synaptic layers obtain inputs from other neurons' axons or dendrites, the interactions of the synaptic signals happen on each branch of dendrites. Subsequently, the membrane layers assemble the interactions and transfer the results to the cell body (soma). Finally, the soma decides whether to fire after comparing the results with its own threshold.

During the training phase, the useful dendrites and the important input feature are kept, while the useless and unnecessary ones are screened out. After that, ALNM acquires a precise dendritic morphology for the problem. Further, the mature neurons of ALNM can be approximately replaced by logic circuits, which contain the comparators and logic NOT, AND and OR gates. ALNM has been applied to deal with several real-world problems, for instance, the forecast of tourist arrivals [24], the diagnosis of liver disorders [10], bankruptcy prediction [27] and computer-aided diagnosis [1]. Compared with other artificial neural models, it can be considered as a more realistic model.

Batch gradient descent (BGD) algorithm has been viewed as a powerful technique for artificial neural model optimization because it can well represent the training samples and be accurate towards the direction of minimum error between predicted values and true values. When the objective function is convex, BGD is able to obtain the globally optimal solution with probability one.

However, when the parameter space is multimodal, BGD will be easy to trap into local minima. In addition, it needs to calculate the gradients of the whole training sample set to update the weights and thresholds of BGD in one iteration; the convergence speed of BGD is slow. Thus, such time-consuming BGD is not suitable for large-scale classification tasks. This motivates us to devise or find a more promising learning algorithm.

In order to handle the above problems, we proposed a novel learning algorithm, termed stochastic adaptive gradient descent (SAGD) algorithm. SAGD adopts stochastic gradient descent information to update the parameters of ALNM, and can adjust the learning rate adaptively. SAGD is a computationally efficient training algorithm, which needs fewer memory demands and is straightforward to implement. The classification performances of the SAGD algorithm is evaluated and compared in our experiment, the results demonstrate its effectiveness and superiority in terms of the average accuracy and the training speed, compared with the original BGD algorithm.

The rest of this article is organized as follows. Section 2 presents a brief introduction of ALNM and its neuronal pruning function. Section 3 shows how SAGD is applied to train ALNM. The experiments and discussion are presented in Sect. 4. Finally, concluding remarks are drawn in Sect. 5.

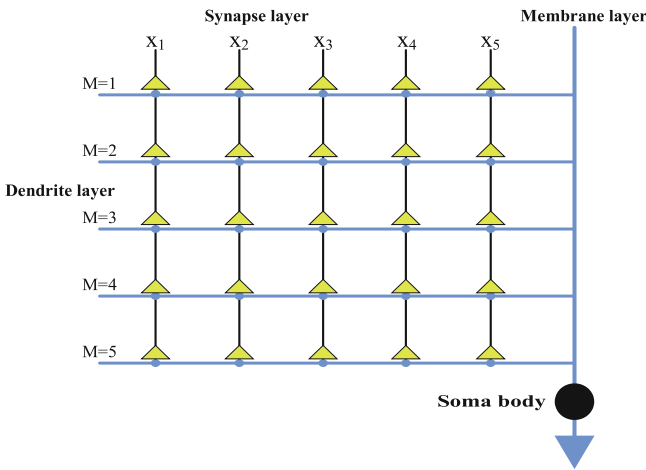


Fig. 1. Architecture of the ALNM model

2 Approximate Logic Neuron Model

The architecture of ALNM is constituted of four layers: the synaptic layer, the dendrite layer, the membrane layer and the soma, which have been illustrated in Fig. 1.

2.1 Synaptic Layer

The synaptic layer is the connection tissue between dendrites and other neurons' axons, and the mechanism of the synaptic layer is to use a receptor to absorb a certain specific ion. Once the receptor takes in an ion, the potential of the receptor will change. Then, it determines whether to become an inhibition synapse or an excitatory synapse [12]. The

modified sigmoid function can be used to express multiple connection states, which has been shown as follows:

$$Y_{im} = \frac{1}{1 + e^{-k(w_{im}x_i - q_{im})}} \tag{1}$$

where x_i is the i -th ($i = 1, 2, 3, \dots, I$) input signal, and its range is $[0, 1]$. w_{im} and q_{im} are the connection state parameters of the synaptic layers on the m -th ($m = 1, 2, 3, \dots, M$) dendrite layer. k is a constant value and set to 5 in our experiments. According to different combinations of w_{im} and q_{im} , the synaptic layers have four connection states, namely, constant 1 connection, constant 0 connection, reversed connection and direct connection, which have been shown in Fig. 2. After the calculation of the synaptic layers, the analog input signals will be converted into digital ones which only consist of “0” and “1”. θ_{im} is the threshold of the synaptic layer, which can be calculated by $\theta_{im} = q_{im}/w_{im}$.

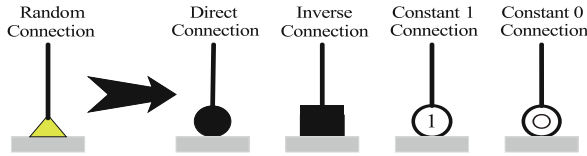


Fig. 2. Connection states of synaptic layers.

Direct Connection. In the direct connection state, when x_i is larger than the threshold θ_{im} , the synaptic layer will output ‘1’. If lower than θ_{im} , it output ‘0’. Biologic explanation indicates that if the input signal has a higher potential than its threshold, the excitatory postsynaptic potential (EPSP) will occur, and the positional potential of the dendrite will rapidly be depolarized. Inversely, a low potential causes an inhibitory synaptic layer, and the inhibitory postsynaptic potential (IPSP) happens, the positional potential will be transiently hyperpolarized [12]. In the logic circuits, a comparator can also implement a similar function.

Case (A): $0 < q_{im} < w_{im}$, e.g.: $w_{im} = 2.0$ and $q_{im} = 1.0$.

Inverse Connection. In the inverse connection state, as opposed to the direct connection state, if input x_i is less than the threshold θ_{im} , the output will be 1, and it causes an EPSP. If the input exceeds the threshold θ_{im} , the output will be 0, and an IPSP occurs. In the logic circuits, the function of the synaptic layer in the inverse connection can be approximated by the combination of a comparator and a logic NOT gate.

Case (B): $w_{im} < q_{im} < 0$, e.g.: $w_{im} = -2.0$ and $q_{im} = -1.0$.

Constant ‘1’ Connection. The constant 1 connection state contains two cases:

Case (C₁): $q_{im} < 0 < w_{im}$, e.g.: $w_{im} = 2.0$ and $q_{im} = -1.0$;

Case (C₂): $q_{im} < w_{im} < 0$, e.g.: $w_{im} = -1.0$ and $q_{im} = -1.5$.

In two cases, whatever the input signal is, the output is always 1. It suggests that, the synapses are constant excitatory and can ignore the input signal and its threshold to trigger an EPSP all the time. The positional potential of the dendrite will be depolarized.

Constant ‘0’ Connection. There are two cases in the constant 0 connection.

Case (D₁): $0 < w_{im} < q_{im}$, e.g.: $w_{im} = 1.0$ and $q_{im} = 1.5$;

Case (D₂): $w_{im} < 0 < q_{im}$, e.g.: $w_{im} = -2.0$ and $q_{im} = 1.5$.

In these cases, the output is independent of the input signal and keeps 0. Meanwhile, the synapse always becomes an inhibitory one that can cause an IPSP. The postsynaptic potential will always be hyperpolarized. The mathematic illustration of all connection cases has been presented in Fig. 3.

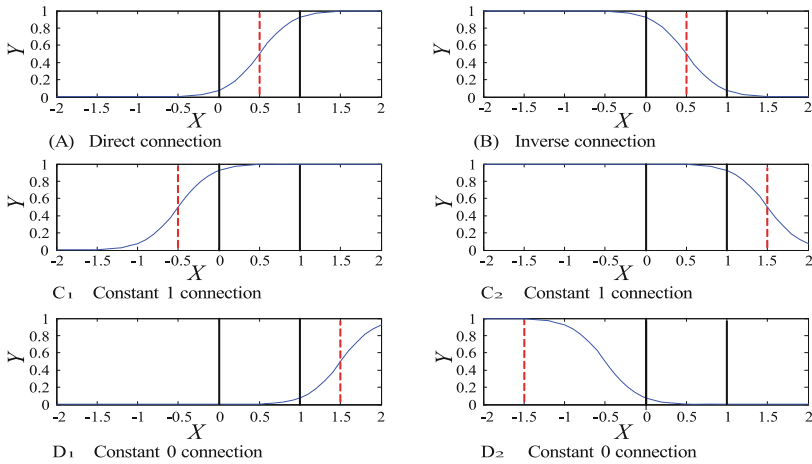


Fig. 3. The functions of synaptic layers in different connection states.

2.2 Dendrite Layer

Dendrites implement the non-linear interaction between synaptic signals on each branch. The multiplication operation has been considered to play an important role in the information processing of the sensory systems, where both visual and auditory processes are thought to be underpinned by multiplication [7, 21]. Inspired by these foundations, the multiplicative operation is also used in the dendrite layer. Because the inputs of the dendrite layers are either 0 or 1, the dendrite layer is equivalent to the logic AND operation. Here, the equation of dendrites can be described as follows:

$$Z_m = \prod_{i=1}^I Y_{im} \quad (2)$$

2.3 Membrane Layer

The membrane layer accumulates all the sublinear summation of the signals in each dendritic branch. Since the inputs of the membrane layers are also either 0 or 1, the function is almost equal to the logic OR operation. The equation is shown as follows:

$$V = \sum_{m=1}^M Z_m \quad (3)$$

2.4 Soma Layer

The cell layer also names soma. It is the core of neurons. The neuron fires depend on whether the membrane potential is larger than its threshold or not. The process can be described by using a sigmoid function of the product terms:

$$O = \frac{1}{1 + e^{-k(V - \theta_{soma})}} \quad (4)$$

where θ_{soma} is the threshold of the cell body, and k is a constant parameter. θ_{soma} and k are 0.5 and 5, respectively.

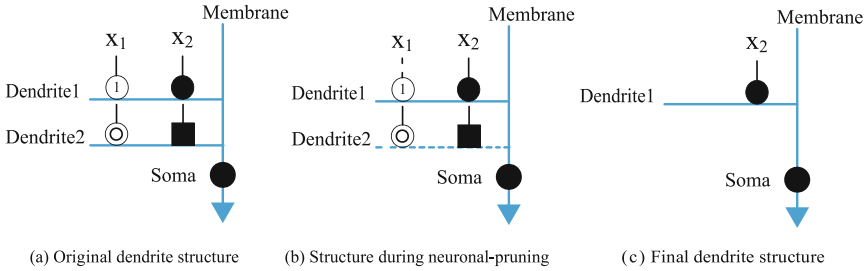


Fig. 4. Neuronal pruning process of the ALNM model.

2.5 Neuronal Pruning Function

Axon pruning: if a synaptic layer receives the input signal from the previous neurons' axon and it locals in the constant '1' connection state, the input signal can be ignored and this kind of connected axons should be discarded. Because the output of the synapse is constant 1, due to the multiplication operation, following the simple rule that an arbitrary value time 1 produces itself, the output of the dendritic layer is independent of the input of the axon. In this way, eliminating the unnecessary axons of ALNM is named as axon pruning function.

Dendritic pruning: if a synaptic layer locals in the constant '0' connection state, its output keeps '0.' According to the mathematic rule that any value multiplied by 0 gets 0, the output of the dendritic layer will become 0, with ignoring all the input signals of synapses in these dendritic branches. Thus, the whole dendritic branch and the synapses should be discarded; we call it dendritic pruning function.

Through the above mechanisms, ALNM can mimic the immature biological neurons to remove the unnecessary dendrites and useless synapses, and achieve the simplified and unique dendritic structure for each problem. To demonstrate the neuronal pruning function, an example is provided in Fig. 4. As shown in Fig. 4(a), the initial structure includes four synapses, two dendritic branches, a membrane layer, and a soma. On the Dendrite-1 layer, since the input X_1 is received by the synapse in the constant '1' connection state, this synaptic layer would be neglected. On the Dendrite-2 layer, because the synapse connecting to the input X_1 locals in the constant '0' connection state, the output of the whole Dendrite-2 will be 0. Thus, the entire Dendrite-2 needs to be deleted, shown by the dotted line in Fig. 4(b). The final structure morphology of ALNM is illustrated in Fig. 4(c), which is much simpler than the original one.

Algorithm 1: Training process of stochastic adaptive gradient descent algorithm. g_t^2 denotes the element-wise square $g_t \odot g_t$. All the operations of vectors are element-wise. The hyperparameters of SAGD are set as follows: $\eta = 0.01$, $\beta_1 = 0.9$, $\beta_2 = 0.999$ and $\varepsilon = 10^{-8}$.

Input:

η : Step size

$\beta_1, \beta_2 \in [0,1)$: Exponential decay rates

ϕ_0 : Initial training parameter vector

Output: ϕ_t : Final training parameter vector

1. Initialize the first moment vector: $m_0 \leftarrow 0$;
 2. Initialize the second moment vector: $v_0 \leftarrow 0$;
 3. Initialize the time step: $t \leftarrow 0$;
 4. while ϕ_t don't meets the stopping criterion do
 5. Obtain the subsample $\chi(t)$ by randomly selecting from the training samples;
 6. Calculate the gradient $g(t)$ at the time step t [29];
 7. Update the first biased moment: $m_t \leftarrow \beta_1 \cdot m_{t-1} + (1 - \beta_1) \cdot g_t$;
 8. Update the second raw moment: $v_t \leftarrow \beta_2 \cdot v_{t-1} + (1 - \beta_2) \cdot g_t^2$;
 9. Compute the first bias-corrected estimate: $\hat{m}_t \leftarrow m_t / (1 - \beta_1^t)$;
 10. Compute the second bias-corrected raw estimate: $\hat{v}_t \leftarrow v_t / (1 - \beta_2^t)$;
 11. Update the parameter vector: $\phi_t \leftarrow \phi_{t-1} - \eta \cdot \hat{m}_t / (\sqrt{\hat{v}_t} + \varepsilon)$;
 12. $t \leftarrow t + 1$;
 13. end
-

3 Stochastic Adaptive Gradient Descent Algorithm

ALNM is a feed-forward neural model, and the functions of all the layers are differential. Thereby, Back propagation (BP) algorithm is employed to train the connection parameters of ALNM. According to the learning rule, a neuron model can minimize the square errors between the actual output O and the desired output T by:

$$Error = \frac{1}{2} \sum_{j=1}^N (T(j) - O(j))^2 \quad (5)$$

where N is the training sample number, $T(j)$ and $O(j)$ represent the j -th actual output and the j -th predicted target, respectively. Training inefficiency and being prone to local minima become two fatal weaknesses of BP algorithm. Consequently, a SAGD algorithm is proposed to improve the training performances of ALNM. The pseudo-code of the proposed algorithm is presented in Algorithm 1. It can be observed that, the hyper-parameters of ALNM include the step size η , exponential decay rate of the first moment estimate β_1 and the exponential decay rate for the second moment estimate β_2 . The training parameters ϕ can be expressed by:

$$\phi = [w_{11} \cdots w_{1M} w_{21} \cdots w_{2M} \cdots w_{IM} q_{11} \cdots q_{1M} \cdots q_{IM}]^T \quad (6)$$

In the training phase, it stochastically selects the training sample subsets to calculate the gradient descent information, then adaptively chooses the learning rate for different training processes. The subsample size depends on the specific task. The gradient descent equation of ϕ can be found in [29].

4 Experimental Results and Discussion

In our experiments, three benchmark classification datasets, namely, XOR, Glass and Cancer, are adopted to evaluate the classification performance of ALNM trained by SAGD. These datasets can be acquired from the University of California at Irvine Machine Learning Repository [28]. Table 1 exhibits their number of instances, number of attributes, and number of classes. The experiments are conducted in 30 independent running times, with the different initial values of w and q . These parameters were assigned uniformly random values between -0.5 and 0.5 . For a fair comparison, SAGD is compared with BGD by using the same parameter setting showed in Table 2. All the experiments are conducted on a PC with 3.20 GHz Intel(R) Core (TM) i5-6500 CPU and 8 GB of RAM by using MATLAB R2016b.

The accuracy is defined as the ratio of the samples whose outputs of the classifier are the same to their targets to the total samples in the testing data set. The average value (Mean) and standard deviation (Std) of the accuracy summarized in Table 3. BGD1 to BGD10 represent the algorithms with different learning rates that vary from 0.01 to 0.1, respectively. It can be observed that SAGD is superior to all the BGDs in terms of ‘Mean \pm Std’ metric, which suggests that SAGD can effectively avoid the

local minima by using the stochastic gradient descent information. Convergence curves can describe the optimization speed of different learning algorithms. The convergence comparison between SAGD and BGD is presented in Fig. 5, 6 and 7. It is easy to find that, the convergence speed of SAGD is much higher than that of BGD, especially in the latter half process, the BGD converges in such a slow level that influences its classification performance. It implies that, adopting an adaptive learning rate will speed up the optimization process and the SAGD can be regarded as a more efficient learning algorithm.

Table 1. Details of the classification data sets

| Data set | Instances | Attributes | Classes |
|----------|-----------|------------|---------|
| XOR | 4 | 2 | 2 |
| Glass | 214 | 9 | 2 |
| Cancer | 699 | 9 | 2 |

Table 2. Parameter settings of SAGD and BGD

| Method | Parameter setting |
|--------|--|
| SAGD | $\eta = 0.01$, $M = 10/11/11$ (XOR/Glass/Cancer), epoch = 1000, $k = 5$, $\theta_{\text{soma}} = 0.5$, $\beta_1 = 0.9$, $\beta_2 = 0.999$, $\varepsilon = 10^{-8}$, the size of Mini-batch is 2/50/50 (XOR/Glass/Cancer) |
| BGD | η from the set{0.01, 0.02, ..., 0.1}, $M = 10$, epoch = 1000, $k = 5$, $\theta_{\text{soma}} = 0.5$ |

Table 3. Experimental results of SAGD and BGDs on three benchmark datasets

| | XOR | Glass | Cancer |
|-------|---------------------------------------|---------------------------------------|---------------------------------------|
| | Mean \pm Std | Mean \pm Std | Mean \pm Std |
| SAGD | 0.9833 \pm 0.0634 | 0.9253 \pm 0.0229 | 0.9547 \pm 0.0085 |
| BGD1 | 0.7083 \pm 0.2085 | 0.8733 \pm 0.0686 | 0.9494 \pm 0.0127 |
| BGD2 | 0.7833 \pm 0.2151 | 0.8900 \pm 0.0593 | 0.9492 \pm 0.0120 |
| BGD3 | 0.8000 \pm 0.2117 | 0.8956 \pm 0.0556 | 0.9519 \pm 0.0098 |
| BGD4 | 0.7917 \pm 0.2186 | 0.9011 \pm 0.0479 | 0.9513 \pm 0.0108 |
| BGD5 | 0.8083 \pm 0.2146 | 0.9087 \pm 0.0418 | 0.9528 \pm 0.0092 |
| BGD6 | 0.8083 \pm 0.2146 | 0.9138 \pm 0.0294 | 0.9547 \pm 0.0090 |
| BGD7 | 0.8083 \pm 0.2146 | 0.9131 \pm 0.0299 | 0.9543 \pm 0.0087 |
| BGD8 | 0.8083 \pm 0.2146 | 0.9118 \pm 0.0316 | 0.9528 \pm 0.0086 |
| BGD9 | 0.8250 \pm 0.2092 | 0.9111 \pm 0.0309 | 0.9531 \pm 0.0086 |
| BGD10 | 0.8250 \pm 0.2092 | 0.9149 \pm 0.0291 | 0.9534 \pm 0.0084 |

In addition, the effectiveness of the neural pruning function is also verified in our experiments. As shown in Fig. 8(a), the original structure of ALNM has 8 dendritic

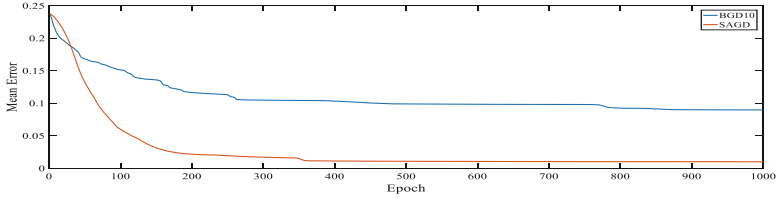


Fig. 5. Convergence comparison of SAGD and BGD10 for the XOR problem.

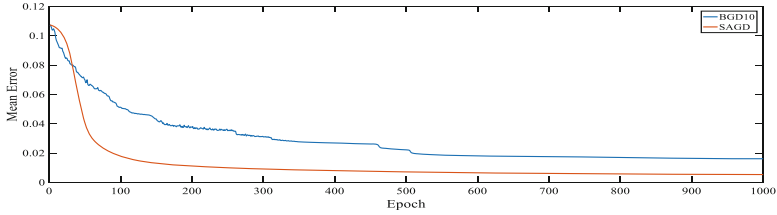


Fig. 6. Convergence comparison of SAGD and BGD10 for the Glass dataset.

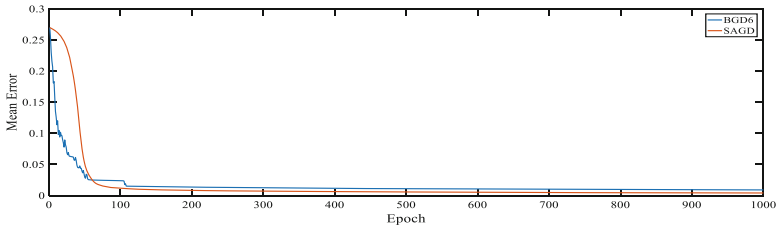


Fig. 7. Convergence comparison of SAGD and BGD6 for the Cancer dataset.

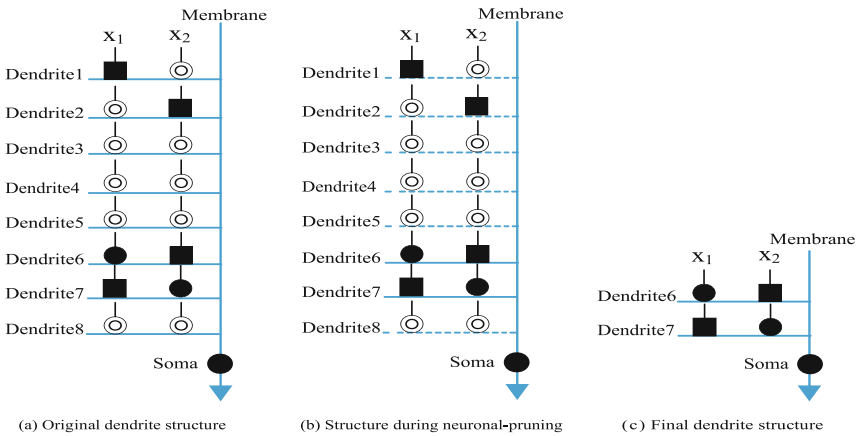


Fig. 8. Structure evaluation of ALNM on the XOR problem through neuronal pruning function.

branches and each branch obtains 2 synapses after the learning process. According to the pruning mechanisms, since the Dendrite-1, 2, 3, 5 and 7 have at least a synapse in the constant 0 connection, all of these branches should be deleted, shown by the dotted line in Fig. 8(b). The final structure is presented in Fig. 8(c), which is much simpler than the original one.

5 Conclusions

In this paper, a novel SAGD algorithm is adopted to train ALNM, which uses stochastic gradient descent information and adaptive learning rate. The experimental results demonstrate that SAGD performs better than BGD on three benchmark datasets, in terms of accuracy and the convergence speed. It can be regarded as a more effective and efficient learning algorithm for ALNM. Further, the neural pruning function of ALNM trained by SAGD is also verified in our experiments. Although SAGD can provide satisfactory optimization performances, the training process is longer than other commonly-used machine learning techniques, such as support vector machine and random forest. It is because calculating the gradient information is time-consuming. In our future research, we will still seek a more efficient learning algorithm of ALNM and apply it to more complex real-world problems.

References

1. Tang, C., et al.: A novel machine learning technique for computer-aided diagnosis. *Eng. Appl. Artif. Intell.* **92**, 103627 (2020)
2. Czajkowski, A., Patan, K., Szymański, M.: Application of the state space neural network to the fault tolerant control system of the plc-controlled laboratory stand. *Eng. Appl. Artif. Intell.* **30**, 168C–178 (2014)
3. Castellani, M., Rowlands, H.: Evolutionary artificial neural network design and training for wood veneer classification. *Eng. Appl. Artif. Intell.* **22**(4–5), 732C–741 (2009)
4. Weimer, D., Thamer, H., Scholz-Reiter, B.: Learning defect classifiers for textured surfaces using neural networks and statistical feature representations. *Procedia CIRP* **7**, 347C–352 (2013)
5. Destexhe, A., Marder, E.: Plasticity in single neuron and circuit computations. *Nature* **431** (7010), 789–795 (2004)
6. Dringenberg, H.C., Hamze, B., Wilson, A., Speechley, W., Kuo, M.C.: Heterosynaptic facilitation of in vivo thalamocortical long-term potentiation in the adult rat visual cortex by acetylcholine. *Cereb. Cortex* **17**(4), 839–848 (2007)
7. Gabbiani, F., Krapp, H.G., Koch, C., Laurent, G.: Multiplicative computation in a visual neuron sensitive to looming. *Nature* **420**(6913), 320–324 (2002)
8. Gu, Q.: Contribution of acetylcholine to visual cortex plasticity. *Neurobiol. Learn. Mem.* **80** (3), 291–301 (2003)
9. Holtmaat, A., Svoboda, K.: Experience-dependent structural synaptic plasticity in the mammalian brain. *Nat. Rev. Neurosci.* **10**(9), 647–658 (2009)
10. Jiang, T., Gao, S., Wang, D., Ji, J., Todo, Y., Tang, Z.: A neuron model with synaptic nonlinearities in a dendritic tree for liver disorders. *IEEJ Trans. Electr. Electron. Eng.* **12**(1), 105–115 (2017)

11. Kanamori, T., Kanai, M.I., Dairyo, Y., Yasunaga, K.i., Morikawa, R.K., Emoto, K.: Compartmentalized calcium transients trigger dendrite pruning in drosophila sensory neurons. *Science* **340**(6139), 1475–1478 (2013)
12. Koch, C.: *Biophysics of Computation: Information Processing in Single Neurons*. Oxford University Press, New York (1998)
13. Koch, C., Poggio, T., Torre, V.: Nonlinear interactions in a dendritic tree: localization, timing, and role in information processing. *Proc. Natl. Acad. Sci.* **80**(9), 2799–2802 (1983)
14. Koch, C., Poggio, T., Torres, V.: Retinal ganglion cells: a functional interpretation of dendritic morphology. *Philos. Trans. Roy. Soc. London B Biol. Sci.* **298**(1090), 227–263 (1982)
15. Losonczy, A., Makara, J.K., Magee, J.C.: Compartmentalized dendritic plasticity and input feature storage in neurons. *Nature* **452**(7186), 436–441 (2008)
16. Low, L.K., Cheng, H.J.: Axon pruning: an essential step underlying the developmental plasticity of neuronal connections. *Philos. Trans. Roy. Soc. London B Biol. Sci.* **361**(1473), 1531–1544 (2006)
17. Luo, L., O’Leary, D.D.: Axon retraction and degeneration in development and disease. *Annu. Rev. Neurosci.* **28**, 127–156 (2005)
18. McCulloch, W.S., Pitts, W.: A logical calculus of the ideas immanent in nervous activity. *Bull. Math. Biophys.* **5**(4), 115–133 (1943)
19. Minsky, M., Papert, S.: *Perceptrons: An Essay in Computational Geometry*. MIT Press (1969)
20. Reynolds, J.N., Wickens, J.R.: Dopamine-dependent plasticity of corticostriatal synapses. *Neural Netw.* **15**(4), 507–521 (2002)
21. Salinas, E., Abbott, L.: A model of multiplicative neural responses in parietal cortex. *Proc. Natl. Acad. Sci.* **93**(21), 11956–11961 (1996)
22. Segev, I.: Sound grounds for computing dendrites. *Nature* **393**(6682), 207–208 (1998)
23. Sjöström, P.J., Rancz, E.A., Roth, A., Häusser, M.: Dendritic excitability and synaptic plasticity. *Physiol. Rev.* **88**(2), 769–840 (2008)
24. Chen, W., Sun, J., Gao, S., Cheng, J.-J., Wang, J., Todo, Y.: Using a single dendritic neuron to forecast tourist arrivals to Japan. *IEICE Trans. Inf. Syst.* **E100-D**, 190–202 (2017)
25. Taylor, W.R., He, S., Levick, W.R., Vaney, D.I.: Dendritic computation of direction selectivity by retinal ganglion cells. *Science* **289**(5488), 2347–2350 (2000)
26. Kwok, T.-Y., Yeung, D.-Y.: Constructive algorithms for structure learning in feedforward neural networks for regression problems. *IEEE Trans. Neural Networks* **8**(3), 630–645 (1997)
27. Yajiao, T., Junkai, J., Todo, Y., et al.: Neural network model for bankruptcy prediction. *Complexity*, 1076–2787 (2019)
28. UCI Repository of Machine Learning Databases. <http://www.ics.uci.edu/~mllearn/MLRepository.html>
29. Ji, J., Gao, S., Cheng, J., Tang, Z., Todo, Y.: An approximate logic neuron model with a dendritic structure. *Neurocomputing* **173**, 1775–1783 (2016)

**Recent Advances in Deep Learning
Methods and Techniques for Medical
Image Analysis**



Detection of COVID-19 by GoogLeNet-COD

Xiang Yu¹, Shui-Hua Wang^{1,2}, Xin Zhang^{3(✉)},
and Yu-Dong Zhang^{1,4(✉)}

- ¹ School of Informatics, University of Leicester, Leicester LE1 7RH, UK
xy144@le.ac.uk, {shuihuawang, yudongzhang}@ieee.org
- ² Guangxi Key Laboratory of Trusted Software, Guilin University of Electronic
Technology, Guilin 541004, China
- ³ Department of Medical Imaging, The Fourth People's Hospital of Huai'an,
Huai'an 223002, Jiangsu Province, China
973306782@qq.com
- ⁴ Department of Information Systems, Faculty of Computing and Information
Technology, King Abdulaziz University, Jeddah 21589, Saudi Arabia

Abstract. The outbreak of COVID-19 has been striking the world for months and caused hundreds of thousands of mortality. Early and accurate detection turns out to be one of the most effective ways to slow the spreading of the virus. To help radiologists interpret images, we developed an automatic CT image-based detection system, which achieved high accuracy on the detection of COVID-19. The proposed model in the detection system is codenamed GoogLeNet-COD, which utilizes one of the state-of-the-art deep convolutional neural networks GooLeNet as the backbone. As GoogLeNet was initially trained on ImageNet, we first replaced the last top two layers with four new layers, which include the dropout layer, two fully-connected layers and the output layer. The dropout technique is utilized to prevent overfitting in the system by inserting a dropout layer in the network. The newly added fully-connected layer serves as a transitional layer that prevents significant information loss while the last fully-connected layer is used to generate possibilities for the final output layer. The hold-out validation method is used to evaluate the performance of the proposed system. The experiment on a private COVID-19 dataset showed a high accuracy of our system.

Keywords: GoogLeNet-COD · Transfer learning · COVID-19

1 Introduction

In December 2019, a new virus, which was later termed as SARS-CoV-2 or COVID-19, suddenly stroke Asia and quickly spread from countries to countries. Transmission of the virus is so quick that over 200 countries have become victims, while thousands of hundreds of people, mainly aged people, died because of the virus. As no vaccine has been produced since then, prevention and early detection turn out to be the only effective way to slow down the spreading of the virus. COVID-19 is highly contagious and spreads rapidly with symptoms including cough, fever, ranging from mild to

severe. Some patients may progress to viral pneumonia and developed into severe and critical illness, and even died.

To effectively diagnose infected people, nucleic acid test and chest imaging techniques are widely used around the world. The nucleic acid test is a quick and well-developed technique to detect the particular sequences of nucleic acid. However, the high false-negative rate impairs the benefit of nucleic acid test and intermittently lower the efficiency of doctors. Compared to the nucleic acid test, the chest CT scanning is becoming a more popular and effective way for screening pneumonia caused by the virus [1]. In CT images, lesions caused by the virus will be imaged and visualizable to humans' eyes. The patchy ground-glass lesions in the lungs and pulmonary consolidation are common findings in chest CT images of patients. Therefore, CT imaging has a higher superiority compared to the nucleic acid test. To relieve the workloads of radiologists in the clinical community, researchers in the computer science community have been quite devoted to developing deep learning-based computer-aided detection (CAD) systems.

Deep learning, which is the advanced Artificial Neural Network (ANN), is one of the gorgeous achievements in the area of Machine Learning (ML). Thanks to the contributions of experts in the field, deep learning has been widely utilized in areas including object detection [2, 3], classification [4, 5] and object segmentation [6–8]. Besides the amazing performance, deep learning enables raw input data to be directly processed without pre-processing procedures as in traditional ML methods. The benefit of deep learning greatly outweighs the shortcomings though it is a fact that visualization and explainability of some deep learning models remain to be improved. Therefore, deep learning has also been widely incorporated in the design of computer-aided design systems of diseases [9–12]. In these systems, convolutional neural networks (CNNs) are generally used in image classification and segmentation because of parameters-friendly and easy training. However, training CNNs can be a time-consuming process that requires a long period of time even when the Graphics Processing Unit (GPU) is available. Transfer learning, a technique that reutilizes pre-trained CNNs, makes it possible to shorten the training time while the performance of the trained CNNs has been improved. By doing this, CNNs do not have to be trained from scratch. The pre-trained CNNs can be trained on a similar dataset but they can also be trained on quite different datasets.

In this paper, we developed an automatic detection system of COVID-19. In the system, chest CT images of patients who are suspected of being infected with COVID-19 are taken as the input of the system. CNN is used as a baseline to classify images into healthy and infected categories. Instead of training CNN in our system from scratch, we used transfer learning by transferring GoogLeNet to our classification task here. We first removed the top layers of GoogLeNet and then replaced new fully-connected layers to meet the classification task here. The dropout technique was used to prevent overfitting problem. Finally, our proposed system achieved high accuracy on a private COVID-19 lung image data. This paper is arranged as follows. In Sect. 2, we will briefly review the related work on the detection of COVID-19, followed by our proposed method in Sect. 3. The experiment, including details of the dataset, settings of the experiment, and results of the experiment will be given in Sect. 4. Discussion and conclusion will be given in Sect. 5.

2 Related Work

Recently, there are substantial works in the field of detecting the COVID-19 virus using deep learning models. Chowdhury et al. developed a deep learning model on a mixed dataset where images in the dataset are from three public datasets [13]. To distinguish pneumonia that could be progressed because of other viruses, 1345 viral pneumonia images are mixed with 190 COVID-19 and 1341 normal chest x-ray images. Data augmentation was used in the training and validation process. Transfer learning technique was applied to four state-of-the-art CNNs: AlexNet [14], ResNet18 [4], DenseNet201 [15] and SqueezeNet [16]. Two classification scenarios are considered in their work: COVID-19 pneumonia vs normal and viral, normal vs COVID-19. Over 98% accuracy was reported in their work. Similar work can be found in [17]. In another work [18], ResNet50 was transferred to detect COVID-19 based on X-ray images. The hold-out validation method was used to evaluate the performance of the developed model. In the hold-out validation, 80% of images in a dataset containing 278 images were partitioned into training set while the rest of them were used for validation. The accuracy of classification reached 98.18%, which supported the conclusion drawn by the authors that X-ray was a useful tool for healthcare. To explore the performance of AI-based image analysis systems, Ophir et al. developed a system that could detect COVID-19 by analyzing 2D and 3D thoracic CT images [19]. By analyzing 3D images, where images are acquired from patients over time, the evolution of the disease can be evaluated. Experiments showed 0.996 AUC on COVID-19 VS Non-COVID-19 classification task.

Though all the above-mentioned models showed high performance on the detection of COVID-19, there are still some challenges to be tackled with. Some units like ReLU (rectified linear unit) and dropout are introduced without further comparisons with models that ignore those units, which weaken the logic behind model designing. One more thing worthies notifying is that the over the complexity of networks introduced in the system. As can be seen from the above models, they showed high accuracy in the detection of COVID-19. But all of the models are featured by large amounts of parameters and high complexity of models, which makes transplantation of the developed models difficult.

Therefore, we proposed a relatively light-weighted detection model GoogLeNet-COD based on GoogLeNet in this paper. To figure out the possible structural improvement of the model, we further explored how units like ReLU and dropout affects the overall performance of the proposed model. Finally, we used the hold-out validation to validate the performance of the proposed model on the dataset.

3 Methodology

In this section, we will introduce our model on the detection of COVID-19. We will briefly introduce GoogLeNet and then move to the process of how transfer learning is carried out in our scenario here.

3.1 GoogLeNet

GoogLeNet is a 22-layer CNN that showed high performance on image classification. In the bottom of GoogLeNet, two pairs of convolution layer and max-pooling layer are used for feature extraction and feature reduction. In the middle of GoogLeNet, inception block, which utilizes parallel convolution that increases the width as well as the depth of networks, secured the first place for GoogLeNet in ILSVRC 2014 competition. There are in total nine inception blocks in GoogLeNet within each inception block there are four parallel paths. Details of each inception block are presented in Fig. 1.

In each inception block, four paths are aiming at extracting rich spatial features. 1×1 convolutions are used to reduce feature dimensions and computational cost. Due to features are concatenated after each inception block, computation costs would blow up just in a few stages with the increase of feature dimensions if no constraints applied. By introducing 1×1 convolutions, the dimensions of the intermediate features are reduced. The sizes of filters in subsequent convolution units in each path vary to make sure different local spatial features can be extracted and combined. It worthies notifying that max-pooling is used in the last path, which brings no more parameters but also serves to extract new features. After combining all of the carefully crafted architecture, GoogLeNet achieved an amazing performance on the ImageNet classification challenge.

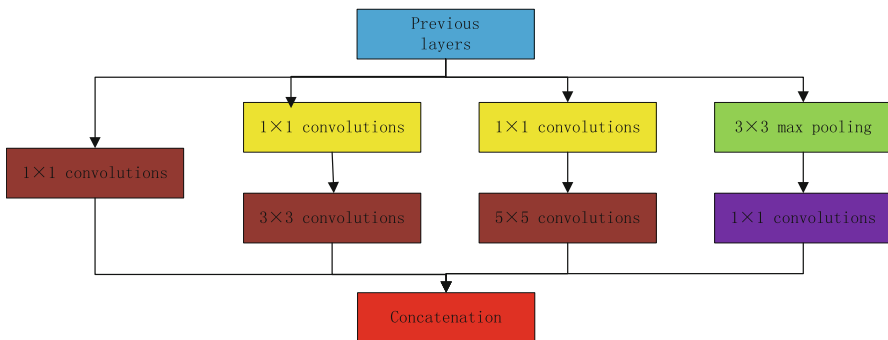


Fig. 1. Inception block.

3.2 GoogLeNet-COD

Considering that GoogLeNet is relatively shallow than the state-of-the-art CNNs while keeping amazing performance, we adapt and transfer GoogLeNet in our detection system here. Initially, GooLeNet was designed for 1000 categories classification. However, only binary classification is considered in our detection system. Therefore, we removed the last two top layers, namely the fully-connected layer and output layer, and replaced with four new top layers: dropout layer, fully-connect layer with 128 neurons, fully-connect layer with 2 neurons and output layer. The dropout layer is employed to prevent overfitting. To reduce information loss, we used a fully-connected

layer with 128 neurons as a transitional layer before final fully-connected layers with 2 neurons. We named the transferred GoogLeNet as GoogLeNet-COD. The procedures for implementing our model can be found in Table 1.

Table 1. Implementation of GoogLeNet-COD.

| |
|--|
| Step1: Load GoogLeNet trained on ImageNet; |
| Step2: Remove the last two top layers; |
| Step3: Add Dropout layer; |
| Step4: Add FC128 and FC2 fully-connected layer; |
| Step5: Add output layer; |
| Step6: Training GoogLeNet-COD with the training set of COVID-19. |

(whereFC128 and FC2 stand for fully-connected layers with 128 and 2 neurons respectively.)

3.3 GoogLeNet-COD Framework

In the GoogLeNet-COD framework, the dataset is first partitioned into a training set and a test set. The training set is then fed to the proposed model to update the parameters. After training, the testing set is taken as the input of the trained model for prediction. Finally, prediction results can be given by the trained model. Detailed information is presented in Fig. 2.

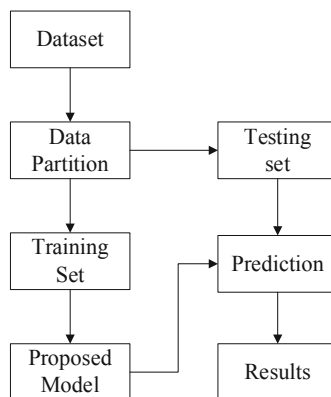


Fig. 2. Flow chart of the GoogLeNet-COD framework.

4 Experiments

In this section, we will briefly introduce the dataset involved in this research. Then we will move to the experiment settings, which will show the details about configurations about the experiment. We then explore the influence of the dropout layer and transitional fully-connected layer exerted to the performance of our model. This section provides a comparison between our method and other state-of-the-art approaches.

This research analyzed 132 COVID-19 pneumonia cases. 66 of them have been confirmed to be infected by COVID-19. To balance the ratio between normal and infected samples, we selected another 148 chests CT images from 66 healthy examiners. Two experienced radiologists collectively read CT images and recorded the diagnostic results while a superior radiologist was referred to achieve agreement on diagnostic results when there were disagreements. For images confirmed with COVID-19, images with the largest level of the lesions were selected; For healthy examiners, random levels of the images were selected instead. Examples of healthy and infected lungs are presented in Fig. 3. 70% of the images in the dataset are partitioned into the training set, while the rest of the images are partitioned into the testing set. The composition of the training set and test set is given in Table 2.

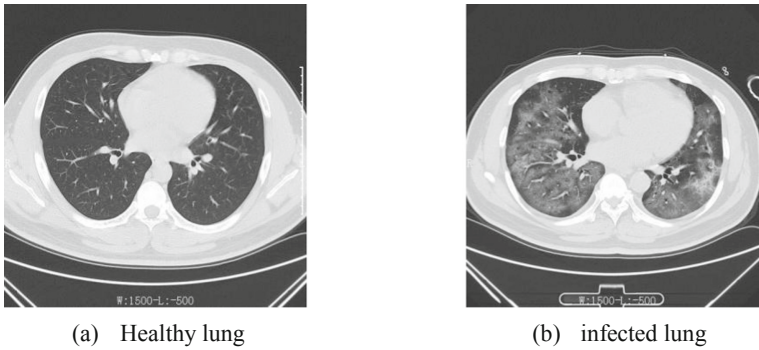


Fig. 3. Examples of images.

Table 2. Composition of training and testing set

| Set | Healthy | COVID-19 | Total |
|----------|---------|----------|-------|
| Training | 104 | 104 | 208 |
| Test | 44 | 44 | 88 |
| Total | 148 | 148 | 296 |

4.1 Experiment Settings and Evaluations

The experiments are conducted out on a personal laptop with 16G RAM and GPU GTX1050(4G). With no other specification, we have 30 as maximum training epoch,

initial learning rate at 10^{-4} , batch size to be 20. While training, the training set shuffles every epoch. The random seed is fixed so that the images in the training set and the testing set remain unchanged when training and validating different models. We use specificity, sensitivity and accuracy to measure the performance of our proposed model. The definitions of the three metrics are:

$$\text{Specificity} = \frac{\text{True Negative}}{\text{True Negative} + \text{False Positive}} \quad (1)$$

$$\text{Sensitivity} = \frac{\text{True Positive}}{\text{True Positive} + \text{False Negative}} \quad (2)$$

$$\text{Accuracy} = \frac{\text{True Negative} + \text{True Positive}}{\text{True Negative} + \text{False Positive} + \text{True Positive} + \text{False Negative}} \quad (3)$$

True Positive means true COVID-19 infected lung images that are correctly classified as infected lung images; True Negative means images from healthy examinees that are correctly classified as healthy images; False Positive and False Negative mean misclassified images from healthy examinees and infected lung images.

4.2 Optimization of Architecture

To explore the influence of the dropout layer and transitional fully-connected layer on the performance of GoogLeNet-COD, we trained GoogLeNet-COD under three different scenarios: GoogLeNet-COD-A with dropout layer and transitional fully-connected layer, GoogLeNet-COD-B without dropout layer but with transitional fully-connected layer, GoogLeNet-COD-C no dropout and the transitional fully-connected layer. The architectures of the three networks are shown in Fig. 4. Block in the dashed rectangle remains the same as GoogLeNet.

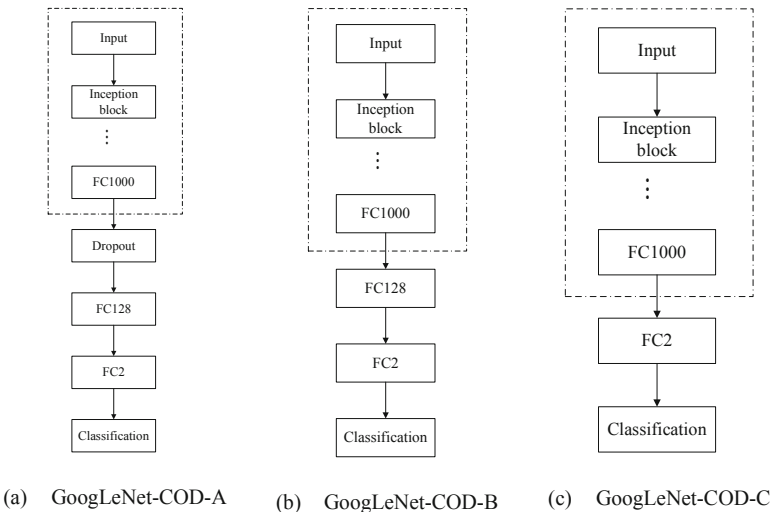


Fig. 4. Architectures of GoogLeNet-COD

4.3 Method Comparison

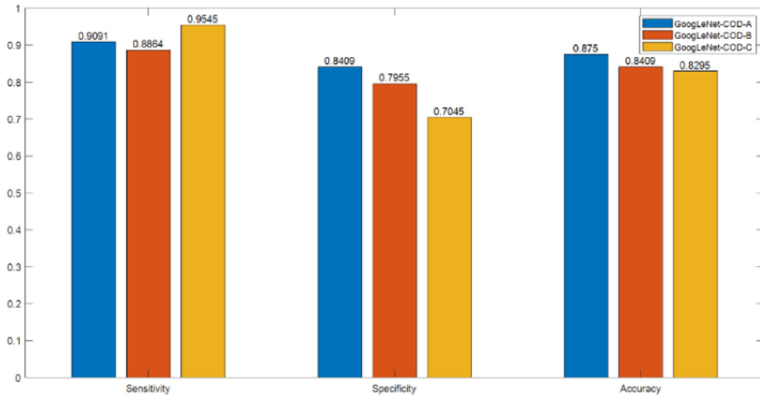


Fig. 5. Model comparison.

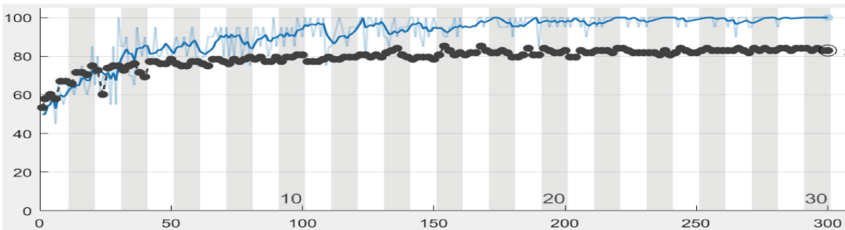
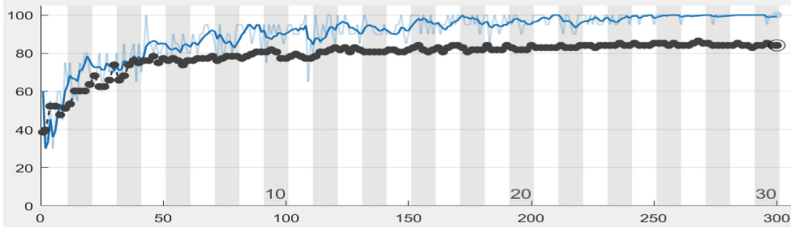
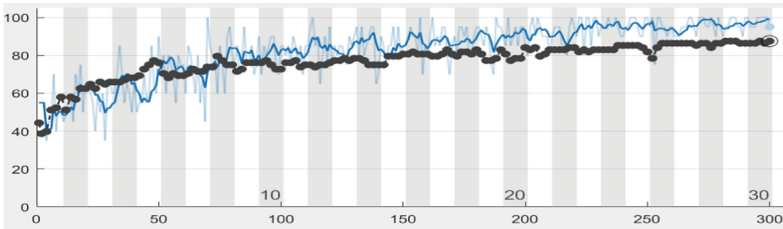


Fig. 6. Training and validation process of three models.

We first compared our models under three different circumstances. The results are shown in Fig. 5. The training process and validation process are shown in Fig. 6.

As can be seen from the training process, GoogLeNet-COD-C that doesn't include the dropout layer and transitional fully-connected layer converged earlier but turns out to be overfitted. The same conclusion can be drawn from the training process of GoogLeNet-COD-B. Nevertheless, GoogLeNet-COD-A showed the best performance amongst all of the three proposed models, which further foster the fact that the dropout layer and transitional layer can be used to avoid overfitting.

Also, we compared our method with existing methods that showed the certain capability of detecting COVID-19. The results are given in Fig. 7. As can be seen, our method performs best in all aspects, which proves the capability of our system on detection of COVID-19.

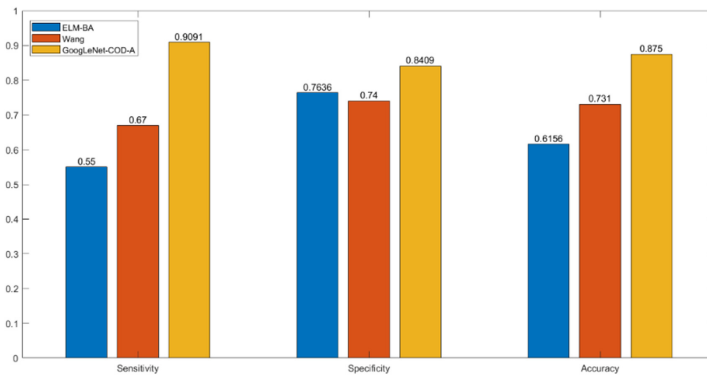


Fig. 7. Comparison of methods.

5 Conclusion

In this paper, we proposed an automatic detection system of COVID-19 by our proposed GoogLeNet-COD. Due to noticeable lesions that can be found in chest CT images, deep learning can be efficiently applied to relieve radiologists from heavy workloads. Based on this, we propose that we can adapt the state-of-the-art networks into a CAD system for COVID-19 detection. By using transfer learning, we slightly adjusted GoogLeNet, which was the champion of ImageNet 2014 on image classification, to construct our GoogLeNet-COD. To design models with the best performance, we explore the necessity of the dropout layer and transitional layer. Experiments show that the dropout layer can effectively mitigate the overfitting problem while transitional fully-connected layer alone does seem to be helpful for mitigating overfitting. Validation of a private dataset proved the efficiency of our system. Comparison with other methods shows our method can achieve comparable accuracy on the detection of COVID-19 by chest CT images.

However, there are still numerous limitations to this research. The accuracy of the proposed models remains to be improved. To resolve this, we will try more state-of-the-art networks to propose new models with better-structured architectures. Also, the size of the dataset, which would significantly affect the performance of networks, is still quite limited. Therefore, we will use larger datasets to contribute to better performance of the proposed models.

Acknowledgment. The paper is partially supported by the Royal Society International Exchanges Cost Share Award, UK (RP202G0230), Medical Research Council Confidence in Concept Award, UK (MC_PC_17171), Hope Foundation for Cancer Research, UK (RM60G0680), and Guangxi Key Laboratory of Trusted Software (kx201901).

References

1. Fang, Y., et al.: Sensitivity of chest CT for COVID-19: comparison to RT-PCR. *Radiology*, 200432 (2020)
2. Ren, S., He, K., Girshick, R., Sun, J.: Faster R-CNN: towards real-time object detection with region proposal networks. In: *Advances in Neural Information Processing Systems*, pp. 91–99 (2015)
3. Zhao, Z.-Q., Zheng, P., Xu, S.-T., Wu, X.: Object detection with deep learning: a review. *IEEE Trans. Neural Netw. Learn. Syst.* **30**(11), 3212–3232 (2019)
4. He, K., Zhang, X., Ren, S., Sun, J.: Deep residual learning for image recognition. In: *Proceedings of the IEEE Conference on Computer Vision and Pattern Recognition*, pp. 770–778 (2016)
5. Szegedy, C., Ioffe, S., Vanhoucke, V., Alemi, A.A.: Inception-v4, inception-ResNet and the impact of residual connections on learning. In: *Thirty-First AAAI Conference on Artificial Intelligence* (2017)
6. Badrinarayanan, V., Kendall, A., Cipolla, R.: SegNet: a deep convolutional encoder-decoder architecture for image segmentation. *IEEE Trans. Pattern Anal. Mach. Intell.* **39**(12), 2481–2495 (2017)
7. Chen, L.-C., Papandreou, G., Kokkinos, I., Murphy, K., Yuille, A.L.: Deeplab: semantic image segmentation with deep convolutional nets, atrous convolution, and fully connected crfs. *IEEE Trans. Pattern Anal. Mach. Intell.* **40**(4), 834–848 (2017)
8. Chen, L.-C., Zhu, Y., Papandreou, G., Schroff, F., Adam, H.: Encoder-decoder with atrous separable convolution for semantic image segmentation. In: Ferrari, V., Hebert, M., Sminchisescu, C., Weiss, Y. (eds.) *ECCV 2018*. LNCS, vol. 11211, pp. 833–851. Springer, Cham (2018). https://doi.org/10.1007/978-3-030-01234-2_49
9. Al-antari, M.A., et al.: An automatic computer-aided diagnosis system for breast cancer in digital mammograms via deep belief network. *J. Med. Biol. Eng.* **38**(3), 443–456 (2018)
10. Mohanty, S.P., Hughes, D.P., Salathé, M.: Using deep learning for image-based plant disease detection. *Front. Plant Sci.* **7**, 1419 (2016)
11. Islam, J., Zhang, Y.: A novel deep learning based multi-class classification method for Alzheimer’s disease detection using brain MRI data. In: Zeng, Y., et al. (eds.) *BI 2017*. LNCS (LNAD), vol. 10654, pp. 213–222. Springer, Cham (2017). https://doi.org/10.1007/978-3-319-70772-3_20
12. Lu, S., Lu, Z., Yang, J., Yang, M., Wang, S.: A pathological brain detection system based on kernel based ELM. *Multimed. Tools Appl.* **77**(3), 3715–3728 (2016). <https://doi.org/10.1007/s11042-016-3559-z>

13. Rahman, T., et al.: Transfer learning with deep convolutional neural network (CNN) for Pneumonia detection using chest X-ray. *Appl. Sci.* **10**(9), 3233 (2020)
14. Krizhevsky, A., Sutskever, I., Hinton, G.E.: Imagenet classification with deep convolutional neural networks. In: *Advances in Neural Information Processing Systems*, pp. 1097–1105 (2012)
15. Huang, G., Liu, Z., Van Der Maaten, L., Weinberger, K.Q.: Densely connected convolutional networks. In: *Proceedings of the IEEE Conference on Computer Vision and Pattern Recognition*, pp. 4700–4708 (2017)
16. Iandola, F.N., Han, S., Moskewicz, M.W., Ashraf, K., Dally, W.J., Keutzer, K.: SqueezeNet: AlexNet-level accuracy with 50x fewer parameters and <0.5 MB model size (2016)
17. Apostolopoulos, I.D., Mpesiana, T.A.: Covid-19: automatic detection from X-ray images utilizing transfer learning with convolutional neural networks. *Phys. Eng. Sci. Med.* **43**(2), 635–640 (2020). <https://doi.org/10.1007/s13246-020-00865-4>
18. Bukhari, S.U.K., Bukhari, S.S.K., Syed, A., Shah, S.S.H.: The diagnostic evaluation of convolutional neural network (CNN) for the assessment of chest X-ray of patients infected with COVID-19 (2020). medRxiv
19. Gozes, O., et al.: Rapid AI development cycle for the coronavirus (covid-19) pandemic: initial results for automated detection & patient monitoring using deep learning CT image analysis (2020). arXiv preprint [arXiv:200305037](https://arxiv.org/abs/200305037)



A Big Data Driven Model for Screening Electricity Customers

Liu Xingping¹(✉), Xie Zhihan², Zhang Chenmin¹, Zhou Chenhui¹,
and Zhuang Chen¹

¹ State Grid ZheJiang Marketing Service Center (Metrology Center),
Hangzhou, China
icic1001@126.com

² Center of Mass Entrepreneurship and Innovation,
State Grid Zhejiang Electric Power Co., Ltd., Hangzhou, China

Abstract. Based on the current corresponding indicators for determining overcapacity electricity consumption, the screening rules for suspected overcapacity electricity customers are scientifically formulated with data analysis methods in this paper. Overcapacity Electricity Consumption refers to the electricity customer's violation of the power supply contract, which exceeds the capacity requested. This is a typical behavior of defaulting electricity and disrupting the normal order of electricity supply and consumption. At present, the inspection system lacks an intuitive visual interface for displaying results analysis and the support from a more scientific and flexible algorithm system. Through the expert's empirical analysis, we have summarized the characteristic indicators of overcapacity customers and formulated the rules for identifying suspected overcapacity electricity customers.

Keywords: Overcapacity electricity · Anomaly detection · Multi-layer cluster

1 Introduction

Overcapacity Electricity Consumption refers to the electricity customer's violation of the power supply contract, which exceeds the capacity requested. This is a typical behavior of defaulting electricity and disrupting the normal order of electricity supply and consumption. At present, the inspection system's screening rules for abnormal (overcapacity) customers is: high-voltage customers, whose actual electricity consumption in the month is greater than the theoretical maximum electricity consumption, are identified as suspected abnormal customers (excluding those experiencing the changing process or the completion of the increase, reduction, suspension, and resumption process is done in the current month).

Some scholars have studied how to identify and detect users' excess capacity. Zheng Songsong et al. (2014) used the electricity information collection system to monitor user load, analyzed the data of overcapacity of users, and investigated and dealt with them on the spot [1]; Bi Kemu et al. (2016) made some suggestions on overcapacity and their investigation and treatment [2]. However, in terms of the determination of overcapacity customers, the system lacks an intuitive visual interface for displaying results analysis

and the support from a more scientific and flexible algorithm system. Through the expert's empirical analysis, we have summarized two characteristic indicators of overcapacity customers: 1. The ratio of actual monthly electricity consumption to the theoretical maximum electricity consumption of the month is often too large; 2. The maximum demand for the month exceeds the actual running capacity.

Based on the corresponding indicators for determining the super-capacity electricity consumption, this paper applies clustering algorithm, model superiority evaluation algorithm (e.g. f1-score) and so on, combined with the multi-dimensional index joint distribution comparison chart (e.g.: KDE), to provide technical support for the screening of suspected overcapacity customers.

2 Feature Engineering

2.1 Basic Data Observations

The characteristic Indicators of New, Old, and Non- Overcapacity Customers are as follows by our observation and analysis:

- 1) Whether it is super-capacity and non-super-capacity users in the distribution of each power ratio overall presents the valley power ratio and peak power ratio and the peak power ratio; Spike Electricity Rate
- 2) The total power ratio of overcapacity users and non-capacity users is very obvious (overcapacity user's total power ratio is mainly above 0.3450);
- 3) The difference between the total power ratio of overcapacity users and non-super-capacity users is obviously mainly caused by the distinction between the valley ratio and the peak power ratio.

3 Modeling

3.1 Modeling a Multi-layer Clustering Based on Two Indicators: Peak and Valley Electricity Rates

We selected two indicator data for clustering: Peak Power Ratio (FDLB) and Valley Power Ratio (GDLB).

Merged Comparison of Multi-dimensional Joint Distribution. We finally confirmed through experiments that the best category for clustering is category 5. Since the method based on a multi-layer clustering scheme can greatly reduce the impact of random sampling on clustering, only one set of sampling data is used for multi-layer clustering in this section. The sampling method is the same as before: 15000 customers are randomly sampled from the full valid non-overcapacity customers, and they are combined with the full customers after filtering to form a new dataset. A multi-layer clustering algorithm is then used to perform clustering based on the peak and valley electricity rates. The resulting five clustering categories are named as A/B/C/D/E (A: blue, B: green, C: orange, D: purple, E: yellow).

It can be seen that the overcapacity customers are mainly distributed in the four cluster categories of “orange”, “green”, “purple” and “yellow”, while rare in the “blue” cluster.

Analysis of Optimal Screening Rules for Overcapacity Customers (Relatively Optimal). The customers in different clustering categories are divided into two groups according to different combinations. Suppose the resulting 5 clustering categories are named as A/B/C/D/E (A: blue, B: green, C: orange, D: Purple, E: yellow), which are combined and divided into overcapacity and non-overcapacity. For all 30 different combinations, the four indicators, namely accuracy, recall rate, F1-score, and F0.5-score, are calculated.

Using F0.5-score as the key indicator, where DE is identified as an overcapacity customer and ABC is identified as a non-overcapacity customer (at this time, the model’s accuracy is 69.89%, recall rate is 49.83%, F1-score is 58.18%, and F0.5-score is 64.68%), achieving a relatively optimal division of overcapacity and non-overcapacity customers.

F1-score believes that the recall rate is as important as accuracy, while F2-score believes that the recall rate is half as important.

Determining Overcapacity and Non-overcapacity Boundaries based on Clustering Results (Relatively Optimal). According to previous analysis, DE (D: purple, E: yellow) is classified as overcapacity, and ABC (A: blue, B: green, C: orange) is classified as non-overcapacity. For the determination of the boundary, we only need to find the boundaries between BD, CD and CE, respectively. The three dividing boundaries are as follows:

BD boundary:

$$-0.2413 * FDLB + 1.3525 * GDLB - 0.7754 = 0 \quad (1)$$

CD boundary:

$$0.6790 * FDLB - 0.6730 * GDLB - 0.2757 = 0 \quad (2)$$

CE boundary:

$$5.5474 * FDLB + 1.1770 * GDLB - 1.4542 = 0 \quad (3)$$

The intersection points of BD/CD and CD/CE boundaries are then calculated to obtain the final overcapacity and non-overcapacity boundary (Fig. 1).

The specific rules are as follows:

$$-0.2413 * FDLB + 1.3525 * GDLB - 0.7754 > 0, \quad \text{if } 0 \leq FDLB < 0.1971 \quad (4)$$

$$0.6790 * FDLB - 0.6730 * GDLB - 0.2757 < 0, \quad \text{if } 0.1971 \leq FDLB < 0.5603 \quad (5)$$

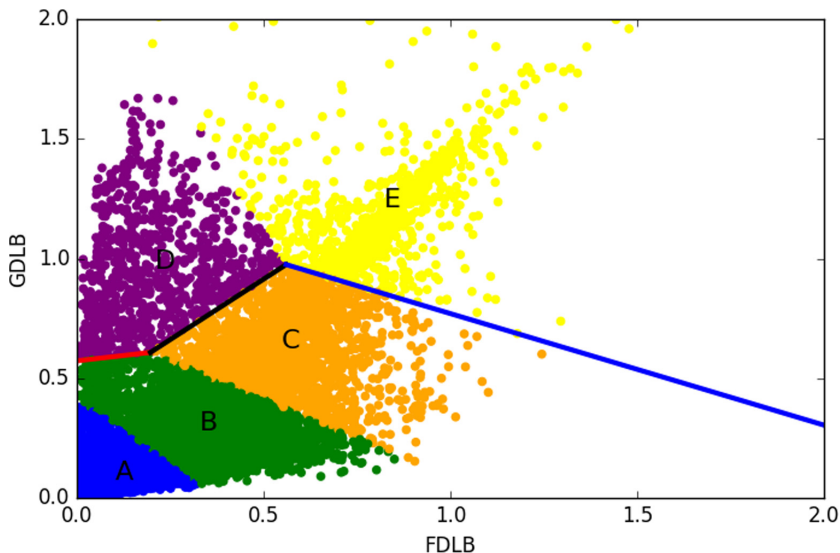


Fig. 1. Overcapacity and non-overcapacity boundary. (Color figure online)

$$0.5474 * FDLB + 1.1770 * GDLB - 1.4542 > 0, \text{ if } 0.5603 \leq FDLB \quad (6)$$

3.2 Modeling a Multi-layer Clustering Based on Two Indicators: Valley and Total Electricity Rates

Two other indicator data are selected for clustering: Valley Ratio (GDLB) and Total Power Ratio (ZDLB).

Merged Comparison of Multi-dimensional Joint Distribution. We finally confirmed through experiments that the best category for clustering is category 5.15000 customers are randomly sampled from the full valid non-overcapacity customers, and they are combined with the full customers after filtering to form a new dataset. A multi-layer clustering algorithm is then used to perform clustering based on the valley and total electricity rates.

It can be seen that the overcapacity customers are mainly distributed in the four cluster categories of “blue”, “orange”, “green” and “yellow”, while rare in the “purple” cluster.

Analysis of Optimal Screening Rules for Overcapacity Customers (Relatively Optimal). The customers in different clustering categories are divided into two groups according to different combinations. Suppose the resulting 5 clustering categories are named as A/B/C/D/E (A: blue, B: green, C: orange, D: Purple, E: yellow), which are combined and divided into overcapacity and non-overcapacity. For all 30 different combinations, the four indicators, namely accuracy, recall rate, F1-score, and F0.5-score, are calculated.

Using F0.5-score as the key indicator, where AC is identified as an overcapacity customer and BDE is identified as a non-overcapacity customer (at this time, the model’s accuracy is 59.74%, recall rate is 56.30%, F1-score is 57.97%, and F0.5-score is 59.02%), achieving a relatively optimal division of overcapacity and non-overcapacity customers.

Determining Overcapacity and Non-overcapacity Boundaries Based on Clustering Results (Relatively Optimal). According to previous analysis, AC (A: blue, C: orange) is classified as overcapacity, and BDE (B: green, D: purple, E: yellow) is classified as non-overcapacity. For the determination of the boundary, we only need to find the boundary between BC (Fig. 2).

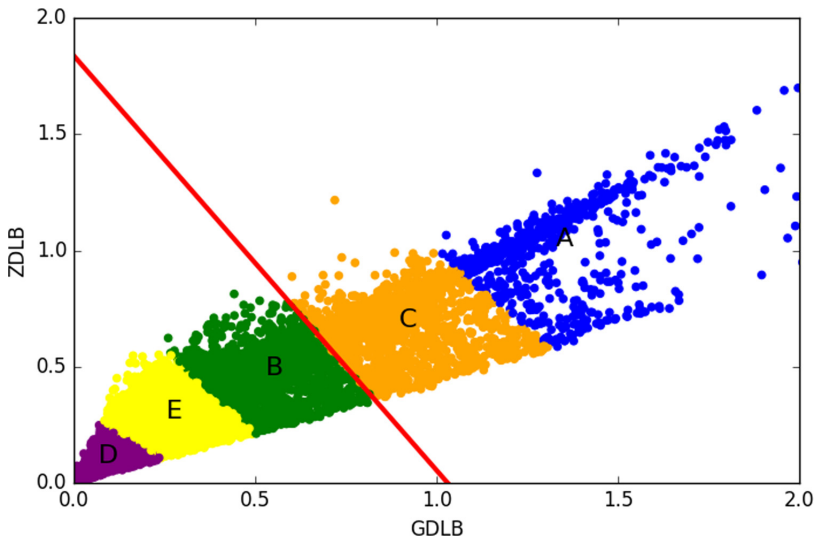


Fig. 2. Overcapacity and non-overcapacity boundary. (Color figure online)

CB boundary:

$$0.7318 * GDLB + 0.4112 * ZDLB - 0.7548 = 0 \tag{7}$$

An overcapacity customer is determined by a positive evaluation of its GDLB and ZDLB in the above formula, otherwise a non-overcapacity customer is determined.

The specific rules are as follows:

$$0.7318 * GDLB + 0.4112 * ZDLB - 0.7548 > 0 \tag{8}$$

4 Experiment

4.1 Comparative Analysis of Modeling Results

From the distribution of the two rounds of data, the correlation between the two indicators (peak and valley electricity rates) in the first round is relatively small, and the data distribution is relatively scattered, thus the regularity is not strong. In contrast, the correlation between the two indicators (valley and total electricity rates) in the second round is large, and the data is mainly distributed on the diagonal (Table 1).

Table 1. From the modeling performance

| | Accuracy | Recall rate | F1-score | F0.5-score |
|------------------|----------|-------------|----------|------------|
| The first round | 69.89% | 49.83% | 58.18% | 64.68% |
| The second round | 59.74% | 56.30% | 57.97% | 59.02% |

In the first round, the accuracy, F1-score, and F0.5-score of the model built using “FDLB” and “GDLB” are better than the results of the model built using “GDLB” and “ZDLB” in the second round. But the recall rate in the first round is lower than the second round.

4.2 Merged Model Results

Since only two indicators are used in the first two rounds of mode construction, the overcapacity and non-overcapacity classification rules constructed in this way may be relatively one-sided, and the magnitude of the suspected overcapacity customers may be relatively large. In order to overcome these two shortcomings, we merge the overcapacity and non-overcapacity screening rules obtained from the first two rounds of model construction.

The final results are shown as below (Table 2):

Table 2. The final results

| | #of real OCs | #of OCs identified by the model | #of real OCs identified by the model | Accuracy | Recall | F1-score | F0.5-score |
|--------------|--------------|---------------------------------|--------------------------------------|---------------|---------------|---------------|---------------|
| 1st Round | 2641 | 1883 | 1316 | 69.89% | 49.83% | 58.18% | 64.68% |
| 2nd Round | 2641 | 2489 | 1487 | 59.74% | 56.30% | 57.97% | 59.02% |
| Merge | 2641 | 1497 | 1134 | 75.75% | 42.94% | 54.81% | 65.71% |

It can be seen from the table that screening rules of the first round have an absolute advantage in F1-score; screening rules of the second round have an absolute advantage in the recall rate; the merged screening rules have an absolute advantage in the accuracy and F0.5-score.

5 Conclusion

We conclude the experiment to draw the following conclusions: The number of suspected overcapacity customers determined by the screening rules of the first and second phase is similar, but the suspected overcapacity customers determined by the screening rules in the second phase include more overcapacity customers. Therefore, the screening rules of the second phase modeling are better than those of the first phase. So, it is finally determined that the screening rules of the second phase are the current optimal screening rules.

Final screening rules for overcapacity customers are as follows.

If the indicator data (FDLB: peak electricity rate, GDLB: valley electricity rate, ZDLB: total electricity rate) meets the following four rules at the same time, an overcapacity customer is determined, otherwise a non-overcapacity customer is determined.

$$(-0.2413 * FDLB + 1.3525 * GDLB - 0.7754 > 0, \text{ if } 0 \leq FDLB < 0.1971 \quad (9)$$

$$0.6790 * FDLB - 0.6730 * GDLB - 0.2757 < 0, \text{ if } 0.1971 \leq FDLB < 0.5603 \quad (10)$$

$$0.5474 * FDLB + 1.1770 * GDLB - 1.4542 > 0 \text{ if } 0.5603 \leq FDLB \quad (11)$$

And

$$0.7318 * GDKB + 0.4112 * ZDLB - 0.7548 > 0 \quad (12)$$

References

1. Song-song, Z., Li, L., Bing-bing, Q.: Over-capacity analysis based on the power information acquisition system. *J. Shanghai Electric Power Coll.* **30**(B04), 44–46 (2014)
2. Bi, K.-M., Zhu, W.-Q., Gu, H.: Analysis of the customer's super-capacity electricity inspection problems
3. Wu, B.-J.: Hazards and prevention of overcapacity electricity consumption by power users (9) (2014)
4. Chen, G.-X., Yang, X.-G.: Properly deal with the overcapacity of electricity customers. *Power Demand Side Management* (5), 58
5. Qu, S.-J.: Reason analysis and prevention and control measures for overcapacity of special transformer users. *Electron. Test* (3) (2017)
6. Wang, Q., Wang, C., Feng, Z.-Y., et al.: Review of K-means clustering algorithm research. *Electron. Des. Eng.* (7), 27–30
7. Gan, J., Tao, Y.: DBSCAN revisited: misclaim, unfixability, and approximation (2015)



The Evaluation Model Research of Power Supply Service Under the Background of “Running Once at Most”

Liu Xingping^(✉), Wang Xiaoyu, and Zhang Chenmin

State Grid ZheJiang Marketing Service Center (Metrology Center),
Hangzhou, China
icic1001@126.com

Abstract. This paper extends the service quality model by using the service blueprint theory. Through combing traditional perceived service quality indicators with the characteristics of service informationization, this paper adds two dimensions of “running once at most” and “information quality”, then, constructs 58 evaluation index systems. Based on data from the random questionnaires of all kinds of electricity users, the empirical results of the service quality model show that: Consumers pay more attention to “running once at most” and information quality. Based on this, author puts forward suggestion on improving service items such as “running once at most” and information quality as well as how to using this extending model.

Keywords: Running once at most · Perceived service quality · Information quality

1 Introduction

Our country’s economy has shifted form a high-speed growth stage to a high-quality development stage. To handle this new stage. It is necessary to update the existing service quality index system and statistical system. State Grid Zhejiang electric power took the initiative to respond to the new situation of the reform and development of the electricity sales side, accelerated the implementation of the “Internet +” marketing service application, and actively promoted the power consumption mode of “purchase electricity first, then use electricity, understand and manage electricity”. It has established an all-weather, online and offline diversified service front-end, including electronic channels, business hall, and customer managers. By the early 2018, electronic channels have been realized The number of customers is 19.37 million, and the electronic channel payment accounts for 16.88% of the total. At the same time, by vigorously promoting smart payment and point exchange business, expanding the scale of smart payment customers, and guiding customers to pay online, etc., all 16 types of businesses such as residential electricity consumption and daily electricity consumption of enterprises and institutions can achieve “not even once Run”, the relatively complex

five types of electricity business of enterprises and institutions have achieved “running once at most”. It can be seen that the service mode from the business hall, 95598 website, etc. to the palm power application, WeChat public service platform and other Internet-based service channels and service methods, these high-quality service development not only put forward the issue of updating the service quality measurement index system, but also provide the basis for summarizing and refining service practice.

Many scholars have also studied the quality of power supply service. Xinan Zhang and PengTian (2005) developed a power supply service quality meter based on SERVQUAL model [2]; Wu (2014) designed the service quality gap model and service quality evaluation index [3]; Lijing He et al. (2017) made a more in-depth study on the power supply service quality evaluation system [1]. However, these studies do not reflect the characteristics of “Internet + mobile power supply service system” in which “Internet +” technology is integrated into mobile power supply services, nor can they reveal and meet the “running once at most” service quality requirements based on Internet technology.

2 Proposed Model and Research Approaches

2.1 Model Design

The quality of power supply service is the process and result of a series of activities that meet the needs of power customers, intangible, and without the change of physical ownership. According to the Finnish scholar Grunrus, the quality of service should consider both the quality of the process and the quality of the results. The quality of results in power supply services mainly refers to the quality of power, including services such as power supply stability and power supply security; and process quality refers to the expansion and installation of electricity in the electricity industry, changes in electricity consumption, electricity bill collection, power failure repair, Energy measurement, customer consultation and complaint handling. According to this, it can be summarized as 1 result quality (power supply quality) and 6 process quality indicators (meter reading billing, fault repair, industrial expansion report installation, business hall services, report complaints and 95598 services).

The “running once at most” service requirement was first proposed by Zhejiang in 2016, and the service industry in various provinces and cities followed up the practice one after another. After three years of exploration, the academic community and the industry began to summarize one after another. The definition of “run once” in relevant services in the provisions on the reform of Zhejiang Province’s security “run once at most” adopted by the Standing Committee of the 13th people’s Congress of Zhejiang Province in November 2018 is defined as: “natural person, legal person and non-legal person organization apply to the administrative organ for handling a matter, if the application materials are complete and conform to the legal form, the handling results

are complete from the time of application to the time of receiving the application.” Only one visit or zero visit is needed, It can be seen that the “number” of business transactions is the result quality dimension of “run once” service quality. These dimensions have not been covered in previous electricity service measurement models. In article 5 of the document, it is also specified that “reduce handling links, integrate handling materials, shorten handling time limit, optimize handling procedures and improve handling efficiency”. It can be seen from these four aspects: the links of service projects, material requirements, processing time limit and effectiveness of results. To sum up, it includes the following five items: the rationality of the frequency of on-site processing of “going to the business hall”, the rationality of relevant materials provided, the simplicity of the process or service procedures, the flexibility of the way of business handling and submission, and the effectiveness of problem solving.

Information quality is the applicability and satisfaction of information to information consumers (users) (Wang R. y, 1996). It has rich connotations and is a multi-dimensional concept (Shirlee Ann knight and Janice burn, 2005). As the evaluation of power supply service quality by users is based on service elements and service links, the perceived information quality is an important element in the service quality of power supply for users, and the information experience and perception of users in the interaction process directly affect the evaluation of information products and information services. However, it is usually evaluated from four aspects: the content of information (including objectivity and accuracy), the overall quality of information (including relevance and soundness), the level of information expression (whether it is clear, concise and easy to understand), and the real-time nature of information (timeliness and matching degree). Due to different industries and use categories, the evaluation indicators of user perceived information quality are not the same. Considering the interactive characteristics of palm power, 95598 intelligent website, Wechat public account, etc., after in-depth interviews with 30 strategic users, under the four frameworks of information content, expression level, real-time and overall quality, information adequacy, consistency and effectiveness are selected Six core indicators, namely, sex, timeliness, security and intelligibility, are used as the evaluation indicators of perceived information quality in the perceived quality of electricity service. Accuracy, simplicity and simplicity of information have been reflected in the dimension of meter reading and payment, so it has not been adopted in the dimension of information quality.

To sum up, based on the user’s perceived quality of power supply quality in addition to 1 result quality index and 6 process quality indicators, increase the “run once quality of service” indicators and “information quality” indicators, comprehensively drawn as shown in Fig. 1 measurement model.

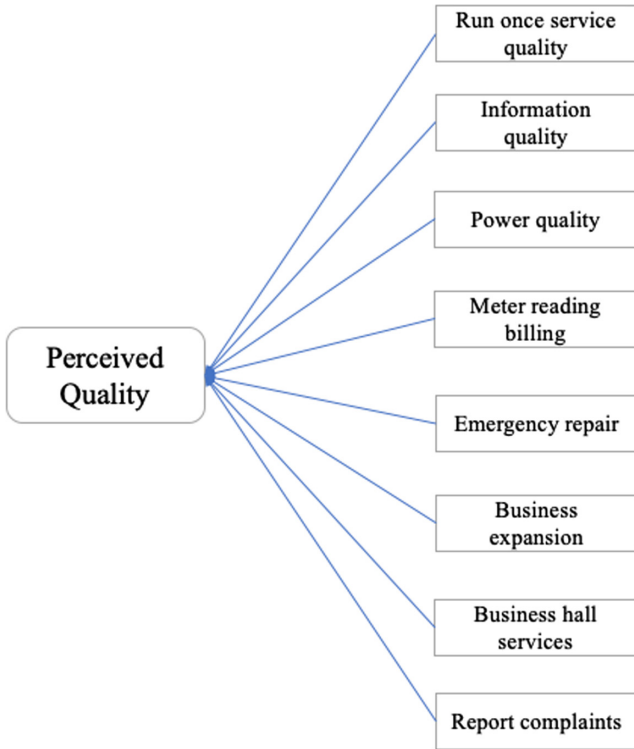


Fig. 1. Measurement model of perceived quality of power supply service under the background of “running once at most”

2.2 Research Design

In order to make the structural measurement model shown in Fig. 1 operational, and to ensure the validity of the secondary indicators, this paper designed a structured in-depth interview questionnaire and conducted interviews with 30 users while referring to relevant research results. Based on the contents of the in-depth interviews and the existing literature results, the three-level indicators under each level of indicators and the four-level indicators that characterize each three-level indicators are extracted and sorted out. Index system, and based on the table, a questionnaire was designed, and the questionnaire was revised after a pre-test. Finally, a combination of face-to-face interviews, telephone interviews, and online interviews was conducted to survey various types of electricity service customers.

Table 1. Service quality evaluation index system for power supply enterprises

| First-level indicators | Second-level indicators | Third-level indicators | Fourth-level indicators |
|---------------------------------|---------------------------------|--|---------------------------|
| Power Service Perceived Quality | Business expansion | Electricity application | Application process |
| | | | Power supply scheme |
| | | | Three no designation |
| | | Acceptance power transmission | Completion acceptance |
| | Timely power transmission | | |
| | Field service service level | | |
| | Power supply quality | Stabilized power supply | Power supply reliability |
| | | | voltage stability |
| | | | Problem solving |
| | | Power off | Announcement channel |
| | Timely and accurate information | | |
| | Planned power outage | | |
| | Meter reading fee | Meter reading | Measurement accuracy |
| | | | Accuracy of meter reading |
| | | | Service behavior |
| | | Pay | Payment convenience |
| | Charging method | | |
| Call back in arrears | | | |
| Business hall services | Network construction | geographical position | |
| | | Environmental facilities | |
| | | Business order | |
| | Service quality | Attitude and behavior | |
| | | service efficiency | |
| Emergency repair | Emergency repair process | Arrival speed | |
| | | processing speed | |
| | | Site management | |
| | Quality of emergency repair | Quality of emergency repair | |
| | | Professional ability | |
| | | Service attitude | |
| Report complaints | complaints and reports | processing speed | |
| | | Processing result | |
| | | Service attitude | |
| | | Treatment level | |
| 95598 | Artificial services | Service attitude (language, initiative, feedback, concentration) | |

(continued)

Table 1. (continued)

| First-level indicators | Second-level indicators | Third-level indicators | Fourth-level indicators | |
|------------------------|-------------------------|------------------------|---|----------------------|
| | | Self-service | Service ability (understanding, feedback, matching) | |
| | | | Waiting time | |
| | | | Answer speed | |
| | | | Operation path facilitate | |
| | Information quality | | | Sufficient agreement |
| | | | | Effective |
| | | | | timely |
| | | | | security |
| | | | | Easy to understand |
| | Running once at most | | | Reasonable material |
| | | | | Flexible way |
| | | | | Simple procedures |
| | | | | Reasonable times |
| | | | | Effective solution |

Table 1 is the items of four-level indicators are set in the form of Likert scale 5. In each item, the quality satisfaction degree of the user is asked, and the higher the score, the higher the satisfaction degree of the user’s perceived service quality.

3 Experiments and Analysis

Considering that the depth and breadth of “run once at most” practice of State Grid Zhejiang electric power company is typical in the whole country, the sample object of this study is grid Zhejiang electric power company randomly selects the surveyed users on the basis of stratified sampling. One city and three counties (among which Zhoushan power supply company is one city and two counties) are selected from 11 Prefecture and city power supply companies. After comprehensive consideration of customer power consumption category, power consumption, reliability requirements and other factors, the survey objects are divided into: (a) residential customers; (b) industrial enterprise customers; (c) commercial service customers; (d) government and utility customers. Random access or invite access to these four types of users. In fact, 5761 valid samples were collected effectively. Through the validity test of evaluation indicators, all the indicators in the valid questionnaire were tested for reliability and validity. After the statistical data of relevant indicators were removed, independent samples were tested for reliability and validity.

3.1 Reliability Test

The reliability test of sample data is a level of consistency between the statistical sample data results. The test results can represent the reliability of the tested indicators and measurement methods. Cronbach's alpha (α) coefficient is often used to test the consistency of the answers to the same question. In this study, spss19.0 software was used to calculate the reliability value of each secondary index, as shown in Table 2. According to the statistical point of view, the Cronbach's alpha (α) coefficient greater than 0.7 can be considered as a high level of statistical data consistency. According to the Cronbach's alpha (α) coefficients of 9 dimensions in Table 2, the Cronbach's alpha (α) values of each secondary indicator are all between 0.843–0.931, indicating that the sample data of this questionnaire survey has a high internal consistency.

Table 2. Reliability analysis table

| Second-level indicators | Cronbach's alpha | Second-level indicators | Cronbach's alpha |
|-------------------------|------------------|-------------------------|------------------|
| Meter reading payment | 0.874 | Business hall services | 0.893 |
| Complaints Report | 0.843 | 95598 services | 0.931 |
| Information quality | 0.915 | Running once | 0.903 |
| Power supply quality | 0.92 | Business expansion | 0.912 |
| Emergency repair | 0.926 | | |

3.2 Validity Test

Validity is the degree to which the statistical sample data of the questionnaire designed based on the evaluation indicators can accurately reflect the evaluation goals (service quality). This paper uses KMO and Bartlett's spherical test to test the structural validity, and then uses factor analysis to isolate the basic design framework in the questionnaire. The KMO and Bartlett spherical tests are performed on the sample statistical data. As shown in Table 3, the KMO test values of the nine secondary indicators are all greater than 0.8, and the sig value of the Bartlett spherical test is 0.000, which indicates that the sample statistical data has good structure validity and is suitable for testing. factor analysis. The principal component analysis method was used to perform factor analysis on various index problems in the sample statistics. Table 4 uses "running once service" and "information quality" as examples. It shows that the expected and actual perceived factor load of each index is 0.736- Between 0.872 (see Table 4 for statistical results), the contribution of each common factor to the total variance of its corresponding item is greater than 67%, indicating that the indicators based on the sample data have a good level of consistency and structural validity.

Table 3. KMO values for Bartlett’s spherical test

| Second-level indicators | KMO | Second-level indicators | KMO |
|-------------------------|-------|-------------------------|-------|
| Meter reading payment | 0.899 | Business hall services | 0.921 |
| Complaints Report | 0.894 | 95598 services | 0.919 |
| Information quality | 0.895 | Running once | 0.907 |
| Power supply quality | 0.88 | Business expansion | 0.923 |
| Emergency repair | 0.917 | | |

Table 4. Factor load factor

| Second-level indicators | Fourth-level indicators | Factor load factor |
|-------------------------|---|--------------------|
| Run at once Service | Rationality of materials provided | 0.813 |
| | Flexibility of delivery method | 0.863 |
| | Simplicity of service procedures | 0.827 |
| | Reasonable number of visits to the site | 0.865 |
| | Problem solving effectiveness | 0.818 |
| | Online channel convenience | 0.746 |
| Information quality | Sufficiency | 0.872 |
| | Uniformity | 0.794 |
| | Effectiveness | 0.839 |
| | timeliness | 0.841 |
| | Safety | 0.837 |
| | Understandability | 0.844 |
| | Operation path | 0.736 |

4 Conclusion

The rapid development of science and technology has profoundly affected the business processes, service channels, product forms and customer expectations of electricity consumption. The basic model of service quality measurement born in the 1980s not only needs to be adjusted according to industry characteristics, but also needs to follow the modern service industry Changes in technology are refactoring in terms of indicator selection and weighting. The power supply service perceived quality evaluation model under the background of “running at most once” has the advantages of strong operability, wide applicability and scientific nature. It can be used at district, city, province and other levels, and can also be used for various types of high voltage users and low voltage users.

References

1. He, W.M., Cheng, Y.M., Li, Y., Zhao, H.-Y., Run, Z.: The research of index system of power supply service quality evaluation. *Power Demand Side Manag.* **19**(5), 41–44, 51 (2017)
2. Zhang, X., Tian, P.: A study on the scale measuring service quality of power supply based on servqual. *J. Ind. Eng. Eng. Manag.* **19**(4), 1–8 (2005)
3. Wu, J.: The research of power supply service quality evaluation system based on service quality gap model. *China New Technol. Prod.* (23), 152 (2014)
4. Zhao, C.-Yan.: The research on power supply service quality comprehensive evaluation system. *Enterp. Reform Manag.* (10), 141 (2014)
5. Huang, X., Mo, Y.: Research on quality monitoring system of power supply service. *Telecommun. Sci.* **30**(2), 147–151 (2014)
6. Liu, B., Zhang, Y.-H.: Empirical study on information quality influencing factors based on network user experience and perception. *J. China Soc. Sci. Tech. Inf.* **32**(6), 663–672 (2013)
7. Wang, Y., Ma, Z., Tan, Y.K., et al.: Day-ahead power market design and market simulation in Guangdong province. *Power Demand Side Manag.* **20**(1), 10–14 (2018)



Customer Characteristics Analysis Module for Operation Platform

Zhang Wei^(✉), Wang Qingjuan, and Lou Fei

State Grid ZheJiang Marketing Service Center (Metrology Center),
Hangzhou, China
icic1002@126.com

Abstract. The general operation support platform can be divided into three parts: data monitoring, business operation and auxiliary management. For operating platforms, it is important to provide services with different priorities for different customers. By analyzing user characteristics, it is very important to help the platform to formulate relevant goals, support the formulation of operational plans, and conduct target customer group screening, customer experience survey analysis, and operational analysis. However, many operating platforms currently do not contain a user feature analysis module for different reasons, which is very disadvantageous for their long term effective and stable use. Therefore, in this paper, we propose a user feature analysis module based on the service operation platform. This module can be directly connected to the existing operation support platform and has high maintain ability. At the same time, it can enhance the operation platform's data analysis of operation work, customer segmentation, experience perception ability, and better support platform work.

Keywords: Customer characteristics analysis · GBDT algorithm

1 Introduction

In Internet applications, the analysis of user characteristics [1, 2] is very important. It can provide different service solutions and promotion information to different users. For the operation platform, the user feature extraction analysis [3] can assist in the formulation of the operation plan, carry out the screening of target customer groups, and improve the efficiency of the operation service platform.

The customer characteristics analysis module for the operating platform needs to meet the following requirements,

- (1) Adopt advanced technology and products, while taking care of the original mature technology, choose mainstream technology architecture and software and hardware platforms for project construction and implementation. High maintainability, easy to load, expand, update and modify features.
- (2) Reliable and stable operation. In order to ensure the uninterrupted and reliable operation of the resource service center, various high availability solutions are provided for key links including databases, hosts, and application deployment.

- (3) Information security. It can protect key operations and sensitive data, and has certain detection and defense capabilities against external attacks and abuses.

In this paper, we draw on the design experience of other Internet applications and propose a new customer characteristics analysis module. Compared with the operating platform that does not include this module, the platform which contain the module proposed in this paper has following advantages,

- Strengthen the ability of data analysis and support for operation. Through the analysis of multidimensional and multilevel data of channel customer behavior data and business data, assist in formulating operational goals and operational plans.
- Enhance customer segmentation capabilities. By improving the perception of customer characteristics and relying on the fine segmentation of customers, we strongly support the operation process to define the target population.
- Enhance the ability to perceive the customer experience. Carry out customer experience surveys, learn about customer channel preferences, customer satisfaction, and suggestions and collect information to quantify customer experience analysis.
- Enhance analysis and management of operations. Carry out statistics, monitoring, evaluation and analysis of personalized operational monitoring indicators, assist in managing operational analysis reports, and improve operational management efficiency.

2 Customer Characteristics Analysis Module

The module proposed in this article is composed of four parts: feature index analysis, data integration, customer characteristics analysis, and customer feature query to achieve data analysis support, customer segmentation, customer experience perception, and operational analysis management capabilities for operational work. Table 1 is the architecture of the customer characteristics analysis module.

Table 1. Architecture of the customer characteristics analysis module

| Module | Unit | Function |
|--|---------------------------------|----------------------|
| Customer characteristics analysis module | Characteristic index management | Defining features |
| | | Define the algorithm |
| | Data integration | Feature extraction |
| | | Data cleansing |
| | Customer feature analysis | Train model |
| Characteristics | | |
| Save model and analysis results | | |
| Feature query | Query | |

2.1 Characteristic Index Management

This section mainly defines the characteristic indicators of the platform user, including the indicator name, the method of extracting the indicator, and the source of the indicator data. Generally, the indicators include, but are not limited to, “name”, “gender”, “age”, “place of residence”, etc. The indicator data can be directly extracted from the user’s operation log records and registered user information on the platform.

2.2 Data Integration

After the user characteristics are defined, the corresponding characteristic indicators need to be extracted from the data source. For “gender” data that is constant, you can directly grab and save it, but for dynamic data such as “click rate”, you need to periodically count the amount of data in a certain period of time to ensure the timeliness of the data. After obtaining the characteristic indicators, the data needs to be cleansed [4] to eliminate the interference caused by malicious or erroneous operations and input of individual users in the data, remove outliers, and ensure the robustness of the model.

2.3 Customer Feature Analysis

After obtaining the user’s characteristics and corresponding indicators, different training data sets can be established for different task objectives, and the customer characteristics are analyzed using the GBDT algorithm [5].

2.4 Feature Query

This section mainly saves the customer characteristics obtained from the feature analysis, so that the platform staff can view and call later to avoid double calculation.

The module collects the defined data, performs customer feature analysis according to the process shown in the Fig. 1, and saves the trained model and the results of the analysis for next use. The analysis results will be fed back to the original operation platform and provide targeted operation solutions.

3 Experiments and Analysis

In order to verify the effectiveness of the modules proposed in this article, we conducted a comparative test on the electricity service operation platform and the network service operation platform, and calculated the revenue of the platform.

For each platform, the original basic framework based on JDBC [6] and Oracle 11 g [7] has not been changed, but different parts of the module have been added for comparison experiments. In the customer characteristics analysis module, the data acquisition and data analysis parts are necessary. The feature query part does not affect the final results. Therefore, in the final experiment, whether the data has been cleansed and the methods of data analysis are compared. Table 2 shows the experiment results.

Algorithm 1 GBDT Regression

Require: train dataset D , maximum iteration time T , Loss function L

Ensure: $f(x)$

- 1: $c = \frac{1}{m} \sum_{i=1}^m y_i$
- 2: $f_0(x) = \underset{c}{\operatorname{argmin}} \sum_{i=1}^m L(y_i, c)$
- 3: **for** $t = 1 \rightarrow T$ **do**
- 4: **for** $t = 1 \text{ to } m$ **do**
- 5: $r_{ti} = - \left[\frac{\partial L(y_i, f(x_i))}{\partial f(x_i)} \right]_{f(x)=f_{t-1}(x)}$
- 6: **end for**
- 7: Use (x_i, r_{ti}) to train a CART regression tree CR_t , which leaves region are $R_{tj}, j = 1, 2, \dots, J$
- 8: **for** $j = 1 \rightarrow J$ **do**
- 9: $c_{tj} = \underset{c}{\operatorname{argmin}} \sum_{x_i \in R_{tj}} L(y_i, f_{t-1}(x_i) + c)$
- 10: **end for**
- 11: $f_t(x) = f_{t-1}(x) + \sum_{j=1}^J c_{tj}, \quad I(x \in R_{tj})$
- 12: **end for**
- 13: $f(x) = f_T(x) = f_0(x) + \sum_{t=1}^T \sum_{j=1}^J c_{tj}, \quad I(x \in R_{tj})$

Fig. 1. Algorithm 1, GBDT Regression

The effectiveness of the operating platform is evaluated using revenue. For simplicity, the table uses the ratio of the original framework's effectiveness to represent the model effect.

It can be seen that no matter which method is adopted, compared with the operation platform without adding the customer characteristic analysis module, the benefits of the added platform have been significantly improved. At the same time, the operation platform using the data cleaning and GBDT methods performs best (Fig. 2).

The module obtains features defined in the feature management module through web data, database, and application log files. After data cleaning, the characteristic representations of different users are obtained. The customer characteristics analysis module uses the user feature training model to obtain clusters for customers and improve the efficiency of the operating platform.

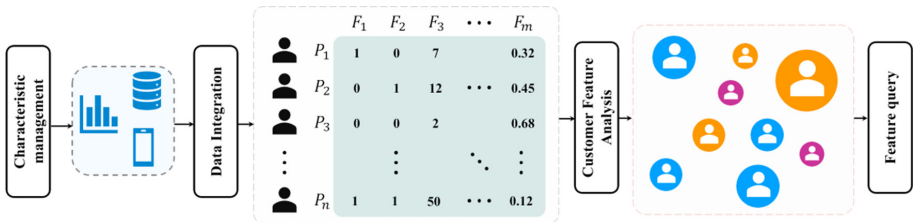


Fig. 2. Data processing flow of the customer characteristics analysis module.

Table 2. Results of profit comparison using different methods

| Method | | | | Electricity | Network |
|----------|-----------|----|------|--------------|--------------|
| Original | Cleansing | RF | GBDT | | |
| √ | | | | 1.0 | 1.0 |
| √ | | √ | | 1.042 | 1.067 |
| √ | | | √ | 1.081 | 1.114 |
| √ | √ | √ | | 1.056 | 1.081 |
| √ | √ | | √ | 1.093 | 1.127 |

4 Conclusion

This paper proposes a novel customer characteristics analysis module that acts on the operating platform. Customer characteristics can be extracted and analyzed through different data sources to help operational platforms specify operational strategies. This module can be directly integrated into the operating platform without changing the original platform framework, has good maintainability and scalability, and significantly improves the efficiency of the operating platform.

References

1. Schigel, T., Goldberg, D.E.: System and method for facilitating network connectivity based on user characteristics. US Patent 8,095,408, 10 January 2012
2. Grunwald, M., Wesemann, D.: Special online consulting for patients with eating disorders and their relatives: analysis of user characteristics and email content. *CyberPsychol. Behav.* **10**(1), 57–63 (2007)
3. De Rivera, J., Gordo, Á., Cassidy, P., Apesteguía, A.: A netnographic study of p2p collaborative consumption platforms' user interface and design. *Environ. Innov. Societal Transitions* **23**, 11–27 (2017)
4. Hernández, M.A., Stolfo, S.J.: Realworld data is dirty: data cleansing and the merge/purge problem. *Data Min. Knowl. Discov.* **2**(1), 9–37 (1998). <https://doi.org/10.1023/A:1009761603038>
5. Friedman, J.H.: Greedy function approximation: a gradient boosting machine. *Ann. Stat.* **29**, 1189–1232 (2001)
6. Hamilton, G., Cattell, R., Fisher, M.: *JDBC Database Access with Java: a Tutorial and Annotated Reference*. Addison Wesley Longman Publishing Co. Inc., Boston (1997)
7. Ashdown, L., Kyte, T.: Oracle database online documentation 11 g release 2 (11.2): Database administration (2014)



Reconstruction and Re-ranking: A Simple and Effective Approach for Question Answering

Shen Ran^{1(✉)}, Wang Yifan¹, Lv Shining¹, Chen Jinwei²,
and Xiong Jianfeng³

¹ State Grid ZheJiang Marketing Service Center (Metrology Center),
Hangzhou, China
icic1003@126.com

² State Grid Zhejiang Jiashan Power Supply Company, Zhejiang, China

³ State Grid Zhejiang Quzhou Power Supply Company, Zhejiang, China

Abstract. With the rapid growth of knowledge bases (KBs), question answering over knowledge base, a.k.a. KBQA has drawn huge attention in recent years. Most of the existing methods follow the simply matching method and search the answer from the whole knowledge bases. Despite the effectiveness of above approaches, there are two key issues should be settled, i.e., how to reconstruct knowledge bases effectively and how to search answer efficiently. In this paper, we introduce a simple model to construct large-scale knowledge base as graph and generate a set of candidate answer from efficient answer search. To verify our model, we conduct extensive experiments on Simple Question benchmarks. The experimental results greatly confirm the effectiveness of our model.

Keywords: Question answering · Knowledge bases · Knowledge graph

1 Introduction

Knowledge Based Question Answering (KBQA) system [3, 8, 11, 12, 17] has drawn great attention in language processing due to the capacity to handle various open-set queries. Given an input query, KBQA system typically transforms it to a KB query and generate the answer from the KB. It is not limited a specific scenario, enabling it available in many areas i.e., intelligent interactions, robotic system etc.

Since several large-scale knowledge bases have proposed i.e., YAGO [5], Freebase [1], SimpleQuestions [3], a lot of language query networks [11, 12] are designed for open-set question answering. In general, the methodological routes of KBQA can be simply divided into two paths. The first one [15, 17, 18] is to tackle Simple- Questions decompose the task into multiple sub-tasks. The others [8, 11] aim to learn a jointly multimodal embedding space to match the query with answers.

Despite the effectiveness of above methods, two key problems in KBQA are still left settled. Firstly, the knowledge base in the KBQA area is usually in the form of a table, where the representation of its structured data is limited. Such issue

makes a great gap for KBQA with generalized question answering. To address this issue, we build a knowledge graph to reconstruct the knowledge base. Specifically, by analyzing heterogeneous and large-scale media information, we extract and integrate the rich semantic information to construct a knowledge graph, providing data support for context-aware interactive semantic search. Secondly, most of approaches pay attention on searching the answer from the whole knowledge bases, which is relatively inefficient and ineffective due to the million-wise search space. Instead, we emphasize on searching the correct answer from a set of candidates. By this way, the irrelevant answers are filtered so that the search process can be conducted in a set of candidate answers. Such solution slightly reduces the computational expense, as well as achieves better performances (Fig. 1).

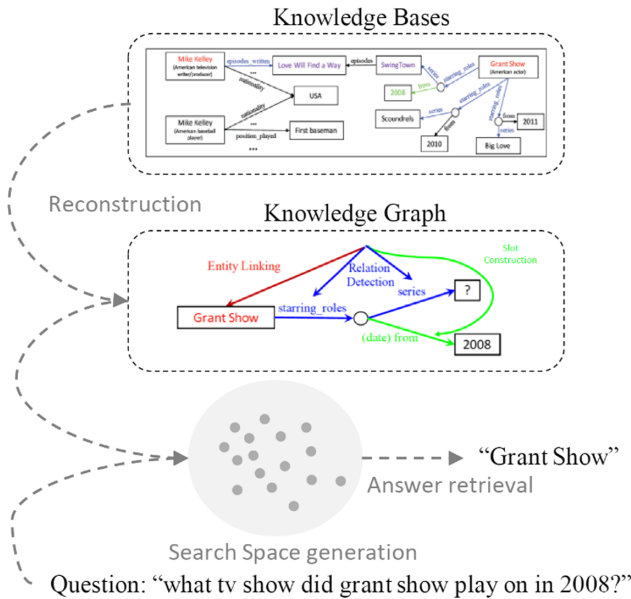


Fig. 1. Schematic of the proposed method, which reconstructs the knowledge base information to a knowledge graph and then generate a set of candidate answers from joint question and knowledge representations, retrieving the correct answer.

2 Related Work

2.1 Knowledge Graph

In general, facts in the knowledge graph are represented by triples, and the number of facts determines the richness of the knowledge graph. There are three typically fact learning methods [2, 9, 10, 13, 16] for machine learning techniques used when constructing according to the knowledge graph. The first [2, 13] is based on full supervision. It requires labeled data as training sets, which can be simply divided into rule-based learning, classification-based labeling, and sequence-based labeling methods.

Another schools [10, 16] tend to leverage semi-supervised methods. It mainly includes self-expanding methods and weakly supervised methods. The former needs to discover new semantic templates based on the initial seed entity pair, while iteratively extracting the corpus to find new entity pairs. The latter heuristically labels the language information using relationships in the knowledge base. Another unsupervised method [9] is mainly based on open-set information extraction by using natural language processing methods. It is not limited to pre-specify the relationship.

2.2 Knowledge Based Question Answering

Knowledge Based Question Answering was first investigated in [7], which used PARALEX as dataset against knowledge base Reverb [6]. With the development of neural networks, utilizing deep learning technology to handle the KBQA, has been extensively researched in recent years. The methods for fact selection can be divided into two routes, i.e., match-scoring models and classification models. The first one [3, 4, 17] is based on deep network such as CNN or LSTM to calculate the similarity between the question and the candidate facts. In the classification models [11, 14, 15], the common practice is to employ deep neural network to directly rank subject-relation pair and retrieve relevant facts. Although classification models perform efficiently, their performance is still behind the match-scoring models. Therefore, we build a simple model based on match-scoring methods, while applying convolutional layer as the basic computational unit for efficiency.

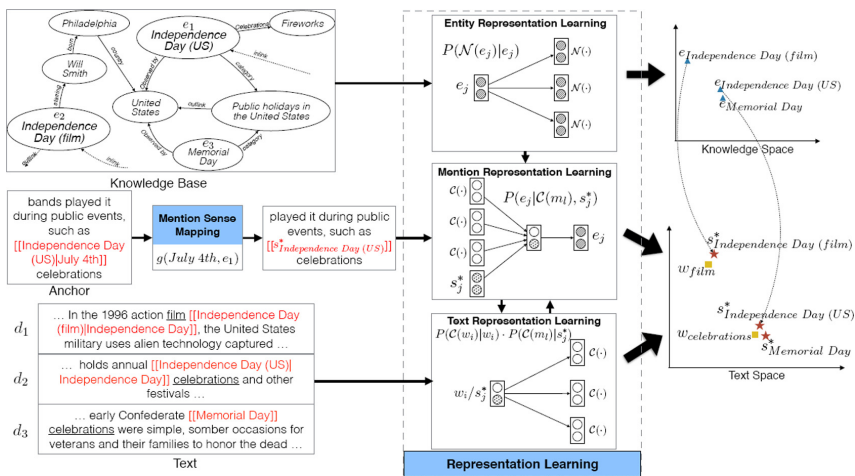


Fig. 2. The Framework of Knowledge Graph Construction. We first leverage three independent model to learn the entity representation, mention representation and text (words) representation. Then, we use a uniform loss to optimize them into a common space, so that aligns them to each other and links each node to constitute knowledge graph.

3 Project Research Content and Implementation Plan

3.1 Knowledge Graph Construction

Named Entity Recognition. Named entity recognition technology is used to annotate the candidate concepts for unstructured text and filter them through domain vocabulary filtering. Meanwhile, it further optimizes the candidate concepts and implicit conceptual information in text. In this paper, we use a distributed model to identify the implicit conceptual relations. The basic assumption of our design is that if two concepts have close semantics with each other, their theme signature and context signature are also similar. The theme signature is regarded as a set of words that appear in the same context with concepts, where the concepts is denoted as c . The context signature is defined as a set including a subset with c as the subject, a subset with c as the object, and a subset of adjectives and nouns to modify c . Then, we define the semantic relevance between concept c and its topic signature as a vector, which is calculated by mutual information method. Finally, our model learns implicit conceptual relationship by logistics regression.

Semantic Slot Construction. In order to establish a framework for semantic slot construction and slot value mining, we integrate the linguistic characteristic and unsupervised online learning into a framework. In particular, we leverage a slot likelihood function to make a soft evaluation for the slots, where the likelihood indicates the confidence probability of a candidate slot. We first generate a slot dictionary, which maps a slot key w to a likelihood function $L(w)$. Besides, each slot is corresponding to a specific list of slot values that stores all possible slot values.

Entity Linking. The purpose of entity linking is to establish the relationship between text documents and structured knowledge base. Therefore, we propose a Multi-Prototype Mention Embedding model (MPME), to jointly learn the representations of words, entities and entity mentions. The core thought is to use both contextual text information and entity knowledge to disambiguate the different meanings of mentions.

Specifically, given a knowledge base denoted as KB , an annotated datasets D and a set of anchor text A , our target is to jointly learn the representations of words, entities and mentions. As shown in Fig. 2., we build a dictionary from wikipedia for $\langle \text{mention}, \text{entity} \rangle$ pairs, denoted as $\langle ml; el \rangle$. Then We design three independent modules to achieve jointly learning for KB , A , D . For simplicity, we utilize a skip-gram model for entity embedding learning, a CBOW model for mentions learning and a joint model for text learning.

Loss Function. Finally, three terms of loss function can be linearly combined as:

$$L_g = L_w + L_e + L_m \quad (1)$$

3.2 Answer Generating Network

Given a question asked by a user, the question answering network aims to match the best fact in the knowledge graph, therefore giving the most relevant answer. Our system is consisted of two designs: (1) the candidate generation method; (2) a candidate re-ranking model. We combine the two modules to generate the accurate answers.

Candidate Generation. In general, a knowledge graph contains millions tuples of answers, which makes it urgent to reduce the search space for applying semantic-based neural approaches. To this end, we design a retrieval system to narrow down the search space in knowledge base and focus on the most relevant information. Solr2 is an inverted index search system, which can help to index all tuples in the processed knowledge graph. Under the efficient index method, the query for the top-k relevant candidates provides a question as the input query. We apply BM25 as metric to rank results.

Candidate Re-ranking. We leverage CNNs to learn the semantic representation for input text. CNNs are easy to learn global semantics due to its order invariant character, as well as to pick the order in short phrases. Such powerful ability enables CNNs ideal for a QA task since users may paraphrase the same question in different ways. Siamese networks are effective CNN-based method and have shown promising results in distance-based learning methods. We take it to learn a similarity metric between questions and answering representations. The candidate re-ranking design is inspired by the great success of neural models in natural language processing. As shown in Fig. 2, a Triplet-Siamese Hybrid Convolutional neural network (TSHCNN) is used to jointly extract and exchange information from the question and tuple inputs. The reason is that we concatenate the pooled outputs of the question and tuple before input to the fully connected network. We provide additional inputs to the network which is the concatenation of both the input question and tuple. Such additional input is matched the need that the network should learn features for both the question and tuple.

Loss Function. The loss is the distance based logistic triplet loss, which is reported in image similarity tasks with better performance. Considering $S_{pos} = S_{neg}$ as the score obtained by the question + positive tuple/question + negative tuple, respectively and L_a as the logistic triplet loss, we have:

$$L_q = \log e(1 + e^{S_{pos} - S_{neg}}) \quad (2)$$

4 Experiments

4.1 Dataset

We test our proposed method on SimpleQuestion dataset, which provides a set of single-relation questions. Each question is accompanied by a ground truth fact, which

is a triple in Freebase. The dataset is split into train (79,590), valid (10,845) and test (21,687) sets.

4.2 Implementation Details

During the training, the word embeddings are initialized by the pretrained Glove with 300 di-mensions. The hidden size of Bi-GRU is set to 200. For optimization, the batch size is set to 64 and dropout of 0.3 is used to regularize Bi-GRU.

4.3 Evaluation

Following the previous works, we use the metric of accuracy to evaluate our models, which calculates the percentage of questions for which the top-ranked candidate fact is correct. It judges a prediction correct when retrieving the correct subject and predicate. In the re-ranking step, top-200 candidates are used as input.

Table 1. Comparisons of answer accuracy for english questions.

| Model | Acc |
|-----------------------|------|
| Mem. NN [3] | 62.7 |
| Attn. NN [8] | 70.9 |
| GRU [11] | 71.2 |
| Bi-LSTM & Bi-GRU [12] | 74.9 |
| CNN & Attn. CNN & | |
| BiLSTM-CRF [17] | 77.2 |

Table 2. Ablation study of the proposed SANN model.

| Model | Acc |
|--------------------------|------|
| Mem. NN [3] | 62.7 |
| Attn. NN [8] | 70.9 |
| SANN (ours) | 77.2 |
| w/o Candidate Re-ranking | 74.2 |
| w/o Candidate Generation | 71.3 |
| w/o Rel words | 66.3 |
| w/o Rel mention | 73.4 |

4.4 Quantitative Analysis

We first compare our method with many classic methods, as shown in Table 1. From Table 1, we find that our method performs better than all of the classic methods with a competitive accuracy. Such results not only attributes to the design of the knowledge graph construction, but also are benefited from the candidate generation and re-ranking

method, which greatly confirms our model. Notably, although the BiLSTMCRF [17] behaves comparatively with our method, it greatly relies on the post-processing method i.e., CRF, leading to a slow processing for realistic application.

Table 3. Recall of top K answer candidates generated by our method.

| K | 1 | 2 | 5 | 10 | 50 | 100 | 200 |
|---|------|------|------|------|------|------|------|
| | 68.4 | 75.3 | 81.2 | 84.3 | 92.1 | 93.1 | 96.4 |

In Table 3, we report candidate generation results. As expected, recall increases as we increase k. The initial step of candidate generation surpasses (Table 1) the original Bordes’ paper [3] and comes close to other complex neural approaches [8, 11]. This is surprising since this initial step is an inverted-index based approach which retrieves the most relevant candidates based on term matching.

In Table 2, we report the ablation results of our method. A first observation is that all designs are useful in our model. Besides, some designs are crucial for the model, such as candidate generation, which filters the most irrelevant answers for the final matchings. The construction of knowledge graph also shows the effectiveness due to its structured representations. Combining all of the above designs, we gain an impressive improvement, i.e., 13.8%, compared to our basic model.

5 Conclusion

In this paper, we propose a simple model for knowledge-based question answering to solve two key issues in question answer i.e., how to reconstruct knowledge bases effectively and how to search answer efficiently. To verify our model, we make a detailed analysis and shows impressive performance of our model over the classic approaches on the SimpleQuestions benchmark. It outperforms many other approaches that use Bi-LSTMs, attention mechanisms or separate segmentation models. We further conduct qualitative analysis, which also highlight the effectiveness of the design of knowledge graph construction and candidate filters.

References

1. Bollacker, K., Evans, C., Paritosh, P., Sturge, T., Taylor, J.: Freebase: a collaboratively created graph database for structuring human knowledge. In: Proceedings of the 2008 ACM SIGMOD International Conference on Management of Data, pp. 1247–1250. ACM (2008)
2. Bordes, A., Usunier, N., Garcia-Duran, A., Weston, J., Yakhnenko, O.: Translating embeddings for modeling multi-relational data. In: Advances in Neural Information Processing Systems, pp. 2787–2795 (2013)
3. Bordes, A., Usunier, N., Chopra, S., Weston, J.: Large-scale simple question answering with memory networks. arXiv [arXiv:1506.02075](https://arxiv.org/abs/1506.02075) (2015)

4. Dai, Z., Li, L., Xu, W.: Cfo: conditional focused neural question answering with largescale knowledge bases. arXiv [arXiv:1606.01994](https://arxiv.org/abs/1606.01994) (2016)
5. Fabian, M.S., Gjergji, K., Gerhard, W., et al.: Yago: a core of semantic knowledge unifying wordnet and wikipedia. In: 16th International World Wide Web Conference, WWW, pp. 697–706 (2007)
6. Fader, A., Soderland, S., Etzioni, O.: Identifying relations for open information extraction. In: Proceedings of the Conference on Empirical Methods in Natural Language Processing, pp. 1535–1545. Association for Computational Linguistics (2011)
7. Fader, A., Zettlemoyer, L., Etzioni, O.: Paraphrase-driven learning for open question answering. In: Proceedings of the 51st Annual Meeting of the Association for Computational Linguistics (Volume 1: Long Papers), pp. 1608–1618 (2013)
8. Golub, D., He, X.: Character-level question answering with attention. arXiv [arXiv:1604.00727](https://arxiv.org/abs/1604.00727) (2016)
9. Jenatton, R., Roux, N.L., Bordes, A., Obozinski, G.R.: A latent factor model for highly multi-relational data. In: Advances in Neural Information Processing Systems, pp. 3167–3175 (2012)
10. Lin, Y., Liu, Z., Sun, M., Liu, Y., Zhu, X.: Learning entity and relation embeddings for knowledge graph completion. In: Twentyninth AAAI Conference on Artificial Intelligence (2015)
11. Lukovnikov, D., Fischer, A., Lehmann, J., Auer, S.: Neural network-based question answering over knowledge graphs on word and character level. In: Proceedings of the 26th International Conference on World Wide Web, pp. 1211–1220. International World Wide Web Conferences Steering Committee (2017)
12. Mohammed, S., Shi, P., Lin, J.: Strong baselines for simple question answering over knowledge graphs with and without neural networks. arXiv [arXiv:1712.01969](https://arxiv.org/abs/1712.01969) (2017)
13. Nickel, M., Tresp, V., Kriegel, H.P.: A three-way model for collective learning on multi-relational data. ICML **11**, 809–816 (2011)
14. Pennington, J., Socher, R., Manning, C.: Glove: global vectors for word representation. In: Proceedings of the 2014 Conference on Empirical Methods in Natural Language Processing (EMNLP), pp. 1532–1543 (2014)
15. Ture, F., Jojic, O.: No need to pay attention: simple recurrent neural networks work! (for answering” simple” questions). arXiv [arXiv:1606.05029](https://arxiv.org/abs/1606.05029) (2016)
16. Wang, Z., Zhang, J., Feng, J., Chen, Z.: Knowledge graph embedding by translating on hyperplanes. In: Twenty-Eighth AAAI Conference on Artificial Intelligence (2014)
17. Yin, W., Yu, M., Xiang, B., Zhou, B., Schtze, H.: Simple question answering by attentive convolutional neural network. arXiv [arXiv:1606.03391](https://arxiv.org/abs/1606.03391) (2016)
18. Yu, M., Yin, W., Hasan, K.S., Santos, C., Xiang, B., Zhou, B.: Improved neural relation detection for knowledge base question answering. arXiv [arXiv:1704.06194](https://arxiv.org/abs/1704.06194) (2017)



Research on Offline State Management Technology of Metered Assets Based on Internet of Things

Linhu^{1(✉)}, Jiang Yong², and Zhang Jimin¹

¹ Zhejiang Wuyi Electric Installation Engineering Company, Hangzhou, Zhejiang, China

icic1004@126.com

² State Grid (Jinhua) Integrated Energy Services Company, Hangzhou, Zhejiang, China

Abstract. Fixed asset management is a key device for trade settlement and operation assessment of power products, but there are still some problems in the operation process: for example, traditional measurement asset management relies on bar codes to manage processes; manual reliance on paper ledger and marketing system Inventory results in a large demand for human resources; on-site verification information can only be viewed with the naked eye, and authenticity cannot be distinguished. To this end, this article proposes to rely on RFID radio frequency technology and mobile operating terminals to realize the automatic identification of metered assets and the interconnection and sharing of marketing systems. They are automatically collected into the marketing business system through a data communication network to realize the identification of metered assets, and then through the opening Computer network to achieve information interaction and sharing, to achieve “transparent” management of items, throughout the planning and design of measurement points, procurement and warehousing, operation and verification, and asset disposal, to achieve a highly intensive asset life-cycle management model.

Keywords: Asset management · RFID radio frequency technology · Automatic identification of measured assets

1 Introduction

With the development of society, fixed asset management has become an indispensable part of the normal operation of an enterprise. The company’s energy measurement device is the power operation equipment, and it is also a key device for the settlement and operation evaluation of power products. The bigger and more difficult the management, the establishment of a complete, precise and accurate measurement device management will be an important basis for the transformation of marketing technology and equipment, but there are still some problems in the operation process: First, traditional measurement asset management relies on barcode To manage the processes. Second, relying on paper ledger and marketing system for manual inventory, resulting

in a large demand for human resources. Third, the on-site verification information can only be viewed with the naked eye, and authenticity cannot be distinguished.

This project relies on RFID radio frequency technology and mobile operation terminals to realize the automatic identification of measurement assets and the interconnection and sharing of marketing systems. They are automatically collected into the marketing business system through a data communication network to realize the identification of measurement assets, and then through an open computer The network realizes information interaction and sharing, realizes “transparent” management of items, runs through the entire process of planning and design of measurement points, procurement and warehousing, operation and verification, and asset disposal, and realizes a highly intensive asset life-cycle management model, which significantly improves Employees work efficiently and meet the following expectations:

1. When the metered assets with RFID tags pass through the RFID access door, the system uses the two-way infrared cutting technology to identify whether it is in or out of the warehouse and changes the status of the metered assets;
2. By transforming warehouse shelves, setting up multi-period automatic inventory of warehouse assets, real-time inventory of the quantity and status of assets in the warehouse area, real-time knowledge of total assets, prevention of asset loss, improvement of measurement asset monitoring level, and prevention of scrapped assets from entering the warehouse the goal of;
3. Use readable and writable RFID tag technology to realize offline management and control of metered assets from inventory management to asset scrapping, including but not limited to current transformer rotation cycle management, operation status inspection, scrap sorting management; carrier equipment operation status changes, Outage warehouse generation, historical information management, etc.

The research results of this project can be directly applied to various application systems of the State Grid Zhejiang Electric Power Co., Ltd. Wuyi Power Supply Company. Throughout the entire life cycle of the metered assets, the ubiquitous connection of physical assets in and out of the warehouse, status, real logistics, information The integration of stream and value stream, a highly intensive asset management model, significantly improves the work efficiency of enterprise employees.

2 Theoretical Basis

2.1 Radio Frequency Identification Technology (RFID)

Radio frequency identification, or Radio Frequency Identification (RFID), is a type of automatic identification technology. It uses wireless radio frequency to perform non-contact two-way data communication, and uses radio frequency to read recording media (electronic tags or radio frequency cards). Write, so as to achieve the goal of identification and data exchange.

2.2 Working Principle of RFID Technology

The basic working principle of RFID technology: After the tag enters the reader, it receives the radio frequency signal sent by the reader, and uses the energy obtained by the induced current to send out the product information (Passive Tag, passive tag or passive tag) stored in the chip, or The tag actively sends a signal of a certain frequency (Active Tag, active tag or active tag), and after the reader reads the information and decodes it, it sends it to the central information system for relevant data processing [1].

2.3 Radio Frequency Identification Technology Components

The complete RFID system consists of a reader, an electronic tag and a data management system, as shown in Fig. 1.

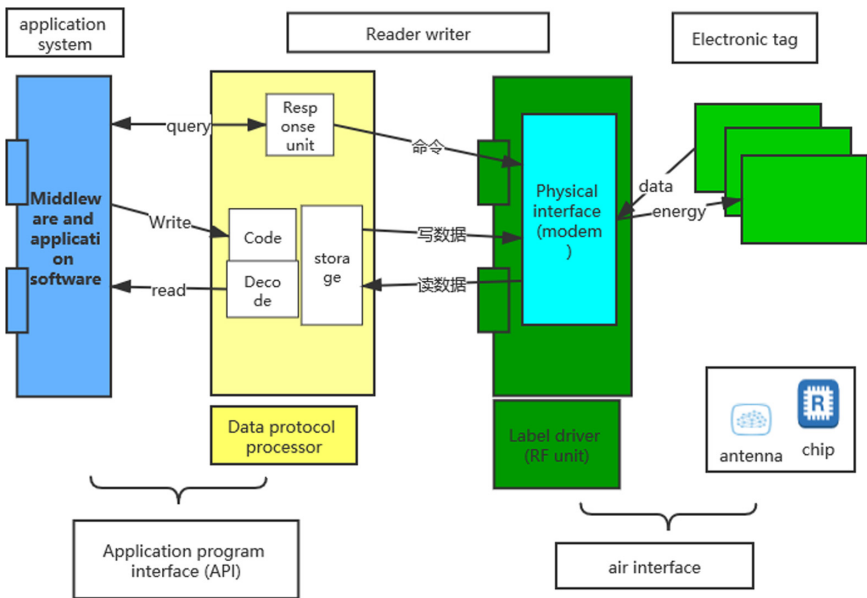


Fig. 1. RFID system architecture.

3 Research Contents

3.1 Research on RFID Tag Security Two-Way Authentication Anti-lost Protocol

When the traditional secure two-way authentication anti-loss protocol encrypts the RFID tag, the encryption effect is poor and the anti-interference ability is not strong. Based on Fisher, a new RFID tag security two-way authentication and loss prevention protocol is researched. The topology of the RFID tag security two-way authentication and loss prevention protocol system is established by using the central network, RFID

access control, management center, and servers. The RFID channel is used to establish a two-way authentication and loss prevention protocol database, and the internal data of the RFID tag is managed through two methods of read-write management and carrier management [2]. The results show that the RFID tag secure two-way authentication and loss prevention protocol based on Fisher research has strong encryption and anti-interference ability, better application effect and higher use value.

Fisher-Based RFID Tag Security Two-Way Authentication Anti-loss Protocol.

Based on Fisher's establishment of RFID tag secure two-way authentication and anti-lost protocols from multiple perspectives, the designed system topology is shown in Fig. 2 below:

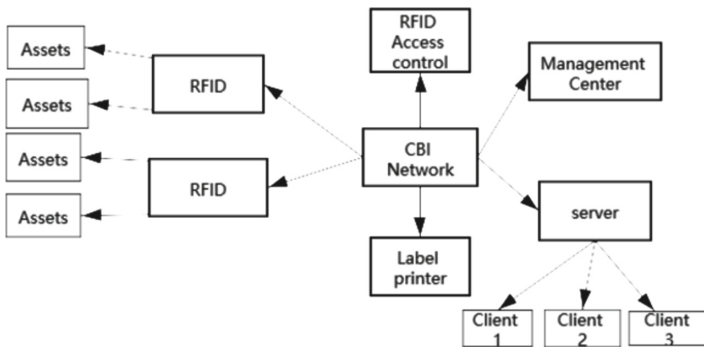


Fig. 2. Topology of RFID tag security two-way authentication loss prevention protocol system.

The topological diagram of the RFID tag security two-way authentication anti-lost protocol system established in Fig. 2 above can more effectively control the measurement assets. The RFID tag security two-way authentication anti-lost protocol is mainly responsible for asset management, storage management, inventory management, offline management, system setting, and statistical reporting. It uses multiple RFID management channels to realize intelligent identification and management [3, 4].

The transformer usually contains an RFID tag inside, which can store the barcode information of the transformer assets, but cannot complete the reading and writing of information. In order to enable offline management of assets, business scenarios need to be considered when setting the RFID tag secure two-way authentication and anti-lost protocol. And business foundation to establish unique identification codes. The system data, RFID tags and metered assets are bound together to facilitate more accurate identification and change of business status [5].

RFID Two-Way Authentication Anti-lost Protocol Database. The RFID standards set for different types of measurement asset management and control business are different. They can not only identify information within the marketing system, but also identify all management items, record all changes, and carry out online and offline business measurement Method [6, 7].

The RFID tag security two-way authentication anti-lost protocol will transfer the measurement assets from the secondary database to the tertiary database when managing the database. The conversion flow chart is shown in Fig. 3 below.

RFID technology is highly intelligent. When using RFID technology to control and analyze assets, the system will automatically determine the status of the assets and lock the physical location of the assets [8]. When the asset is removed from the secondary warehouse, the RFID technology will automatically set the asset and adjust the status to the state of “departed”; when the asset is entered from the secondary warehouse, the RFID technology will adjust the state to the “deposited” state. Each state record needs to set detailed parameters to facilitate later analysis. Once abnormalities are found in the work process, abnormal reminders are promptly given.

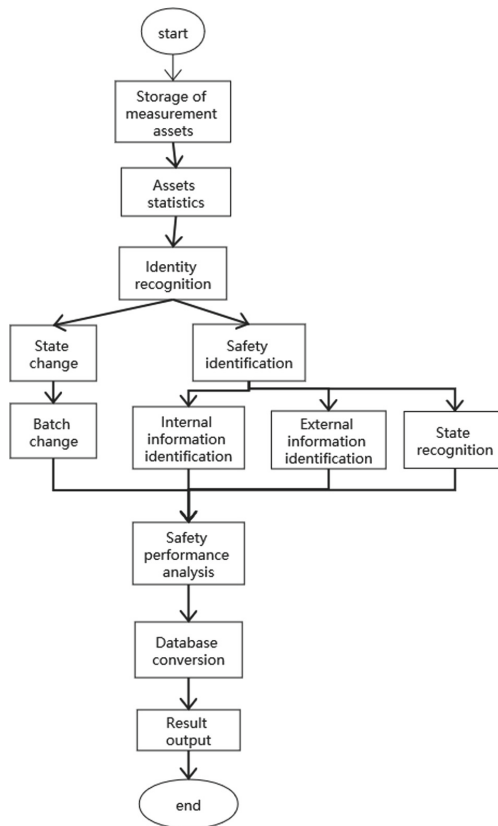


Fig. 3. Flow chart of transformation of measurement Assets Database under RFID Technology.

The database established by the RFID tag secure two-way authentication anti-lost protocol is shown in Fig. 4 below:

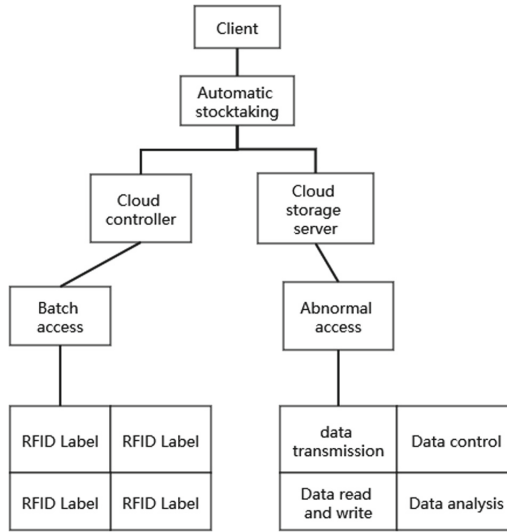


Fig. 4. RFID tag security two-way authentication anti loss protocol database.

RFID tags are readable and writable tags. They can calculate all assets and set a fixed management cycle. There are two management methods. The specific content is as follows:

The first type: use a readable and writable method to record RFID tags, analyze the status of measured assets, and mark in three places: inventory status, running status, and stop status. The asset content in the RFID tag must be updated regularly, and the offline control must be consistent with the marketing status, and it must be compared with the resources in the database in a timely manner. Once an abnormal phenomenon is found, it is timely reported to the staff [9, 10].

The second type: establish a carrier in the database, assign various codes in RFID to the carrier, manage various acquisition devices offline, and compare the status of various devices.

The database based on the RFID tag security two-way authentication and anti-lost protocol designed by this project can complete the monitoring work and inventory work at the same time when applied, and can perform large-scale measurement work. The measured content will be uploaded to the central module for statistics immediately.

3.2 Research on Anti-theft Methods Based on Transformer RFID Tags

Transformer is an important measurement basic data acquisition equipment in the power industry. After the popularization of smart meters, the objects of power theft

gradually shifted from meters to transformers. The phenomenon of stealing electricity by replacing large transformers with transformers is becoming more and more common. Stealers will change the nameplates of transformers while stealing the transformers.

To this end, this research method places an RFID electronic tag in the transformer nameplate. The nameplate tag and the transformer are injection molded together during the production of the transformer. Disassembling the nameplate will destroy the electronic tag, make the tag unreadable, and prevent the transformer from being disassembled. Change, play a role in preventing theft of electricity. In order to timely and effectively manage the RF tag data of the transformer, it is used in conjunction with a mobile operating terminal. The mobile work terminal realizes automatic matching and identification with RFID electronic tags through the range sensing capability based on radio frequency tags. After successful matching, the mobile work terminal realizes its data sharing and exchange through the RFID electronic tag data exchange and management system [12].

Based on this principle, an anti-theft method based on mutual inductor RFID electronic tags is proposed. The specific flowchart 6 is as follows:

Transformer Label Initialization. The transformer's own conversion ratio information is stored in the transformer label. The initialization of the transformer label is to verify and verify the transformer's ratio information. The specific process is:

First of all, after the power customer provided the personal assets current transformer to the power company, the power company's measurement center carried out the equipment verification work, mainly through the equipment to further confirm whether the transformation ratio of the transformer was consistent with the declaration. Then, for the transformer that passed the verification, the RFID electronic tag is paired with the transformer to form a unique correspondence relationship. Then, the mobile terminal is used to write the initial verification information such as the RFID's unique code of the transformer, the number of the power transformer, the transformation ratio, and the verification time to the RFID tag for reading and writing and data exchange. save. Finally, the equipment is sealed for the RFID electronic tags that have been verified, which facilitates the unified distribution and security of the equipment, and completes the initialization of the entire RFID electronic tags [13].

Daily Site Inspection. After the initialization of the RFID electronic tag of the transformer is completed, the subsequent power workers will conduct regular on-site inspections of the transformer according to the requirements of the inspection task. During the inspection process, power workers used mobile operating terminals to read the last written information of the RFID electronic tag, and judged whether the user had theft or illegal power consumption behavior based on the intact state of the RFID electronic tag and the transformer ratio information. The specific process is shown in Fig. 5:

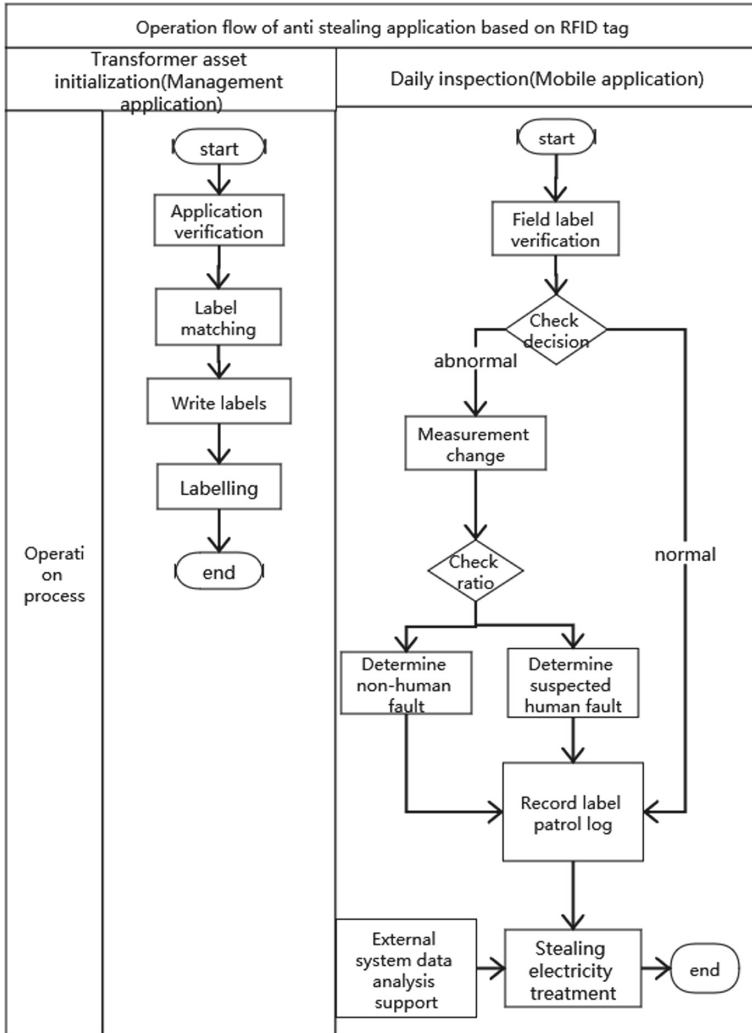


Fig. 5. Application operation flow chart.

4 Conclusion

This system is used to build a warehouse asset management and control information collection application. The query software of the information management platform sends out statistics and inventory signals to intelligently complete the information statistics. Based on RFID tags and access control equipment, it can automatically enter and leave the warehouse. With the help of RFID tags and mobile operations The terminal implements anti-counterfeit verification of high-voltage transformers. It is connected to the tag scanning equipment through the existing mobile operation terminal, and reads the RFID tag information on the site through the scanning equipment

and feeds back to the mobile operation terminal to verify the results. The automatic inventory analysis of the measured asset inventory reduces the warehouse management Staff manual inventory.

References

1. Xiong, J., Wang, J.: Research on RFID secure two-way authentication protocol based on HASH function. *China Test* **43**(3), 87–90 (2017)
2. Liu, B., Liu, N., Yang, Y., et al.: Bidirectional authentication protocol for radio frequency identification based on elliptic curve cryptography. *Comput. Eng.* **43**(1), 196–200 (2017)
3. Liu, Y., Yang, L., Yang, Y.: Scalable RFID two-way authentication protocol based on Rabin algorithm. *Comput. Eng. Appl.* **53**(2), 15–20 (2017)
4. Liu, Y., Xie, Y., Shi, Y., et al.: Research and implementation of lightweight RFID security protocol based on SASI protocol. *Commun. Technol.* **50**(6), 1284–1289 (2017)
5. Li, X., Sun, C., Zheng, W.: RFID two-way authentication protocol based on pseudo-random function. *Comput. Eng. Appl.* **32**(24), 233–243 (2018)
6. Ma, Y., Liu, D.: An improved RFID two-way authentication protocol for backward security. *Comput. Eng. Appl.* **53**(9), 136–140 (2017)
7. Su, T.: Security authentication protocol for passive RFID. *Comput. Eng. Des.* **38**(7), 1697–1701 (2017)
8. Wang, P., Zhou, Z., Li, J.: An improved scheme of RFID security authentication protocol without backend database. *J. Front. Comput. Sci. Technol.* **44**(4), 93–100 (2018)
9. Zhu, X.: Research on anti-collision of RFID tags with two-slot algorithm in ship communication network. *Ship Sci. Technol.* (8), 76–78 (2017)
10. Dong, N., Ma, W., Chen, X., et al.: Research on fall prevention management system based on BIM and RFID. *Constr. Econ.* **38**(2), 53–57 (2017)
11. Jiang, H., Sun, L., Zhang, X.: Research and application of anti-counterfeit authentication system based on RFID and NFC technology. *J. Comput. Appl. Softw.* **34**(9), 317–321 (2017)
12. Su, Q., Li, Q., Peng, J., et al.: Wireless key generation protocol for encrypted RFID system based on pseudonym identification. *Comput. Eng.* **43**(8), 173–177 (2017)
13. Liu, H., Cao, K., An, Q.: Research on anti-counterfeiting mechanism of RFID-based traceability system products. *J. Yulin Univ.* **27**(2), 76–78 (2017)



Assessment and Application Research on the Carrying Capacity of Township Power Supply Station Based on Big Data Analysis

Pan Weiwei^(✉), Shen Guang, Wu Yuebo, and Huang Xiang

State Grid Zhejiang Power Co., Ltd, Hangzhou, China
icicl005@126.com

Abstract. At present, the grid division of township power supply stations lacks guiding opinions, the grid division principle of each unit is not unified, and the assessment of the carrying capacity of each station has not formed a unified and reasonable assessment plan. As the power grid data resources of township power supply stations show typical big data characteristics, it is urgent to use big data analysis tools in the business analysis of township power supply stations. Based on this, this paper uses the clustering algorithm and subjective and objective weighting method to evaluate the scores and weights of each evaluation index from the dimensions of customer scale, line loss of the substation area and collaborative work order, and obtains the carrying capacity of each substation area and managers of each substation area, and studies the business application scenario of this model.

Keywords: Big data analysis · Township power supply station · Carrying capacity of substation area

1 Introduction

In recent years, the State Grid Corporation of China has continued to carry out the work of grasping the foundation, building standards, and improving service quality at the township power supply stations¹. Consequently, the professional management level and work quality of the power supply stations have got a great deal of promotion. However, with the continuous changes in the service needs of the majority of electricity customers, some problems have been exposed: first, the power grid data resources show typical big data characteristics, and the use of big data analysis tools in the analysis of the township power supply stations is insufficient²; second, the current grid division of power supply stations lacks guiding opinions, the grid division principle of each unit is not uniform, the assessment of the carrying capacity of each substation area has not formed a unified and reasonable assessment plan, and the number of substation areas covered by each grid responsibility area has not fully evaluated the carrying capacity of each substation area manager and grid management, which is not conducive to maximizing the subjective initiative of the grid responsible person. Therefore, there is an urgent need to establish a scientific grid management carrying capacity model based on big data tools to evaluate the grid substation area configuration. This paper

uses the clustering algorithm and subjective and objective weighting method to evaluate the scores and weights of each evaluation index from the dimensions of customer scale, line loss of the substation area and collaborative work order, and obtains the carrying capacity of each substation area and managers of each substation area. Combined with the work ability of the substation area manager, the work of the substation area manager was redistributed to achieve “ make the best possible use of men”.

2 Construction of the Evaluation Model of the Carrying Capacity of Substation Area

Collect the basic information about substation area of one city in 2018 (substation area number, number of low-voltage substation area users, power supply area, area type, substation area manager), and operation information about the substation area (substation area number, line loss rate, number of collaborative work orders),and the average time for processing work orders in rural substation areas and urban substation areas, processing missing data and outliers, analysis of the difficulty of work in the substation area, analysis of the workload of the management of the substation area, scoring of the carrying capacity of the substation area, and scoring of the carrying capacity of the substation area managers.

2.1 Coefficient of Work Difficulty in Substation Area

Calculation formula of work difficulty coefficient using different service area types:

Urban work difficulty coefficient:

$$M_{\text{town}} = 1 \tag{1}$$

Rural work difficulty coefficient:

$$M_{\text{village}} = T_{\text{village}}/T_{\text{town}} \tag{2}$$

Among them, T_{town} means the average work order processing time of all substation areas in rural types, and T_{village} means the average work order processing time of all substation areas in urban types. The calculation results are as follows:

Urban work difficulty coefficient:

$$M_{\text{town}} = 1 \tag{3}$$

Rural work difficulty coefficient:

$$M_{\text{village}} = \frac{3.47}{3.88} = 0.89 \tag{4}$$

2.2 Management Workload of Substation Area

Line Loss Rate Indicator of Substation Area. A total of 20,409 data from the processed 2048 substation areas are clustered based on the k-means algorithm³. Combined with actual business scenarios (the higher the line loss rate in substation area, the greater the workload, and the growth rate of workload is gradually increasing; the line loss rate score is mainly concentrated in the 60–80 interval), and the line loss rate indicator is finally determined. The scoring rules are as follows (Table 1):

Table 1. Segmental scoring rules for line loss rate indicators.

| Class | Line loss rate interval | Score | Number of substation areas | Proportion |
|-------|-------------------------|-----------|----------------------------|------------|
| 1 | [0,1.56) | [0, 60) | 3416 | 16.7% |
| 2 | [1.56,4.73) | [60, 80) | 13442 | 65.9% |
| 3 | [4.73,7.63) | [80, 100) | 3392 | 16.6% |
| 4 | > = 7.63 | 100 | 159 | 0.8% |

As shown in the table above, the scoring rules in different line loss rate interval segments are different, and the line loss rate index score in each interval segment is linearly related to the line loss rate. The scoring rules are expressed as follows, R means line loss rate:

$$\text{line loss rate index score} = \begin{cases} \frac{1500}{39} * R, R \in [0, 1.56) \\ \frac{2000}{317} * (R - 1.56) + 60, & R \in [1.56, 4.73) \\ \frac{200}{29} * (R - 4.73) + 80, & R \in [4.73, 7.63) \\ 100, R \in [7.63, \infty) \end{cases} \quad (5)$$

Evaluation of User Scale Indicators in Substation Area. Based on the k-means algorithm, the processed substation area and its user quantity index are clustered separately. At the same time, combined with the actual business scenario (the larger the number of low-voltage users in substation area, the greater the workload, and the growth rate of workload is gradually increasing), the final grading rules for the number of low-voltage stations are as follows (Table 2):

Table 2. Segmental scoring rules for the number of low-voltage substation area

| Class | Low-voltage user quantity interval | Score | Number of substation areas | Proportion |
|-------|------------------------------------|-----------|----------------------------|------------|
| 1 | [0,53) | [0, 60) | 522 | 25.49% |
| 2 | [53,178) | [60, 80) | 1225 | 59.81% |
| 3 | [178,270) | [80, 100) | 209 | 10.21% |
| 4 | > = 270 | 100 | 92 | 4.49% |

As shown in the table above, the scoring rules in different low-voltage user quantity interval segments are different, and the index score of the low-voltage user quantity index in each interval segment has a linear relationship with the number of low-voltage users. The scoring rules are expressed as follows, N means the number of low-voltage users:

$$\text{low - voltage user quantity score} = \begin{cases} \frac{60}{53} * N, & N \in [0, 53) \\ 0.16 * (N - 53) + 60, & N \in [53, 178) \\ \frac{5}{23} * (N - 178) + 80, & N \in [178, 270) \\ 100, & N \in [270, \infty) \end{cases} \tag{6}$$

2.3 Evaluation of the Carrying Capacity of Substation Area

The number of collaborative work orders refers to the number of system work orders excluding outsourced work orders. Since the data of collaborative work order index is all zero, the weighting of collaborative work order indicators can only be determined using the subjective weighting method (expert scoring). For the other two indicators that affect the management workload of the substation area, the line loss rate of the substation area and the customer size (the number of low-voltage users) are weighted using the subjective and objective comprehensive weighting method. The weights of the three indicators of line loss rate, user scale, and number of collaborative work orders in the station area are 0.4, 0.4, and 0.2, respectively. The specific results are as follows (Table 3):

Table 3. Weight of the carrying capacity of the substation area.

| | Plan | Line loss rate | User scale | Number of collaborative work orders |
|------------------------|------------------------------------|----------------|------------|-------------------------------------|
| Expert experience | Expert scoring | 0.50 | 0.30 | 0.2 |
| Metric data dimension | Entropy weight discriminant model | 0.28 | 0.52 | – |
| | Principal component analysis model | 0.52 | 0.28 | – |
| | Coefficient of variation model | 0.33 | 0.47 | – |
| Grey correlation model | | 0.40 | 0.40 | 0.2 |
| Final weight | | 0.40 | 0.40 | 0.2 |

The carrying capacity score of the substation area is mainly the final score obtained by combining the management workload of the substation area and the work difficulty coefficient of the substation area. Since the number of collaborative work orders and the

index data are all zero, all the recorded data of the index are assigned a value of 100. The specific calculation formula is:

Management workload score = Line loss rate * 0.4 + User scale * 0.4 + Number of collaborative work orders * 0.2.

Carrying Capacity Score = Management workload score * Work Difficulty Coefficient.

By calculating processed records, the distribution of the carrying capacity score of the substation area is as follows (Fig. 1):

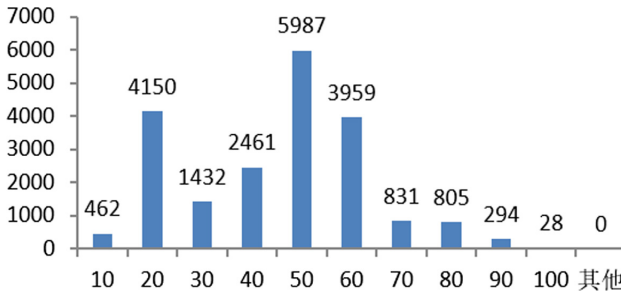


Fig. 1. Distribution map of the carrying capacity of the substation area.

The above figure is a histogram of the carrying capacity distribution of the substation area. The data scale under the horizontal axis indicates the upper limit of each interval segment (for example, “10” indicates the interval is [0,10], “20” indicates the interval is (10,20)). It can be seen from the above figure that the carrying capacity of the substation area is mainly distributed between 10-60, but the high point appears at [10,20], the reason is that there are many substation areas with the area of the platform area between [0,1].

2.4 Evaluation of the Carrying Capacity of Substation Area Manager

The work capacity of the substation area manager is the sum of the carrying capacity of all the substation areas under its jurisdiction. Calculated as follows:

$$B_{manager} = \sum_{i=1}^n b_i \tag{7}$$

Among them, $B_{manager}$ means the carrying capacity of the substation area manager, which means the carrying capacity of the i -th substation area, and n means that the substation area manager has jurisdiction over a total of n stations. Calculate the carrying capacity of the managers in the substation area and obtain the following distribution (Fig. 2):

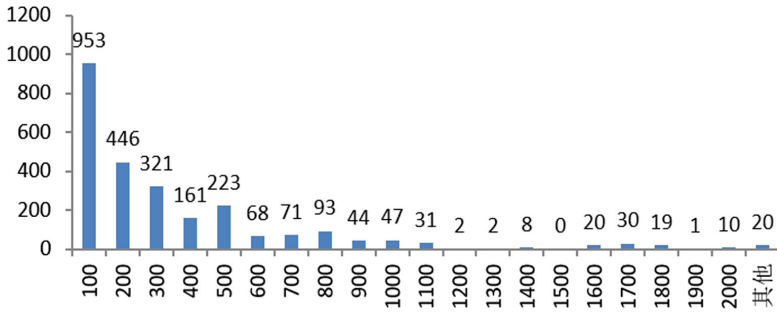


Fig. 2. Distribution map of the carrying capacity of the substation area manager.

According to the capacity data of substation area managers, cluster the values based on the k-means algorithm respectively, and obtain the results of the classification of the capacity of substation managers in the following (Table 4):

Table 4. Criteria of the carrying capacity rank of substation area managers.

| Carrying Capacity Grade | Ability of Managers | Capacity Interval | Number of Managers | Proportion |
|-------------------------|---------------------|-------------------|--------------------|------------|
| Extremely high | – | $[973, \infty)$ | 150 | 5.84% |
| High | A | $[630, 973)$ | 229 | 8.91% |
| Higher | B | $[335, 630)$ | 428 | 16.65% |
| Medium | C | $[72, 335)$ | 979 | 38.09% |
| Lower | D | $[32, 72)$ | 494 | 19.22% |
| Low | E | $[0, 32)$ | 290 | 11.28% |

It can be seen that the carrying capacity of the substation area managers is mostly concentrated at the middle level. The corresponding manager’s ability is C. According to their ability, they can manage 6–10 substations area with a carrying capacity score of 60 or 7–12 substations area with a carrying capacity score of 50.

3 Business Application Based on Assessment of Carrying Capacity of Substation Area

3.1 Equipment and Service Monitoring in Substation Area

Taking the substation area as the basic unit, through the evaluation of the substation area’s carrying capacity, and using data visualization to display4, the content includes the substation area’s overview, equipment characteristics, safety index, reliability index, economic index, and service index. The display is as follows (Fig. 3):

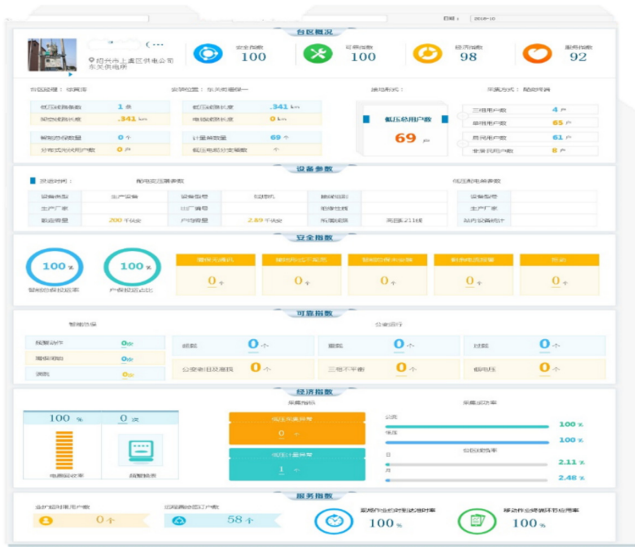


Fig. 3. Equipment and service monitoring scenarios in the substation area.

Based on the equipment and service monitoring scenarios in the assessment of the carrying capacity of the substation area, it can intuitively monitor the key indicators of the substation area and realize the supervision of special tasks, which reduces the work burden of the employees at the grass-roots power supply station to a certain extent, at the same time, it provides data support for equipment expansion, transformation, and diversion of equipment in the substation area, achieving precise investment and improving input-output efficiency.

3.2 Substation Area Manager Business Management Monitoring

Taking the substation area manager as the basic unit, through the evaluation of the substation area manager’s carrying capacity, the data visualization is used to display. The content includes basic information, skill level, work quantity, work potential, and work quality. The display is as follows (Fig. 4):

Based on the assessment of the manager’s carrying capacity, the manager’s business management and monitoring can carry out personnel information management, intuitively monitor the managerial capabilities of the managers in each substation area, and redistribute the work of the managers in the substation area, so as to achieve the purpose of “make the best possible use of men”, and provide data support for personnel performance, personnel training, personnel promotion and other work.

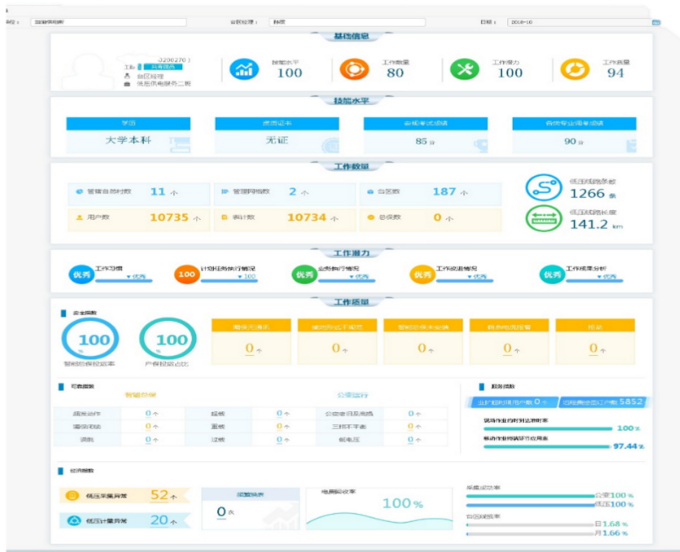


Fig. 4. The business management and monitoring scene of the substation area manager.

4 Conclusion

With the continuous development of science and technology, the world today has gradually entered the era of big data. Under this background, new requirements have been put forward for the development of various industries, and the development of State Grid Corporation is no exception. To achieve the improvement of the operation efficiency and quality of township power supply, big data analysis tools must be used in its business management [4]. This paper uses clustering algorithms and subjective and objective weighting methods to evaluate the scores and weights of each evaluation index from the dimensions of customer size, line loss in the substation area, and the status of collaborative work orders. Meanwhile, the business application of this model is studied.

References

1. Min, L., Yanhua, Z., Weibin, L.: Deepen the construction of “all-round” township power supply stations. *Rural Power Manag.* **278**(01), 69 (2019)
2. Lin, Y., Wei, L.: Research and application of the power supply station big data business model. *Power Syst. Big Data* **5**, 31–34 (2016)
3. Zhou, A., Yu, Y.: The research about clustering algorithm of K-Means. *Comput. Technol. Dev.* **21**(2), 62–65 (2011)
4. Liu, S., Song, Y., Zhu, Y.: Research on data storage for smart grid condition monitoring using Hadoop. *Comput. Sci.* **40**(1), 81–84 (2013)
5. Xiaosheng, P., Diyuan, D., Shijie, C.: Key technologies of electric power big data and its application prospects in smart grid. *Proc. CSEE* **35**(3), 503–511 (2015)



Research on the Optimization of Mobile Work Terminal Positioning Function Based on LBS

Pan Weiwei^(✉), Shen Guang, Wu Yuebo, and Huang Xiang

State Grid Zhejiang Power Co., Ltd, Hangzhou, China
icic1005@126.com

Abstract. In view of the weak support of GPS positioning function of mobile terminal, this paper uses in-depth research and analysis, using Unicom network auxiliary positioning service, according to the security control requirements of the national network information system, adopting the method of adding strong isolation device, proposes a basis Location, Service (LBS) is a safe, efficient, and responsive technical design method that satisfies the positioning needs of mobile operating terminals under harsh operating conditions, and provides services such as on-site job sign-in, equipment information collection, and regional management based on location data information support.

Keywords: LBS · Mobile work terminal · Positioning · Security

1 Introduction

With the continuous deepening of mobile business applications in the power marketing business, higher requirements have been placed on the support capabilities of mobile operation terminals. Not only need to meet daily business processing needs, but also need to continuously expand support capabilities [4, 5] to achieve user location information and trajectory information, on-site equipment location, on-site check-in information and other location data are collected and uploaded to the township power supply monitoring platform to provide work order processing and information upload and update assistants for on-site services to achieve intelligent management, visual monitoring and information scheduling [6]. Due to the extremely high requirements for information security in the power industry, mobile applications involve a series of issues such as secure access to internal and external networks, data security, and application development models [7]. The current positioning functions of mobile operating terminals mainly rely on GPS. Affected by weather and location, the positioning speed response is slow, and the search time is long, which cannot support the development of related businesses.

In order to improve the location service function of mobile operating terminals, through in-depth research and analysis, this paper proposes a safe and efficient network-aided system design method based on location services (LBS) to meet the positioning needs of mobile operating terminals under harsh operating conditions, based on Provide support for the on-site operation of location data information, equipment information collection, area management and other business development.

A complete LBS system consists of four parts, including positioning system, mobile service center, communication network and mobile intelligent terminal, as shown in Fig. 1:

Among them, the positioning system includes a GP positioning system and a base station positioning system. Positioning technology is the core technology of the entire LBS system, which is responsible for information interaction with mobile terminals and network interconnection of various sub-centers (location servers, content providers, etc.) to complete the classification, recording and forwarding of various information and the flow of business information between sub-centers, and monitors the entire networks

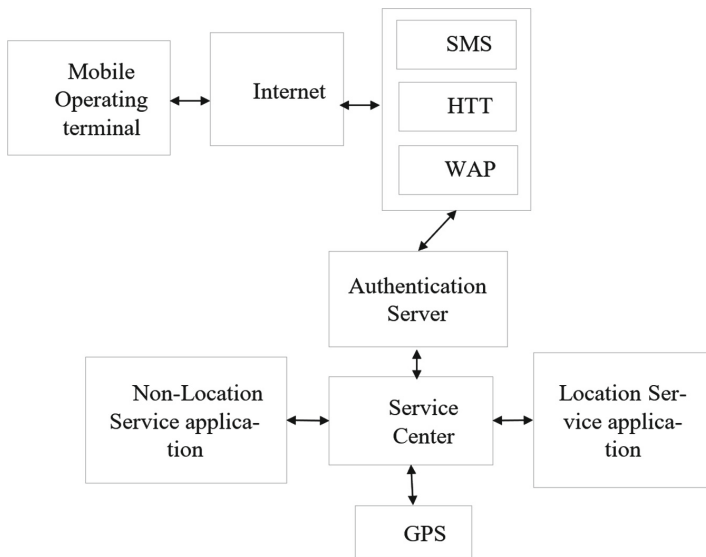


Fig. 1. LBS system diagram Auxiliary positioning system design

2 Auxiliary Positioning System Design

2.1 System Overall Architecture Design

As shown in Fig. 2, the system is mainly divided into 4 layers, namely the data layer, business layer, transmission layer, and display layer. The data layer is divided into a server data layer and a terminal data layer. The server data layer is mainly responsible

for the storage of spatial data, attribute data, and SVG map data, and the terminal data layer is responsible for the storage of system pictures and so on. The business layer is divided into EJB business and Web business, among them EJB business is responsible for data reading, transformation, analysis and answering Web request, Web business is responsible for client data request and response. The transport layer is responsible for data transmission, mainly through the power VPN dedicated network. The display layer is responsible for data (attribute data and spatial data) display, as well as data manipulation.

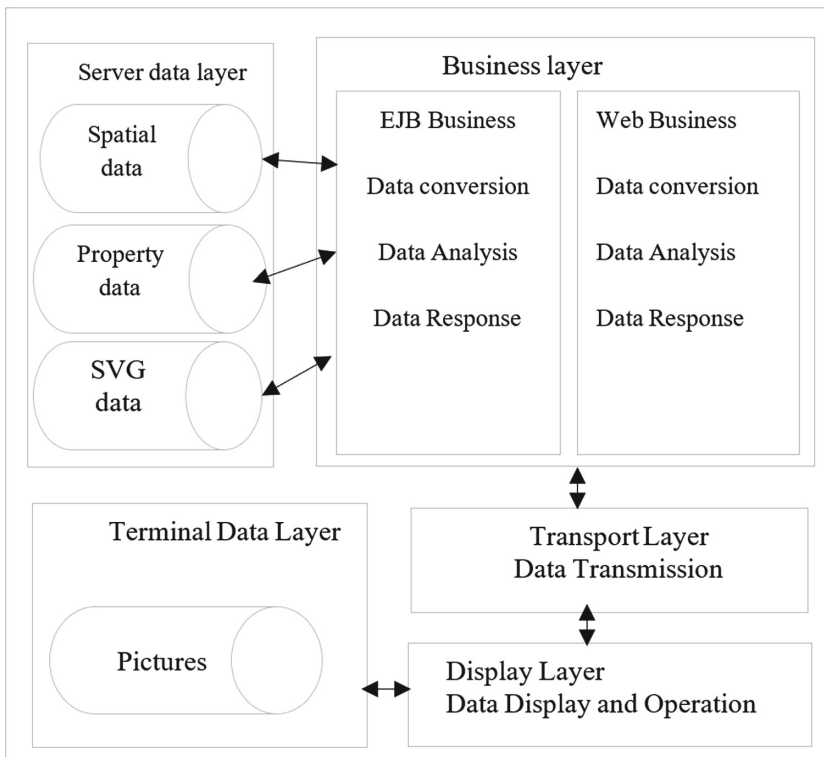


Fig. 2. LBS overall architecture diagram

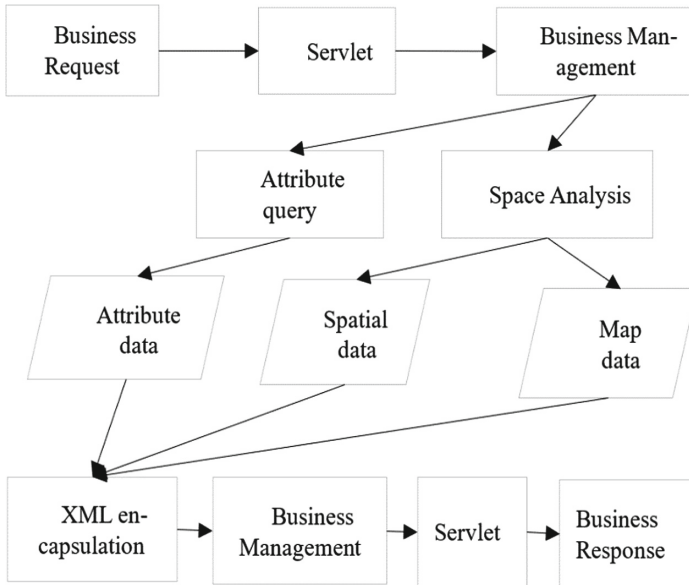


Fig. 3. Functional architecture of LBS server system

2.2 System Function Module Design

2.2.1 Server-Side Functional Design

The server is for the client, used to handle user business requests. The main functions include receiving client business requests, performing spatial calculation and analysis, searching response data from the server database, packaging response data, and sending response data. The functional framework of the server-side system is shown in Fig. 3.

The server-side Servlet component is responsible for accepting the business request sent by the customer and sending the response result; the data encapsulation is completed by JavaBeans; the business request data is managed by the business management module and handed over to the attribute query, spatial analysis and sending module for business processing or data reading Fetch, analyze, transform, encapsulate XML, and answer the client.

2.2.2 Client Function Design

As shown in Fig. 4, the user issues a service request and obtains response data from the server according to the service type. The business types are divided into positioning business and non-positioning business.

Coordinate positioning and name positioning belong to the type of positioning business, and distance measurement, location information and mail services belong to the type of non-positioning business; in the transportation service, the query of the traffic station is the positioning business, and the query of the transportation route is the non-positioning business. The positioning service response data includes spatial positioning data and attribute data. The non-location service response data is divided into status response data and non-location request result data.

When the user operates the terminal map, the graphic operation module is called. Graphic operations include full image display, zoom in, zoom out, roaming, layer control, etc.

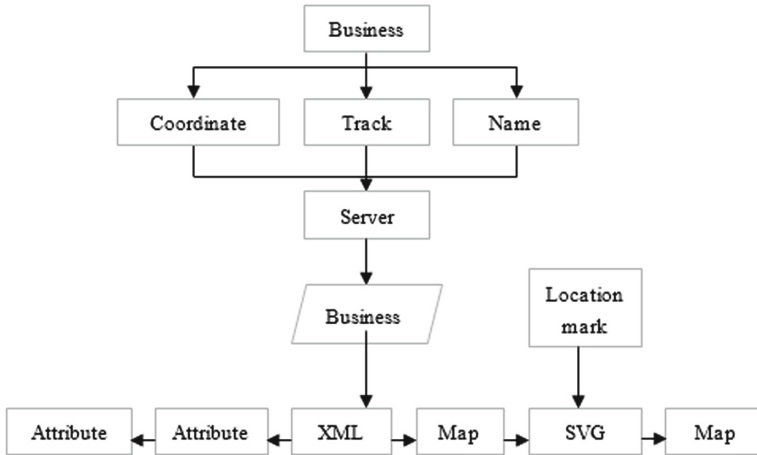


Fig. 4. Application architecture diagram

3 Research on Secure Access of Network Assisted Positioning System

3.1 Security Architecture Design

As shown in Fig. 5, in order to meet the requirements of State Grid’s security management and control, this paper proposes the following security arrangements (Fig. 6):

The LBS positioning system server is arranged outside the power information network, and the positioning-related applications are arranged on the power information external network. At the same time, safety isolation devices are added at the power information internal and external network boundaries and the external network private network boundary to achieve safe penetration.

In the specific application process, the mobile service application network-assisted positioning system accesses the power intranet through a secure access platform; when the mobile terminal initiates a positioning-related business application request, the request is transmitted to the power through the power private network APN through the power external network. The secure access platform of the network is connected to the marketing mobile application platform by the secure access platform. When a positioning request is initiated, the mobile operating platform accesses the location service of the power external network server through the strong isolation device and calls the external network location service.

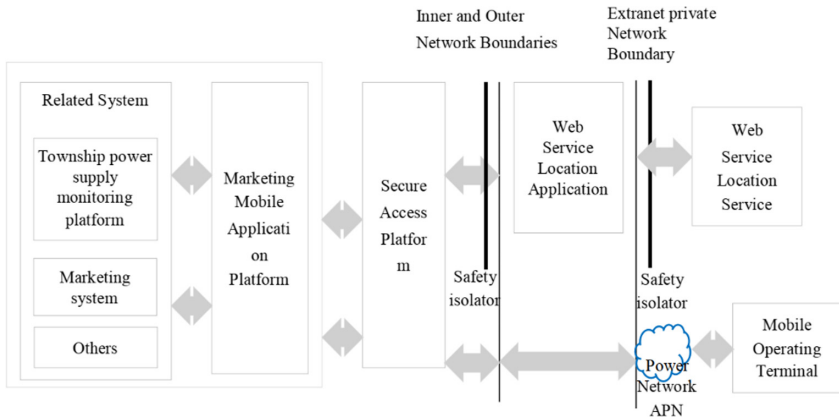


Fig. 5. Data Application framework

3.2 Research on Security Guarantee Strategy

In order to further improve the security performance of the system, security design research was conducted in terms of communication data encryption, access control, and strengthening of Internet border management and control, as follows:

3.2.1 Communication Data Encryption

In order to provide a secure communication environment for the LBS-based network-assisted positioning system and provide reliable privacy protection, it is necessary to provide encryption services for all information transmission in the system. The encryption module not only provides the authentication between the user and the server, but also realizes the function of all data encryption, ensuring the security of the network-assisted positioning system. There are many technologies in the application layer to achieve secure communication, such as Https, SSL/TLS protocols, etc., but these protocols have some problems when applied in this system, such as Https need to deploy digital certificates, but they need to apply for trusted digital certificates on a regular basis and cost more, and are less scalable in heterogeneous computing environments, which is not conducive to multi-terminal access to the system. Therefore, the LBS-based network-assisted positioning system designs and implements an encryption module.

The first step for users to use LBS-based power inspection is to establish a secure connection with the server. After establishing a secure connection, all data in the communication channel needs to be encrypted to ensure the safety of the power inspection system. In this process, two types of encryption algorithms are involved. After weighing, the asymmetric encryption algorithm is used to establish a secure connection, and the symmetric encryption algorithm is used to encrypt the data in the communication channel.

3.2.2 Access Control

Access control refers to designing user application operation permissions and key resource access permissions on the server side. Application permissions are hierarchically refined according to function modules, application interfaces, and operation buttons; access to key resources is controlled according to database tables and key records.

Currently, there are three main user roles in the LBS-based network-assisted positioning system: platform administrator, application administrator, and business user. The platform administrator has access to all functional modules of the network-assisted positioning system. The main job is to carry out role management, user management, menu management and role permission configuration, according to the nature of the work, to manage the user information using the system; the main job of the application administrator is to manage related applications of the system.

4 Strengthen Internet Border Control Measures

In order to strengthen the control of the Internet boundary, the network-assisted positioning system is accessed through a secure access platform, and the following management and control strategies are adopted at the same time:

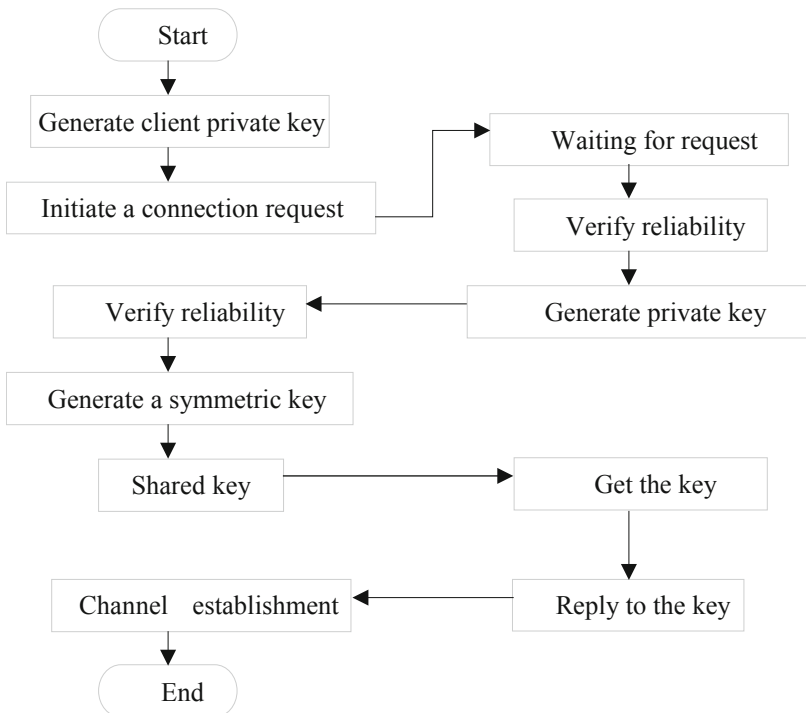


Fig. 6. Secure connection process

- 1) Adopt the existing firewall at the provincial company's Internet border and configure access control strategies to achieve the network isolation and access control of the provincial company's information extranet and the Internet.
- 2) The existing IDS equipment of the provincial company's Internet boundary is used to realize the prevention of border network intrusion, record all kinds of information such as user access record, system operation log, system operation state, and so on, after being standardized, filtered, integrated and alarm analysis, etc., centralized storage and management in the form of logs in a unified format.
- 3) Application firewall (WAF) is used to protect application layer attacks, and the protection rule base is updated in time.
- 4) Deploy intrusion prevention equipment to monitor and prevent intrusion attacks such as port scanning at the boundary and Trojan backdoor attacks.

5 Conclusion

Aiming at the problem that the GPS positioning function of current mobile operation terminals is weak, this paper designs and develops an LBS-based network-assisted positioning system based on specific business requirements through in-depth research and analysis. At the same time, in order to meet the requirements of State Grid's information security control, specific management and control strategies are proposed in terms of deployment methods, access methods, and security management and control strategies. Among them, in terms of deployment, the server is deployed externally, data is accessed by deploying a security isolation device, and the security access platform is used to uniformly access the intranet. Data encryption, access control, and Internet border management are used to achieve specific Security guarantee to meet the positioning requirements under the harsh operating conditions of mobile operation terminals, and provide support for the development of business such as on-site operation check-in, equipment information collection, and area management based on location data information.

References

1. Li, J.: Application of mobile operation terminal to realize intelligent emergency repair. *Power Demand Side Manage.* **4**, 29 (2014)
2. Hu, C., Bi, J.: Design of mobile application for power job visualization based on LBS map. *Automation & Instrumentation* **5** (2019)
3. Wang, L.-N., Wu, Q.-J., Li, R.: Design of visual mobile application for electric power operation based on LBS[J]. *Telecom Power Technol.* **36**(04), 48–49
4. Hu, R.-Y., Qu, Z.-Q., Xu, Q.-C., et al.: Self-service fault repair based on LBS. *Power Demand Side Manage.* **s1**(11–12), 15
5. Li, J.-B., Guo, B.: Application of mobile operation terminal in the power supply service. *Power Demand Side Manage.* **2**, 55–58 (2014)

6. Zhang, Y., Wang, Y., Shi, L., et al.: Research and discussion on the fusion of mobile operation terminal. *Power Demand Side Manage.* **21**(01), 76–78+86
7. Ling, X.-L., Wang, W., Fan, A.-J., et al.: Research on security and protection of mobile operation in electric power marketing. *Electric Power Inf. Commun. Technol.* **7**, 114–119



Study on Line Loss Prediction of Low-Voltage Platform Area Based on Internet of Things

Sun Gang^(✉), Gu Hongjie, and He Yun

State Grid ZheJiang Marketing Service Center (Metrology Center),
Hangzhou, China
icic1006@126.com

Abstract. Under the background of smart power grid and big data, improving the level of line loss prediction in low-voltage platform area plays an important role in realizing standardized management of line loss, reducing line loss in platform area and improving economic benefits. Firstly, the intelligent diagnosis architecture of line loss based on ubiquitous Internet of things and the data preprocessing process to realize the platform diagnosis are analyzed. Secondly, in view of the big data collected in the smart grid environment, the PCA method is proposed to reduce the dimensionality of data and extract the main components affecting the prediction of line loss. Then the users in the platform area to be predicted will adopt the IK-means algorithm for clustering processing. The ACO-ELM algorithm is used to optimize the initial value of the extreme learning machine. Finally, experimental simulation and comparison show that, compared with ELM and GA-BP algorithms, ACO-ELM method has the smallest error between the predicted line loss rate and the measured line loss rate, which verifies the effectiveness of the proposed method.

Keywords: Line loss predict · Ant colony optimization · Extreme learning machine

1 Introduction

Line loss refers to the energy consumed in the form of thermal energy when electrical energy is transmitted on power lines, and includes all electrical energy losses from power plants to power users [1, 2]. Among them, the line loss rate refers to the percentage of active energy loss and input active power. Line loss management affects the economic benefits of power companies, and platform area line loss management is greatly restricted due to meter reading and metering technologies. Therefore, the construction of an intelligent line loss management platform in platform area is particularly important [3, 4]. The construction and operation of “Strong Smart Grid” and “Ubiquitous Electricity Internet of Things” are important material foundations for building a world-class energy Internet enterprise. Further digging the application value of the data collected by the electricity information collection system in the line loss management of platform area. It is of great significance to improve the standardization of line loss management in low-voltage platforms, reduce the line loss in platforms, and improve the economic efficiency of enterprises.

At present, power supply companies have built a unified big data platform in accordance with the three-layer architecture of data collection, analysis, and application, and realized the separation of source-side data collection and data application display. However, there are still some problems in the intelligent diagnosis of line losses in low-voltage platform area using big data platforms. For example, the system’s diagnosis and treatment suggestions are not comprehensive and abundant. The platform area manager needs to handle the problems based on previous experience in the process of use. The level of intelligent is not high enough, and the research results of line loss models based on massive data at home and abroad are relatively few. In order to improve the accuracy of line loss prediction and anomaly diagnosis, this paper proposes an improved SVM algorithm to provide useful guidance for improving line loss management and increasing business efficiency [5].

2 Line Loss Prediction of Low-Voltage Platforms Area Based on ACO-ELM

2.1 PCA Data Reduction

Due to the data overlap and redundancy between the partitioned data, in order to improve the processing speed of the prediction model, the principal component analysis (PCA) was used to reduce the dimensionality of data [6–8]. The principle of PCA is as follows:

Suppose there are N samples and each sample contains n parameters, then the samples can be expressed as: $\mathbf{X} = (x_{ij})_{N \times n}$.

1. Standardize \mathbf{X} .
2. Construct the correlation coefficient matrix: $\mathbf{R} = (r_{ij})_{n \times n} = \mathbf{X}'\mathbf{X}$.

$$\mathbf{R} = \begin{bmatrix} r_{11} & r_{12} & \cdots & r_{1n} \\ r_{21} & r_{22} & \cdots & r_{2n} \\ \cdots & \cdots & \cdots & \cdots \\ r_{n1} & r_{n2} & \cdots & r_{nn} \end{bmatrix} \tag{1}$$

$r_{ij} = (i, j = 1, 2, \dots, p)$ is the correlation coefficient of x_i, x_j , $r_{ij} = r_{ji}$, Solving process is:

$$r_{ij} = \frac{\sum_{k=1}^n (x_{ki} - \bar{x}_i)(x_{kj} - \bar{x}_j)}{\sqrt{\sum_{k=1}^n (x_{ki} - \bar{x}_i)^2 \sum_{k=1}^n (x_{kj} - \bar{x}_j)^2}} \tag{2}$$

3. Find the characteristic root and characteristic vector of R , $\lambda_1 \geq \lambda_2 \geq \dots \geq \lambda_n \geq 0$. Find the feature vector corresponding to each feature root.

$$\mathbf{a}_1 = \begin{bmatrix} a_{11} \\ a_{21} \\ \vdots \\ a_{n1} \end{bmatrix}, \mathbf{a}_2 = \begin{bmatrix} a_{12} \\ a_{22} \\ \vdots \\ a_{n2} \end{bmatrix}, \dots, \mathbf{a}_n = \begin{bmatrix} a_{1n} \\ a_{2n} \\ \vdots \\ a_{nn} \end{bmatrix} \quad (3)$$

4. Write out the principal components and take m parameters instead of the original data ($m < n$).

$$F_i = a_{1i}X_1 + a_{2i}X_2 + \dots + a_{ni}X_n (i = 1, 2, \dots, n) \quad (4)$$

$$\mathbf{X}_{PCA} = [F_1, F_2, \dots, F_m] = \mathbf{X}[a_1, a_2, \dots, a_m] \quad (5)$$

5. Calculate the contribution rate of the main component of each parameter.

$$\gamma_i = \lambda_i / \sum_{j=1}^n \lambda_j (i = 1, \dots, n) \quad (6)$$

$\gamma_i (i = 1, \dots, n)$ is the degree of correlation between the various parameters. If γ_i is larger, it means that the parameter contributes more to the original data set. Generally take

$$\sum_{i=1}^m \lambda_i / \sum_{j=1}^n \lambda_j = \beta, \beta \geq 0.85 \quad (7)$$

In order to improve the stability of clustering, an IK-means algorithm is proposed to determine the clustering center [9–12].

2.2 ACO-ELM Algorithm

2.2.1 Mathematical Model of Extreme Learning Machine

The mathematical model of ELM is shown in Fig. 1:

The ELM learning method is as follows:

Training set: $\{(x_i, t_i)\}_{i=1}^N \subset R^n \times R^m$, The hidden layer excitation function $g(\cdot)$ is a non-linear function. There are L hidden neurons.

- (1) Randomly select the hidden layer node parameter $(a_i, b_i), i = 1, \dots, L$, a_i is the input weight of the i -th hidden layer neuron, and b_i is the i -th hidden layer neuron threshold [13–15].

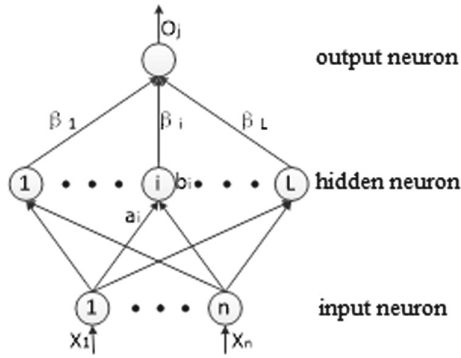


Fig. 1. Mathematical model diagram of extreme learning machine

(2) Calculate the output node matrix of the hidden layer $H = g(a_i, b_i, x_i)$,

$$H = \begin{bmatrix} h(x_1) \\ \vdots \\ h(x_n) \end{bmatrix} = \begin{bmatrix} g(a_1, b_1, x_1) & \cdots & g(a_L, b_L, x_1) \\ \vdots & \cdots & \vdots \\ g(a_1, b_1, x_n) & \cdots & g(a_L, b_L, x_n) \end{bmatrix}_{n \times L} \quad (8)$$

(3) Calculate the output weight β from the hidden layer to the output layer:

$$\beta = H^+ \cdot T, \quad \beta = \begin{bmatrix} \beta_1^T \\ \vdots \\ \beta_L^T \end{bmatrix}_{L \times m}, \quad T = \begin{bmatrix} t_1^T \\ \vdots \\ t_n^T \end{bmatrix}_{n \times m} \quad (9)$$

Where H^+ is the left pseudo-inverse matrix of the hidden layer output matrix H and T is the target output, i.e. $T = \{t_j\}_{j=1}^n$.

(4) Calculate the output value O_j . When the training error ($|O_j - T_j|$) is less than the preset constant ε , ELM can approach these training samples:

$$O_j = \sum_{i=1}^L \beta_i g(a_i, b_i, x_i), \quad |O_j - T_j| \leq \varepsilon, j = 1, \dots, n \quad (10)$$

(5) Find the error:

$$E_{(a_i, b_i)} = \sqrt{\sum_{j=1}^n (O_j - T_j)^2} \tag{11}$$

Among them, (a_i, b_i) is the input weight and threshold of the hidden node, respectively. T_j is the actual output value of the j -th group of data, and O_j is the predicted output value of the j -th group of data.

2.2.2 Ant Colony Algorithm Mathematical Model

Step 1: Initialize the parameters;

Generate M ants as the initial population $Y(0)$; evolution algebra $maxgen$; number of nodes n ; fitness of the i -th path fit_i ; η_{ij} is a heuristic factor; τ_{ij} is the amount of pheromone on the edge (i, j) . The amount of pheromone left by the k -th ant on the edge (i, j) in this iteration $\Delta\tau_{ij}^k$; pheromone evaporation coefficient ρ ; the probability of ant k transferring from node i to node j at time t $P_{ij}^k(t)$; t is time [14, 15].

Step 2: Calculate fitness $fit(y)$;

$$fit(y) = [y_1, y_2, \dots, y_M]^T \tag{12}$$

$$y_i = \frac{1}{m} \sum_{j=1}^m (O_j - T_j)^2 \tag{13}$$

Among them, m is the total number of input data, O_j is the j -th predicted output value, and T_j is the j -th actual output value.

Step 3: release the pheromone according to the fitness;

$$\tau_{ij}(t+n) = (1 - \rho) \cdot \tau_{ij}(t) + \Delta\tau_{ij} \tag{14}$$

$$\Delta\tau_{ij} = \sum_{k=1}^m \Delta\tau_{ij}^k \tag{15}$$

$$\Delta\tau_{ij}^k = \begin{cases} \frac{Q}{fit_k}, & \text{Ant } k \text{ travels through } ij \text{ this time}(i, j) \\ 0, & \text{Ant } k \text{ travels without } ij(i, j) \end{cases} \tag{16}$$

Among them, Q is a normal number, fit_k is the fitness of ant k walking the path. Initial $\tau_{ij}(0) = C, \Delta\tau_{ij}(0) = C$.

Step 4: Calculate transition probability $P_{ij}^k(t)$ and traverse all nodes;

$$P_{ij}^k = \frac{[\tau_{ij}(t)]^\alpha \cdot [\eta_{ij}(t)]^\beta}{\sum_{s \in J_k(i)} [\tau_{is}(t)]^\alpha \cdot [\eta_{is}(t)]^\beta}, j \in J_k(i); P_{ij}^k = 0, j \notin J_k(i) \quad (17)$$

Where α is the relative importance of the pheromone, β is the relative importance of the heuristic factor, and $J_k(i)$ is the set of nodes selected by ant k in the next step. Heuristic factor calculation formula: $\eta_{ij} = 1/d_{ij}$.

Step 5: Record the path of this iteration, update the current optimal path, and clear the tabu list;

Step 6: Determine whether the maximum number of iteration steps has been reached, or whether stagnation has occurred. If yes, the algorithm ends and the current optimal path is output; otherwise, go to step 2 for the next iteration.

2.2.3 Ant Colony Optimization Extreme Learning Machine Algorithm

Step 1: Initialize the pheromone P_j of L elements, and then start M ants from the ant nest, and perform step 2 for each one.

$$P_j = 1, j = 1, 2, \dots, L \quad (18)$$

Step 2: Start with the first element and select an element in the interval $[-1, 1]$ each time according to the path selection rule, and increase I to its pheromone (I represents the pheromone increase amount). Ants choose paths based on probability:

$$pro_j = P_j / \sum_{i=1}^L P_i \quad (19)$$

Step 3: Calculate the fitness of each ant's path, and select the maximum fitness and its path.

$$fit = \frac{1}{n} \sum_{i=1}^n |O_i - T_i| \quad (20)$$

Among them, n is the number of samples, O_i is the predicted output of the sample, and T_j is the actual output of the sample.

Step 4: Adjust the path of the ant according to the fitness of the sample, perform Gaussian mutation on the path of the ant with small fitness, and update the crawling speed. Then update the pheromone.

$$pro_{xj} = pro_j + Q * [(fit_{max} - fit_j) / (fit_{max} - fit_{min})] \tag{21}$$

Among them, pro_{xj} is the updated pheromone, pro_j is the pheromone before update, Q is the pheromone enhancement coefficient, and the fitness maximum value fit_{max} and fitness minimum value fit_{min} in each generation.

Step 5: The loop is executed to the number of genetic generations N , from the maximum fitness value of each generation, select the maximum fitness value and find the corresponding path.

$$fit_{end} = \max(fit_{i_{max}}), i = 1, 2, \dots, N \tag{22}$$

After the optimal path is selected, the corresponding weights and thresholds are the optimized ones.

2.3 Calculation of Line Loss in Low-Voltage Platform Area

After the pre-processing, principal component analysis and cluster analysis of the platform area data, a line loss ACO-ELM model is established for each type of platform area. The input of the model is the principal elements after clustering analysis of each partition, and the output is the line loss rate. A model between the line loss rate and the influence factor is established, and the relationship between each influence factor and the line loss rate is analyzed, so as to provide a reduction in the line loss rate support. In summary, the research process of the line loss prediction model for low-voltage platform area is shown in Fig. 2.

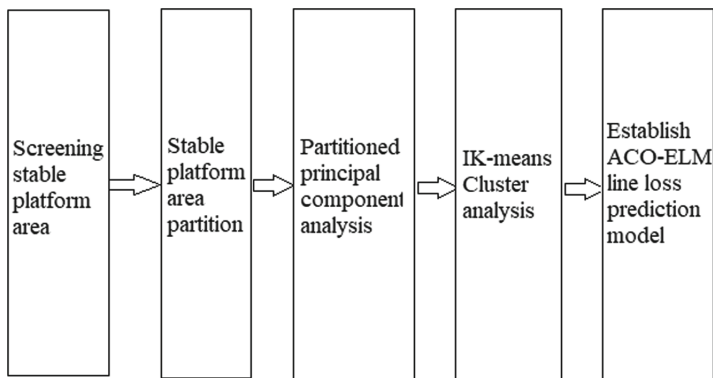


Fig. 2. Research process of low-voltage platform area line loss prediction model

3 Experiment and Analysis

3.1 Experimental Setup

Based on the data of 130,089 platforms in Zhejiang Province, after processing by stable platforms area, 75,159 rural stable platforms area and 18,638 urban stable platforms area were determined. Taking the rural area as an example, the PCA method is used to determine the principal components of various types of residents, and then the ACO-ELM algorithm is used to predict the line loss rate of the platforms area. The principal component analysis data features include: total number of users, number of residents, number of non-residents, capacity of residents, capacity of non-residents, capacity of transformers, power supply, proportion of residents' capacity, and capacity of residents. After PCA calculation, it can be known that the sum of the first five data features is 86.21% > 85%, so the first five features are taken as the main component of the prediction. After selecting the principal components of the data, the input sample data is classified and processed, and then ACO-ELM is used for line loss prediction. Line loss prediction results are shown in Fig. 3 and Table 1.

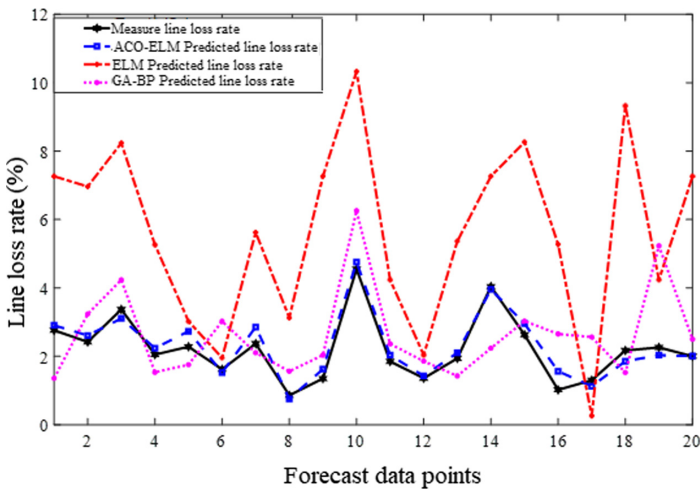


Fig. 3. Comparison chart of line loss prediction

Table 1. Comparison results of line loss prediction

| Category of platform area | Measure line loss rate (%) | ACO-ELM predicted line loss rate (%) | ELM predicted line loss rate (%) | GA-BP predicted line loss rate (%) |
|---------------------------|----------------------------|--------------------------------------|----------------------------------|------------------------------------|
| Inferior category1 | 2.76 | 2.906107 | 7.2635 | 1.3562 |
| Inferior category1 | 2.42 | 2.610274 | 6.96523 | 3.2365 |
| Inferior category1 | 3.37 | 3.107871 | 8.2365 | 4.235 |

(continued)

Table 1. (continued)

| Category of platform area | Measure line loss rate (%) | ACO-ELM predicted line loss rate (%) | ELM predicted line loss rate (%) | GA-BP predicted line loss rate (%) |
|---------------------------|----------------------------|--------------------------------------|----------------------------------|------------------------------------|
| Inferior category2 | 2.05 | 2.236542 | 5.2655 | 1.5325 |
| Inferior category2 | 2.28 | 2.73206 | 3.023 | 1.7562 |
| Mid-range category1 | 1.62 | 1.5268 | 1.95623 | 3.02356 |
| Mid-range category1 | 2.37 | 2.8565 | 5.625 | 2.1036 |
| Mid-range category1 | 0.86 | 0.75698 | 3.128 | 1.5623 |
| Mid-range category2 | 1.35 | 1.62589 | 7.2653 | 2.036 |
| Mid-range category2 | 4.55 | 4.7526 | 10.3256 | 6.2563 |
| Mid-range category2 | 1.85 | 2.03562 | 4.23651 | 2.365 |
| Mid-range category3 | 1.36 | 1.425698 | 2.03562 | 1.8562 |
| Mid-range category3 | 1.94 | 2.10356 | 5.3659 | 1.4268 |
| Mid-range category4 | 4.04 | 3.95624 | 7.2658 | 2.2365 |
| Mid-range category4 | 2.63 | 2.9562 | 8.2634 | 3.032 |
| Premium category1 | 1.02 | 1.56235 | 5.268 | 2.653 |
| Premium category1 | 1.3 | 1.1268 | 0.2586 | 2.563 |
| Premium category1 | 2.17 | 1.85623 | 9.3256 | 1.526 |
| Premium category2 | 2.26 | 2.03256 | 4.2365 | 5.23 |
| Premium category2 | 2 | 2.003245 | 7.263 | 2.5125 |

3.2 Result Analysis

The PCA method is used to perform dimensionality reduction on the user characteristic data of the platform area. The sample data to be predicted is clustered using the IK-means algorithm, and then the ACO-ELM algorithm is used to intelligently diagnose the line loss of the platform area user. From the results in Fig. 5 and Table 1, it can be seen that the ACO-ELM method proposed in this paper has a significantly better fit between the predicted line loss rate and the actual measured line loss rate than the ELM and GA-BP algorithms, verifying that the ACO- The ELM algorithm is suitable for line loss rate prediction.

4 Conclusions

After using PCA to reduce the dimensionality of power user data in low-voltage platforms, users are clustered using the IK-means algorithm, and the corresponding category library model is selected according to the user's category, that is, the corresponding ACO-ELM prediction model for low-voltage Line losses in platform area are forecasted. Experimental results verify that the prediction accuracy of this method is significantly higher than that of ELM and GA-BP algorithms, and it has a positive guiding significance for improving the intelligent diagnosis of line losses in low-voltage platform area.

References

1. Yongkai, Z., Huan, M., Wei, Z., Zhe, X., Xiaoxu, B., Weiyu, W.: Forecasting method of corresponding period monthly line loss in a distribution network and its application considering time of use. *Power Syst. Clean Energ.* **33**(10), 67–73 (2017)
2. Shouxiang, W.A.N.G., Kai, Z.H.O.U., Yun, S.U.: Line loss rate estimation method of transformer district based on random forest algorithm. *Electr. Power Autom. Equipmen* **37** (11), 39–45 (2017)
3. Haitao, Y., Yang, Z., Haifeng, T., Jieqing, X.: Interval estimation for line loss rates of low-voltage transformer zones considering uncertainty of load distribution. *Water Resour. Power* **36**(08), 181–184 (2018)
4. Weili, L., Qichang, H.: Diagnosis model for low-voltage district line loss management based on support vector machine. *East Chin. Electr. Power* **41**(02), 401–405 (2013)
5. Shangyuan, H., Lei, Y., Bin, Z., Jinmu, C.: Basic data system for line loss delicacy project in low-voltage transformer areas. *East Chin. Electr. Power* **39**(10), 1687–1690 (2011)
6. Yongbo, T., Weihua, G., Tao, P., Wei, O.: Transformer fault diagnosis model based on PCA and KICA feature extraction. *High Voltage Eng.* **40**(02), 557–563 (2014)
7. Peiliang, W., Chunjiang, X.: Fault detection and self-learning identification based on PCA-PDBNs. *Chin. J. Sci. Instr.* **36**(05), 1147–1154 (2015)
8. Jun, Ma., Zhao Feile, X., Xiao, C.S.: Fault diagnosis of analog circuit based on optimized BP neural network with MRA-PCA-PSO technology. *J. Electr. Meas. Instrum.* **32**(03), 73–79 (2018)
9. Yanjuan, L.I., Mengting, N.I.U., Linhui, L.I.: Research on remote sensing image clustering based on bee colony algorithm. *Comput. Eng. Appl.* **55**(06), 151–159 (2019)
10. Su, H., Zhe, H., Zejun, W.: A K-Means/Spport vector machine based self-adaptive online fault diagnosis method for fuel cell systems. *J. Tongji Univ. (Natural Sci.)* **47**(02), 255–260 (2019)
11. Ya, L., Liping, L., Baiqing, L., Jun, Y., Zezhong, W., Shiming, T.: Calculation of line loss rate in transformer district based on improved k-means clustering algorithm and BP neural network. *Proc. CSEE* **36**(17), 4543–4552 (2016)
12. Shuang, L.I., Ruirui, C.H.E.N., Nan, L.I.N.: K-means clustering algorithm with Hadoop framework for large data mining. *Comput. Eng. Des.* **39**(12), 3734–3738 (2018)
13. Yan, W., Zhen, W., Minxiang, H., Zhenqi, C., Mengmeng, Y.: Ultra-short-term wind power prediction based on OS-ELM and Bootstrap method. *Autom. Electr. Power Syst.* **38**(06), 14–19+122 (2014)

14. Hua, F., Xinrui, W., Zhijun, W., Yuhong, W., Naiwei, T., Yaosong, X.: Research on the soft sensor of coal and gas outburst based on PCA and PSO-ELM. *Chin. J. Sens. Actuators* **27** (12), 1710–1715 (2014)
15. Yinghao, S., Qing, F., Xuan, G., Changya, Z.: Combined forecasting of photovoltaic power generation in microgrid based on the improved BP-SVM-ELM and SOM-LSF with particlization. *Proc. CSEE* **36**(12), 3334–3343 (2016)



Research on Unstructured Electronic Archives Query Based on Visual Retrieval Technology

Hui Yang^(✉)

E-Energy Tech Ltd., Hangzhou, Zhejiang, China
icic1008@126.com

Abstract. Digitalization of enterprise archives is the mainstream trend of archive management. This paper proposes a digital archive index management framework based on visual retrieval technology for unstructured digital archive management problems. The framework adopts the current mainstream deep local feature extraction scheme DELF Pipeline to carry out feature extraction for digital archives, and use the distributed inverted indexing framework Lucene to build an efficient indexing and retrieval system for digital archives. Through a large number of simulation experiments, it is proved that the framework can be well used for the management of enterprise unstructured digital archives, which supports dynamic incremental index construction and has high retrieval efficiency.

Keywords: Electronic archive management · Visual retrieval · Inverted index

1 Introduction

In this era of big data, whether it is enterprise digitization or the data management thinking that managers often talk about, is in the “popular fashion”, and the digitization of enterprise archives is also one of the mainstream trends. File digitization is to store information in a computer database by scanning and entering paper documents to achieve fast and convenient retrieval, quick and easy synchronous backup, small storage space, convenient maintenance, and safety. The digitization of archives management is an inevitable requirement in the information age, and the focus of building digitized archives is to facilitate retrieval. A good file management system often has a multiplier effect for file management workers to complete all file management tasks. It can not only improve economic efficiency, but also greatly improve office efficiency.

Many research work at home and abroad has also carried out related research on the digital management of archives [1–3] technology. Dede E et al. [4] proposed the integration method of NoSQL data storage and MapReduce in non-Java application scenarios, and analyzed the advantages and disadvantages of different methods. Corcoglioniti Francesco et al. [5] described a scalable, fault-tolerant open source storage system. Do Bao H, Wu Andrew, Biswal Sandip, etc. [6] formed a radiology file based on semantic search and Web by using RADTF, which provided an effective solution for storing and retrieving radiology cases. Wu Qunhui et al. [7] pointed out that social network data has unstructured characteristics, and proposed a new natural disaster event discovery model. Yang Jiachen et al. [8] believed that the analysis of

unstructured image data source conversion must first undergo a form conversion, and construct a method that can quickly retrieve images.

However, most of the existing digital archive management systems are based on structured digital archives. The pre-construction of such archives requires a lot of manpower and time for the structural processing of electronic data. And more enterprise electronic archive data is only obtained by scanning. This type of digital archive data is not structured data, and it cannot use mature database storage and retrieval methods, which brings new challenges to digital archive management.

This paper proposes a digital archive index management framework based on visual retrieval technology for the problem of unstructured digital archive management. The framework uses the current mainstream deep local features to abstractly describe digital archives, and uses the distributed inverted index framework Lucence to efficiently index digital archives for subsequent real-time retrieval. Experiments prove that the framework can be well used for the management of enterprise unstructured digital archives, which supports dynamic incremental index construction, and has a high retrieval efficiency. For the user's retrieval needs, in a digital archive with a scale of millions, the user retrieval results can be returned within milliseconds.

2 The Framework

Many electronic documents are difficult to generate structured information, so they can only be treated as image data. The retrieval of such electronic documents is difficult and cannot be achieved through database-related retrieval techniques. Aiming at the problems of unstructured archive retrieval, this paper designs an unstructured digital archive retrieval framework based on deep DELF features. The overall framework of the index retrieval system for electronic documents is shown in Fig. 1:

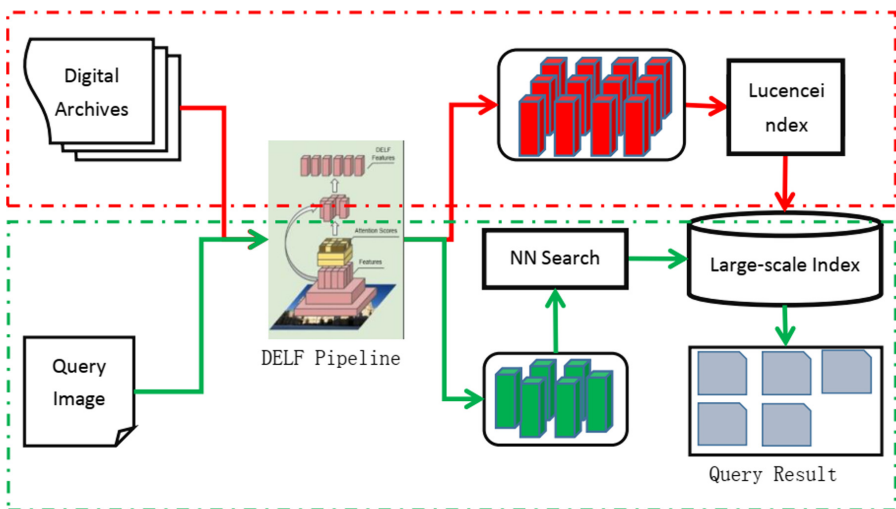


Fig. 1. The framework of digital archives query system (Color figure online)

We can see from Fig. 1 that the digital archive index retrieval system framework mainly includes two channels:

The channel in the red box is mainly for offline preprocessing of the electronic digital archive. The channel extracts the local visual features of each electronic document in the archive through the DELF pipeline. Based on these local features, the Lucence inverted index retrieval framework is used to build a large-scale visual index library for retrieval in another channel.

The channel in the green box is mainly used to process the search request submitted in real time. This channel extracts features through the DELF Pipeline for the search image input by the user, and performs approximate nearest neighbor search on the large-scale index database that has been built based on these features, and finally feeds back the search results to the user.

3 Digital Archives Query System Based on Visual Retrieval Techniques

3.1 Pretreatment of Digital Archives Based on Automatic White Balance Method

White balance is a very important concept in the field of videography. It can solve a series of problems in color reproduction and tone processing. Therefore, the white balance processing method is also widely used in image preprocessing to solve the problem of uneven illumination of pictures. This article chooses the automatic white balance algorithm of dynamic threshold adjustment. This algorithm is similar to the gray world method and the perfect reflection algorithm. The execution of the algorithm is divided into two steps: white point detection and white point adjustment. The white point detection is mainly responsible for completing the white reference point detection, and the white point adjustment is to complete the correction of the point color by adjusting each color component. The specific selection and adjustment process can be found in the document [9].

3.2 Extract Deep Local Features for Digital Archives

After preprocessing, the illumination and rotation angle of the digital archive image have been corrected. Then we need to abstract the digital archive image, that is, extract features from the digital archive image. Large-scale image retrieval is one of the research hotspots in computer vision. In the past ten years, image retrieval systems have gradually developed from the original manual features and indexing algorithms to establish methods for global image description through convolutional neural networks (CNNs). Many research efforts have attempted to achieve retrieval based on the global features of CNN, and have achieved very good experimental results on small and medium-sized data. Then when the data set is large-scale and is affected by factors such as complex background, occlusion, viewing angle and lighting changes, for example, in the face of large-scale digital archive images, its performance is limited. The global expression is hard to match the patch-level matching between images well, which

makes it difficult to complete the partial matching image retrieval when the occlusion and the background are complex. Recently, the literature [10–12] used CNN to extract local features to achieve block-level matching. However, these methods are not specifically designed for image retrieval tasks, so their performance in detecting features with semantic information is limited, and the accuracy obtained in practical applications is not high.

The retrieval system designed in this paper is based on local features. Common image local features include manual features (such as: SIFT [13], SURF [14], ORB [15], etc.) and deep local features (such as DELF [16]). The local feature extraction in this paper is done by DELF Pipeline. First, in order to select the key points of local features, this paper measures the correlation scores between local features by training a landmark classifier with attention. To achieve this training, features are processed using weighted summation pooling, where the pooled weights are obtained by the attention network. Then, the full convolutional neural network is used to extract the local features of key points, the model is ResNet50, and the output layer is conv4_x. In order to solve the problem of scale transformation, an image pyramid is constructed, and FCN is used to process the image at each scale separately. Use ResNet50 pre-trained on ImageNet as a benchmark, and fine-tune the significance of the enhanced local description. Considering the application in landmark recognition, the training uses landmark images with annotation information, and the loss function uses standard cross-entropy loss for image classification problems. A square area is cropped from the center of the image, and the scale is uniformly transformed to 250×250 , and a 224×224 image is randomly cropped for training. The network summary structure is shown in Fig. 2:

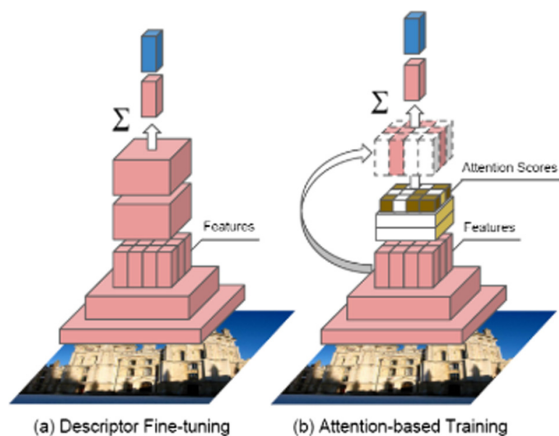


Fig. 2. DELF pipeline as local feature extractor [16]

3.3 Construct Large-Scale Index Based on Lucence

Lucene [17] is a simple and powerful Java-based search library, which can be used in any application to search for functions. Lucene is an open source project which is

extensible. Its high-performance library for indexing and searching almost any type of document. The Lucene library provides the core business of any search application required. In this paper, the local features in the digital document are regarded as the visual words in the document, and the Lucene engine is used to build the indexing and retrieval system.

Since the visual dictionary is not a standard dictionary, the first step in building an index system is to generate a visual dictionary. In this paper, the K-Means algorithm is used to generate a visual vocabulary dictionary based on deep local features through clustering. Then use a visual dictionary to quantize each local feature in the digital document, and build an index on the quantized visual words. The index construction process is completed by the Index Writer component provided by Lucene. The specific construction process is shown in Fig. 3:

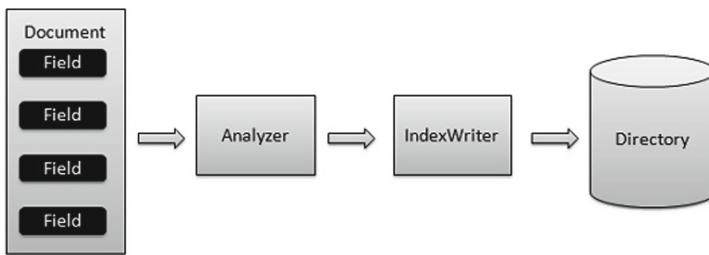


Fig. 3. Index process of Lucene Framework

The Index Writer module is mainly used to update or create index. After each digital document is analyzed by the analyzer, the Index Writer module is used to create index. The Index Writer module can also be used to store, update, open, and edit index, and supports incremental addition and dynamic updates of index in digital archives.

3.4 Query of Digital Archives

The retrieval of archives is based on the core retrieval module of the Lucene engine.

Figure 4 illustrates the search process and the classes used. Index Searcher is the most important and core component in the search process.

We first create the directory containing the index, and then pass it to Index Searcher, which uses Index Reader to open the directory. Then, create a deadline query to make the search using Index Searcher pass the search to the query. Index Searcher returns the Top Docs object contains the search information along with the document ID of the document that it is the result of the search operation.

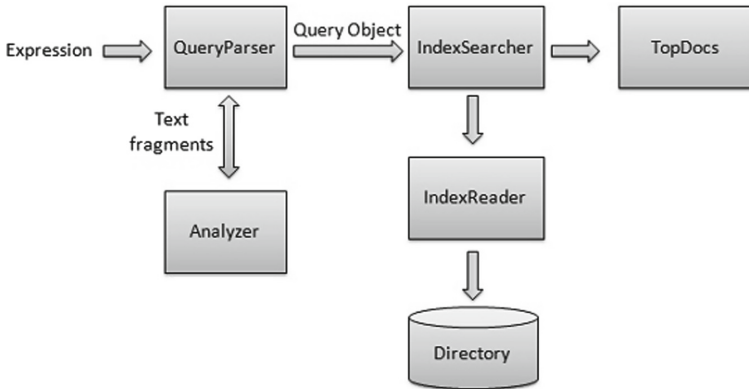


Fig. 4. The detail search process on Lucene Framework

4 Experiment Results and Analysis

4.1 Experiment Setup

In order to verify the method proposed in this paper, we conducted simulation experiments on the electronic document database of the power service system. The database contains: various types of electronic documents such as user contracts, application forms, electricity meter pictures, ID card scans, etc., totaling about 1 million copies. These more than one million electronic documents will be used as system libraries to build offline indexes for retrieval. At the same time, we also prepared 1,000 copies of paper materials, which were scanned and pre-processed as test data.

The hardware platform of the experiment is: Xeon CPU 1, 64 G memory, GPU card 1080Ti X2, hard disk 5T, software platform includes: Ubuntu 16.0 operating system, Pytorch deep neural network platform for building Delf Pipeline deep network procedures, pre-trained Basic network Resnet50, Lucene software and other required software packages.

4.2 Experiment Results and Analysis

Different dictionary sizes directly affect the accuracy and efficiency of retrieval results. In order to find a suitable dictionary size, this paper conducts experiments on different dictionary sizes. The dictionary generation uses the KMeans algorithm. We generate visual dictionaries of their respective sizes, and the generation time is shown in Table 1 below:

Table 1. Time cost of visual dictionary generation

| dictionary size | 1000 | 2000 | 5000 | 10000 | 20000 | 50000 |
|----------------------|------|------|------|-------|-------|-------|
| Generation Times (s) | 57 | 181 | 556 | 2056 | 4012 | 11056 |

Different dictionary sizes also affect the accuracy of retrieval results. Usually, a dictionary that is too small is not conducive to distinguishing visual words, while a visual dictionary that is too large is too sparse. In order to get a higher accuracy of the results, you need to choose a suitable dictionary size. To this end, this paper conducted a set of experiments for different dictionary sizes, and the experimental results are shown in Fig. 5. As can be seen from the figure, when the dictionary size is 20,000 visual words, the system’s retrieval effect is the best. Therefore, this paper chooses 20000 as the size of the visual dictionary.

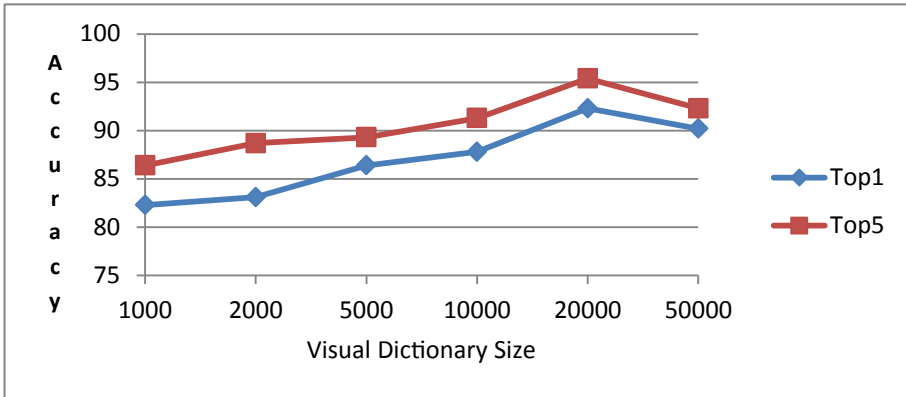


Fig. 5. The variation of accuracy in different visual dictionary sizes

In order to verify the throughput capacity of the framework proposed in this paper for archives of different capacities, this paper sets six digital archives of different sizes and conducts corresponding experiments. The average search time on digital archives of different sizes is shown in Table 2:

Table 2. Retrieval time and archive size

| Archive size | AVG retrieval time (ms) |
|--------------|-------------------------|
| 20000 | 3.31 |
| 50000 | 3.52 |
| 100000 | 3.89 |
| 200000 | 4.02 |
| 500000 | 4.16 |
| 1000000 | 4.35 |

As can be seen from the average retrieval time of Table 2, as the size of the archive increases, the single retrieval time also increases, but the growth rate is much slower than the growth rate of the archive, the main reason is that the Lucene framework uses

inverted index Technology makes the retrieval time almost independent of the size of the archives, but with the size of the visual dictionary.

5 Conclusion

Enterprise file digitization is the mainstream trend of file management. This paper proposes a digital archive index management framework based on visual retrieval technology for the problem of unstructured digital archive management. The framework uses the current mainstream deep local feature extraction scheme DELF Pipeline to extract features from digital archives and uses distributed inverted index framework Lucence to build an efficient indexing and retrieval system for digital archives. Through a large number of simulation experiments, it is proved that the framework can be well used for the management of enterprise unstructured digital archives, supports dynamic incremental index construction, and has high retrieval efficiency.

References

1. Aihara, K., Takasu, A., Adachi, J.: A distributed index system for efficient query processing in peer-to-peer Networks. *Commun. Comput. Signal Process.* **1**, 139–142 (2003)
2. Kanwar, R., Trivedi, P., Singh, K.: No SQL, a solution for distributed database management system. *Int. J. Comput. Appl.* **67**(2), 6–9 (2013)
3. Mansuri, I.R., Sarawagi, S.: Integrating unstructured data into relational databases. In: *Proceedings of the 22nd International Conference on Data Engineering* (2006)
4. Dede, E., Sendir, B., Kuzlu, P., et al.: Processing cassandra datasets with Hadoop- streaming based approaches. *IEEE Trans. Serv. Comput.* **9**(1), 46–58 (2016)
5. Corcoglioniti, F., Rospocher, M., Cattoni, R., et al.: The knowledge store: a storage framework for interlinking unstructured and structured knowledge. *Int. J. Semant. Web Info. Syst.* **11**(2), 1–35 (2015)
6. Do, B.H., Wu, A., Biswal, S., et al.: Informatics in radiology: RADTF: a semantic search-enabled, natural language processor-generated radiology teaching file. *Radio Graph. Rev. Publ. Radiol. Soc. North America Inc.* **30**(7), 2039–2048 (2010)
7. Wu, Q., Ma, S., Liu, Y.: Sub-event discovery and retrieval during natural hazards on social media data. *World Wide Web* **19**(2), 277–297 (2015). <https://doi.org/10.1007/s11280-015-0359-8>
8. Yang, J., Jiang, B., Li, B., et al.: A fast image retrieval method designed for network big data. *IEEE Trans. Ind. Inform.* **PP**(99), 1 (2017)
9. Weng, C.-C., Chen, H., Fuh, C.-S.: A novel automatic white balance method for digital still cameras. In: *IEEE International Symposium on Circuits & Systems*, 26 June 2005
10. Wang, Q., et al.: Image classification based on deep local feature coding. In: *International Symposium on Intelligent Signal Processing & Communication Systems* (2017)
11. Lan, Z., Zhu, Y., Hauptmann, A.G.: Deep local video feature for action recognition (2017)
12. Zhu, Q., et al.: A deep-local-global feature fusion framework for high spatial resolution imagery scene classification. *Remote Sens.* **10**(4), 568 (2018)
13. David, G.L.: Object recognition from local scale-invariant features. In: *International Conference on Computer Vision, Corfu, Greece, September 1999*, pp. 1150–1157 (1999)

14. Bay, H., Tuytelaars, T., Van Gool, L.: SURF: speeded up robust features. In: Leonardis, A., Bischof, H., Pinz, A. (eds.) ECCV 2006. LNCS, vol. 3951, pp. 404–417. Springer, Heidelberg (2006). https://doi.org/10.1007/11744023_32
15. Rublee, E., et al.: ORB: an efficient alternative to SIFT or SURF. In: International Conference on Computer Vision IEEE (2012)
16. Noh, H., et al.: Large-scale image retrieval with attentive deep local features. In: 2017 IEEE International Conference on Computer Vision (ICCV). IEEE (2017)
17. Zhou, D., Xie, K.: Lucene search engine. *Comput. Eng.* **33**(18), 95–97 (2007)



Gingivitis Detection by Fractional Fourier Entropy and Standard Genetic Algorithm

Yan Yan^{1,2(✉)} and Elijah Nguyen³

¹ School of Informatics, University of Leicester,
University Road, Leicester LE1 7RH, UK
yanyan899@outlook.com

² Educational Information Center, Liming Vocational University,
Quanzhou 362000, Fujian, China

³ College of Science and Engineering, Flinders University,
Bedford Park, South Australia, Australia

Abstract. Early detection of gingivitis is crucial for oral health. Dental diagnosis and treatment require very high standards of care and a great deal of experience. To reduce the diagnostic difficulties of dentists, this work proposes a classification method for gingivitis based on fractional Fourier entropy and standard genetic algorithm. The fractional Fourier transform was used to extract the eigenvector fractional Fourier entropy, and the eigencoefficient was substituted into the classifier of standard genetic algorithm for the classification of healthy gingival images and pathological gingival images. Experimental results show that this approach has better performance than existing methods and is effective in image classification of gingivitis.

Keywords: Gingivitis detection · Fractional Fourier entropy · Standard genetic algorithm · Feedforward neural network · Image processing

1 Introduction

In recent years, although people tend to pay more attention to the health of teeth, they often neglect the fact that invisible lesions in the teeth can be a big problem and therefore miss the best time for diagnosis and treatment. Oral health has many negative impacts on many countries and individuals. According to the World Health Organization, oral diseases are estimated to affect 3.5 billion people, particularly periodontitis, which accounts for about 10 percent of the world's population [1]. First, in terms of countries, most low - and middle-income countries are largely unable to provide prevention and treatment due to the high cost of oral health care. Secondly, for individuals, oral health seems to have little impact on death. Nonetheless, it leaves people in a state of long-term suffering, which can lead to mental and physical problems. With in-depth follow-up interviews with 19 adults with gingivitis researched by Pyo, et al. [2], showing that periodontal disease can lead to tooth loss, seriously affecting important dietary problems in humans. Most oral problems can be prevented, and early detection and treatment can effectively control the occurrence of oral diseases. Diagnosis of gingivitis, an unhealthy dental condition in which gums bleed and swell, is still a big

challenge for dentists as it is difficult to be detected and chronic inflammation can lead to possible misdiagnosis by inexperienced physicians. Therefore, Dental records were particularly important because routine oral examinations relied on previous experience significantly [3].

There are various research topics focused on artificial intelligence-based dental diagnosis in recent years. The main research models are mainly used to detect and predict or enhance the color of diagnoses images. The study of models for detection and prediction improves the performance of automatic detection. Li, et al. [3] found producing data recording through a combination of three approaches, including a contrast-limited adaptive histogram equalization, Gray Level Co-Occurrence Matrices, and an extreme learning machine, were more effective when compared to other advanced methods. Thakur, et al. [4] used sigmoid-based multilayer neural networks and the Levenberg-Marquardt training algorithm to identify early symptoms and risk factors in periodontal disease and gingivitis. According to Sudheera, et al. [5], the research of the K-means method was used to detect the amount of dental plaque in the dental area to support image segmentation and tooth image diagnosis. The research by JH, et al. [6], using GoogLeNet Inception v3 CNN and 3000 dental X-ray images to diagnose and predict premolars and molars caries and periodontal damage teeth. Aberin and Goma [7] proposed that the microscopic plaque image detection based on the neural network can be divided into healthy and unhealthy, and tested the AlexNet architecture as the best architectural model for using convolutional neural network. Zhu, et al. [8] proposed automatic tooth detection and segmentation based on natural-color images of mask R-CNN, and the model can support a small number of modifications to adapt to other types of detection segmentation and evaluation. You, et al. [9] proposed an AI model for the detection of dental plaque that has been tested to a clinically acceptable level. Most families can easily afford video cameras, making it easier to monitor children's oral hygiene. The study of models for color enhancement provides higher quality images for detection. To assist in the classification of gum disease, Rana, et al. [10] proposed a CNN with annotation training by dental professionals to provide color-enhanced pixel-level segmentation of intra-oral images. Hatvani, et al. [11] studied a method based on two CNN architectures, a subpixel network, and U-net network to enhance and improve the resolution of dental CT images. Hu, et al. [12] used the antagonistic network generated by Wasserstein generative adversarial (WGAN) to perform enhanced correction for low-dose dental CT imaging.

The above methods have achieved some results in image enhancement, segmentation, and detection, but each method has the error calculation caused by image quality requirements or insufficient test data. Therefore, we provide a new and more efficient algorithm. The development of the algorithm was based on the feature vectors of gingivitis images extracted by fractional Fourier entropy (FRFE), as well as the usage of a standard genetic algorithm (SGA) for neural network optimization and image classification. This combination of the algorithm is superior to other advanced gingivitis detection methods owing to the algorithm improves the image accuracy and simplifies the detection space and process. Our contribution is to propose a model characterized by high quality, high precision, and low time consumption, which can improve the overall diagnostic efficiency, with the provision of early prevention information reduce the incidence of gingivitis.

The remnant of this paper is organized as follows. Section 2 introduces the method used in our experiment. Section 3 mainly describes the data used in the experiment and discusses the experimental results. Section 4 concludes this research and forecasts future research in different fields.

2 Methodology

In this study, we used a new detection method. A detection model by using the fractional Fourier entropy (FRFE) and standard genetic algorithm (SGA). We first used the two-dimensional fractional Fourier transform (2D - FRFT) for gingivitis images and then used Shannon entropy to extract the eigenvectors of the 2D - FRFT spectrum. A standard genetic algorithm was used to optimize weights and biases in feedforward neural network (FNN) for modeling. Finally, the model was used to classify gingivitis images. The progress shown in Fig. 1.

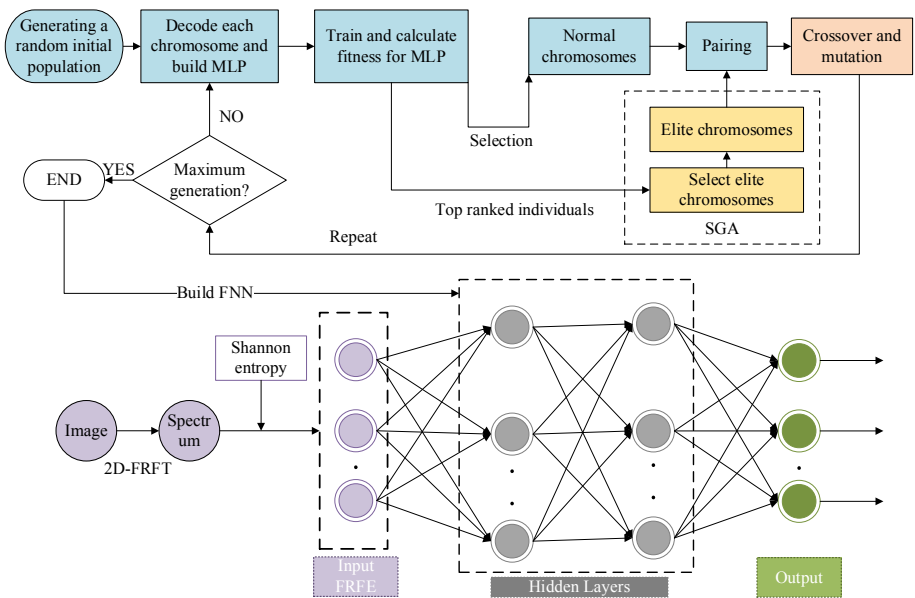


Fig. 1. Image classification based on FRFE and SGA

2.1 Fractional Fourier Entropy

The fractional Fourier entropy (FRFE) can be regarded as an images feature, which was first proposed by Wang, et al. [13]. In the field of image classification, although discrete wavelet transform (DWT) has more advantages than traditional Fourier transform as a common method, DWT is easily affected by the selection of optimal decomposition level and optimal wavelet function. Moreover, FRFE has better performance and

precision than DWT. Therefore, we choose to extract FRFE as the eigenvector for image preprocessing.

FRFE is based on feature vectors extracted from original images, which can greatly reduce the unnecessary detection space, improve the accuracy by directly detecting feature vectors, and reduce the time needed for detection and analysis. The core principle of getting fractional Fourier entropy is to extract features by Shannon entropy through fractional two-dimensional Fourier transform (2D - FRFT) spectrum. The value of α -angle obtained by the fractional Fourier transform (FRFT) [14, 15] of a specific function $z(t)$ is defined as φ_α , and its equation is as follows:

$$\varphi_\alpha(w) = \int_{-\infty}^{+\infty} K_\alpha(t, w)z(t)dt \tag{1}$$

In this formula, w refers to frequency, t represents time. The transformation kernel function K [16], where i was defined as Imaginary units which can be interpreted as:

$$K_\alpha(t, w) = (1 - icota)^{\frac{1}{2}} \times \exp(i\pi(w^2cota - 2wtcsca + t^2cota)) \tag{2}$$

2D - FRFT is transformed by FRFT, where 2D - FRFT contains two angles, a and b , and the angles are represented by $\varphi_{a,b}$. Meanwhile, Shannon entropy is used to extract the entropy of the 2D - FRFT as H , Suppose the probability mass function of a value set $\{c_1, c_2, \dots, c_j\}$ is $S(C)$, C is a discrete random variable belonging to the value set. $S(C)$ shows below:

$$H(C) = F[-\ln(S(C))] \tag{3}$$

The expected value is defined as F , then the following:

$$H(C) = \sum_{j=1}^n S(C_j) [-\ln(S(C_j))] \tag{4}$$

Hence, the FRFE formula of the Gum image represented by D is assumed to be:

$$D[-\ln(S(C_j))] = H[\varphi_{a,b}[-\ln(S(C_j))]] \tag{5}$$

2.2 Feedforward Neural Network

As one of the most widely used and rapidly developed artificial neural networks, feedforward neural network (FNN) has the advantages of good generalization ability and back-propagation learning. The FNN we adopted is attributed to its easy implementation of multidimensional data processing. The model with well-trained weights can avoid manual feature selection and manual image processing.

FNN is a network that does not consider the type of data entry, where the data can possibly have any special structures. FNN is a unidirectional multi-layer structure consists of three parts: an input layer, a flexible number of hidden layers, and a final

output layer. The main process shows in the bottom right in Fig. 1 is to reach the expected output target after the given input parameters are processed by hidden layer neurons.

The FNN has strong fitting ability. As for a hidden layer containing enough neurons, the multi-layer FNN can approach the continuous function of arbitrary complexity with arbitrary precision.

It is necessary to establish the overall structure of neural network before training weights and biases to make the best work of FNN. The use of an approximation theorem [17–19] can improve the fitting degree of FNN and make it closer to the high-performance model needed by the experiment [20]. The framework of FNN is influenced by the number of hidden layers and hidden states, and the optimal number of hidden layers and the number of neurons can improve the speed and efficiency of FNN by controlling and deleting some layers and nodes [21]. Finally, FNN is trained with various optimization algorithms including back-propagation [22] and particle swarm optimization [23] to obtain the best weights and biases.

However, it's a complex process to design FNN that requires designers to focus on the optimization of various design parameters. It requires a large number of data and tuning parameters, and it requires a better hardware configuration of the computer. These methods cannot get perfect results completely, because the over-fitting state may occur due to the ultra-high or ultra-low values in the operation process. At the same time, the problem of gradient disappearance may arise. Besides, the specific definition of the hidden layer also hard to find a breakthrough solution.

2.3 Standard Genetic Algorithm

Several algorithms have been used to detect gingivitis. According to the studies of predictive methods for periodontal disease by Papantonopoulos, et al. [24], the best predictive results were found to be artificial neural networks with an efficiency of 90–98%. Compared with the local optimal solution of the optimization problem and the solution result strongly depends on the initial value of the traditional optimization algorithm, the genetic algorithm can find the global optimal solution of the optimization problem and the optimization result is independent of the initial conditions. The advantage of the genetic algorithm lies in its powerful and fast random searching ability. A genetic algorithm starts with a group, retains potential possibilities, and compares multiple individuals at the same time. With randomness and extensibility, it can carry out probability iteration and is easy to be combined with other algorithms.

As the pioneer of presenting genetic algorithms, John Holland has brought this concept forward according to the natural evolution theory proposed by Charles Darwin and the idea of inherited traits [25]. Because it can imitate the natural evolution of the population to obtain improved adaptability through iteration, this algorithm is widely used in optimization problems [26].

The genetic algorithms process can be interpreted as: a group of selected random individuals is considered as initial samples, where the highly adaptive ones with the best genetic factors inherited from multiple generations are chosen, and those with extraneous conditions are eliminated through evaluation and calculation. Moreover, those with 'elite genes' will be screened and continuous crossover and mutation, and

inherit excellent genes. This iterative process continues until a given number of generations or reached termination conditions, which means the fitness function is minimized [27].

Although genetic algorithms can obtain the global optimal solution, it shows weakness in local searchability. In the iteration process, the parameters tend to converge prematurely, and the iteration results are easily affected by the parameters, resulting in the deterioration of the iteration quality.

2.4 10-Fold Cross Validation

Ten-fold cross-validation is a common method to test the accuracy of algorithms [28]. A 10-fold cross-validation scheme was used to prevent neural network over-fitting during training [29]. The implementation of the scheme is to randomly divide the data set into 10 folding subsets of equal size. After 10 times of iteration and learning, nine folds were used in turn to build the model, while the rest part was used for test data. The final observed value is obtained by averaging the results of the 10 iterations. The process of Ten-fold cross-validation is shown in Fig. 2. P represents the algorithm precision;

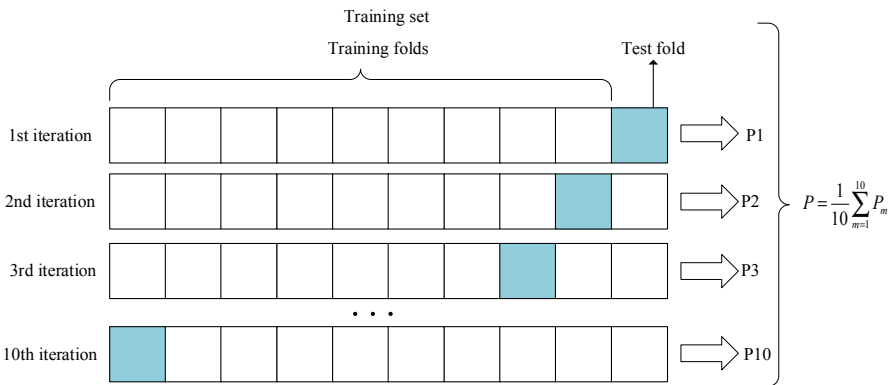


Fig. 2. Ten-fold cross validation

The repeatability of Ten-fold cross-validation is a vital factor for its reliability. The possibility of variation leads to single cross-validation that does not have the authoritative ability to get the best model. For robust model selection, it is necessary to summarize loss function based on the repeated Ten-fold cross-validation. However, there are some cases that shows even Ten-fold cross-validation is not substantive different from Five-fold cross-validation or Twenty-fold nested cross-validation.

3 Experiment Results and Discussions

3.1 Dataset

We obtained the dataset from five patients who suffered from gingivitis from Nanjing Stomatological hospital [3]. The two digital single lens reflex (DSLR) were leveraged to collect the teeth images from the patients randomly. Our dataset contains 180 teeth images in total, 90 of gingivitis and 90 of normal control. The field of view ranges from 51 mm to 200 mm and the voxel resolution ranges from 0.1 mm to 0.39 mm. In order to get a clear view of the teeth areas, the width and length of the samples were manually adjusted. The two samples of the two classes are presented below in Fig. 3.

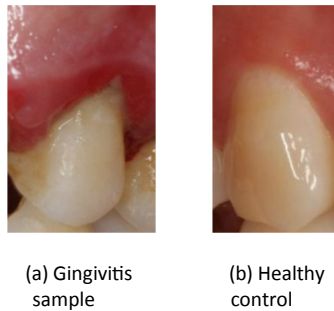


Fig. 3. Samples of our dataset

3.2 The Results of Fractional Fourier Entropy

Take Fig. 3(a) as example, the fractional Fourier transform (FRFT) results are shown in Fig. 4. illustrates 25 FRFT decompositions from an image of gingivitis. 25 different (a, b) combinations are adopted, and both a and b fall into the set of $\{0.1, 0.3, 0.5, 0.7, 0.9\}$. In the coordinates composed of (a,b), each point has a specific radian and Angle, forming the frequency domain of two-dimensional space. In the experiment, we chose 25 vector angles. For each dimension, the value varies from 0.1 to 0.9 with an increase of 0.2, therefore a dimension has five values. After the combination, we have a total of 25 vector angles, that are (0.1, 0.1) (0.1, 0.3),... (0.1, 0.9) (0.3, 0) (0.3, 0.3)... (0.3, 0.9)... (0.9, 0.1) (0.9, 0.2),... (0.9, 0.9). When the two angles are closed to zero, FRFT is an operator that contains no spectral information. If each Angle is increased by nearly one, FRFT tends to be downgraded to standard Fourier transform (FT).

We compute the entropy of the spectrum function. The fractional Fourier entropy (FRFE) of Fig. 4 is shown in Table 1 displayed the eigenvalue of FRFE. As we can see, the smaller the FRFE value, the clearer the image. FRFE is a very effective feature and 25 FRFE features can be used to distinguish between gingivitis and normal gums.

Through the inverse FRFT, the image is processed with contour enhancement and pseudo-color mixing to obtain a clearer image. In other words, the higher the frequency of the frequency domain, the higher the image resolution. The comparison of wavelet entropy, wavelet energy and fractional Fourier entropy with the data set was verified for

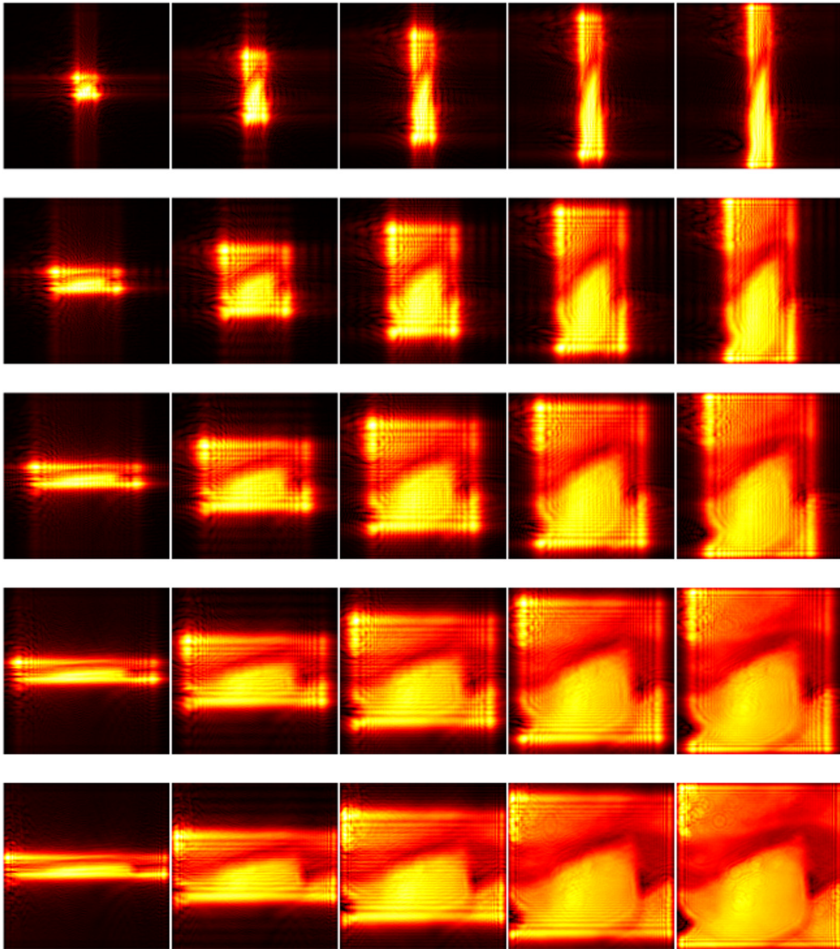


Fig. 4. Result of FRFT

Table 1. Entropy of FRFT results

| | | | | |
|--------|--------|--------|--------|--------|
| 7.2419 | 7.4880 | 7.7129 | 7.2583 | 5.9228 |
| 7.5116 | 7.6508 | 7.7715 | 7.2006 | 6.0655 |
| 7.6872 | 7.7672 | 7.6223 | 6.8215 | 6.0606 |
| 7.2089 | 7.1218 | 6.7780 | 6.2063 | 5.7013 |
| 5.7594 | 5.8675 | 5.9138 | 5.6230 | 5.2195 |

10 times by k-fold stratified cross validation [13] showed that the precision of fractional Fourier entropy was significantly better than the other two, which proved that FRFE had better performance. Therefore, FRFE is an effective feature and 25 FRFE features can be used to distinguish between gingivitis and normal gums.

3.3 The Results of Standard Genetic Algorithm

This part is a performance test obtained by 10 cross verifications of fractional Fourier entropy and standard genetic algorithm (FRFE - SGA) method. Five criteria of sensitivity, specificity, precision, accuracy and F1 score were compared in the validation set. The results of the proposed FRFE - SGA method is shown in Table 2, with the last row showing the mean and standard deviation values. The sensitivity, specificity, precision, accuracy, and F1 score of our method were $78.00 \pm 2.71\%$, 76.56 ± 3.00 , 76.97 ± 2.29 , 77.28 ± 1.90 , and 77.43 ± 1.92 .

Table 2. Result of proposed FRFE-SGA method

| Run | Sen | Spc | Prc | Acc | F1 |
|---------|------------------|------------------|------------------|------------------|------------------|
| 1 | 80.00 | 75.56 | 76.64 | 77.78 | 78.25 |
| 2 | 81.11 | 72.22 | 74.54 | 76.67 | 77.68 |
| 3 | 77.78 | 72.22 | 73.69 | 75.00 | 75.66 |
| 4 | 77.78 | 78.89 | 78.66 | 78.33 | 78.21 |
| 5 | 75.56 | 76.67 | 76.42 | 76.11 | 75.96 |
| 6 | 77.78 | 81.11 | 80.47 | 79.44 | 79.10 |
| 7 | 82.22 | 76.67 | 77.88 | 79.44 | 79.99 |
| 8 | 72.22 | 76.67 | 75.58 | 74.44 | 73.82 |
| 9 | 78.89 | 81.11 | 80.68 | 80.00 | 79.78 |
| 10 | 76.67 | 74.44 | 75.09 | 75.56 | 75.84 |
| Mean+SD | 78.00 ± 2.71 | 76.56 ± 3.00 | 76.97 ± 2.29 | 77.28 ± 1.90 | 77.43 ± 1.92 |

3.4 Comparison to State-of-the-Art Approaches

The proposed fractional Fourier entropy and standard genetic algorithm (FRFE - SGA) method is compared with the most advanced method, as shown in Table 3. The Sensitivity, Specificity and Accuracy of Naive Bayes classifier (NBC) [30] were 66%, 62% and 64%, respectively. The second method, using the classification method of Wavelet-energy (WE) [31], gained the values of 62% (sensitivity), 68% (specificity) and 65% (Accuracy). The third method, Grey-level cooccurrence matrix and Extreme learning machine (GLCM - ELM) [32], showed a Sensitivity of 72%, a Specificity of 70% and an Accuracy of 71%. The last method is Contrast-limited adaptive equalization, Gray-level cooccurrence matrix, and Extreme learning machine (CLAHE - GLCM - ELM) [3]. This method has the highest values of Sensitivity, Specificity, and Accuracy, 75%, 73%, and 74%, respectively. However, the values of Sensitivity, Specificity and Accuracy in our FRFE+SGA were $78.00 \pm 2.71\%$, $76.56 \pm 3.00\%$ and $77.28 \pm 1.90\%$, respectively. The results fully demonstrate the superiority of FRFE+SGA algorithm.

Table 3. Comparison with state-of-the-art algorithms

| Approach | Sen | SpC | Acc |
|--------------------|---------------|---------------|---------------|
| NBC [30] | 66% | 62% | 64% |
| WE [31] | 62% | 68% | 65% |
| GLCM-ELM [32] | 72% | 70% | 71% |
| CLAHE-GLCM-ELM [3] | 75% | 73% | 74% |
| FRFE-SGA (Ours) | 78.00 ± 2.71% | 76.56 ± 3.00% | 77.28 ± 1.90% |

4 Conclusions

In this paper, a new gingivitis detection method combining fractional Fourier entropy (FRFE) and standard genetic algorithm (SGA) is proposed. Different from previous methods, the image segmentation before classification only requires extraction of feature vectors and automatic processing of the algorithm, which can obtain better feature image quality than the current methods. The quality of the image affects the detection result of the classifier. The FRFE - SGA method is tested to have a better detection effect than the latest algorithm, which indicates that the FRFE - SGA method can effectively assist doctors in diagnosis and improve the diagnosis efficiency.

Our algorithm may be further applied to other pathological tests in future studies, and meanwhile, the overall algorithm can be improved and optimized in the subsequent experiments to reduce the overfitting problem and improve the detection accuracy. This research will help not only dentists but also other types of doctors get rid of the difficult task of diagnosis. In the future, deep learning [33–35] approaches will be tested to help enhance the gingivitis detection performance.

References

1. Oral Health (2020). <https://www.who.int/news-room/fact-sheets/detail/oral-health>
2. Pyo, J., Lee, J.H., Lee, M., Ock, M.: Quality of life and health for patients with chronic periodontitis: a qualitative study (2020)
3. Li, W., Chen, Y., Sun, W., Brown, M., Zhang, X., Wang, S., et al.: A gingivitis identification method based on contrast-limited adaptive histogram equalization, gray-level co-occurrence matrix, and extreme learning machine. *Int. J. Imaging Syst. Technol.* **29**, 77–82 (2019)
4. Thakur, A., Guleria, P., Bansal, N.: Symptom & risk factor based diagnosis of Gum diseases using neural network, pp. 101–104 (2016)
5. Sudheera, P., Sajja, V.R., Kumar, S.D., Rao, N.G.: Detection of dental plaque using enhanced K-means and silhouette methods, pp. 559–563 (2016)
6. Lee, J.H., Kim, D.H., Jeong, S.N., Choi, S.H.: Detection and diagnosis of dental caries using a deep learning-based convolutional. *J. Dent.* **77**, 106–111 (2018). <https://doi.org/10.1016/j.jdent.2018.07.015>
7. Aberin, S.T.A., de Goma, J.C.: Detecting periodontal disease using convolutional neural networks, pp. 1–6 (2018)
8. Zhu, G., Piao, Z., Kim, S.C.: Tooth detection and segmentation with mask R-CNN, pp. 070–072 (2020)

9. You, W., Hao, A., Li, S., Wang, Y., Xia, B.: Deep learning-based dental plaque detection on primary teeth: a comparison with clinical assessments. *BMC Oral Health* **20**, 1–7 (2020)
10. Rana, A., Yaune, G., Wong, L.C., Gupta, O., Muftu, A., Shah, P.: Automated segmentation of gingival diseases from oral images, pp. 144–147 (2017)
11. Hatvani, J., Horváth, A., Michetti, J., Basarab, A., Kouamé, D., Gyöngy, M.: Deep learning-based super-resolution applied to dental computed tomography. *IEEE Trans. Radiat. Plasma Med. Sci.* **3**(2), 120–128 (2019)
12. Hu, Z., Jiang, C., Sun, F., Zhang, Q., Ge, Y., Yang, Y., et al.: Artifact correction in low-dose dental CT imaging using wasserstein generative adversarial networks. *Med. Phys.* **46**, 1686–1696 (2019)
13. Wang, S., Zhang, Y., Yang, X., Sun, P., Dong, Z., Liu, A., et al.: Pathological brain detection by a novel image feature—fractional fourier entropy. *Entropy* **17**, 8278–8296 (2015)
14. Cattani, C., Rao, R.: Tea category identification using a novel fractional fourier entropy and jaya algorithm. *Entropy* **18**(3), 77 (2016)
15. Li, J.: Detection of left-sided and right-sided hearing loss via fractional fourier transform. *Entropy* **18**(5), 194 (2016)
16. Zhang, Y.D., Chen, S., Wang, S.H., Yang, J.F., Phillips, P.: Magnetic resonance brain image classification based on weighted-type fractional fourier transform and nonparallel support vector machine. *Int. J. Imaging Syst. Technol.* **25**, 317–327 (2015)
17. Jiang, X.: Fingerspelling identification for chinese sign language via AlexNet-based transfer learning and adam optimizer. *Sci. Program.* **2020**, 3291426 (2020)
18. Wang, S.H., Muhammad, K., Hong, J., Sangaiah, A.K., Zhang, Y.D.: Alcoholism identification via convolutional neural network based on parametric ReLU, dropout, and batch normalization. *Neural Comput. Appl.* **32**(3), 665–680 (2018). <https://doi.org/10.1007/s00521-018-3924-0>
19. Zhang, Y.D., Dong, Z., Chen, X., Jia, W., Du, S., Muhammad, K., Wang, S.H.: Image based fruit category classification by 13-layer deep convolutional neural network and data augmentation. *Multimedia Tools Appl.* **78**(3), 3613–3632 (2017). <https://doi.org/10.1007/s11042-017-5243-3>
20. Wang, S.H., Zhang, Y., Li, Y.J., Jia, W.J., Liu, F.Y., Yang, M.M., et al.: Single slice based detection for Alzheimer’s disease via wavelet entropy and multilayer perceptron trained by biogeography-based optimization. *Multimedia Tools Appl.* **77**(9), 10393–10417 (2018)
21. Ramchoun, H., Amine, M., Idrissi, J., Ghanou, Y., Ettaouil, M.: Multilayer perceptron: architecture optimization and training. *Int. J. Interact. Multimedia Artif. Intell.* **4**(1), 26–30 (2016)
22. Ahmad, M.T., Kumar, N., Singh, B.: Fast multilayer perceptron neural network-based control algorithm for shunt compensator in distribution systems. *IET Gener. Transm. Distrib.* **10**(15), 3824–3833 (2016)
23. Ji, G.: A comprehensive survey on particle swarm optimization algorithm and its applications. *Math. Prob. Eng.*, p. 931256 (2015)
24. Papantonopoulos, G., Takahashi, K., Bountis, T., Loos, B.G.: Artificial neural networks for the diagnosis of aggressive periodontitis trained by immunologic parameters. *PLoS ONE* **9**, e89757 (2014)
25. Wang, S., Lu, Z., Wei, L., Ji, G., Yang, J.: Fitness-scaling adaptive genetic algorithm with local search for solving the multiple depot vehicle routing problem. *Simulation* **92**, 601–616 (2015)
26. Galán, C.O., Lasheras, F.S., de Cos Juez, F.J., Sánchez, A.B.: Missing data imputation of questionnaires by means of genetic algorithms with different fitness functions. *J. Comput. Appl. Math.* **311**, 704–717 (2017)

27. Ji, G.: Genetic pattern search and its application to brain image classification. *Math. Prob. Eng.*, p. 580876 (2013)
28. Fushiki, T.: Estimation of prediction error by using K-fold cross-validation. *Stat. Comput.* **21**, 137–146 (2009)
29. Singh, G., Panda, R.: Daily sediment yield modeling with artificial neural network using 10-fold cross validation method: a small agricultural watershed, Kapgari, India. *Int. J. Earth Sci. Eng.* **4**(6), 443–450 (2011)
30. Zhou, X.: Detection of pathological brain in MRI scanning based on wavelet-entropy and naive bayes classifier. In: *International Conference on Bioinformatics and Biomedical Engineering (IWBBIO)*, Granada, Spain, pp. 201–209 (2015)
31. Yang, G., et al.: Automated classification of brain images using wavelet-energy and biogeography-based optimization. *Multimedia Tools Appl.* **75**(23), 15601–15617 (2015). <https://doi.org/10.1007/s11042-015-2649-7>
32. Brown, M.: Gingivitis identification via grey-level cooccurrence matrix and extreme learning machine. *Adv. Soc. Sci. Educ. Hum. Res.* **250**, 486–492 (2018)
33. Chen, Y.: Cerebral micro-bleeding identification based on a nine-layer convolutional neural network with stochastic pooling. *Concurrency Comput. Pract. Experience* **31**, e5130 (2020)
34. Wang, S.H., Sun, J., Phillips, P., Zhao, G., Zhang, Y.D.: Polarimetric synthetic aperture radar image segmentation by convolutional neural network using graphical processing units. *J. Real-Time Image Proc.* **15**(3), 631–642 (2017). <https://doi.org/10.1007/s11554-017-0717-0>
35. Huang, C.: Multiple sclerosis identification by 14-layer convolutional neural network with batch normalization, dropout, and stochastic pooling. *Front. Neurosci.* **12**, 818 (2018)



Logical Analysis and Enlightenment of Credit Management System Design in Electricity Market

Ye Hongdou^{1(✉)} and Chen Xiaoxiao²

¹ Zhejiang Marketing Service Center (Metrology Center), Hangzhou, China
icic1007@126.com

² State Grid Zhejiang Electric Power Research Institute (Data Center),
Hangzhou, China

Abstract. Credit management system is an important part of electricity market construction. Firstly, this paper expounds the necessity and basic requirements of credit management in electricity market. Then it comprehensively compares and analyses the credit management system of PJM, ERCOT and Guangdong electricity market. On the basis of the above research, the paper takes full account of the factors such as market risk management system, types of electricity transactions, market settlement cycle and so on. The key factors and the general rules to be followed in the design of electricity market credit system are analyzed for four aspects: credit limit requirements, calculation of unsecured credit limit, calculation of guaranteed credit limit and credit risk assessment. Finally, regarding to China's national conditions, the paper puts forward some opinions and suggestions on the construction of credit management system in China's electricity market for four parts: the construction of credit rating system, the establishment of risk coverage period and risk calculation index, the acquisition method of guarantee credit line and the object of credit management.

Keywords: Electricity market · Credit management · Credit limit · Credit risks · System design

1 Introduction

Credit management is a specialized technique for creditors to scientifically manage credit transactions to control credit risk [1]. As a special commodity, electricity cannot be stored in large quantities, and the production and consumption of electricity must be completed at the same time. Due to the special nature of power commodities, the delivery and settlement of power commodities are usually not synchronized, which is the main reason for the credit risk in the power market. The role of the power market credit management system is to assess the credit risk of market entities, and to avoid market credit risk through a series of management measures to reduce the possibility of bad debts in the market [2].

The United States is one of the countries with the largest credit economy, the most developed credit management industry, and the most complete social credit system in the world. The construction of the US regional power market credit management

system is based on the development of the US credit system for more than 200 years, and is closely related to the industry credit information system, credit service agencies, credit demand entities, credit supervision, and credit guarantee and support systems. In 1996, the US Federal Energy Regulatory Commission FERC issued Order 888, which requires the opening of transmission networks and encourages the establishment of power operators, marking the beginning of the market-oriented reform of the US power industry. After the promulgation of the regulations, the United States gradually established 10 regional power markets, all of which have established a relatively complete power market credit management system [3–11]. In all regional power markets, the marketization level of PJM and ERCOT is relatively mature, the risk management capabilities are relatively sound, and the power market credit management system implemented is the most typical.

Compared with the United States, the current domestic legal provisions are not yet complete, the credit management system is not yet perfect, and the credit evaluation of the power industry is still in the primary stage of development. In June 2015, the China Electricity Council issued four credit evaluation standards for the power industry, including the “Credit Evaluation Standards for Power Enterprises”, which was the first industry credit evaluation standard issued by China [12]. In March 2015, “Several Opinions on Further Deepening the Reform of the Electric Power System” of the Central Committee of the Communist Party of China (Zhongfa No. 9) was officially released, marking the official start of the power system reform, while clearly proposing the relevant requirements for establishing and improving the credit system of market entities. The pilot provinces of the electricity market have successively issued measures for credit management of the electricity market according to the actual situation: In January 2018, Yunnan Province issued the “Credit Evaluation Mechanism for Subject Transaction Behaviors of Yunnan Electricity Market (Trial)” [13], establishing a “three-tier five-tier system” credit evaluation system. In August 2018, Guangdong Province issued the “Guangdong Electricity Market Transaction Credit Management Measures (Trial)” and established a credit management system based on bank performance guarantees [14]. Compared with the United States, China’s credit management mechanism is relatively backward, mainly reflected in the fact that the credit assessment does not consider the financial status and assets of market entities. Meanwhile, The market risk assessment is relatively coarse-grained and the management objects are relatively limited.

This article first expounds the universality requirements of the credit management system of the electricity market, and then takes the US PJM electricity market, ERCOT electricity market and Guangdong electricity market as examples to analyze the credit management systems of the three electricity markets in detail. On this basis, for the key elements of the power market credit management system, including credit limit requirements, unsecured credit limit calculation, secured credit limit calculation, and credit risk assessment, we analyze the internal logic of the power market credit management system construction.

Based on the above analysis conclusions, combined with China’s national conditions and network conditions, China’s power market credit management system is recommended.

2 Basic Requirements for Credit Management in the Electricity Market

The unsynchronized delivery and settlement of power commodities is the main cause of credit risk in the power market. In the power market, the Central Counter Party (Central Counter Party) is generally introduced as the settlement subject. It is connected between the contract counterparties and becomes the “buyer’s seller” and “seller’s buyer”, as the only counterparties of all settlement participants [15]. After the central counterparty accesses the contractual relationship between the buyer and the seller, it assumes the credit risk of all settlement participants. In order to control the risks borne by the central counterparty, the basic requirements for credit management that market entities need to meet are:

$$R \leq L \tag{1}$$

In the formula, R is the credit risk of market entities, and L is the credit limit of market entities.

The credit risk of market entities refers to the unpaid debts of the market entities, the unsettled transaction amount and the default costs of market members. Credit risk is usually evaluated based on historical transaction data, and the corresponding historical transaction period referred to as the risk lookback period [16]. Taking PJM as an example, the long-term credit risk will be determined with reference to the historical 52-week transaction amount every April/October, and the risk retrospective period is 52 weeks. According to the risk management requirements, each market must clarify how long the future transaction costs need to be covered by credit risk, and the length of time covered is called the risk coverage period. Different markets have different risk coverage periods due to different trading varieties, different evaluation methods, and different management requirements.

The credit limit of a market entity refers to the credit transaction limit given by the market entity according to its business, management, and financial conditions. Most power market credit lines are divided into unsecured credit lines and secured credit lines. The former is given by market credit management agencies or settlement agencies, and the latter is obtained by market entities paying collateral or collateral. Different power markets count There are different types of mortgage guarantees for guarantee lines of credit. That is, the credit limit of the market entity can be expressed as:

$$L = L_c + L_{uc} \tag{2}$$

In the formula, L_c is the secured credit limit, and L_{uc} is the unsecured credit limit.

The unsecured credit limit L_{uc} usually takes the product of a certain type of asset of the market entity and a specific ratio, and the unsecured credit limit generally has a maximum amount requirement:

$$L_{uc} = kA \quad (3)$$

$$L_{uc} \leq L_{uc-cap} \quad (4)$$

In the formula, k is the asset ratio, which represents the percentage of certain types of assets of the market entity included in the unsecured credit limit; A is certain amounts of assets for market entities; L_{uc-cap} is the upper limit of the unsecured credit limit.

The asset ratio k is directly related to the credit score or credit rating of the market entity. The higher the credit score or credit rating, the higher the asset ratio k , and the higher the corresponding unsecured credit limit. A certain amounts of assets of market entity A usually refers to the tangible net assets of the market entity, and some markets use the total assets of the market entity minus the total debt. At the same time, each market also puts forward corresponding requirements on the unsecured credit limit upper limit L_{uc-cap} according to its degree of risk preference, market entity's operating status, financial status, etc.

3 Introduction to the Credit Management System of Major Power Markets in the US and China

3.1 PJM Power Market Credit Management System

3.1.1 Credit Line Management Requirements

PJM limits the amount of transactions by calculating the credit limit of each market entity. The calculation method of the credit limit is shown in formula (2). If the market settlement agency finds that the credit limit of the market entity has not met the requirements, it will require the collateral to be added within 2 working days, otherwise it will impose a fine on the defaulting entity; when the collateral cannot be added or the penalty is paid, the default allocation mechanism will be activated, And restrict the entity's trading behavior, the defaulting entity will not be able to quote and trade until the default is lifted [7, 8].

3.1.2 Unsecured Credit Limit Calculation

The calculation method of the unsecured credit limit of the PJM market entity is the same as formula (3). The asset ratio used to calculate the unsecured credit limit is as follows:

$$k_{PJM} = 2.5\% \times (SC - 40)/60 \quad (5)$$

In the formula, k_{PJM} is the asset ratio of the unsecured credit line of the PJM market entity, and SC is the credit score of the PJM market entity.

PJM uses a combination of external agency ratings and internal ratings to calculate the credit score of market entities. The rating of external institutions generally adopts Senior Unsecured Debt ratings for market entities. If the ratings of two external rating agencies are different, the average value is taken. Any market entity with a rating of BB+ or below cannot be unsecured.

3.1.3 Calculation of Guaranteed Credit Line

PJM market subject guarantee credit lines mainly include cash or letters of credit issued by financial institutions (external ratings of A or above). If the financial institution that issued the letter of credit has a rating other than A, another financial institution with a rating of A is required to guarantee the institution.

The long-term credit risk is based on the historical weekly transaction amount as the evaluation basis, and the maximum value of the sum of the actual transaction amount of the consecutive 1–3 weeks in the past six months is calculated:

$$E_{three-week-peak} = \max[P_N, \text{sum}(P_N, P_{N+1}), \text{sum}(P_N, P_{N+1}, P_{N+2})], N \in \text{last 24 weeks} \tag{6}$$

In the formula, $E_{three-week-peak}$ is the long-term credit risk of market entities, and P_N is the total trading volume of market entities in week N . This value is reset to $E_{three-week-peak}$ in the past 52 weeks every April/October. The total credit limit of market entities needs to be consistently higher than long-term credit requirements, namely:

$$L_{uc} + L_c \geq E_{three-week-peak} \tag{7}$$

The short-term credit risk mainly covers the amounts of unpaid bills, the amount that has not yet been settled in the settlement system, and the risk arising from the expected market behavior. PJM market entities need to ensure that the short-term credit risk does not exceed 75% of the total credit limit (also known as operating credit Limit).

$$0.75 \times (L_{uc} + L_c) \geq E_{short} \tag{8}$$

In the formula, E_{short} is short-term credit risk.

In addition, the financial transmission right (FTR) as a pure financial transaction has its additional risks, so PJM requires market participants participating in FTR transactions to pay additional collateral.

3.2 ERCOT Power Market Credit Management System

3.2.1 Credit Line Management Requirements

ERCOT requires that the sum of financial guarantees (composed of mortgage guarantee amount, remaining guarantee amount, etc.) of all market entities and unsecured credit amount needs to be greater than or equal to the total potential credit risk (Total Potential Exposure). The total potential risk TPE can be divided into two parts, TPES and TPEA, which reflect the credit risk of market participants participating in the blocking of income rights and the credit risk of participating in other trading varieties. ERCOT requires that the market subject’s TPES must be less than the mortgage guarantee amount, and the TPEA must be less than the sum of the unsecured credit limit and the remaining guarantee amount:

$$TPES \leq L_{sc} \text{ and } TPEA \leq L_{uc} + L_{rc} \quad (9)$$

In the formula, L_{sc} is the mortgage guarantee amount of the market entity. In the ERCOT power market, it specifically refers to the sum of the letter of credit, performance guarantee, and cash provided by the market entity; L_{rc} is the remaining guarantee amount of the market entity.

If the above conditions are not met, ERCOT can cancel the market subject's right to conduct transactions until the above conditions are met. During this period, market entities need to manage market transactions, reduce transaction risks, or increase credit lines by adding financial guarantees.

3.2.2 Unsecured Credit Limit Calculation

On the basis of meeting the upper limit of unsecured credit limit proposed by FERC, ERCOT divided the unsecured credit limit of market entities into four categories for discussion: The first category is unpublished power cooperatives or rural public utility services with a tangible net worth of less than US\$100 million (satisfying the relevant terms) distribution or electricity supply borrowers. The second category is municipal public utilities with unpublished ratings or tangible net assets of less than US\$100 million. The third category is publicly rated companies with tangible net assets greater than US\$100 million. The fourth category is companies with undisclosed ratings and tangible net assets greater than US\$100 million. ERCOT has discretionary power over the unsecured credit lines of market entities, and can propose market entities to provide necessary financial information to support calculations based on actual needs.

3.2.3 Calculation of Guaranteed Credit Line

ERCOT accepts market entities to provide financial guarantees in four ways: (1) Individuals who already have unsecured credit lines in the market can provide central counterparties with a guarantee of up to US\$50 million; (2) Unconditional, irrevocable letters of credit whose beneficiary is ERCOT, which limits the amount of letters of credit for different credit ratings of letters of credit; (3) The beneficiary is ERCOT's performance guarantee, which has credit requirements for the performance guarantee issuing company, and the maximum amount of each performance guarantee is USD 10 million; (4) Provide cash guarantee. The latter three methods are collectively called mortgage guarantees, corresponding to L_{sc} in Eq. (9).

3.2.4 Credit Risk Assessment

The total potential risk TPE is divided into TPEA and TPES. TPEA considers estimated debt according to the type of transaction, mainly including real-time market estimated debt, day-to-day market estimated debt, OTC bilateral transaction estimated debt, and also considered unsettled debt and unpaid items. TPES mainly considers the debt that may arise from blocking equity transactions. Congestion Revenue Rights (CRR) is a financial instrument. When the ERCOT transmission network is congested a few days ago or in the real-time market, it can avoid the congestion risk caused by the node's marginal electricity price by charging CRR holders or giving congestion compensation.

CRR is divided into two types: point-to-point liability and point-to-point option. TPES mainly considers the possible risk exposure of these two transactions.

3.3 Guangdong Electricity Market Credit Management System

3.3.1 Credit Limit Management Requirements

In Guangdong power market, the credit limit of the market subject is divided into trading credit limit and settlement credit limit. If the market subject participates in medium-term and long-term market transactions, the transaction credit amount shall be greater than or equal to the trading performance risk, and if the market entity participates in the settlement of the electricity market, the settlement credit amount shall be greater than or equal to the settlement performance risk:

$$L_{s,trade} \geq E_{trade} \text{ and } L_{s,settle} \geq E_{settle} \tag{10}$$

In the formula, $L_{s,trade}$ is the market performance guarantee, $L_{s,settle}$ is the settlement performance guarantee letter of the market entity, E_{trade} is the transaction performance risk of the market entity. E_{settle} is the settlement performance risk of market entities.

If the market entity's transaction credit occupancy limit is equal to or greater than 100%, its trading qualification in the medium and long-term market is suspended, and the typical curve contract of the medium-term and long-term electric energy market is forced to be processed; If the market entity's settlement market credit occupancy amount is equal to or greater than 100%, then the holding of medium-term and long-term contracts such as the year, month, and week of the delivery month, spot market transaction results, and related retail contract settlement qualifications will be suspended.

3.3.2 Calculation of Guaranteed Credit Limit

The Guangdong Electricity Market has not yet conducted an unsecured credit limit assessment of market entities. It mainly accepts the establishment of guarantee credit lines for market entities in the form of performance guarantees. Depending on the situation, cash guarantees can also be used on the premise of the market entity's willingness.

3.3.3 Credit Risk Assessment

Market performance risk is divided into transaction performance risk and settlement performance risk. The transaction performance risk mainly considers all the single-symbol holding contract transaction risk, and the settlement performance risk mainly considers the historical arrears of the market subject, the outstanding bill fee, the liquidated transaction fee and the unliquidated transaction fee.

4 Logical Analysis of the Credit Management System of Power Market

Credit management system is an important link in the power market, its design should be coordinated with the top design of the power market, combined with the actual situation of the market, fully consider the market risk management system, power trading varieties, market settlement cycle and other factors of the overall principle. To this end, this section will have an in-depth discussion on some key elements of the electricity market credit management system, including credit limit requirements, unsecured quota calculation, secured quota calculation, credit risk assessment, etc., and analyze the internal logic and the law of universality.

4.1 Basis for Formulating Credit Limit Requirements

The credit limit requirement is the most important rule in the credit management system, and is the criterion for judging whether the market subject can continue to participate in the transaction. The basic idea of setting the credit limit requirements in each power market is the same, that is, the credit limit of the market subject is sufficient to cover credit risk, reduce the settlement risk of the central counterparty in the market, and reduce the possible bad debts in the market. Based on the above research results, under the premise of observing the basic ideas, each market has different requirements for the refinement of the credit limit, mainly from two dimensions, namely the transaction cycle and the transaction type (Table 1).

Table 1. Comparisons of major electricity markets in the United States and China

| District | Credit limit requirements | Unsecured amount calculation | Guarantee dissonation calculation | Credit Risk Assessment |
|-----------|---------------------------------|---|-----------------------------------|---|
| PJM | Formula (2), (7) Formula (8) | External ratings combined with internal scoring | Letter of credit cash | Long-term credit risk, short-term credit risk, FTR trading risk |
| | | Rating scoring corresponds to asset ratio | | |
| ERCOT | Formula (2), (9) | Calculated by user | Letter of guarantee | Credit risk of blocking income rights transactions Credit risk of other trading products |
| | | Have discretion | Performance guarantee cash | |
| Guangdong | Formula (10) | / | Performance Guarantee Cash | Transaction performance risk Settlement performance risk |

From the perspective of transaction cycle, power market operating agencies generally put forward long-term credit limit requirements and short-term credit limit

requirements. The long-term and short-term referred to here are relative concepts: it can be a trading cycle that strictly corresponds to the market trading varieties. For example, the Guangdong market considers the transaction performance guarantee to cover the risk of medium-term and long-term contract transactions, and the settlement performance guarantee covers the medium-term and long-term, day-to-day, and real-time transactions risk; it can also be corresponding to the time of resetting the credit limit, such as PJM's long-term credit requirements are reset once a week, and short-term credit requirements are reset once every billing day. In terms of transaction types, most markets have additional credit requirements for pure financial transaction types. For example, PJM requires additional collateral for market entities participating in FTR transactions and ERCOT for market entities participating in CRR transactions.

In addition, the credit limit requirements of different power markets will be implemented in conjunction with corresponding credit limit warning, credit supplement management and other measures.

4.2 Selection of Calculation Methods for Unsecured Credit

The unsecured credit limit of market entities must be established on a sound social credit system, including the legal guarantee mechanism for information disclosure, the market-oriented operation mode of credit information services, the wide application of credit rating products, and the strong credit awareness of market entities. As can be seen from the comparison of the power markets in China and the United States, due to the current imperfect social credit system in China, it is impossible to assess the unsecured credit lines of market entities for the time being.

The calculation of unsecured credit lines depends on the credit ratings of market entities. Credit ratings can be provided by a third-party credit agency recognized by the settlement agency or through the internal credit rating method of the settlement agency. Most power market settlement agencies tend to encourage market members to carry out third-party credit agency ratings. ERCOT market settlement institutions accept the credit ratings of market entities in Standard and Poor's, Fitch and Moody, and use this as the basis for calculating unsecured credit lines; PJM's highest score for market participants participating in internal scoring is only 86.5 points, and the highest score for market participants participating in third-party credit agency ratings is 100 points, which also shows that market settlement agencies trust the third-party credit agencies more.

The policy tendency of the electricity market is also an influencing factor for unsecured credit lines. Taking ERCOT as an example, a higher asset ratio is provided to public institutions as the basis for calculating the unsecured credit limit. In addition, it is worth mentioning that the unsecured credit limit is essentially a leverage for market transactions. If the market transaction leverage is too high, it means that the overall market risk is increased. Therefore, most power markets make restrictions on the unsecured credit limit of market entities limit.

4.3 Selection of Calculation Method of Guaranteed Credit Line

In all power markets, cash is the basic way to provide guaranteed credit lines, and it is also the least efficient way to operate the market. It is reflected in two aspects: if only

cash is used as a guaranteed credit line, it will occupy a lot of resources for market risk prevention, not It is conducive to the effective operation of the market; at the same time, the way of using cash as the guarantee credit line ignores the difference between market entities, which is unfair to market entities with good reputation.

Based on the support of the social credit system, the electricity market has expanded the method of obtaining guaranteed credit lines, allowing market entities to provide letters of credit, performance guarantees, and guarantees as guarantee credit lines. On the one hand, this approach reduces the proportion of cash flow in the guaranteed credit line and improves the market’s operational efficiency; on the other hand, it transfers market risks to banks and insurance companies to improve the market’s ability to resist risks.

In some markets, out of control over market risks, there are credit rating regulations and guarantee limits for companies that provide letters of credit, performance guarantees, and guarantees.

4.4 Credit Risk Assessment Method

The credit risk assessment of the power market is based on historical transaction sourcing, assessing historical debt, outstanding debt, outstanding debt, the cost of default of market entities and potential future risks. Credit risk assessment focuses on the choice of risk coverage and risk backtracking. The risk coverage period is related to the market trading variety, trading cycle, settlement period and settlement process, while the risk retrospective period is mainly related to the requirements of market members.

The following is an example of the impact of the settlement process on credit risk assessment. Considering the pre-date trading varieties of a market, the settlement method is “day-clearing week closing”. Suppose that a week is defined as Sunday to Saturday, the bill is issued on Thursday of the week after the delivery of electricity and expires on Wednesday, two weeks after the delivery, and that the market entity is a power company, and that the user agent relationship needs to be transferred one week after the default is prohibited from trading in the market, the time series is as follow (Table 2):

Table 2. Time series table of market participants

| | Sunday | Monday | Tuesday | Wednesday | Thursday | Friday | Saturday |
|--------------|---------------------------------------|--------|---------|---------------------------|---------------------------|--------|------------------------------------|
| Week n-2 | 5.20 | 5.21 | 5.22 | 5.23 | 5.24 | 5.25 | 5.26 |
| | Unexpired debt amount (bill 6.6 due) | | | | | | |
| Week n-1 | 5.27 | 5.28 | 5.29 | 5.30 | 5.31 | 6.1 | 6.2 |
| | Unexpired debt amount (bill 6.13 due) | | | | | | |
| Current week | 6.3 | 6.4 | 6.5 | 6.6 | 6.7 | 6.8 | 6.9 |
| | Delivered but not settled | | | Future risk | | | |
| Week n | | | | Week n-2 bill expiry date | Week n-1bill Issuing date | | Week n Agent Relationship transfer |

If a market entity is banned from market transactions on June 6, according to the settlement process, the unpaid fees of the market entity cover three complete weeks, so when assessing credit risk, the risk coverage period is set to three weeks is relatively safe. When the settlement mechanism is “daily settlement and monthly settlement”, the risk coverage period should be set longer.

The risk assessment of market entities is relatively complex and requires comprehensive consideration. According to the requirements of market settlement agencies for credit risk management, different markets have different requirements for the risk coverage period and risk retrospective period.

5 Conclusion

Credit management system is an important part of the power market construction. This article expounds the basic requirements of power market credit management, and explains in detail the necessity of power market credit management, the basic requirements of credit management and related calculation methods. Taking the American PJM, ERCOT, and Guangdong power markets as examples, the credit management system is introduced and analyzed from four aspects: credit limit requirements, unsecured credit limit calculation, secured credit limit calculation, and credit risk assessment. On the basis of the above research, fully consider the factors including market risk management system, power trading varieties, market settlement cycle, etc., make an in-depth discussion and analysis of the top-level design of the power market credit management system, and finally put forward the China power market credit management system in light of China’s national conditions thinking about construction. It is hoped that the research results of this article can provide useful help for China’s future electricity market reform.

References

1. Liu, C.: Credit Management. Economy & Management. Publishing House (2010)
2. Chen, X.D., Tian, L., Gan, B.Y., Ji, T.Y.: Appraisal mechanism analysis on credit limit quantification of wholesale electricity markets in the United States. *Autom. Electr. Power Syst.* **42**(19), 98–105 (2018)
3. CAISO business practice manual for credit management & marketclearing, version [EB/OL], 18 April 2019. https://bpmcm.caiso.com/BPM%20Document%20Library/Credit%20Management%20and%20Market%20Clearing/Credit%20Management%20and%20Market%20Clearing%20V11_clean.doc
4. ERCOT nodal protocols: Section 16 registration and qualification of market participants [EB/OL], 18 April 2019. http://www.ercot.com/content/wcm/current_guides/53528/16-110117_Nodal.doc
5. NYISO market administration and control area service tariff: K-credit worthiness requirements for customers [EB/OL], 18 April 2019. http://www.nyiso.com/public/markets_operations/documents/tariffviewer/index.jsp
6. ISO New England financial assurance policy [EB/OL], 18 April 2019. https://www.iso-ne.com/static-assets/documents/2017/09/sect_i_ex_ia.pdf

7. PJM open access transmission tariff: Q-PJM credit policy [EB/OL], 18 April 2019. <http://www.pjm.com/directory/mergedtariffs/oatt.pdf> (2019)
8. PJM credit overview and supplement [EB/OL], 18 April 2019. <http://www.pjm.com/-/media/documents/agreements/pjmcredit-overview.ashx?la=en>
9. ORDER F.Credit reforms in organized wholesale electric markets [EB/OL], 18 April 2019. http://www.ercot.com/content/wcm/training_courses/109642/Credit_Management_August_2016.pdf
10. NYISO revisions to NYISO credit worthiness policies for credit scoring [EB/OL], 18 April 2019. http://www.nyiso.com/public/webdocs/markets_operations/committees/bic_spwg_cptf/meeting_materials/2009-04-20/042009_CPTF_Credit_Scoring_Enhancements_4152009_
11. NYISO accounting and billing manual [EB/OL], 18 April 2019. http://www.nyiso.com/public/webdocs/markets_operations/documents/Manuals_and_Guides/Manuals/Administrative/acctbillmnl.pdf
12. Power Industry Standards of the People's Republic of China: Power Enterprise Credit Evaluation Standards (DL/T1381-2014) [EB/OL], 18 April 2019. <http://www.csres.com/detail/252256.html>
13. Yunnan Electricity Market Subject Trading Behavior Credit Evaluation Mechanism (Trial) [EB/OL], 18 April 2019. http://www.sohu.com/a/193648097_99908709
14. Guangdong Electricity Market Transaction Credit Management Measures (Trial) [EB/OL], 18 April 2019. http://www.sohu.com/a/201486843_99908709
15. Liu, X.: The role of central counter-party mechanism in OTC derivatives trading regulation —based on huge loss event of JP Morgan chase. *Shanghai Finance* **383**(06), 49–52 (2012)
16. Liu, J., Zhang, J.N., Ji, W.X.: Experience comparison and enlightenment of the construction of credit system in international mature electricity market. *Price Theory Pract.* **2**, 71–74 (2018)
17. Zhou, M., Yan, Y., Ding, Q., Wu, S.Y.: Transaction and settlement mechanism for foreign countries and enlightenment and policy suggestions for China. *Autom. Electr. Power Syst.* **41**(618), 1–8 (2017)
18. Wang, Y.P., Liu, L., Zhu, M., Zhu, G.Y.: Research on credit rating model of players in Guizhou power trading market. *Power Demand Side Manage.* **115**(05), 52–55 (2018)

Author Index

- Ahmad, Iftikhar II-290
Al-Qershi, Osamah M. III-611
Al-Shebani, Qasim III-611
Altini, Nicola I-342, I-398
Amaro, Ernesto García III-98
Ayala de la Vega, Joel I-291
Ayala Niño, Daniel I-291
- Ban, Ming-Yang III-41
Bao, Wenzheng II-432, II-446
Barbiero, Pietro I-172
Bilal, Diyar Khalis III-121
Biswas, Arindam I-282
Bontempo, Gianpaolo II-32
Brunetti, Antonio I-342, I-398
Brunetti, Gioacchino I-342
- Cabrera, Josué Espejel III-98
Calderón Zavala, Guillermo I-291
Canales, Jair Cervantes III-98
Cantarini, Michela I-207
Cao, Ge I-367, III-87
Cao, Mei-Yuan II-316
Cao, Rui-Fen III-447
Cao, Yi II-432, II-446
Carnimeo, Leonarda I-342
Cascarano, Giacomo Donato I-342, I-398
Castilla, José Sergio Ruiz III-98
Cervantes Canales, Jair I-291
Chen, Bolin II-21, II-161
Chen, Guangyi I-231
Chen, Guanyuan I-17
Chen, Jian II-145
Chen, Shuo II-607
Chen, Wen-Sheng III-378
Chen, Xiangtao III-455
Chen, Yan-Ping I-311
Chen, Yiqiong II-290
Chen, Yuehui II-432, II-446
Chen, Yuhui II-103
Chen, Zhan-Heng II-239, II-279, II-348, III-542
Chen, Zhuang I-510
- Cheng, Huanhuan III-531
Cheng, Jia-Jun II-14
Cheng, Li II-270
Cheng, Xueying III-355, III-476
Chenhui, Zhou I-510
Chenmin, Zhang I-510, I-517
Chou, Hsin-Hung II-251
Cilia, Nicole Dalia I-53
Ciravegna, Gabriele I-172
Cirrincione, Giansalvo I-160, I-172, I-259, II-32
Cui, Yan II-3
- De Stefano, Claudio I-53
Ding, Cheng III-51
Ding, Li II-216
Dong, Chao-Qun III-467
Dong, Jun I-430
Dong, Minhui I-471, I-484
Du, Jixiang III-145
Du, Yuchuan I-183
- Fang, Hanfeng II-145
Fang, Sheng I-105
Fang, Yun I-81
Fei, Lou I-526
Feng, Cong III-624
Feng, Jie I-128
Feng, Jing III-280
Feng, Naiqin I-115
Feng, Xiao-Bei III-291
Ficarra, Elisa I-172, II-32
Fontanella, Francesco I-53
Franco, Leonardo III-258
Fu, Qiming II-103
Fukuda, Hisato III-28, III-110
- Gabrielli, Leonardo I-207
Gan, Xiaobing II-457
Gang, Sun I-565
Gao, Huacheng II-3
Gao, Kai Tai III-520
Gao, Li II-21

- Gao, Na II-145
 Gao, Yan I-17
 Gao, Ying-Lian II-537
 Gao, Yujia II-290
 García Lamont, Farid I-291
 Geng, Yu-Shui II-188, II-262
 Ghali, Fawaz III-484
 Gopalakrishnan, Chandrasekhar II-514
 Guan, Linting III-314
 Guang, Shen I-548, I-556
 Guerriero, Andrea I-342, I-398
 Gulan, Maja II-469
 Guo, Wenxiang III-237
 Guo, Zhen-Hao II-279, II-339, II-348, II-505, III-271
 Gupta, Phalguni I-282

 Ha, Cheolkeun III-224
 Han, Fei I-105
 Han, Pengyong II-514
 Hao, Chengqian I-430
 He, Keren I-17, II-399
 He, Ying I-484, II-67, II-79
 Higashita, Risa II-413
 Hongdou, Ye I-597
 Hongjie, Gu I-565
 Hou, Ling-Ying I-302
 Hsieh, Sun-Yuan II-251
 Hsu, Ching-Tien II-251
 Hu, Chao II-607
 Hu, Donghui I-413
 Hu, Lun II-524, II-621, III-271
 Hu, Pengwei II-524, II-621
 Hu, Peng-Wei III-367, III-400
 Hu, Yan II-413
 Huang, Chengcheng I-355
 Huang, De-Shuang II-339
 Huang, Han I-323
 Huang, Huajuan III-388, III-420
 Huang, Kaishan II-469, III-567
 Huang, Peizhi II-594, II-607
 Huang, Qian-Jing I-311
 Huang, Qinhua III-555
 Huang, Wenzhun II-326
 Huang, Yu III-624
 Huang, Yu-An II-316, II-326
 Huang, Zhi-An II-326
 Huang, Zhichao II-583
 Huang, Zhi-Kai I-302
 Hussain, Abir III-301, III-408, III-484

 Islam, Md Mafiqul III-28

 Ji, Bo-Ya II-227, III-271, III-400
 Ji, Junkai I-471, I-484
 Jianfeng, Xiong I-531
 Jiang, Bo III-498, III-520
 Jiang, Han-Jing III-271
 Jiang, Jing I-105
 Jiang, Tengsheng II-103
 Jiang, Wei II-384
 Jiang, Xue-Song II-262
 Jiang, Yonghong III-455
 Jimin, Zhang I-539
 Jin, Li-Ting III-291
 Jin, Luoxin III-579
 Jing, Xiaozhu II-384
 Jinwei, Chen I-531
 Jo, Kanghyun I-367
 Jo, Kang-Hyun III-133
 Jo, Kang-hyun III-87
 Joshi, Basanta III-3
 Juarez, Gustavo III-258

 Kadhim, Inas Jawad III-611
 Kang, Hee-Jun III-177, III-190, III-202
 Kang, Hee-Jung III-16
 Khan, Sohail Ahmed III-301
 Khan, Wasiq III-301, III-408
 Kleanthous, Natasa III-408
 Kobayashi, Yoshinori III-28, III-110
 Kong, Xiang-Zhen II-537
 Koole, Sander L. II-175
 Kuno, Yoshinori III-28, III-110

 Lam, Antony III-28, III-110
 Lamont, Farid García III-98
 Le, Phu-Nguyen III-16
 Lee, Hong-Hee III-213
 Leng, Qiangkui III-355, III-476
 Li, Ai-Min II-188
 Li, Bo II-14
 Li, Haiou II-103
 Li, Hao-Yuan II-227, II-270, III-367
 Li, Heng II-413
 Li, Huan-Yi I-311
 Li, Jinxin I-17, II-216, II-399
 Li, Junyi II-384
 Li, Lingjie II-549
 Li, Lingyue I-329

- Li, Li-Ping II-132, II-279, II-371, III-542
 Li, Pei-Fang III-280
 Li, Ruiyang II-121
 Li, Sanqian II-413
 Li, Shaochun II-524
 Li, Wen II-302
 Li, Xiangna III-476
 Li, Xiao II-481, II-493
 Li, Yuan II-571
 Li, Yuchen I-413
 Li, Zhengwei I-150, II-514
 Li, Zheng-Wei II-109, III-367
 Li, Zhipeng I-241
 Liang, Gaoyuan I-140, III-467
 Liang, Wan-Yun I-105
 Liang, Wen Long III-510
 Lin, Chongqing III-341
 Lin, Fan I-192
 Lin, Qiuzhen II-549, II-607
 Lin, Wenjun II-413
 Lin, Wu II-571
 Lin, Xiaoli II-361
 Linhu I-539
 Liu, Dian III-62
 Liu, Fang II-216
 Liu, Feilin III-314
 Liu, Hang Yu III-510
 Liu, Huan III-579
 Liu, Jiang II-413
 Liu, Jie III-247
 Liu, Jin-Xing I-81, II-537
 Liu, Juan III-280
 Liu, Peng II-413
 Liu, Si III-624
 Liu, Song II-188
 Liu, Tong III-291
 Liu, Xiao-yu I-458
 Liu, Xiyu III-237
 Liu, Yudong III-247
 Liu, Yunxia III-601, III-624
 Lovino, Marta I-172, II-32
 Lu, Haitao I-430
 Lu, Qin II-188
 Lu, Weizhong II-103
 Lu, Xinguo I-17, II-216, II-399, III-455
 Lu, Yonggang III-432
 Lu, Yu III-498, III-520
 Lu, Yuanyuan II-3
 Lui, Alison III-484
 Luo, Gong-Xu II-348
 Luo, Jiawei II-201
 Luo, Naili II-571, II-594
 Lv, Chengcong III-329
 Ma, Haiying I-445
 Ma, Lianbo I-28, I-41
 Ma, Lijia II-560, II-583
 Ma, Wenzheng II-446
 Ma, Yan I-458
 Ma, Yong-Li I-323
 Ma, Zhiyu II-290
 Mao, Fubing II-583
 Marino, Francescomaria I-342
 Mason, Alex III-408
 Mei, Jing II-524
 Mi, Jian-Xun I-128
 Miao, Fahui I-67
 Min, Xu II-524
 Ming, Zhong II-549
 Mo, Haoran I-140, III-467
 Ng, Kenney II-524
 Nguyen, Duy-Long III-213
 Nguyen, Elijah I-585
 Nguyen, Van-Cuong III-202
 Nicholas, Kasper III-161
 Nie, Ru I-150
 Ning, Yi-Ning I-302
 Niu, Ben III-567, III-579
 Otaño, Paula III-258
 Ouyang, Weimin III-555
 Pahareeya, Jankisharan III-484
 Pan, Binbin III-378
 Pan, Jie II-121, II-132
 Panday, Sanjeeb Prasad III-3
 Pandey, Rom Kant III-3
 Pang, Menghua III-601
 Pasero, Eros I-160, I-259
 Patiño, Daniel III-258
 Paviglianiti, Annunziata I-160
 Peng, Xiaoxiao III-145
 Premaratne, Prashan III-611
 Prencipe, Berardino I-342, I-398
 Principi, Emanuele I-207
 Pu, Wei Jian III-510
 Pucheta, Julián III-258

- Qi, Shun II-145
 Qi, Zhixin I-329
 Qiao, Chen II-145
 Qiao, Ying I-140
 Qin, Lei I-81
 Qin, Lijuan I-115
 Qin, Xiao I-183, I-241, I-355, I-378, I-387,
 II-67, II-79, II-90
 Qin, Yuping III-355, III-476
 Qingjuan, Wang I-526
 Qiu, Daowen III-341
 Qiu, Jin II-103
 Qiu, Ze-Yang III-291
 Qu, Qiang I-17
- Ramalingam, Rajasekaran II-514
 Ran, Shen I-531
 Randazzo, Vincenzo I-160, I-172, I-259
 Ren, Chenxia II-514
 Ren, Fei III-247
 Ren, Jiadong I-430
 Ren, Kai II-145
 Ren, Liang-Rui II-537
 Rivero, Cristian Rodriguez III-258
- Scardapane, Arnaldo I-342
 Sengupta, Debapriya I-282
 Serafini, Luca I-207
 Shakya, Aman III-3
 Shang, Li I-95
 Shang, Xuequn II-21, II-161
 Shen, Cong II-201
 Shen, Xiaolong I-28, I-41
 Shen, Zhen II-67, II-79
 Shi, Pengfei I-413
 Shining, Lv I-531
 Shrestha, Manish III-3
 Siviero, Mattia I-172
 Sneddon, Jenny III-408
 Song, Shuangbao I-471
 Song, Xiao-Yu III-291
 Song, Yuqing I-273
 Squartini, Stefano I-207
 Su, Xiao-Rui II-339, II-481
 Sun, Bin I-115
 Sun, Guorong I-445
 Sun, Hui III-593
 Sun, Jin II-432
 Sun, Lan I-3
- Sun, Tao II-188, II-262
 Sun, Yue III-291
 Sun, Yue-Lin III-74
- Taleb, Hamdan I-241
 Tan, Lijing III-579
 Tang, Cheng I-471, I-484
 Tang, Qing I-367, III-87
 Tang, Weidong III-388
 Tang, Zefang II-524
 Tao, Rui I-273
 Tian, Guang-yue I-458
 Tian, Lei II-57
 Tian, Tianhai II-45
 Tian, Wei-Dong III-41, III-51, III-62, III-74
 Tran, Huy Q. III-224
 Treur, Jan II-175, III-161
 Triggiani, Vito I-342
 Truong, Thanh Nguyen III-177, III-190
 Tu, Nguye Hoang II-201
 Tunc, Lutfi Taner III-121
- Uddin, Md Kamal III-110
 Ullah, Nimat II-175
 Unel, Mustafa III-121
- Vial, Peter James III-611
 Villani, Laura I-342
 Vo, Anh Tuan III-177, III-190
 Vohra, Rajan III-484
- Wan, Sizhe I-387
 Wang, Chao I-387
 Wang, Chuxin I-140
 Wang, Fei I-241
 Wang, Haiyu I-423
 Wang, Hanli I-183
 Wang, Hao-Ching II-251
 Wang, Hong III-531
 Wang, Huan I-302
 Wang, Jing III-447
 Wang, Jingwei I-28
 Wang, Jing-Yan I-140, III-467
 Wang, Juan I-81
 Wang, Lei I-150, II-109, II-227, II-239,
 II-371
 Wang, Ling III-498, III-510, III-520
 Wang, Mei-Neng II-371, III-542
 Wang, Nan-Xun III-74

- Wang, Shiqiang II-560
 Wang, Shui-Hua I-499
 Wang, Shu-Lin II-57, II-302
 Wang, Siguo II-67, II-79
 Wang, Teng II-161
 Wang, Wei II-201
 Wang, Xianfeng I-223
 Wang, Xiao-Feng I-311
 Wang, Xiaojuan II-621
 Wang, Xin-Gang II-188, II-262
 Wang, Xinyu II-216
 Wang, Yadong II-384
 Wang, Yan-Bin II-279, II-348
 Wang, Zhen I-223
 Wang, Zhibo III-467
 Wang, Zhonglie III-247
 Wei, Xiaohui III-455
 Wei, Xiuxi III-388, III-420
 Wei, Zhang I-526
 Weiwei, Pan I-548, I-556
 Wen, Chang-Gang I-81
 Wen, Lihua III-133
 Wong, Leon II-239, II-316, II-505, III-271
 Wu, Di I-183, I-378, I-387
 Wu, Hongjie I-183, I-241, I-378, I-387,
 II-67, II-79, II-90, II-103
 Wu, Junhua I-355
 Wu, Ronghui II-399
 Wu, Yan III-314
 Wu, Yong I-387
 Wu, Yubo III-455
 Wu, Zhi-Ze I-311

 Xi, Xian-Chang I-302
 Xi, Yue III-432
 Xian, Shi I-329
 Xiang, Huang I-548, I-556
 Xiang, Laisheng III-237
 Xiao, Baoyu II-457, III-567
 Xiaoxiao, Chen I-597
 Xiaoyu, Wang I-517
 Xie, Wenfang I-231
 Xie, Xue-Jun III-542
 Xingping, Liu I-510, I-517
 Xu, Caixia II-514
 Xu, Junlin II-302
 Xu, Minqi II-361

 Xu, Yan I-28
 Xue, Yuan II-3

 Yan, Rui III-247
 Yan, Xin II-109, II-371
 Yan, Yan I-585, II-45
 Yang, Bin II-423
 Yang, Hongwei I-378
 Yang, Hui I-576
 Yang, Jialiang II-302
 Yang, Long III-400
 Yang, Xinneng III-314
 Yang, Zhen-Yu II-262
 Yao, Li I-67
 Yi, Hai-Cheng II-279, II-339, II-348, II-481,
 II-505
 Yifan, Wang I-531
 Yong, Jiang I-539
 Yong, Yibo I-41
 You, Zhuhong II-121, II-524
 You, Zhu-Hong II-109, II-132, II-227,
 II-239, II-270, II-279, II-316, II-326,
 II-339, II-348, II-371, II-481, II-493,
 II-505, III-271, III-291, III-367, III-400,
 III-542
 Yu, Changqing II-121
 Yu, Chang-Qing II-132, II-326
 Yu, Haiping II-361
 Yu, Qiyuan II-594
 Yu, Xiang I-499
 Yuan, Changan I-183, I-241, I-355, I-378,
 I-387, II-67, II-79, II-90
 Yuan, Lin II-188, II-262
 Yuan, Yue II-216
 Yue, Zhenyu II-290
 Yuebo, Wu I-548, I-556
 Yun, He I-565

 Zeng, Qianwen III-378
 Zeng, Tao II-290
 Zhan, Xinke II-121
 Zhan, Xin-ke II-132
 Zhang, Aihua III-329
 Zhang, Bo III-447
 Zhang, ChengYong I-150
 Zhang, Churong III-567

- Zhang, Fa III-247
 Zhang, Hongbo III-145
 Zhang, Jian III-280
 Zhang, Jingkuan II-583
 Zhang, Kun I-183
 Zhang, Lijun I-183, I-241
 Zhang, Ping II-493, II-505
 Zhang, Qinhu II-67, II-79, II-90
 Zhang, Rui II-3
 Zhang, Shanwen I-223, II-326
 Zhang, Wei I-192, II-423
 Zhang, Xiao II-560
 Zhang, Xin I-499
 Zhang, Xinan II-45
 Zhang, Yindong II-90
 Zhang, Youhua II-290
 Zhang, Yuan II-524
 Zhang, Yu-Dong I-499
 Zhang, Zhiqiang III-329
 Zhang, Zhongqing II-384
 Zhao, Bo-Wei II-493, II-505
 Zhao, Hongguo III-601, III-624
 Zhao, Huan I-150
 Zhao, Jiajun I-471, I-484
 Zhao, Jing II-188, II-262
 Zhao, Junfeng I-28, I-41
 Zhao, Xiaojie I-67
 Zhao, Xingming I-183, I-241, I-378, I-387,
 II-67, II-79, II-90
 Zhao, Zhongqiu I-378, I-413
 Zhao, Zhong-Qiu III-41, III-51, III-62, III-74
 Zheng, Chunhou III-247
 Zheng, Chun-Hou II-3, II-537, III-447
 Zheng, Kai II-109, II-227, II-239, II-371
 Zheng, Shuli I-413
 Zheng, Yawen I-67
 Zhihan, Xie I-510
 Zhong, Shen II-594
 Zhong, Xing II-57
 Zhou, Ji-Ren II-270, II-481, II-493, III-367,
 III-400
 Zhou, Pan I-458
 Zhou, Tie Hua III-498, III-510, III-520
 Zhou, Xi II-270, II-316
 Zhou, Yan I-95
 Zhu, Lin III-291
 Zhu, Yu-hang I-458
 Zhu, Zhenghao II-399
 Zonneveld, Eric III-161
 Zou, Le I-311